University of Oxford

Department of Chemistry



Alkaline earth complexes supported by chelating diamido ligands

Matthew Haynes

The Queen's College

October 2024

This Thesis is submitted in partial fulfilment of the requirement for the degree of

Doctor of Philosophy at the University of Oxford

Preface

The work described in this Thesis was carried out in the Chemistry Research Laboratory at the University of Oxford between April 2021 and October 2024 under the supervision of Professor Dermot O'Hare and Doctor Zoë Turner, and in the Department of Chemistry and Pharmacology at the University of Erlangen-Nuremberg between September 2023 and November 2023 in collaboration with Professor Sjoerd Harder. All work was performed by the author unless otherwise stated, and no part has been previously submitted for another degree at this or any other university.

Part of the work contained in this Thesis has been published in the following journal paper:

A. O'Reilly, **M. D. Haynes**, Z. R. Turner, C. L. McMullin, S. Harder, D. O'Hare, J. R. Fulton and M. P. Coles, Chem. Commun., 2024, **60**, 7204–7207.

And presented at the following conferences:

44th International Conference on Coordination Chemistry **August 2022** – Rimini: *poster*;

Dalton 2023 **April 2023** – Warwick: *poster*;

Canadian Chemistry Conference and Exhibition **June 2023** – Vancouver: *poster*;

Dalton Young Members' Event **August 2023** – Birmingham: *oral*;

RSC Main Group Interest Group Meeting **April 2023** – Birmingham: *poster*.

Matthew Haynes

The Queen's College

October 2024

Abstract

Alkaline earth complexes supported by chelating diamido ligands

Matthew Haynes **D.Phil Thesis**

The Queen's College **October 2024**

The alkaline earth metals magnesium, calcium, strontium and barium have received increasing attention in recent years due to their high abundance, low cost and biocompatibility. Homogeneous alkaline earth complexes supported by dianionic ligands have generally received less attention than those supported by monoanionic ligands. Therefore, the aims of this Thesis were i) to prepare new alkaline earth complexes supported by chelating di(amido) ligands and ii) to assess the suitability of these complexes as precursors for the synthesis of reactive heterobimetallic s-block species.

The Thesis begins with an introduction of alkaline earth coordination chemistry. Alkaline earth-mediated redox-neutral reactivity is discussed, followed by a summary of recent advancements made in the field of low-valent alkaline earth chemistry. Relevant examples of systems employing both monoanionic and dianionic ligands are presented.

The attempted synthesis of monomeric alkaline earth complexes supported by 1,8-*bis*(silylamido)naphthalene ligands, ($[^{R_3}L]^{2-}$ = $[1,8\text{-}\{(R_3Si)N\}_2C_{10}H_6]^{2-}$) resulted in the isolation of two magnesium complexes. Conversely, the persistence of intermediate species and, in some cases, a competing thermal degradation reaction hindered the isolation of analogous complexes of the heavier alkaline earth elements. The exact composition of the reaction mixture was found to be dependant on the exact combination of metal, ligand substituents and temperature employed in each case, with these varying outcomes rationalised based on competing electronic and steric demands.

A THF-free synthetic route enabled the isolation and characterisation of a new family of dimeric calcium, strontium and barium complexes bearing phenyl-substituted 1,8-*bis*(silylamido)naphthalene ligands, which display two distinct dimerisation modes and form unstable monomeric adducts when dissolved in THF.

The alternative use of highly basic alkyl-substituted 1,8-*bis*(silylamido)naphthalene ligands resulted in the isolation of new bimetallic alkaline earth complexes displaying a diverse range of structural motifs, as well as a solvent-separated ion pair.

The more flexible di(amido)siloxane ligand ($[^{NON\text{-}Dipp}L]^{2-}$ = $[O(SiMe_2NDipp)_2]^{2-}$) enabled the isolation of another new family of dimeric THF-free alkaline earth complexes. These were compared with a series of THF adducts characterised in collaboration with Prof. Martyn Coles and co-workers. The attempted reduction of a dimeric di(amido)siloxane magnesium complex resulted in the characterisation of two dimeric heterobimetallic molecular magnesium hydroxide complexes featuring a rearranged ligand backbone that results from a 1,3-silyl retro-Brook rearrangement.

Acknowledgements

Firstly, I would like to thank Professor Dermot O'Hare for giving me the opportunity to study within his research group. I am particularly grateful for the flexibility I have been afforded during my time in Oxford, which has enabled me to pursue my own ideas and enjoy my time both in and out of the lab.

I am also especially thankful to Zoë. From detailed technical advice and help with challenging crystal structures to incredibly thorough proof-reading, every stage of my DPhil has been made easier by your support and encouragement. I am also extremely thankful to Louis for all his help in the lab, for supervising Alice while I was in Germany and for all his invaluable ideas and suggestions.

I am very grateful for all the technical support that I have received. Thank you to Coral for accommodating my many NMR requests, to Amber, Kirsten, Zoë, Aisling, Louis, Clem and Jens for all their help with single crystal X-ray diffraction, and to Peace and Phil for their support in the lab during a challenging COVID-dominated period. I am also grateful to everyone in the CTL for making the many Fridays spent demonstrating so rewarding, and to Saskia for the many outreach and teaching opportunities I was able to take part in.

I am also extremely fortunate to have spent three months working in Erlangen in the group of Professor Sjoerd Harder, to whom I am very thankful for the opportunity and for all the logistical support and Belgian beers he provided. I immensely enjoyed my time in Germany, during which I learned a huge amount in the lab while benefiting from the invaluable experience of living abroad. In particular, I would like to thank Michi, Stefan,

Dawid, Ollie, Marcel, Tim and Jens for being so welcoming and providing the support that enabled my short stay to be so productive, rewarding and memorable. Thanks also to the OxICFM CDT, The Queen's College and the RSC for funding both this placement and my attendance at multiple conferences, which greatly enhanced my D.Phil experience and development as a researcher. I am also grateful to Prof. Martyn Coles, Prof. J. Robin Fulton and Ms. Andrea O'Reilly for their willingness to share results and work together as part of a productive and rewarding collaboration.

I have been lucky to have shared my time in Oxford with such fantastic colleagues. Thank you to everyone in the O'Hare group, which has been great to be part of both in the CRL and at the pub. A big thank you to Rebecca for all her patient support in the lab and for showing that there is a light at the end of the alkaline earth tunnel (as well as for not killing me after Taylor Swift came out at The 1975). Gabi, I hope our hard-earned friendship outlasts the atmosphere in the S2 glovebox. Alex, our shared Glastonbury obsession made the long final months in S3 much more enjoyable. Thanks to Aisling for all the chaos and for not burning down the flat, and to Justin, Katie and Sam for all the help and procrastination along the way. Alice, I couldn't have had a better Part II student. Thanks also to the Langton and Faulkner groups, especially Xiangyu, Elba, Shaun, Charlotte and Jonny for the many enjoyable lunch breaks. I am also very fortunate to have been part of the 2020 OxICFM cohort, with a turbulent start to Oxford life during lockdown made much more enjoyable by our two-hour lunch breaks, Geoguessr interludes and the support of the administration team.

To my friends: thanks to Youssef and Dana for brightening up the dark nights at Venneit Close, to Joe and Liam for the many joyous hours spent in the Lamb and Flag since the wonderful day it reopened, and to Chloe, Helen, Maya, Leo, Theo, Ella, Dan, Molly,

Alex, Ben, Khalil, Zsofia, Vlad, Annabelle, Izzy, Fergal, Lou, Sophie, Nic and Diana for the many enjoyable weekends and trips that have kept me sane. Thanks also to Helen, Freyja and the cats for being so welcoming and to Chris for all the free beer.

I can't thank my family enough for all their love and support. Thanks to my Mum and Dad for putting up with me yet again both during lockdown and while I wrote up, it says a lot that I still love being at home even after surviving both periods here! Thanks to Dan for providing an endless source of football-related topics to bicker over and for the increasingly excellent pizzas and music recommendations, I commend your brave decision to pursue a PhD even after watching me finish mine.

Finally, to Charlie. We did it! I would say thank you but that does not begin to describe the gratitude I feel for all the love, support and good times you have provided since I was lucky enough to meet you in the CDT office in the middle of a pandemic. I simply could not have done it without you. You have made me a better person, a better chemist and definitely a better cook. I am so unbelievably proud of everything you have achieved, and can't wait for what's next. It seems strange that in amongst the thousands of words in this thesis I only get to spend a paragraph on you, but I guess the only words that really matter are that I love you.

Nomenclature

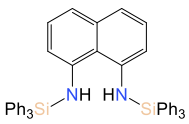
Below is a summary of some of the commonly used terms throughout the Thesis.

Term	Definition
$\{^1H\}$	Proton decoupled
Å	Ångström, 10^{-10} m
Ar	Aryl
br	Broad
BDI	β-diketiminato
BDE	Homolytic bond dissociation energy
^{n}Bu	*n*-butyl, C_4H_9
CAAC	Cylic alkylaminocarbene
COSY	2D correlation spectroscopy
χ	Pauling electronegativity
d	Doublet
d	Deuterated
δ	Chemical shift
DFT	Density Functional Theory
Dipp	2,6-Di*iso*propylphenyl
DiPeP	2,6-Di*iso*pentylphenyl
eq.	Equivalents
Et	Ethyl
Et_2O	Ether

FTIR	Fourier transform infrared
hept	heptet
HMBC	Heteronuclear multiple bond correlation
HN"	Hexamethyldisilazane, $HN(SiMe_3)_2$
HSQC	Heteronuclear single quantum coherence
Hz	Hertz, s^{-1}
^{i}Pr	*Iso*propyl, $CHMe_2$
J	Coupling constant
IE	Ionisation Energy
IR	Infrared
L	Ligand
$[L]^-$	Monoanionic ligand
$[L]^{2-}$	Dianionic ligand
m	Multiplet
Me	Methyl
μ	Bridging
N"	Hexamethydisilazide, $[N(SiMe_3)_2]^-$
NMR	Nuclear magnetic resonance
NOESY	Nuclear Overhauser Effect Spectroscopy
$^{NON\text{-}Dipp}LH_2$	$O(SiMe_2NHDipp)_2$
$[^{NON\text{-}Dipp}L]^{2-}$	$[O(SiMe_2NDipp)_2]^{2-}$
Ph	Phenyl, C_6H_5
ppm	Parts per million
q	Quartet

r	Radius
ρ	Charge density
ROP	Ring-opening polymerisation
$^{R_3}LH_2$	1,8-*bis*(silylamino)naphthalene, 1,8-{$(R_3Si)NH\}_2C_{10}H_6$
$[^{R_3}L]^{2-}$	1,8-*bis*(silylamido)naphthalene, $[1,8\text{-}\{(R_3Si)N\}_2C_{10}H_6]^{2-}$
$[^{R_3}LH]^-$	$[1\text{-}\{(R_3Si)N\}\text{-}8\text{-}\{(R_3Si)NH\}\text{-}C_{10}H_6]^-$
$[^{R_3\text{-}\mu\text{-}R_2}L]^-$	$[8\text{-}\{(R_3Si)N\}\text{-}1\text{-}N\text{-}(N,N'\text{-}SiR_2)\text{-}C_{10}H_6]^-$
s	Singlet
SSIP	Solvent-separated ion pair
t	Triplet
^{t}Bu	*Tert*-butyl, CMe_3
TCHP	2,4,6-Tricyclohexylphenyl
Θ	Oxophilicity
THF	Tetrahydrofuran, C_4H_8O
$(THF)_n$	An unknown number of equivalents of coordinated THF
THP	Tetrahydropyran
Trip	Tri*iso*propylphenyl
VT	Variable temperature
WCA	Weakly-coordinating anion
XRD	X-ray diffraction

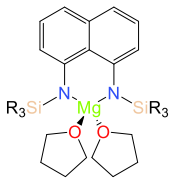
Compounds described in this Thesis



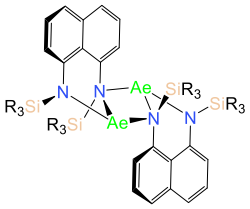
(**1**)



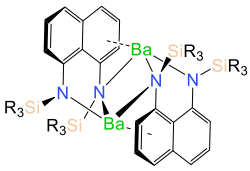
R = H (**2**)
R = $SiMe_2H$ (**3**)



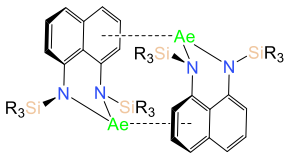
R_3 = Me_3 (**4**)
R_3 = $Me_2{}^tBu$ (**5**)



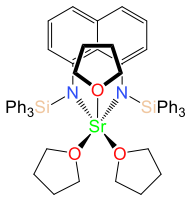
R_3 = Ph_2Me, Ae = Ca (**6**)
R_3 = Ph_2Me, Ae = Sr (**7**)
R_3 = Ph_3, Ae = Ca (**9**)



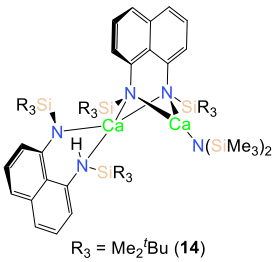
R_3 = Ph_2Me (**8**)



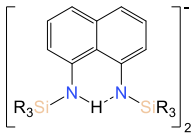
R_3 = Ph_3, Ae = Sr (**10**)
R_3 = Ph_3, Ae = Ba (**11**)
R_3 = $Me_2{}^tBu$, Ae = Ca (**13**)



(**12**)

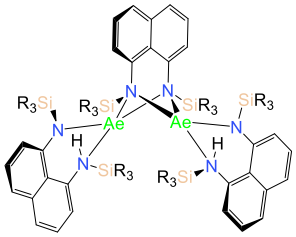


R_3 = $Me_2{}^tBu$ (**14**)

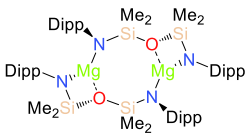


$[Ca(THF)_6]^{2+}$

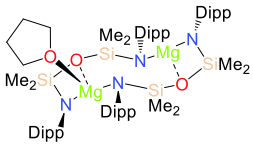
R_3 = $Me_2{}^tBu$ (**15**)



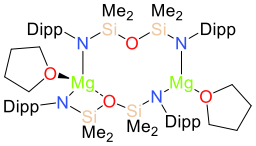
R_3 = $Me_2{}^tBu$, Ae = Sr (**16**)
R_3 = $Me_2{}^tBu$, Ae = Ba (**17**)



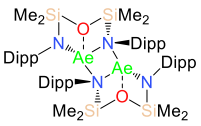
(**18**)



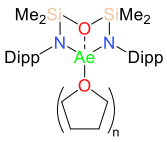
(**18·THF**)



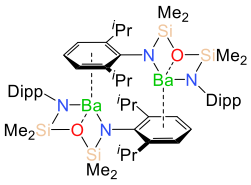
(**18·THF_2**)



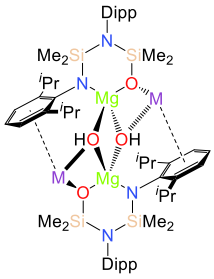
Ae = Ca (**19**)
Ae = Sr (**20**)
Ae = Ba (**21**)



n = 2, Ae = Ca (**19·THF_2**)
n = 3, Ae = Sr (**20·THF_3**)
n = 3, Ae = Ba (**21·THF_3**)



(**21a**)



M = Na (**22**)
M = K (**23**)

Compound nomenclature

Number	Name	Number	Name
1	$^{Ph_3}LH_2$	**18**	$[(^{NON\text{-}Dipp}L)Mg]_2$
2	$^{\mu\text{-}Me_2}LH_2$	**18·THF**	$[\{(^{NON\text{-}Dipp}L)Mg\}_2(THF)]$
3	$^{Me_2H\text{-}\mu\text{-}Me_2}LH$	**18·THF$_2$**	$[(^{NON\text{-}Dipp}L)Mg(THF)]_2$
4	$[(^{Me_3}L)Mg(THF)_2]$	**19**	$[(^{NON\text{-}Dipp}L)Ca]_2$
5	$[(^{Me_2tBu}L)Mg(THF)_2]$	**19·THF$_2$**	$[(^{NON\text{-}Dipp}L)Ca(THF)_2]$
6	$[(^{Ph_2Me}L)Ca]_2$	**20**	$[(^{NON\text{-}Dipp}L)Sr]_2$
7	$[(^{Ph_2Me}L)Sr]_2$	**20·THF$_3$**	$[(^{NON\text{-}Dipp}L)Sr(THF)_3]$
8	$[(^{Ph_2Me}L)Ba]_2$	**21/21a**	$[(^{NON\text{-}Dipp}L)Ba]_2$
9	$[(^{Ph_3}L)Ca]_2$	**21·THF$_3$**	$[(^{NON\text{-}Dipp}L)Ba(THF)_3]$
10	$[(^{Ph_3}L)Sr]_2$	**22**	$[(^{NNO\text{-}Dipp}L)Mg(\mu\text{-}OH)Na]_2$
11	$[(^{Ph_3}L)Ba]_2$	**23**	$[(^{NNO\text{-}Dipp}L)Mg(\mu\text{-}OH)K]_2$
12	$[(^{Ph_3}L)Sr(THF)_3]$		
13	$[(^{Me_2tBu}L)Ca]_2$		
14	$[(^{Me_2tBu}LH)Ca(\mu\text{-}^{Me_2tBu}L)CaN'']_2$		
15	$[^{Me_2tBu}LH]_2[Ca(THF)_6]$		
16	$[\{(^{Me_2tBu}LH)Sr\}_2(\mu\text{-}^{Me_2tBu}L)]$		
17	$[\{(^{Me_2tBu}LH)Ba\}_2\ (\mu\text{-}^{Me_2tBu}L)]$		

Table of Contents

Chapter 1 - Introduction **1**

1.1 Main group elements for sustainable chemistry **1**

1.2 Alkaline earth chemistry **2**

1.2.1 Coordination chemistry of the divalent alkaline earth cations 2

1.2.1.1 Metal-ligand bonding 3

1.2.1.2 Stability and the Schlenk equilibrium 4

1.2.2 Redox-neutral reactivity 6

1.2.2.1 Polarised insertion 6

1.2.2.2 Sigma-bond metathesis 7

1.2.3 Alkaline earth-mediated catalysis 8

1.3 Alkaline earth complexes supported by monoanionic ligands **8**

1.3.1 Synthesis 9

1.3.2 Beta-diketiminate ligands 10

1.3.3 Heteroleptic complexes 11

1.3.3.1 Synthesis 11

1.3.3.2 Reactivity 13

1.3.4 Low-valent alkaline earth compounds 17

1.3.4.1 Synthesis of low-valent beryllium and magnesium complexes 17

1.3.4.2 Reactivity 20

1.3.5 Low-valent chemistry of the heavier alkaline earth elements 22

1.4 Alkaline earth complexes supported by chelating dianionic ligands **23**

1.4.1 Synthesis 24

1.4.2 Redox non-innocent dianionic ligands 24

1.4.3 Deprotonated dianionic ligands 25

1.5 Heterobimetallic alkaline earth complexes supported by dianionic ligands **26**

1.5.1 Diamido alkaline earth complexes as precursors for heterobimetallic species 27

1.5.1.1 Inspiration from low-valent aluminium chemistry 27

1.5.1.2 Additional diamido alkaline earth precursors 29

1.5.2 Heterobimetallic alkaline earth complexes supported by redox non-innocent α-diimine ligands 31
1.5.3 Heterobimetallic alkaline earth complexes supported by chelating *bis*(silylamido) ligands 31
1.5.4 Heterobimetallic alkaline earth complexes supported by chelating NON-xanthene ligands 34
1.6 Scope of thesis 38
1.7 References 39

Chapter 2 – Synthesis and characterisation of monomeric 1,8-*bis*(silylamido)naphthalene alkaline earth complexes 49
2.1 Introduction 49
2.1.1 Overview 49
2.1.2 Previously reported 1,8-*bis*(silylamido)naphthalene metal complexes 50
2.2 Proligand synthesis and characterisation 52
2.2.1 Succesful proligand synthesis 52
2.2.1.1 NMR spectroscopic analysis 53
2.2.1.2 X-ray crystallographic analysis 55
2.2.2 Attempted synthesis of $^{Me_2H}LH_2$ 56
2.2.2.1 NMR spectroscopic analysis 57
2.2.2.2 X-ray crystallographic analysis of $^{Me_2H\text{-}\mu\text{-}Me_2}LH$ (**3**) 59
2.2.2.3 Proposed mechanism 59
2.3 Synthesis and characterisation of 1,8-*bis*(silylamido)naphthalene magnesium complexes 61
2.3.1 Synthesis of monomeric magnesium complexes 61
2.3.2 *In situ* NMR spectroscopic analysis 62
2.3.3 NMR spectroscopic analysis of $[(^{R_3}L)Mg(THF)_2]$ (R_3 = Me_3 (**4**) and $Me_2{}^tBu$ (**5**)) 63
2.3.4 X-ray crystallographic analysis of $[(^{R_3}L)Mg(THF)_2]$ (R_3 = Me_3 (**4**) and $Me_2{}^tBu$ (**5**)) 64
2.4 Reactivity of $^{R_3}LH_2$ with $[(THF)_2AeN"_2]$ in THF 67
2.4.1 *In situ* NMR spectroscopic analysis 68
2.4.1.1 $[(^{R_3}LH)AeN"]$ 68
2.4.1.2 $[(^{R_3}L)Ae(THF)_n]$ 71
2.4.1.3 $[(^{R_3\text{-}\mu\text{-}R_2}L)AeN"(THF)_n]$ 74
2.4.1.4 Metal steric effects 78

2.4.1.5 Ligand steric effects 81
2.4.1.6 Metal electronic effects 82
2.4.1.7 Ligand electronic effects 83
2.4.2 Deuterium labelling experiments 85
2.4.2.1 Proligand deuteration 85
2.4.2.2 Mechanistic studies 86
2.4.3 Investigation of Schlenk equilibria 88
2.4.3.1 Solution-state structure of [(^{R3}LH)AeN"(THF)$_n$] 88
2.4.3.2 Solution-state structure of [($^{R3\text{-}\mu\text{-}R2}$L)AeN"(THF)$_n$] 92
2.5 Conclusions 94
2.6 References 96

Chapter 3 – Synthesis and characterisation of phenyl-substituted 1,8-*bis*(silylamido)naphthalene alkaline earth complexes 98
3.1 Introduction 98
3.1.1 Overview 98
3.1.2 Dimeric complexes supported by 1,8-*bis*(silylamido)naphthalene and related ligands 98
3.2 Synthesis of dimeric THF-free alkaline earth complexes 100
3.3 X-ray crystallographic analysis of nitrogen-bridged dimers 101
3.3.1 Crystal structure of [(^{Ph3}L)Ca]$_2$ (**9**) 102
3.3.2 Crystal structures of [(^{Ph2Me}L)Ae]$_2$, (Ae = Ca (**6**), Sr (**7**) and Ba (**8**)) 105
3.3.2.1 Crystal structures of [(^{Ph2Me}L)Ca]$_2$ (**6**) and [(^{Ph2Me}L)Sr]$_2$ (**7**) 105
3.3.2.2 Crystal structure of [(^{Ph2Me}L)Ba]$_2$ (**8**) 106
3.4 X-ray crystallographic analysis of naphthalene-bridged dimers 110
3.4.1 Crystal structure of [(^{Ph3}L)Sr]$_2$ (**10**) 110
3.4.2 Crystal structure of [(^{Ph3}L)Ba]$_2$ (**11**) 114
3.5 X-ray crystallographic analysis of monomeric THF adducts 116
3.5.1 Crystal structure of [(^{Ph3}L)Sr(THF)$_3$] (**12**) 116
3.5.2 Comparison between X-ray crystallographic data and *in situ* NMR spectra recorded in THF-d_8 119
3.6 *In situ* NMR spectroscopic analysis 121
3.6.1 *In situ* NMR spectroscopic analysis of [(^{Ph3}L)Ca$_2$N"$_2$] 123
3.6.2 *In situ* NMR spectroscopic analysis of [(^{Ph3}L)Ca]$_2$ (**9**) 125

3.7 NMR spectroscopic analysis of 6–11 in THF-d_8 126
3.7.1 Comparative ^{29}Si NMR spectroscopic analysis 128
3.7.2 Degradation of **6**–**11** in THF 130
3.8 Conclusions 133
3.9 References 134

Chapter 4 – Synthesis and characterisation of alkyl-substituted 1,8-*bis*(silylamido)naphthalene alklaine earth complexes 136
4.1 Introduction 136
4.1.1 Overview 136
4.1.2 Weakly-coordinating anions and solvent-separated ion pairs 137
4.2 Synthesis of alkyl-substituted alkaline earth complexes 139
4.3 Characterisation of calcium compounds 141
4.3.1 X-ray crystal structure of [(^{Me_2tBu}L)Ca]$_2$ (**13**) 141
4.3.2 X-ray crystal structure of [(^{Me_2tBu}LH)Ca(μ-^{Me_2tBu}L)CaN''] (**14**) 145
4.3.2.1 Comparison with *in situ* NMR spectroscopic data 150
4.3.3 IR spectroscopic analysis 151
4.3.4 *In situ* NMR spectroscopic analysis 151
4.3.5 NMR spectroscopic analysis in THF-d_8 155
4.3.5.1 NMR spectroscopic analysis of [(^{Me_2tBu}L)Ca]$_2$ (**13**) 155
4.3.5.2 NMR spectroscopic analysis of [(^{Me_2tBu}LH)Ca(μ-^{Me_2tBu}L)CaN''] (**14**) 156
4.3.6 X-ray crystallographic analysis of [^{Me_2tBu}LH]$_2$[Ca(THF)$_6$] (**15**) 159
4.3.6.1 Comparison with previously reported WCAs and SSIPs 166
4.3.6.2 Factors influencing the formation of a SSIP 167
4.3.6.3 Outlook 168
4.4 Characterisation of strontium and barium complexes 169
4.4.1 X-ray crystallographic analysis 169
4.4.1.1 Crystal structure of [{(^{Me_2tBu}LH)Sr}$_2$(μ-^{Me_2tBu}L)] (**16**) 170
4.4.1.2 Crystal structure of [{(^{Me_2tBu}LH)Ba}$_2$(μ-^{Me_2tBu}L)] (**17**) 174
4.4.2 Discussion of "triple-decker" formation 175
4.4.3 IR spectroscopic analysis 177
4.4.4 *In situ* NMR spectroscopic analysis 177
4.4.5 NMR spectroscopic analysis in THF-d_8 180

4.4.6 Comparative ^{1}H NMR spectroscopic analysis 183
4.4.6.1 [(^{Me_2tBu}LH)CaN"(THF)$_n$] and [(^{Me_2tBu}LH)$_2$Ae(THF)$_n$] (Ae = Sr and Ba) 183
4.4.6.2 [(^{Me_2tBu}L)Ae(THF)$_n$] 184
4.4.7 Comparative ^{29}Si NMR spectroscopic analysis 185
4.5 Conclusions 189
4.6 References 190

Chapter 5 – Synthesis, characterisation and reactivity of di(amido)siloxane alkaline earth complexes 192
5.1 Introduction 192
5.1.1 Overview 192
5.1.2 Di(amido)siloxane ligands 192
5.2 Proligand synthesis 195
5.3 Synthesis of di(amido)siloxane magnesium complexes 196
5.3.1 X-ray crystallographic analysis 198
5.3.1.1 X-ray crystal structure of [($^{NON\text{-}Dipp}$L)Mg]$_2$ (**18**) 198
5.3.1.2 X-ray crystal structures of [{($^{NON\text{-}Dipp}$L)Mg}$_2$(THF)] (**18·THF**) and [($^{NON\text{-}Dipp}$L)Mg(THF)]$_2$ (**18·THF$_2$**) 200
5.3.2 NMR spectroscopic analysis 204
5.4 Synthesis of calcium, strontium and barium complexes 206
5.4.1 X-ray crystallographic analysis 207
5.4.1.1 X-ray crystal structures of nitrogen-bridged [($^{NON\text{-}Dipp}$L)Ae]$_2$ (Ae = Ca (**19**), Sr (**20**) and Ba (**21**)) 207
5.4.1.2 X-ray crystal structure of aryl-bridged [($^{NON\text{-}Dipp}$L)Ba]$_2$ (**21a**) 211
5.4.1.3 X-ray crystal structures of [($^{NON\text{-}Dipp}$L)Ae(THF)$_n$] 214
5.4.2 NMR spectroscopic analysis 217
5.5 Attempted synthesis of low-valent alkaline earth complexes 219
5.5.1 Synthesis of [($^{NNO\text{-}Dipp}$L)Mg(μ-OH)M]$_2$ (M = Na (**22**) and K (**23**)) 219
5.5.2 Attempted reduction of [($^{NON\text{-}Dipp}$L)Ae]$_2$ (Ae = Ca (**19**), Sr (**20**) and Ba (**21**)) 220
5.5.3 X-ray crystallographic analysis 221
5.5.4 NMR spectroscopic analysis 224
5.5.5 Discussion of **22** and **23** and comparison with low-valent complexes 226
5.6 Conclusions 230
5.7 References 232

Chapter 6 – Experimental details and characterisation data 235
6.1 General details 235
6.1.1 Air- and moisture-sensitive compounds 235
6.1.2 Commercially supplied reagents 235
6.1.3 Synthesis of literature compounds 236
6.1.4 Solvent preparation 236
6.1.5 Solution NMR spectroscopy 237
6.1.6 Fourier transform infrared (FTIR) spectroscopy 237
6.1.7 Elemental analysis 238
6.1.8 Single crystal X-ray diffraction (XRD) 238
6.1.9 Ligand numbering schemes 239
6.2 Experimental details for Chapter 2 239
6.2.1 Synthesis of $^{Ph_3}LH_2$ (**1**); adapted from reference 2. 239
6.2.2 Synthesis of $^{\mu\text{-}Me_2}LH_2$ (**2**) and $^{Me_2H\text{-}\mu\text{-}Me_2}LH$ (**3**) 240
6.2.3 Synthesis of [(^{Me_3}L)Mg(THF)$_2$] (**4**) 241
6.2.4 Synthesis of [($^{Me_2tBu}L$)Mg(THF)$_2$] (**5**) 242
6.2.5 General procedure for the reaction of $^{R_3}LH_2$ with [(THF)$_2$AeN"$_2$] in THF-d_8 243
6.2.6 Synthesis of $^{Me_3}LD_2$ 245
6.2.7 Synthesis of $^{Ph_2Me}LD_2$ 246
6.3 Experimental details for Chapter 3 247
6.3.1 Synthesis of [($^{Ph_2Me}L$)Ca]$_2$ (**6**) 247
6.3.2 Synthesis of [($^{Ph_2Me}L$)Sr]$_2$ (**7**) 248
6.3.3 Synthesis of [($^{Ph_2Me}L$)Ba]$_2$ (**8**) 249
6.3.4 Synthesis of [(^{Ph_3}L)Ca]$_2$ (**9**) 250
6.3.5 Synthesis of [(^{Ph_3}L)Sr]$_2$ (**10**) 251
6.3.6 Synthesis of [(^{Ph_3}L)Ba]$_2$ (**11**) 252
6.3.7 Synthesis of [(^{Ph_3}L)Sr(THF)$_3$] (**12**) 253
6.4 Experimental details for Chapter 4 253
6.4.1 Synthesis of [($^{Me_2tBu}L$)Ca]$_2$ (**13**) 253
6.4.2 Synthesis of [($^{Me_2tBu}LH$)Ca(μ-$^{Me_2tBu}L$)Ca{N(SiMe$_3$)$_2$}] (**14**) 255
6.4.3 Synthesis of [$^{Me_2tBu}LH$]$_2$[Ca(THF)$_6$] (**15**) 256

6.4.4 Synthesis of [{($^{Me_2{}^tBu}$LH)Sr}$_2$(μ-$^{Me_2{}^tBu}$L)] (**16**) 257
6.4.5 Synthesis of [{($^{Me_2{}^tBu}$LH)Ba}$_2$(μ-$^{Me_2{}^tBu}$L)] (**17**) 259
6.5 Experimental details for Chapter 5 260
6.5.1 Synthesis of [($^{NON\text{-}Dipp}$L)Mg]$_2$ (**18**) 260
6.5.2 Synthesis of [{($^{NON\text{-}Dipp}$L)Mg}$_2$(THF)] (**18·THF**) 261
6.5.3 Synthesis of [($^{NON\text{-}Dipp}$L)Mg(THF)]$_2$ (**18·THF$_2$**) 262
6.5.4 Synthesis of [($^{NON\text{-}Dipp}$L)Ca]$_2$ (**19**) 262
6.5.5 Synthesis of [($^{NON\text{-}Dipp}$L)Ca(THF)$_2$] (**19·THF$_2$**) 263
6.5.6 Synthesis of [($^{NON\text{-}Dipp}$L)Sr]$_2$ (**20**) 263
6.5.7 Synthesis of [($^{NON\text{-}Dipp}$L)Sr(THF)$_3$] (**20·THF$_3$**) 264
6.5.8 Synthesis of [($^{NON\text{-}Dipp}$L)Ba]$_2$ (**21**) 265
6.5.9 Synthesis of [($^{NON\text{-}Dipp}$L)Ba(THF)$_3$] (**21·THF$_3$**) 266
6.5.10 Synthesis of [($^{NNO\text{-}Dipp}$L)Mg(μ-OH)Na]$_2$ (**22**) 266
6.5.11 Synthesis of [($^{NNO\text{-}Dipp}$L)Mg(μ-OH)K]$_2$ (**23**) 266
6.6 References 268

Chapter 7 - Conclusions 269

Appendix – Supplementary data for Chapters 2–5 ..... A-1
A.1 Appendix for Chapter 2 ..... A-1
A.1.1 NMR spectra of isolated compounds A-1
A.1.2 *In situ* NMR spectra A-6
A.1.3 X-ray crystallographic data A-15
A.2 Appendix for Chapter 3 ..... A-21
A.2.1 NMR spectra of isolated compounds A-21
A.2.2 X-ray crystallographic data A-27
A.3 Appendix for Chapter 4 ..... A-31
A.3.1 NMR spectra of isolated compounds A-31
A.3.2 X-ray crystallographic data A-35
A.4 Appendix for Chapter 5 ..... A-39
A.4.1 NMR spectra of isolated compounds A-39
A.4.2 *In situ* NMR spectra A-44
A.4.3 X-ray crystallographic data A-45

Chapter 1

Introduction

1.1 Main group elements for sustainable chemistry

The global chemical industry remains highly profitable, with total worldwide revenues of $5.72 trillion in 2022.[1] However, the impact its current manifestation has on both human health and natural ecosystems has become increasingly apparent.[2–6] While the changes required for the chemical industry to move towards a more sustainable "circular economy" are manifold,[7,8] the replacement of rare and toxic transition metals that are used extensively for industrial-scale homogeneous catalysis is one field that has received attention.[9]

Consequently, recent decades have seen a growing body of literature dedicated to the development of coordination complexes of main group elements that display "transition metal-like" chemistry, with a view to providing viable alternatives to well-established d-block catalysis.[10,11] Much of this work has focused on the "orbital-engineering" of complexes featuring electronegative p-block elements.[10,11] However, recent decades have also seen growing interest in electropositive s-block metals, including the alkaline earth elements.

1.2 Alkaline earth chemistry

While the use of beryllium and radium is generally hindered by their respective toxicity and radioactivity,[12,13] the other alkaline earth elements are often presented as attractive candidates for sustainable chemistry. Magnesium (7th), calcium (5th), strontium (17th) and barium (14th) are among the most abundant elements in the earth's crust.[14] This results in significantly lower costs than many industrially relevant transition metals – for instance, while platinum costs $1600/troy oz, magnesium and calcium cost only $0.13/troy oz and $0.005/troy oz respectively.[9] However, magnesium has been designated as a critical element with a supply risk, despite its high terrestrial abundance.[15] Consequently, interest has grown in the development of reactive coordination complexes of calcium, strontium and barium, which do not face supply concerns.[15,16] With the exception of barium, which interferes with transmembrane potassium ion channels *in vivo*,[17] these elements also possess very low toxicity and are therefore biocompatible. While these properties confer both economic and sustainability benefits to the alkaline earth elements relative to many d- and some p-block elements, homogeneous alkaline earth complexes have generally received significantly less academic interest due to some of the fundamental challenges associated with their coordination chemistry and reactivity.[18]

1.2.1 Coordination chemistry of the divalent alkaline earth cations

While the isolation of low-valent complexes exhibiting Ae(0) or Ae(I) oxidation states has been reported in recent years (see **Sections 1.3** and **1.5**), the chemistry of the alkaline earth elements is dominated by the high stability of their divalent Ae(II) oxidation state. This results from their low first and second ionisation energies, which enable the facile oxidation of metallic Ae(0) to Ae(II) (**Table 1.1**).[19] Consequently, the vast majority of alkaline earth coordination complexes feature dicationic Ae^{2+} centres that are incapable

of redox chemistry. However, variations in bonding and reactivity are observed as Ae^{2+} size increases, with the contracted ionic radii of beryllium (0.45 Å) and magnesium (0.72 Å) resulting in higher electronegativities and charge densities than those of the radially expanded heavier congeners calcium (1.00 Å), strontium (1.18 Å) and barium (1.36 Å) (**Table 1.1**, **Figure 1.1**).[20,21]

Table 1.1 Selected physical quantities of the alkaline earth (Ae) elements: first and second ionisation energies (IE_1 and IE_2 respectively),[19] ionic radius (r)[20], charge density (ρ), Pauling electronegativity (χ)[21] and oxophilicity (Θ).[38]

Ae	IE_1 / kJ mol^{-1}	IE_2 / kJ mol^{-1}	r / Å	ρ / Å^{-1}	χ	Θ
Be	899.7	1757.1	0.45	5.24	1.57	0.4
Mg	737.7	1450.7	0.72	1.28	1.31	0.6
Ca	589.8	1145.4	1.00	0.48	1.00	0.7
Sr	549.5	1064.2	1.18	0.29	0.95	0.5
Ba	502.9	965.2	1.36	0.19	0.89	0.3

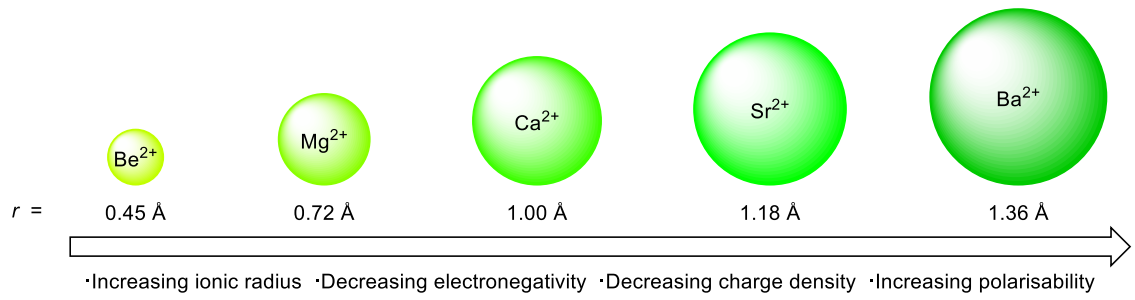


Figure 1.1 Illustration of variations in ionic radius and related periodic trends as group 2 is descended.

1.2.1.1 Metal-ligand bonding

The bonding of the radially contracted lighter congeners Be^{2+} and Mg^{2+} has an appreciable covalent contribution due to their more compact valence orbitals,[12,22] whereas the bonding of the more diffuse Ca^{2+}, Sr^{2+} and Ba^{2+} dications is increasingly dominated

by non-directional ionic interactions.[23,24] Therefore, Be^{2+} and Mg^{2+} complexes generally exhibit lower coordination numbers that result from their preferential interaction with "hard" monodentate donors such as alkoxides and amides. Conversely, the coordination of polydentate ligands enables the coordinative saturation of the large Ca^{2+}, Sr^{2+} and Ba^{2+} cations.[25] This often manifests through the stabilisation of formally low-coordinate heavy Ae^{2+} centres *via* the formation of "softer" π-facial interactions with alkenes/arenes[26–31] and/or agostic interactions with electron rich C-H,[32] C-F[33–35] or Si-H[36,37] bonds. Notably however, the Ca^{2+} cation has the highest quantified oxophilicity (Θ = 0.7) of the series due to the competing influences of both electronegativity and "hardness" on this parameter.[38] This has resulted in the isolation of a number of solvent-separated ion pairs (SSIPs) in which the Ca^{2+} cation is preferentially coordinated by the neutral oxygen donors of solvents such as tetrahydrofuran (THF), with charge balance provided by stable weakly coordinating anions (WCAs).[39–45]

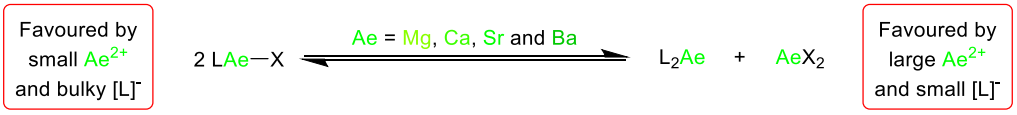
1.2.1.2 Stability and the Schlenk equilibrium

The strong metal-ligand bonds formed by magnesium have enabled the synthesis of stable organomagnesium compounds, with Grignard reagents (RMgX, $[R]^-$ = carbanion, $[X]^-$ = halide) now well-established in both inorganic and organic synthesis.[46] However, this stability can hinder their reactivity, with magnesium complexes often displaying significantly slower turnover rates than their heavier congeners when applied to catalysis.[9]

The predominantly electrostatic interactions formed between Ae^{2+} and anionic ligands are weakened as group 2 is descended due to the decrease in charge density that results from increasing Ae^{2+} ionic radius (**Table 1.1**). Consequently, the weak metal-ligand bonds formed by the heavier Ae^{2+} congeners confer increasingly high rates of ligand

exchange, enabling even anionic ligands to readily exchange between highly labile Ae^{2+} centres.[15] This property can be exploited to enable the rapid exchange of substrates and products, and is therefore attractive as a means of achieving high rates of catalytic turnover.[47]

However, the ancillary ligands (L) used to control the structure and reactivity of alkaline earth complexes also become increasingly labile upon their coordination to the heavier Ae^{2+} congeners. Consequently, heteroleptic alkaline earth complexes of the form [LAeX] ($[L]^-$ = monoanionic ancillary ligand, $[X]^-$ = alkoxide, amide, halide, hydride, alkyl etc.) are prone to solution-phase decomposition *via* the Schlenk equilibrium. This results in ligand redistribution and the formation of the homoleptic species [L_2Ae] and [AeX_2] (**Scheme 1.1**).[24]



Scheme 1.1 Schlenk equilibrium showing the ligand redistribution between the heteroleptic alkaline earth complex [LAeX] and the homoleptic species [L_2Ae] and [AeX_2] ($[L]^-$ = monoanionic ancillary ligand and $[X]^-$ = labile monoanionic ligand).

This process is driven by the additional thermodynamic stability gained upon i) the coordinative saturation of Ae^{2+} that results from the coordination of a second multidentate ancillary ligand in [L_2Ae] and ii) the generally high lattice enthalpy of the [AeX_2] salt that is eliminated upon the coordination of two small monodentate ligands to Ae^{2+}.[25] Efforts have therefore centred on the development of sufficiently bulky ancillary ligands that enforce excessive steric congestion in [L_2Ae], thereby rendering [LAeX] kinetically stable. However, steric bulk and coordination number must be appropriately tuned to

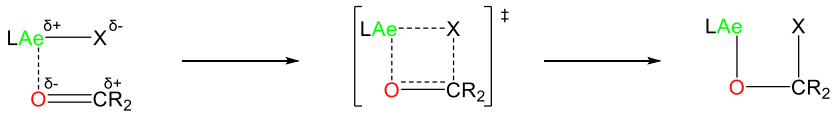
ensure that the reactivity of the Ae^{2+} complex is not significantly inhibited, meaning the competing demands of complex stability and reactivity must be carefully balanced.[9,24]

1.2.2 Redox-neutral reactivity

While d-orbital involvement has been suggested for some heavier alkaline earth complexes,[48–51] the highly stable Ae^{2+} oxidation state precludes transition-metal like reactivity such as oxidative addition and reductive elimination. Consequently, heteroleptic complexes of the heavier alkaline earth elements are yet to achieve industrial viability. However, an array of impressive redox-neutral reactivity has been reported for heteroleptic Ae^{2+} complexes,[47,52] which generally results from the highly polarity and lability of their $Ae^{\delta+}$-$X^{\delta-}$ bonds. This can generally be categorised as either polarised insertion or σ-bond metathesis.[9,52]

1.2.2.1 Polarised insertion

Polarised insertion consists of the nucleophilic attack of the $Ae^{\delta+}$-$X^{\delta-}$ bond on an unsaturated multiple bond (**Scheme 1.2**).



Scheme 1.2 Polarised insertion of a $Ae^{\delta+}$-$X^{\delta-}$ bond across an unsaturated carbonyl bond *via* a concerted four-membered transition state.

This process is generally facile for polarised substrates such as carbonyls and imines. These substrates are further polarised upon the coordination of their heteroatoms to Ae^{2+} prior to nucleophilic attack, increasing their electrophilicity. Furthermore, heteroatom coordination to Ae^{2+} stabilises the accumulation of negative charge that results from nucleophilic attack.[9,47] While alkenes are more challenging substrates due to their

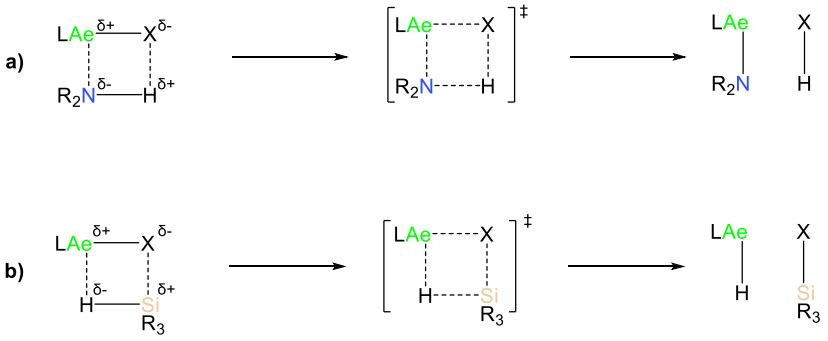
reduced degree of polarisation, the use of sufficiently reactive alkaline earth complexes has enabled polarised insertion across their C=C double bonds (*vide infra*).[52]

1.2.2.2 Sigma-bond metathesis

The polarised $Ae^{\delta+}$-$X^{\delta-}$ bond can also react with saturated species *via* σ-bond metathesis.[9,48] This redox-neutral reactivity is well-established for trivalent lanthanide complexes, the bonding of which is also primarily governed by highly polarised metal-ligand bonds.[54] In general, σ-bond metathesis consists of the cleavage of two polarised σ-bonds present in the reactants and the formation of two new σ-bonds in a concerted manner (**Scheme 1.3**).[52] However, in some cases an alternative stepwise mechanism has been reported for alkaline earth-mediated σ-bond methathesis.[54]

The outcome of the σ-bond metathesis reaction is determined by the predisposed polarity of the incoming substrate. This is exemplified by the deprotonation of species with protic $E^{\delta-}$-$H^{\delta+}$ bonds such as alcohols and amines, which enables the isolation of the corresponding alkoxide or amide. Indeed, this susceptibility to "protonolysis" is commonly exploited when synthesising novel alkaline earth complexes (see **Sections 1.3.1** and **1.4.1**),[55–58] and is also responsible for their high moisture sensitivity.

Conversely, the reaction of $Ae^{\delta+}$-$X^{\delta-}$ with species such as silanes and boranes that contain hydridic $E^{\delta+}$-$H^{\delta-}$ bonds instead results in the nucleophilic attack of $[X]^-$ at an electrophilic centre and the formation of an alkaline earth hydride (**Scheme 1.3b**). Notably, silane metathesis of this kind has been employed for both the stoichiometric synthesis of isolable alkaline earth hydrides[59] and for the generation of catalytically active hydride intermediates.[52]



Scheme 1.3 σ-bond metathesis of a polarised $Ae^{\delta+}$-$X^{\delta-}$ bond with **a)** a protic $E^{\delta-}$-$H^{\delta+}$ bond and **b)** a hydridic $E^{\delta+}$-$H^{\delta-}$ bond *via* concerted four-membered transition states.

1.2.3 Alkaline earth-mediated catalysis

The ability of kinetically labile heteroleptic alkaline earth complexes to engage in both polarised insertion with unsaturated substrates and σ-bond metathesis with saturated substrates that have orthogonal polarities has enabled the construction of various alkaline earth-mediated catalytic cycles.[9,23,24,47,52] Notable examples include imine hydrogenation,[60,61] amine carbonylation,[62] the ring-opening polymerisation (ROP) of lactide *via* a coordination-insertion mechanism[63,64] and the dehydrocoupling of hydridic silanes with protic species including amines,[54,65–72] alcohols,[73] boronic acids[74] and even terminal alkynes.[65,66] The catalytic hydrogenation of both conjugated and unactivated alkenes by alkaline earth hydrides has also been reported.[47,75–79]

1.3 Alkaline earth complexes supported by monoanionic ligands

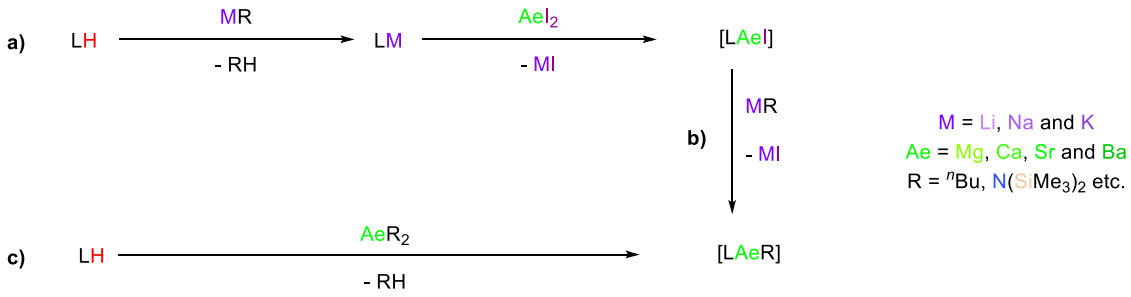
While reactive alkaline earth complexes supported by both neutral[77,78,80,81] and dianionic (**Sections 1.4** and **1.5**) ancillary ligands have been reported, homogeneous alkaline earth chemistry has largely been dominated by heteroleptic species supported by monoanionic ancillary ligands.

1.3.1 Synthesis

Heteroleptic alkaline earth complexes of the form [LAeX] are generally synthesised by either salt metathesis or protonolysis procedures (**Scheme 1.4**).

Salt metathesis requires the initial isolation of an alkali metal salt of the monoanionic ancillary ligand, [LM], *via* the deprotonation of the proligand LH with a suitable alkali metal base. The reaction of [LM] with an anhydrous alkaline earth halide, often the iodide AeI_2, then affords [LAeI], with one equivalent of the alkali metal iodide MI eliminated (**Scheme 1.4a**).[82,83] This has proven a useful means of directly synthesising heteroleptic iodides as precursors for the synthesis of reduced low-valent species.[25,84–87] Further salt metathesis of [LAeI] with alkali metal salts is also possible, enabling the exchange of the halide for an alternative $[R]^-$ ligand (**Scheme 1.4b**).

Alternatively, protonolysis utilises alkaline earth bases of the form $[AeR_2]$ such as di-*n*-butylmagnesium (Mg^nBu_2) and the alkaline earth *bis*(hexamethyldisilazides) ($[AeN''_2]$, $N'' = [N(SiMe_3)_2]^-$) to directly deprotonate LH, producing [LAeR] and eliminating one equivalent of RH (**Scheme 1.4c**).[88–91]



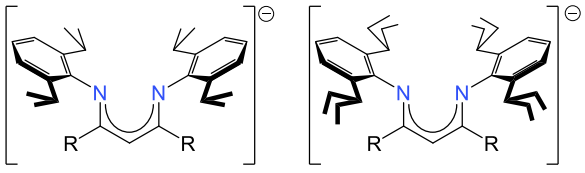
Scheme 1.4 General scheme for the synthesis of heteroleptic alkaline earth complexes supported by monoanionic ligands ($[L]^-$) *via* **a)** and **b)** salt metathesis and **c)** protonolysis.

A wide array of monoanionic ligands have now been reported to stabilise heteroleptic alkaline earth complexes.[83,90,92–94] A comprehensive summary of these is beyond the

scope of this introduction. However, many of the most notable recent achievements have been made using β-diketiminate (BDI) ligands, and so these are presented herein as representative examples.

1.3.2 Beta-diketiminate ligands

β-diketiminates ($^{R\text{-}R'}$[BDI]$^-$ = [CH{CR′NR}$_2$]$^-$) are ubiquitous monoanionic ligands that have been utilised for the synthesis of coordination complexes of elements from across the periodic table, in part due to their facile synthesis.[95] The use of bulky N-aryl substituents to flank the metal binding pocket has enabled the isolation of many reactive main group species,[96] with the [$^{Dipp\text{-}R}$BDI]$^-$ ([CH{CRNDipp}$_2$]$^-$, Dipp = 2,6-di*iso*propylphenyl, R = Me and ^{t}Bu) ligands proving particularly effective for alkaline earth chemistry. Harder and co-workers have also recently reported the bulkier [$^{DiPeP\text{-}R}$BDI]$^-$ ligands ([CH{CR(NDiPeP)}$_2$]$^-$, DiPeP = 2,6-di*iso*pentylphenyl, R = Me and ^{t}Bu), consisting of N-aryl groups with bulky 3-pentyl substituents (**Chart 1.1**).[97] The 3-pentyl substituents of these ligands confer additional kinetic stability in addition to improved hydrocarbon solubility, thus stabilising low-coordinate or low-valent alkaline earth centres and enabling the use of inert alkane solvents.[32] Other variants of the BDI ligand have also been applied to alkaline earth chemistry, including unsymmetrical ligands with two different N-aryl substituents,[31,98] pendant amino donors[87] and tethered systems.[99,100]



[$^{Dipp\text{-}R}$BDI]$^-$
Dipp = 2,6-di*iso*propylphenyl
R = Me and ^{t}Bu

[$^{DiPeP\text{-}R}$BDI]$^-$
DiPeP = 2,6-di*iso*pentylphenyl
R = Me and ^{t}Bu

Chart 1.1 Structures of the [$^{Dipp\text{-}R}$BDI]$^-$ (R = Me and ^{t}Bu) and superbulky [$^{DiPeP\text{-}R}$BDI]$^-$ ligands (R = Me and ^{t}Bu).

1.3.3 Heteroleptic complexes

1.3.3.1 Synthesis

The early years of the 21st century saw the isolation of the heteroleptic BDI-supported alkaline earth amides [($^{Dipp\text{-}Me}$BDI)Ae(THF)$_n$N''] (n = 0, Ae = Mg (**I-Mg**), Ae = Ca (**I-Ca**); n = 1, Ae = Ca (**II-Ca**), Sr (**II-Sr**) and Ba (**II-Ba**), **Chart 1.2**).[101–103] While the magnesium and calcium congeners have proved to be useful precursors to more reactive heteroleptic species, the Dipp substituents of the [$^{Dipp\text{-}Me}$BDI]$^-$ ligand were found to be insufficient to suppress Schlenk equilibria in the case of **II-Sr** and **II-Ba**.

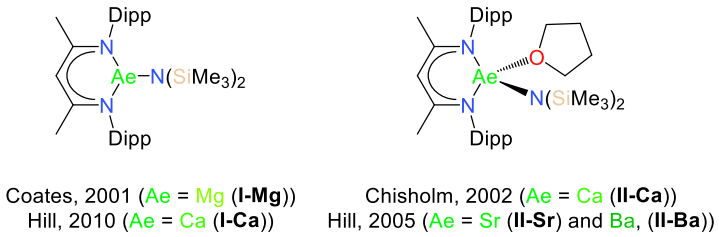
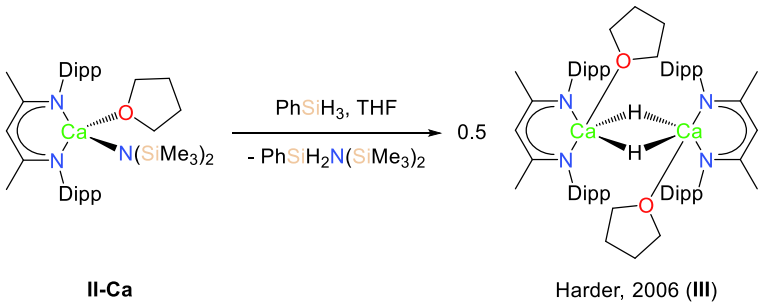


Chart 1.2 Heteroleptic alkaline earth amides supported by the [$^{Dipp\text{-}Me}$BDI]$^-$ ligand.

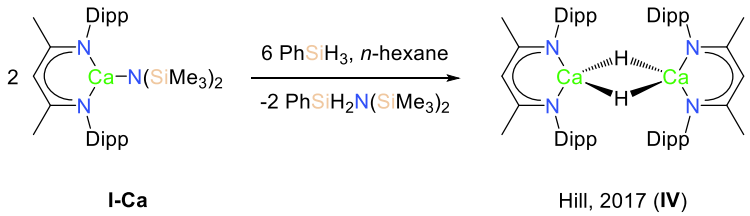
In 2006, Harder and co-workers reported the first isolable molecular calcium hydride [($^{Dipp\text{-}Me}$BDI)Ca(THF)(μ-H)]$_2$ (**III**) *via* the σ-bond metathesis of **II-Ca** with one equivalent of phenylsilane in THF (**Scheme 1.5**).[104]



Scheme 1.5 Synthesis of [(^{Dipp}BDI)Ca(THF)(μ-H)]$_2$ (**III**) *via* silane metathesis.

Attempts to synthesise the analogous THF-free molecular calcium hydride [($^{Dipp\text{-}Me}$BDI)Ca(THF)(μ-H)]$_2$ (**IV**) were initially unsuccessful.[105] However, it was

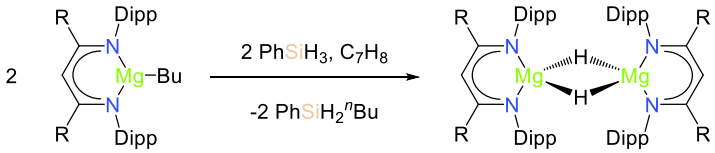
eventually reported in 2017 by Hill and co-workers, who employed the reaction of a threefold excess of phenylsilane with **I-Ca** in *n*-hexane (**Scheme 1.6**).[75]



I-Ca Hill, 2017 (**IV**)

Scheme 1.6 Synthesis of [($^{Dipp\text{-}Me}$BDI)Ca(THF)(μ-H)]$_2$ (**IV**) *via* silane metathesis in *n*-hexane.

In 2008, Jones reported the isolation of the dimeric THF-free magnesium hydrides [($^{Dipp\text{-}R}$BDI)Mg(μ-H)]$_2$ (R = Me (**Va**) and ^{t}Bu (**Vb**)) following a similar silane metathesis procedures that employed heteroleptic alkylmagnesium precursors (**Scheme 1.7**).[106]

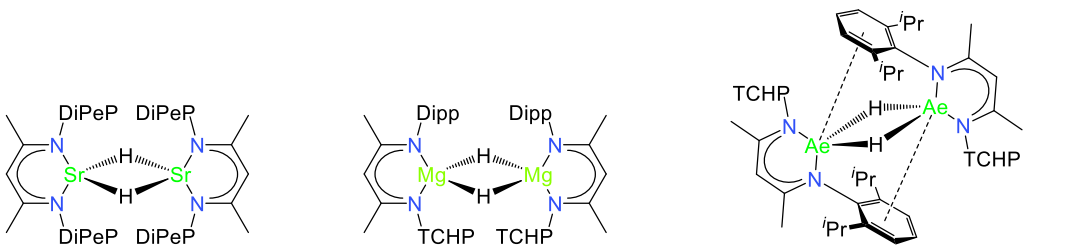


Jones, 2010
R = Me (**Va**) and ^{t}Bu (**Vb**)

Scheme 1.7 Synthesis of [($^{Dipp\text{-}R}$BDI)Mg(μ-H)]$_2$ (R = Me (**Va**) and ^{t}Bu (**Vb**)) *via* silane metathesis.

Recent reports have since demonstrated the ability of even bulkier BDI ligands to supress Schlenk equilibria[32] and enable the synthesis of stable molecular strontium and barium hydrides *via* the same silane metathesis route used for the synthesis of **III**–**V**.[31,107] In 2019, Harder and co-workers successfully isolated the dimeric strontium hydride [($^{DiPeP\text{-}Me}$BDI)Sr(μ-H)]$_2$ (**VI, Chart 1.3**).[107] The bulky 3-pentyl arms of the [$^{DiPeP\text{-}Me}$BDI]$^-$ ligand provide enhanced steric protection and form stabilising agostic interactions with the low-coordinate strontium centre. In addition, the improved hydrocarbon solubility of **VI** enables its dissolution in inert alkane solvents, thus facilitating its onward reactivity (*vide infra*). Very recently, Jones, Hill and co-workers reported a series of dimeric hydrides bearing an unsymmetrical BDI ligand with both N-Dipp and N-TCHP (TCHP

= 2,4,6-tricyclohexylphenyl) substituents ([($^{Dipp\text{-}TCHP\text{-}Me}$BDI)Ae(μ-H)]$_2$, Ae = Mg (**VII-Mg**), Ca (**VII-Ca**), Sr (**VII-Sr**) and Ba (**VII-Ba**), **Chart 1.3**).[31] In this case, stabilisation of the low-coordinate Ae^{2+} centres of the heavier congeners was provided by the formation of π-facial interactions with the less bulky Dipp substituent. While the heavier **VII-Ae** congeners (Ae = Ca, Sr and Ba) were found to be stable in the solid state, they exhibited poor solubility in non-coordinating solvents and decomposed rapidly when dissolved in THF. This example demonstrates that further investigation of the solution-phase structures and reactivity of alkaline earth complexes that are readily isolated and characterised in the solid state can be challenging.



Harder, 2019 (**VI**)

Jones, 2024 (**VII-Mg**)

Jones, 2024
Ae = Ca (**VII-Ca**), Sr (**VII-Sr**) and Ba (**VII-Ba**)

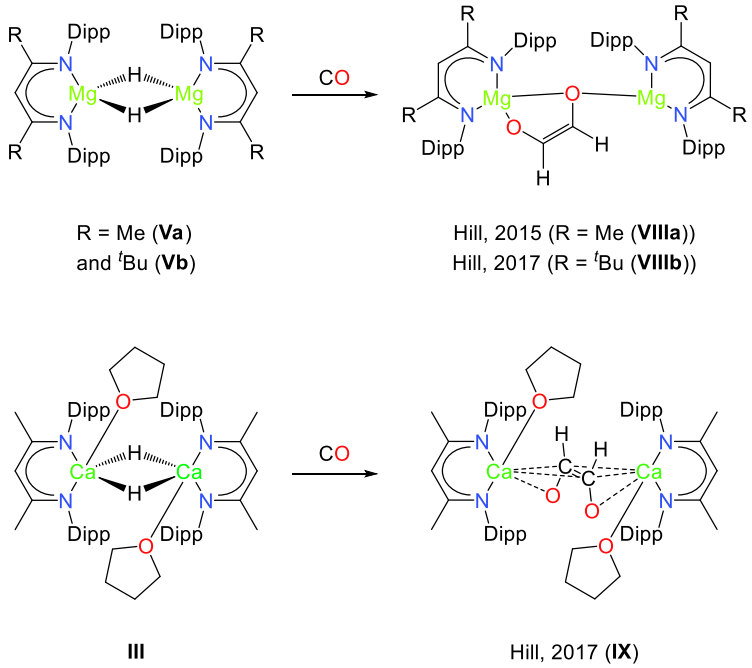
Chart 1.3 Selected molecular alkaline earth hydrides supported by bulky BDI ligands.

Together, the syntheses of compounds **I**–**VII** exemplify the sensitivity of reactive heteroleptic alkaline complexes to reaction conditions (particularly the solvent), Ae^{2+} size and ligand bulk.

1.3.3.2 Reactivity

An array of both stoichiometric and catalytic reactivity has been reported for **I**–**VII**. While the application of **I-Sr** and **I-Ba** to catalysis was hindered by significant ligand redistribution in solution, the more well-defined lighter congeners **I-Mg** and **I-Ca** were shown to catalyse both the ROP of lactide and the intramolecular hydroamination of aminoalkenes.[108,109] Hill and co-workers have also reported the stoichiometric reactions

of **III**, **Va** and **Vb** with carbon monoxide, which resulted in the homologation of the latter to form the enediolate complexes [{($^{Dipp\text{-}R}$BDI)Ae(THF)$_n$}$_2$(μ-C$_2$H$_2$O$_2$)] (Ae = Mg, n = 0, R = Me (**VIIIa**), R = ^{t}Bu (**VIIIb**), Ae = Ca, n = 1, R = Me (**IX**), **Scheme 1.8**).[110,111]

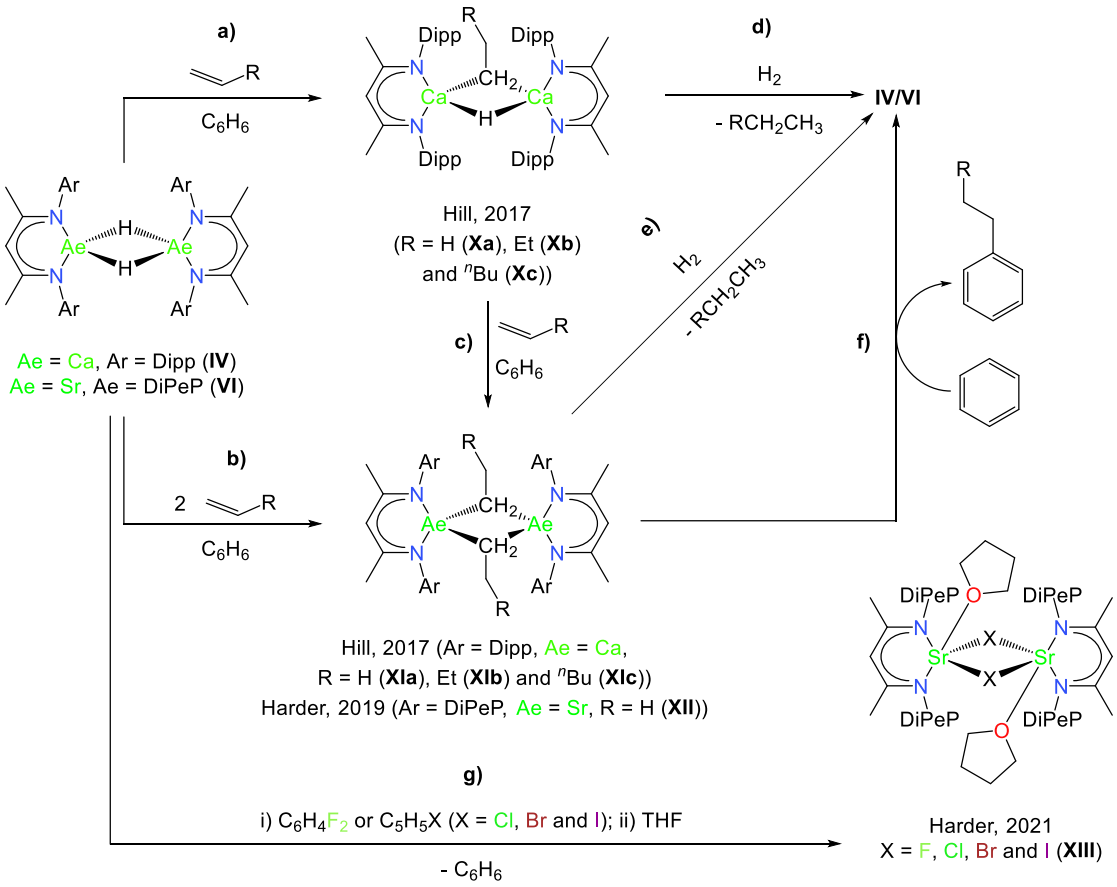


Scheme 1.8 Reactions of alkaline earth hydrides with carbon monoxide to form enediolate complexes.

The catalytic reduction of CO with phenylsilane was also reported for **Va**,[110] while **III** and **Vb** were each shown to enable both the stoichiometric carbonylation of amines and the catalytic hydro-deoxygenation of the resulting formamidates with pinacol borane.[111] Very recently, Crimmin and co-workers also reported the both the deoxygenative coupling of carbon monoxide[99] and its cross-coupling with an isocyanide[112] by a tetrametallic magnesium hydride complex supported by a related tethered BDI ligand.

Harder and co-workers have also reported the stoichiometric reactions of **III** with an array of polarised multiple bonded species,[113] as well as the ability of **III** to catalyse the hydrogenation of conjugated alkenes.[114] However, **III** was shown to be inert with respect to unactivated alkenes.[113] In contrast, the four-coordinate calcium centre of **IV** was found

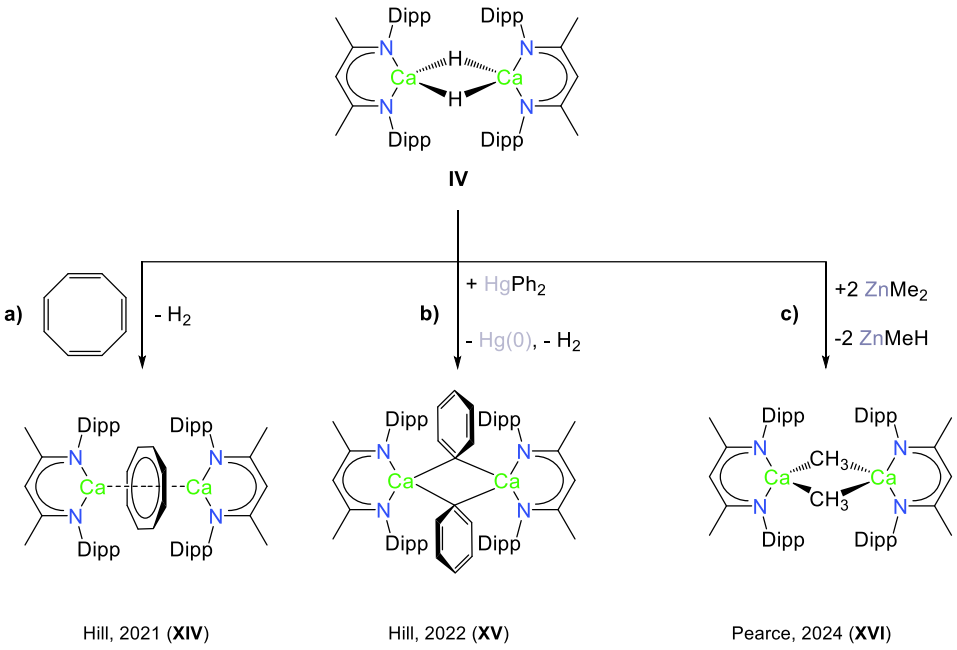
to significantly enhance its reactivity towards unactivated alkenes relative to **III**, with its vacant coordination site enabling the coordination and polarisation of the C=C π-bond. The reactions of **IV** with terminal alkenes *via* polarised insertion afforded the dimeric calcium hydride-alkyl complexes [{($^{Dipp\text{-}Me}$BDI)Ca}$_2$(μ-R)(μ-H)] (R = C_2H_5 (**Xa**), C_4H_9 (**Xb**) and C_6H_{13} (**Xc**)) and the dimeric calcium alkyl complexes [($^{Dipp\text{-}Me}$BDI)Ca(μ-R)]$_2$ (R = C_2H_5 (**XIa**), C_4H_9 (**XIb**) and C_6H_{13} (**XIc**), **Scheme 1.9a**, **b** and **c**).[75,76]



Scheme 1.9 **a)** Synthesis of dimeric alkaline earth mixed hydride-alkyls; **b)** and **c)** synthesis of dimeric alkaline earth alkyls; **d)** and **e)** heterolysis of dihydrogen by alkaline-earth alkyls, resulting in the catalytic hydrogenation of unactivated alkenes; **f)** nucleophilic alkylation of benzene by alkaline earth alkyls; **g)** hydrodehalogenation of haloarenes by strontium alkyls.

Both **X** and **XI** were subsequently shown to facilitate the heterolysis of dihydrogen *via* σ-bond metathesis, with the consequent regeneration of the hydride complex **IV** enabling the alkaline-earth mediated catalytic hydrogenation of unactivated alkenes (**Scheme 1.9d** and **e**).[76] The unique reactivity of these highly polarised calcium alkyls was further demonstrated by their ability to facilitate the nucleophilic alkylation of benzene *via* an anionic Meisenheimer-type intermediate,[75] the first reported example of this mode of reactivity (**Scheme 1.9f**). In a subsequent 2019 report, Harder and co-workers described similar reactivity for the strontium hydride **VI**, which was found to react with ethene to form an ethyl complex (**XII**) that also facilitated the nucleophilic alkylation of benzene. Notably, **VI** was also shown to react with carbon-halogen bonds, enabling the hydrodehalogenation of halogenated arenes (**Scheme 1.9g**).[115] However, the resulting strontium halide complexes (**XIII**) did not react with hydridic substrates, precluding catalytic reactivity.

In 2021, the reaction of **IV** with 1,3,5,7-cyclooctatetraene was reported by Hill and co-workers.[116] This resulted in the elimination of dihydrogen and the formation of an inverse sandwich complex of the cyclooctatetraenyl dianion ([{($^{Dipp\text{-}Me}$BDI)Ca}$_2$(C_8H_8)], **XIV**, **Scheme 1.10**). The reactivity of **IV** with d-block compounds has also been explored. Hill, Pearce and co-workers have recently reported the reaction of **IV** with diarylmercury reagents, which afforded the molecular calcium phenyl [($^{Dipp\text{-}Me}$BDI)Ca(μ-Ph)]$_2$ (**XV**, **Scheme 1.10**)[117] as well as other calcium aryl complexes.[118] Notably, the reaction of **XV** with aryl bromides was found to enable the stoichiometric synthesis of biaryls. In addition, a subsequent report described the reaction of **IV** with dimethylzinc, which afforded the molecular calcium methyl [(^{Dippp}BDI)Ca(μ-Me)]$_2$ (**XVI**, **Scheme 1.10**).[119]



Scheme 1.10 Synthesis of **a)** [{($^{Dipp\text{-}Me}$BDI)Ca}$_2$(C_8H_8)] (**XIV**), **b)** [($^{Dipp\text{-}Me}$BDI)Ca(μ-Ph)]$_2$ (**X**) and **c)** [($^{Dipp\text{-}Me}$BDI)Ca(μ-Me)]$_2$ (**XVI**).

Crimmin and co-workers have also investigated the reactivity of alkaline earth hydrides with transition metal complexes. This resulted in the isolation of the first hexagonal planar transition metal complex in 2019 following the reaction of **Va** with a palladium(II) precursor.[120] This was followed by recent reports of both magnesium-[121] and calcium-stabilised[122] transition metal formyl complexes formed upon the respective reactions of **III** and **Va** with transition metal carbonyls.

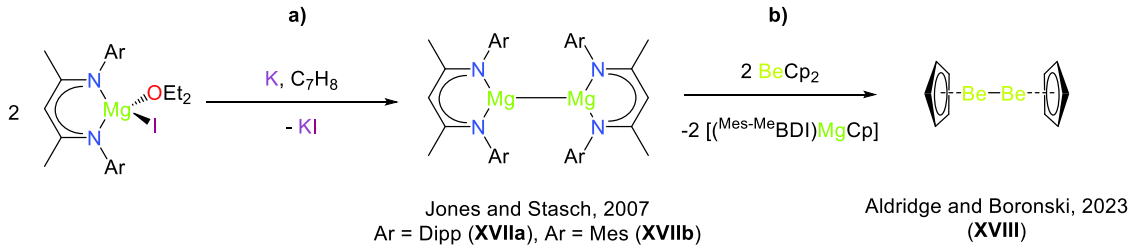
1.3.4 Low-valent alkaline earth compounds

1.3.4.1 Synthesis of low-valent beryllium and magnesium complexes

A seminal 2007 report by Jones, Stasch and co-workers described the synthesis of [($^{Dipp\text{-}Me}$BDI)Mg-Mg($^{Dipp\text{-}Me}$BDI)] (**XVIIa**) as well as a guanidinate supported analogue, the first examples of low-valent Mg(I) complexes featuring Mg-Mg bonds.[123] The N-Mesityl (Mes = 2,4,6-trimethylphenyl) substituted variant [(^{Mes}BDI)Mg-Mg(^{Mes}BDI)]

(**XVIIb**) was also reported in 2010.[124] In all cases, the synthesis involved the reduction of heteroleptic iodide precursors with potassium metal (**Scheme 1.11a**). Notably, computational calculations determined the Mg-Mg bond to be the first reported example of a non-nuclear attractor (NNA), an electron density maximum not associated with any particular nucleus.[125] Additional Mg(I) dimers supported by other monoanionic ligands have subsequently been reported.[126,127]

Furthermore, in 2023 Aldridge, Boronski and co-workers reported the synthesis of diberyllocene (CpBeBeCp, Cp = $[C_5H_5]^-$, **XVIII**, **Scheme 1.11b**), the first low-valent Be(I) compound featuring a Be(I)-Be(I) bond, through the reduction of beryllocene (Cp_2Be) with **XVIIb**.[128] This synthesis exploited the energetic preference for the stronger Be-Be bond over the Mg-Mg bond (homolytic bond dissociation energy (BDE) = 300 kJ mol^{-1} (Be) and 202 kJ mol^{-1} (Mg))[129] that results from the former's more compact valence orbitals.[125] **XVIII** has since been utilised to synthesise additional low-valent beryllium compounds with Be-Be bonds.[130]



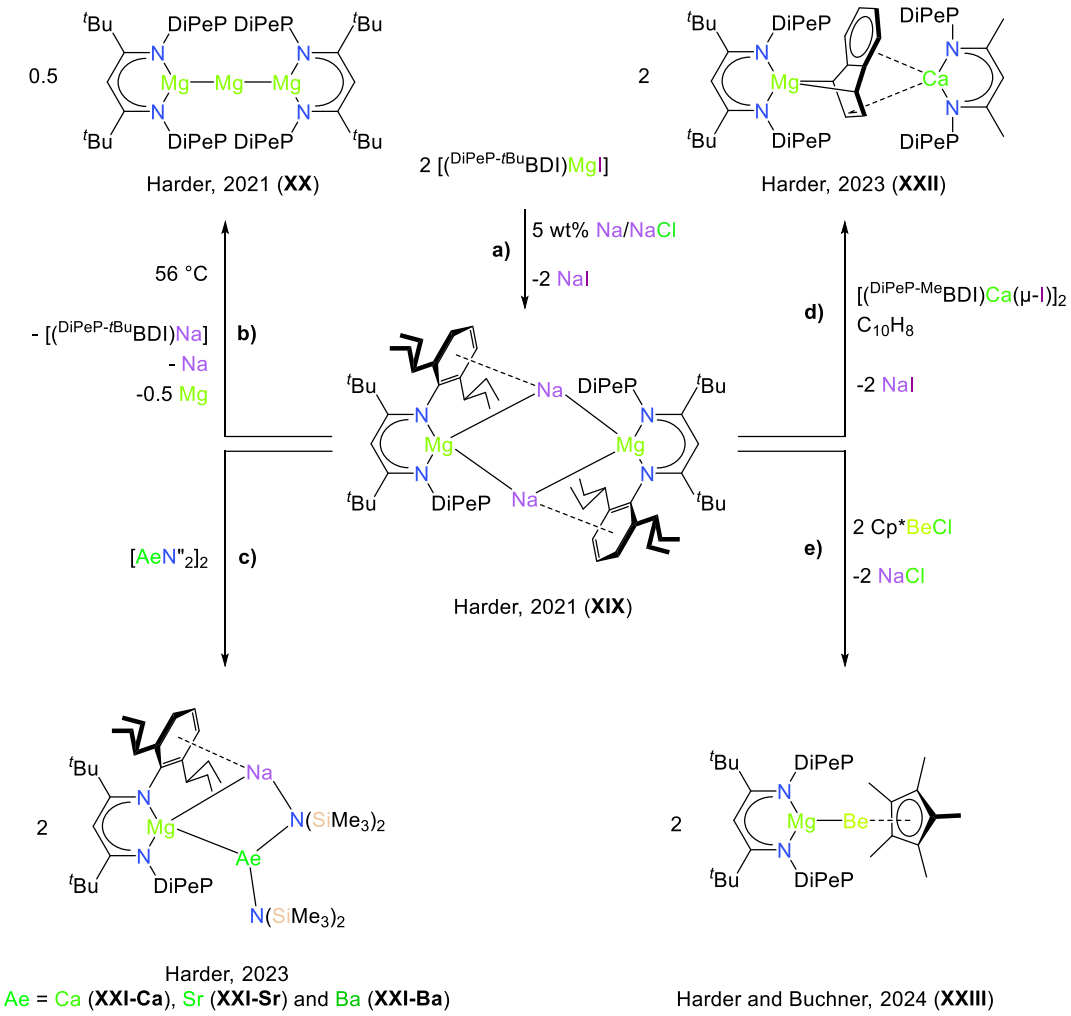
Scheme 1.11 Synthesis of Mg(I) and Be(I) dimers.

Notably, improved multigram, high-yielding syntheses of **XVIIa** using 5 wt% Na/NaCl and 5 wt% K/KI reducing agents were reported subsequently by Jones and co-workers.[131] Additionally, reports describing the mechanochemical reduction of both BDI- and guanidinate-supported heteroleptic magnesium iodides with these novel reducing agents by Harder and co-workers has enabled the isolation of proposed solid-state monomeric

Mg(I) radicals, which could be trapped as Mg(II)-CAAC adducts (CAAC = cyclic alkylaminocarbene).[132,133]

In 2018, Harder and co-workers reported a Mg(I) dimer analogous to **XVII** supported by the bulkier [$^{DiPeP\text{-}Me}$BDI]$^-$ ligand, which exhibited an elongated Mg-Mg bond (3.0513(8) Å).[97] More remarkably, a subsequent 2021 report described the use of the even bulkier [$^{DiPeP\text{-}t\text{Bu}}$BDI]$^-$ ligand in the isolation of the first reported magnesium(0) complex [{($^{DiPeP\text{-}t\text{Bu}}$BDI)Mg}Na]$_2$ (**XIX**, **Scheme 1.12a**).[134] Unlike previously reported Mg(I) dimers, it was noted that the $[Mg_2Na_2]^{2+}$ core of **XIX** does not consist of a NNA, with electron density instead concentrated at the Mg(0) centres. Heating a benzene solution of **XIX** at 56 °C resulted in the extrusion of sodium metal and the formation of another novel Mg(0) complex, [{($^{DiPeP\text{-}t\text{Bu}}$BDI)Mg}$_2$Mg] (**XX**, **Scheme 1.12b**), which was found to consist of a $[Mg_3]^{2+}$ core with two Mg-Mg bonds that each feature NNAs.

XIX has since been demonstrated to act as a nucleophilic source of magnesium. This has enabled Harder and co-workers' isolation of the first Mg-Ae (Ae = Ca, Sr and Ba) bonds through cation-anion exchange between **XIX** and [AeN"$_2$]$_2$ to form the heterotrimetallic species [{($^{DiPeP\text{-}t\text{Bu}}$BDI)Mg}Na(μ-N")AeN"] (Ae = Ca (**XXI-Ca**), Sr (**XXI-Sr**) and Ba (**XXI-Ba**), **Scheme 1.12c**).[135] While the reaction of **XIX** with [($^{DiPeP\text{-}Me}$BDI)Ca(μ-I)]$_2$ in benzene resulted in the C-H activation of the solvent,[136] the addition of naphthalene to the reaction mixture instead afforded [{($^{DiPeP\text{-}t\text{Bu}}$BDI)Mg}(μ-$C_{10}H_8$){Ca($^{DiPeP\text{-}t\text{Bu}}$BDI)}] (**XXII**, **Scheme 1.12d**), implying the formation of a transient Mg-Ca interaction. This outcome contrasted with a subsequent report in which [($^{DiPeP\text{-}t\text{Bu}}$BDI)MgBeCp*] (Cp* = $[C_5Me_5]^-$, **XXIII**, **Scheme 1.12e**), the first reported example of a Mg-Be bond, was successfully isolated by Harder, Buchner and co-workers *via* salt metathesis.[137]

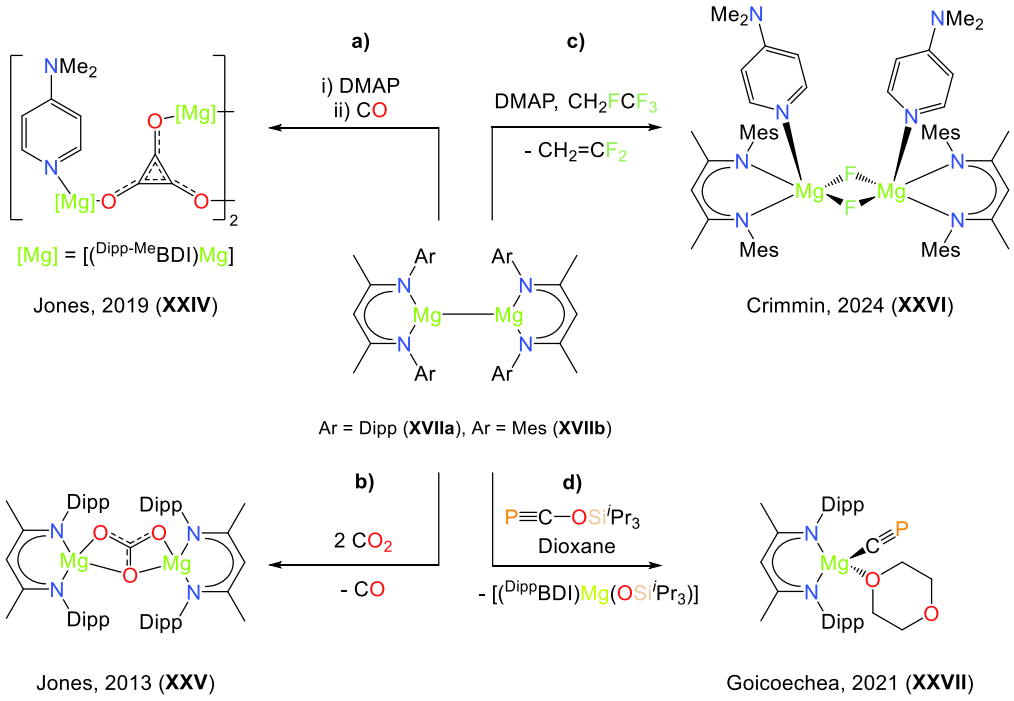


Scheme 1.12 Synthesis of **a)** [{(DiPeP-^{t}Bu)BDI)Mg}Na]$_2$ (**XIX**), **b)** [{(DiPeP-^{t}Bu)BDI)Mg}$_2$Mg] (**XX**), **c)** [{(DiPeP-^{t}Bu)BDI)Mg}Na(μ-N")AeN"] (Ae = Ca (**XXI-Ca**), Sr (**XXI-Sr**) and Ba (**XXI-Ba**)) **d)** [{(DiPeP-^{t}Bu)BDI)Mg}(μ-C$_{10}$H$_8$){Ca(DiPeP-MeBDI)}] (**XXII**), and **e)** [(DiPeP-^{t}Bu)BDI)MgBeCp*] (**XXIII**).

1.3.4.2 Reactivity

Magnesium(I) dimers are now established as electron-precise soluble reducing agents with applications across organic and inorganic synthesis,[84] including a number of notable recent examples. While the Mg(I) dimer **XVII** does not react with either dinitrogen, dihydrogen or carbon monoxide, Jones and co-workers have since reported that unsymmetrical Lewis base adducts of **XVIIa** with significantly lengthened Mg-Mg bonds facilitate the reductive trimerisation of carbon monoxide to the deltate anion (**XXIV**,

Scheme 1.13a),[138] as well as the reductive disproportionation of carbon dioxide (**XXV**, **Scheme 1.13b**).[139] Furthermore, Jones and co-workers also reported the reductive hexamerisation of CO to the benzenehexolate anion by **XVIIb** in the presence of $Mo(CO)_6$. Crimmin and co-workers have reported the stereoselective insertion of cyclopropenes into the Mg-Mg bond of **XVIIa**,[140] as well as the defluorination of both Teflon[141] and hydrofluorocarbons[142] (**XXVI**, **Scheme 1.13c**) using **XVIIb**. In 2021, Goicoechea and co-workers reported the synthesis of [($^{Dipp\text{-}Me}$BDI)Mg(CP)(dioxane)] (**XXVII**, **Scheme 1.13d**), the first s-block cyaphide complex, through the reduction of PCO(Si^{i}Pr$_3$) with **XVIIa**.[143] The high polarity of the resulting $Mg^{\delta+}$-$C^{\delta-}$ bond was found to enable the synthesis of various novel p- and d-block cyaphide complexes *via* salt metathesis reactions that employ **XXVII** as a "cyaphide transfer reagent" with Grignard-like reactivity.[144]



Scheme 1.13 Reactions of Mg(I) dimers with **a)** carbon monoxide, **b)** carbon monoxide, **c)** hydrofluorocarbons and **d)** PCO(Si^{i}Pr$_3$). DMAP = 4-dimethylaminopyridine.

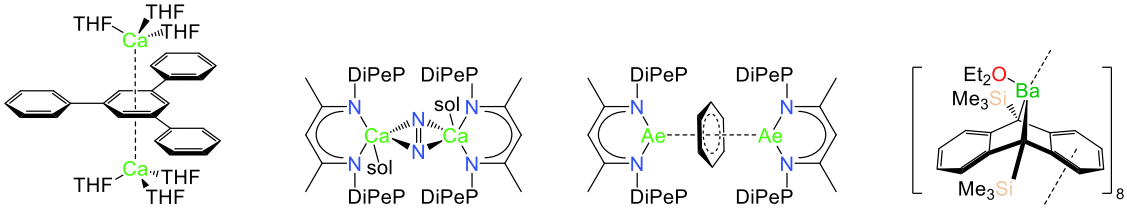
The magnesium(0) complexes **XIX** and **XX** were found to exhibit enhanced reactivity relative to **XVII**, enabling the activation of dihydrogen.[134] The proposed solid-state Mg(I) radicals reported by Harder and co-workers also display enhanced (though more poorly controlled) reactivity relative to Mg(I) dimers when dissolved in solution, including the activation of dihydrogen and benzene.[132,133]

1.3.5 Low-valent chemistry of the heavier alkaline earth elements

Low-valent homobimetallic Ae(I) dimers of the heavier congeners calcium, strontium and barium have so far proven inaccessible. The more diffuse valence orbitals of these elements result in Ae(I)-Ae(I) bonds with weaker computed BDEs (123 kJ mol^{-1} (Ca), 106 kJ mol^{-1} (Sr) and 90.9 kJ mol^{-1} (Ba))[129] than the isolable Mg(I) and Be(I) dimers **XVII** and **XVIII** (*vide supra*).[125] However, various attempts to isolate heavier Ae(I) or Ae(0) complexes have resulted in the isolation of a number of notable species.

In 2009, Westerhausen and co-workers reported the inverse sandwich complex $[\{(THF)_3Ca\}_2(\mu\text{-}1,3,5\text{-}Ph_3C_6H_3)]$ (**XXVIII**).[145] While a Ca(I) oxidation state was proposed, this has since been the subject of debate.[146] In a subsequent seminal report in 2021, the attempted synthesis of a Ca(I)-Ca(I) bonded species analogous to **XVII** resulted in the isolation of the first calcium dinitrogen complex $[\{(^{DiPeP\text{-}Me}L)Ca(sol)\}_2(\mu\text{-}N_2)]$ (sol = THF or THP, THP = tetrahydropyran, **XXIX**, **Chart 1.4**).[147] **XXIX** was proposed to form *via* the reaction of a transient low-valent Ca(I) intermediate with dinitrogen. The reaction of **XXIX** with various small molecules, including dihydrogen, resulted in the oxidation of the bridging $[N_2]^{2-}$ dianion and the release of dinitrogen. Consequently, **XXIX** was described as a "low-valent synthon" of the originally targeted Ca(I) dimer. The synthesis of **XXIX** required the use of an inert alkane solvent, as the presence of benzene was found to result in conversion to $[\{(^{DiPeP\text{-}Me}BDI)Ca\}_2(\mu\text{-}C_6H_6)]$ (**XXX-Ca,**

Chart 1.4), an inverse sandwich complex of the benzene dianion. **XXX-Ca** was also found to act as a low-valent synthon capable of activating a wide array of small molecules.[148] In 2022, Harder and co-workers also reported an analogous strontium complex (**XXX-Sr**, **Chart 1.4**) and showed that both **XXX-Ca** and **XXX-Sr** can facilitate the alkaline earth-mediated dehydrogenative C-C coupling of benzene to form biphenyl.[149] The synthesis of a "Ba(0) synthon" consisting of Ba^{2+} sandwiched by dianionic anthracene ligands *via* metal vapour deposition has also been reported recently by Harder and co-workers (**XXXI**).[150]



Westerhausen, 2009 (**XXVIII**)

Harder, 2021 (**XXIX**) sol = THF and THP

Harder, Ae = Ca, 2021 (**XXX-Ca**) Ae = Sr, 2022 (**XXX-Sr**)

Harder, 2023 (**XXXI**)

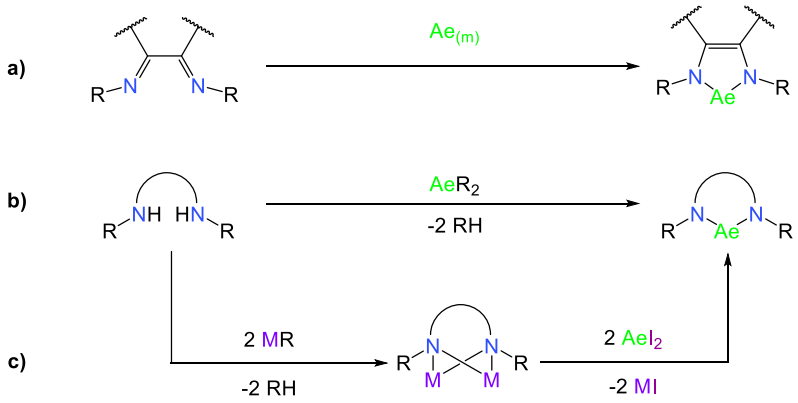
Chart 1.4 Selected examples of compounds relevant to the low-valent chemistry of the heavier alkaline earth elements calcium, strontium and barium.

1.4 Alkaline earth complexes supported by chelating dianionic ligands

The field of homogeneous alkaline earth chemistry has largely been dominated by monoanionic ligand systems due to their ability to support reactive heteroleptic and low valent species, with dianionic ancillary ligands ($[L]^{2-}$) receiving less attention. These ligands preclude the coordination of another anionic $[X]^-$ substituent to the Ae^{2+} centre in the absence of an additional metal cation, resulting in complexes of the form [LAe]. Various examples supported by a range of dianionic ligands have been reported, often as monomeric THF adducts of the form $[LAe(THF)_n]$.

1.4.1 Synthesis

Alkaline earth complexes of the form [LAe] can be synthesised *via* three routes, depending on the form of the neutral proligand employed. One approach is the reduction of redox non-innocent aprotic proligands such as α-diimines with metallic Ae(m), resulting in the formation of a reduced dianionic ligand coordinated to Ae(II) (**Scheme 1.14a**).[151] Conversely, proligands with two protic functionalities such as *bis*(amines) can be deprotonated and converted into diamido alkaline earth complexes *via* either protonolysis (**Scheme 1.14b**)[56] or salt metathesis (**Scheme 1.14c**).[152]



Scheme 1.14 General scheme for the synthesis of alkaline earth complexes of the form [LAe] by **a)** reduction of a redox non-innocent proligand, **b)** protonolysis and **c)** salt metathesis of a protonated proligand.

1.4.2 Redox non-innocent dianionic ligands

A number of α-diimine proligands such as bisiminoacenaphthalenes,[153,154] 1,4-diaza-1,3-dienes[155] and phenanthrene diimines[156,157] have been used to synthesise diamido alkaline earth complexes.[158] Fedushkin and co-workers have demonstrated the ability of alkaline earth complexes supported by bisiminoacenaphthalene ligands, [{$C_{12}H_6$(NDipp)$_2$}Ae(THF)$_n$] (**XXXII**, **Chart 1.5**) to both activate small molecules (such as CO_2,[159] phenylacetylene[160] and nitriles[161]) and form extended metal-organic

frameworks[162] due to the twinned redox non-innocent and basic properties of their ligands. Both these bisiminoacenaphthalene complexes[154,163] and similar phenanthrene diamine-based complexes[156] have also been reported to catalyse lactide ROP.

1.4.3 Deprotonated dianionic ligands

A number of [LAe] complexes consisting of Ae^{2+} coordinated by two deprotonated anionic donors have also been reported. Any further reactivity of complexes of this form often results from the high basicity of $[L]^{2-}$ conferring non-innocent behaviour.

Harder and co-workers have reported a series of monomeric alkaline earth complexes supported by dianionic bora-amidinate ligands [{$HB(NDipp)_2$}$Ae(THF)_n$] (Ae = Mg, Ca and Sr; **XXXIII**, **Chart 1.5**).[164] Despite their lack of a labile $[X]^-$ ligand, these were shown to be competent catalysts for the intramolecular hydroamination of aminoalkenes. This reactivity was attributed to the formation of heteroleptic intermediates capable of polarised insertion into the C=C double bond following the deprotonation of the aminoalkene substrates by the basic bora-amidinate ancillary ligand.

Panda and co-workers have previously reported alkaline earth complexes supported by both *bis*(phosphinoselenoicamides) and *bis*(phosphinosulfonicamides), [{CH_2NPPh_2E}$_2$$Ae(THF)_3$] (E = S and Se; Ae = Mg, Ca, Sr and Ba; **XXXIV**, **Chart 1.5**),[165,166] which were found to catalyse lactide ROP in the absence of a co-initiator. The attack of the P=E functionalities of **XXXIV** on the first lactide monomer to form an anionic initiating group that could polymerise additional monomers *via* a coordination-insertion mechanism was proposed. A later report described the polymerisation of ε-caprolactam into nylon-6 by analogous complexes which consisted of borane functionalities that initiated polymerisation through the deprotonation of the first ε-caprolactam monomer to form a catalytically active heteroleptic species.[167]

O'Hare and co-workers very recently reported a series of alkaline earth complexes supported by a dianionic *bis*(phenoxyimine) "NOON" ligand based on a rigid naphthalene scaffold (**XXXV**, **Chart 1.5**).[152] While lactide polymerisation proceeded *via* a conventional activated monomer mechanism in the presence of a co-initiator, ROP also occurred even in the absence of a co-initiator. It was proposed that the deprotonation of lactide by the "NOON" ligand resulted in the formation of a catalytically active heteroleptic species in the latter case, the poorly defined nature of which resulted in more poorly controlled polymerisation.[168]

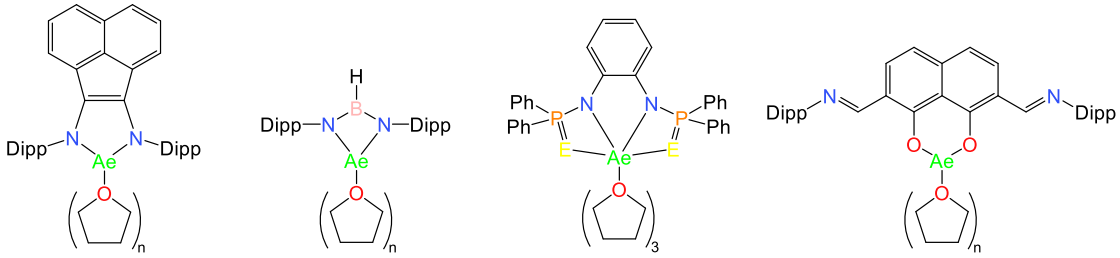


Chart 1.5 Selected examples of catalytically active alkaline earth complexes supported by chelating dianionic ligands.

1.5 Heterobimetallic alkaline earth complexes supported by dianionic ligands

The reactivity of alkaline earth complexes supported by chelating dianionic ligands has generally lagged behind the significant advancements facilitated by monoanionic ancillary ligands (**Section 1.3**). While the coordination of only a single dianionic ligand to Ae^{2+} prevents ligand redistribution *via* Schlenk equilibria, the absence of a labile $Ae^{\delta+}$-$X^{\delta-}$ bond in [LAe] generally precludes redox-neutral reactivity such as polarised

insertion and σ-bond metathesis (except in cases where the ancillary ligand participates in these processes, *vide supra*).

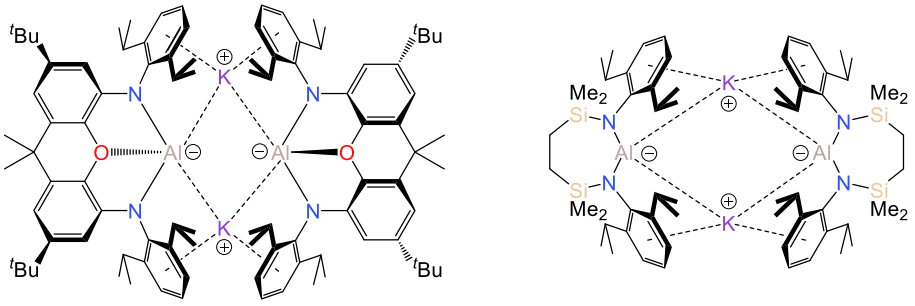
However, recent years have seen a rapid growth in the development of alkaline earth complexes supported by chelating dianionic ligands for use as precursors in the synthesis of reactive heterobimetallic s-block species. These can be divided into heteroleptic "ate" complexes with labile $[X]^-$ ligands ([LAeXM]), low-valent magnesium complexes with Mg(I)-Mg(I) bonds ([LMg(I)-Mg(I)L]M_2) and low-valent "synthons" consisting of a reduced bridging dianion, [LAe(μ-X)AeL]M_2 (M = alkali metal cation). Various dianionic ligands have been assessed as scaffolds for these systems, with both their steric bulk and backbone flexibility shown to exert a significant influence on the structures and reactivity of the heterobimetallic species reported to date.

1.5.1 Diamido alkaline earth complexes as precursors for heterobimetallic species

1.5.1.1 Inspiration from low-valent aluminium chemistry

Recent advancements in the field of low-valent aluminium chemistry have seen the successful synthesis of heterobimetallic assemblies consisting of nucleophilic aluminyl anions supported by chelating dianionic ligands. The first example of an aluminyl anion, [{($^{Dipp\text{-}t\text{Bu}}NON_{xanth}$)Al}K]$_2$ ($[^{Dipp\text{-}t\text{Bu}}NON_{xanth}]^{2-}$ = 4,5-bis(2,6-di*iso*propylanilido)-2,7-di-tert-butyl-9,9-dimethylxanthene, **XXXVI**, **Chart 1.6**) was reported by Aldridge, Goicoechea and co-workers in 2018.[169] The synthesis of **XXXVI** employed a "NON" ligand with a rigid xanthene backbone. A number of other dianionic ligand systems have since been shown to support analogous aluminyl species.[170] Of particular relevance to alkaline earth chemistry, Hill and co-workers reported [{($CH_2SiMe_2NDipp)_2$Al}K]$_2$ in 2019 (**XXXVII**, **Chart 1.6**).[171] The aluminyl anion in **XXXVII** consists of a

seven-membered aluminacycle supported by a more flexible *bis*(silylamido) ligand that coordinates in a N,N′-chelating manner.

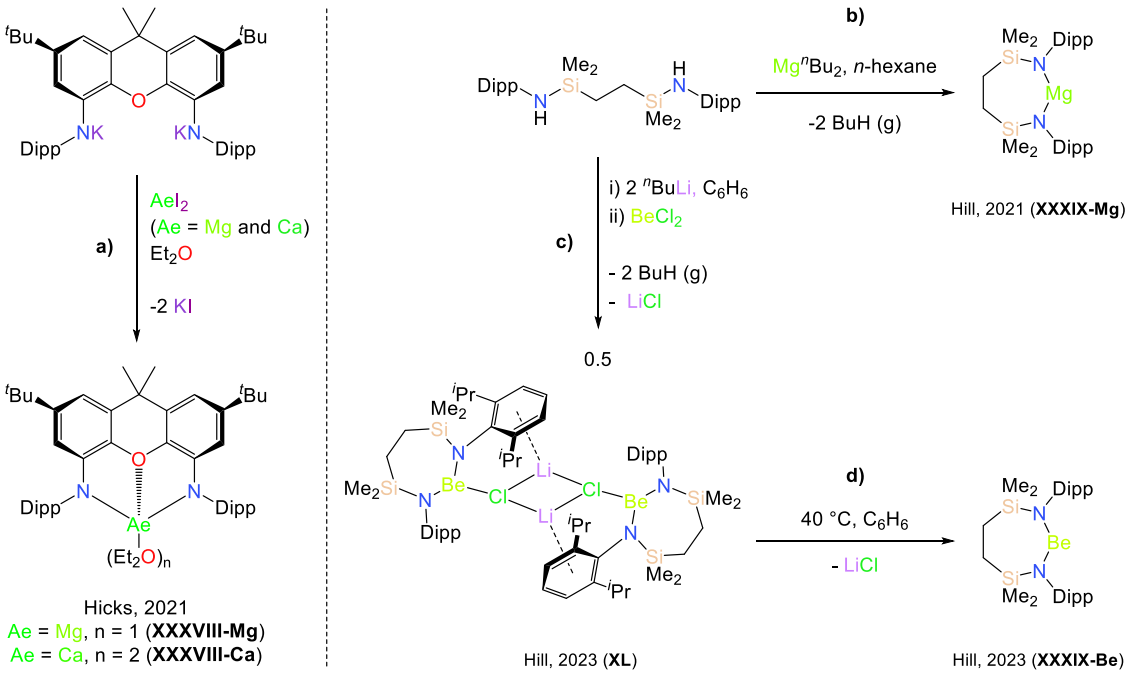


Aldridge and Goicochea, 2018 (**XXXVI**) Hill, 2019 (**XXXVII**)

Chart 1.6 The potassium aluminyl compounds [{($^{Dipp\text{-}tBu}$NON$_{xanth}$)Al}K]$_2$ (**XXXVI**) and [{(CH$_2$SiMe$_2$NDipp)$_2$Al}K]$_2$ (**XXXVII**) supported by chelating diamido ligands relevant to alkaline earth chemistry.

Following the successful application of these ligands to low-valent aluminium chemistry, they have each been utilised subsequently for the synthesis of alkaline earth complexes. Hicks and co-workers have reported the isolation of the neutral alkaline earth complexes [($^{Dipp\text{-}tBu}$NON$_{xanth}$)Ae(Et$_2$O)$_n$] (Ae = Mg, n = 1 (**XXXVIII-Mg**); Ae = Ca, n = 2 (**XXXVIII-Ca**), **Scheme 1.15a**) supported by the same "NON" ligand employed in **XXXVI**, which were found to form rare fluoroarene adducts when crystalised from fluorobenzene.[55] Furthermore, Hill and co-workers have isolated the beryllium and magnesium complexes [(CH$_2$SiMe$_2$NDipp)$_2$Ae] (Ae = Be (**XXXIX-Be**) and Mg (**XXXIX-Mg**)) supported by the *bis*(silylamido) ligand that was first used in **XXXVII**.[56,172] While **XXXIX-Mg** was accessed *via* a simple alkane elimination procedure (**Scheme 1.15b**), the synthesis of **XXXIX-Be** required a temperature of 40 °C to induce lithium chloride elimination from the dimeric lithium chloroberyllate [(CH$_2$SiMe$_2$NDipp)$_2$Be(μ-Cl)Li]$_2$ (**XL**) that formed initially following salt metathesis

(**Scheme 1.15c** and **d**). Subsequent reports have detailed the outcomes of the attempted reductions of **XXXVIII-Ae**, **XXXIX-Ae** and **XL** (see **Section 1.5.3** and **1.5.4**).[56,173]



Scheme 1.15 a) synthesis of [($^{Dipp\text{-}tBu}$NON$_{xanth}$)Ae(Et$_2$O)$_n$] (Ae = Mg, n = 1 (**XXXVIII-Mg**); Ae = Ca, n = 2 (**XXXVIII-Ca**), **b)** synthesis of [(CH$_2$SiMe$_2$NDipp)$_2$Mg] (**XXXIX-Mg**), **c)** synthesis of [(CH$_2$SiMe$_2$NDipp)$_2$Be(μ-Cl)Li]$_2$ (**XL**) and **d)** synthesis of [(CH$_2$SiMe$_2$NDipp)$_2$Be] (**XXXIX-Be**).

1.5.1.2 Additional diamido alkaline earth precursors

Jones and co-workers have very recently reported a number of neutral alkaline earth complexes supported by chelating diamido ligands with bulky N-aryl substituents, also with a view to employing them as precursors for heterobimetallic low-valent species. The use of *para*-terpheynyl-*bis*(anilido) ligands ([^{Ar}Terph]$^{2-}$ = [*p*-C$_6$H$_4${*o*-C$_6$H$_4$(NAr)}$_2$]$^{2-}$, Ar = Dipp and TCHP) resulted in the isolation of the monomeric complex [(^{Ar}Terph)Mg] (**XLI, Chart 1.7**) and the dimeric species [(^{Ar}Terph)Ae]$_2$ (Ae = Ca, Sr and Ba, **XLII, Chart 1.7**), with the latter bridged by Ae^{2+}-aryl π-facial interactions.[174] Conversely, attempts to isolate a monometallic beryllium congener instead resulted in the formation of the bimetallic heteroleptic complex [(^{Dipp}Terph)(BePh)$_2$] (**XLIII**) due to beryllium's

smaller size precluding the full deprotonation of the proligand with a single equivalent of diphenylberyllium. The attempted reduction of these complexes with alkali metal reducing agents resulted in the formation of intractable product mixtures, thus demonstrating that not all rigid and bulky ligand scaffolds are suitable for the isolation of reactive heterobimetallic s-block species. Together, this series of compounds also illustrates the structural diversity that can result from the coordination of Ae^{2+} cations of varying sizes to dianionic ligands featuring both hard amido donors and soft π-systems.

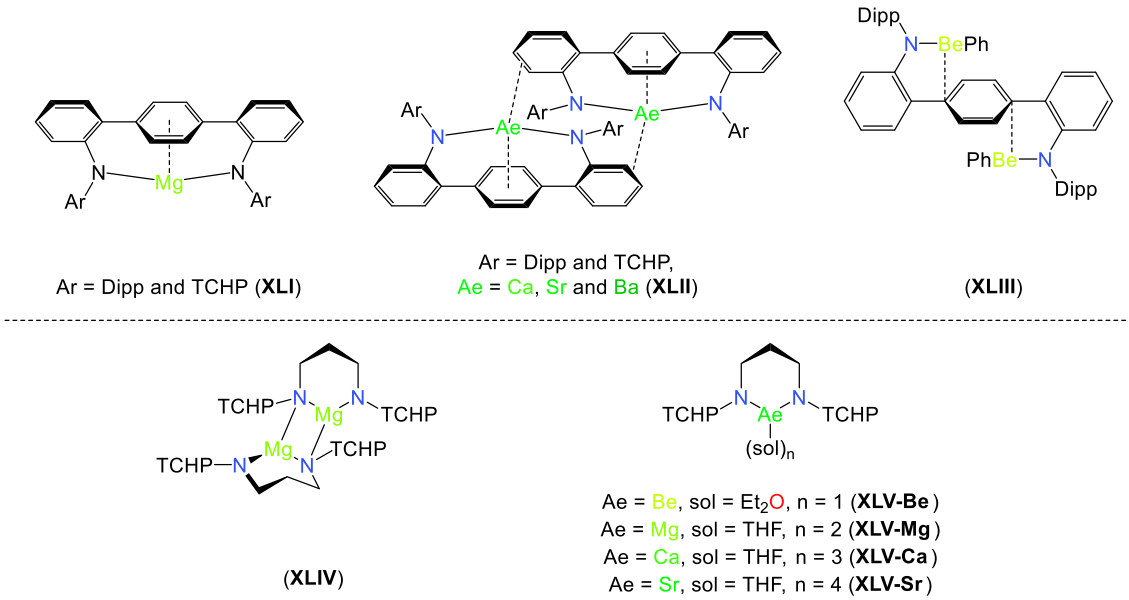


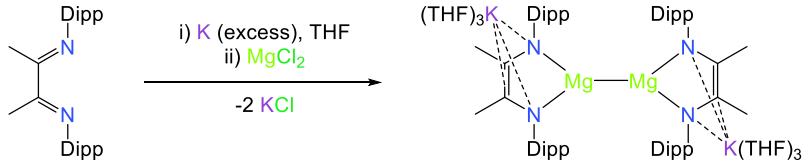
Chart 1.7 Alkaline earth complexes supported by bulky diamido ligands reported by Jones and co-workers.

Jones and co-workers have also very recently reported a bulky 1,3-diamidopropane ligand ($[^{TCHP}NCN]^{2-}$ = $[CH_2\{CH_2N(TCHP)\}_2]^{2-}$),[175] which was utilised to isolate the dimeric N-bridged magnesium complex $[(^{TCHP}NCN)Mg]_2$ (**XLIV, Chart 1.7**) as well as the monomeric adducts $[(^{TCHP}NCN)Ae(sol)_n]$ (sol = Et_2O, Ae = Be (**XLV-Be**), n = 1; sol = THF, Ae = Mg, n = 2 (**XLV-Mg**); Ae = Ca (**XLV-Ca**), n = 3, Ae = Sr, n = 4 (**XLV-Sr**); **Chart 1.7**).[57] It was noted that attempts to isolate the monomeric barium congener resulted in decomposition to the proligand and the precipitation of barium

metal, demonstrating that in some cases the synthesis of alkaline earth precursors supported by bulky dianionic ligands can be less than straightforward.

1.5.2 Heterobimetallic alkaline earth complexes supported by redox non-innocent α-diimine ligands

The first example of a Mg(I) dimer supported by a dianionic ligand was reported by Wu, Yang and co-workers in 2009 using a 1,4-diaza-1,3-diene proligand (**XLVI, Scheme 1.16**).[176] The resultant dianionic charge of the $[LMg\text{-}MgL]^{2-}$ fragment in **XLVI** was found to be stabilised by the interaction of two K^+ cations with the conjugated π-system of the ligand within a heterobimetallic assembly. This was followed by reports of similar complexes supported by related diamido-*o*-phenylene and phenanthrene-diimine ligands.[155,157] However, no significant differences between the reactivity of these "anionic" Mg(I) dimers and their neutral analogues were found.



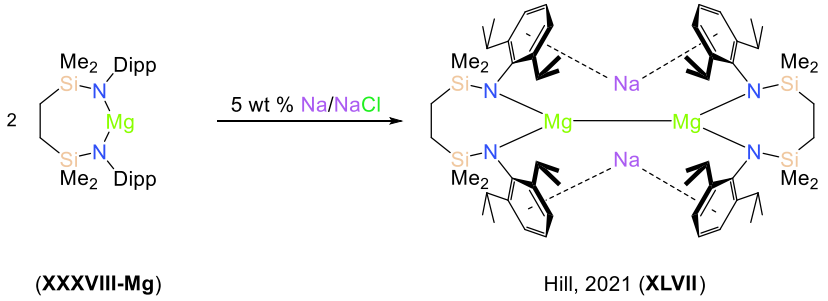
Wu & Yang, 2009 (**XLVI**)

Scheme 1.16 Synthesis of the first reported Mg(I) dimer supported by a dianionic ligand.

1.5.3 Heterobimetallic alkaline earth complexes supported by chelating *bis*(silylamido) ligands

In 2021 Hill and co-workers reported the reduction of **XXXIX-Mg** with 5 wt% Na/NaCl, which resulted in the isolation of $[\{(CH_2SiMe_2NDipp)_2Mg\}Na]_2$ (**XLVII**, **Scheme 1.17**). This low-valent heterobimetallic complex was found to consist of a $[Mg_2Na_2]^{2+}$ core supported by a chelating *bis*(silylamido) ligand. The Mg-Mg bond in **XLVII** was found to be significantly lengthened (3.2124(11) Å) relative to the reported range for

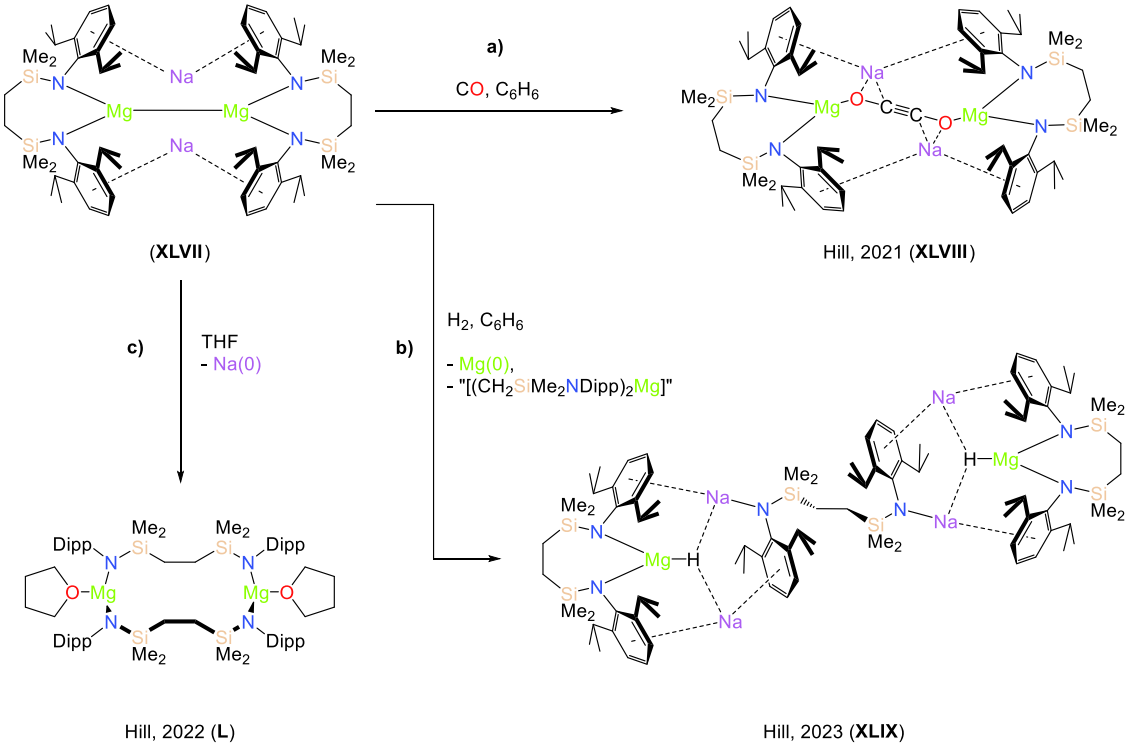
magnesium(I) dimers supported by monoanionic ligands (2.971–3.196 Å).[177,178] Computational calculations revealed that while a Mg-Mg interaction is present, this is only one component of a contiguous $[Mg_2Na_2]^{4+}$ core which does not consist of a NNA, making **XLVII** more reminiscent of the Mg(0) complex **XIX** than previously reported Mg(I) dimers.



(**XXXVIII-Mg**) Hill, 2021 (**XLVII**)

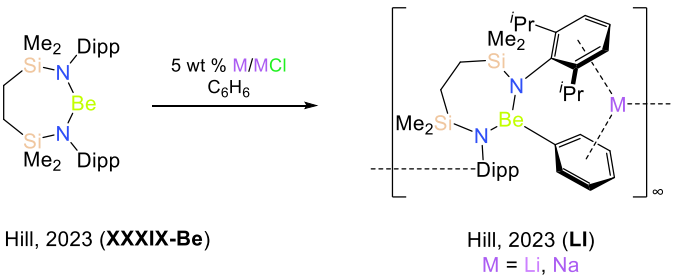
Scheme 1.17 Synthesis of $[\{(CH_2SiMe_2NDipp)_2Mg\}Na]_2$ (**XLVII**).

This has since been borne out by **XLVII**'s distinct reactivity. The reaction of **XLVII** with carbon monoxide resulted in the reductive coupling of the latter to form the ethynediolate anion (**XLVIII**, **Scheme 1.18a**).[56] This contrasts with the reactivity of the homobimetallic Mg(I) dimer **XVII**, to which the coordination of a Lewis base was required to enable the reductive trimerisation of carbon monoxide to the deltate anion (**Scheme 1.13a**, *vide supra*).[138] **XLVII** has since been shown to activate a range of other small molecues.[179] Notably, the reaction of **XLVII** with dihydrogen resulted in conversion to a heterobimetallic magnesium hydride (**XLIX, Scheme 1.18b**),[180] an outcome that also contrasted with the reactivity of neutral Mg(I) dimers. Remarkably, another report showed that Na(0) is extruded upon the coordination of THF to **XLVII**, which resulted in full conversion to a macrocyclic Mg(II) complex (**L**, **Scheme 1.18c**).[181]



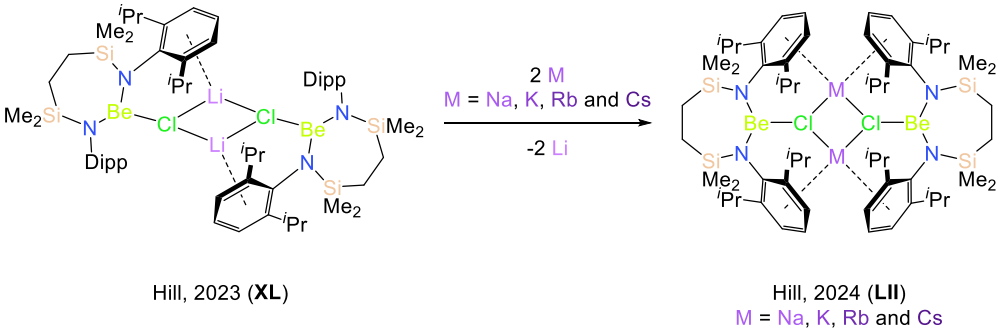
Scheme 1.18 Reactions of [{$(CH_2SiMe_2NDipp)_2Mg$}$Na]_2$ (**XLVII**) with **a)** carbon monoxide, **b)** dihydrogen and **c)** THF.

The attempted synthesis of a Be(I) analogue of **XLVII** *via* the reduction of the diamido beryllium precursor **XXXIX-Be** with either 5 wt% Li/LiCl or 5 wt% Na/NaCl resulted in the C-H activation of the benzene solvent by transient low-valent species and the formation of the polymeric lithium and sodium phenylberyllates [{$(CH_2SiMe_2NDipp)_2Be$}(μ-Ph)M]$_\infty$ (M = Li and Na, **LI**, **Scheme 1.19**).[172]



Scheme 1.19 C-H activation of benzene resulting from the attempted reduction of [{$(CH_2SiMe_2NDipp)_2Be$] (**XXXIX-Be**) with alkali metal reducing agents

The attempted reduction of the related lithium chloroberyllate **XL** with various alkali metals also did not afford reduction to Be(I). Remarkably however, the interchange of the alkali metal cation to form the heavier alkali metal chloroberyllates [{($CH_2SiMe_2NDipp)_2Be$}(μ-Cl)M]$_2$ (M = Na, K, Rb and Cs, **LII**, **Scheme 1.20**) was observed and found to be reversible in some cases.[182] A subsequent recent report detailed the influence of crown ether encapsulation of the alkali metal on the thermodynamics of this process.[183]

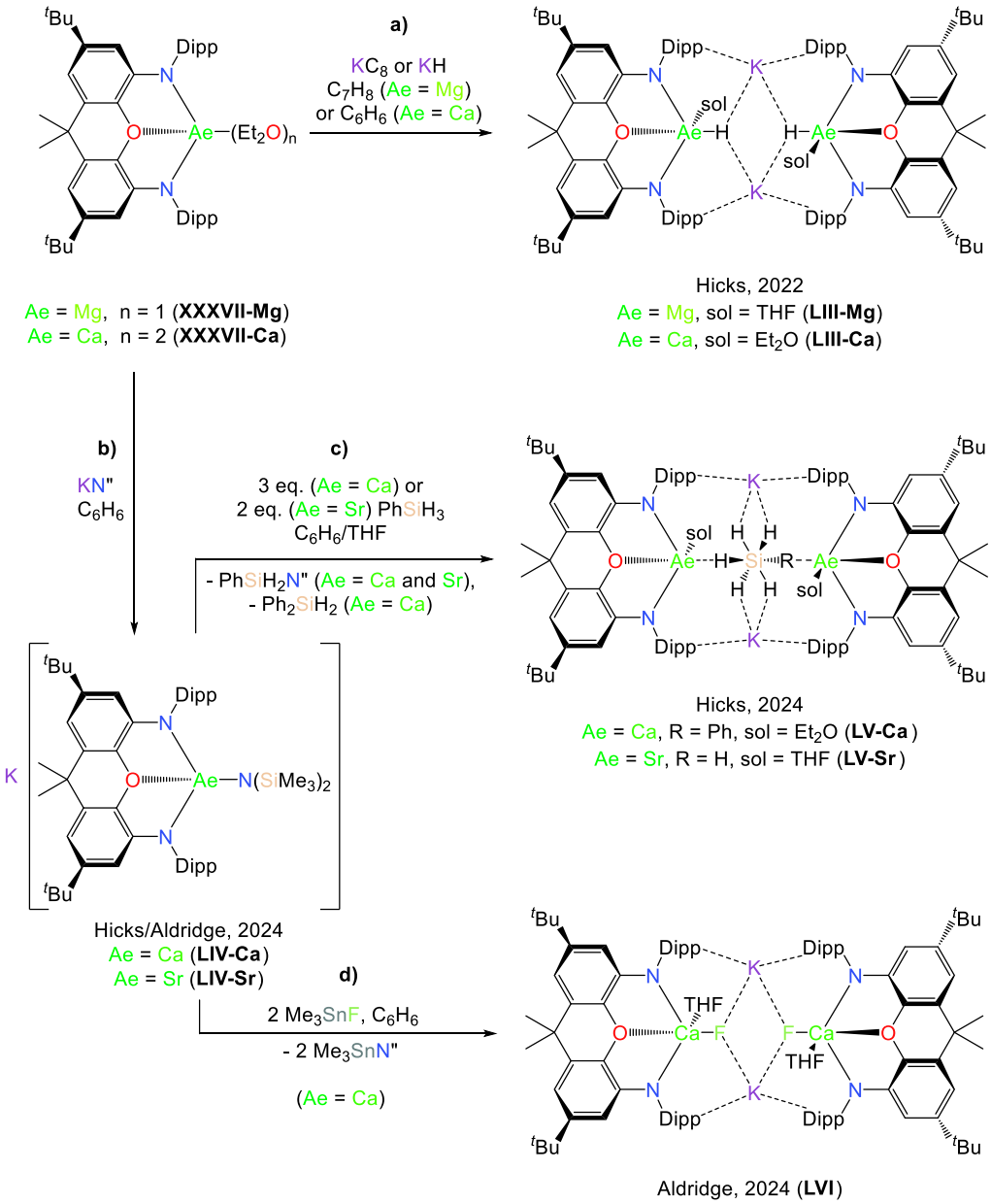


Scheme 1.20 Alkali metal cation exchange resulting from the attempted reduction of the [{($CH_2SiMe_2NDipp)_2Be$(μ-Cl)Li] (**XL**) with the heavier alkali metals (M = Na, K, Rb and Cs).

1.5.4 Heterobimetallic alkaline earth complexes supported by chelating NON-xanthene ligands

In 2022, Hicks and co-workers reported the attempted reduction of **XXXVII-Mg** and **XXXVII-Ca** with potassium graphite, which resulted in the isolation of the heterobimetallic dimeric hydrides [($^{Dipp\text{-}t\text{Bu}}NON_{xanth}$)Ae(sol)(μ-H)K]$_2$ (Ae = Mg, sol = THF (**LIII-Mg**), Ae = Ca, sol = Et_2O (**LIII-Ca**), **Scheme 1.21a**).[173] Hydride abstraction was attributed to the C-H activation of the solvent (toluene or benzene) by transient Ae(I) radical species. **LIII-Mg** and **LIII-Ca** could also be synthesised deliberately (though in poorer yields) using potassium hydride, and were further shown to react with CO to form

cis-ethenediolate complexes which could be converted into value-added silyl ethers upon their reaction with silyl chlorides.



Scheme 1.21 Heterobimetallic alkaline earth "ate" complexes with polarised $Ae^{\delta+}$-$X^{\delta-}$ bonds supported by the $[^{Dipp\text{-}t^{Bu}}NON_{xanth}]^{2-}$ ligand.

Hicks and co-workers have also very recently reported attempts to synthesise an analogous heterobimetallic strontium hydride. This involved the synthesis of the heterobimetallic amides $[(^{Dipp\text{-}t^{Bu}}NON_{xanth})Ae(\mu\text{-}N")K]$ (Ae = Ca (**LIV-Ca**), Ae = Sr,

(**LIV-Sr**), **Scheme 1.21b**), which were then reacted with phenylsilane. While the synthesis of the previously reported calcium hydride **LIII-Ca** *via* this route was successful, the unexpected hypersilyl complexes [{($^{Dipp\text{-}tBu}$NON$_{xanth}$)AeK}$_2$(μ-SiH$_5$R)] (Ae = Ca, R = H (**LV-Ca**); Ae = Sr, R = Ph (**LV-Sr**), **Scheme 1.21c**) were also isolated, with any molecular strontium hydride analogous to **LIII-Mg** and **LIII-Ca** determined to be a transient intermediate *en-route* to **LV-Sr**.[184]

Aldridge and co-workers have subsequently reported the independent synthesis of the same heterobimetallic Ca/K amide **LIV-Ca**, which was found to exist in equilibrium with the homometallic **XXXVII-Ca** and KN" in solution. The reaction of **LIV-Ca** with trimethyltin flouride resulted in the isolation of the dimeric complex [{($^{Dipp\text{-}tBu}$NON$_{xanth}$)Ca}(μ-F)K]$_2$ (**LVI**, **Scheme 1.21d**), with the conversion of **LVI** into a monomeric crown ether adduct also demonstrated.[185] These represented the first examples of terminal, non-bridging Ca-F bonds, overcoming the high lattice enthalpy of fluorspar ($\Delta H_L(CaF_2) = -2360$ kJ mol^{-1}),[186] and were shown to facilitate fluoride delivery to organic substrates.

The influence of ligand bulk on the outcomes of these reactions has been demonstrated by Jones and co-workers, who reported the reduction a calcium complex supported by a NON-xanthene ligand with even bulkier N-aryl substituents in 2022. This resulted in dinitrogen activation and the isolation of the heterobimetallic dimeric complex [{($^{TCHP\text{-}Et}$NON$_{xanth}$)CaK}$_2$(μ-N$_2$)] (Et = ethyl, **LVII**, **Chart 1.8**) rather than the formation of a Ca(I)-Ca(I) bond. This outcome was consistent with the isolation of the BDI-supported homometallic calcium dinitrogen complex **XXIX** by Harder and co-workers, in which the μ-η^2:η^2 coordination mode of the $[N_2]^{2-}$ anion is the same as that

observed in **LVII**.[187] However, the low-yielding synthesis and poor solubility of **LVII** precluded an assessment of its reactivity.

A subsequent 2023 report described the isolation of the first magnesium dinitrogen complex [{($^{TCHP\text{-}Et}NON_{xanth}$)MgK}$_2$(μ-$N_2$)] (**LVIII**, **Chart 1.8**) using the same bulky xanthene ligand.[188] Notably, the $[N_2]^{2-}$ dianion is coordinated in a μ-κ_1:κ_1 manner in this case. **LVIII** was found to react with carbon monoxide, dihydrogen (in both cases in a similar manner to that reported for the low-valent Mg_2Na_2 complex **XLVII**) and ethylene. **LVIII** was subsequently shown to facilitate the Birch-type reduction of benzene, naphthalene and anthracene, as well as the C-H activation of toluene and C-F activation of fluorobenzene, and has been described as a "masked magnesium(I) diradical".[189]

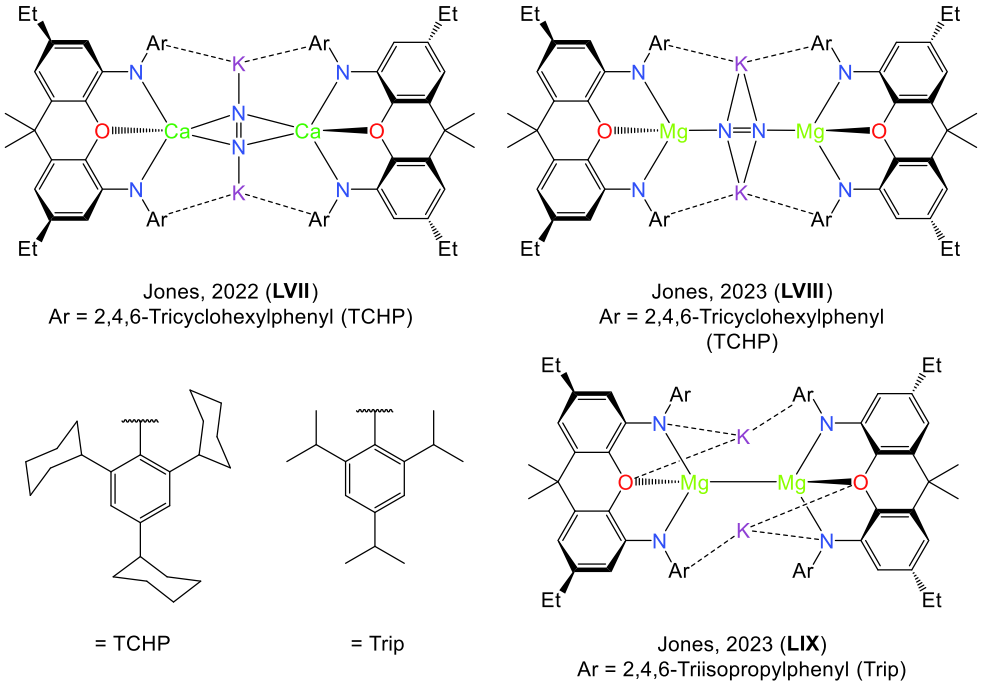


Chart 1.8 Heterobimetallic alkaline earth dinitrogen complexes and a heterobimetallic Mg(I) dimer supported by extremely bulky [$^{Ar\text{-}Et}NON_{xanth}$]$^{2-}$ (Ar = Trip and TCHP) ligands.

Jones and co-workers have also reported the use of the [$^{Trip\text{-}Et}NON_{xanth}$]$^{2-}$ (Trip = 2,4,6-tri*iso*propylphenyl) ligand, the steric bulk of which is intermediate to that of its TCHP- and Dipp-substituted analogues. The reduction of the magnesium complex

[($^{Trip\text{-}Et}NON_{xanth}$)Mg] resulted in the isolation of the anionic Mg(I) dimer [K($^{Trip\text{-}Et}NON_{xanth}$)Mg(I)-Mg(I)($^{Trip\text{-}Et}NON_{xanth}$)K] (**LIX**, **Chart 1.8**), rather than dinitrogen activation. However, **LIX** was found to have similar reactivity to **LVIII**, forming the same ethynediolate and hydride complexes upon its reaction with CO and H_2 respectively. These results, which contrast significantly with those reported by Hicks and co-workers, demonstrated the significant influence that ligand bulk exerts on the reactivity of the transient low-valent Ae(I) radicals proposed to form upon reduction in each case.

1.6 Scope of thesis

The primary aims of this thesis are: (i) to synthesise novel alkaline earth complexes supported by bulky chelating di(amido) ligands and (ii) assess their suitability as precursors for heterobimetallic alkali metal/alkaline earth complexes.

Chapter 2 details the attempted synthesis and characterisation of novel alkaline earth complexes bearing rigid 1,8-*bis*(silylamido)naphthalene ancillary ligands. The unexpected synthetic challenges faced when the synthesis of monomeric THF adducts was attempted will be discussed.

Chapter 3 describes the successful isolation and characterisation of dimeric donor-free alkaline earth complexes bearing phenyl-substituted 1,8-*bis*(silylamido)naphthalene ligands.

Chapter 4 discusses the successful isolation and characterisation of bimetallic donor-free alkaline earth complexes bearing bulky alkyl-substituted 1,8-*bis*(silylamido)naphthalene ligands, which display a diverse range of novel structural

motifs. The characterisation of an unexpected solvent-separated ion pair (SSIP) featuring a new weakly coordinating anion (WCA) is also discussed.

Chapter 5 presents the synthesis and characterisation of novel alkaline earth complexes bearing more flexible di(amido)siloxane ligands, followed by an investigation of their attempted reduction to low-valent species. Results obtained in collaboration with Ms. Andrea O'Reilly and Prof. Martyn Coles at Victoria University of Wellington are also discussed.

1.7 References

1 Global chemical industry revenue 2022 | Statista, https://www.statista.com/statistics/302081/revenue-of-global-chemical-industry/, (accessed 18 July 2024).

2 Defossilising the chemical industry (RSC policy briefing), 2024.

3 R. Geyer, J. R. Jambeck and K. L. Law, *Sci. Adv.*, 2017, **3**, e1700782.

4 D. K. A. Barnes, F. Galgani, R. C. Thompson and M. Barlaz, *Philos. Trans. R. Soc. B Biol. Sci.*, 2009, **364**, 1985–1998.

5 R. Marfella, F. Prattichizzo, C. Sardu, G. Fulgenzi, L. Graciotti, T. Spadoni, N. D'Onofrio, L. Scisciola, R. La Grotta, C. Frigé, V. Pellegrini, M. Municinò, M. Siniscalchi, F. Spinetti, G. Vigliotti, C. Vecchione, A. Carrizzo, G. Accarino, A. Squillante, G. Spaziano, D. Mirra, R. Esposito, S. Altieri, G. Falco, A. Fenti, S. Galoppo, S. Canzano, F. C. Sasso, G. Matacchione, F. Olivieri, F. Ferraraccio, I. Panarese, P. Paolisso, E. Barbato, C. Lubritto, M. L. Balestrieri, C. Mauro, A. E. Caballero, S. Rajagopalan, A. Ceriello, B. D'Agostino, P. Iovino and G. Paolisso, *N. Engl. J. Med.*, 2024, **390**, 900–910.

6 Y. Li, L. Tao, Q. Wang, F. Wang, G. Li and M. Song, *Environ. Heal.*, 2023, **1**, 249–257.

7 T. Keijer, V. Bakker and J. C. Slootweg, *Nat. Chem. 2019 113*, 2019, **11**, 190–195.

8 *Clim. Chang. 2022 - Mitig. Clim. Chang.*, 2023, 1161–1244.

9 M. S. Hill, D. J. Liptrot and C. Weetman, *Chem. Soc. Rev.*, 2016, 45, 972–988.

10 P. P. Power, *Nature*, 2010, **463**, 171–177.

11 C. Weetman and S. Inoue, *ChemCatChem*, 2018, **10**, 4213–4228.

12 M. R. Buchner, *Chem. Commun.*, 2020, **56**, 8895–8907.

13 P. L. Brown, A. V. Matyskin and C. Ekberg, *Radiochim. Acta*, 2022, **110**, 505–513.

14 K. Hans Wedepohl, *Geochim. Cosmochim. Acta*, 1995, **59**, 1217–1232.

15 S. Harder and J. Langer, *Nat. Rev. Chem. 2023 712*, 2023, **7**, 843–853.

16 P. Gao, J. Jiang, S. Maeda, K. Kubota and H. Ito, *Angew. Chemie Int. Ed.*, 2022, **61**, e202207118.

17 B. S. Bhoelan, C. H. Stevering, A. T. J. Van Der Boog and M. A. G. Van Der Heyden, *Clin. Toxicol.*, 2014, **52**, 584–593.

18 S. Harder, *Chem. Rev.*, 2010, **110**, 3852–3876.

19 N. Wiberg, G. Fischer and E. Wiberg, *Lehrb. der Anorg. Chemie*, 2007, 2146–2147.

20 R. D. Shannon, *Acta Crystallogr. A*, 1976, **32**, 751–767.

21 A. L. Allred, *J. Inorg. Nucl. Chem.*, 1961, **17**, 215–221.

22 K. M. Fromm, *Coord. Chem. Rev.*, 2020, **408**, 213193.

23 M. R. Crimmin and M. S. Hill, *Top. Organomet. Chem.*, 2013, **45**, 191–242.

24 P. M. Chapple and Y. Sarazin, *Eur. J. Inorg. Chem.*, 2020, **2020**, 3321–3346.

25 L. A. Freeman, J. E. Walley and R. J. Gilliard, *Nat. Synth.*, 2022, **1**, 439–448.

26 K. Thum, J. Martin, H. Elsen, J. Eyselein, L. Stiegler, J. Langer and S. Harder, *Eur. J. Inorg. Chem.*, 2021, **2021**, 2643–2653.

27 J. Pahl, S. Brand, H. Elsen and S. Harder, *Chem. Commun.*, 2018, **54**, 8685–8688.

28 K. Thum, A. Friedrich, J. Pahl, H. Elsen, J. Langer and S. Harder, *Chem. Eur. J.*, 2021, **27**, 2513–2522.

29 J. Pahl, A. Friedrich, H. Elsen and S. Harder, *Organometallics*, 2018, **37**, 2901–2909.

30 L. J. Morris, N. A. Rajabi, M. F. Mahon, I. Manners, C. L. McMullin and M. S. Hill, *Dalton Trans.*, 2020, **49**, 10523–10534.

31 D. B. Kennedy, M. J. Evans, D. D. L. Jones, J. M. Parr, M. S. Hill and C. Jones, *Chem. Commun.*, 2024, **60**, 10894–10897.

32 T. X. Gentner, B. Rösch, K. Thum, J. Langer, G. Ballmann, J. Pahl, W. A. Donaubauer, F. Hampel and S. Harder, *Organometallics*, 2019, **38**, 2485–2493.

33 Y. Sarazin, B. Liu, T. Roisnel, L. Maron and J. F. Carpentier, *J. Am. Chem. Soc.*, 2011, **133**, 9069–9087.

34 Y. Sarazin and J. F. Carpentier, *CHAPTER 4: Secondary (Agostic Si-H/Electrostatic C-F) interactions in alkaline earth-based catalysts*, Royal Society of Chemistry, 2019.

35 J. Hammoud, F. Abou-Khalil, T. Roisnel, V. Dorcet, C. Bour, V. Gandon, D.

Lebœuf, J. F. Carpentier and Y. Sarazin, *Dalton Trans.*, 2020, **49**, 13017–13028.

36 B. Liu, T. Roisnel, J.-F. Carpentier, Y. Sarazin, B. Liu, T. Roisnel, J.-F. Carpentier and Y. Sarazin, *Angew. Chemie Int. Ed.*, 2012, **51**, 4943–4946.

37 Y. Sarazin, D. Roşca, V. Poirier, T. Roisnel, A. Silvestru, L. Maron and J. F. Carpentier, *Organometallics*, 2010, **29**, 6569–6577.

38 K. P. Kepp, *Inorg. Chem.*, 2016, **55**, 9461–9470.

39 S. Krieck, H. Görls and M. Westerhausen, *Inorg. Chem. Commun.*, 2008, **11**, 911–913.

40 S. Krieck, H. Görls and M. Westerhausen, *Organometallics*, 2008, **27**, 5052–5057.

41 S. Harder, F. Feil and T. Repo, *Chem. Eur. J.*, 2002, **8**, 1991–1999.

42 S. Harder, S. Müller and E. Hübner, *Organometallics*, 2004, **23**, 178–183.

43 I. L. Fedushkin, A. N. Lukoyanov, S. Dechert and H. Schumann, *Eur. J. Inorg. Chem.*, 2004, **2004**, 2421–2424.

44 B. Liu, V. Dorcet, L. Maron, J. F. Carpentier and Y. Sarazin, *Eur. J. Inorg. Chem.*, 2012, **2012**, 3023–3031.

45 C. Lichtenberg, P. Jochmann, T. P. Spaniol and J. Okuda, *Angew. Chemie Int. Ed.*, 2011, **50**, 5753–5756.

46 D. Seyferth, *Organometallics*, 2009, **28**, 1598–1605.

47 A. G. M. Barrett, M. R. Crimmin, M. S. Hill and P. A. Procopiou, *Proc. R. Soc. A*, 2010, **466**, 927–963.

48 A. Rovaletti, L. De Gioia, C. Greco and F. Arrigoni, *Dalton Trans.*, 2023, **52**, 7966–7974.

49 Q. Wang, S. Pan, Y. B. Wu, G. Deng, J. H. Bian, G. Wang, L. Zhao, M. Zhou and G. Frenking, *Angew. Chemie Int. Ed.*, 2019, **58**, 17365–17374.

50 M. Zhou and G. Frenking, *Acc. Chem. Res.*, 2021, **54**, 3071–3082.

51 P. Stegner, C. Färber, J. Oetzel, U. Siemeling, M. Wiesinger, J. Langer, S. Pan, N. Holzmann, G. Frenking, U. Albold, B. Sarkar and S. Harder, *Angew. Chemie Int. Ed.*, 2020, **59**, 14615–14620.

52 Y. Sarazin and J. F. Carpentier, *Chem. Rec.*, 2016, **16**, 2482–2505.

53 R. Waterman, *Organometallics*, 2013, **32**, 7249–7263.

54 J. F. Dunne, S. R. Neal, J. Engelkemier, A. Ellern and A. D. Sadow, *J. Am. Chem. Soc.*, 2011, **133**, 16782–16785.

55 J. S. McMullen, A. J. Edwards and J. Hicks, *Dalton Trans.*, 2021, **50**, 8685–8689.

56 H.-Y. Liu, R. J. Schwamm, S. E. Neale, M. S. Hill, C. L. McMullin and M. F. Mahon, *J. Am. Chem. Soc.*, 2021, **143**, 17851–17856.

57 C. Jones, D. T. Nguyen and C. Helling, *Chem. – An Asian J.*, 2024, **19**,

e202400498.

58 D. T. Nguyen, C. Helling, M. J. Evans and C. Jones, *Inorg. Chem.*, 2024, **63**, 5718–5726.

59 M. J. Evans and C. Jones, *Chem. Soc. Rev.*, 2024, **53**, 5054–5082.

60 H. Elsen, J. Langer, M. Wiesinger and S. Harder, *Organometallics*, 2020, **39**, 4238–4246.

61 H. Bauer, M. Alonso, C. Färber, H. Elsen, J. Pahl, A. Causero, G. Ballmann, F. De Proft and S. Harder, *Nat. Catal.*, 2018, **1**, 40–47.

62 M. D. Anker, C. E. Kefalidis, Y. Yang, J. Fang, M. S. Hill, M. F. Mahon and L. Maron, *J. Am. Chem. Soc.*, 2017, **139**, 10036–10054.

63 B. Liu, T. Roisnel, J. P. Guégan, J. F. Carpentier and Y. Sarazin, *Chem. Eur. J.*, 2012, **18**, 6289–6301.

64 Y. Sarazin and J. F. Carpentier, *Chem. Rev.*, 2015, 115, 3564–3614.

65 M. Rauch, R. C. Roberts and G. Parkin, *Inorg. Chim. Acta*, 2019, **494**, 271–279.

66 F. Buch and S. Harder, *Organometallics*, 2007, **26**, 5132–5135.

67 M. S. Hill, D. J. Liptrot, D. J. Macdougall, M. F. Mahon and T. P. Robinson, *Chem. Sci.*, 2013, **4**, 4212–4222.

68 C. Bellini, C. Orione, J. F. Carpentier and Y. Sarazin, *Angew. Chemie Int. Ed.*, 2016, **55**, 3744–3748.

69 C. Bellini, T. Roisnel, J. F. Carpentier, S. Tobisch and Y. Sarazin, *Chem. Eur. J.*, 2016, **22**, 15733–15743.

70 C. Bellini, V. Dorcet, J. F. Carpentier, S. Tobisch and Y. Sarazin, *Chem. Eur. J.*, 2016, **22**, 4564–4583.

71 C. Bellini, J.-F. Carpentier, S. Tobisch and Y. Sarazin, *Angew. Chemie Int. Ed.*, 2015, **54**, 7679–7683.

72 A. Baishya, T. Peddarao and S. Nembenna, *Dalton Trans.*, 2017, **46**, 5880–5887.

73 L. J. Morris, M. S. Hill, M. F. Mahon, I. Manners, F. S. McMenamy and G. R. Whittell, *Chem. Eur. J.*, 2020, **26**, 2954–2966.

74 E. Le Coz, V. Dorcet, T. Roisnel, S. Tobisch, J. F. Carpentier and Y. Sarazin, *Angew. Chemie Int. Ed.*, 2018, **57**, 11747–11751.

75 A. S. S. Wilson, M. S. Hill, M. F. Mahon, C. Dinoi and L. Maron, *Science*, 2017, **358**, 1168–1171.

76 A. S. S. Wilson, C. Dinoi, M. S. Hill, M. F. Mahon and L. Maron, *Angew. Chem. Int. Ed.*, 2018, **57**, 15500–15504.

77 T. Höllerhage, T. P. Spaniol, A. Carpentier, L. Maron and J. Okuda, *Inorg. Chem.*, 2022, **61**, 3309–3316.

78 D. Schuhknecht, C. Lhotzky, T. P. Spaniol, L. Maron and J. Okuda, *Angew.*

Chemie Int. Ed., 2017, **56**, 12367–12371.

79 M. Wiesinger, B. Maitland, C. Färber, G. Ballmann, C. Fischer, H. Elsen and S. Harder, *Angew. Chemie Int. Ed.*, 2017, **56**, 16654–16659.

80 V. Leich, T. P. Spaniol, L. Maron and J. Okuda, *Angew. Chemie Int. Ed.*, 2016, **55**, 4794–4797.

81 T. Höllerhage, T. P. Spaniol, U. Englert and J. Okuda, *Inorg. Chim. Acta*, 2022, **543**, 121198.

82 R. Kumar, V. Sharma, S. Jain, H. Sharma, K. Vanka and S. S. Sen, *ChemCatChem*, 2022, **14**, e202101788.

83 C. Knüpfer, J. Langer and S. Harder, *ZAAC*, 2023, **650**, e202300226.

84 A. Stasch and C. Jones, *Dalton Trans.*, 2011, **40**, 5659–5672.

85 S. Harder and B. Rösch, *Chem. Commun.*, 2021, **57**, 9354–9365.

86 I. V. Basalov, A. A. Kissel, E. N. Nikolaevskaya, N. O. Druzhkov, A. V. Cherkasov, J. Long, J. Larionova, G. K. Fukin and A. A. Trifonov, *Dalton Trans.*, 2022, **51**, 1995–2004.

87 Y. Liu, K. Zhu, L. Chen, S. Liu and W. Ren, *Inorg. Chem.*, 2022, **61**, 20373–20385.

88 J. Pan, L. Zhang, Y. He, Q. Yu and G. Tan, *Organometallics*, 2021, **40**, 3365–3369.

89 M. Arrowsmith, M. S. Hill and G. Kociok-Köhn, *Organometallics*, 2011, **30**, 1291–1294.

90 M. P. Stevens, E. Spray, I. J. Vitorica-Yrezabal, K. Singh, V. M. Timmermann, L. Sotorrios, S. A. Macgregor and F. Ortu, *Dalton Trans.*, 2022, **51**, 11922–11936.

91 D. W. Stephen, D. Sharma, A. P. Andrews and A. Venugopal, *Dalton Trans.*, 2023, **52**, 1533–1537.

92 M. Luna Barros, M. G. Cushion, A. D. Schwarz, Z. R. Turner and P. Mountford, *Dalton Trans.*, 2019, **48**, 4124–4138.

93 P. M. Chapple, M. Cordier, V. Dorcet, T. Roisnel, J. F. Carpentier and Y. Sarazin, *Dalton Trans.*, 2020, **49**, 11878–11889.

94 P. M. Chapple, S. Kahlal, J. Cartron, T. Roisnel, V. Dorcet, M. Cordier, J. Y. Saillard, J. F. Carpentier and Y. Sarazin, *Angew. Chem. Int. Ed.*, 2020, **59**, 9120–9126.

95 L. Bourget-Merle, M. F. Lappert and J. R. Severn, *Chem. Rev.*, 2002, **102**, 3031–3065.

96 M. Zhong, S. Sinhababu and H. W. Roesky, *Dalton Trans.*, 2020, **49**, 1351–1364.

97 T. X. Gentner, B. Rösch, G. Ballmann, H. L. Jens and S. E. Harder, *Angew. Chemie Int. Ed.*, 2019, **58**, 607–611.

98 G. M. Richardson, M. J. Evans, T. Rajeshkumar, J. A. J. McCone, S. A. Cameron, L. Maron, C. Jones and M. D. Anker, *Chem. Eur. J.*, 2024, **30**, e202400681.

99 W. Yang, A. J. P. White and M. R. Crimmin, *Angew. Chemie Int. Ed.*, 2024, **136**, e202319626.

100 P. Rinke, H. Görls, P. Liebing and R. Kretschmer, *Organometallics*, 2023, **19**, 29.

101 B. M. Chamberlain, M. Cheng, D. R. Moore, T. M. Ovitt, E. B. Lobkovsky and G. W. Coates, *J. Am. Chem. Soc.*, 2001, **123**, 3229–3238.

102 M. H. Chisholm, J. Gallucci and K. Phomphrai, *Chem. Commun.*, 2003, 48–49.

103 A. G. Avent, M. R. Crimmin, M. S. Hill and P. B. Hitchcock, *Dalton Trans.*, 2005, 278–284.

104 S. Harder, J. Brettar, S. Harder and J. Brettar, *Angew. Chemie Int. Ed.*, 2006, **45**, 3474–3478.

105 A. Causero, G. Ballmann, J. Pahl, C. Färber, J. Intemann and S. Harder, *Dalton Trans.*, 2017, **46**, 1822–1831.

106 S. P. Green, C. Jones and A. Stasch, *Angew. Chemie Int. Ed.*, 2008, **47**, 9079–9083.

107 B. Rösch, T. X. Gentner, H. Elsen, C. A. Fischer, J. Langer, M. Wiesinger and S. Harder, *Angew. Chem. Int. Ed.*, 2019, **58**, 5396–5401.

108 M. R. Crimmin, I. J. Casely and M. S. Hill, *J. Am. Chem. Soc.*, 2005, **127**, 2042–2043.

109 M. R. Crimmin, M. Arrowsmith, A. G. M. Barrett, I. J. Casely, M. S. Hill and P. A. Procopiou, *J. Am. Chem. Soc.*, 2009, **131**, 9670–9685.

110 M. D. Anker, M. S. Hill, J. P. Lowe and M. F. Mahon, *Angew. Chemie Int. Ed.*, 2015, **54**, 10009–10011.

111 M. D. Anker, C. E. Kefalidis, Y. Yang, J. Fang, M. S. Hill, M. F. Mahon and L. Maron, *J. Am. Chem. Soc*, 2017, **139**, 10036–10054.

112 W. Yang, A. J. P. White and M. R. Crimmin, *Chem. Sci.*, 2024, **15**, 11807–11813.

113 J. Spielmann and S. Harder, *Chem. Eur. J.*, 2007, **13**, 8928–8938.

114 J. Spielmann, F. Buch and S. Harder, *Angew. Chemie*, 2008, **120**, 9576–9580.

115 M. Wiesinger, B. Rösch, C. Knüpfer, J. Mai, J. Langer and S. Harder, *Eur. J. Inorg. Chem.*, 2021, **36**, 3731– 3741.

116 M. S. Hill, M. F. Mahon, A. S. S. Wilson, C. Dinoi, L. Maron and E. Richards, *Chem. Commun.*, 2019, **55**, 5732–5735.

117 K. G. Pearce, C. Dinoi, M. S. Hill, M. F. Mahon, L. Maron, R. S. Schwamm and A. S. S. Wilson, *Angew. Chemie Int. Ed.*, 2022, **61**, e202200305.

118 K. G. Pearce, C. Dinoi, R. J. Schwamm, L. Maron, M. F. Mahon, M. S. Hill, K. G. Pearce, R. J. Schwamm, M. F. Mahon and M. S. Hill, *Adv. Sci.*, 2023, **10**, 2304765.

119 K. G. Pearce, S. E. Neale, C. L. McMullin, M. F. Mahon and M. Hill, *Chem. Commun.*, 2024, **60**, 7882–7885.

120 M. Garçon, C. Bakewell, G. A. Sackman, A. J. P. White, R. I. Cooper, A. J. Edwards and M. R. Crimmin, *Nat. 2019 5747778*, 2019, **574**, 390–393.

121 J. M. Parr, A. J. P. White and M. R. Crimmin, *Chem. Sci*, 2022, **13**, 6592–6598.

122 J. M. Parr, A. J. P. White and M. R. Crimmin, *Chem. Commun.*, 2023, **59**, 9840–9843.

123 S. P. Green, C. Jones and A. Stasch, *Science*, 2007, **318**, 1754–1757.

124 A. J. Martín, T. Shinagawa and J. Pérez-Ramírez, *Chem*, 2019, **5**, 263–283.

125 J. T. Boronski, *Dalton Trans.*, 2023, **53**, 33–39.

126 A. Stasch, *Angew. Chemie Int. Ed.*, 2014, **53**, 10200–10203.

127 A. J. Boutland, I. Pernik, A. Stasch and C. Jones, *Chem. Eur. J.*, 2015, **21**, 15749–15758.

128 J. T. Boronski, A. E. Crumpton, L. L. Wales and S. Aldridge, *Science*, 2023, **380**, 1147–1149.

129 M. A. Gosch and D. J. D. Wilson, *Organometallics*, 2023, **42**, 2185–2196.

130 J. T. Boronski, A. E. Crumpton, A. F. Roper and S. Aldridge, *Nat. Chem.*, 2024, **16**, 1295–1300.

131 J. Hicks, M. Juckel, A. Paparo, D. Dange and C. Jones, *Organometallics*, 2018, **37**, 4810–4813.

132 D. Jędrzkiewicz, J. Langer and S. Harder, *ZAAC*, 2022, **648**, e202200138.

133 D. Jędrzkiewicz, J. Mai, J. Langer, Z. Mathe, N. Patel, S. DeBeer and S. Harder, *Angew. Chemie*, 2022, **61**, e202200511.

134 B. Rösch, T. X. Gentner, J. Eyselein, J. Langer, H. Elsen and S. Harder, *Nature*, 2021, **592**, 717–720.

135 J. Mai, J. Maurer, J. Langer and S. Harder, *Nat. Synth.*, 2024, **3**, 368–77.

136 J. Mai, B. Rösch, N. Patel, J. Langer and S. Harder, *Chem. Sci.*, 2023, **14**, 4724–4734.

137 C. Berthold, J. Maurer, L. Klerner, S. Harder and M. R. Buchner, *Angew. Chemie Int. Ed.*, 2024, **63**, e202408422.

138 K. Yuvaraj, I. Douair, A. Paparo, L. Maron and C. Jones, *J. Am. Chem. Soc.*, 2019, **141**, 8764–8768.

139 R. Lalrempuia, A. Stasch, A. Stasch and C. Jones, *Chem. Sci.*, 2013, **4**, 4383–4388.

140 F. Rekhroukh, L. Zhang, R. Y. Kong, A. J. P. White and M. R. Crimmin, *Chem. Commun.*, 2022, **58**, 8282–8285.

141 D. J. Sheldon, J. M. Parr and M. R. Crimmin, *J. Am. Chem. Soc.*, 2023, **145**,

10486–10490.

142 D. J. Sheldon, J. M. Parr and M. R. Crimmin, *Dalton Trans.*, 2024, **53**, 6524–6528.

143 D. W. N. Wilson, S. J. Urwin, E. S. Yang and J. M. Goicoechea, *J. Am. Chem. Soc.*, 2021, **143**, 10367–10373.

144 T. Görlich, P. Coburger, E. Yang, J. Goicoechea, H. Grützmacher, C. Müller, E. S. Yang, P. Coburger, H. Grützmacher, E. S. Yang and J. M. Goicoechea, *Angew. Chemie Int. Ed.*, 2023, **62**, e202217749.

145 S. Krieck, H. Görls, L. Yu, M. Reiher and M. Westerhausen, *J. Am. Chem. Soc.*, 2009, **131**, 2977–2985.

146 B. Rösch, T. X. Gentner, J. Langer, C. Färber, J. Eyselein, L. Zhao, C. Ding, G. Frenking and S. Harder, *Science*, 2021, **371**, 1125–1128.

147 B. Rösch, T. X. Gentner, J. Langer, C. Färber, J. Eyselein, L. Zhao, C. Ding, G. Frenking and S. Harder, *Science*, 2021, **371**, 1125–1128.

148 J. Mai, B. Rösch, J. Langer, S. Grams, M. Morasch, S. Harder, J. Mai, B. Rösch, J. Langer, S. Grams, M. Morasch and S. Harder, *Eur. J. Inorg. Chem.*, 2023, **26**, e202300421.

149 J. Mai, M. Morasch, D. Jędrzkiewicz, J. Langer, B. Rösch and S. Harder, *Angew. Chemie Int. Ed.*, 2022, **62**, e202212463.

150 O. P. E. Townrow, C. Färber, U. Zenneck and S. Harder, *Angew. Chemie Int. Ed.*, 2023, **63**, e202318428.

151 I. L. Fedushkin, A. A. Skatova, V. A. Chudakova, G. K. Fukin, S. Dechert and H. Schumann, *Eur. J. Inorg. Chem.*, 2003, **2003**, 3336–3346.

152 R. L. Jones, Z. R. Turner, J.-C. Buffet and D. O'Hare, *Organometallics*, 2024, **43**, 414–426.

153 I. L. Fedushkin, V. A. Chudakova, A. A. Skatova, N. M. Khvoinova, Y. A. Kurskii, T. A. Glukhova, G. K. Fukin, S. Dechert, M. Hummert and H. Schumann, *ZAAC*, 2004, **630**, 501–507.

154 I. L. Fedushkin, A. G. Morozov, V. A. Chudakova, G. K. Fukin and V. K. Cherkasov, *Eur. J. Inorg. Chem.*, 2009, **33**, 4995–5003.

155 J. Gao, Y. Liu, Y. Zhao, X. J. Yang and Y. Sui, *Organometallics*, 2011, **30**, 6071–6077.

156 B. Gao, D. Zhao, X. Li, Y. Cui, R. Duan and X. Pang, *RSC Adv.*, 2014, **5**, 440–447.

157 M. Ma, H. Wang, J. Wang, L. Shen, Y. Zhao, W. H. Xu, B. Wu and X. J. Yang, *Dalton Trans.*, 2019, **48**, 2295–2299.

158 T. K. Panda, H. Kaneko, O. Michel, K. Pal, H. Tsurugi, K. W. Törnroos, R. Anwander and K. Mashima, *Organometallics*, 2012, **31**, 3178–3184.

159 M. V. Moskalev, A. A. Skatova, D. A. Razborov, A. A. Bazanov, N. L. Bazyakina,

V. G. Sokolov and I. L. Fedushkin, *Eur. J. Inorg. Chem.*, 2021, **2021**, 1890–1896.

160 I. L. Fedushkin, N. M. Khvoinova, A. A. Skatova and G. K. Fukin, *Angew. Chemie Int. Ed.*, 2003, **42**, 5223–5226.

161 I. L. Fedushkin, A. G. Morozov, O. V. Rassadin and G. K. Fukin, *Chem. Eur. J.*, 2005, **11**, 5749–5757.

162 N. L. Bazyakina, V. M. Makarov, S. Y. Ketkov, A. S. Bogomyakov, R. V. Rumyantcev, V. I. Ovcharenko and I. L. Fedushkin, *Inorg. Chem.*, 2021, **60**, 3238–3248.

163 A. G. Morozov, M. V. Moskalev, D. A. Razborov and I. L. Fedushkin, *J. Organomet. Chem.*, 2020, **927**, 121535.

164 B. Freitag, C. A. Fischer, J. Penafiel, G. Ballmann, H. Elsen, C. Färber, D. F. Piesik and S. Harder, *Dalton Trans.*, 2017, **46**, 11192–11200.

165 R. K. Kottalanka, H. Adimulam, J. Bhattacharjee, H. Vignesh Babu and T. K. Panda, *Dalton Trans.*, 2014, **43**, 8757–8766.

166 J. Bhattacharjee, A. Harinath, H. P. Nayek, A. Sarkar and T. K. Panda, *Chem. Eur. J.*, 2017, **23**, 9319–9331.

167 J. Bhattacharjee, A. Harinath, A. Sarkar and T. K. Panda, *ChemCatChem*, 2019, **11**, 3366–3370.

168 R. L. Jones, Z. R. Turner, J.-C. Buffet and D. O'Hare, *Polym. Chem.*, 2024, **15**, 1767–1776.

169 J. Hicks, P. Vasko, J. M. Goicoechea and S. Aldridge, *Nature*, 2018, **557**, 92–95.

170 M. P. Coles and M. J. Evans, *Chem. Commun.*, 2023, **59**, 503–519.

171 R. J. Schwamm, M. P. Coles, M. S. Hill, M. F. Mahon, C. L. McMullin, N. A. Rajabi and A. S. S. Wilson, *Angew. Chemie Int. Ed.*, 2020, **59**, 3928–3932.

172 K. G. Pearce, M. S. Hill and M. F. Mahon, *Chem. Commun.*, 2023, **59**, 1453–1456.

173 J. S. McMullen, R. Huo, P. Vasko, A. J. Edwards and J. Hicks, *Angew. Chemie Int. Ed.*, 2022, **62**, e2022152.

174 C. Jones, D. T. Nguyen, C. Helling and M. J. Evans, *Inorg. Chem.*, 2024, **63**, 5718–5726.

175 D. T. Nguyen, M. J. Evans and C. Jones, *J. Organomet. Chem.*, 2024, **1012**, 123143.

176 Y. Liu, S. Li, X. J. Yang, P. Yang and B. Wu, *J. Am. Chem. Soc.*, 2009, **131**, 4210–4211.

177 J. C. Mullins, K. Yuvaraj, Y. Jiang, G. P. Van Trieste, A. Maity, D. C. Powers and C. Jones, *Chem. Eur. J.*, 2022, **28**, e202202103.

178 S. P. Green, C. Jones and A. Stasch, *Angew. Chemie Int. Ed.*, 2008, **47**, 9079–9083.

179 H.-Y. Liu, S. E. Neale, M. S. Hill, M. F. Mahon, C. L. McMullin and E. Richards, *Organometallics*, 2024, **43**, 879–888.

180 H.-Y. Liu, S. E. Neale, M. S. Hill, M. F. Mahon, C. L. McMullin and B. L. Morrison, *Chem. Commun.*, 2023, **59**, 3846–3849.

181 H.-Y. Liu, S. E. Neale, M. S. Hill, M. F. Mahon, C. L. Mcmullin, E. Richards, M. S. Hill and C. L. M C Mullin, *Angew. Chemie Int. Ed.*, 2022, **62**, e202213670.

182 K. G. Pearce, H.-Y. Liu, S. E. Neale, H. M. Goff, M. F. Mahon, C. L. McMullin and M. S. Hill, *Nat. Commun.*, 2023, **14**, 1–5.

183 M. Hill, K. G. Pearce, S. E. Neale, M. F. Mahon and C. L. McMullin, *Chem. Commun.*, 2024, **60**, 8391–8394.

184 R. Huo, A. J. Armstrong, G. R. Nelmes, D. J. Lawes, A. J. Edwards, C. L. McMullin and J. Hicks, *Chem. Eur. J.*, 2024, **30**, e202400662.

185 J. J. C. Struijs, M. A. Ellwanger, A. E. Crumpton, V. Gouverneur and S. Aldridge, *Nat. Chem.*, 2024, **16**, 1473–1480.

186 C. Patel, E. André-Joyaux, J. A. Leitch, X. M. de Irujo-Labalde, F. Ibba, J. Struijs, M. A. Ellwanger, R. Paton, D. L. Browne, G. Pupo, S. Aldridge, M. A. Hayward and V. Gouverneur, *Science*, 2023, **381**, 302–306.

187 R. Mondal, K. Yuvaraj, T. Rajeshkumar, L. Maron and C. Jones, *Chem. Commun.*, 2022, **58**, 12665–12668.

188 R. Mondal, M. J. Evans, T. Rajeshkumar, L. Maron and C. Jones, *Angew. Chem. Int. Ed*, 2023, **62**, e202308347.

189 M. J. Evans, J. Mullins, R. Mondal and C. Jones, *Chem. Eur. J.*, 2024, **30**, e202401005.

Chapter 2

Synthesis and characterisation of monomeric 1,8-*bis*(silylamido)naphthalene alkaline earth complexes

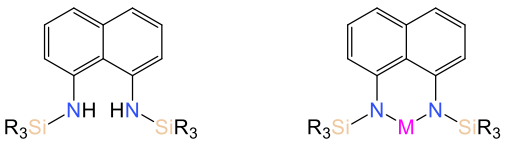
2.1 Introduction

2.1.1 Overview

This chapter discusses the outcomes of attempts to synthesise novel diamido alkaline earth complexes bearing dianionic 1,8-*bis*(silylamido)naphthalene ligands ($[^{R_3}L]^{2-}$ = $[1,8\text{-}\{(R_3Si)N\}_2C_{10}H_6]^{2-}$). Protonolysis reactions of the corresponding 1,8-*bis*(silylamino)naphthalene proligands ($^{R_3}LH_2$, $1,8\text{-}\{(R_3Si)NH\}_2C_{10}H_6$) with alkaline earth *bis*(hexamethyldisilazide) ($[AeN"_2]$, N" = $[N(SiMe_3)_2]^-$) bases in THF were attempted. The isolation and characterisation of both novel proligand species and two monomeric magnesium complexes is presented. This is followed by a discussion of the unexpected synthetic challenges faced when the synthesis of heavier alkaline earth (Ae = Ca, Sr and Ba) complexes was attempted *via* this route.

2.1.2 Previously reported 1,8-*bis*(silylamido)naphthalene metal complexes

1,8-*bis*(silylamino)naphthalene proligands ($^{R3}LH_2$ = 1,8-{$(R_3Si)NH\}_2C_{10}H_6$) consist of a rigid naphthalene backbone bridging between two amino groups, which are each functionalised with bulky silyl substituents. These can be doubly deprotonated to form dianionic 1,8-*bis*(silylamido)naphthalene ligands ($[^{R3}L]^{2-}$ = 1,8-{$(R_3Si)N\}_2C_{10}H_6$) coordinated to a cationic metal centre (**Chart 2.1**).



$^{R3}LH_2$ $[(^{R3}L)M]$

Chart 2.1 A generic 1,8-bis(silylamino)naphthalene proligand, $^{R3}LH_2$, and a generic 1,8-bis(silylamido)naphthalene metal complex, $[(^{R3}L)M]$.

The rigidity and small N-N distances of these ligands render their metal binding pocket extremely basic, as evidenced by the marketing of the related species 1,8-*bis*(dimethylamino)naphthene as "proton sponge".[1] The straightforward synthesis of $^{R3}LH_2$ from 1,8-diaminonaphthalene and a wide array of commercially available silylchlorides enables the facile modulation of both the steric and electronic properties of these proligands.[2] The trimethyl-substituted derivative $^{Me3}LH_2$ has been known since the 1970s, when it was first reported and used to synthesise the Sn(II) complex $[(^{Me3}L)Sn]$.[3,4] This was followed in 1998 by reports from Gade and co-workers of the dilithium salt $[(^{Me3}L)\{Li(THF)\}_2]$,[5] which was used to prepare dithallium and mixed lithium/thallium complexes *via* salt metathesis.[6] A number of additional $^{R3}LH_2$ variants (R_3 = Et_3, $^iPr_3$, $Me_2{}^tBu$, $PhMe_2$ and Ph_2Me) were subsequently reported by Gade and co-workers.[2] A range of transition metal complexes supported by $[^{R3}L]^{2-}$ ligands have subsequently been

reported.[7–11] A number of reports also relate to notable p-block species (**Chart 2.2**), including In-In[6] and Tl-Tl[2] bonded dimers reported by Gade and co-workers (**I** and **II** respectively). Roesky, Stalke and co-workers have since described the isolation of a Bi(II)-Bi(II) bonded dimer (**III**).[12] Subsequently, Chitnis and co-workers have reported a number of notable heavy p-block species supported by $[^{R}3L]^{2-}$, including the first reported example of a Bi-Sb bond (**IV**)[13] and reactive antimony hydrides capable of hydrostibination.[14] A computational study suggested that dispersion interactions between the bulky silyl substituents of the $[^{R}3L]^{2-}$ ligands play a major role in stabilising these relatively weak bonds between heavy elements.[15] Conversely, an attempt by Andrada and co-workers to reduce the aluminium iodide complex $[(^{Me}3L)AlI]$ resulted in the activation of the benzene solvent (**V**) rather than the formation of an Al-Al bond or an anionic aluminyl compound.[15] In addition, the lead complex $[(^{Me}3L)Pb]$ has also been reported and shown to react with ammonia due to the high basicity of its Pb-N bonds. This enabled the isolation of the mixed amino/amido species $[(\kappa^1\text{-N-}^{Me}3LH)Pb(\mu\text{-}NH_2)]_2$ (**VI**), which could be trapped at −40 °C.[16]

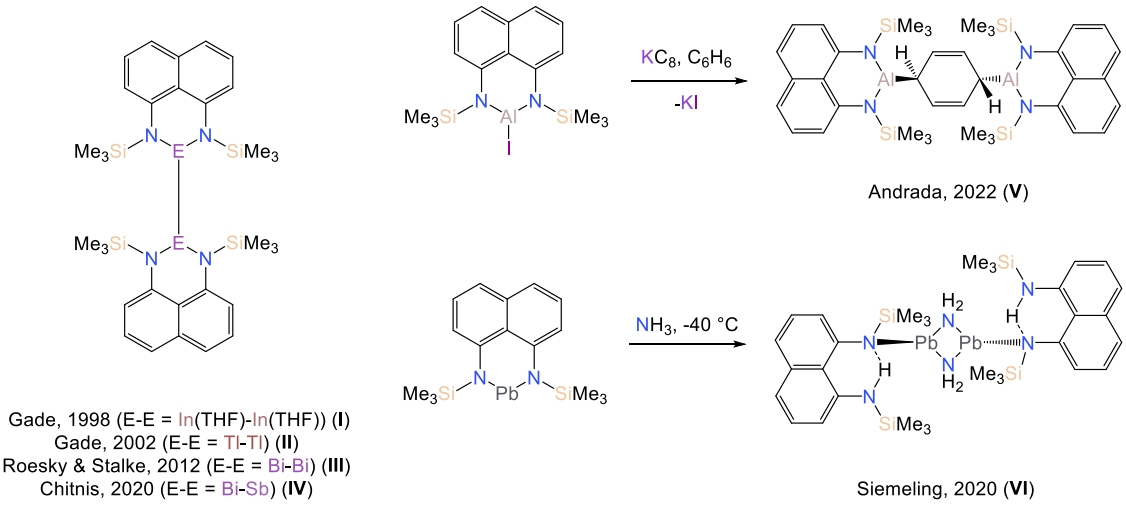


Chart 2.2 Selected examples of previously reported p-block complexes supported by 1,8-*bis*(silylamido)naphthalene ligands.

In contrast, there have been relatively few reports of s-block complexes bearing 1,8-*bis*(silylamido)naphthalene ligands, excluding dilithium salts which have often been employed as salt metathesis reagents.[2,5,17,18] A mixed Mg/Li complex has also been reported,[18] while in 2017 Kays and co-workers reported both mono- and bimetallic Mg(II) complexes (**VII** and **VIII** respectively, **Chart 2.3**).[10] Heavier alkaline earth complexes (Ae = Ca, Sr and Ba) supported by $[^{R3}L]^{2-}$ have not been previously reported, and so the monomeric THF adducts $[(^{R3}L)Ae(THF)_n]$ were chosen as the initial synthetic targets of this Thesis research.

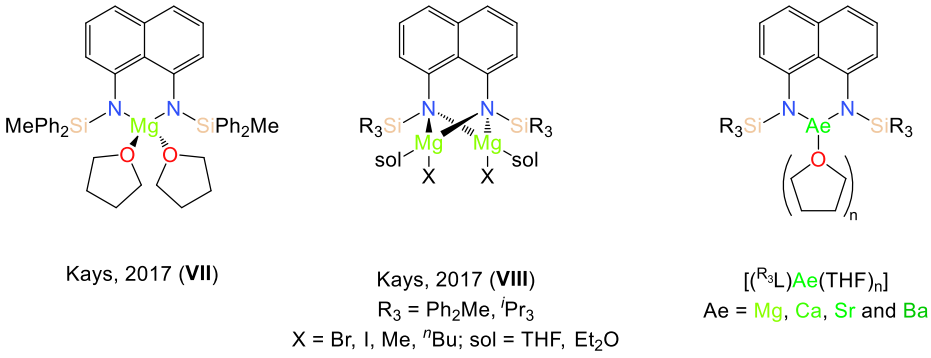


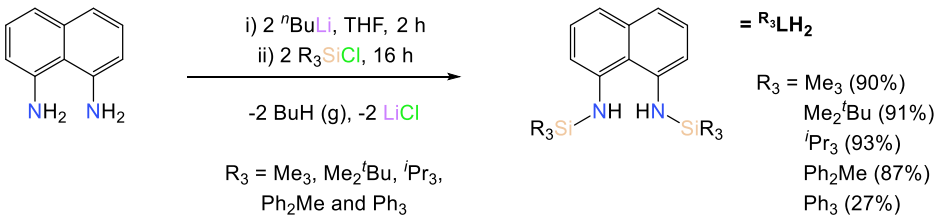
Chart 2.3 Selected examples of previously reported magnesium complexes supported by 1,8-*bis*(silylamido)naphthalene proligands, and the synthetic targets of this chapter, $[(^{R3}L)Ae(THF)_n]$.

2.2 Proligand synthesis and characterisation

2.2.1 Succesful proligand synthesis

The proligands $^{R3}LH_2$ (R_3 = Me_3, $Me_2{}^tBu$, $^iPr_3$ and Ph_2Me) were prepared using a previously reported two-step procedure (**Scheme 2.1**).[2] The dilithiation of 1,8-diaminonaphthalene was achieved using two equivalents of *n*-butyllithium in THF at –30 °C. The subsequent *in situ* reaction of the dilithium salt with two equivalents of the

appropriate silyl chloride afforded $^{R3}LH_2$ as off-white powders in 87–93% yield. The novel proligand $^{Ph3}LH_2$ (**1**) was also prepared *via* this route, though in lower yield (27%)



Scheme 2.1 Synthesis of $^{R3}LH_2$ (R_3 = Me_3, $Me_2{}^tBu$, $^iPr_3$, Ph_2Me and Ph_3).

2.2.1.1 NMR spectroscopic analysis

The ^1H NMR spectra of all previously reported proligands agreed well with those found in the literature.[2] The novel proligand **1** was analysed by multinuclear NMR spectroscopy, with the ^1H spectrum of **1** presented as a representative example (**Figure 2.1**). The aromatic region consists of three naphthyl signals (δ = 7.11, 6.86 and 6.74 ppm) which resonate at lower frequencies than three phenyl signals (δ = 7.53, 7.31 and 7.20 ppm). In addition, a singlet integrating to two at δ = 6.67 ppm corresponds to the two amino protons. This spectrum reflects the C_{2v}-symmetric structure of $^{R3}LH_2$ in

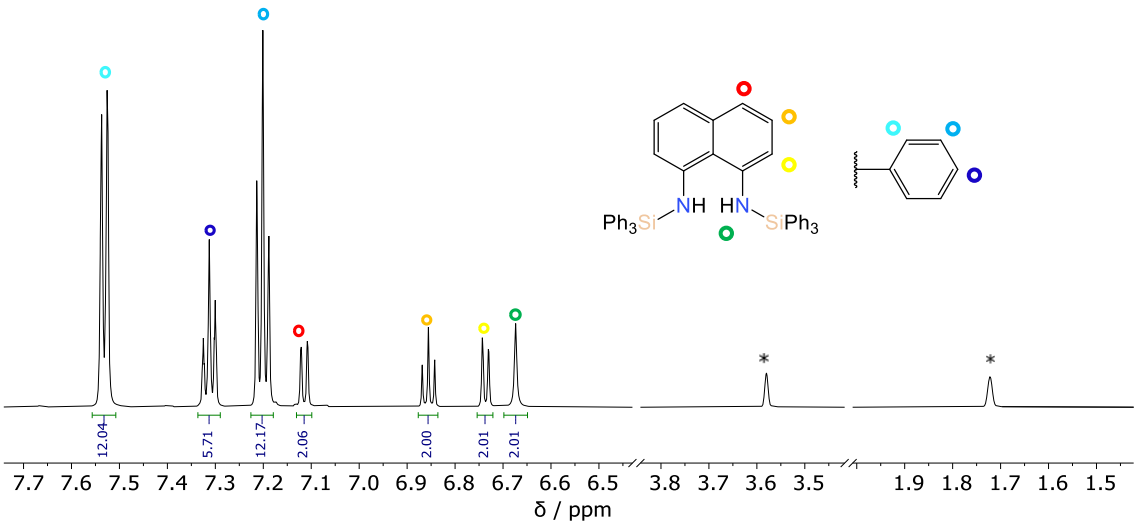


Figure 2.1 ^1H NMR spectrum (C_4D_8O, 298 K, 600.4 MHz) of $^{Ph3}LH_2$ (**1**).

* denotes residual protio fraction of C_4D_8O.

solution, with both amino protons sharing the same chemical environment. This symmetry is confirmed by the presence of six naphthyl resonances in the $^{13}C\{^{1}H\}$ spectrum of **1** and one signal at δ = 19.89 ppm in its ^{29}Si spectrum.

The chemical shifts of the amino protons of $^{R_3}LH_2$, δ(N-H), act as a useful probe for determining the relative acidities of these proligands (**Table 2.1**). The amino singlet moves to a higher frequency in the order Ph_3 > Ph_2Me > Me_3 > $Me_2{}^tBu$ > $^iPr_3$. This demonstrates the electron-withdrawing influence exerted by phenyl substituents, which result in more acidic and deshielded amino protons. Conversely, bulky *tert*-butyl and *iso*-propyl groups result in more shielded and less acidic amino functionalities due to the electron-donating influence of these bulky substituents. The δ(N-H) value of the least bulky proligand $^{Me_3}LH_2$ is consequently intermediate between its phenyl- and bulky alkyl-substituted analogues. This trend was found to significantly influence the reactivity of these proligands with $[(THF)_2AeN''_2]$ (Ae = Ca, Sr and Ba, **Section 2.4**).

Table 2.1 Chemical shifts of the amino signals, δ(N-H), in the ^1H NMR spectra (THF-d_8, 298 K, 400 MHz of the proligands $^{R_3}LH_2$ (R_3 = Ph_3, Ph_2Me, Me_3, $Me_2{}^tBu$ and $^iPr_3$).

R_3	δ(N-H) / ppm
$^iPr_3$	5.39
$Me_2{}^tBu$	6.11
Me_3	6.38
Ph_2Me	6.65
Ph_3	6.67

2.2.1.2 X-ray crystallographic analysis

Large colourless single crystals of **1** suitable for X-ray diffraction analysis grew from a saturated toluene/*n*-pentane solution (**Figure 2.2a**, **Table A.3**). Proligand **1** crystallises in the $P\bar{1}$ space group with two crystallographically independent $^{Ph3}LH_2$ molecules in the asymmetric unit. There is no statistically significant difference between the metrical parameters of these, so only one set of metrics is discussed. Notably, the crystal structure of **1** consists of two distinct amino proton environments. One proton sits in the plane of the naphthalene backbone and forms an intramolecular NH--N hydrogen bond between the two amino groups (N(1)-H(2) = 2.11(2) Å, (N(1)-H(2)-N(2) = 140(2)°). Conversely, the other amino proton is projected out of the plane of the naphthalene backbone. This structure agrees well with those reported previously for $^{Ph2Me}LH_2$ and $^{iPr3}LH_2$,[10] and demonstrates the high basicity of the N,N pocket.[1] This contrasts with the C_{2v}-symmetric structures of $^{R3}LH_2$ inferred from NMR spectroscopic analysis, suggesting that in solution the two amino protons rapidly exchange between the two distinct positions they occupy in the solid state.

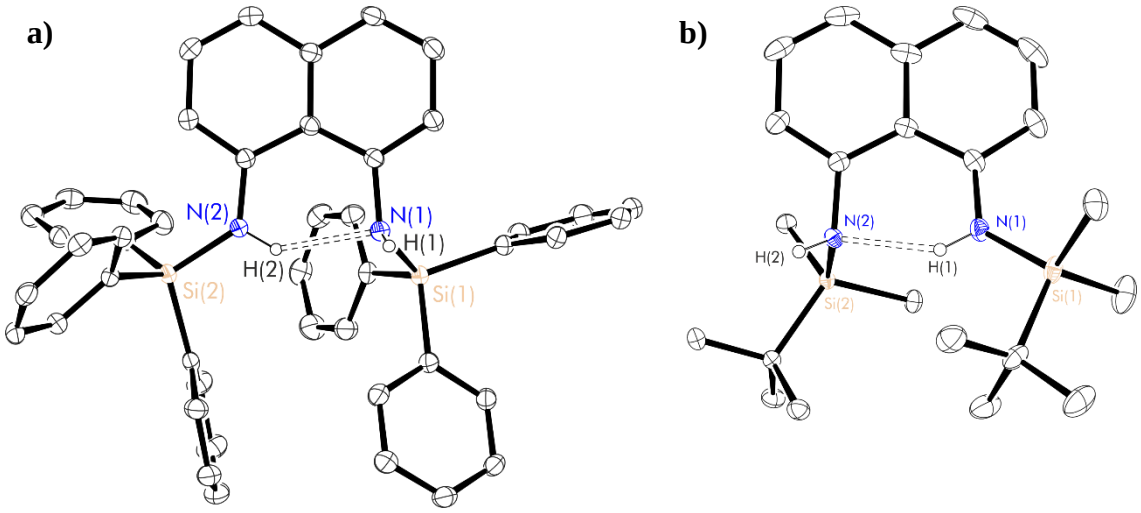


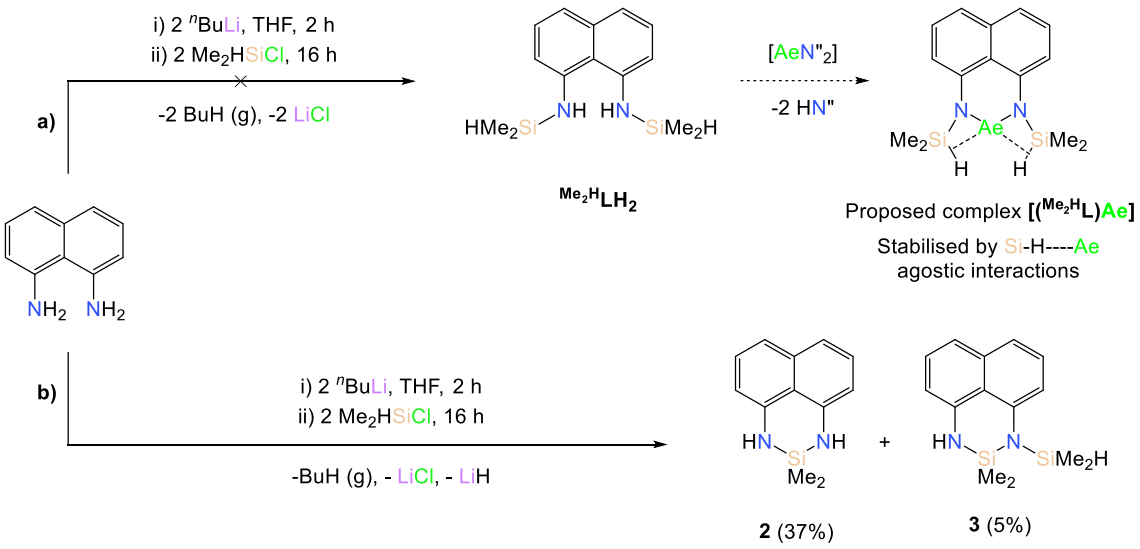
Figure 2.2 Thermal displacement ellipsoid drawings (30%) of **a)** $^{Ph3}LH_2$ (**1**) and **b)** $^{Me2tBu}LH_2$.

All non-amino hydrogen atoms have been omitted for clarity.

While the proligands $^{Me3}LH_2$ and $^{Me2tBu}LH_2$ have been reported previously,[2] they have not been characterised in the solid state. Consequently, single crystals of $^{Me3}LH_2$ and $^{Me2tBu}LH_2$ were grown by slow evaporation of saturated pentane solutions at –30 °C. Their solid-state structures were determined by X-ray diffraction (**Table A.3**) to allow for comparison with both other proligands and novel complexes. The crystal structure of $^{Me2tBu}LH_2$ is presented as a representative example (**Figure 2.2b**, see **Figure A.27** for $^{Me3}LH_2$). These structures are very similar to those already discussed, and notably also each feature an intramolecular hydrogen bond between their two amino groups. This is consistent with the results of subsequent protonolysis reactions, which showed that the deprotonation of both amino groups can be challenging due to a preference for the retention of the strong intramolecular hydrogen-bond observed in the solid-state (*vide infra*).

2.2.2 Attempted synthesis of $^{Me2H}LH_2$

The synthesis of the novel dimethylsilyl-substituted proligand $^{Me2H}LH_2$ was also attempted using the same previously reported literature procedure. It was hypothesised that the presence of Si-H moieties capable of forming agostic interactions with low-coordinate Ae^{2+} centres would stabilise the corresponding alkaline earth complexes (**Scheme 2.2a**). However, this instead resulted in the unexpected isolation of $^{\mu\text{-}Me2}LH_2$ (1,8-$(NH)_2$-(N,N′-Me_2Si)-$C_{10}H_6$, **2**) and the novel compound $^{Me2H\text{-}\mu\text{-}Me2}LH$ (1-(NH)-(N,N′-$SiMe_2$)-8-{$(Me_2HSi)N$}-$C_{10}H_6$, **3**) as the major (37%) and minor (5%) products respectively (**Scheme 2.2b**).



Scheme 2.2 a) Attempted synthesis of $^{Me_2H}LH_2$ for the proposed synthesis of [(^{Me_2H}L)Ae], **b)** unexpected isolation of $^{\mu\text{-}Me_2}LH_2$ (**2**) and $^{Me_2H\text{-}\mu\text{-}Me_2}LH$ (**3**).

2.2.2.1 NMR spectroscopic analysis

Unlike for the other proligands, ^{1}H HMR spectra of the crude reaction mixture revealed the presence of two species, neither of which could be assigned as the expected product $^{Me_2H}LH_2$. Fractional crystallisation from *n*-pentane enabled the separation of the two products and the recording of clean NMR spectra for each. Comparison of the ^{1}H NMR spectrum of the major product with a report from Lappert and co-workers confirmed its identity as **2**, which was originally synthesised deliberately *via* an alternative route.[19] Conversely, the minor product **3** has not been reported previously. The ^{1}H NMR spectrum of **3** (**Figure 2.3**) consists of six naphthyl resonances between 7.30–6.25 ppm which each integrate to one, suggesting that the plane of symmetry through the C(9)-C(10) axis of the naphthalene backbone (which is present in both **2** and $^{R_3}LH_2$) has been lost. This asymmetry is confirmed by the presence of 10 naphthyl peaks in the ^{13}C{^{1}H} NMR spectrum of **3**, as well as two signals at δ = –6.75 and –13.00 ppm in the ^{29}Si NMR spectrum. Furthermore, the methyl region in the ^{1}H NMR spectrum consists of a doublet

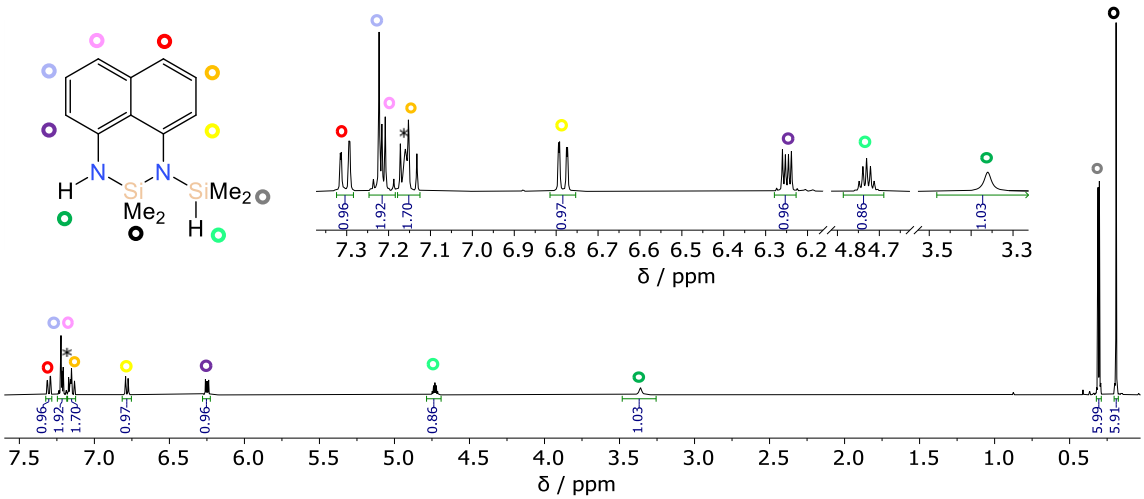


Figure 2.3 ^{1}H NMR spectrum (C_6D_6, 298 K, 400 MHz) of $^{Me_2H\text{-}\mu\text{-}Me_2}$LH (**3**).

* denotes residual protio fraction of C_6D_6. Expansion shows non-methyl proton environments.

(δ = 0.31 ppm) and a singlet (δ = 0.19 ppm) that each integrate to six, with a ^{1}H-^{1}H COSY spectrum confirming the mutual coupling of the doublet with a heptet at δ = 4.73 ppm ($^{3}J_{H\text{-}H}$ = 3.6 Hz). Combined, these three signals imply the presence of both N-SiMe$_2$H and N-SiMe$_2$-N groups in **3**. The ^{29}Si-^{1}H HMBC spectrum of **3** contains a $^{3}J_{Si\text{-}H}$ correlation between the SiMe$_2$H septet in the ^{1}H NMR spectrum and the signal at δ = –6.75 ppm in the ^{29}Si NMR spectrum. This confirms that **3** contains the same N-SiMe$_2$-N group as **2**, as the correlation of the Si-H proton and N-SiMe$_2$-N silicon results from the two silicon atoms being bonded to the same nitrogen atom. Furthermore, the amino singlet at δ = 3.36 ppm in the ^{1}H NMR spectrum only integrates to one relative to the combined integrals of the six naphthyl protons, confirming the loss of three protons from the 1,8-diaminonaphthalene starting material as opposed to the two expected. Notably, this singlet resonates at a significantly lower frequency than those in the ^{1}H NMR spectra of ^{R_3}LH$_2$ (**Table 2.1**), which is assumedly due to the absence of an intramolecular hydrogen bond in **3**.

2.2.2.2 X-ray crystallographic analysis of $^{Me_2H\text{-}\mu\text{-}Me_2}$LH (3)

Storage of a concentrated *n*-pentane solution of **3** at -30 °C resulted in the growth of pink crystals suitable for X-ray diffraction. **3** crystallises in the $P2_1/c$ space group (**Figure 2.4**, **Table A.4**), Gratifyingly, the crystal structure of **3** agrees well with the connectivity proposed based on NMR spectroscopic analysis, exhibiting both the asymmetry and absence of intramolecular hydrogen bonding that results from the presence of both N-$SiMe_2H$ and N-$SiMe_2$-N groups.

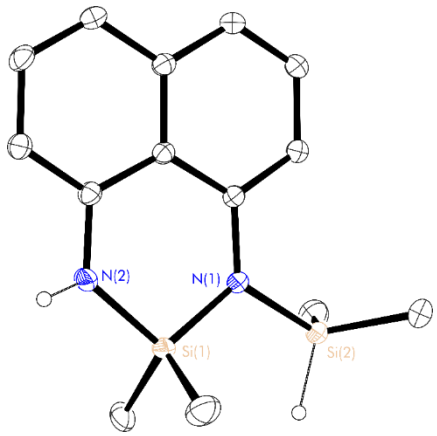


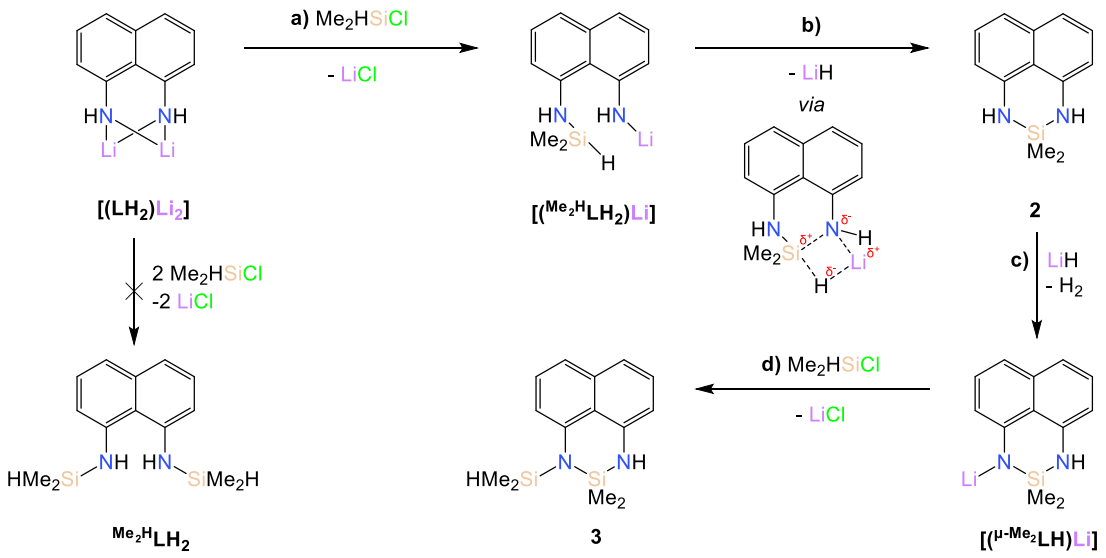
Figure 2.4 Thermal displacement ellipsoid drawings (30%) of $^{Me_2H\text{-}\mu\text{-}Me_2}$LH (**3**).

All hydrogen atoms, excluding N-H and Si-H atoms, have been omitted for clarity.

2.2.2.3 Proposed mechanism

The mechanism for the formation of **2** and **3** is not immediately obvious, as it requires the unexpected cleavage of a Si-H bond. Based on the available evidence, a four-step mechanism is proposed in which **2** forms initially followed by its partial conversion to **3** (**Scheme 2.3**). In the first step (**a**), the reaction of [$(LH_2)Li_2$] with the first equivalent of Me_2HSiCl results in the formation of the expected intermediate species [($^{Me_2H}LH_2$)Li]. However, this clearly does not react with a second equivalent of the silylating agent as expected. Instead, it is proposed that an intramolecular σ-bond metathesis reaction, which

proceeds *via* a concerted four-membered transition stage,[20] results in the elimination of lithium hydride (**b**). This results in Si-H bond cleavage and the formation of a new N-Si bond, affording **2**. Further deprotonation of **2** then results from its reaction with the equivalent of lithium hydride released in the previous step, resulting in the formation of the intermediate [($^{\mu\text{-Me}_2\text{H}}$LH)Li] and the evolution of dihydrogen (**c**). [($^{\mu\text{-Me}_2\text{H}}$LH)Li] then reacts with the second equivalent of Me_2HSiCl, affording **3** (**d**). The incomplete conversion of **2** into **3** is attributed to the low solubility of lithium hydride. A ^{7}Li NMR spectrum of the precipitate formed over the course of the reaction contains a very broad signal ranging from 0.0 to 1.8 ppm. This signal is inconclusive, but does not exclude the elimination of both lithium hydride and lithium chloride.[21] In addition, the evolution of gas was observed following the addition of the silyl chloride, supporting the suggestion that H_2 is released. This proposed mechanism agrees well with a previous report which described the fragmentation of lithiated derivatives of the [^{Me_3}L]$^{2-}$ ligand *via* the elimination of methylithium.[19]



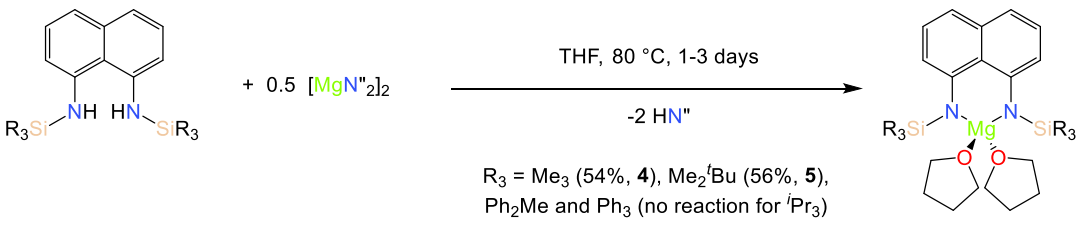
Scheme 2.3 Proposed mechanism for the formation of **2** and **3**.

Neither **2** or **3** were of interest for use as proligands due to the occupation of their proposed metal binding pockets by a N-SiMe$_2$-N group. However, the crystallographic verification of the unsymmetrical structure of compound **3** proved useful subsequently when determining the structures of alkaline earth complexes featuring similar motifs (**Section 2.4.1.3**). The synthesis of $^{Me_2H}LH_2$ was not pursued further.

2.3 Synthesis and characterisation of 1,8-*bis*(silylamido)naphthalene magnesium complexes

2.3.1 Synthesis of monomeric magnesium complexes

While [(^{Ph_2Me}L)Mg(THF)$_2$] (**VIII**, **Chart 2.2**) has been reported previously by Kays and co-workers,[10] no other monometallic magnesium complexes supported by [^{R_3}L]$^{2-}$ are known. The synthesis of [(^{R_3}L)Mg(THF)$_n$] (R$_3$ = Me$_3$, Me$_2$^{t}Bu, ^{i}Pr$_3$ and Ph$_3$) was therefore targeted. Each proligand was reacted with [MgN"$_2$]$_2$ in a 2:1 ratio (**Scheme 2.4**) in THF-d_8, with the reactions monitored *in situ* by ^{1}H NMR spectroscopy. This showed quantitative (>99%) conversion to [(^{R_3}L)Mg(THF)$_n$] in most cases (R$_3$ = Me$_3$, Me$_2$^{t}Bu and Ph$_3$). Subsequently, the R$_3$ = Me$_3$ (**4**) and Me$_2$^{t}Bu (**5**) derivatives were isolated in 54% and 56% yields respectively and additionally characterised by multi-nuclear NMR and IR spectroscopy, X-ray diffraction, and elemental analysis. However, degradation during work-up prevented the isolation of [(^{Ph_3}L)Mg(THF)$_2$].



Scheme 2.4 Synthesis of [(^{R_3}L)Mg(THF)$_2$] (R$_3$ = Me$_3$ (**4**), Me$_2$^{t}Bu (**5**), Ph$_2$Me and Ph$_3$).

2.3.2 *In situ* NMR spectroscopic analysis

In all cases, minimal reactivity was observed at 25 °C. However, conversion to the target diamido complexes [(^{R3}L)Mg(THF)$_n$] and the concomitant release of two equivalents of HN" was afforded in most cases upon heating the reaction mixture at 80 °C (**Figure 2.5**).

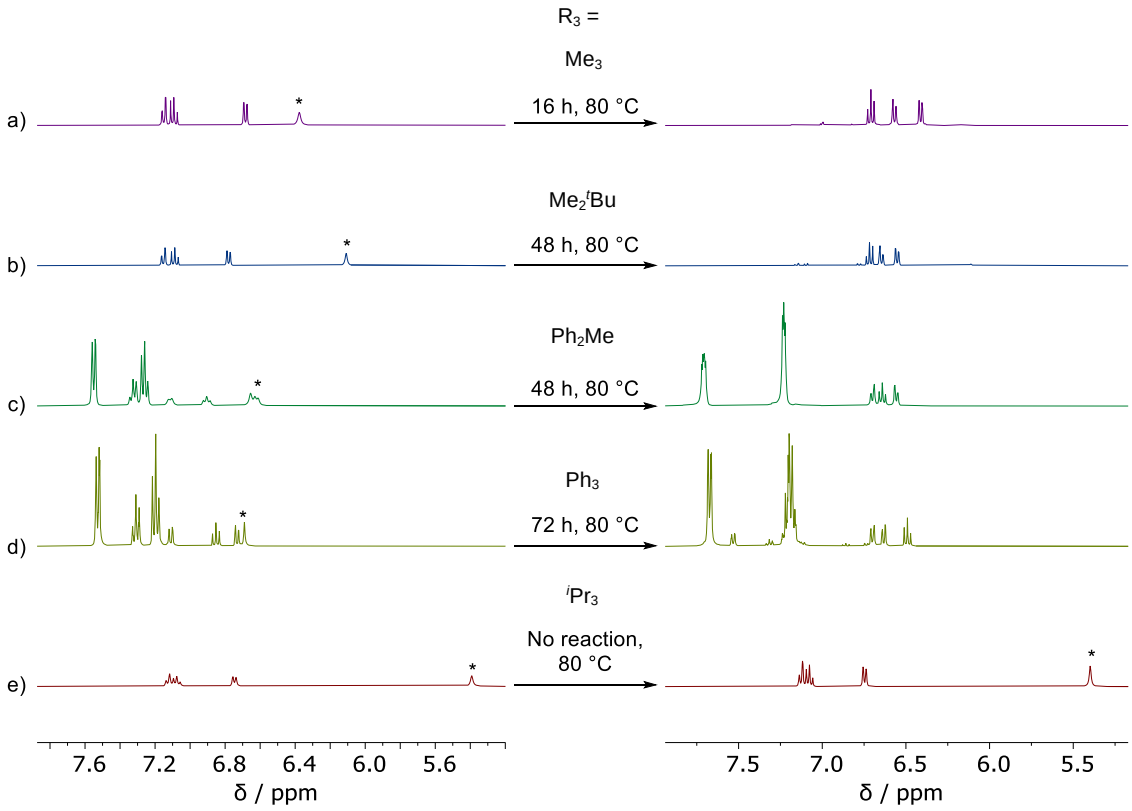


Figure 2.5 Aromatic regions of ^{1}H NMR spectra (C_4D_8O, 298 K, 400 MHz) taken of the reaction mixtures resulting from the addition of 2 eq. $^{R3}LH_2$ (R_3 = Me_3 (**a**), $Me_2{}^tBu$ (**b**), Ph_2Me (**c**), Ph_3 (**d**) and $^iPr_3$ (**e**)) to 1 eq. $[MgN"_2]_2$ in THF-d_8 after 10 minutes at 25 °C (left) and after heating to 80 °C for various time intervals (right). * denotes the amino signals of $^{R3}LH_2$.

Quantitative conversion was achieved within 16 hours in the case of the least bulky proligand $^{Me3}LH_2$ (**a**), with 2–3 days required for the bulkier phenyl and *tert*-butyl substituted proligands (**b-d**). Consumption of the proligands is demonstrated by the absence of their amino singlets, with the growth of new naphthyl signals at lower frequencies relative to the corresponding proligand signals implying the formation of

[(^{R3}L)Mg(THF)$_n$]. However, minimal (1%>) conversion of the bulkiest proligand ^{iPr3}LH$_2$ was observed even after heating at 80 °C for over a week (**e**). The relatively small ionic radius of Mg^{2+} assumedly results in a high activation barrier and therefore a slow rate for the protonolysis reaction between the two bulky reagents even at elevated temperature. This barrier is presumably raised by increasing the steric bulk of ^{R3}LH$_2$, seemingly to a prohibitive extent in the case of ^{iPr3}LH$_2$. In all cases, no intermediate species or thermal degradation products were observed, in contrast with the results obtained for the heavier alkaline earth elements (**Section 2.4**). It is proposed that any higher coordinate intermediate species are disfavoured on steric grounds due to the smaller ionic radius of Mg^{2+}, resulting in their rapid consumption and the prevention of unwanted side reactions.

2.3.3 NMR spectroscopic analysis of [(^{R3}L)Mg(THF)$_2$] (R$_3$ = Me$_3$ (4) and Me$_2$^{t}Bu (5))

While complexes **4** and **5** are poorly soluble in hydrocarbon solvents, NMR spectra could be recorded in THF-d_8. The ^{1}H NMR spectrum of **4** is presented as a representative example (**Figure 2.6**). The spectrum consists of three naphthyl signals in the aromatic region (δ = 6.71, 6.57 and 6.41 ppm) and a single methyl signal at δ = 0.11 ppm. This confirms the retention of a plane of symmetry through the C(9)-C(10) axis, conferring C_{2v} symmetry in solution. In all cases these signals resonate at higher frequencies than the analogous signals in the ^{1}H NMR spectrum of ^{Me3}LH$_2$, a result of the accumulation of negative charge on the dianionic [^{Me3}L]$^{2-}$ ligand. The full consumption of the proligand is confirmed by the absence of its amino singlet, an observation that is supported by the absence of N-H absorbances in the IR spectra of solid samples of **4** and **5**. Signals corresponding to the two equivalents of coordinated THF are also present, though these are presumably in exchange with the THF-d_8 solvent.

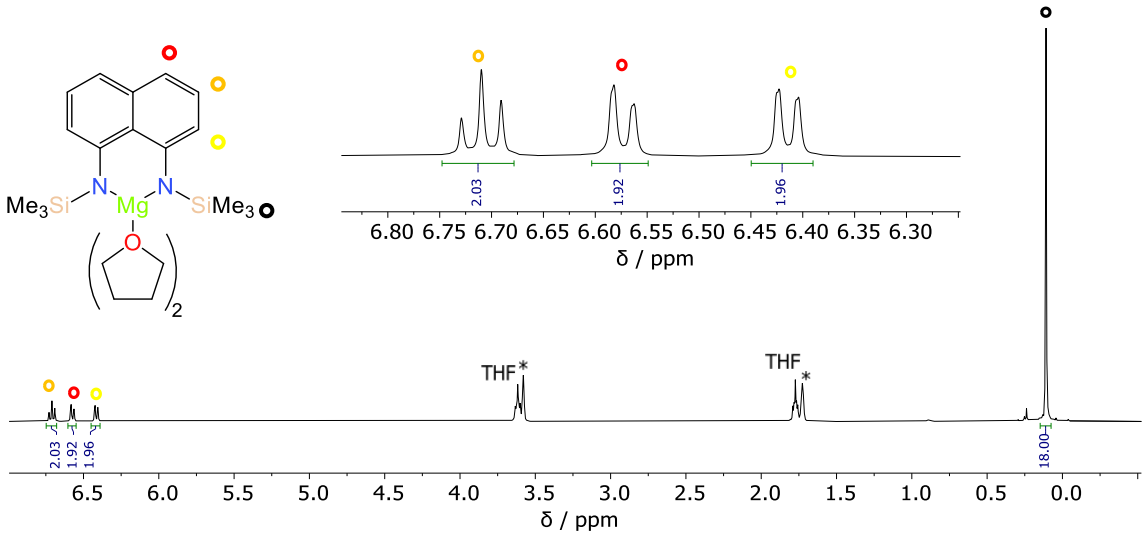


Figure 2.6 ^{1}H NMR spectrum (C_4D_8O, 298 K, 400 MHz) of [(^{Me3}L)Mg(THF)$_2$] (**4**).

* denotes residual protio fraction of C_4D_8O. Expansion shows naphthyl region.

2.3.4 X-ray crystallographic analysis of [(^{R3}L)Mg(THF)$_2$] (R$_3$ = Me$_3$ (4) and Me$_2$^{t}Bu (5))

Single crystals of complexes **4** and **5** suitable for X-ray diffraction were grown by storing saturated THF/*n*-pentane (1:1) solutions at –30 °C, enabling the determination of their crystal structures (**Figure 2.7**, **Table 2.2**). Both **4** and **5** crystallise in the $P2_1/c$ and $P\bar{1}$ space groups respectively, and have very similar structures. In both cases, a four-coordinate Mg^{2+} centre is chelated by the [^{R3}L]$^{2-}$ ligand in a κ^2-N,N'-bidentate manner. Two THF molecules are also coordinated, resulting in a somewhat distorted tetrahedral coordination geometry (τ_4 = 0.83 (**4**) and 0.79 (**5**)).[22] The retention of two equivalents of coordinated THF by isolated samples of **4** and **5** was confirmed by elemental analysis. The tricyclic structures each consist of a six-membered MgN_2C_3 metallacycle, with magnesium residing in the plane (Mg(1)-plane$_{C(1)-C(10)}$ = 0.013(2) Å (**4**), 0.151(2) (**5**)) of a naphthalene backbone which has significantly distorted from planarity (C(1–10)-plane$_{C(1)-C(10)}$ = 0.006(1)–0.182(2) Å (**4**), 0.003(1)–0.202(1) Å (**5**)) in

order to better accommodate Mg^{2+} within a widened metal binding pocket. This is reflected by substantial increases in the N(1)-N(2) distances of **4** (3.013(1) Å) and **5** (3.016(1) Å) relative to those of the corresponding proligands $^{Me3}LH_2$ (2.754(2) Å) and $^{Me2tBu}LH_2$ (2.812(2) Å). Distortion of the $[^{iPr3}L]^{2-}$ ligand to accommodate the coordination of the similarly sized Zn^{2+} cation (ionic radius = 0.74 Å)[23] within the plane of the naphthalene backbone has been reported previously.[7] That such a large distortion is necessary to accommodate the relatively small Mg^{2+} cation suggests that the larger Ae^{2+} congeners may be too large to be coordinated within the plane of the naphthalene backbone (see **Chapters 3** and **4**).

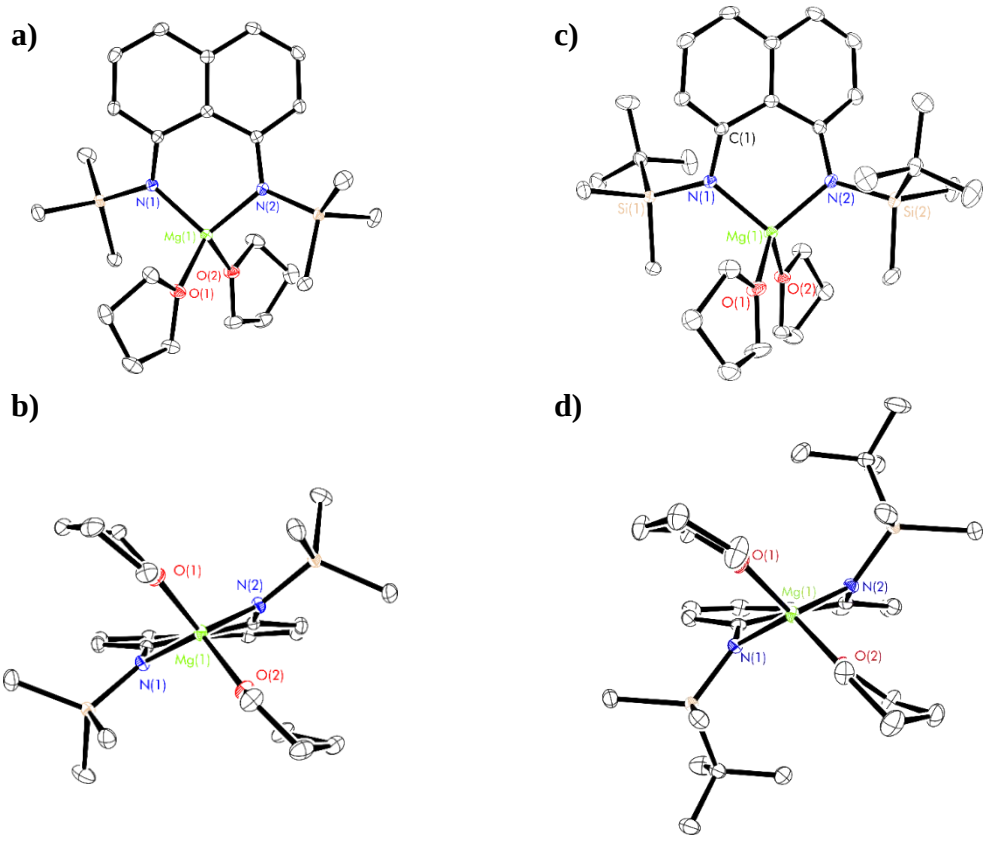


Figure 2.7 Thermal displacement ellipsoid drawings (30%) of **a)** face-on and **b)** side-on views of $[(^{Me3}L)Mg(THF)_2]$ (**4**); **c)** face-on and **d)** side-on views of $[(^{Me2tBu}L)Mg(THF)_2]$ (**5**). All hydrogen atoms have been omitted for clarity.

In contrast, the previously reported X-ray crystal structure of [(^{Ph_2Me}L)Mg(THF)$_2$] (**VIII**) exhibits a somewhat different structure (**Figure 2.8**, **Table 2.2**).[10]

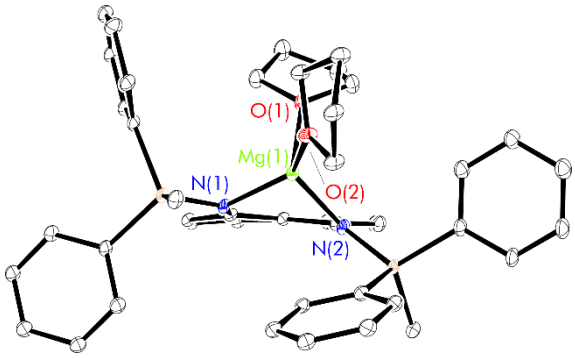


Figure 2.8 Thermal displacement ellipsoid drawings (30%) of [(^{Ph_2Me}L)Mg(THF)$_2$] (**VIII**), produced using data from reference 10. All hydrogen atoms have been omitted for clarity.

Table 2.2 Selected experimental metrical parameters (bond lengths (Å) and angles (°)) for [(^{R_3}L)Mg(THF)$_2$] (R_3 = Me_3 (**4**), $Me_2{}^tBu$ (**5**) and Ph_2Me (**VIII**).[10]

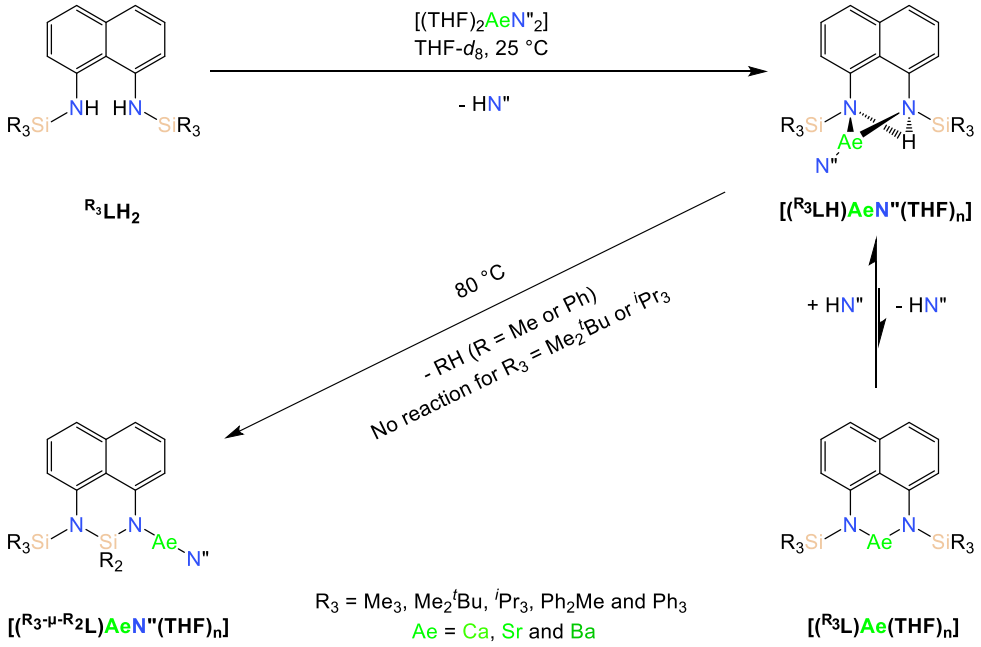
	4	**5**	**VIII**[10]
Space group	$P2_1/c$	$P2_1/c$	$P\bar{1}$
Mg(1)-N(1)	1.9796(9)	1.982(1)	2.007(8)
Mg(1)-N(2)	1.9826(9)	1.9831(9)	1.965(6)
Mg(1)-O(1)	2.0229(9)	2.0358(9)	2.025(6)
Mg(1)-O(2)	2.0175(9)	2.037(1)	2.010(7)
N(1)-N(2)	3.013(1)	3.016(1)	2.940(9)
Mg(1)-plane$_{C(1)-C(10)}$	0.013(2)	0.151(2)	1.079(8)
Min. C(1−10)-plane $_{C(1)-C(10)}$	0.006(1)	0.003(1)	0.002(6)
Max. C(1−10)-plane $_{C(1)-C(10)}$	0.182(2)	0.202(1)	0.100(6)
N(1)-Mg(1)-N(2)	99.00(4)	99.03(5)	95.5(3)
τ_4	0.83	0.79	0.75

While the Mg-N and Mg-O bond lengths in **VIII** are of similar lengths to those in **4** and **5** (**Table 2.2**), the Mg^{2+} centre in the former sits much further (Mg(1)-plane$_{C(1)-C(10)}$ = 1.079(8) Å) from the mean plane of a significantly less distorted naphthalene backbone (C(1–10)-plane$_{C(1)-C(10)}$ = 0.006(6)–0.100(6) Å) with a correspondingly smaller N-N distance (2.940(9) Å). However, there is no obvious explanation for the structural variance of **VIII** relative to **4** and **5**, which may simply arise due to changes in crystal packing forces.

It was found that **4** and **5** are both insoluble in alkane and arene solvents. Furthermore, degradation of analytically pure crystalline samples of **4** and **5** to their respective proligands was observed over time upon their dissolution in THF. Unfortunately, this precluded any further investigation of their reactivity.

2.4 Reactivity of $^{R_3}LH_2$ with $[(THF)_2AeN"_2]$ in THF

The synthesis of solvated monomeric 1,8-*bis*(silylamido)naphthalene complexes of the heavier alkaline earth elements, $[(^{R_3}L)Ae(THF)_n]$ (R_3 = Me_3, $Me_2{}^tBu$, $^iPr_3$, Ph_2Me and Ph_3; Ae = Ca, Sr and Ba), was targeted *via* an analogous protonolysis route to that successfully employed for magnesium. The 1:1 reactions of $^{R_3}LH_2$ with $[(THF)_2AeN"_2]$ (Ae = Ca, Sr and Ba) in THF-d_8 were monitored *in situ* by ^{1}H NMR spectroscopy, which revealed a complex reactivity profile. The formation of three different types of complex, $[(^{R_3}LH)AeN"(THF)_n]$, $[(^{R_3}L)Ae(THF)_n]$ and $[(^{R_3\text{-}\mu\text{-}R_2}L)AeN"(THF)_n]$, is possible depending on the ligand substituents, alkaline earth metal and temperature employed in a given reaction (**Scheme 2.5**). As these complexes form in THF-d_8, the number of THF molecules coordinated to Ae^{2+}, $(THF)_n$, is unclear in the absence of crystallographic data. Full details of the outcomes of all reactions can be found in the **Tables 2.3**–**2.5**.

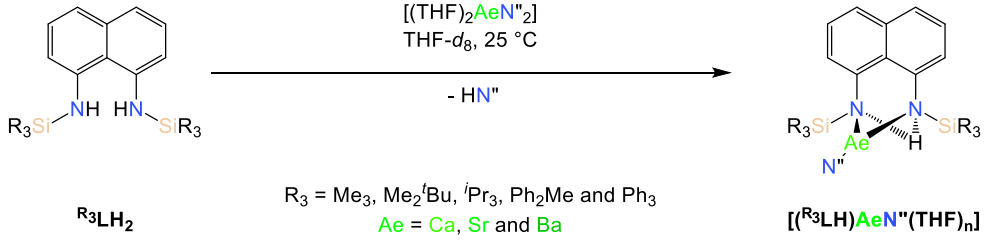


Scheme 2.5 General scheme for the 1:1 reaction of $^{R3}LH_2$ (R_3 = Me_3, Ph_2Me, Ph_3, $Me_2{}^tBu$ and $^iPr_3$) with $[(THF)_2AeN"_2]$ (Ae = Ca, Sr and Ba) in THF-d_8. Coordinated THF is excluded for clarity.

2.4.1 *In situ* NMR spectroscopic analysis

2.4.1.1 [(^{R3}LH)AeN"]

In general, the reaction mixture immediately takes on a bright yellow colour. The formation of the singly deprotonated intermediate species $[(^{R3}LH)AeN"(THF)_n]$ is generally rapid at 25 °C (**Scheme 2.6**).



Scheme 2.6 Formation of $[(^{R3}LH)AeN"(THF)_n]$ in THF-d_8. Coordinated THF is excluded for clarity.

The formation of [(^{R3}LH)AeN"(THF)$_n$] was observed for all metal and ligand combinations, with initial ^{1}H NMR spectra recorded after *ca*. 10 minutes showing full consumption of the proligand in most cases (**Table 2.3**).

Table 2.3 Maximum percentage conversion of ^{R3}LH$_2$ (R$_3$ = Me$_3$, Me$_2$^{t}Bu, ^{i}Pr$_3$, Ph$_2$Me and Ph$_3$) into [(^{R3}LH)AeN"(THF)$_n$] (Ae = Ca, Sr and Ba) in THF-d_8 with relevant reaction temperatures and times.

R$_3$	Ca	Sr	Ba
Me$_3$	>99% after 10 mins at 25 °C. Intermediate.	>99% after 10 mins at 25 °C. Intermediate.	>99% after 10 mins at 25 °C. Intermediate.
Me$_2$^{t}Bu	44% after 16 at 80 °C. Equilibrium mixture.	>99% after 10 mins at 25 °C. Final product.	>99% after 10 mins at 25 °C. Final product.
^{i}Pr$_3$	55% after 72 h at 80 °C. Equilibrium mixture.	50% after 24 h at 80 °C Equilibrium mixture.	90% after 10 mins at 25 °C. Equilibrium mixture.
Ph$_2$Me	>99% after 10 mins at 25 °C. Intermediate.	>99% after 10 mins at 25 °C. Intermediate.	>99% after 10 mins at 25 °C. Intermediate.
Ph$_3$	>99% after 16 h at 25 °C. Intermediate.	>99% after 10 mins at 25 °C. Intermediate.	>99% after 10 mins at 25 °C. Intermediate.

A representative ^{1}H NMR spectrum of [(^{Me3}LH)BaN"(THF)$_n$] (**Figure 2.9**) contains a diagnostic resonance at δ = 12.37 ppm with an integration value of one. This is assigned as the bridging amino proton, (N,N)μ_2-H, that has been retained by the strongly basic binding pocket. The sharing of protons between donor atoms is widely reported to result in high frequency chemical shifts.[24,25] There are also numerous reported examples of factors including the insufficient basicity of [AeN"$_2$] (pKa(HN") = 25.8),[26] persistence of HN" in solution and preference of the heavier Ae elements for softer monoanionic ligands resulting in the incomplete deprotonation of proligands by [AeN"$_2$] bases.[27–33]

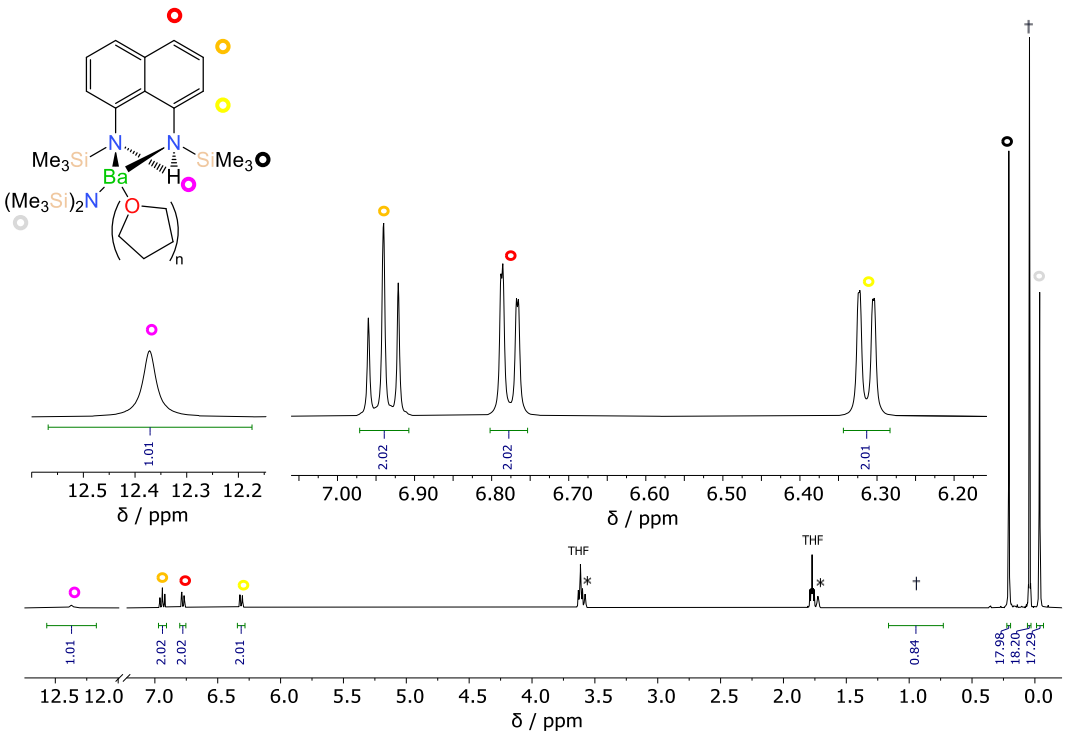


Figure 2.9 ^{1}H NMR spectrum (C_4D_8O, 298 K, 400 MHz) of [(^{Me3}LH)BaN"(THF)$_n$] prepared *in situ* from $^{Me3}LH_2$ and [BaN"$_2$(THF)$_2$]. † denotes HN", * denotes residual protio fraction of C_4D_8O.

Note: this is a time-averaged spectrum of homo- and heteroleptic species (see ***Section 2.4.3****).*

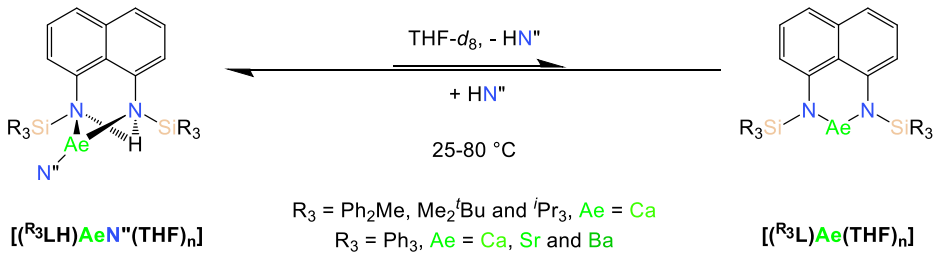
The coordination of [^{R3}LH]$^-$ to the metal centre in a κ^2-N,N′-bidentate manner is inferred from the presence of only three resonances, each integrating to two, in the aromatic region of the spectrum at δ = 6.94, 6.78 and 6.31 ppm. Three methyl signals, each integrating to 18, account for the methyl groups of the [^{Me3}LH]$^-$ and [N"]$^-$ fragments (δ = 0.21 and –0.03 ppm respectively) as well as those of the single equivalent of HN" that has been released (δ = 0.05 ppm). A bidentate coordination mode is further evidenced by the presence of six resonances in the aromatic region of the ^{13}C{^{1}H} NMR spectrum, confirming the retention of a plane of symmetry through the C(9)-C(10) axis of the naphthalene backbone. This suggests that the (N,N)μ$_2$-H proton is rapidly exchanging between two nitrogen donors which are both coordinated to Ba^{2+}, resulting in a time-averaged spectrum that exhibits the coordination of [^{Me3}LH]$^-$ to Ba^{2+} in a

symmetrical manner. A similar phenomenon observed in the NMR spectra of heteroleptic Ae^{2+} complexes featuring a mixed amino/amido monoanionic ligand has been reported previously by Fedushkin and coworkers.[34–36] Furthermore, the $[^{Me3}LH]^-$ fragment has previously been crystallographically characterised in a Pb(II) complex (**VI**, **Chart 2.2**), though in this case it was found to coordinate in an unsymmetrical κ^1-N-monodentate manner both in the solid state and in solution.[16] This difference likely results from the preference of the heavier Ae^{2+} cations to form complexes with higher coordination numbers dominated by non-directional ionic bonding. Conversely, the p-block element lead forms more covalent metal-ligand bonds and has a stereochemically active lone pair that influences its coordination geometry.[37]

Additional spectra of $[(^{R3}LH)AeN''(THF)_n]$ complexes synthesised *in situ* featuring different metal and ligand combinations are fully consistent with these observations (see **Appendix**). These spectra all notably contain a diagnostic (N,N)μ_2-H signal, the chemical shift of which varies between δ = 12–16 ppm (**Figure A.19**). Unfortunately, the isolation of $[(^{R3}LH)AeN''(THF)_n]$ was not possible due to decomposition during solvent removal *in vacuo*, with crystallisation also precluded by the high solubility and dynamic solution-phase structures of $[(^{R3}LH)AeN''(THF)_n]$ in THF (*vide infra*).

2.4.1.2 $[(^{R3}L)Ae(THF)_n]$

The further reactivity of $[(^{R3}LH)AeN''(THF)_n]$ is highly sensitive to the exact combination of alkaline earth metal and ligand substituents employed in a given reaction. In some cases, the target diamido complex $[(^{R3}L)Ae(THF)_n]$ is accessible (R_3 = Ph_2Me, $Me_2{}^tBu$ and $^iPr_3$, Ae = Ca; R_3 = Ph_3, Ae = Ca, Sr and Ba; **Table 2.4**), and forms *in situ* with the concomitant release of a second equivalent of HN'' (**Scheme 2.7**).



Scheme 2.7 Formation of [(^{R3}L)Ae(THF)$_n$]. Coordinated THF is excluded for clarity.

Table 2.4 Maximum percentage conversion of $^{R3}LH_2$ (R_3 = Me_3, $Me_2{}^tBu$, $^iPr_3$, Ph_2Me and Ph_3) into [(^{R3}L)Ae(THF)$_n$] (Ae = Ca, Sr and Ba) in THF-d_8 with relevant reaction temperatures and times.

R_3	Ca	Sr	Ba
Me_3	Not observed.	Not observed.	Not observed.
$Me_2{}^tBu$	39% after 16 h at 80 °C. Equilibrium mixture.	Not observed.	Not observed.
$^iPr_3$	4% after 72 h at 80 °C. Equilibrium mixture.	Not observed.	Not observed.
Ph_2Me	>99% after 16 h at 25 °C. Reversible.	Not observed.	Not observed.
Ph_3	>99% after 3 h at 80 °C. Reversible.	63% after 2 h at 60 °C. Reversible.	31% after 24 h at 25 °C. Reversible.

The ^{1}H NMR spectra of [(^{Ph3}LH)CaN"(THF)$_n$] and [(^{Ph3}L)Ca(THF)$_n$] are presented as representative examples (**Figure 2.10**). The 1:1 reaction of $^{Ph3}LH_2$ with [(THF)$_2$CaN"$_2$] results in the exclusive formation of [(^{Ph3}LH)CaN"(THF)$_n$] after 16 hours at 25 °C (**a**). Heating the reaction mixture at 80 °C (the same approach that enabled the isolation of the magnesium complexes **4** and **5**) for a further 3 hours results in full conversion to [(^{Ph3}L)Ca(THF)$_n$] (**b**). This is demonstrated by the growth of new phenyl (δ = 7.70, 7.16

and 7.03 ppm) and naphthyl (δ = 6.64, 6.62 and 6.55 ppm) resonances and the absence of the (N,N)μ_2-H signal previously present at δ = 15.98 ppm. The integral value of the singlet corresponding to HN" also doubles from 18 to 36 as a second equivalent of the amine is released. The presence of only three naphthyl resonances confirms the retention of a plane of symmetry through the C(9)-C(10) axis. These resonances are shifted to a lower frequency (Δδ = 0.12–0.58 ppm) with respect to the naphthyl resonances of [(^{Ph3}LH)CaN"(THF)$_n$]. This shift is observed consistently for [(^{R3}L)Ae(THF)$_n$] relative to [(^{R3}LH)AeN"(THF)$_n$], suggesting that more electron density is donated to the Ae^{2+} centre by $[^{R3}L]^{2-}$ than by $[^{R3}LH]^{-}$. Further heating for two weeks at 80 °C does not result in the

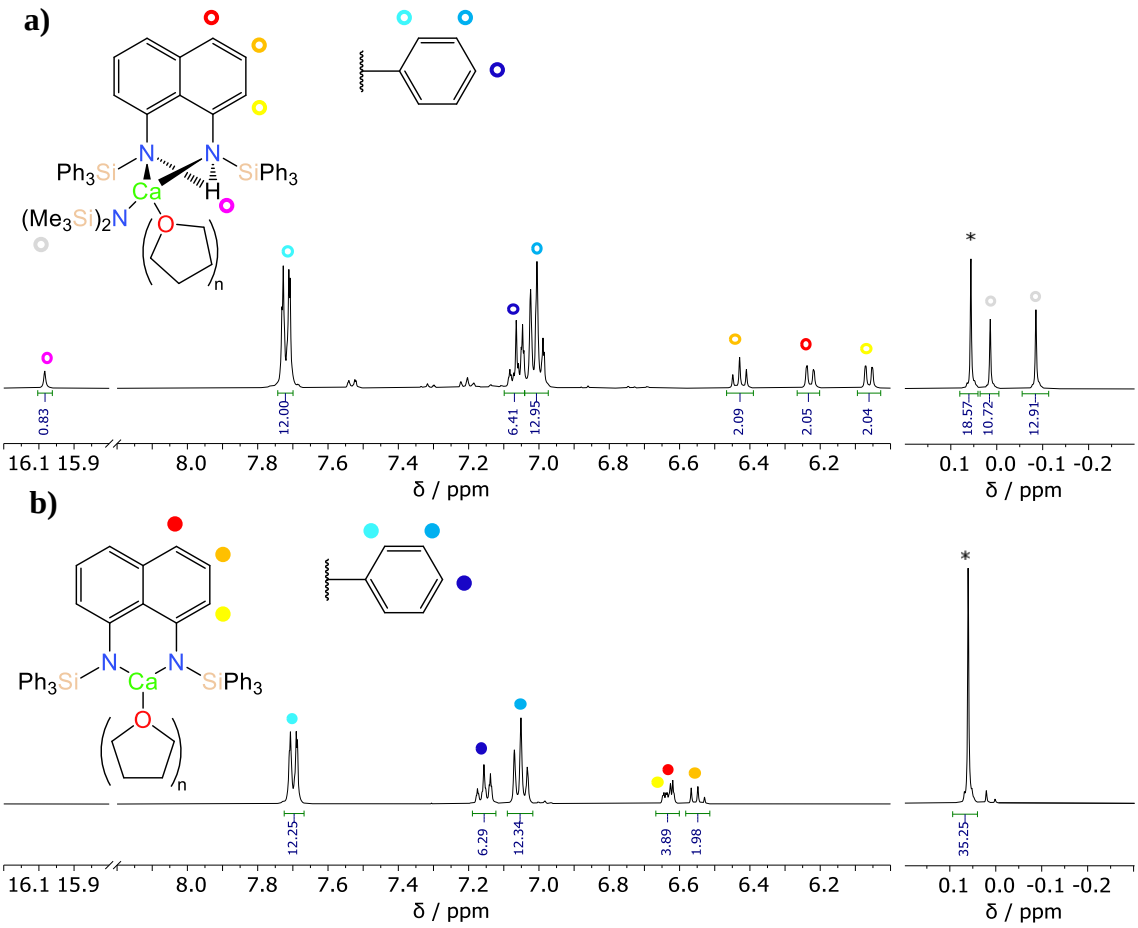


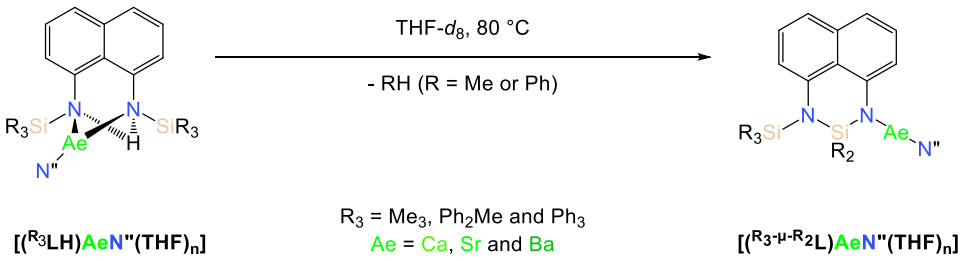
Figure 2.10 *in situ* ^{1}H NMR spectra (C_4D_8O, 298 K, 400 MHz) of **a)** [(^{Ph3}LH)CaN"(THF)$_n$] and **b)** [(^{Ph3}L)Ca(THF)$_n$], prepared by heating the sample in a) for 16 h at 80 °C. * denotes HN".

decomposition of [(^{Ph3}L)Ca(THF)$_n$], which, like the magnesium complexes [(^{R3}L)Mg(THF)$_2$], is seemingly stable in solution at this temperature (though subsequent heating at 110 °C did result in thermal degradation, *vide infra*).

However, the formation of [(^{R3}L)Ae(THF)$_n$] is only possible for some ligand and metal combinations (**Table 2.4**). Even in these cases [(^{R3}L)Ae(THF)$_n$] generally forms reversibly, with an equilibrium with [(^{R3}LH)AeN"(THF)$_n$] favouring the intermediate in most cases. (**Sections 2.4.14**−**7**). This has precluded the isolation of the heavier congeners [(^{R3}L)Ae(THF)$_n$] (Ae = Ca, Sr and Ba) *via* this route, even in cases such as [(^{Ph3}L)Ca(THF)$_n$] which forms exclusively in solution. This contrasts with the stability of the isolable magnesium congeners **4** and **5**. This is attributed to the increased concentration of HN" that occurs during solvent removal *in vacuo* favouring the reverse reaction and resulting in the isolation of impure samples (83%> by NMR). Efforts to crystallise [(^{R3}L)Ae(THF)$_n$] from the reaction mixture also proved unsuccessful (though the crystal structure of [(^{Ph3}L)Sr(THF)$_3$] (**12**) was determined subsequently, **Section 3.5.1**).

2.4.1.3 [($^{R3\text{-}\mu\text{-}R2}$L)AeN"(THF)$_n$]

In other cases, an intramolecular thermal degradation reaction irreversibly converts [(^{R3}LH)AeN"(THF)$_n$] into the unsymmetrical thermodynamic product [($^{R3\text{-}\mu\text{-}R2}$L)AeN"(THF)$_n$] (**Scheme 2.8**, **Table 2.5**). This process occurs when R_3 = Me_3, Ph_2Me or Ph_3, resulting in the concomitant release of one equivalent of either methane (R = Me) or benzene (R = Ph). However, no reaction of this kind is observed when R_3 = $Me_2{}^tBu$ or $^iPr_3$ (**Section 2.4.1.5**). While this form of degradation has not been previously reported for metalation reactions of $^{R3}LH_2$, it is reminiscent of the catalytic



Scheme 2.8 Formation of [($^{R_3\text{-}\mu\text{-}R_2}$L)AeN"(THF)$_n$]. Coordinated THF is excluded for clarity.

Table 2.5 Maximum percentage conversion of $^{R_3}LH_2$ (R_3 = Me_3, $Me_2{}^tBu$, $^iPr_3$, Ph_2Me and Ph_3) into [($^{R_3\text{-}\mu\text{-}R_2}$L)AeN"(THF)$_n$] (Ae = Ca, Sr and Ba) in THF-d_8 with relevant reaction temperatures and times.

R_3	Ca	Sr	Ba
Me_3	>99% after 16 h at 80 °C. Final product.	>99% after 16 h at 80 °C. Final product.	>99% after 16 h at 80 °C. Final product.
$Me_2{}^tBu$	Not observed.	Not observed.	Not observed.
$^iPr_3$	Not observed.	Not observed.	Not observed.
Ph_2Me	>99% after 16 h at 80 °C. Final product.	>99% after 16 h at 80 °C. Final product.	>99% after 16 h at 80 °C. Final product.
Ph_3	>99% after 1 month at 110 °C. Final product	>99% after 16 h at 80 °C. Final product.	>99% after 3 h at 50 °C. Final product.

dehydrocoupling of silanes and amines by the alkaline earth hexamethyldisilazides reported by Hill and co-workers.[32] The insertion of benzonitrile into the N-Si bonds of the $[^{Me3}L]^{2-}$ ligand has also been reported previously, demonstrating that these ligands can display non-innocent behaviour.[17] The ^{1}H NMR spectrum of [($^{Me_3\text{-}\mu\text{-}Me_2}$L)BaN"(THF)$_n$] is presented as a representative example (**Figure 2.11**). Heating a sample of [(^{Me3}LH)BaN"(THF)$_n$] at 80 °C for 16 hours results in the

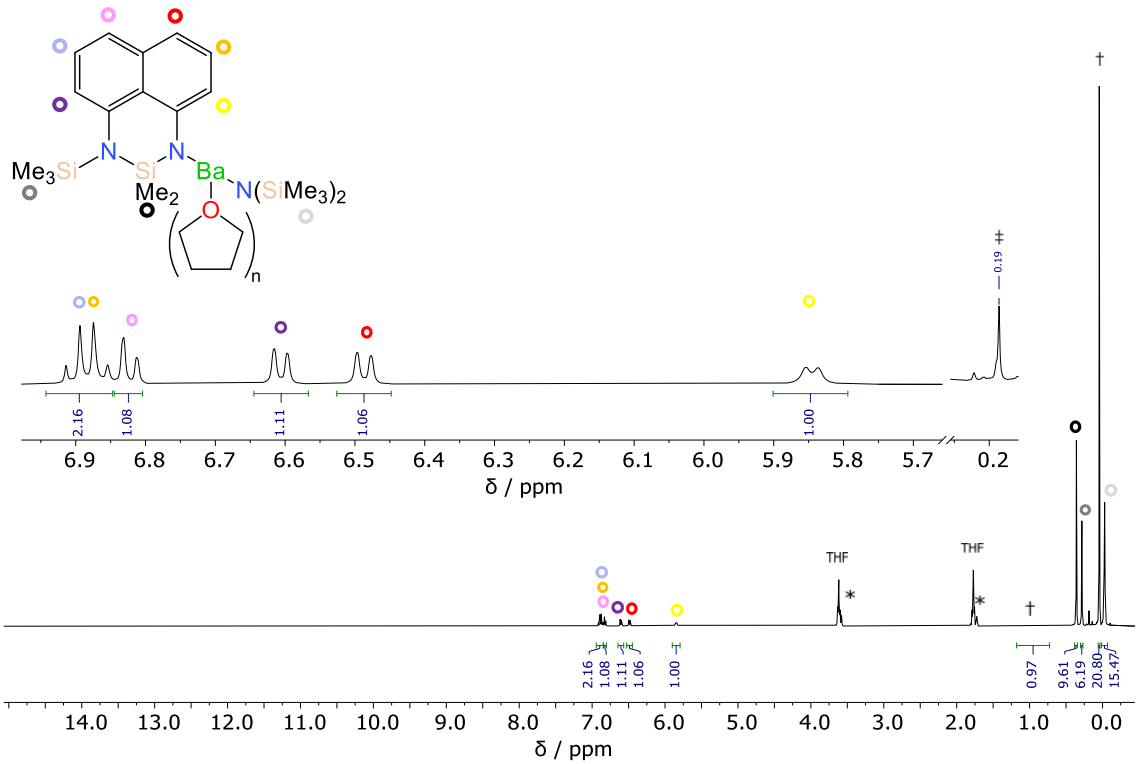


Figure 2.11 ^{1}H NMR spectrum (C_4D_8O, 298 K, 400 MHz) of [($^{Me3\text{-}\mu\text{-}Me2}$L)BaN"(THF)$_n$] prepared *in situ* by heating $^{Me3}LH_2$ and [BaN"$_2$(THF)$_2$] at 80 °C for 16 h. ‡ denotes CH_4, † denotes HN", * denotes residual protio fraction of C_4D_8O.

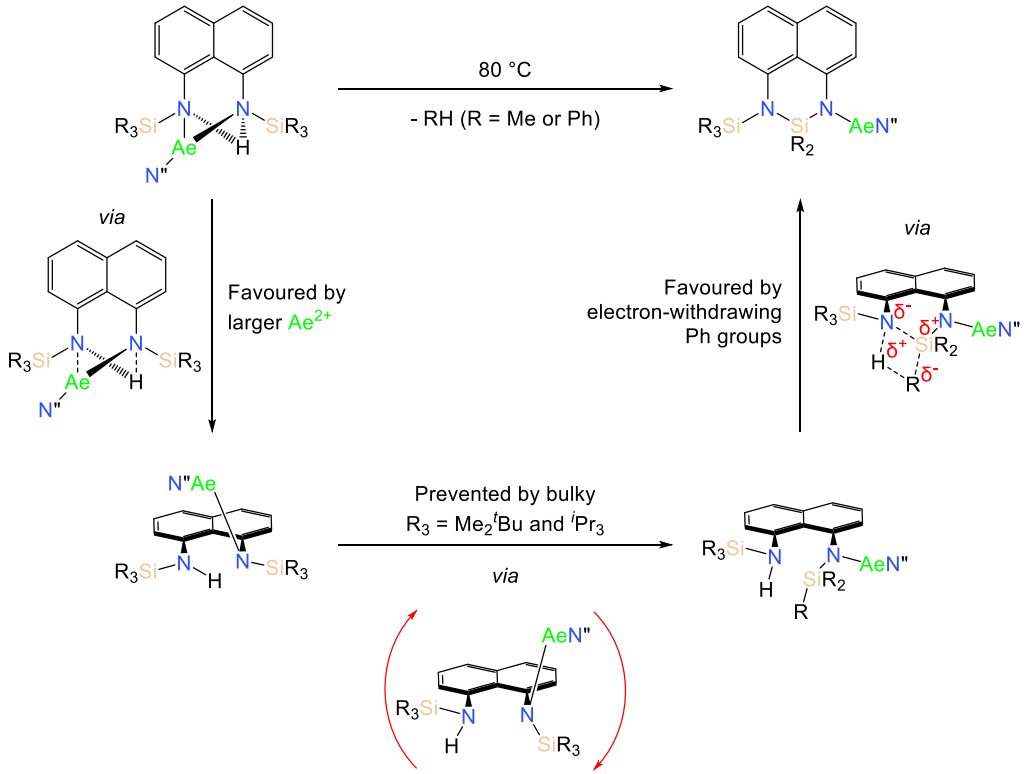
*Note: this is a time-averaged spectrum of homo- and heteroleptic species (see **Section 2.4.3**).*

consumption of the diagnostic (N,N)μ$_2$-H signal at δ = 12.37 ppm, and the appearance of a characteristic singlet at δ = 0.19 ppm which indicates the evolution of methane. The aromatic region now consists of six signals (δ = 6.89, 6.87, 6.82, 6.61, 6.49 and 5.84 ppm) each integrating to one, in contrast with the three signals each integrating to two present in the ^{1}H spectrum of [(^{Me3}LH)BaN"(THF)$_n$] (**Figure 2.9**). This demonstrates the descent in symmetry that occurs upon thermal degradation, which is further evidenced by the presence of 10 signals in the aromatic region of the ^{13}C{^{1}H} NMR spectrum (**Figure A.23**). Further, the methyl region of the ^{1}H NMR spectrum now contains two signals at δ = 0.36 and 0.28 ppm, which integrate to nine and six and correspond to the terminal $SiMe_3$ and bridging $SiMe_2$ groups of the [$^{Me3\text{-}\mu\text{-}Me2}$L]$^-$ fragment respectively. The ^{29}Si-^{1}H

HMBC NMR spectrum shows $^{2}J_{Si\text{-}H}$ correlations between these ^{1}H NMR signals and two ^{29}Si NMR signals (δ = –0.46 and –16.36 ppm, **Figure A.25**). Contrastingly, only one resonance at δ = –7.99 ppm in the ^{29}Si NMR spectrum of [(^{Me3}LH)BaN"(THF)$_n$] is assigned to the [^{Me3}LH]$^-$ fragment. Additional spectra recorded for the calcium and strontium congeners are also consistent with these observations (**Figure 2.17, Section 2.4.3**). Thermal degradation of the phenyl-substituted variants of [(^{R3}LH)AeN"(THF)$_n$] (R_3 = Ph_2Me and Ph_3) resulted in spectra that were more challenging to fully assign due to the presence of multiple overlapping aromatic signals (**Figure 2.12b**). It is proposed that the complexity of these spectra result from the same loss of C_{2v} symmetry confirmed by simpler spectra of the methyl substituted complexes [($^{Me3\text{-}\mu\text{-}Me2}$L)AeN"(THF)$_n$]. The growth of a diagnostic singlet at δ = 7.30 ppm supports the notion that degradation occurs *via* the protonation of a phenyl substituent and results in the formation of both benzene and [($^{R3\text{-}\mu\text{-}R2}$L)AeN"(THF)$_n$].

Unfortunately, while [($^{Me3\text{-}\mu\text{-}Me2}$L)AeN"(THF)$_n$] (Ae = Ca, Sr and Ba) could be isolated as powders, these samples were contaminated by the homoleptic species [($^{Me3\text{-}\mu\text{-}Me2}$L)$_2$Ae(THF)$_n$] and [(THF)$_2$AeN"]$_2$ due to ligand redistribution *via* Schlenk equilibria (**Section 2.4.3**). These dynamic solution-phase processes seemingly also precluded the crystallisation of [($^{R3\text{-}\mu\text{-}R2}$L)AeN"(THF)$_n$] and their characterisation by X-ray diffraction. However, the similarities between the ^{1}H NMR spectra of [($^{Me3\text{-}\mu\text{-}Me2}$L)BaN"(THF)$_n$] and compound **3** (**Figures 2.11** and **2.3** respectively) combined with the crystallographic verification of the structure of the latter (**Figure 2.4**) provide strong evidence for the proposed structure of the [$^{R3\text{-}\mu\text{-}R2}$L]$^-$ fragment. It is proposed that this thermal degradation process occurs *via* an intramolecular σ-bond metathesis reaction following the coordinative rearrangement of [(^{R3}LH)AeN"(THF)$_n$] into an active

conformation (**Scheme 2.9**). This mechanism, and the experimental evidence supporting it, is discussed further in the following sections.

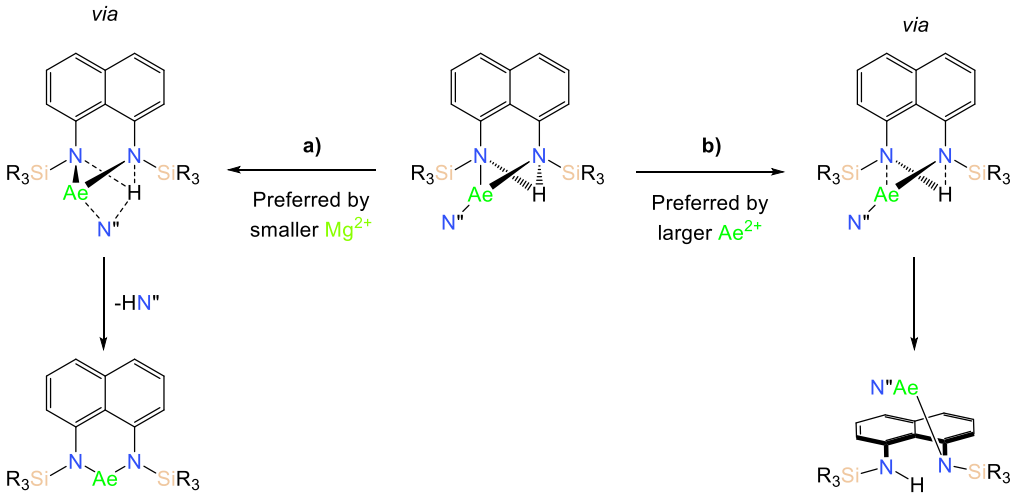


Scheme 2.9 Conversion of [(^{R3}LH)AeN"(THF)$_n$] into [($^{R3\text{-}\mu\text{-}R2}$L)AeN"(THF)$_n$] *via* a proposed three-step mechanism that is influenced by various steric and electronic factors. Coordinated THF is excluded for clarity.

2.4.1.4 Metal steric effects

The initial formation of [(^{R3}LH)AeN"(THF)$_n$] proceeds fastest for the largest cations Sr^{2+} and Ba^{2+} (>99% conversion after 10 minutes at 25 °C for all proligands except ^{iPr3}LH$_2$, **Table 2.3**), reflecting their higher rates of ligand exchange. For Ca^{2+}, the reaction generally proceeds at room temperature (unlike for Mg^{2+}), but at a slower rate than for the heavier congeners. This is exemplified by the relatively slow formation of [(^{Ph3}LH)CaN"(THF)$_n$] (**Figure 2.10a**, *vide supra*) - full conversion is only reached after 16 hours at 25 °C, in contrast with the heavier congeners (Ae = Sr and Ba) which form effectively instantaneously (**Table 2.3**).

Furthermore, the larger ionic radii of Sr^{2+} and Ba^{2+} appear to strongly bias the equilibrium between [(^{R3}LH)AeN"(THF)$_n$] and [(^{R3}L)Ae(THF)$_n$] towards the former, with the formation of [(^{R3}L)Ae(THF)$_n$] (Ae = Sr and Ba) only observed when $R_3 = Ph_3$ (maximum conversions of 63% and 31% achieved respectively, 1%> otherwise) . This is presumably due to the increased coordinative saturation of the large Ae^{2+} cations that is provided by the additional $[N"]^-$ donor of [(^{R3}LH)AeN"(THF)$_n$], as well as their preference for "softer" monoanionic ligands. This is consistent with the observation that the conversion of $^{R3}LH_2$ into [(^{R3}L)Mg(THF)$_n$] proceeds without the sterically congested intermediate species [(^{R3}LH)MgN"(THF)$_n$] being observed, assumedly due to the rapid consumption of the latter *via* the release of HN" (**Scheme 2.10a**). This can be attributed to the smaller Mg^{2+} cation preferring the coordination of a single "hard" dianionic ligand rather than two bulky monoanionic ligands.



Scheme 2.10 a) Coordinative rearrangement of [(^{R3}LH)AeN"(THF)$_n$] into a conformation in which the [^{R3}LH]$^-$ ligand is coordinated to Ae^{2+} in a κ^1-N-monodentate manner; **b)** the release of HN" from [(^{R3}LH)AeN"(THF)$_n$] to form [(^{R3}L)Ae(THF)$_n$]. Coordinated THF is excluded for clarity.

In contrast, the rate of conversion of [(^{R3}LH)AeN"(THF)$_n$] into [($^{R3\text{-}\mu\text{-}R2}$L)AeN"(THF)$_n$] *via* thermal degradation was found to rise as Ae^{2+} ionic radius increases. While no

reactivity of this kind is observed for Mg^{2+}, the reaction proceeds at progressively lower temperatures for Ca^{2+}, Sr^{2+} and Ba^{2+}. This effect is most pronounced for the formation of [($^{Ph3\text{-}\mu\text{-}Ph2}$L)AeN''(THF)$_n$] from [(^{Ph3}LH)AeN''(THF)$_n$] (Ae = Ca, Sr and Ba, **Table 2.5**). For calcium, heating a solution of [(^{Ph3}LH)CaN''(THF)$_n$] at 80 °C for 3 hours results in clean conversion to [(^{Ph3}L)Ca(THF)$_n$] (**Figure 2.10**). Only trace amounts of benzene are released by the competing thermal degradation after further heating at 80 °C for two weeks, though full conversion to [($^{Ph3\text{-}\mu\text{-}Ph2}$L)CaN''(THF)$_n$] was achieved after one month at 110 °C. In contrast, while some conversion of [(^{Ph3}LH)SrN''(THF)$_n$] to [(^{Ph3}L)Sr(THF)$_n$] was observed at 60 °C (**Figure 2.12a**), heating a solution of the strontium congener at 80 °C for 24 hours resulted in full conversion to [($^{Ph3\text{-}\mu\text{-}Ph2}$L)SrN''(THF)$_n$] (**Figure 2.12b**). For the barium congener, significant amounts of benzene are released even at room temperature, with full conversion to [($^{Ph3\text{-}\mu\text{-}Ph2}$L)BaN''(THF)$_n$] achieved after 3 hours at 50 °C.

This suggests that the greater kinetic lability of the heavier congeners more readily facilitates the thermal degradation reaction, supporting the notion that [(^{R3}LH)AeN''(THF)$_n$] must first undergo coordinative rearrangement into an active conformation for the elimination of RH to occur. It is therefore proposed that the symmetric κ^2-N,N′-bidentate coordination mode is broken, with the [^{R3}LH]$^-$ fragment subsequently ligated to Ae^{2+} in an unsymmetrical, κ^1-N-monodentate manner (**Scheme 2.10b**). The proposed structure of this intermediate is similar to that of [(^{R3}LH)Pb(μ-NH_2)]$_2$ (**VI, Chart 2.2**).[16] This process is made possible by the greater lability of the larger Ae^{2+} cations, from which a neutral amino donor can reversibly dissociate. Further tautomerisation of this intermediate species then enables conversion to [($^{R3\text{-}\mu\text{-}R2}$L)AeN''(THF)$_n$] (*vide infra*).

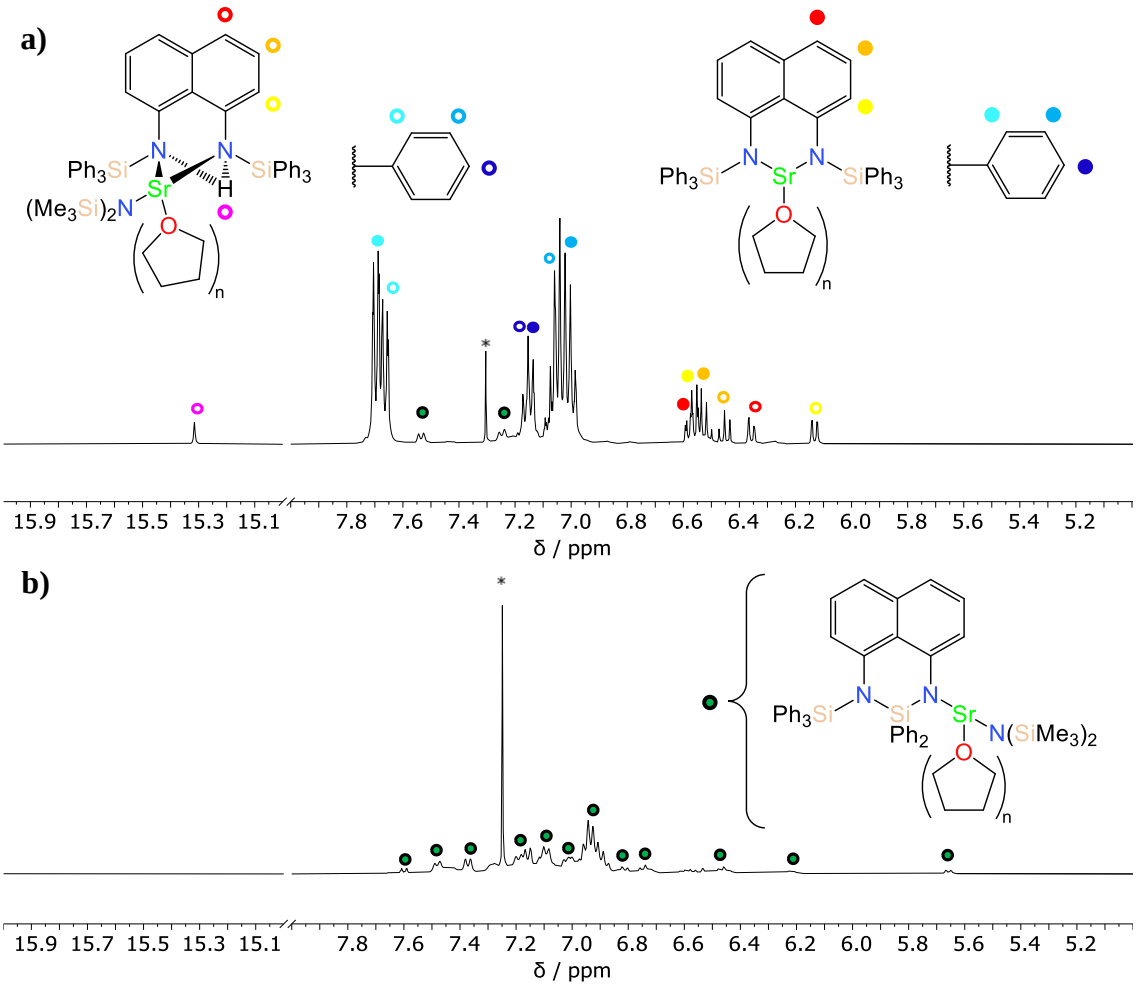
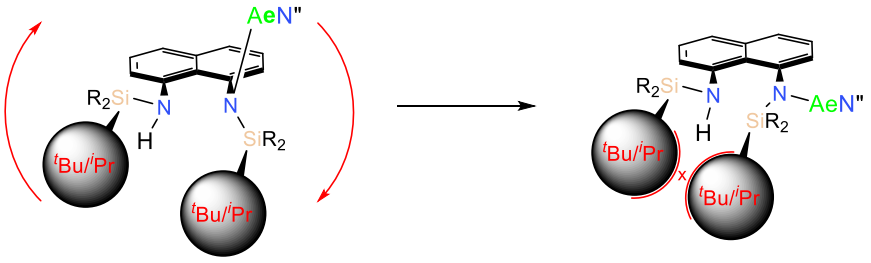


Figure 2.12 Aromatic regions of *in situ* ^{1}H NMR spectra (C_4D_8O, 298 K, 400 MHz) of **a)** a mixture of [(^{Ph3}LH)SrN"(THF)$_n$] (35%) and [(^{Ph3}L)Sr(THF)$_n$] (63%) formed after 2 h at 60 °C; **b)** [($^{Ph3\text{-}\mu\text{-}Ph2}$L)SrN"(THF)$_n$], prepared by heating the sample in a) for 16 h at 80 °C. * denotes benzene.

2.4.1.5 Ligand steric effects

For all metals the formation of [(^{R3}LH)AeN"(THF)$_n$] is incomplete when R_3 = ^{i}Pr$_3$ (**Table 2.3**), with a maximum conversion of 90% observed for the largest metal barium (**Figure A.17**). This can be attributed to increased steric congestion at the metal centre that results from the coordination of ^{iPr3}LH$_2$. Notably, no thermal degradation of [(^{R3}LH)AeN"(THF)$_n$] to [($^{R3\text{-}\mu\text{-}R2}$L)AeN"(THF)$_n$] was observed for any metal when R_3 = Me$_2$^{t}Bu or ^{i}Pr$_3$, even after heating at 110 °C for one month. This suggests that the bulky *tert*-butyl and *iso*-propyl substituents prohibit this mode of reactivity on steric

grounds. It is proposed that the necessary rotational rearrangement of the $[\kappa^1\text{-N-}^{R_3}LH]^-$ fragment into an active conformation from which RH can be eliminated is precluded by bulky alkyl substituents (**Scheme 2.11**).



Scheme 2.11 Conformational rearrangement of $[(\kappa^1\text{-N-}^{R_3}LH)AeN"(THF)_n]$ into an active conformation *via* a rotation which is prohibited by excessively bulky silyl substituents.

2.4.1.6 Metal electronic effects

Analysis of $\delta(\mu_2\text{-H})$, the chemical shifts of the (N,N)-μ_2H signals in ^{1}H NMR spectra of $[(^{R_3}LH)AeN"(THF)_n]$ (Ae = Ca, Sr and Ba; R_3 = $Me_2{}^tBu$, $^iPr_3$, Ph_2Me and Ph_3), provides insight into the impact of varying the metal centre on the electronics of the $[^{R_3}LH]^-$ fragment (**Figure 2.13**). For a given ligand, $\delta(\mu_2\text{-H})$ always decreases as Ae^{2+} size increases ($\delta_{Ca} > \delta_{Sr} > \delta_{Ba}$). This is due to the increasing polarisation of the $Ae^{\delta+}\text{-}N^{\delta-}$ bonds as they become more ionic with greater Ae^{2+} size and electropositivity. Consequently, the nitrogen donor atoms retain more electron density and become more basic, resulting in a more tightly bound (N,N)μ_2-H proton that is shielded more effectively. This rationalises the observation that the deprotonation of $[(^{R_3}LH)AeN"(THF)_n]$ to form $[(^{R_3}L)Ae(THF)_n]$ becomes increasingly challenging and reversible for the larger Ae^{2+} cations, whereas the formation of $[(^{R_3}L)Mg(THF)_n]$ is generally facile and irreversible. However, this argument does seem somewhat counterintuitive when considering the faster rates of thermal degradation that result from increasing Ae^{2+} size, suggesting that steric factors dominate in this case (**Section 2.4.1.4**).

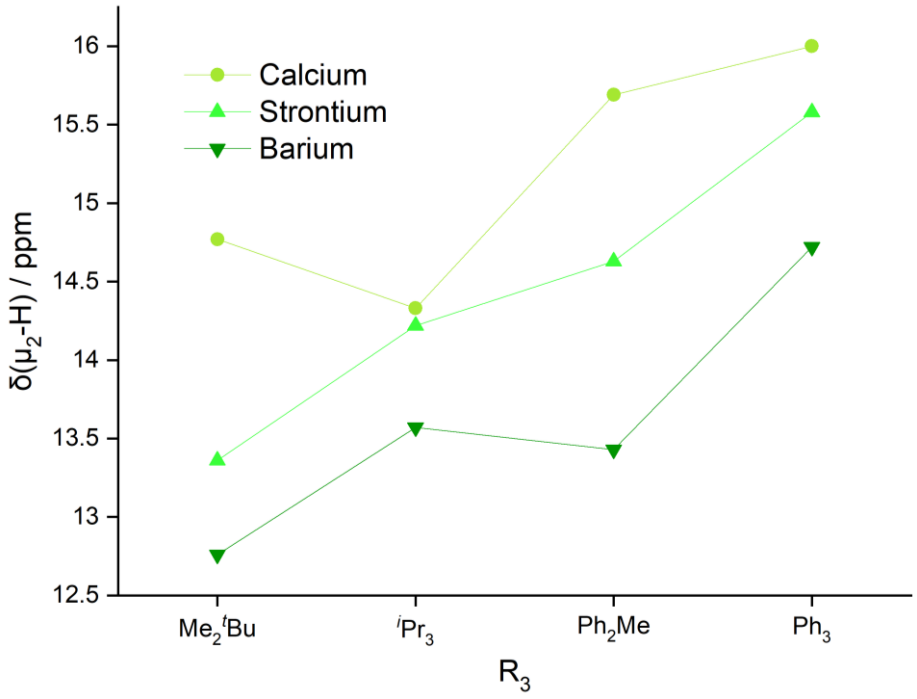


Figure 2.13 Variation in the chemical shift of the (N,N)μ$_2$-H proton, δ(μ$_2$-H), in the *in situ* ^{1}H NMR spectra of [(^{R3}LH)AeN"(THF)$_n$] (R$_3$ = Me$_2$^{t}Bu, ^{i}Pr$_3$, Ph$_2$Me and Ph$_3$, Ae = Ca, Sr and Ba).

See **Figure A.19** for the (N,N)μ$_2$-H regions of the relevant ^{1}H spectra (THF-d_8, 400 MHz, 298 K).

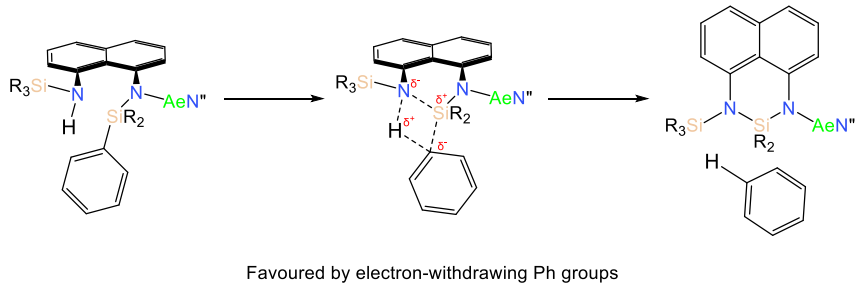
2.4.1.7 Ligand electronic effects

The bulky alkyl-substituted strontium and barium complexes [(^{Me2tBu}LH)AeN"(THF)$_n$] and [(^{iPr3}LH)AeN"(THF)$_n$] (Ae = Sr and Ba) do not react further even upon prolonged heating. In the case of the calcium congeners, the composition of the reaction mixture is highly temperature sensitive with ^{R3}LH$_2$, [(^{R3}LH)CaN"(THF)$_n$] and [(^{R3}L)Ca(THF)$_n$] (R$_3$ = Me$_2$^{t}Bu and ^{i}Pr$_3$) all present in varying proportions (**Tables 2.3**–**4**). While the lack of thermal degradation can be explained based on steric factors (**Section 2.4.1.5**), the influence of electronic factors must be considered to rationalise the reluctance of the bulkier variants of [(^{R3}LH)AeN"(THF)$_n$] to release HN". The latter outcome results from bulky, electron-donating alkyl substituents increasing the basicity of the [^{R3}LH]$^-$ fragment, stabilising [(^{R3}LH)AeN"(THF)$_n$].

Conversely, the phenyl-substituted complexes [(^{Ph_2Me}L)Ca(THF)$_n$] (**Figure A.20**) and [(^{Ph_3}L)Ca(THF)$_n$] (**Figure 2.10b**) each form exclusively after 16 hours at 25 °C and 80 °C respectively. The triphenyl-substituted complexes [(^{Ph_3}L)Sr(THF)$_n$] (**Figure 2.12a**) and [(^{Ph_3}L)Ba(THF)$_n$] also form as the major (63%) and minor (31%) products respectively after 2 hours at 60 °C (Sr) and 16 hours at 25 °C (Ba), with full conversion not possible in these cases due to the competing formation of [($^{Ph_3\text{-}\mu\text{-}Ph_2}$L)AeN"(THF)$_n$] (**Section 2.4.1.4**). This suggests that phenyl groups have an electron withdrawing effect, reducing the basicity of the nitrogen donor atoms of the [^{R_3}LH]$^-$ fragment and facilitating the abstraction of the (N,N)μ_2-H proton. It is also possible that phenyl substituents form π-facial interactions with Ae^{2+}, conferring additional stability to [(^{R_3}L)Ae(THF)$_n$] in these cases (**Chapter 3**).

The influence of the electron-withdrawing/donating nature of amido substituents on the reactivity of other diamido alkaline earth complexes has been reported previously.[38] That the acidity of (N,N)μ_2-H is modulated by the silyl substituents of [(^{R_3}LH)AeN"(THF)$_n$] is confirmed by an analysis of δ(μ_2-H) (**Figure 2.13**). For a given metal, the (N,N)μ_2-H signal generally increases in frequency in the order $\delta_{Ph_3} > \delta_{Ph_2Me} > \delta_{iPr_3} > \delta_{Me_2tBu}$, with δ_{Ph_3} the largest in the case of all three metals. This electronic consideration rationalises the observation that the rate of thermal degradation increases in the order $Ph_3 > Ph_2Me > Me_3$, despite the steric bulk of the SiR_3 group also increasing in the same manner. The withdrawal of electron density by phenyl substituents enhances both their own basicity and the acidity of the amino proton, with the abstraction of the latter by the former favoured as a consequence. This provides evidence for the formation of [($^{R_3\text{-}\mu\text{-}R_2}$L)AeN"(THF)$_n$] and loss of RH in a concerted manner *via* an intramolecular σ-bond metathesis reaction (**Scheme 2.12**). Following the rearrangement of

[(^{R3}LH)AeN"(THF)$_n$] into an active conformation (**Schemes 2.10** and **2.11**), the amino proton is abstracted by a methyl or phenyl silyl substituent. The basicity of these silyl substituents is enhanced by the negative charge of the [^{R3}LH]$^-$ fragment. The proposed four-membered transition state is assumedly lowered in energy by the enhanced polarisation induced by phenyl substituents, resulting in faster increased rates of thermal degradation. Ultimately, this results in the concomitant formation of a new N-Si and C-H bonds and generates both the unsymmetrical monodentate [$^{R3\text{-}\mu\text{-}R2}$L]$^-$ ligand and one equivalent of either methane or benzene.

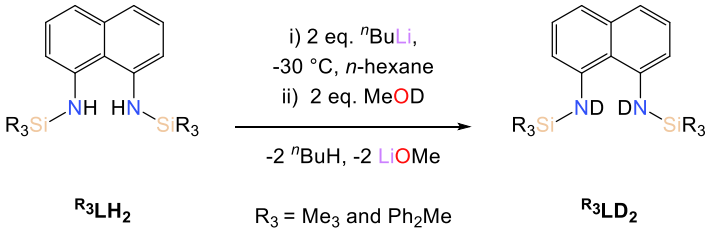


Scheme 2.12 Proposed pathway for the thermal degradation of [(^{R3}LH)AeN"(THF)$_n$] into [($^{R3\text{-}\mu\text{-}R2}$L)AeN"(THF)$_n$] *via* an intramolecular σ-bond metathesis reaction that results in the elimination of benzene. Coordinated THF is excluded for clarity.

2.4.2 Deuterium labelling experiments

2.4.2.1 Proligand deuteration

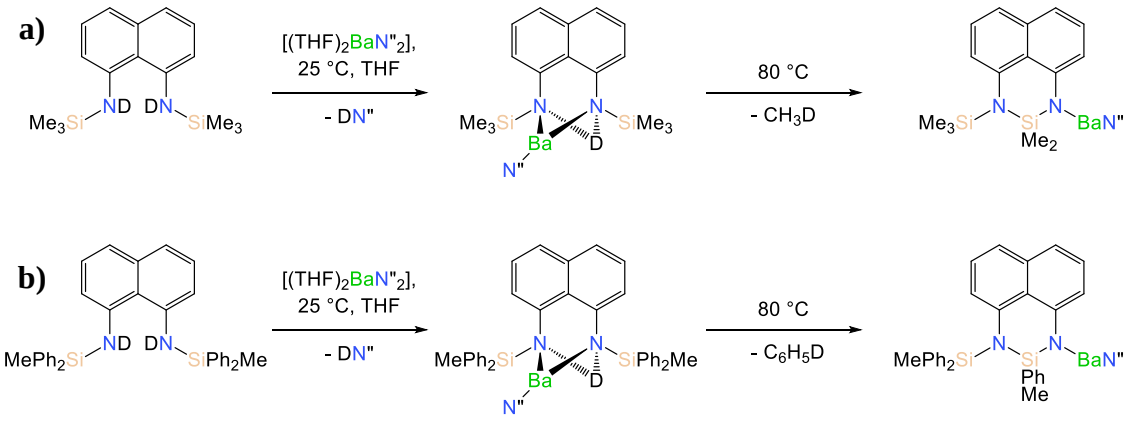
The deprotonation of ^{R3}LH$_2$ (R$_3$ = Me$_3$ and Ph$_2$Me) with two equivalents of *n*-butyllithium in *n*-hexane followed by the addition of two equivalents of methanol-*d*$_1$ afforded the deuterated proligands ^{R3}LD$_2$ (**Scheme 2.13**). Full suppression of the N-H signal was observed in the ^{1}H spectra of ^{R3}LD$_2$, with corresponding N-D singlets instead present in their ^{2}H spectra.



Scheme 2.13 Synthesis of the deuterated proligands $^{R3}LD_2$ (R_3 = Me_3 and Ph_2Me).

2.4.2.2 Mechanistic studies

The deuterium labelled proligands $^{R3}LD_2$ were employed to further investigate the mechanism of the thermal degradation reaction. The 1:1 reaction of $^{Me3}LD_2$ with [$(THF)_2$BaN"$_2$] was conducted in both THF and THF-d_8 (**Scheme 2.14a**) and monitored by ^{2}H and ^{1}H NMR spectroscopy respectively (**Figure 2.14**). An initial ^{1}H NMR spectrum showed the full suppression of the (N,N)μ_2-H signal at δ = 12.37 ppm. A corresponding resonance in the ^{2}H NMR spectrum (**a**) is present at δ = 12.14 ppm, corresponding to the (N,N)μ_2-D atom of [(^{Me3}LD)BaN"(THF)$_n$]. This spectrum also contains a resonance at δ = 0.93 ppm, corresponding to the amino signal of the single equivalent of DN" that has been released. A ^{1}H NMR spectrum of the THF-d_8 sample taken after 16 hours at 80 °C shows full conversion to [($^{Me3\text{-}\mu\text{-}Me2}$L)BaN"(THF)$_n$] as



Scheme 2.14 a) 1:1 reaction of $^{Me3}LD_2$ with [$(THF)_2$BaN"$_2$] in THF,

b) 1:1 reaction of $^{Ph2Me}LD_2$ with [$(THF)_2$BaN"$_2$]. Coordinated is THF excluded for clarity.

expected (**b**). In addition, a 1:1:1 triplet ($^2J_{D\text{-}H}$ = 2.0 Hz) at δ = 0.17 ppm is now present, and is attributed to the methyl protons of methane-d_1 (CH_3D). In the analogous ^2H NMR spectrum (**c**), the singlet at δ = 12.14 ppm has been fully consumed while the DN" signal remains. A 1:3:3:1 quartet ($^2J_{D\text{-}H}$ = 1.9 Hz) present at δ = 0.15 ppm is assigned as the

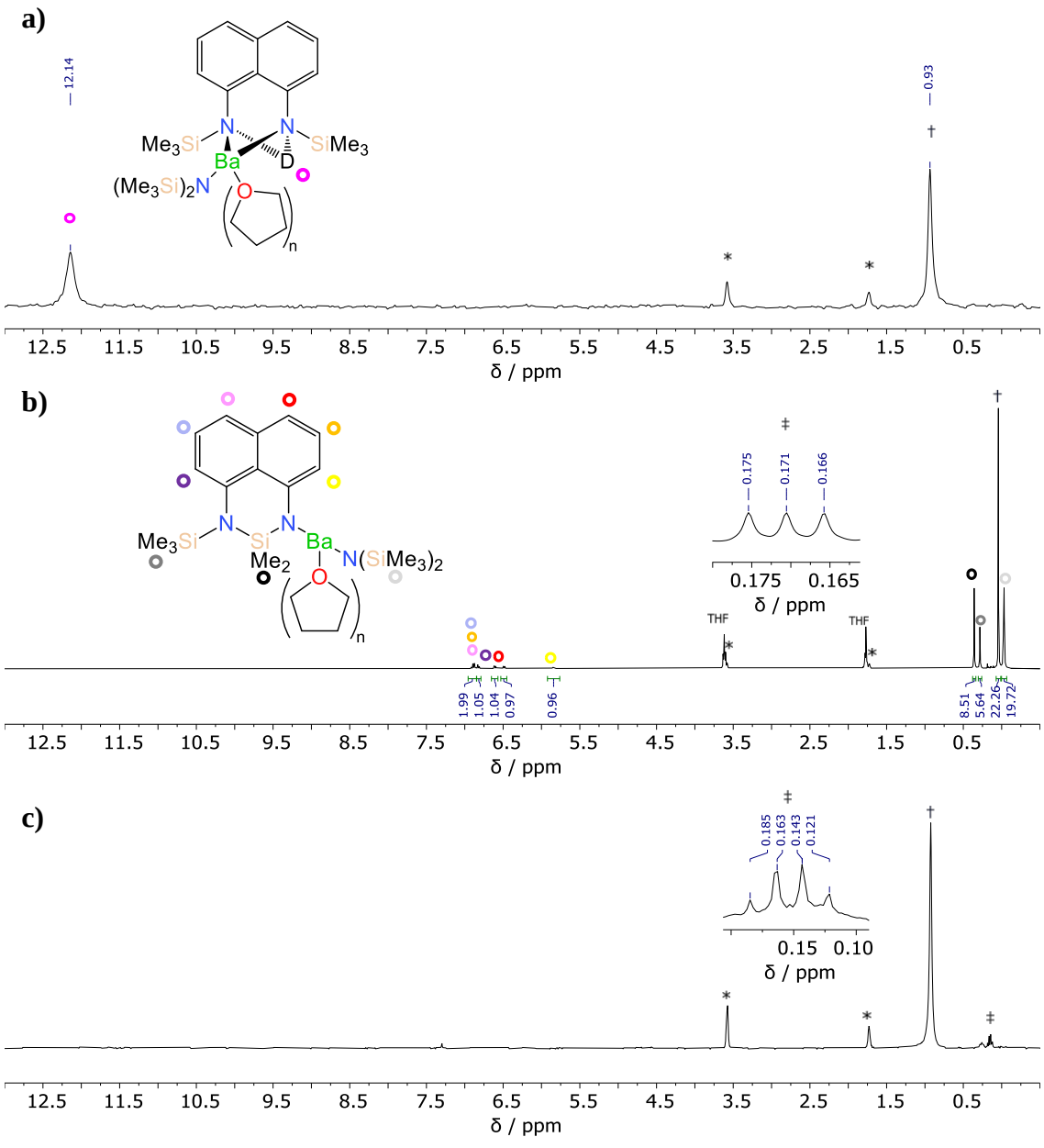


Figure 2.14 a) ^2H NMR spectrum (C_4H_8O, 298 K, 77 MHz) of [(^{Me3}LD)BaN"(THF)$_n$], **b)** ^1H NMR spectrum (C_4D_8O, 298 K, 400 MHz) of [($^{Me3\text{-}\mu\text{-}Me2}$L)BaN"(THF)$_n$] and **c)** ^2H NMR spectrum (C_4H_8O, 298 K, 77 MHz) of [($^{Me3\text{-}\mu\text{-}Me2}$L)BaN"(THF)$_n$]. Expansions in **b)** and **c)** show CH_3D signals. ‡ denotes CH_3D, † denotes DN", * denotes residual protio/deuterio fraction of THF-d_8/THF.

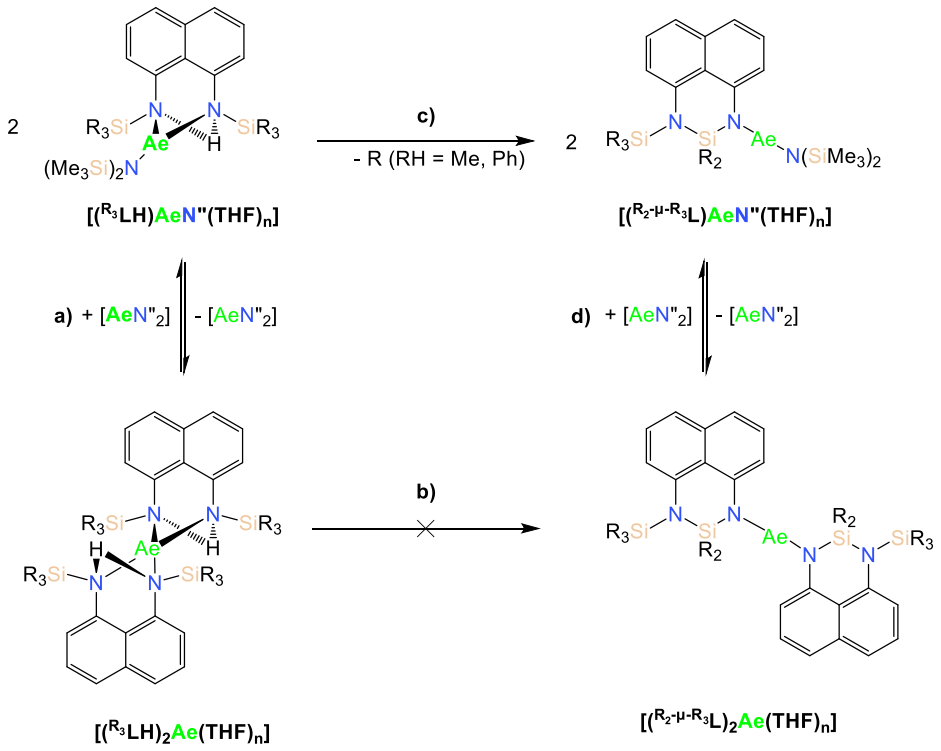
single deuterium atom of the CH_3D by-product. Together, these results confirm the abstraction of the (N,N)μ_2-D atom of [(^{Me3}LD)BaN"(THF)$_n$] by one of its methyl substituents upon its conversion into [($^{Me3\text{-}\mu\text{-}Me2}$L)BaN"(THF)$_n$].

The analogous reaction of $^{Ph2Me}LD_2$ with [(THF)$_2$BaN"$_2$] was also conducted (**Scheme 2.14b**) and monitored *in situ* by NMR spectroscopy (**Figure A.26**). The initial ^{1}H NMR spectrum once again showed the suppression of the (N,N)μ_2-H signal, with a (N,N)μ_2-D signal instead observed in the ^{2}H NMR spectrum at δ = 12.91 ppm along with the diagnostic DN" peak. Heating at 80 °C resulted in the full consumption of the (N,N)μ_2-D signal and the observation of diagnostic benzene singlets resulting from the formation of C_6H_5D in both the ^{1}H and ^{2}H NMR spectra. Notably, no CH_3D was observed. This confirms the exclusive loss of a phenyl group from the $SiPh_2Me$ moiety, further demonstrating the influence their electron-withdrawing effect has on the thermal degradation reaction (**Section 2.4.1.7**).

2.4.3 Investigation of Schlenk equilibria

2.4.3.1 Solution-state structure of [(^{R3}LH)AeN"(THF)$_n$]

The proposed structure of [(^{R3}LH)AeN"(THF)$_n$] is heteroleptic, as this is the expected product of the 1:1 reaction of $^{R3}LH_2$ with [(THF)$_2$AeN"$_2$]. Variable temperature NMR studies were conducted to investigate the presence of any Schlenk equilibria with the homoleptic species [(^{R3}LH)$_2$Ae(THF)$_n$] and [(THF)$_n$AeN"$_2$] in solution (**Scheme 2.15a**).



Scheme 2.15 General scheme for **a)** interconversion of [(^{R3}LH)AeN"(THF)$_n$] and [(^{R3}LH)$_2$Ae(THF)$_n$]; **b)** conversion of [(^{R3}LH)$_2$Ae(THF)$_n$] into [($^{R3\text{-}\mu\text{-}R2}$L)$_2$Ae(THF)$_n$] (not observed); **c)** conversion of [(^{R3}LH)AeN"(THF)$_n$] into [($^{R3\text{-}\mu\text{-}R2}$L)AeN"(THF)$_n$]; and **d)** interconversion of [($^{R3\text{-}\mu\text{-}R2}$L)AeN"(THF)$_n$] and [($^{R3\text{-}\mu\text{-}R2}$L)$_2$Ae(THF)$_n$]. Coordinated THF is excluded for clarity.

The ^{1}H NMR spectrum of [(^{Me3}LH)SrN"(THF)$_n$] at 25 °C (**Figure 2.15**) shows significant broadening of the (N,N)μ$_2$-H signal at δ = 12.37 ppm. Additional spectra recorded at lower temperatures (**Figure 2.15**) show further broadening of both this signal and the three naphthyl signals from 0 °C to –40 °C. Further cooling results in full divergence into two sets of resonances at –60 °C that sharpen significantly at –80 °C. The low coalescence temperature (for the 3,6-C$_{10}H_6$ triplet at δ = 6.92 ppm: T_c = 233 K, Δν = 243 Hz and $\Delta G^{\ddagger}$(233 K) = 49 kJ mol^{-1})[39] suggests that both [(^{Me3}LH)SrN"(THF)$_n$] and [(^{Me3}LH)$_2$Sr(THF)$_n$] are present in solution and are in rapid exchange at room temperature, resulting in a time-averaged spectrum.

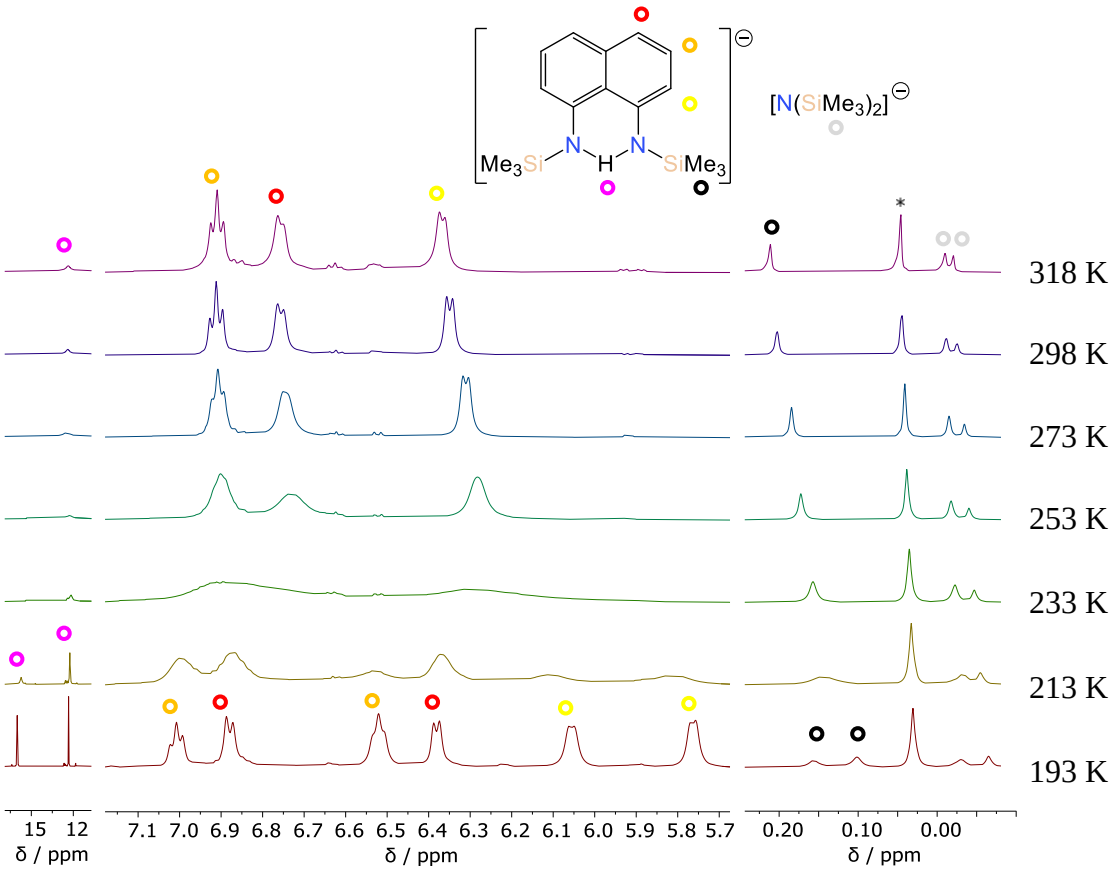


Figure 2.15 Variable temperature ^{1}H NMR spectra (C_4D_8O, 499.99 MHz) of [(^{Me3}LH)SrN"(THF)$_n$] prepared *in situ* from ^{Me3}LH$_2$ and [SrN"$_2$(THF)$_2$]. * denotes HN". The [^{Me3}LH]$^-$ and [N"]$^-$ ligands are shown as an anions as they are present in [(^{Me3}LH)SrN"(THF)$_n$], [(^{Me3}LH)$_2$Sr(THF)$_n$] and [(THF)$_n$AeN"$_2$].

Similar low temperature spectra of [(^{Me3}LH)BaN"(THF)$_n$] showed some signal broadening but no divergence, suggesting that exchange between the two species is still rapid even at very low temperatures due to the greater lability of Ba^{2+}. However, [(^{Me3}LH)$_2$Ba(THF)$_n$] could be synthesised rationally via a 2:1 reaction between ^{Me3}LH$_2$ and [(THF)$_2$BaN"$_2$], as evidenced by the absence of the [N"]$^-$ methyl resonance at δ = –0.03 ppm in the ^{1}H NMR spectrum (**Figure 2.16c**) that is present when 1:1 and 1:2 reactions are conducted (**a** and **b** respectively).

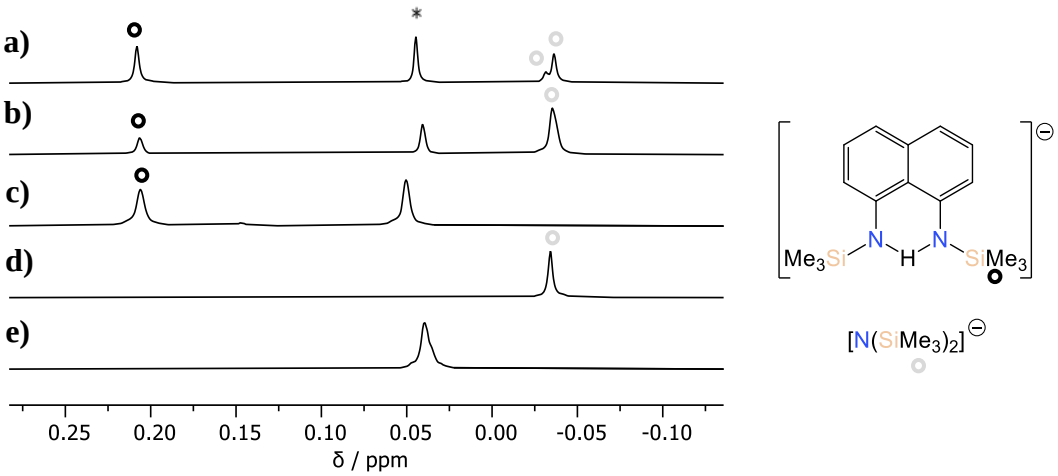


Figure 2.16 Methyl regions of the ^{1}H NMR spectra (C_4D_8O, 298 K, 400 MHz) of **a)** 1:1 reaction of $^{Me3}LH_2$ and $[(THF)_2BaN"_2]$, **b)** 1:2 reaction of $^{Me3}LH_2$ and $[(THF)_2BaN"_2]$, **c)** 2:1 reaction of $^{Me3}LH_2$ and $[(THF)_2BaN"_2]$, **d)** $[(THF)_2BaN"_2]$ and **e)** HN". The $[^{Me3}LH]^-$ and $[N]^-$ ligands are shown as anions as they are present in $[(^{Me3}LH)BaN"(THF)_n]$, $[(^{Me3}LH)_2Ba(THF)_n]$ and $[(THF)_nBaN"_2]$.

Contrastingly, spectra of bulkier variants of $[(^{R3}LH)AeN"(THF)_n]$ (R_3 = $Me_2{}^tBu$, $^iPr_3$, Ph_2Me and Ph_3) taken at 25 °C generally displayed sharp resonances, with lower temperatures not showing any divergence into multiple species. Similarly, the 2:1 reactions of $^{R3}LH_2$ with $[(THF)_nAeN"_2]$ resulted in spectra showing a 1:1 ratio of $^{R3}LH_2$ to $[(^{R3}LH)AeN"(THF)_n]$, rather than $[(^{R3}LH)_2Ae(THF)_n]$. This suggests that only the least bulky ligand $[^{Me3}L]^-$ enables interconversion between $[(^{R3}LH)AeN"(THF)_n]$ and $[(^{R3}LH)_2Ae(THF)_n]$, and that bulkier silyl substituents disfavour ligand redistribution of this kind. Consequently, the $\delta(\mu_2\text{-H})$ data for $[(^{Me3}LH)AeN"(THF)_n]$ were excluded from **Figure 2.13**. Notably, heating a sample of $[(^{Me3}LH)_2Ba(THF)_n]$ prepared *in situ* (**Figure 2.16c**) at 80 °C for 16 hours resulted in no significant changes to the ^{1}H NMR spectrum. This suggests that thermal degradation of $[(^{Me3}LH)_2Ae(THF)_n]$ to form $[(^{Me3\text{-}\mu\text{-}Me2}L)_2Ae(THF)_n]$ does not occur directly (**Scheme 2.15b**) and that it is the

heteroleptic species [(^{Me3}LH)AeN"(THF)$_n$] that undergoes thermal degradation (**Scheme 2.15c**). Furthermore, this implies that [($^{R3\text{-}\mu\text{-}R2}$L)AeN"(THF)$_n$] does initially form as a heteroleptic species *via* the mechanism proposed in **Scheme 2.9**.

2.4.3.2 Solution-state structure of [($^{R3\text{-}\mu\text{-}R2}$L)AeN"(THF)$_n$]

However, the ^{1}H NMR spectra of [($^{Me3\text{-}\mu\text{-}Me2}$L)AeN"(THF)$_n$] (Ae = Ca, Sr and Ba, **Figure 2.17**) showed that the homoleptic species [($^{Me3\text{-}\mu\text{-}Me2}$L)$_2$Ae(THF)$_n$] are also present in solution (**Scheme 2.15d**). The room temperature spectrum of the calcium congener (**a**) shows the broadening and in some cases divergence of the naphthyl and methyl resonances. This implies the presence of both homo- and heteroleptic complexes containing [$^{Me3\text{-}\mu\text{-}Me2}$L]$^-$ ligands which are in slow exchange with one another. The corresponding resonances in the analogous spectrum of the strontium congener (**b**) are significantly broadened, but with no divergence observed. Conversely, barium's higher

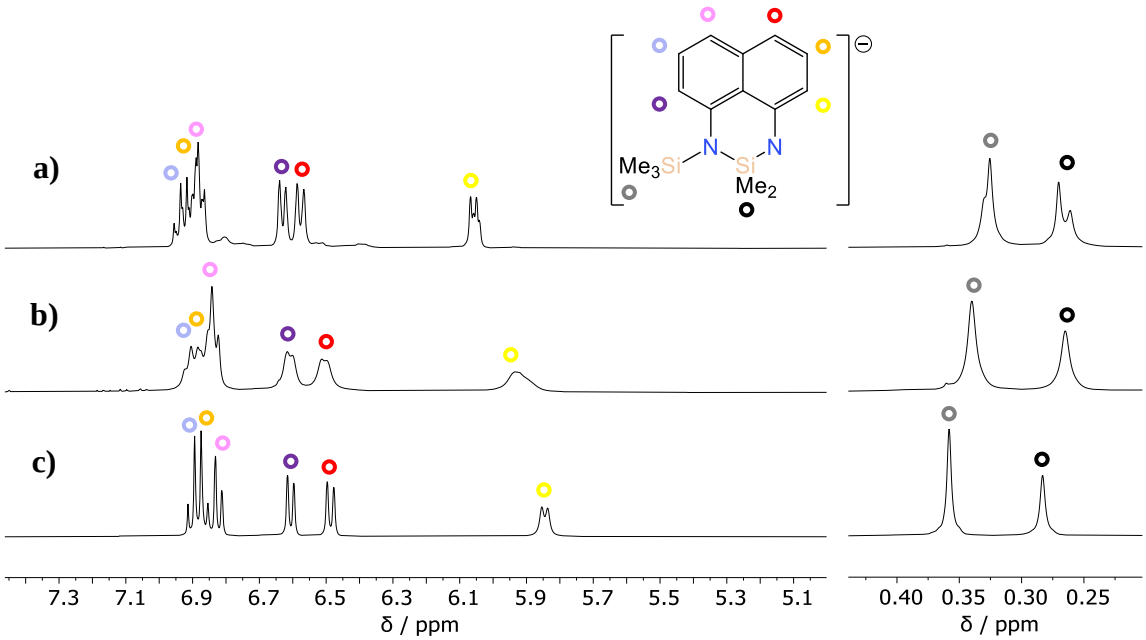


Figure 2.17 Naphthyl and methyl regions of the ^{1}H NMR spectra (C_4D_8O, 298 K, 400 MHz) of [($^{Me3\text{-}\mu\text{-}Me2}$L)AeN"(THF)$_n$] (Ae = Ca (**a**), Sr (**b**) and Ba (**c**)). The [$^{Me3\text{-}\mu\text{-}Me2}$L]$^-$ ligand is shown as an anion as it is present in both [($^{Me3\text{-}\mu\text{-}Me2}$L)AeN"(THF)$_n$] and [($^{Me3\text{-}\mu\text{-}Me2}$L)$_2$Ae(THF)$_n$].

kinetic lability results in relatively sharp time-averaged signals (**c**). In all cases, lower temperature spectra show further divergence of the naphthyl and methyl signals as the rate of exchange between [($^{Me3\text{-}\mu\text{-}Me2}$L)AeN"(THF)$_n$] and [($^{Me3\text{-}\mu\text{-}Me2}$L)$_2$Ae(THF)$_n$] slows (**Figures A.21** and **A.22**). Variable temperature spectra of [($^{Me3\text{-}\mu\text{-}Me2}$L)SrN"(THF)$_n$] are presented as a representative example (**Figure 2.18**).

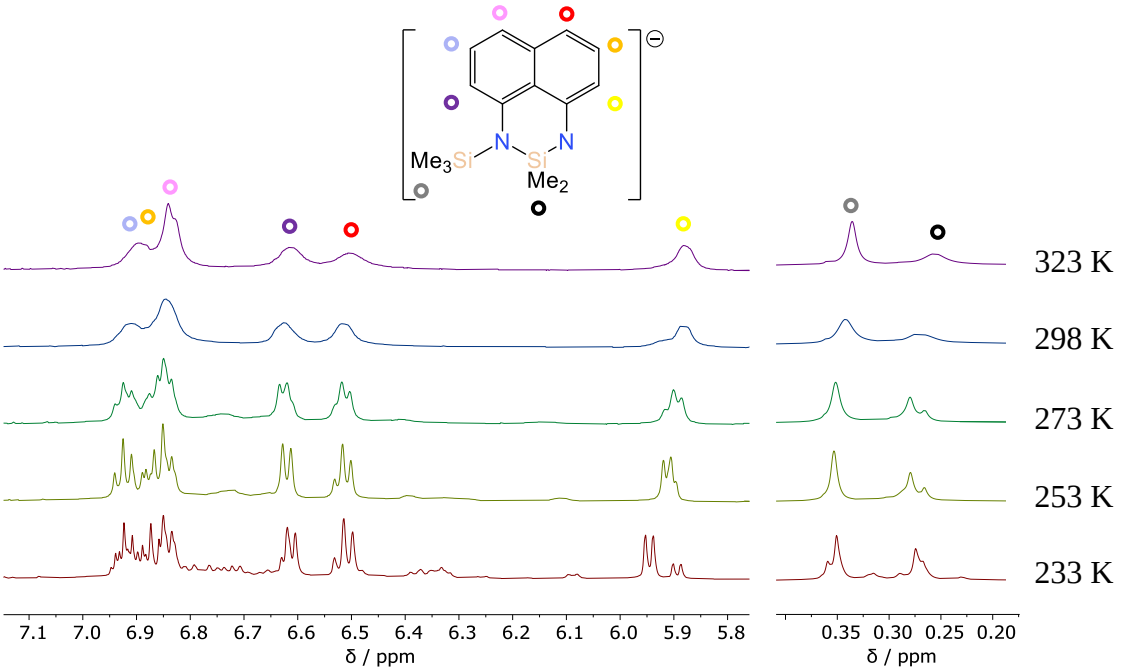


Figure 2.18 Variable temperature ^{1}H NMR spectra (C_4D_8O, 499.9 MHz) of [($^{Me3\text{-}\mu\text{-}Me2}$L)SrN"(THF)$_n$]. The [$^{Me3\text{-}\mu\text{-}Me2}$L]$^-$ ligand is shown as an anion as it is present in both [($^{Me3\text{-}\mu\text{-}Me2}$L)SrN"(THF)$_n$] and [($^{Me3\text{-}\mu\text{-}Me2}$L)$_2$Sr(THF)$_n$].

Together, these spectra demonstrate that the redistribution of the monodentate [$^{Me3\text{-}\mu\text{-}Me2}$L]$^-$ and [N"]$^-$ ligands occurs readily, with an increasing rate of exchange as group 2 is descended. While room temperature spectra of [($^{Ph3\text{-}\mu\text{-}Ph2}$L)AeN"(THF)$_n$] (Ae = Sr and Ba, see **Figure 2.12b**) were more challenging to assign due to their overlapping aromatic signals, they show significant signal broadening which can be attributed to ligand redistribution. That the monodentate ligands [$^{R3\text{-}\mu\text{-}R2}$L]$^-$ do not prevent Schlenk equilibria, while the chelating bidentate ligands [^{R3}LH]$^-$ (excluding R_3 = Me_3)

seemingly do, demonstrates the importance of employing suitable ligand systems for solution-phase alkaline earth chemistry, and is fully consistent with literature precedent.[40–42]

2.5 Conclusions

A series of 1,8-*bis*(silylamino)naphthalene proligands $^{R_3}LH_2$ (R_3 = Me_3, $Me_2{}^tBu$, $^iPr_3$, Ph_2Me and Ph_3) have been synthesised, including the novel triphenyl variant $^{Ph_3}LH_2$ (**1**). The related compounds $^{\mu\text{-}Me_2}LH_2$ (**2**) and $^{Me_2H\text{-}\mu\text{-}Me_2}LH$ (**3**) were also isolated following the attempted synthesis of $^{Me_2H}LH_2$. These proligands were investigated as a platform for the synthesis of monomeric diamido alkaline earth complexes. Two novel 1,8-*bis*(silylamido)naphthalene magnesium complexes [(^{R_3}L)Mg(THF)$_2$] (R_3 = Me_3 (**4**) and $Me_2{}^tBu$ (**5**)) have been synthesised *via* the protonolysis of $^{R_3}LH_2$ with [MgN"$_2$]$_2$ in THF. Complexes **1–5** were characterised by multinuclear NMR spectroscopy and, in most cases, X-ray crystallography, infra-red spectroscopy and elemental analysis.

The synthesis of the heavier congeners [(^{R_3}L)Ae(THF)$_n$] (Ae = Ca, Sr and Ba) *via* the protonolysis of $^{R_3}LH_2$ with [(THF)$_2$AeN"$_2$] in THF was also attempted. *In situ* NMR spectroscopic analysis revealed the formation of complex reaction mixtures that were highly sensitive to the ligand substituents, alkaline earth metal and temperature employed in a given reaction. The intermediate species [(^{R_3}LH)AeN"(THF)$_n$] and thermal degradation product [($^{R_3\text{-}\mu\text{-}R_2}$L)AeN"(THF)$_n$] were also identified in addition to [(^{R_3}L)Ae(THF)$_n$].

Increasing the size of Ae^{2+} was found to destabilise [(^{R_3}L)Ae(THF)$_n$] and favour the formation of [($^{R_3\text{-}\mu\text{-}R_2}$L)AeN"(THF)$_n$] *via* thermal degradation. The presence of bulky

alkyl substituents was found to stabilise the intermediate species [(^{R3}LH)AeN"(THF)$_n$] and prevent any thermal degradation, whereas electron withdrawing phenyl substituents favoured further deprotonation to form either [(^{R3}L)Ae(THF)$_n$] or [($^{R3\text{-}\mu\text{-}R2}$L)AeN"(THF)$_n$] (**Chart 2.4**).

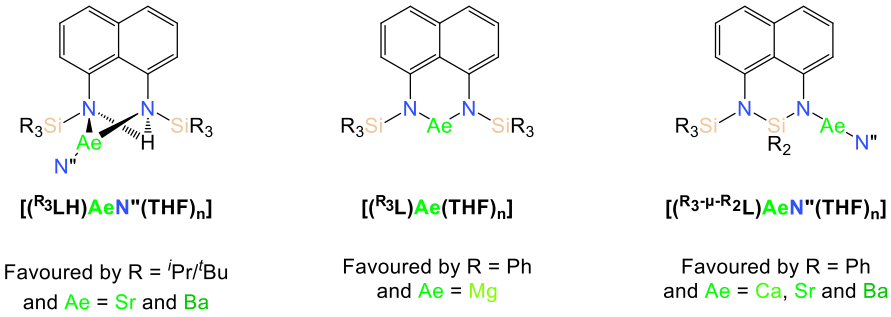


Chart 2.4 Summary of factors influencing the formation of [(^{R3}LH)AeN"(THF)$_n$], [(^{R3}L)Ae(THF)$_n$] and [($^{R3\text{-}\mu\text{-}R2}$L)AeN"(THF)$_n$]. Coordinated THF excluded for clarity.

The factors influencing these varying outcomes could be rationalised by considering various steric and electronic effects. This enabled the proposition of a mechanism for the thermal degradation reaction, which consists of an intramolecular σ-bond metathesis reaction following the rearrangement of [(^{R3}LH)AeN"(THF)$_n$] into an active conformation. This mechanism was further supported by deuterium labelling experiments. Variable temperature NMR spectra demonstrated that both [($^{R3\text{-}\mu\text{-}R2}$L)AeN"(THF)$_n$] and [(^{Me3}LH)AeN"(THF)$_n$] are in equilibrium with their homoleptic analogues, whereas the bulkier variants of [(^{R3}LH)AeN"(THF)$_n$] were stable with respect to ligand redistribution.

The use of THF as the solvent enabled the observation of many species *in situ* by NMR spectroscopy. However, the high solubility and dynamic solution-phase structures of these complexes in THF precluded their isolation and solid-state characterisation. Consequently, **Chapters 3** and **4** describe the use of a THF-free synthetic route to enable

the more straightforward isolation of heavier alkaline earth complexes supported by $[^{R3}L]^{2-}$. These subsequent investigations were aided significantly by the insight provided by results discussed in this Chapter.

2.6 References

1 R. L. Benoit, D. Lefebvre and M. Fréchette, *Can. J. Chem.*, 1987, **65**, 996–1001.

2 L. H. Gade, C. H. Galka, K. W. Hellmann, R. M. Williams, L. De Cola, I. J. Scowen and M. McPartlin, *Chem. Eur. J.*, 2002, **8**, 3732–3746.

3 J. L. Smith, J. L. Beck and W. J. A. Vandenheuvel, *Org. Mass Spectrom.*, 1971, **5**, 473–480.

4 C. D. Schaeffer and J. J. Zuckerman, *J. Am. Chem. Soc.*, 1974, **96**, 7160–7162.

5 K. W. Hellmann, C. Galka, L. H. Gade, T. Kottke and D. Stalke, *Chem. Commun.*, 1998, 549–550.

6 K. W. Hellmann, C. H. Galka, I. Rüdenauer, L. H. Gade, I. J. Scowen, M. McPartlin, M. Saunders, R. Berger, A. Jaffe, J. M. McBride, J. ONeill, R. Breslow, J. M. Hoffman, C. Perchonock, E. Wasserman, R. S. Hutton, V. J. Kuck, H. Jiao, P. R. von Schleyer, Y. Mo, M. A. McAllister and T. T. Tidwell, *Angew. Chem. Int. Ed*, 1998, **37**, 272.

7 A. J. Blake, N. L. Gillibrand, G. J. Moxey and D. L. Kays, *Inorg. Chem.*, 2009, **48**, 10837–10844.

8 K. Nomura, N. Naga and K. Takaoki, *Macromolecules*, 1998, **31**, 8009–8015.

9 C. H. Lee, Y. H. La and J. W. Park, *Organometallics*, 2000, **19**, 344–351.

10 M. A. Bradley, C. Birchall, A. J. Blake, W. Lewis, G. J. Moxey and D. L. Kays, *Dalton Trans.*, 2017, **46**, 4101–4110.

11 M. V. Yakovenko, N. Y. Udilova, T. A. Glukhova, A. V. Cherkasov, G. K. Fukin and A. A. Trifonov, *New J. Chem.*, 2015, **39**, 1083–1093.

12 B. Nekoueishahraki, P. P. Samuel, H. W. Roesky, D. Stern, J. Matussek and D. Stalke, *Organometallics*, 2012, **31**, 6697–6703.

13 K. M. Marczenko and S. S. Chitnis, *Chem. Commun.*, 2020, **56**, 8015–8018.

14 K. M. Marczenko, J. A. Zurakowski, K. L. Bamford, J. W. M. MacMillan and S. S. Chitnis, *Angew. Chem. Int. Ed.*, 2019, **58**, 18096–18101.

15 N. J. Roberts, E. R. Johnson and S. S. Chitnis, *Organometallics*, 2022, **41**, 2180–2187.

16 R. Guthardt, C. Bruhn, C. Färber and U. Siemeling, *Organometallics*, 2020, **39**, 4174–4177.

17 D. M. Lyubov, A. V. Cherkasov, G. K. Fukin, K. A. Lyssenko, E. A. Rychagova, S. Y. Ketkov and A. A. Trifonov, *Dalton Trans.*, 2018, **47**, 438–451.

18 C. H. Galka, D. J. M. Tro, I. Ru, L. H. Gade, I. Scowen and M. Mcpartlin, *Inorg. Chem.*, 2000, **39**, 4615–4620.

19 S. Danièle, C. Drost, B. Gehrhus, S. M. Hawkins, P. B. Hitchcock, M. F. Lappert, P. G. Merle and S. G. Bott, *Dalton Trans.*, 2001, 3179–3188.

20 R. Waterman, *Organometallics*, 2013, **32**, 7249–7263.

21 K. H. Chan, J. L. Hong and A. C. Su, *J. Polym. Res.*, 2004, **11**, 133–140.

22 L. Yang, D. R. Powell and R. P. Houser, *Dalton Trans.*, 2007, 955–964.

23 R. D. Shannon, *Acta Crystallogr. A*, 1976, **32**, 751–767.

24 R. L. Jones, L. J. Morris, C. G. Collins Rice, Z. R. Turner and D. O'Hare, *Phys. Chem. Chem. Phys.*, 2023, **25**, 15463–15468.

25 R. L. Jones, Z. R. Turner, J.-C. Buffet and D. O'Hare, *Polym. Chem.*, 2024, **15**, 1767–1776.

26 R. R. Fraser, T. S. Mansour and S. Savard, *J. Org. Chem.*, 1985, **50**, 3232–3234.

27 T. K. Panda, H. Kaneko, O. Michel, K. Pal, H. Tsurugi, K. W. Törnroos, R. Anwander and K. Mashima, *Organometallics*, 2012, **31**, 3178–3184.

28 B. Freitag, C. A. Fischer, J. Penafiel, G. Ballmann, H. Elsen, C. Färber, D. F. Piesik and S. Harder, *Dalton Trans.*, 2017, **46**, 11192–11200.

29 V. Lorenz, C. G. Hrib, D. Grote, L. Hilfert, M. Krasnopolski and F. T. Edelmann, *Organometallics*, 2013, **32**, 4636–4642.

30 L. Orzechowski, G. Jansen and S. Harder, *J. Am. Chem. Soc.*, 2006, **128**, 14676–14684.

31 L. Orzechowski and S. Harder, *Organometallics*, 2007, **26**, 5501–5506.

32 M. S. Hill, D. J. Liptrot, D. J. Macdougall, M. F. Mahon and T. P. Robinson, *Chem. Sci.*, 2013, **4**, 4212–4222.

33 M. Arrowsmith, M. S. Hill and G. Kociok-Köhn, *Organometallics*, 2010, **29**, 4203–4206.

34 I. L. Fedushkin, N. M. Khvoinova, A. A. Skatova and G. K. Fukin, *Angew. Chemie Int. Ed.*, 2003, **42**, 5223–5226.

35 I. L. Fedushkin, A. G. Morozov, O. V. Rassadin and G. K. Fukin, *Chem. Eur. J.*, 2005, **11**, 5749–5757.

36 A. G. Morozov, M. V. Moskalev, D. A. Razborov and I. L. Fedushkin, *J. Organomet. Chem.*, 2020, **927**, 121535.

37 P. P. Power, *Nature*, 2010, **463**, 171–177.

38 P. C. Stegner, J. Eyselein, G. M. Ballmann, J. Langer, J. Schmidt and S. Harder, *Dalton Trans.*, 2021, **50**, 3178–3185.

39 A. G. Palmer, *Annu. Rev. Biophys. Biomol. Struct.*, 2001, **30**, 129–155.

40 M. R. Crimmin and M. S. Hill, *Top. Organomet. Chem.*, 2013, **45**, 191–242.

41 M. S. Hill, D. J. Liptrot and C. Weetman, *Chem. Soc. Rev.*, 2016, 45, 972–988.

42 P. M. Chapple and Y. Sarazin, *Eur. J. Inorg. Chem.*, 2020, **2020**, 3321–3346.

Chapter 3

Synthesis and characterisation of phenyl-substituted 1,8-*bis*(silylamido)naphthalene alkaline earth complexes

3.1 Introduction

3.1.1 Overview

Building on the work described in **Chapter 2**, this chapter discusses the isolation of phenyl-substituted 1,8-*bis*(silylamido)naphthalene alkaline earth complexes *via* a THF-free synthetic route. In total, the synthesis and characterisation of seven novel complexes of the heavier alkaline earth elements (Ae = Ca, Sr and Ba) is presented. These include six homobimetallic dimers that display two distinct structural motifs, as well as one monomeric THF adduct.

3.1.2 Dimeric complexes supported by 1,8-*bis*(silylamido)naphthalene and related ligands

A number of aggregated species supported by1,8-*bis*(silylamido)naphthalene ligands, ($[^{R_3}L]^{2-}$ = $[1,8\text{-}\{(R_3Si)N\}_2C_{10}H_6]^{2-}$) have been reported previously, the X-ray crystal structures of which display a range of structural motifs. In 2009, Kays and co-workers

reported the dimeric zinc complex [(^{Me3}L)Zn]$_2$ (**I**, **Chart 3.1**).[1] This nitrogen-bridged species consists of a central Zn_2N_2 core in which the two [^{Me3}L]$^{2-}$ ligands each chelate one Zn^{2+}centre in a κ^2-N,N′-bidentate manner, with a μ_2-N donor also bridging to the other zinc dication. This motif has also been reported for ytterbium(II) and europium(II) complexes supported by a related naphthalene-bridged *bis*(guanidinate) ligand.[2,3] O'Hare and co-workers have also very recently reported a series of dimeric alkaline earth complexes supported by a related *bis*(phenoxyimine) "NOON" ligand, which also contains a rigid naphthalene backbone (**II-Ae**, Ae = Mg, Ca, Sr and Ba, **Chart 3.1**).[4] The X-ray crystal structures of **II-Ae** revealed a central Ae_2O_2 diamond core, with Ae^{2+} also coordinated by one imine donor of the "NOON" ligand and THF. When dissolved in THF, these dimeric species were found to exist in equilibrium with their monomeric analogues, which could be isolated as 18-crown-6 adducts. The ability of **II-Ae** (Ae = Ca, Sr and Ba) to catalyse the ring-opening polymerisation of lactide both in the presence and absence of a co-initiator has also been demonstrated.[5]

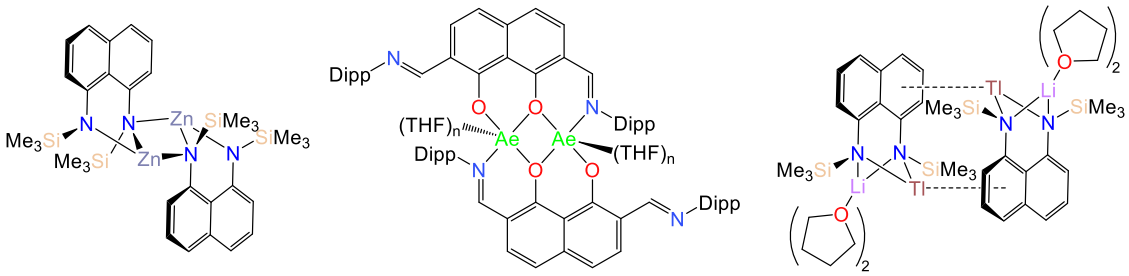


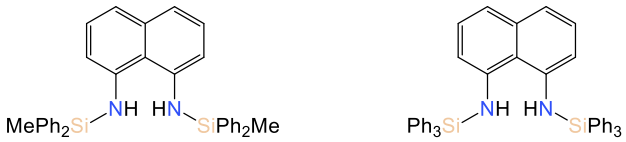
Chart 3.1 Selected examples of dimeric complexes supported by dianionic chelating ligands with rigid naphthalene backbones.

Conversely, dimerisation is also possible through the formation of π-facial interactions between metal cations and the naphthalene backbone. This mode of dimerisation has been reported previously for both the dilithium salt [(^{Me3}L)Li{Li(THF)}]$_2$ and the mixed

thalium/lithium dimer [(^{Me3}L)Tl{Li(THF)$_2$}]$_2$ (**III**, **Chart 3.1**), in which dimerisation results from η^3- and η^6-π-facial interactions respectively.[6] Dimeric alkaline earth complexes supported by chelating diamido ligands that dimerise *via* both bridging amido donors[7] and Ae^{2+}-aryl π-facial interactions[7,8] have also been reported recently by Jones and co-workers (see **Chart 1.7**, **Chapter 1**). These compounds show an increasing preference for the formation of "soft" π-facial interactions by the larger Ae^{2+} congeners.

3.2 Synthesis of dimeric THF-free alkaline earth complexes

The *in situ* NMR spectroscopic data discussed in **Chapter 2** revealed that the phenyl-substituted proligands ^{Ph2Me}LH$_2$ and especially ^{Ph3}LH$_2$ (**1**) (**Chart 3.2**) were more readily deprotonated than their alkyl-substituted analogues. This was attributed to the increased acidity of their amino protons that results from their electron-withdrawing phenyl substituents. Consequently, these proligands were chosen as candidates for the synthesis of donor-free alkaline earth.

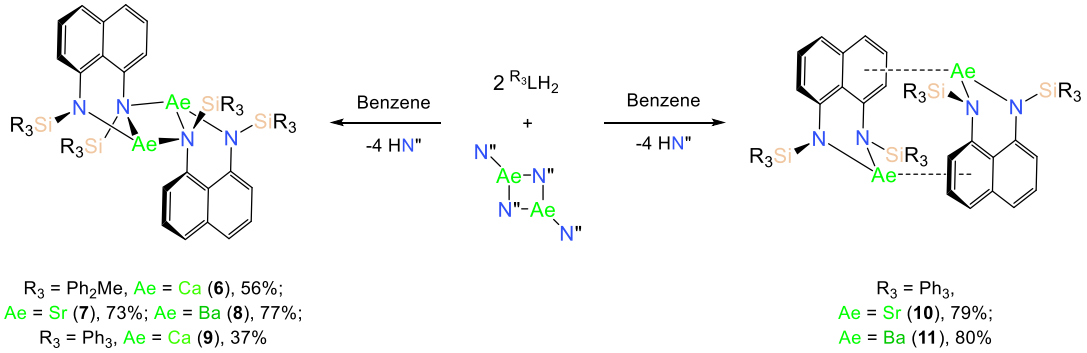


^{Ph2Me}LH$_2$ ^{Ph3}LH$_2$ (1)

Chart 3.2 The phenyl-substituted 1,8-*bis*(silylamino)naphthalene proligands ^{Ph2Me}LH$_2$ and ^{Ph3}LH$_2$ (**1**).

Two equivalents of ^{R3}LH$_2$ (R$_3$ = Ph$_2$Me and Ph$_3$) were reacted with one equivalent of the THF-free dimeric alkaline earth bases [AeN"$_2$]$_2$ (Ae = Mg, Ca, Sr and Ba) in benzene (**Scheme 3.1**). Unfortunately, the [MgN"$_2$]$_2$ reactions proved unproductive (*vide infra*). Gratifyingly however, the reactions of the heavier congeners afforded the dimeric alkaline earth complexes [(^{R3}L)Ae]$_2$ (R$_3$ = Ph$_2$Me, Ae = Ca (**6**), 56%, Sr (**7**), 73% and Ba

(**8**), 77%; R_3 = Ph_3, Ae = Ca (**9**), 37%, Sr (**10**), 79% and Ba (**11**), 80%) as bright yellow crystalline solids. The solid-state structures of complexes **6**–**11** are dependent on the exact combination of metal and ligand substituents present in each case, and exhibit either nitrogen- or naphthalene-bridged centrosymmetric dimeric motifs (**Sections 3.3** and **3.4**). With the exception of **9** (*vide infra*), **6**–**11** all precipitate directly from the reaction mixture, enabling their facile isolation and characterisation by X-ray crystallography, NMR spectroscopy, IR spectroscopy and elemental analysis.



Scheme 3.1 Synthesis of **6**–**11** *via* the 2:1 reaction of $^{R_3}LH_2$ (R_3 = Ph_2Me and Ph_3) with $[AeN''_2]_2$ (Ae = Ca, Sr and Ba) in benzene.

3.3 X-ray crystallographic analysis of nitrogen-bridged dimers

Complexes **6–9** all crystallise as nitrogen-bridged dimers. However, they are not completely isostructural. The key structural features of these complexes will first be discussed using $[(^{Ph_3}L)Ca]_2$ (**9**) as a representative example. The structures of $[(^{Ph_2Me}L)Ae]_2$, (Ae = Ca (**6**), Sr (**7**) and Ba (**8**)) will then be presented in turn, with any notable variations discussed in each case. The crystal structures of **6**–**9** are shown in **Figures 3.1**–**3**, with selected metrical parameters presented in **Table 3.1**.

3.3.1 Crystal structure of [(^{Ph_3}L)Ca]$_2$ (9)

Unlike in other cases, crystals of **9** did not grow directly from the reaction mixture. However, lyophilisation of the reaction mixture afforded a bright yellow powder which could be recrystallised from boiling benzene, affording yellow single crystals suitable for an X-ray diffraction study. Notably, **9** crystallises in the $P\overline{1}$ space group and has a structure consisting of four crystallographically distinct [(^{Ph_3}L)Ca]$_2$ molecules, unlike **6**–**8** (*vide infra*). However, there is little metrical variance between these four dimeric units, which all display the same nitrogen-bridged dimeric motif. Consequently, a single representative [(^{Ph_3}L)Ca]$_2$ molecule is discussed herein.

The asymmetric unit of **9** (**Figure 3.1a**) consists of a monomeric [(^{Ph_3}L)Ca] unit, in which Ca^{2+} is chelated by the dianionic [^{Ph_3}L]$^{2-}$ ligand in a κ^2-N,N′-bidentate manner *via* two deprotonated amide donors. Coordinative saturation is provided by the formation of both η^1- and η^2-π-facial interactions between Ca^{2+} and two phenyl substituents (one from each $SiPh_3$ group). This provides crystallographic evidence that phenyl substituents stabilise [(^{R_3}L)Ae] fragments and thus facilitate the full deprotonation of $^{R_3}LH_2$ by [AeN"$_2$]$_2$. These observation are consistent with the formation of the phenyl-substituted monomeric complexes [(^{R_3}L)Ae(THF)$_n$] (R_3 = Ph_2Me and Ph_3) when the same synthetic route is attempted in THF rather than benzene (**Section 2.4.1.7**). Various examples of stabilising Ae^{2+}-arene interactions have also been reported in the literature.[8–16]

The Ca^{2+} centre lies 0.564(2) Å from the mean plane defined by the naphthalene backbone. While this is further than for the monomeric magnesium complexes **4** and **5**, the accommodation of the larger Ca^{2+} cation relatively close to the plane of the [^{Ph_3}L]$^{2-}$ ligand has again necessitated a significant distortion of the naphthalene backbone away

from planarity (C(1–10)-Plane$_{C(1)-C(10)}$ = 0.002(1)–0.170(1) Å, see **Figure 3.7g**). This results in a significant increase in the N-N distance of **9** (2.964(2) Å) relative to that of the proligand $^{Ph3}LH_2$ (2.827(2) Å) as the metal binding pocket widens to facilitate the coordination of Ca^{2+}. This small metal binding pocket results in an acute N(1)-Ca(1)-N(2)

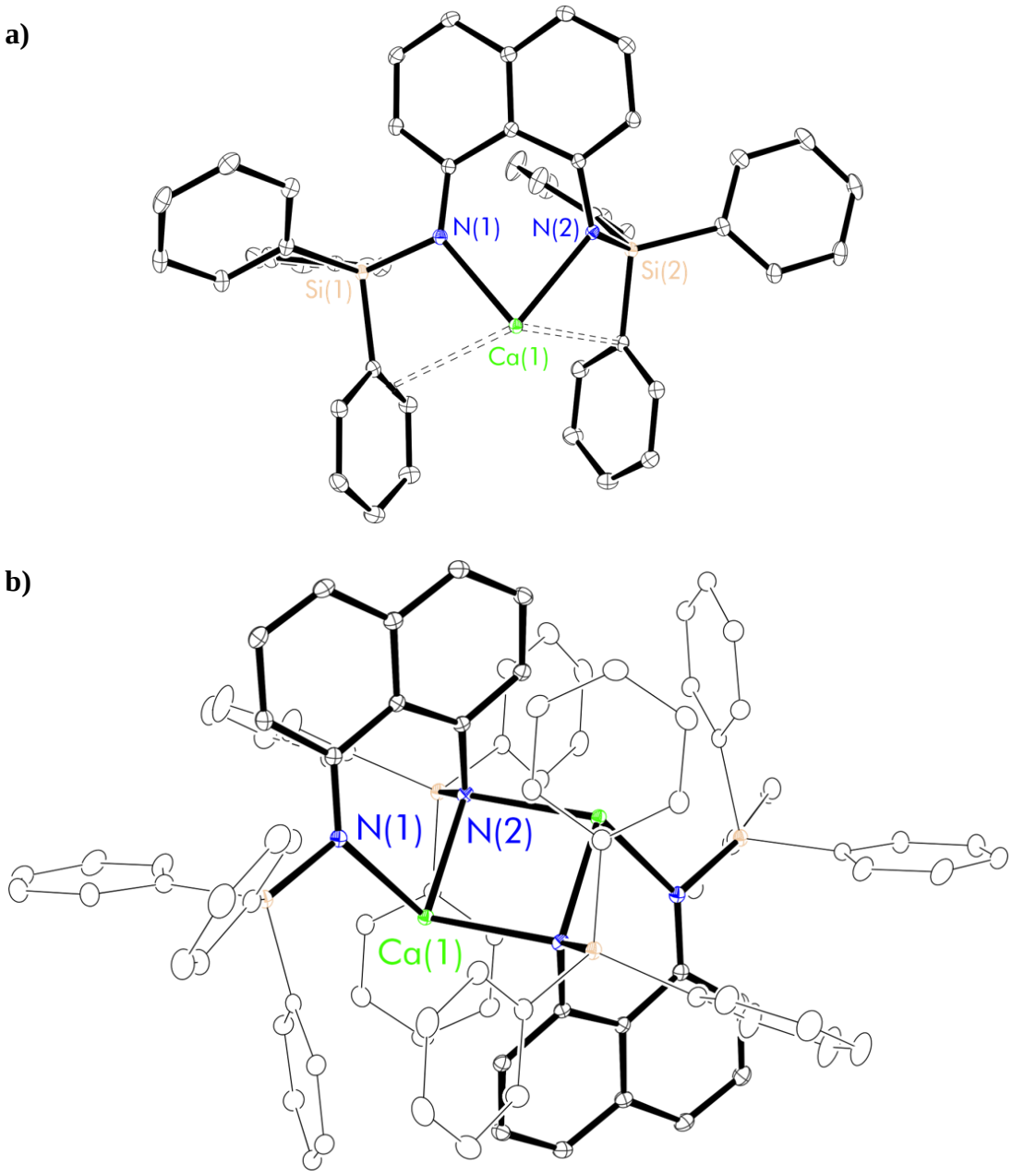


Figure 3.1 Thermal displacement ellipsoid drawings (30% probability) of **a)** the asymmetric unit and **b)** full dimeric structure of [(^{Ph3}L)Ca]$_2$ (**9**) generated by a (–X, –Y+2, –Z+1) symmetry operation. All hydrogen atoms have been omitted and phenyl groups are wireframed in b) for clarity.

bite angle of 78.85(4)°. The Ca^{2+} centre is therefore exposed and consequently forms further stabilising interactions that result in dimerisation.

The full dimeric structure of **9** (**Figure 3.1b**) is generated by a by a (–X, –Y+2, –Z+1) symmetry operation, which generates an inversion centre at the centroid of a planar four-membered Ae_2N_2 diamond core. This dimerisation mode has previously been reported for the 1,8-bis(silylamido)naphthalene Zn(II) complex **I** (**Chart 3.1**);[1] Eu(II)[17] and Yb(II)[3] complexes supported by a related ligand; as well as a range of alkaline earth complexes bearing both chelating diamido ligands[8,18–20] and a related *bis*(phenoxyimine) ligand with a naphthalene backbone (**II-Ae**, **Chart 3.1**).[4] This central Ca_2N_2 ring bridges between two monomeric [(^{Ph_3}L)Ca] units that are necessarily orientated antiparallel with respect to one other. This motif results in an interplanar hinge angle of 0° between the mean planes defined by the two naphthalene backbones and a short Ca-Ca distance of 3.4485(4) Å.

The dimeric structure is bridged by a μ_2-N donor which has a tetrahedral geometry ($\Sigma\{\angle N(2)\}$ = 655.1(2)°), while the other terminal amide donor is trigonal planar ($\Sigma\{\angle N(1)\}$ = 360.0(2)°). The calcium centre is formally three-coordinate, with a distorted trigonal pyramidal coordination geometry ($\Sigma\{\angle Ca(1)\}$ = 289.07(7)°). While the bridging Ca-N bond is the longest of the three (Ca(1)-N(1) = 2.311(1) Å < Ca(1)-N(2) = 2.357(1) Å < Ca(1)-N(2)* = 2.478(1) Å, where * refers to symmetry related atoms), it is similar in length to the other Ca-N distances in this case. This reflects the strength of the ionic Ca-N bonds formed by the relatively hard Ca^{2+} cation, which results in dimerisation occurring *via* the bridging μ_2-N donors.

This trigonal pyramidal coordination geometry results in the exposure of one face of the Ca^{2+} cation, which is stabilised by additional π-facial interactions with both phenyl

substituents (*vide supra*) and the naphthalene backbone of the opposing $[^{Ph_3}L]^{2-}$ ligand. However, Ca^{2+} does not reside directly above the opposing naphthalene ring (Ca(1)-centroid$_{C(5)\text{-}C(10)}$ = 3.8029(8) Å). Together, these factors result in a "relaxed" ladder-like structure with both a relatively small fold angle between the respective Ca_2N_2 and naphthalene planes (57.00(5)°) and a short interplanar distance between the two naphthalene planes (1.992(4) Å). This can be attributed to the preference of the (relatively) small Ca^{2+} cation to maximise its interactions with the hard amide donors of the $[^{Ph_3}L]^{2-}$ ligand rather than the softer π-system of the naphthalene backbone. This "relaxed" structure also helps to relieve steric congestion between the bulky $SiPh_3$ groups.

3.3.2 Crystal structures of [(^{Ph_2Me}L)Ae]$_2$, (Ae = Ca (6), Sr (7) and Ba (8))

Yellow single crystals of [(^{Ph_2Me}L)Ae]$_2$ (Ae = Ca (**6**), Sr (**7**) and Ba (**8**)) suitable for X-ray diffraction studies were grown by layering a benzene solution of $^{Ph_2Me}LH_2$ (2 eq.) over a benzene solution of the appropriate [AeN"$_2$]$_2$ precursor (1 eq.). Complexes **6**–**8** all crystallise in the *P*2$_1$/*c* space group, with structures consisting of only a single centrosymmetric [(^{Ph_2Me}L)Ae]$_2$ dimer.

3.3.2.1 Crystal structures of [(^{Ph_2Me}L)Ca]$_2$ (6) and [(^{Ph_2Me}L)Sr]$_2$ (7)

The structure of **6** is unsurprisingly very similar to that of **9**, with their composition only differing due to the substitution of a phenyl group for a methyl group. This results in very similar metrical parameters, especially within their respective asymmetric units (**Table 3.1**). However, **6** has a slightly less "relaxed" dimeric structure (**Figure 3.2a**), evidenced by a larger Ae_2N_2-naphthyl fold angle (62.354(2)°) and a widened interplanar distance between the two naphthalene rings (2.331(6) Å). This slight structural "contraction" is likely enabled by the reduced degree of steric congestion conferred by the smaller methyl

substituents in **6**. This facilitates the accommodation of an enhanced Ca^{2+}-naphthyl interaction, reflected by a slight shortening of the Ca(1)-centroid$_{C(5)-C(10)}$ distance to 3.736(11) Å in **6**.

The structure of the strontium congener **7** (**Figure 3.2b**) also varies relatively little from those of **6** and **9**. The increased ionic radius of Sr^{2+} relative to Ca^{2+} results in lengthened Sr-N bond lengths (Sr(1)-N(1) = 2.461(2) Å, Sr(1)-N(2) = 2.487(2) Å, Sr(1)-N(2)* = 2.677(2) Å) and a more acute N(1)-Sr(1)-N(2) bite angle (74.13(8)°) as Sr^{2+} necessarily sits further from the $[^{Ph_2Me}L]^{2-}$ ligand than Ca^{2+}. **7** has a similarly "relaxed" structure - while the interplanar distance between the two naphthalene rings in **7** has increased to 2.64469(7) Å, this is due to the extension of the Ae-N bonds (*vide supra*) rather than a large increase in the Ae_2N_2-naphthyl fold angle (62.354(2)° (**6**) vs 63.407(2)° (**7**)).

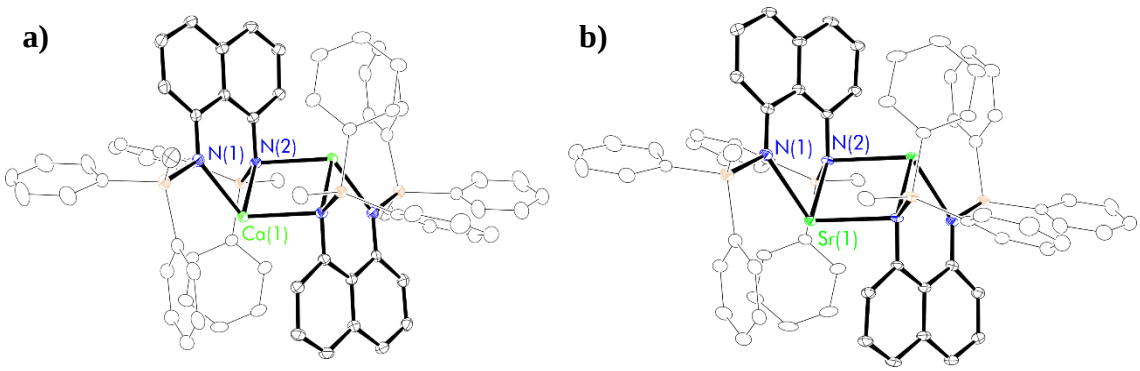


Figure 3.2 Thermal displacement ellipsoid drawings (30% probability) of **a)** $[(^{Ph_2Me}L)Ca]_2$ (**6**) and **b)** $[(^{Ph_2Me}L)Sr]_2$ (**7**), which are each generated by (–X+1, –Y+1, –Z+1) symmetry operations. All hydrogen atoms have been omitted and phenyl groups are shown as ball and stick models for clarity.

3.3.2.2 Crystal structure of $[(^{Ph_2Me}L)Ba]_2$ (8)

The structure of the barium congener **8** (**Figure 3.3**) displays some significant differences from those of **6**, **7** and **9**. Within the asymmetric unit, the extremely large Ba^{2+} cation sits

significantly further from the plane of the naphthalene backbone (Ae^{2+}-$plane_{C(1)-C(10)}$ = 0.60372(2) Å (**7**) vs 1.433(4) Å (**8**), see **Figures 3.7e** and **f**). Consequently, the N(1)-Ba(1)-N(2) bite angle (67.73(7)°) is contracted, while the N(1)-N(2) distance in **8** (2.935(3) Å) is the shortest of the four nitrogen-bridged dimers. This reflects the more planar naphthalene backbone of **8** (C(1–10)-$plane_{C(1)-C(10)}$ = 0.002(3)–0.077(2) Å): the Ba^{2+} cation is so large that it must sit out of plane, so the $[^{Ph_2Me}L]^{2-}$ ligand has not distorted significantly in order to accommodate it. The full dimeric structure of **8** is significantly "contracted" relative to those of **6**, **7** and **9**, as evidenced by its significantly increased Ae_2N_2-naphthyl fold angle (95.00(9)°) and a naphthalene-naphthalene interplanar distance (4.395(6) Å) that is more than double that of **9** (1.992 (4) Å). The twist angle between the central Ae_2N_2 ring and the two naphthalene mean planes is also greatly increased (30.004(3)° (**7**) vs 61.87(7)° (**8**)), reflecting the more distorted structure of **8**. This results from the formation of a

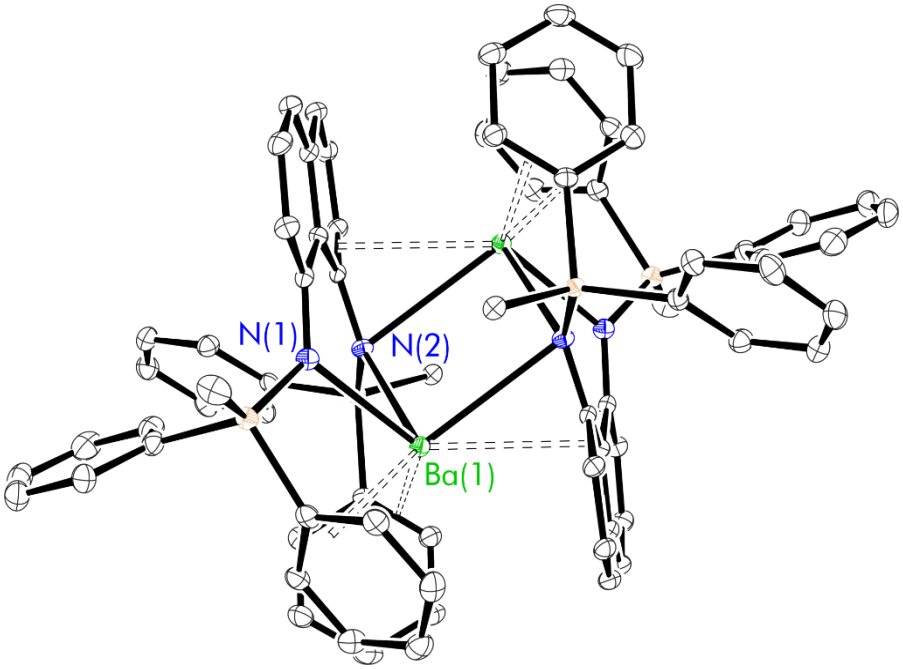
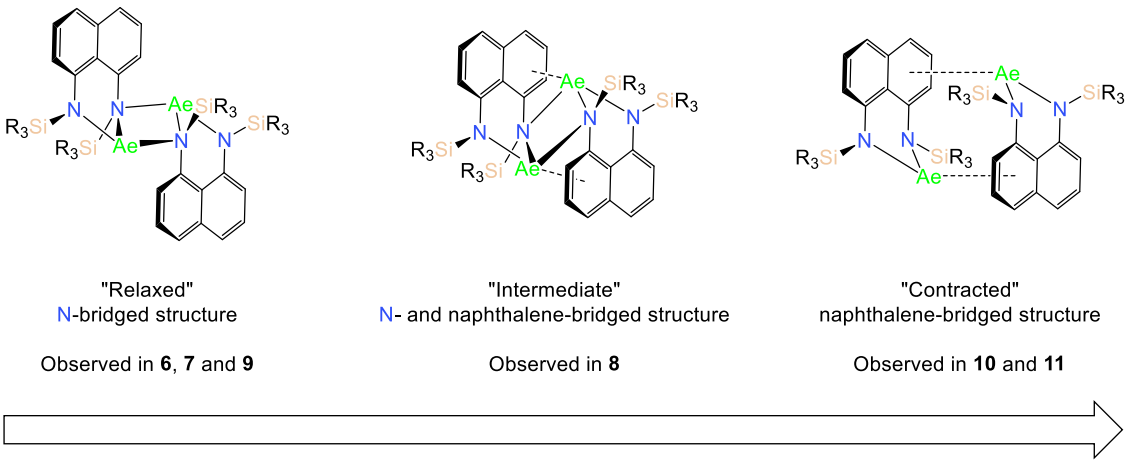


Figure 3.3 Thermal displacement ellipsoid drawing (30% probability) of $[(^{Ph_2Me}L)Ba]_2$ (**8**) generated by a (–X, –Y+1, –Z) symmetry operation. All hydrogen atoms have been omitted for clarity.

strong η^2-π-facial Ba^{2+}-naphthyl interaction, with Ba^{2+} lying above the opposing naphthalene ring (Ba(1)-centroid$_{C(5)\text{-}C(10)}$ = 3.282(1) Å). All three Ae-N bond lengths (Ba(1)-N(1) = 2.621(2) Å, Ba(1)-N(2) = 2.647(2) Å, Ba(1)-N(2)* = 3.088(2) Å) are lengthened in **8** relative to **7** due to the larger ionic radius of Ba^{2+}. However, the bridging Ae(1)-N(2)* distance has increased by 0.411(3) Å, whereas the chelating Ae(1)-N(1) and Ae(1)-N(2) distances have each only increased by 0.160(3) Å. This reflects a weakening of the nitrogen-bridged dimerisation mode that results from the softness of the large Ba^{2+} dication, which instead exhibits a greater preference for multihaptic π-facial interactions with the softer phenyl and naphthyl donors. Consequently, the structure of **8** can be viewed as somewhat intermediate between the more "relaxed" nitrogen-bridged complexes **6**, **7** and **9** and the "contracted" naphthalene-bridged dimers **10** and **11** (*vide infra*). As such, **8** acts as a "structural snapshot" of the tautomerisation process that assumedly results in the conversion of intermediate nitrogen-bridged species into naphthalene-bridged dimers in some cases (**Scheme 3.2**).



Scheme 3.2 "Structural snapshots" of the proposed tautomerisation of a "relaxed" nitrogen-bridged $[(^{R_3}L)Ae]_2$ dimer into a "contracted" naphthalene-bridged form *via* an intermediate species in which both interactions are present. Each of the three motifs has been crystallographically characterised.

Table 3.1 Experimental metrical parameters (bond lengths in Å and angles in °) in $[(^{R_3}L)Ae]_2$ ($R_3 = Ph_2Me$, Ae = Ca (**6**), Sr (**7**) and Ba (**8**); $R_3 = Ph_3$, Ae = Ca (**9**)). * refers to symmetry related atoms. *a*: atom labels altered for clarity.

	6	**7**	**8**[a]	**9**
Space group	$P2_1/c$	$P2_1/c$	$P2_1/c$	$P\bar{1}$
Ae(1)-N(1)	2.308(2)	2.461(2)	2.621(2)	2.311(1)
Ae(1)-N(2)	2.479(2)	2.487(2)	2.647(2)	2.357(1)
Ae(1)-N(2)*	2.332(2)	2.677(2)	3.088(2)	2.478(1)
Ae(1)-Ae(1)*	3.4870(8)	3.7726(4)	4.2476(2)	3.4485(4)
N(1)-N(2)	2.956(3)	2.983(4)	2.935(3)	2.964(2)
Ae(1)-$Plane_{C(1)-C(10)}$	0.522(4)	0.60372(2)	1.433(4)	0.564(2)
Ae(1)-$Plane_{C(1)-C(10)}$*	1.809(3)	2.04097(5)	2.9616(18)	1.4283(19)
$Plane_{C(1)-C(10)}$ -$Plane_{C(1)-C(10)}$*	2.331(6)	2.6447(1)	4.395(6)	1.992(4)
N(1)-Ae(1)-N(2)	79.14(7)	74.13(8)	67.73(7)	78.85(4)
N(1)-Ae(1)-N(2)*	117.04(7)	114.35(8)	104.41(7)	121.18(4)
N(2)-Ae(1)-N(2)*	87.14(7)	86.22(7)	84.73(6)	89.04(4)
Σ{∠Ae(1)}	283.32(12)	274.70(13)	256.87(12)	289.07(7)
$Plane_{C(1)-C(10)}$- $Plane_{Ca(1)_2N(2)_2}$ fold angle	62.354(2)	63.407(2)	95.00(9)	57.00(5)

3.4 X-ray crystallographic analysis of naphthalene-bridged dimers

Layering benzene solutions of $^{Ph_3}LH_2$ (2 eq.) over benzene solutions of $[AeN"_2]_2$ (1 eq., Ae = Sr and Ba) resulted in the spontaneous crystallisation of the dimeric complexes $[(^{Ph_3}L)Ae]_2$ (Ae = Sr (**10**) and Ba (**11**)) directly from the reaction mixture. Like **6–8**, **10** and **11** both crystallise in the $P2_1/c$ space group, with two identical $[(^{R_3}L)Ae]$ units orientated antiparallel with respect to one another within a centrosymmetric dimeric structure. However, they display a markedly different naphthalene-bridged dimerisation mode. As the structures of **10** and **11** are very similar, their shared structural features will be discussed using **10** as a representative example, with specific aspects of the structure of **11** then presented for the sake of comparison.

3.4.1 Crystal structure of $[(^{Ph_3}L)Sr]_2$ (10)

The asymmetric unit of **10** (**Figure 3.4a**) consists of a fully deprotonated $[(^{Ph_3}L)Sr]$ fragment, in which the $[^{Ph_3}L]^{2-}$ ligand is coordinated to Sr^{2+} in a κ^2-N,N′-bidentate manner. As neither nitrogen donor is bonded to the other symmetry related Sr^{2+} cation, the two N-Sr bond lengths are of very similar lengths (N(1)-Sr(1) = 2.462(2) Å, N(2)-Sr(1) = 2.445(2) Å). Similarly to **6**–**9**, the Sr^{2+} cation forms η^3- and η^1-π-facial interactions with one phenyl substituent from each $SiPh_3$ group. The dianionic $[^{Ph_3}L]^{2-}$ ligand is highly planar (C(1–10)-plane$_{C(1)-C(10)}$ = 0.001(2)–0.033(2) Å), resulting in a relatively short N(1)-N(2) distance of 2.900(3) Å. This is due to Sr^{2+} lying 1.210(3) Å from the plane of the naphthalene backbone, which consequently has not distorted to accommodate it in-plane (**Figure 3.7h**). This notably contrasts with the asymmetric unit of the analogous $[^{Ph_2Me}L]^{2-}$-supported strontium complex **7**, in which Sr^{2+} sits closer (Sr(1)-plane$_{C(1)-C(10)}$ = 0.60372(2) Å) to the plane of a more distorted

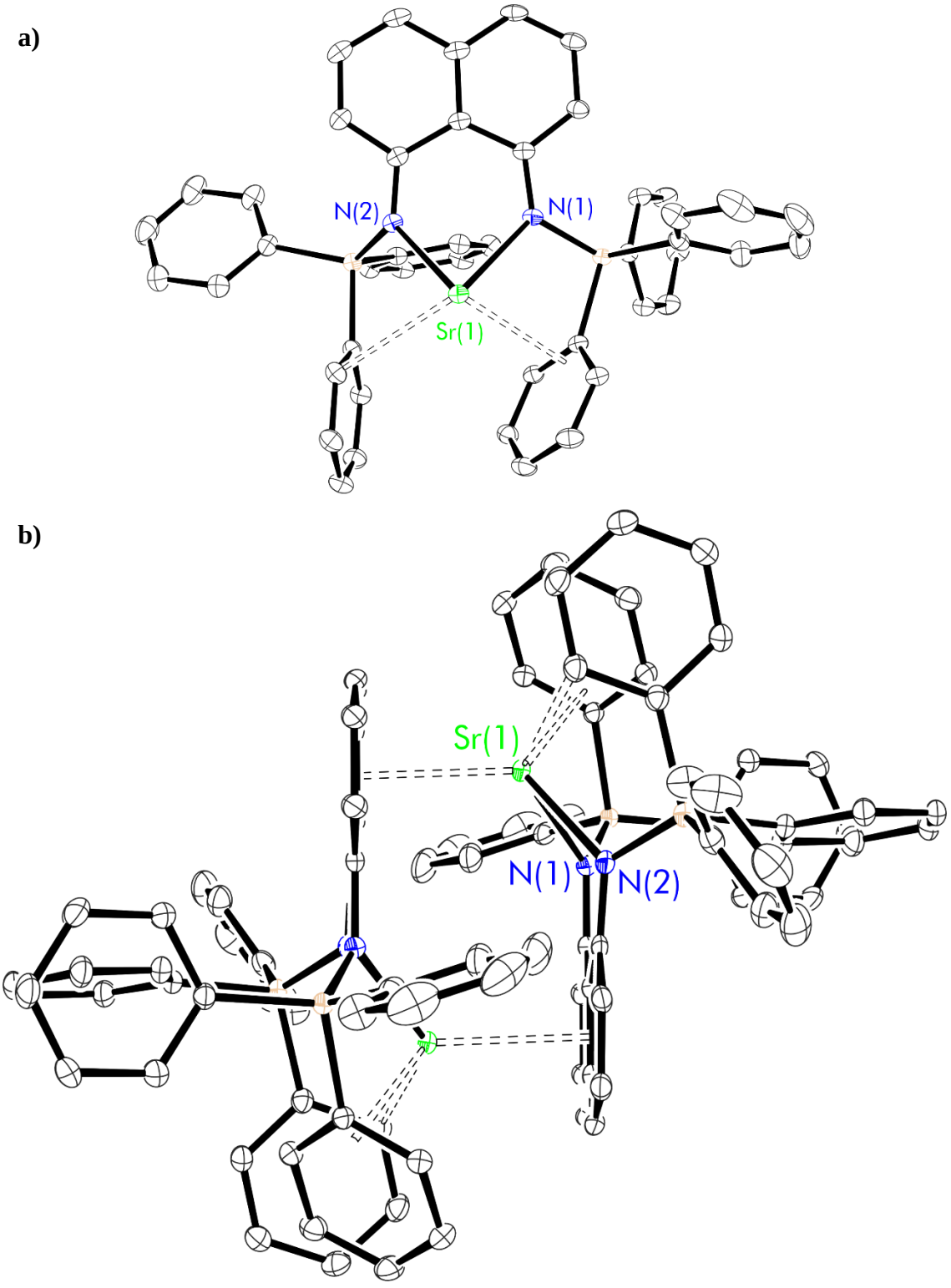


Figure 3.4 Thermal displacement ellipsoid drawing (30% probability) of **a)** asymmetric unit and **b)** full dimeric structure of $[(^{Ph_3}L)Sr]_2$ (**10**) generated by a (–X+1, –Y+1, –Z+1) symmetry operation. All hydrogen atoms have been omitted for clarity.

(C(1–10)-plane$_{C(1)-C(10)}$ = 0.015(3)–0.100(3) Å) naphthalene backbone (**Figure 3.7e**). This variation arises from the change in dimerisation mode between **7** and **10**, as Sr^{2+} sits further out of plane in **10** in order to maximise its η^6-π-facial interaction with the opposing naphthalene ring.

The full dimeric structure of **10** shows that the four-membered Sr_2N_2 ring present in both the $[SrN''_2]_2$ precursor[21] and the nitrogen-bridged dimers **6**–**9** has been broken. This is evidenced by a Sr(1)-N(2)* distance of 4.090(2) Å (*ca.* 1.5 Å greater than Σr_{cov}(Sr,N) = 2.56 Å)[22] and the trigonal planar geometries of both nitrogen donors ($\Sigma\{\angle N(1)\}$ = 358.7(2)°, $\Sigma\{\angle N(2)\}$= 359.3(2)°). Instead, **10** dimerises *via* the formation of two η^6-π-facial Sr^{2+}-naphthyl interactions, resulting in a short Sr^{2+}-centroid$_{C(5)-C(10)}$ distances of 2.748(9) Å. This contrasts with the analogous distances in **6–9**, the shortest of which is 3.282(1) Å in **8** (which itself displays an intermediate nitrogen/naphthalene-bridged structure, *vide supra*). Consequently, **10** has a highly "contracted" dimeric structure characterised by a large Sr_2N_2-naphthyl fold angle (105.82(6)°) and a wide interplanar separation between the two naphthalene rings (3.944(3) Å).

10 can be viewed as a dimeric "piano-stool" complex in which one face of the Sr^{2+} cation is coordinated by two nitrogen donors within the same [(^{Ph_3}L)Sr] unit, while the other face is capped by the opposing naphthalene ring. This structural motif has been previously reported for the 1,8-*bis*(silylamido)naphthalene-supported mixed thallium/lithium complex **III** (**Chart 3.1**) as well as a related dilithium dimer.[6] **10** and **11** are also reminiscent of a series of aryl-bridged alkaline earth dimers supported by bulky chelating diamido ligands which were reported recently by Jones and co-workers (**Chart 1.7**).[8]

It is notable that simply exchanging a methyl group for an additional phenyl group results in such a marked shift in dimerisation mode between the two strontium complexes **7** and **10**. In contrast, the same substitution did not result in any significant structural variation between the analogous calcium complexes **6** and **9**. Though steric congestion between bulky $SiPh_3$ substituents would assumedly be relieved by reducing the number of bulky amide donors coordinated to Ca^{2+}, this does not preclude the accommodation of a nitrogen-bridged dimerisation mode by the smaller Ca^{2+} cation in **9**. This suggests that the shift to a naphthalene-bridged structure in **10**, which contains a larger Sr^{2+} cation, cannot solely result from steric factors. Instead, it is proposed that the presence of an additional electron-withdrawing phenyl group reduces the charge density of the N-donor atoms. The significant electron-withdrawing influence exerted by phenyl groups is supported by analysis of the chemical shifts of both the (N,N)μ_2-H signals in ^{1}H NMR spectra of [(^{R_3}LH)AeN"(THF)$_n$] (**Figure 2.13**, **Section 2.4.1.6**) and the SiR_3 signals in ^{29}Si NMR spectra of **6–11** in THF-d_8 (**Figure 3.11**, **Section 3.7.1**).

Consequently, the bridging Sr(1)-N(2)* interaction (which likely forms initially on account of its presence in the [SrN"$_2$]$_2$ precursor) is significantly weakened and is subsequently outcompeted by the formation of a Sr^{2+}-naphthyl interaction (**Scheme 3.2**). That this tautomerisation process occurs for Sr^{2+} and Ba^{2+} but not for Ca^{2+} when $R_3 = Ph_3$ reflects the preference of the heavier congeners for the formation of multihaptic interactions with "soft" π-systems that are better able to saturate their large coordination spheres.[23] In contrast, the subtle electronic modulation of the strength of the amide donors causes little variation between the structures of the calcium congeners **6** and **9** due to the stronger preference of Ca^{2+} for harder monodentate donors.[24]

3.4.2 Crystal structure of [(^{Ph_3}L)Ba]$_2$ (11)

Similarly, the structure of the barium congener **11** (**Figure 3.5**) shows less variance relative to the analogous [^{Ph_2Me}L]$^{2-}$-supported complex **8**, as the latter already contains a significant Ba^{2+}-naphthyl interaction in addition to its Ba_2N_2 ring. Consequently, the reduced charge density of the N-donor atoms in **11** that results from their $SiPh_3$ substituents again results in full cleavage of the Ba(1)-N(2)* bond (which is already lengthened in **8**, *vide supra*) and conversion to a solely naphthalene-bridged structure.

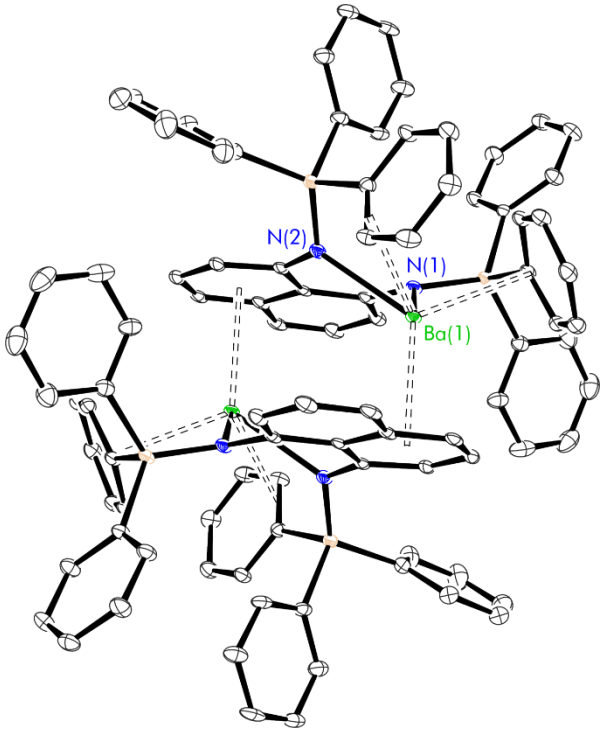


Figure 3.5 Thermal displacement ellipsoid drawing (30% probability) of [($^{Ph_{23}}$L)Ba]$_2$ (**11**) generated by a (–X+1, –Y+1, –Z+1) symmetry operation. All hydrogen atoms have been omitted for clarity.

Both the asymmetric unit and full dimeric structure of **11** vary little from those of the strontium congener **10**, not-withstanding the expected increases in Ba-N (Ba(1)-N(1) = 2.625(3) Å, Ba(1)-N(2) = 2.593(3) Å) and Ba-centroid$_{C(5)\text{-}C(10)}$ (2.9128(3) Å) distances, as well as a consequently narrower N(1)-Ba(1)-N(2) bite angle

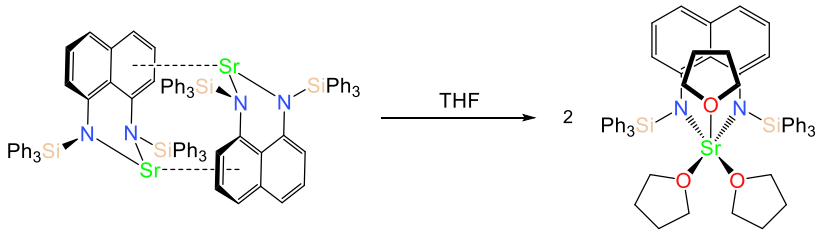
(68.60(8)°), that result from the larger ionic radius of Ba^{2+}. While the N(1)-N(2) distance in **11** is somewhat larger (2.941(4) Å) than in **10**, inspection of the structure shows that this results from an in-plane widening of the metal-binding pocket rather than distortion of the highly planar naphthalene backbone (C(1–10)-$plane_{C(1)\text{-}C(10)}$ = 0.001(1)–0.023(1) Å).

Table 3.2 Experimental metrical parameters (bond lengths in Å and angles in °) in $[(^{Ph_3}L)Ae]_2$ (R_3 = Ph_3 Ae = Sr (**10**) and Ba (**11**)). * refers to symmetry related atoms.

	10	**11**
Space group	$P2_1/c$	$P2_1/c$
Ae(1)-N(1)	2.462(2)	2.625(3)
Ae(1)-N(2)	2.445(2)	2.593(3)
Ae(1)-N(2)*	4.090(2)	4.276(3)
Ae(1)-Ae(1)*	4.8750(5)	4.98330(5)
N(1)-N(2)	2.900(3)	2.9414(4)
Ae(1)-$Centroid_{C(5)\text{-}C(10)}$*	2.7348(9)	2.91287(3)
Ae(1)-$Plane_{C(1)\text{-}C(10)}$	1.210(3)	1.44113(1)
$Plane_{C(1)\text{-}C(10)}$-$Plane_{C(1)\text{-}C(10)}$*	3.944(3)	4.334402(5)
N(1)-Ae(1)-N(2)	72.47(6)	68.60(8)
N(1)-Ae(1)-$Centroid_{C(5)\text{-}C(10)}$*	117.31(5)	116.6599(7)
N(2)-Ae(1)-$Centroid_{C(5)\text{-}C(10)}$*	119.98(5)	123.3939(3)
$Plane_{C(1)\text{-}C(10)}$-$Plane_{Ca(1)_2N(2)_2}$ fold angle	105.82(6)	106.3350(7)

3.5 X-ray crystallographic analysis of monomeric THF adducts

Complexes **6–11** all dissolve readily in THF. This results in the disruption of their dimeric structures by the strong donor solvent and full conversion into the monomeric THF adducts [(^{R_3}L)Ae(THF)$_n$] (R_3 = Ph_2Me and Ph_3, Ae = Ca, Sr and Ba) This property was primarily exploited to enable the recording of NMR spectra in THF-d_8 (**Section 3.7**). However, large block-like yellow crystals of the monomeric THF adduct [(^{Ph_3}L)Sr(THF)$_3$] (**12**) unexpectedly grew when a THF solution of **10** was left to stand (**Scheme 3.3**), enabling its structural characterisation by X-ray diffraction.



10 **12**

Scheme 3.3 Conversion of [(^{Ph_3}L)Sr]$_2$ (**10**) into the solvated monomer [(^{Ph_3}L)Sr(THF)$_3$] (**12**) in THF.

3.5.1 Crystal structure of [(^{Ph_3}L)Sr(THF)$_3$] (12)

Complex **12** crystallises in the $P2_1/c$ space group, with two crystallographically independent [(^{Ph_3}L)Sr(THF)$_3$] molecules in the asymmetric unit. However, the metrical parameters of these two distinct molecules vary little, so only one [(^{Ph_3}L)Sr(THF)$_3$] unit (**Figure 3.6**) and selected metrical parameters from it (**Table 3.3**) are presented here.

The [^{Ph_3}L]$^{2-}$ ligand remains coordinated to Sr^{2+} in the same κ^2-N,N′-bidentate manner observed in the dimeric THF-free strontium complex **10**. The Sr-N bond lengths (N(1)-Sr(1)) = 2.465(1) Å, N(2)-Sr(1)) = 2.437(1) Å) and N(1)-Sr(1)-N(2) bite angle (73.37(4)°) in **12** are statistically indistinguishable from those in **10**.

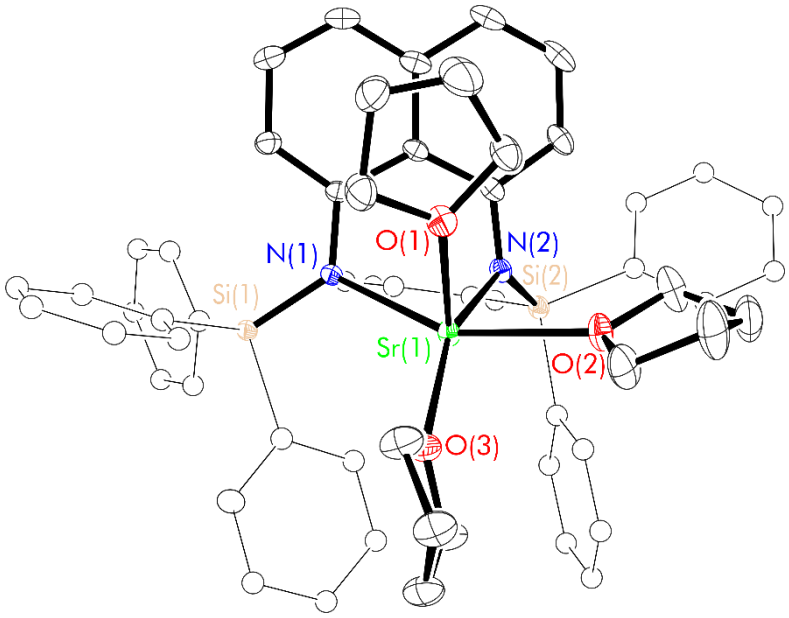


Figure 3.6 Thermal displacement ellipsoid drawing (30% probability) of [(^{Ph_3}L)Sr(THF)$_3$] (**12**). All hydrogen atoms have been omitted and phenyl groups are shown in ball-and-stick form for clarity.

Table 3.3 Selected experimental metrical parameters (bond lengths (Å) and angles (°)) for [(^{Ph_3}L)Sr(THF)$_3$] (**12**). Analogous metrics for **10** and [(^{R_3}L)Mg(THF)$_2$] (R_3 = Me_3 (**4**), $Me_2{}^tBu$ (**5**), and Ph_2Me (**A**)[26]) are also presented for comparison.

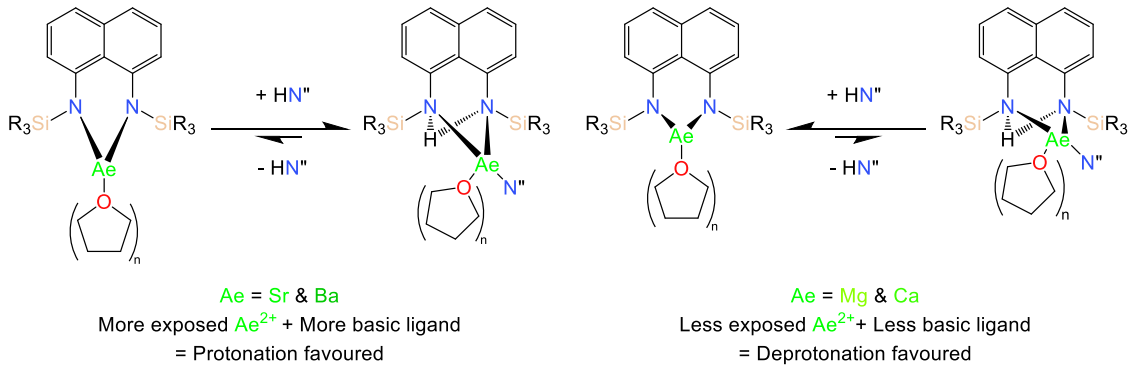
	12	**10**	**4**	**5**	**A**[26]
Space group	$P2_1/c$	$P2_1/c$	$C2/c$	$P\bar{1}$	$P\bar{1}$
Ae(1)-N(1)	2.465(1)	2.462(2)	1.9796(9)	2.007(8)	2.007(8)
Ae(1)-N(2)	2.437(1)	2.445(2)	1.9826(9)	1.965(6)	1.965(6)
Ae(1)-O(1)	2.557(1)	-	2.0229(9)	2.025(6)	2.025(6)
Ae(1)-O(2)	2.571(1)	-	2.0175(9)	2.010(7)	2.010(7)
Ae(1)-O(3)	2.557(2)	-	-	-	-
N(1)-N(2)	2.929(2)	2.900(3)	3.013(1)	3.016(1)	2.940(9)
Ae(1)-plane$_{C(1)-C(10)}$	1.8654(17)	1.210(3)	0.0130(15)	0.1508(17)	1.079(8)
N(1)-Ae(1)-N(2)	73.37(4)	72.47(6)	99.00(4)	99.03(5)	95.5(3)

The $[^{Ph_3}L]^{2-}$ ligand in **12** remains highly planar (C(1–10)-plane$_{C(1)\text{-}C(10)}$ = 0.004(2)–0.071(1) Å), though with a slightly lengthened N(1)-N(2) distance (2.929(2) Å). The Sr^{2+} cation lies 0.6554 Å further from the naphthalene plane in **12** than in **10** in order to accommodate the coordination of three THF molecules. Furthermore, the Sr^{2+}-phenyl π-facial interactions that are present within the $[(^{Ph_3}L)Sr]$ unit of **10** are less prevalent in **12**. This results in a five-coordinate strontium centre with a square pyramidal coordination geometry ($\tau_5 = 0.075$).[25] The apical position is occupied by a THF molecule that is projected above the naphthalene backbone, blocking any dimerisation *via* the formation of a Sr^{2+}-naphthyl π-facial interaction. The equatorial positions are occupied by the amide donors of the chelating $[^{Ph_3}L]^{2-}$ ligand and two additional THF molecules that are necessarily *cis* to one another. The coordination of any additional THF molecules is seemingly blocked by the phenyl substituents of the $[^{Ph_3}L]^{2-}$ ligand.

The Sr-O bond lengths in **12** vary little with respect to one another and are all between 2.557(1)–2.571(1) Å in length. The coordination of three THF molecules contrasts with the monomeric magnesium complexes $[(^{R_3}L)Mg(THF)_2]$ ($R_3 = Me_3$ (**4**), $Me_2{}^tBu$ (**5**) and Ph_2Me[26] (**A**)), in which the smaller Mg^{2+} cation is coordinated by only two THF molecules in distorted tetrahedral arrangements. The structure of **12** is most similar to that of **A**, as in both cases the $[Ae(THF)_n]^{2+}$ group lies out of the naphthalene plane on one face of a more planar $[^{R_3}L]^{2-}$ ligand (**Figures 3.7c** and **j**). Conversely, in **4** and **5** the in-plane accommodation of Mg^{2+} results in significant distortion of the naphthalene backbone (**Figure 3.7a** and **b**).

3.5.2 Comparison between X-ray crystallographic data and *in situ* NMR spectra recorded in THF-d_8

While additional crystal structures of [(^{R3}L)Ae(THF)$_n$] have not been obtained, the solid-state characterisation of of **6–12** provides insight into the solution-phase behaviour of their monomeric analogues when synthesised *in situ* in THF-d_8 (**Section 2.4**). The Ae^{2+} cations in both **12** and the dimeric strontium and barium complexes **7** (to a lesser extent), **8**, **10** and **11** are highly exposed, as they are too large to fit within the small metal-binding pocket (**Figure 3.7**). Consequently, HN" (which is persistent in solution when the synthesis of [(^{R3}L)Ae(THF)$_n$] is attempted in THF) can coordinate to Ae^{2+} and protonate the $[^{R3}L]^{2-}$ ligand (pKa(HN") = 25.8,[27] **Scheme 3.4**). This effect is compounded by the enhanced basicity of $[^{R3}L]^{2-}$ that results from its coordination to the larger, more electropositive Ae^{2+} cations (**Section 2.4.1.6**). Combined, these steric and electronic factors strongly favour the reverse reaction to form the intermediate species [(^{R3}LH)AeN"(THF)$_n$], the long-lived nature of which then enables its thermal degradation into [($^{R3\text{-}\mu\text{-}R3}$LH)AeN"(THF)$_n$]. This provides a structural explanation for the difficulties faced when attempting to synthesise [(^{R3}L)Ae(THF)$_n$] (Ae = Sr and Ba) in THF-d_8.



Scheme 3.4 Influence of Ae^{2+} size on the equilibrium between [(^{R3}L)Ae(THF)$_n$] and [(^{R3}LH)AeN"(THF)$_n$].

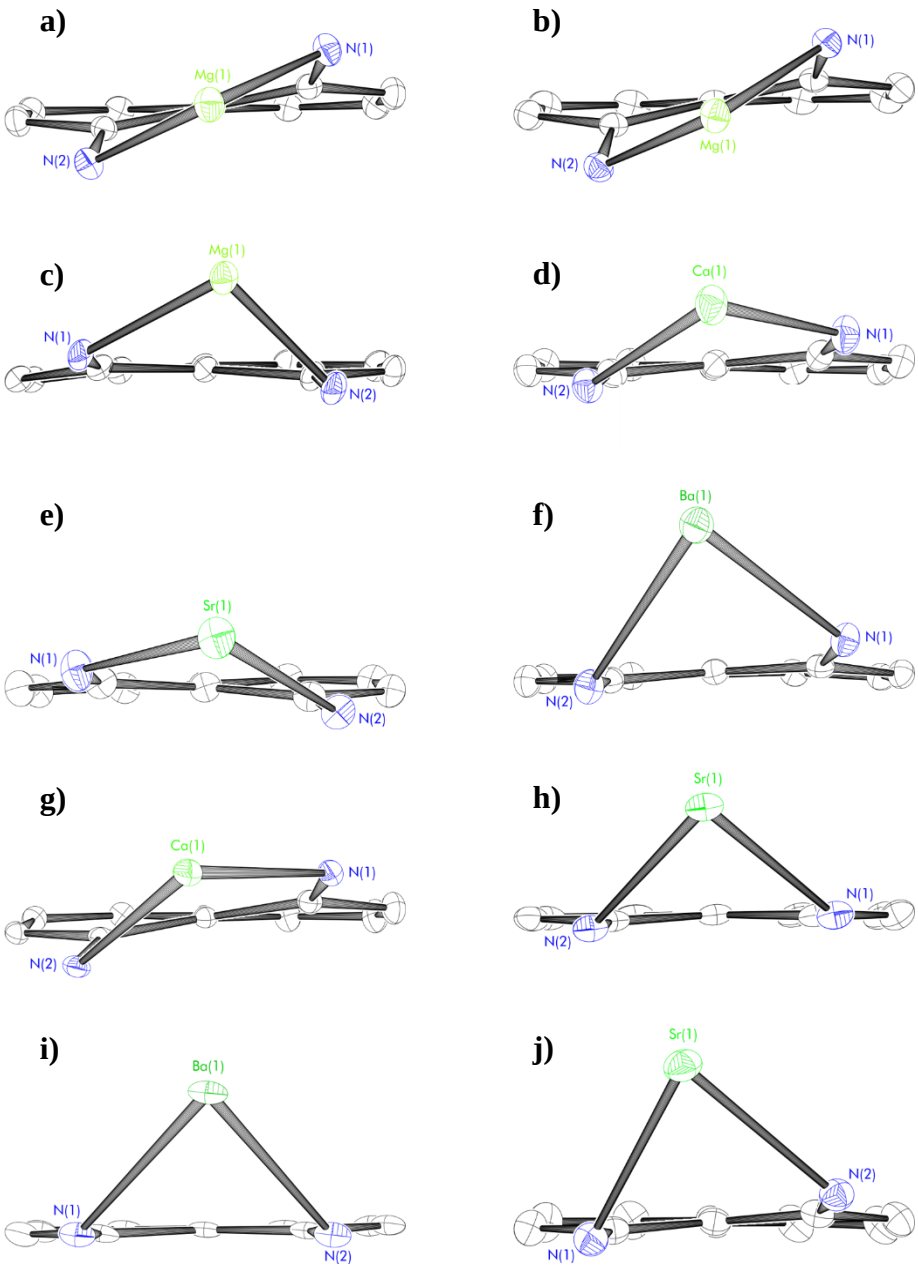


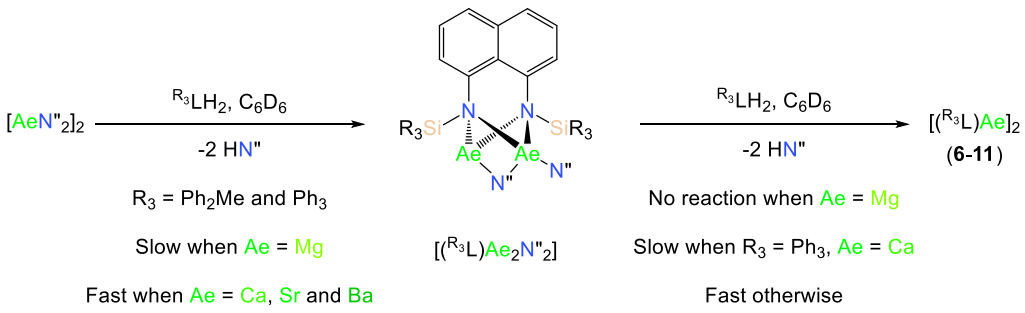
Figure 3.7 Thermal displacement ellipsoid drawings (30% probability) of the [(1,8-$C_{10}H_6N_2$)Ae] units of **a) 4**, **b) 5**, **c) A**,[26] **d) 6**, **e) 7**, **f) 8**, **g) 9**, **h) 10**, **i) 11** and **j) 12** viewed down their C(9)-C(10) axes, illustrating the general increase in Ae^{2+} exposure that results from greater Ae^{2+} size. All hydrogen atoms have been omitted for clarity.

Conversely, the stability of the magnesium complexes **4** and **5** and the calcium complexes [(^{R_3}L)Ca(THF)$_n$] (R_3 = Ph_2Me and Ph_3) when formed *in situ* can be attributed to the smaller Mg^{2+} and Ca^{2+} cations being less exposed due to their smaller size (**Scheme 3.4**).

This assertion is supported directly by the crystal structures of **4** and **5** and those of the dimeric calcium complexes **6** and **9**. Unfavourable solution-phase processes are avoided entirely in the THF-free system as a consequence of the crystallisation of the **6–11** (excluding **9**) directly from the reaction mixture.

3.6 *In situ* NMR spectroscopic analysis

Unfortunately, the insolubility of crystalline samples of **6**–**11** in benzene and toluene precluded the recording of NMR spectra in arene solvents at room temperature. While higher temperatures did enable the dissolution of **6**–**11** in these solvents in some cases, this resulted in decomposition, precluding a direct assessment of the solution-state structures of these dimeric compounds. However, the 2:1 reactions of $^{R3}LH_2$ (R_3 = Ph_2Me and Ph_3) with $[AeN''_2]_2$ (Ae = Mg, Ca, Sr and Ba) in C_6D_6 could be monitored by ^{1}H NMR spectroscopy, providing insight into the mechanism by which **6**–**11** form (**Scheme 3.5**).



Scheme 3.5 General scheme for the synthesis of $[(^{R3}L)Ae]_2$ *via* the intermediate species $[(^{R3}L)Ae_2N''_2]$ (R_3 = Ph_2Me and Ph_3; Ae = Mg, Ca, Sr and Ba).

Gratifyingly, the THF-free reactions proved much simpler than the analogous reactions in THF-d_8 (**Section 2.4**). In all cases, no intermediate species with high frequency (N,N)μ_2-H signals or thermal degradation products were observed. With the exception of **9** (*vide infra*), initial ^{1}H NMR spectra recorded after *ca*. 10 minutes showed that in all

cases full deprotonation of both equivalents of $^{R3}LH_2$ had occurred. The rapid crystallisation of **6**, **7**, **8**, **10** and **11** resulted in spectra with broad, low intensity ligand signals that were dominated by a sharp singlet at δ = 0.10 ppm corresponding to the by-product HN". The crystallisation of $[(^{R3}L)Ae]_2$ presumably provides a large thermodynamic sink that strongly biases the solution-phase equilibria that were observed in THF, driving full conversion to the dimeric product when benzene is employed as the solvent. Consequently, any intermediate species bearing $[^{R3}LH]^-$ ligands are not observed due to their rapid consumption *via* the effectively irreversible elimination of HN". The formation of $[(^{R3}L)Ae]_2$ therefore outcompetes any thermal degradation *via* the elimination of benzene under these conditions.

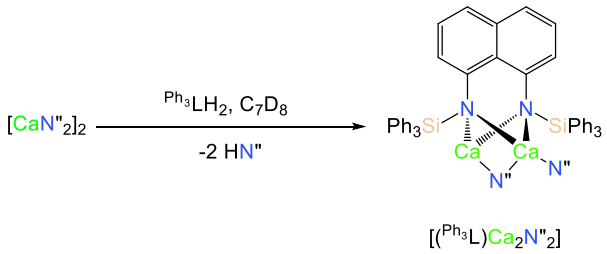
However, $[(^{Ph3}L)Ca]_2$ (**9**) forms more slowly and remains dissolved in solution, providing insight into the mechanism of its formation and enabling its characterisation by ^{1}H NMR spectroscopy. The slower formation of **9** is likely due to steric congestion that results from the combination of the smaller Ca^{2+} cation with the bulkier $^{Ph3}LH_2$ proligand. This is consistent with the analogous reaction in THF-d_8, which also proceeded more slowly than the $^{Ph2Me}LH_2$/[CaN"$_2$] and $^{Ph3}LH_2$/[AeN"$_2$] (Ae = Sr and Ba) reactions (**Table 2.4**).

An initial spectrum recorded after *ca.* 10 minutes showed the formation of a mixture of the product **9**, an intermediate species assigned as $[(^{Ph3}L)Ca_2N"_2]$ (**Section 3.6.1**) and some as-yet unconsumed proligand. Full conversion to **9** was then achieved after 16 hours at 25 °C. This suggests that while the initial 1:1 reaction between $^{Ph3}LH_2$ and $[CaN"_2]_2$ proceeds rapidly, steric congestion results in a substantially slower reaction between the resulting intermediate species $[(^{Ph3}L)Ca_2N"_2]$ and the second equivalent of proligand (**Scheme 3.5**). The intermediate species $[(^{R3}L)Ae_2N"_2]$ presumably also forms during the

synthesis of **6**, **7**, **8**, **10** and **11**, but is not observed in these cases due to its rapid consumption. Conversely, the 2:1 reactions of $^{R3}LH_2$ with $[MgN"_2]_2$ result in the slow formation of $[(^{R3}L)Mg_2N"_2]$ and no further reaction to form $[(^{R3}L)Mg]_2$. This contrasts with the facile synthesis of the monomeric THF adducts $[(^{R3}L)Mg(THF)_2]$ (**Section 2.3**), reflecting the increased degree of steric congestion at Mg^{2+} that results from the retention of an aggregated structure in the absence of a donor solvent.

3.6.1 *In situ* NMR spectroscopic analysis of $[(^{Ph3}L)Ca_2N"_2]$

The intermediate species $[(^{Ph3}L)Ca_2N"_2]$ was synthesised rationally *via* the 1:1 reaction of $^{Ph3}LH_2$ with $[CaN"_2]_2$ in toluene-d_8 and characterised *in situ* by NMR spectroscopy in order to obtain a better understanding of its solution-state structure (**Scheme 3.6**).



Scheme 3.6 Synthesis of $[(^{Ph3}L)Ca_2N"_2]$.

A ^1H NMR spectrum recorded at 25 °C (**Figure 3.8a**) notably contains two broad overlapping singlets at δ = –0.28 and –0.43 ppm with a combined integral value of 36, which are assigned as the methyl protons of the two coordinated $[N"]^-$ ligands. This suggests that in solution $[(^{Ph3}L)Ca_2N"_2]$ has a fluxional structure in which the two monodentate amide ligands are exchanging between two positions. This is further supported by the presence of only three naphthyl (δ = 7.51, 7.13 and 6.77 ppm) and three phenyl signals (δ = 7.68, 7.27 and 7.18 ppm) in the aromatic region, consistent with the presence of a plane of symmetry through the C(9)-C(10) axis that is perpendicular to the

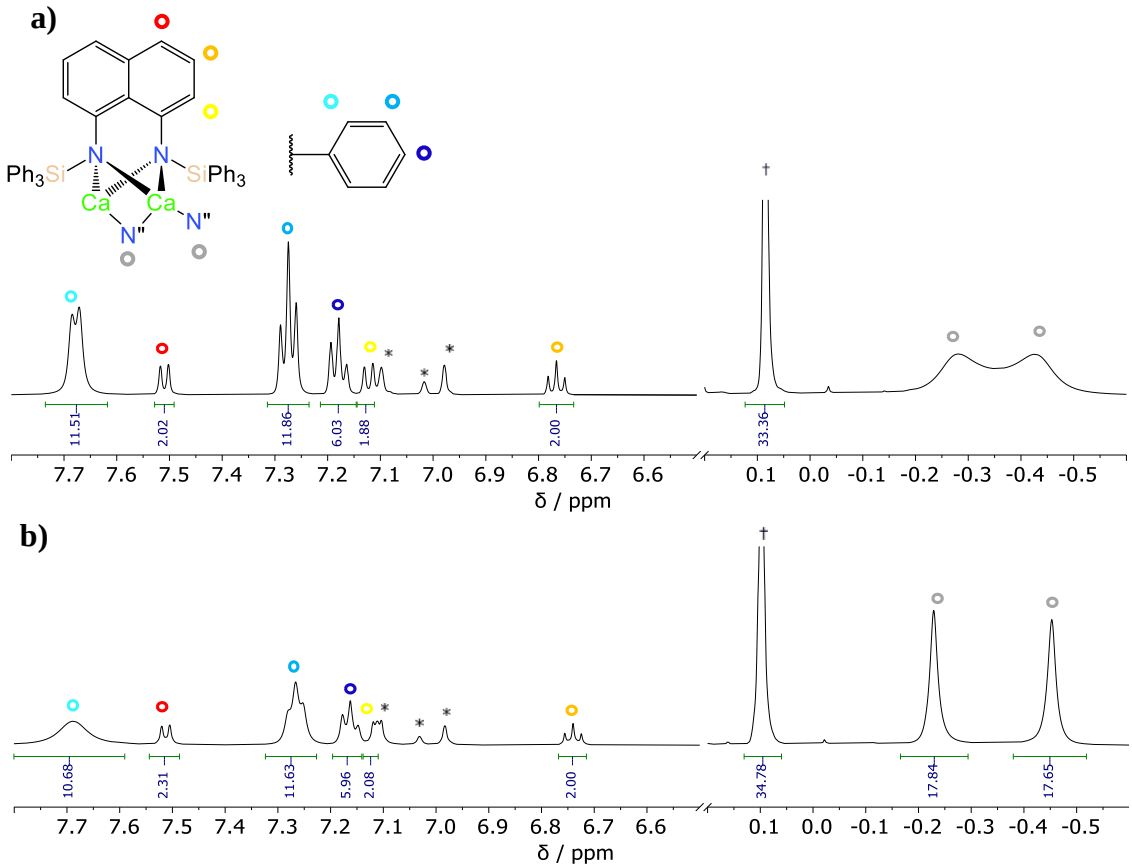


Figure 3.8 *in situ* ^{1}H NMR spectra (C_7D_8, 499.9 MHz) of [(^{Ph3}L)Ca_2N"$_2$], prepared *via* the 1:1 reaction of $^{Ph3}LH_2$ and [CaN"$_2$]$_2$, at **a)** 298 K and **b)** 273 K. † denotes HN", * denotes residual protio fraction of C_7D_8.

naphthalene ring. An analogous spectrum recorded at 0 °C (**Figure 3.8b**) shows the divergence of the [N"]$^-$ signal into two sharp singlets. These signals further diverge and sharpen at lower temperatures as the rate of exchange between terminal and bridging positions slows and an unsymmetrical structure becomes observable ($\delta_{193\ K}$ = –0.13 and –0.47 ppm, T_c = 303 K, $\Delta\nu$ = 170 Hz, $\Delta G^{\ddagger}$(303 K) = 59 kJ mol^{-1}).[28] However, the C_2 symmetry of the phenyl and naphthyl signals is retained even upon cooling to –80 °C, with no signal divergence observed. This suggests that the intermediate possesses a Ca_2N_2 ring that is bridged by the [^{Ph3}L]$^{2-}$ ligand, which coordinates to both metal cations in κ^2-N,N′-bidentate manner *via* two μ_2-N donors in order to maximise the coordination number of the two Ca^{2+} centres. The proposed structure of [(^{Ph3}L)Ca_2N"$_2$] consists of a

$[(\mu\text{-}^{R3}L)Ae_2]^{2+}$ motif that has been crystallographically verified in the alkyl-substituted complexes **14**, **16** and **17**, **Chapter 4**). However, crystals of $[(^{Ph3}L)Ca_2N''_2]$ suitable for X-ray diffraction could not be obtained, and so this solution-state structure is proposed tentatively.

3.6.2 *In situ* NMR spectroscopic analysis of $[(^{Ph3}L)Ca]_2$ (9)

The ^{1}H NMR spectrum of **9** recorded *in situ* in C_6D_6 (**Figure 3.9**) consists of three naphthyl (δ = 7.05, 6.76 and 6.67 ppm) and three phenyl (δ = 7.55, 7.05 and 6.88 ppm) signals in the aromatic region, consistent with a C_{2v}-symmetric structure, as well as the expected two equivalents of HN" per ligand. This contrasts with the unsymmetrical dimeric solid-state structure of **9** (*vide infra*), suggesting that in solution **9** may have a fluxional structure that results in a time-averaged C_{2v}-symmetric spectrum. This phenomenon has been reported for the NMR spectra of the dimeric precursors $[AeN''_2]_2$,

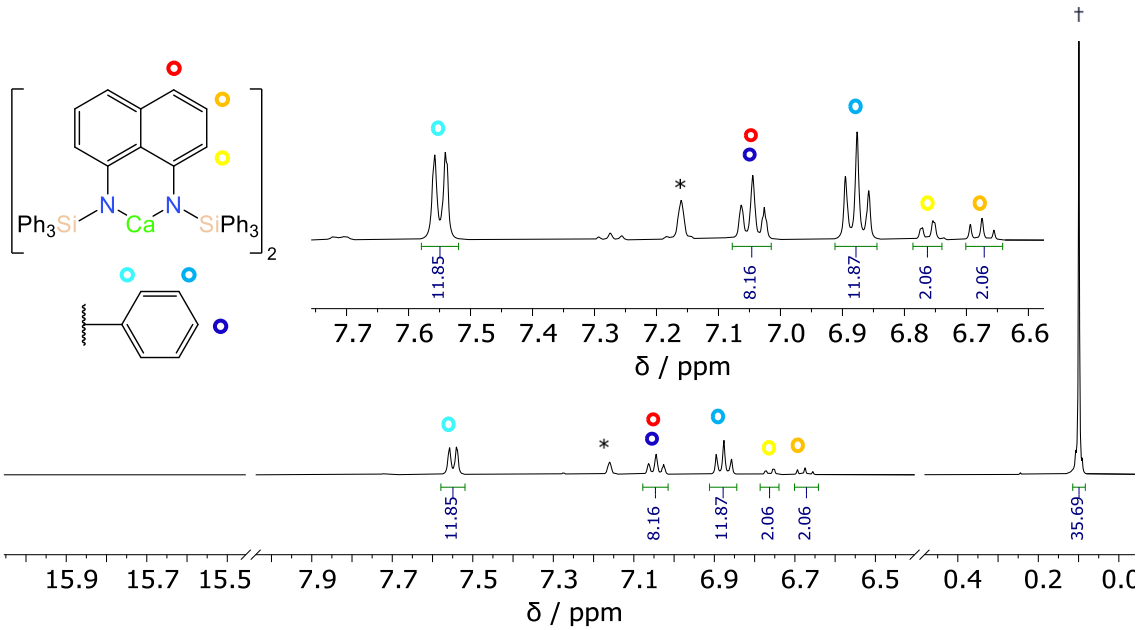


Figure 3.9 ^{1}H NMR spectrum (C_6D_6, 298 K, 400 MHz) of $[(^{Ph3}L)Ca]_2$ (**9**) prepared *in situ via* the 2:1 reaction of $^{Ph3}LH_2$ with $[CaN''_2]_2$ (spectrum taken after 16 h at 25 °C). Expansion shows the aromatic region. † denotes HN", * denotes residual protio fraction of C_6D_6.

in which the distinct terminal and bridging [N"]$^-$ ligands observed in the solid state produce a single signal at room temperature as they exchange rapidly in solution due to the kinetic lability of Ae^{2+}.[29] It is also possible that in solution **9** may exist as a monomer due to the reversible coordination of HN" to Ca^{2+}, with dimerisation only occurring upon the removal of the amine by-product *in vacuo*. Notably, the solubility of **9** in benzene is greatly reduced following its isolation *via* lyophilisation, providing further evidence that its initial solution state-structure may differ from its final solid-state form.

While **9** does not crystallise directly from the reaction mixture, it is stable in solution at 25 °C, with no thermal degradation *via* the elimination of benzene observed. This is consistent with analogous spectra recorded in THF-d_8 (**Figure 2.10**, **Section 2.4.1.2**) which showed that the monomeric analogue [(^{Ph_3}L)Ca(THF)$_n$] does not suffer from thermal degradation unless heated to 110 °C (**Table 2.4**). This contrasts with most other metal and proligand combinations, and suggests that in this case full deprotonation is favoured regardless of whether benzene or THF is employed as the solvent.

3.7 NMR spectroscopic analysis of 6–11 in THF-d_8

While poorly soluble in hydrocarbons, **6**–**11** dissolve readily in THF. This results in their instantaneous conversion into the analogous monomeric THF adducts [(^{R_3}L)Ae(THF)$_n$] (R_3 = Ph_2Me and Ph_3; Ae = Ca, Sr and Ba), as demonstrated by the X-ray crystal structure of **12** (**Figure 3.6**). This enabled their full characterisation by multinuclear NMR spectroscopy in THF-d_8. The ^{1}H, ^{13}C{^{1}H} and ^{29}Si NMR spectra of the [^{Ph_2Me}L]$^{2-}$-supported complexes **6**–**8** closely resemble one another, as do the analogous spectra of the [^{Ph_3}L]$^{2-}$-supported complexes **9**–**11**. The ^{1}H NMR spectrum of **10** is presented as representative example (**Figure 3.10**).

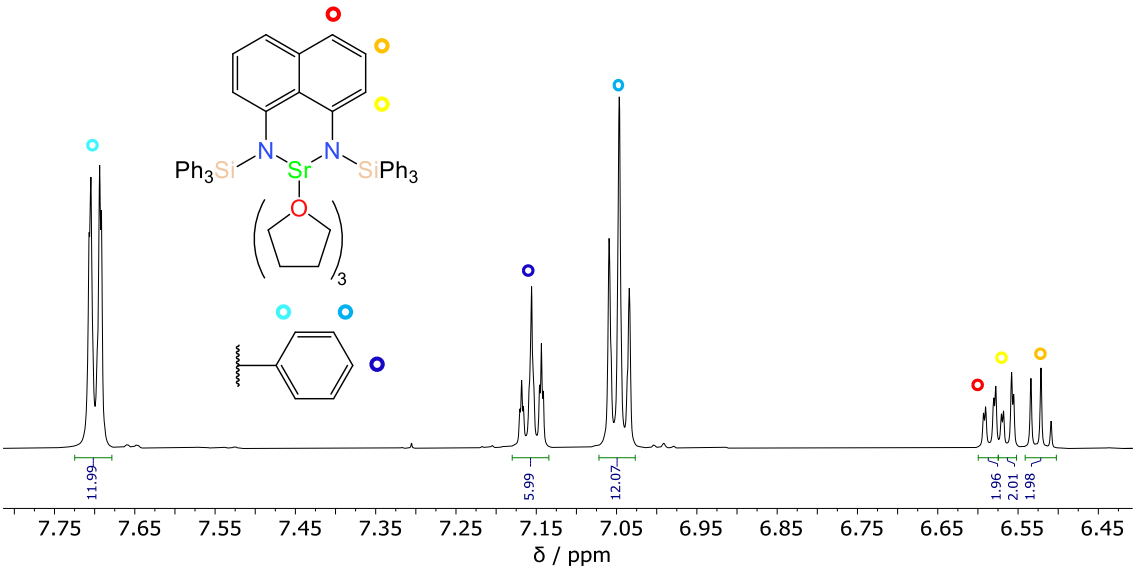


Figure 3.10 Aromatic region of the ^{1}H NMR spectrum (C_4D_8O, 298 K, 600.4 MHz) of [(^{Ph3}L)Sr(THF)$_3$] (**12**), formed when [(^{Ph3}L)Sr]$_2$ (**10**) is dissolved in THF.

The spectrum, which consists of an aromatic region with three phenyl (δ = 7.70, 7.16 and 7.05 ppm) and three naphthyl (δ = 6.59, 6.56 and 6.52 ppm) resonances, is consistent with C_{2v} molecular symmetry. Additionally, the ^{13}C{^{1}H} NMR spectrum consists of four phenyl and six naphthyl signals, while the ^{29}Si NMR spectrum consists of a single signal at δ = –32.92 ppm. No amino signals corresponding to unconsumed proligand or a (N,N)μ$_2$-H bridging proton are observed, confirming the full deprotonation of the proligand to form the dianionic [^{Ph3}L]$^{2–}$ ligand. This is fully consistent with both the X-ray crystal structures (*vide supra*) and solid-state IR spectra of **6**–**11**, with the latter also showing the absence of any N-H absorbances. Together, these spectra confirm the C_{2v}-symmetric structures of [(^{R3}L)Ae(THF)$_n$] in solution, with the [^{R3}L]$^{2–}$ ligand coordinated to Ae^{2+} in a κ^2-N,N′-bidentate manner. Furthermore, the ^{1}H NMR spectra of isolated samples of **6**–**11** agree well with both those of the magnesium complexes **4** and **5** (**Section 2.3**) and those in which complexes assigned as [(^{R3}L)Ae(THF)$_n$] were generated *in situ* in THF-d_8 (**Section 2.4.1.2**).

The irreversible conversion of **6**–**11** into monomeric THF adducts contrasts with the solution-phase behaviour of the related dimeric alkaline earth complexes **II-Ae** (**Chart 3.1**).[4,5] NMR spectra of **II-Ae** revealed that they exist in equilibrium with their monomeric analogues when dissolved in THF, with full conversion to the monomeric species only achieved upon addition of a crown ether. This reflects the additional coordinative saturation provided by the *bis*(phenoxyimine) "NOON" ligand, which stabilises the aggregated dimeric form in the presence of a donor solvent. Conversely, the Ae^{2+} cations in **6**–**11** are highly exposed (**Figure 3.7**), enabling their facile conversion into monomeric THF adducts.

3.7.1 Comparative ^{29}Si NMR spectroscopic analysis

The ^{29}Si NMR spectra of **6**–**11** in THF-d_8 each consist of a low frequency singlet, corresponding to the silicon atoms of their SiR_3 substituents. This ^{29}Si NMR spectroscopic signal acts as a useful probe for investigating the influence of both the coordinated Ae^{2+} cation and the substituents of the SiR_3 group on the electronic properties of the $[^{R_3}L]^{2-}$ ligand. The chemical shifts of the relevant ^{29}Si signals, $\delta(SiR_3)$, are presented in **Table 3.4** and **Figure 3.11**.

This analysis reveals two clear trends. Firstly, the ^{29}Si signal of a given ligand shifts to a lower frequency as the size and electropositivity of the Ae^{2+} cation to which it is coordinated increases. This results in more ionic Ae-N bonds and the retention of more charge density on the anionic amide donors, with the adjacent silicon atoms more shielded as a consequence. Secondly, the ^{29}Si NMR signal of the $[^{Ph_3}L]^{2-}$ ligand consistently resonates at a lower frequency than the corresponding $[^{Ph_2Me}L]^{2-}$ signal upon their coordination to same Ae^{2+} centre, with a near-uniform change in chemical shift observed across the three metals ($\Delta\delta(SiR_3)$ = 3.59 (Ca), 3.53 (Sr) and 3.59 (Ba) ppm).

Table 3.4 Chemical shifts of the SiR_3 ^{29}Si NMR spectroscopic signals, δ(SiR_3), of [(^{R_3}L)Ae(THF)$_n$] (R_3 = Ph_2Me and Ph_3; Ae = Ca, Sr and Ba), formed when **6**–**11** are dissolved in THF-d_8.

Compound	**Ae**	**R_3**	**δ(SiR_3)**
6	Ca	Ph_2Me	–27.98
7	Sr	Ph_2Me	–29.39
8	Ba	Ph_2Me	–30.64
9	Ca	Ph_3	–31.57
10	Sr	Ph_3	–32.92
11	Ba	Ph_3	–34.23

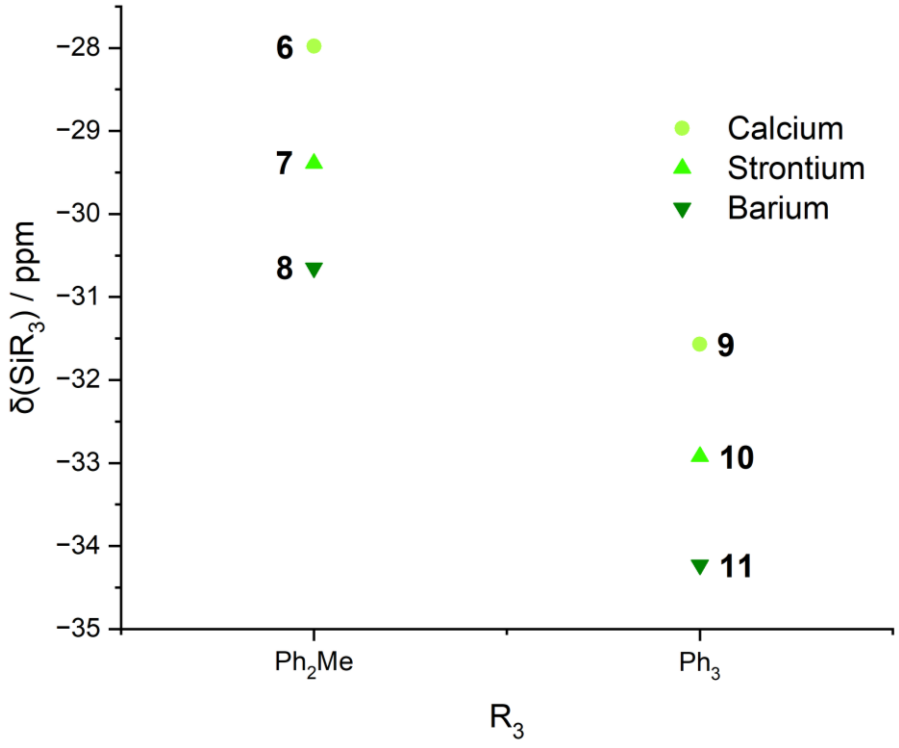


Figure 3.11 Chemical shifts of the SiR_3 ^{29}Si NMR spectroscopic signals, δ(SiR_3), of [(^{R_3}L)Ae(THF)$_n$] (R_3 = Ph_2Me and Ph_3; Ae = Ca, Sr and Ba), formed when **6**–**11** are dissolved in THF-d_8.

This demonstrates the additional electron withdrawing effect that results from the presence of an extra phenyl substituent, which results in $SiPh_3$ groups that withdraw more electron density from the electron-rich $[1,8\text{-}C_{10}H_6N_2]^{2-}$ π-system and consequently have more shielded silicon centres than their $SiPh_2Me$ analogues. Consequently, the ^{29}Si NMR signals of $[(^{Ph_2Me}L)Ca(THF)_n]$ and $[(^{Ph_3}L)Ba(THF)_n]$ are the least and most shielded respectively due to the combination of these ligand and metal effects, with the $\delta(SiR_3)$ values of the other phenyl-substituted $[(^{R_3}L)Ae(THF)_n]$ complexes intermediate between these extreme cases. These conclusions are fully consistent with those made based on analysis of the chemical shifts of the (N,N)μ_2-H signals of $[(^{R_3}LH)AeN''(THF)_n]$ (**Figure 2.13**, **Section 2.4.1.6**).

3.7.2 Degradation of 6–11 in THF

Isolated crystalline samples of **6**–**11** were shown to be analytically pure by elemental analysis, and are stable indefinitely when stored under an inert atmosphere. However **6**–**11** were all found to decompose following their conversion into $[(^{R_3}L)Ae(THF)_n]$ when dissolved in THF at 25 °C. This decomposition process is generally slow at room temperature with appreciable quantities of benzene released only after several hours, enabling clean NMR spectra of freshly prepared THF samples to be prepared.

However, repeated attempts to obtain clean spectra of $[(^{Ph_3}L)Ba]_2$ (**11**) were unsuccessful, despite elemental analysis confirming the purity of crystalline samples of the dimeric compound. While the expected signals assigned as $[(^{Ph_3}L)Ba(THF)_n]$ still dominate (**Figure 3.12a**), additional ligand signals are also present. These signals, including a high frequency (N,N)μ_2-H resonance (δ = 14.49 ppm), are similar to those present in the ^1H NMR spectrum of $[(^{Ph_3}LH)BaN''(THF)_n]$ generated *in situ* (**Figure 3.12b**). This

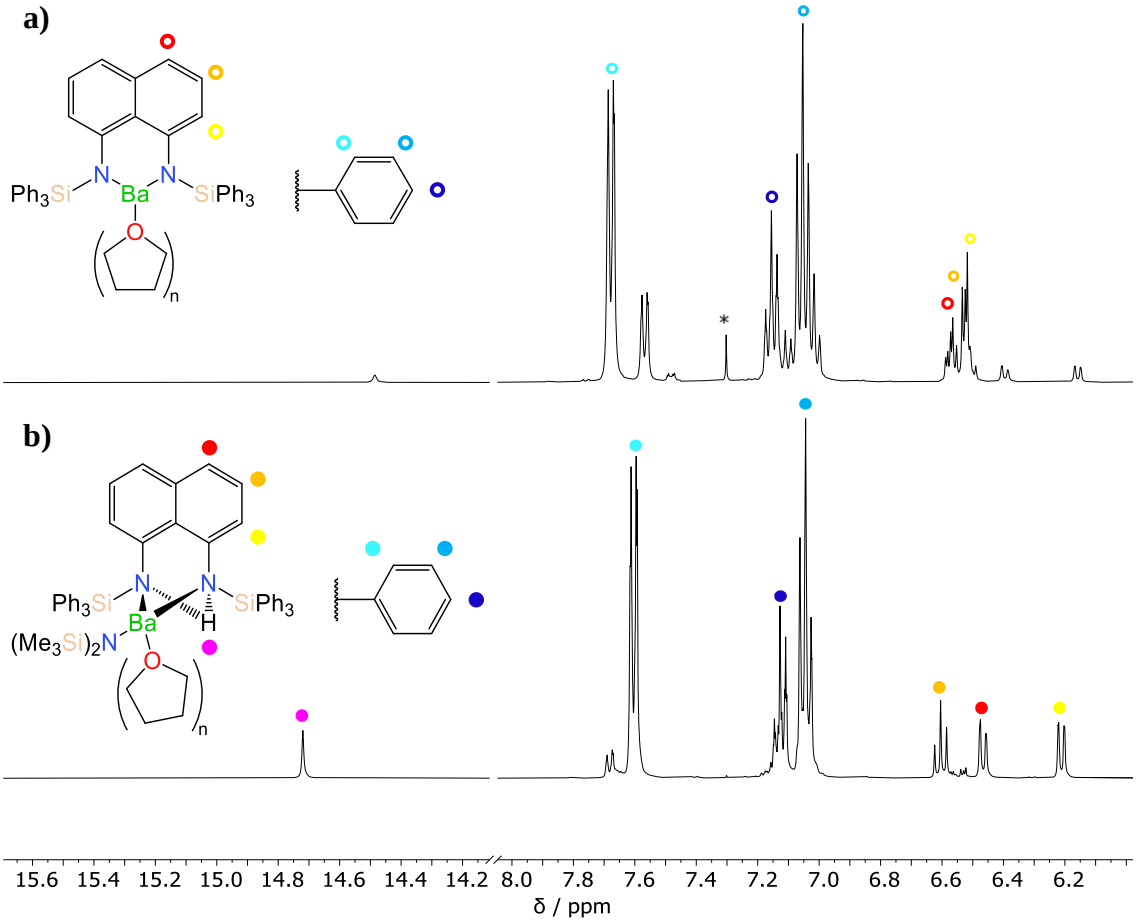
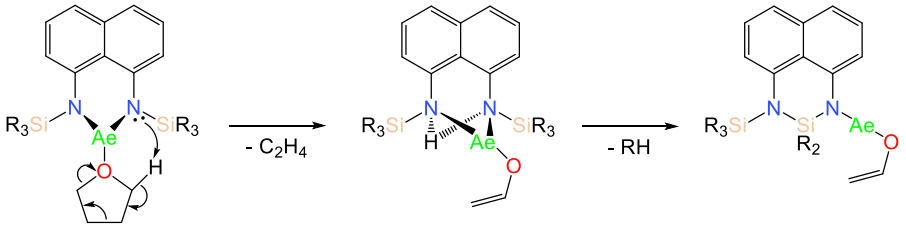


Figure 3.12 (N,N)μ$_2$-H and aromatic regions of the ^{1}H NMR spectra (C_4D_8O, 298 K, 400 MHz) of **a)** impure [(^{Ph3}L)Ba(THF)$_n$] formed when [(^{Ph3}L)Ba]$_2$ (**11**) is dissolved in THF-d_8; **b)** [(^{Ph3}LH)BaN"(THF)$_n$] formed *in situ via* the 1:1 reaction of ^{Ph3}LH$_2$ with [(THF)$_2$BaN"$_2$] at 25 °C in THF-d_8. * denotes benzene present due to its co-crystallisation with **11** and its release upon degradation.

suggests that solution-phase decomposition is especially rapid in this case, and results in the formation of a [^{Ph3}LH]$^-$ fragment. The absence of any (N,N)μ$_2$-H proton in solid samples of **11** was confirmed by IR spectroscopy, implying that its presence in solution results from degradation. Subsequent spectra recorded at later time intervals showed the full consumption of both sets of resonances, along with the concomitant growth of new ligand signals and the release of significant amounts of benzene. While the many broad and overlapping signals could not be confidently assigned, the resulting spectrum is very

similar to those resulting from the *in situ* formation of [($^{Ph_3\text{-}\mu\text{-}Ph_2}$L)AeN"(THF)$_n$] (**Figure 2.12b**). This suggests that further decomposition results in the irreversible conversion of the [^{Ph_3}LH]$^-$ ligand into a [$^{Ph_3\text{-}\mu\text{-}Ph_2}$L]$^-$ fragment *via* the mechanism discussed in **Section 2.4**. Qualitative observations confirmed that the rate of degradation of [(^{R_3}L)Ae(THF)$_n$] increases with larger Ae^{2+} size and is faster both when R_3 = Ph_3 (relative to R_3 = Ph_2Me). These trends are fully consistent with those discussed in **Chapter 2**, and rationalise the observation that **11** is especially prone to decomposition.

The thermal degradation reaction *in situ* is easily attributed to the persistence of HN", which readily protonates [(^{R_3}L)Ae(THF)$_n$] to form the intermediate species [(^{R_3}LH)AeN"(THF)$_n$] that subsequently degrades. However, it is less obvious where a proton is abstracted from when isolated samples of **6**–**11** are dissolved in THF and no HN" is present. It is possible that the very high basicity of [^{R_3}L]$^{2-}$ enables the deprotonation of a THF molecule, the C-H bonds of which are activated upon coordination to the Lewis acidic Ae^{2+} centre. This provides the proton required for further degradation (**Scheme 3.7**). The reaction of highly basic alkaline earth complexes with THF in this manner has been reported previously.[30,31]



Scheme 3.7 Possible mechanism for the degradation of [(^{R_3}L)Ae(THF)$_n$] *via* the C-H activation of coordinated THF. Additional coordinated THF molecules not shown for clarity.

3.8 Conclusions

Full deprotonation of the phenyl-substituted proligands $^{Ph_3}LH_2$ and $^{Ph_2Me}LH_2$ *via* protonolysis with $[AeN"_2]_2$ (Ae = Ca, Sr and Ba) in benzene afforded the six novel dimeric 1,8-*bis*(silylamido)naphthalene alkaline earth complexes $[(^{R_3}L)Ae]_2$ ($R_3 = Ph_2Me$, Ae = Ca (**6**), Sr (**7**), and Ba (**8**); $R_3 = Ph_3$, Ae = Ca (**9**), Sr (**10**) and Ba (**11**)). X-ray crystallographic analysis showed that **6**, **7** and **9** crystallise as nitrogen bridged dimers. Conversely, **10** and **11** instead display a naphthalene-bridged motif, while the structure of **8** is intermediate between the two distinct classes. The variance between these structures was rationalised based on the electron-withdrawing influence of the phenyl substituents of their ligands and the preferential formation of "soft" multihaptic π-facial interactions by the larger Sr^{2+} and Ba^{2+} cations.

NMR spectroscopic analysis of isolated samples of **6**–**11** in THF-d_8 confirmed their conversion into the monomeric THF adducts $[(^{R_3}L)Ae(THF)_n]$, with crystallographic verification provided by the X-ray crystal structure of $[(^{Ph_3}L)Sr(THF)_3]$ (**12**). Comparative analysis of the ^{29}Si NMR spectra of **6**–**11** confirmed the influence of both the coordinated Ae^{2+} cation and the substituents of the SiR_3 group on the electronic properties of the $[^{R_3}L]^{2-}$ ligand. Unfortunately, the insolubility of **6**–**11** in arene solvents and their degradation when dissolved in THF precluded any further assessment of their reactivity in solution. However, the results presented in **Chapter 2** suggested that while alkyl-substituted 1,8-bis(silylamido)naphthalene alkaline earth complexes may be more challenging to synthesise, they are generally less prone to decomposition. Consequently, the synthesis of THF-free alkaline earth complexes using the proligand $^{Me_2tBu}LH_2$ is discussed in **Chapter 4**.

3.9 References

1 A. J. Blake, N. L. Gillibrand, G. J. Moxey and D. L. Kays, *Inorg. Chem.*, 2009, **48**, 10837–10844.

2 Q. Liu, C. Wang, X. Zhang, M. Xue, Y. Yao, Y. Zhang and Q. Shen, *New J. Chem.*, 2016, **40**, 10447–10454.

3 C. Wang, X. Zhang, M. Xue, Y. Zhang and Q. Shen, *Organometallics*, 2013, **32**, 3618–3624.

4 R. L. Jones, Z. R. Turner, J.-C. Buffet and D. O'Hare, *Organometallics*, 2024, **43**, 414–426.

5 R. L. Jones, Z. R. Turner, J.-C. Buffet and D. O'Hare, *Polym. Chem.*, 2024, **15**, 1767–1776.

6 K. W. Hellmann, C. Galka, L. H. Gade, T. Kottke and D. Stalke, *Chem. Commun.*, 1998, 549–550.

7 C. Jones, D. T. Nguyen and C. Helling, *Chem. – An Asian J.*, 2024, **19**, e202400498.

8 D. T. Nguyen, C. Helling, M. J. Evans and C. Jones, *Inorg. Chem.*, 2024, **63**, 5718–5726.

9 K. Thum, J. Martin, H. Elsen, J. Eyselein, L. Stiegler, J. Langer and S. Harder, *Eur. J. Inorg. Chem.*, 2021, **2021**, 2643–2653.

10 K. G. Pearce, C. Dinoi, R. J. Schwamm, L. Maron, M. F. Mahon, M. S. Hill, K. G. Pearce, R. J. Schwamm, M. F. Mahon and M. S. Hill, *Adv. Sci.*, 2023, **10**, 2304765.

11 L. Münzfeld, S. Gillhuber, A. Hauser, S. Lebedkin, P. Hädinger, N. D. Knöfel, C. Zovko, M. T. Gamer, F. Weigend, M. M. Kappes and P. W. Roesky, *Nature*, 2023, **620**, 92–96.

12 J. Pahl, S. Brand, H. Elsen and S. Harder, *Chem. Commun.*, 2018, **54**, 8685–8688.

13 L. Garcia, M. D. Anker, M. F. Mahon, L. Maron and M. S. Hill, *Dalton Trans.*, 2018, **47**, 12684–12693.

14 J. Pahl, A. Friedrich, H. Elsen and S. Harder, *Organometallics*, 2018, **37**, 2901–2909.

15 K. Thum, A. Friedrich, J. Pahl, H. Elsen, J. Langer and S. Harder, *Chem. Eur. J.*, 2021, **27**, 2513–2522.

16 O. P. E. Townrow, C. Färber, U. Zenneck and S. Harder, *Angew. Chemie*, 2023, **63**, e202318428.

17 Q. Liu, C. Wang, X. Zhang, M. Xue, Y. Yao, Y. Zhang and Q. Shen, *New J. Chem.*, 2016, **40**, 10447–10454.

18 P. Stegner, C. Färber, J. Oetzel, U. Siemeling, M. Wiesinger, J. Langer, S. Pan, N. Holzmann, G. Frenking, U. Albold, B. Sarkar and S. Harder, *Angew. Chemie Int. Ed.*, 2020, **59**, 14615–14620.

19 M. J. C. Dawkins, A. N. Simonov and C. Jones, *Dalton Trans.*, 2020, **49**, 6627–6634.

20 L. Lameyer, O. A. Salah, S. Deuerlein, T. Stey and D. Stalke, *ZAAC*, 2004, **630**, 1801–1806.

21 M. Westerhausen and W. Schwarz, *ZAAC*, 1991, **606**, 177–190.

22 P. Pyykkö, *J. Phys. Chem. A*, 2015, **119**, 2326–2337.

23 P. M. Chapple and Y. Sarazin, *Eur. J. Inorg. Chem.*, 2020, **2020**, 3321–3346.

24 S. Harder, *Chem. Rev.*, 2010, **110**, 3852–3876.

25 A. W. Addison, T. N. Rao, J. Reedijk, J. Van Rijn and G. C. Verschoor, *J. Chem. Soc. Dalt. Trans.*, 1984, 1349–1356.

26 M. A. Bradley, C. Birchall, A. J. Blake, W. Lewis, G. J. Moxey and D. L. Kays, *Dalton Trans.*, 2017, **46**, 4101–4110.

27 R. R. Fraser, T. S. Mansour and S. Savard, *J. Org. Chem.*, 1985, **50**, 3232–3234.

28 A. G. Palmer, *Annu. Rev. Biophys. Biomol. Struct.*, 2001, **30**, 129–155.

29 M. Westerhausen, *Inorg. Chem.*, 1991, **30**, 96–101.

30 K. Izod and P. G. Waddell, *Organometallics*, 2015, **34**, 2726–2730.

31 S. Harder and J. Langer, *Nat. Rev. Chem.*, 2023, **7**, 843–853.

Chapter 4

Synthesis and characterisation of alkyl-substituted 1,8-*bis*(silylamido)naphthalene alkaline earth complexes

4.1 Introduction

4.1.1 Overview

This chapter builds on the work discussed in **Chapter 3**, in which the isolation and characterisation of the complexes $[(^{R_3}L)Ae]_2$ ($[^{R_3}L]^{2-}$ = $[1,8\text{-}\{(R_3Si)N\}_2C_{10}H_6]^{2-}$; R_3 = Ph_2Me, Ae = Ca (**6**), Sr (**7**) and Ba (**8**); R_3 = Ph_3, Ae = Ca (**9**), Sr (**10**) and Ba (**11**), **Chart 4.1**) was discussed. The same THF-free synthetic route is employed in the isolation of novel complexes of the heavier alkaline earth elements calcium, strontium and barium bearing alkyl-substituted 1,8-*bis*(silylamido)naphthalene ligands. Based on results in **Chapter 2**, it was hypothesised that these bulky alkyl substituents would confer improved solution-phase stability. The $^{Me_2tBu}LH_2$ proligand was selected, as protonolysis reactions of the $^{iPr_3}LH_2$ proligand had been hindered by its excessive steric bulk. In total, the synthesis and characterisation of five novel compounds is discussed. This includes a calcium dimer with a naphthalene-bridged dimeric structure analogous to **10** and **11**.

However, the other four compounds display new structural motifs that result from the basicity and steric bulk of their alkyl-substituted ligands. Notably, the crystal structure of a solvent-separated ion pair (SSIP) consisting of an unexpected weakly-coordinating anion (WCA) was obtained.

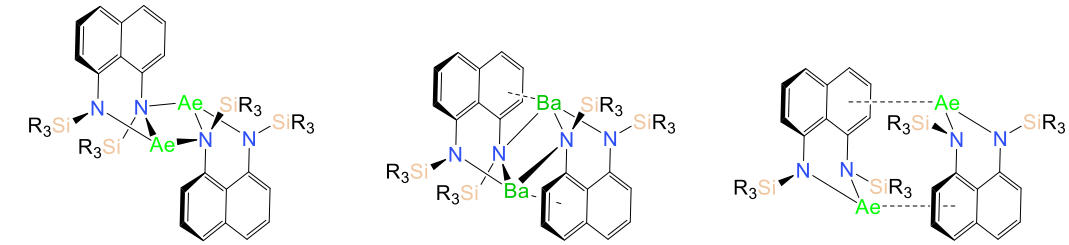


Chart 4.1 Complexes **6**–**11**, presented for comparison with the complexes discussed in **Chapter 4**.

4.1.2 Weakly-coordinating anions and solvent-separated ion pairs

WCAs consist of a diffuse negative charge that is delocalised across many atoms.[1] Notable examples that have found widespread synthetic utility[2] include the poly-fluorinated $[B(C_6F_5)_4]^-$, $[H_2N\{B(C_6F_5)_3\}_2]^-$ and $[Al\{OC(CF_3)_3\}_4]^-$ anions.[3–5] While full non-coordination is impossible,[6] the electronegative fluorine atoms of these WCAs are extremely weak Lewis bases that are only capable of forming very weak dative interactions, thus enabling the synthesis of discrete cationic metal complexes.[7] A number of heteroleptic alkaline earth complexes of the form [(L)Ae][WCA] have been reported. These consist of both a monoanionic coordinating ligand ($[L]^-$) and a WCA, resulting in the release of cationic $[(L)Ae]^+$ complexes in solution.

Sarazin, Carpentier and co-workers have reported, bulky phenolate-[8,9] (**I**, **Chart 4.2**) and BDI-supported[10] cationic alkaline earth complexes, the high Lewis acidity of which was found to enable significantly enhanced rates of lactide ROP *via* an activated monomer mechanism. Furthermore, Harder and co-workers have employed WCAs to enable the

isolation of various cationic BDI-supported alkaline earth arene and alkene complexes (**II**, **Chart 4.2**).[11–15]

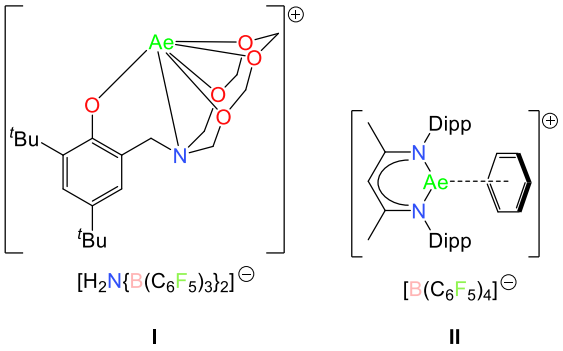
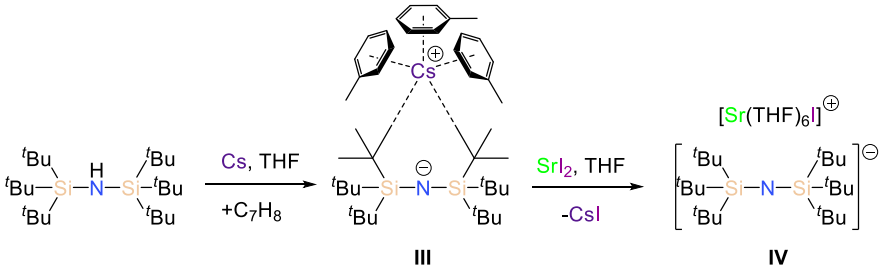


Chart 4.2 Selected examples of cationic alkaline earth complexes (Ae = Mg and Ca) accessed using weakly-coordinating anions (WCAs).

Notably, Harder and co-workers also very recently reported the bulky amine $(^{t}Bu_3Si)_2NH$.[16] While the extreme steric bulk of $(^{t}Bu_3Si)_2NH$ precluded its deprotonation by most common bases, reduction with a Cs^{+}/e^{-} electride in THF followed by crystallisation from toluene afforded $[\{(^{t}Bu_3Si)_2N\}Cs(C_7H_8)_3]$ (**III**, **Scheme 4.1**). The $[(^{t}Bu_3Si)_2N]^{-}$ ligand has a near-linear geometry in the crystal structure of **III**, and only interacts with the large Cs^{+} cation through agostic interactions formed *via* the C-H bonds of its bulky alkyl substituents. No interaction was observed between Cs^{+} and the highly encumbered anionic nitrogen donor, which is stabilised by negative hyper-conjugation with the adjacent silyl groups. Salt metathesis reactions with alkaline earth iodide reagents proved unselective, but did yield crystals of the SSIP $[(THF)_6SrI][(^{t}Bu_3Si)_2N]$ (**Scheme 4.1**, **IV**). The $[(^{t}Bu_3Si)_2N]^{-}$ anion acts as a WCA in both **III** and **IV** despite the localisation of negative charge on its anionic nitrogen donor, in contrast with most conventional WCAs.



Scheme 4.1 Synthesis of [{(^{t}Bu$_3$Si)$_2$N}Cs(C$_7$H$_8$)$_3$] (**III**) and [(^{t}Bu$_3$Si)$_2$N][Sr(THF)$_6$I] (**IV**), in which the bulky amide [(^{t}Bu$_3$Si)$_2$N]$^-$ acts as a weakly-coordinating anion (WCA).

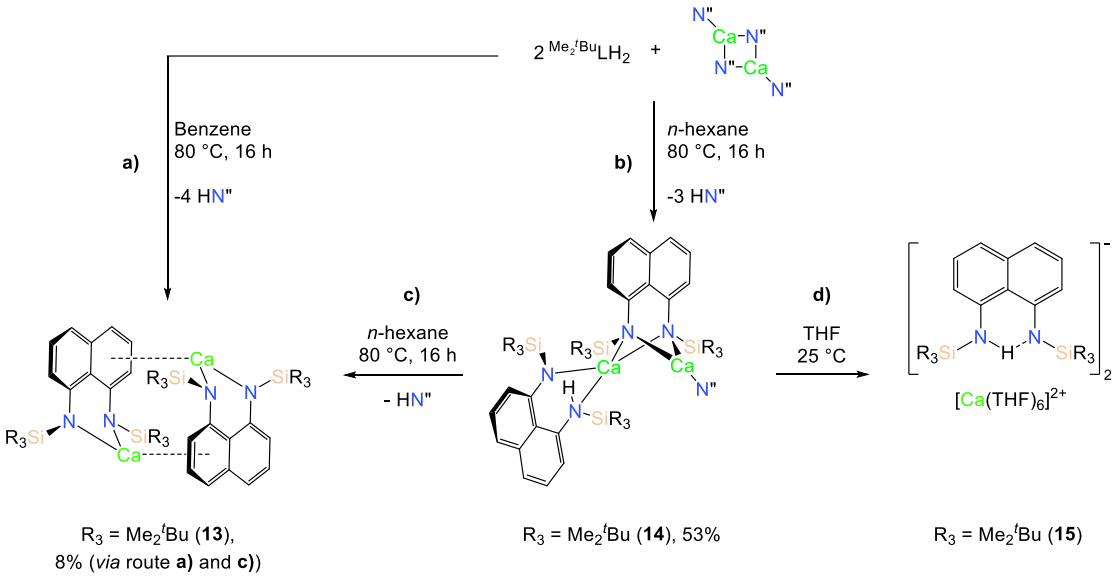
4.2 Synthesis of alkyl-substituted alkaline earth complexes

Gratifyingly, the 2:1 reaction of ^{Me2tBu}LH$_2$ with [CaN"$_2$]$_2$ in benzene at 80 °C proved successful (**Scheme 4.2**). A small crop of yellow crystals grew upon slow cooling of the reaction mixture after heating at 80 °C for 16 hours. This enabled the isolation of [(^{Me2tBu}L)Ca]$_2$ (**13**, **Scheme 4.2a**), which has the same naphthalene-bridged dimeric structure as [(^{Ph3}L)Ae]$_2$ (Ae = Sr (**10**) and Ba (**11**)), in low yield (8%).

Subsequent attempts to isolate greater quantities of **13** by instead using *n*-hexane as the reaction solvent once again resulted in the crystallisation of small crops of **13** after 16 hours at 80 °C. Unfortunately, this approach did not improve the isolated yield. However, concentration of the *n*-hexane filtrate (obtained following the isolation of **13** *via* filtration) resulted in the crystallisation of the unexpected bimetallic intermediate species [(^{Me2tBu}LH)Ca(μ-^{Me2tBu}L)CaN"] (**14**, **Scheme 4.2b**) in moderate yield (53%). Heating the reaction mixture at 80 °C for 1 week in either benzene or *n*-hexane did not significantly change the isolated yields of **13** and **14**, suggesting that at this temperature they are in equilibrium as the minor and major species respectively. Unfortunately, the poor hydrocarbon solubility of isolated samples of **14** precluded a direct assessment of its conversion into **13** when the three equivalents of HN" released during the formation

of **14** *in situ* are excluded. However, the low isolated yield (8%) of **13** reflects the relative stability of **14**, with only partial conversion of the former into the latter possible (**Scheme 4.2c**). Consequently, **14** is the major product of the reaction in both benzene and *n*-hexane (though was only isolated in the latter case).

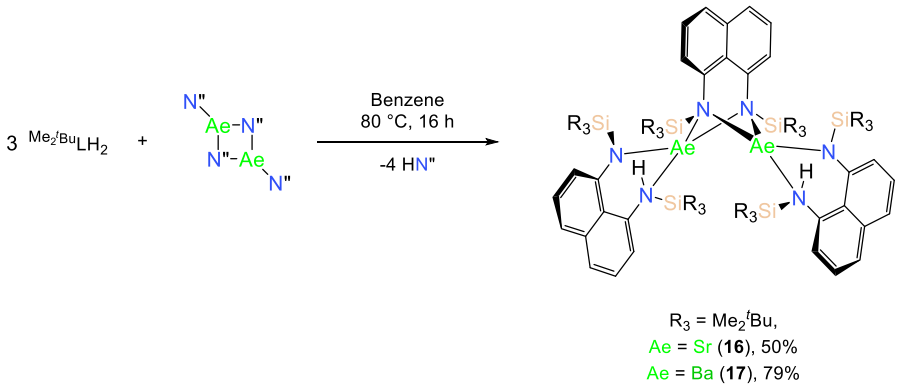
Remarkably, the SSIP $[^{Me_2tBu}LH]_2[Ca(THF)_6]$ (**15**, **Scheme 4.2d**), in which the $[^{Me_2tBu}LH]^-$ fragment acts as a WCA, crystallised when THF solutions of **14** were left to stand at 25 °C. Unfortunately, pure samples of **15** could not be isolated due to its decomposition *in vacuo*.



Scheme 4.2 a) Synthesis of $[(^{Me_2tBu}L)Ca]_2$ (**13**) and **b)** $[(^{Me_2tBu}LH)Ca(\mu\text{-}^{Me_2tBu}L)CaN"]$ (**14**) *via* the 2:1 reaction of $^{Me_2tBu}LH_2$ with $[CaN"_2]_2$ in benzene and *n*-hexane respectively, **c)** partial conversion of **14** into **13** *in situ* in *n*-hexane and **d)** conversion of **14** into $[^{Me_2tBu}LH]_2[Ca(THF)_6]$ (**15**) in THF.

Conversely, the analogous 2:1 reactions involving the heavier alkaline earth congeners strontium and barium resulted in the crystallisation of the unexpected bimetallic "triple-decker" complexes $[\{(^{Me_2tBu}LH)Ae\}_2(\mu\text{-}^{Me_2tBu}L)]$ (Ae = Sr (**16**) and Ba (**17**)). Higher

yields of **16** (50%) and **17** (79%) could be achieved *via* a deliberate synthesis employing a 3:1 ratio of $^{Me_2{}^tBu}LH_2$ to $[AeN''_2]_2$ (**Scheme 4.3**).



Scheme 4.3 Synthesis of $[\{(^{Me_2{}^tBu}LH)Ae\}_2(\mu\text{-}^{Me_2{}^tBu}L)]$ (Ae = Sr (**16**) and Ba (**17**)) *via* the 3:1 reaction of $^{Me_2{}^tBu}LH_2$ with $[AeN''_2]_2$ (Ae = Sr and Ba) in benzene.

Notably, the temperature of 80 °C required for conversion to **13**, **14**, **16** and **17** contrasts with the formation of **6**–**11** (**Chart 4.1**) at 25 °C. This observation, combined with the low isolated yield of **13** and the stability of **14**–**17**, reflects the high basicity of the $[^{Me_2{}^tBu}LH]^-$ fragment. Compounds **13**–**17** were characterised by X-ray crystallography and, excluding **15**, multinuclear NMR spectroscopy, IR spectroscopy and elemental analysis.

4.3 Characterisation of calcium compounds

4.3.1 X-ray crystal structure of $[(^{Me_2{}^tBu}L)Ca]_2$ (13)

Complex **13** crystallises in the $P2_1$ space group. Like the phenyl-substituted complexes **10** and **11**, **13** crystallises as a naphthalene-bridged dimer (**Figure 4.1**, **Table 4.1**). However, in this case the asymmetric unit consists of the full dimer rather than a single $[(^{R_3}L)Ae]$ unit. The two $[(^{Me_2{}^tBu}L)Ca]$ units present in **13**, which each consist of the

$[^{Me_2tBu}L]^{2-}$ ligand chelating Ca^{2+} in the expected κ^2-N,N′-bidentate manner, are crystallographically independent and therefore not related by inversion. Consequently, the mean planes defined by the two naphthalene rings are not parallel with respect to one another (unlike in **6**–**11**), resulting in a small interplanar fold angle of 1.55(3)°. Excluding this asymmetry, the dimeric "piano-stool" structure of **13** is largely similar to those of **10** and **11**, with short Ca-centroid distances (Ca(1)-centroid$_{C(27)-C(32)}$ = 2.4583(7) Å, Ca(2)-centroid$_{C(1)-C(6)}$ = 2.4629(7) Å) the result of the smaller ionic radius of Ca^{2+} with respect to the heavier congeners. The four Ca-N bonds are all of very similar lengths (2.263(1)–2.272(1) Å), and are notably shorter than those formed by the nitrogen-bridged calcium dimers **6** and **9**. This is likely due to the absence of a third Ca-N bond in **13** resulting in reduced steric congestion at Ca^{2+}, which forms two shorter Ca-N bonds as opposed to three longer ones.

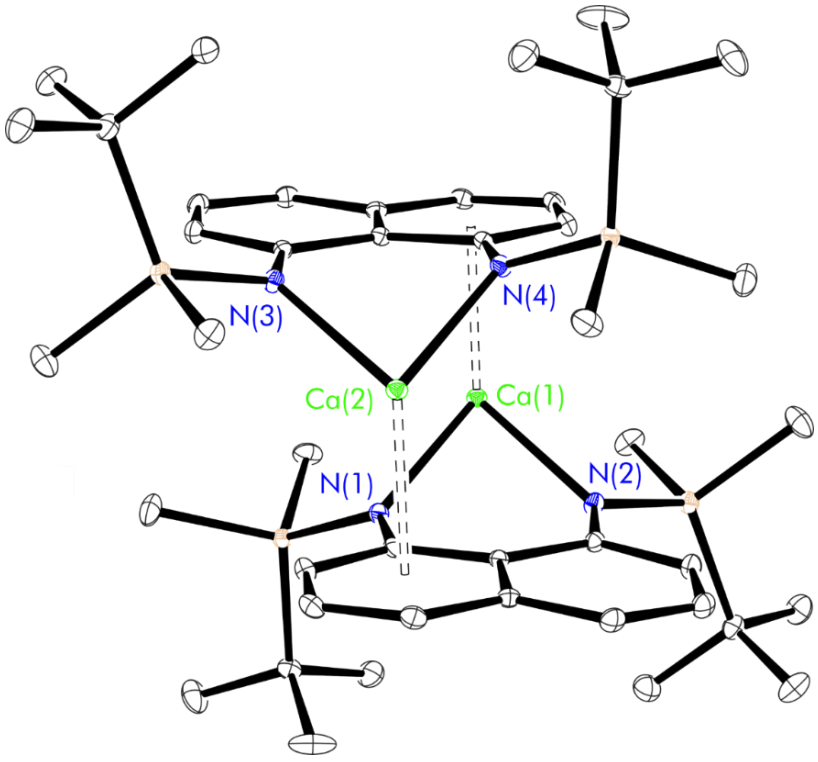


Figure 4.1 Thermal displacement ellipsoid drawing (30% probability) of $[(^{Me_2tBu}L)Ca]_2$ (**13**).

All hydrogen atoms have been omitted for clarity.

Table 4.1 Experimental metrical parameters (bond lengths in Å and angles in °) in $[(^{Me_2{}^tBu}L)Ca]_2$ (**13**).

Space group	$P2_1$
N(1)-Ca(1)	2.266(1)
N(2)-Ca(1)	2.268(1)
N(3)-Ca(2)	2.263(1)
N(4)-Ca(2)	2.272(1)
$Ca(1)\text{-Centroid}_{C(27)\text{-}C(32)}$	2.458(1)
$Ca(2)\text{-Centroid}_{C(1)\text{-}C(4),C(9),C(10)}$	2.464(1)
$Ca(1)\text{-Plane}_{C(1)\text{-}C(10)}$	1.204(2)
$Ca(2)\text{-Plane}_{C(23)\text{-}C(32)}$	1.195(2)
N(1)-N(2)	2.870(2)
N(3)-N(4)	2.875(2)
Ca(1)-Ca(2)	4.425(1)
N(1)-Ca(1)-N(2)	78.55(5)
$N(1)\text{-Ca(1)-Centroid}_{C(27)\text{-}C(32)}$	122.32(4)
$N(2)\text{-Ca(1)-Centroid}_{C(27)\text{-}C(32)}$	121.57(4)
N(3)-Ca(2)-N(4)	78.67(5)
$N(3)\text{-Ca(2)-Centroid}_{C(1)\text{-}C(4),C(9),C(10)}$	121.37(4)
$N(2)\text{-Ca(1)-Centroid}_{C(1)\text{-}C(4),C(9),C(10)}$	122.46(4)
$Plane_{C(1)\text{-}C(10)}\text{-}Plane_{C(23)\text{-}C(32)}$ fold angle	1.55(3)

In the absence of the Ae^{2+}-phenyl π-facial interactions that are present in **6**–**11**, each calcium centre in **13** is stabilised by agostic interactions with the C-H bonds of one methyl substituent from each flanking $SiMe_2{}^tBu$ group (Ca-H_{Me} = 2.6968(4)–2.8649(5) Å). The Ca^{2+} centres in **13** sit further out of plane than those in **6** and **9** in order to engage in the η^6-π-facial Ca^{2+}-naphthyl interactions that result in dimerisation (Ca(1)-$plane_{(1)\text{-}C(10)}$ = 1.204(2) Å, Ca(2)-$plane_{C(23)\text{-}C(32)}$ = 1.195(2) Å). Consequently, both $[^{Me_2{}^tBu}L]^{2-}$ ligands are highly planar (C(1–10)-$plane_{C(1)\text{-}C(10)}$ = 0.003(1)–0.054(1) Å; (C(23–32)-$plane_{C(23)\text{-}C(32)}$ = 0.011(1)–0.057(1) Å) having not distorted to accommodate Ca^{2+} in plane, with short N-N distances (N(1)-N(2) = 2.870(2) Å, N(3)-N(4) = 2.875(2) Å). Despite this, the N-Ca-N bite angles in **13** (N(1)-Ca(1)-N(2) = 78.55(5)°, N(3)-Ca(2)-N(4) = 78.67(5)°) are very similar to those in **6** and **9**.

It is notable that **13** crystallises as a naphthalene-bridged dimer, whereas the phenyl-substituted calcium dimers **6** and **9** have nitrogen-bridged structures. A consideration of electronic factors would suggest that the bulky electron-donating *tert*-butyl groups of **13** should increase the charge density of its amide donors, making a nitrogen-bridged structure even more favourable. While this rationale seemingly applies for other complexes bearing $[^{Me_2{}^tBu}L]^{2-}$ and $[^{Me_2{}^tBu}LH]^{-}$ ligands (*vide infra*), it is not borne out in this case. Instead, the formation of a naphthalene-bridged structure can be attributed to the relief of significant steric congestion that likely results from the coordination of three bulky $[RN(SiMe_2{}^tBu)]^{-}$ donors to Ca^{2+} in an intermediate nitrogen-bridged structure. This contrasts with the shift from the nitrogen-bridged strontium and barium complexes **7** and **8** to their naphthalene-bridged analogues **10** and **11** (**Scheme 3.2**), where electronic factors seemingly predominated. This underlines the greater

influence of steric factors on the smaller Ca^{2+} cation relative to the heavier congeners.[17] Unfortunately, incomplete conversion of the intermediate species **14** into **13** resulted in the isolation of insufficient quantities of pure material to investigate its onward reactivity.

4.3.2 X-ray crystal structure of [(^{Me_2tBu}LH)Ca(μ-^{Me_2tBu}L)CaN"] (14)

Complex **14** crystallises in the *P*1 space group, (**Figure 4.2**, **Table 4.2**). The structure of **14** consists of a fully deprotonated [μ-^{Me_2tBu}L]$^{2-}$ ligand bridging between Ca^{2+} cations, with each metal centre coordinated in a κ^2-N,N′-bidentate manner *via* two μ$_2$-N donors. These form four Ca-N bonds which are of very similar lengths (2.372(1)–2.4120(9) Å). This results in a central [(μ-^{Me_2tBu}L)Ca_2]$^{2+}$ moiety consisting of a Ca_2N_2 core with a long Ca(1)-Ca(2) distance (3.8219(5) Å). Unlike in the centrosymmetric nitrogen-bridged dimers **6**–**9**, the Ca_2N_2 ring in **14** is not planar, resulting in Ca(1)-N(3-N(4)-Ca(2) and

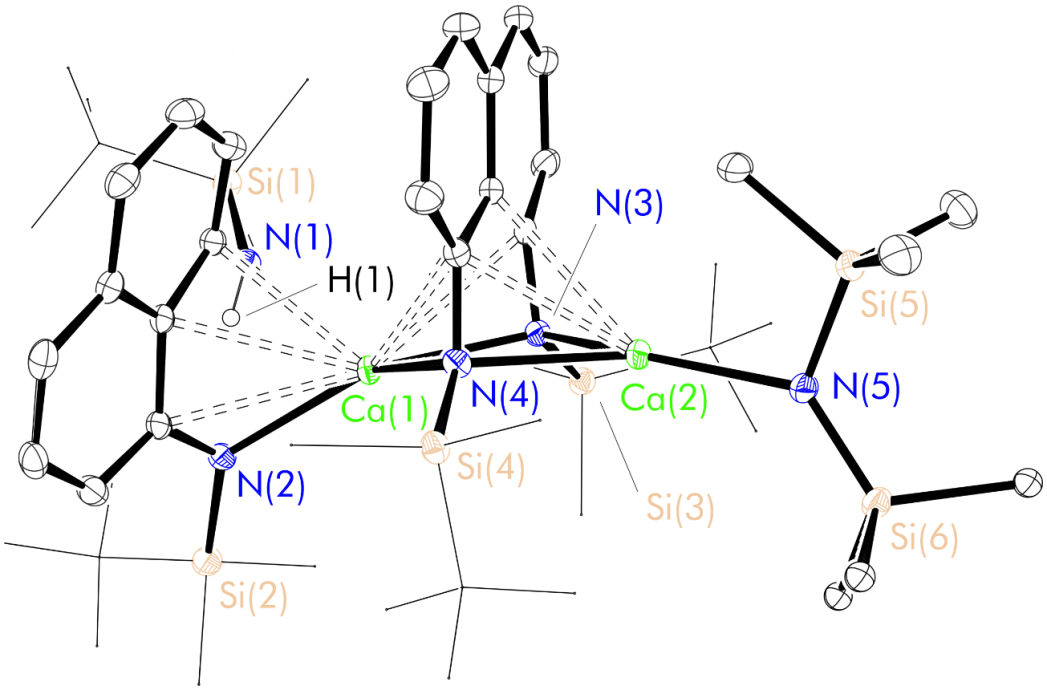


Figure 4.2 Thermal displacement ellipsoid drawing (30% probability) of [(^{Me_2tBu}LH)Ca(μ-^{Me_2tBu}L)CaN"] (**14**). All non-amino hydrogen atoms have been omitted and SiMe_2^{t}Bu substituents are wireframed for clarity.

N(3)-Ca(1)-Ca(2)-N(4) torsion angles of 168.32(5)° and 164.50(7)° respectively. Both calcium cations necessarily lie out of the plane of the bridging [μ-$^{Me_2{}^tBu}$L]$^{2-}$ ligand (Ca(1)-plane$_{C(23)\text{-}C(32)}$ = 1.7616(13) Å, Ca(2)-plane$_{C(23)\text{-}C(32)}$ = 2.0340(12) Å). Consequently, the naphthalene backbone is highly planar (C(23-32)-plane$_{C(23)\text{-}C(32)}$ = 0.002(1)–0.049(1) Å) with a N-N distance (N(3)-N(4) = 2.8719(16) Å) that is very similar to those of **13** and significantly shorter than those of the more distorted **6** and **9** (2.956(3) and 2.964(2) Å respectively). Each face of the naphthalene ring also forms a η^3-π-facial interaction with a Ca^{2+} cation (Ca(1)-centroid$_{C(23),(32),C(23)}$ = 2.688(1) Å, Ca(2)-centroid$_{C(1),C(10),C(8)}$ = 2.5875(1) Å). Each metal centre is capped by a monoanionic ligand. The four-coordinate calcium centre, Ca(1), is coordinated by both [$^{Me_2{}^tBu}$LH]$^-$ and [$^{Me_2{}^tBu}$L]$^{2-}$ ligands in a κ^2-N,N′-bidentate manner, resulting in a highly distorted tetrahedral coordination geometry (Σ{∠Ca(1)} = 667.93(10)°, τ_4 = 0.54[18]). This distortion results from the geometric constraints imposed by the narrow bite angles of both the [μ-$^{Me_2{}^tBu}$L]$^{2-}$ (N(3)-Ca(1)-N(4) = 74.09(4)°) and [$^{Me_2{}^tBu}$LH]$^-$ (N(1)-Ca(1)-N(2) = 66.37(4)°) ligands, which are rotated with respect to one another to minimise steric clash between their bulky silyl substituents. This arrangement results in an interplanar fold angle of 16.21(3)° between the planes defined by the two non-parallel naphthalene rings. Conversely, the other Ca^{2+} centre, Ca(2), is coordinated by a terminal monodentate [N"]$^-$ group that has been retained from the [CaN"$_2$]$_2$ precursor,[19] resulting in the shortest of the seven Ca-N bonds (Ca(2)-N(5) = 2.291(1) Å). Consequently, Ca(2) has a three-coordinate trigonal planar coordination geometry (Σ{∠Ca(2)} = 358.72(11)°). The SiMe$_3$ groups of the [N"]$^-$ ligand are orientated such that steric clash with the bulky SiMe$_2{}^t$Bu groups of the opposing [μ-$^{Me_2{}^tBu}$L]$^{2-}$ ligand is minimised.

Table 4.2 Experimental metrical parameters (bond lengths in Å and angles in °) in [($^{Me_2{}^tBu}$LH)Ca(μ-$^{Me_2{}^tBu}$L)CaN''] (**14**).

Space group	*P*1
Ca(1)-N(1)	2.620(1)
Ca(1)-N(2)	2.409(1)
Ca(1)-N(3)	2.3946(9)
Ca(1)-N(4)	2.372(1)
Ca(2)-N(3)	2.415(1)
Ca(2)-N(4)	2.4120(9)
Ca(2)-N(5)	2.291(1)
N(1)-H(1)	0.82(2)
N(2)-H(1)	2.08(3)
Ca(1)-Ca(2)	3.8219(5)
N(1)-N(2)	2.758(2)
N(3)-N(4)	2.872(2)
Ca(1)-Plane$_{C(1)-C(10)}$	2.069(1)
Ca(1)-Plane$_{C(23)-C(32)}$	1.762(1)
Ca(2)-Plane$_{C(27)-C(32)}$	2.034(1)
N(1)-Ca(1)-N(2)	66.37(4)
N(3)-Ca(1)-N(4)	74.09(4)
N(3)-Ca(2)-N(4)	73.03(4)
Ca(1)-N(3)-N(4)-Ca(2)	168.32(5)
N(3)-Ca(1)-Ca(2)-N(4)	164.50(7)
Plane$_{C(1)-C(10)}$-Plane$_{C(23)-C(32)}$ fold angle	16.21(3)

The amino proton of the $[^{Me_2tBu}LH]^-$ fragment, H(1), is necessary for charge balance, with its retention resulting from only three equivalents of the four possible being released from the $[CaN"_2]_2$ precursor. H(1) was located in the difference map and freely refined, with its presence also confirmed by ^{1}H NMR and IR spectroscopy (*vide infra*). H(1) is localised on a neutral amino donor (N(1)-H(1) = 0.82(2) Å), and forms an intramolecular hydrogen-bond with the adjacent amido donor (N(2)-H(1) = 2.08(3) Å, N(1)-H(1)-N(2) = 140(2)°).

The localisation of negative charge on the deprotonated amido donor is confirmed by a Ca-N bond that is of similar length (Ca(1)-N(2) = 2.409(1) Å) to those formed by the amide donors of the $[\mu\text{-}^{Me_2tBu}L]^{2-}$ ligand (*vide supra*). In contrast, the corresponding Ca-NH bond (Ca(1)-N(1) = 2.620(1) Å) formed by the protonated amine donor is around 0.2 Å longer. While the coordination geometry at Ca(1) clearly demonstrates the presence of a Ca-NH interaction, this is longer than the combined covalent radii of calcium and nitrogen (Σr_{cov}(Ca,N) = 2.42 Å[20]). H(1) lies close to the plane (H(1)-plane$_{C(1)\text{-}C(10)}$ = 0.45(2) Å) of a somewhat distorted naphthalene backbone (C(1–10)-plane$_{C(1)\text{-}C(10)}$ = 0.009(1)–0.141(1) Å). The N(1)-N(2) distance of the $[^{Me_2tBu}LH]^-$ ligand (2.758(2) Å) is shortened relative to that of the proligand $^{Me_2tBu}LH_2$ (2.8121(16) Å), a result of the attractive interactions between the nitrogen donors and both the amino proton and a Ca^{2+} dication that lies significantly out of plane (Ca(1)-plane$_{C(1)\text{-}C(10)}$ = 2.069(1) Å). This N-N distance is contracted to an even greater extent relative to those of the dianionic $[^{R_3}L]^{2-}$ fragments observed in **6**–**14** due to the absence of intramolecular hydrogen bonds in the latter.

The [$^{Me_2{}^tBu}$LH]$^-$ ligand in **14** closely resembles the [^{Me_3}LH]$^-$ ligand in the ammonolysis product [(^{Me_3}LH)Pb(μ-NH$_2$)]$_2$ (**V**, **Figure 4.3a**), the only previously reported example of a crystallographically characterised [^{R_3}LH]$^-$ ligand.[21] Furthermore, the metrical parameters of the former are statistically indistinguishable from those of the proligand $^{Me_2{}^tBu}$LH$_2$ (where N(1)-H(1) = 0.83(2) Å, N(2)-H(1) = 2.11(2) Å and N(1)-H(1)-N(2) = 142(2)°; **Figure 4.3b**). This rationalises the observation that removing a single proton from ^{R_3}LH$_2$ *via* protonolysis is generally facile in THF-d_8 at 25 °C (see **Section 2.4.1**), as this results in little overall structural change. The κ^2-N,N′(H)-bidentate coordination of the [$^{Me_2{}^tBu}$LH]$^-$ ligand to Ca^{2+} in **14** contrasts with **V**, in which the [^{Me_3}LH]$^-$ ligand coordinates to Pb(II) in a κ^1-N-monodentate manner. This reflects calcium's preference for higher coordination numbers and non-directional ionic bonding.[17] In contrast, the combination of lead's higher electronegativity (χ_{Ca} = 1.00, χ_{Pb} = 1.87)[22] and the inert pair effect results in the formation of three more covalent Pb-N bonds that are near-orthogonal,[23] with the coordination of a fourth N-donor

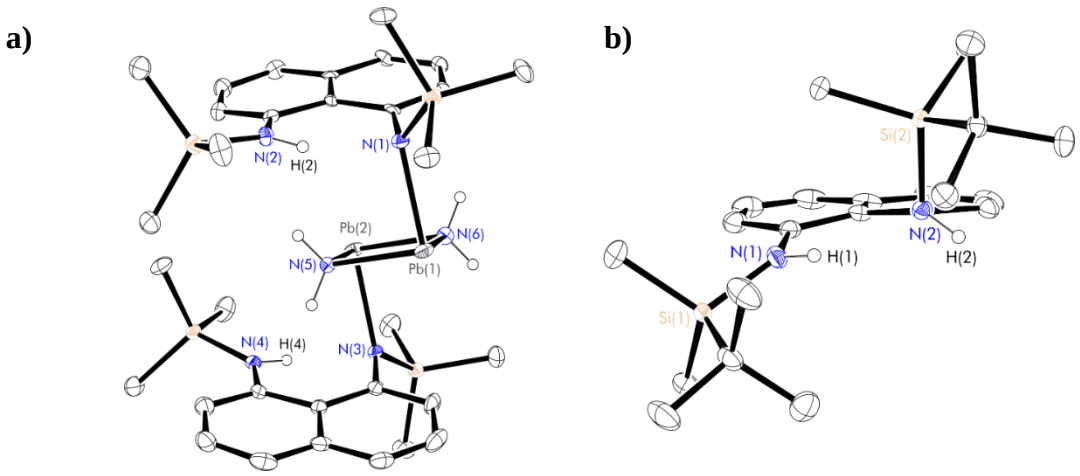


Figure 4.3 Thermal displacement ellipsoid drawing (30% probability) of **a)** [(^{Me_3}LH)Pb(μ-NH$_2$)]$_2$ (**V**), reproduced from reference 21, and **b)** $^{Me_2{}^tBu}$LH$_2$; for comparison with the X-ray crystal structure of **14**. All non-amino hydrogen atoms have been omitted for clarity.

precluded. Finally, the Ca^{2+} cation in **14** is further stabilised by a η^3-π-facial interaction with the naphthalene ring of the $[^{Me_2tBu}LH]^-$ ligand (Ca(1)-centroid$_{C(1),(10),C(8)}$ = 2.608(1) Å), with no analogous interaction present in **V**.

4.3.2.1 Comparison with *in situ* NMR spectroscopic data

The crystal structure of **14** provides crystallographic verification for the formation of stable heteroleptic intermediates species consisting of singly deprotonated $[^{R_3}LH]^-$ ligands. This provides strong support for the proposed structures of the monomeric intermediate species $[(^{R_3}LH)AeN''(THF)_n]$ in THF-d_8 (**Section 2.4.1.1**). However, the asymmetry of the $[^{Me_2tBu}LH]^-$ ligand that results from the localisation of its amino proton on a single nitrogen atom in the solid state differs from the proposed C_s-symmetric solution-phase structures of $[(^{R_3}LH)AeN''(THF)_n]$. This supports the assertion that the rapid shuttling of the (N,N)μ_2-H proton between N-donors in solution results in time averaged NMR spectra, and is consistent with NMR spectra of **14** recorded in THF-d_8 (*vide infra*).

Complex **14** can be viewed as resulting from the aggregation of a $[(^{Me_2tBu}LH)CaN'']$ unit with a $[(^{Me_2tBu}L)Ca]$ unit. This is consistent with the analogous reaction in THF-d_8, where $[(^{Me_2tBu}LH)CaN''(THF)_n]$ and $[(^{Me_2tBu}L)Ca(THF)_n]$ coexist in solution in proportions that vary with temperature (**Tables 2.3** and **2.4**). The incomplete conversion of the intermediate species **14** into the fully deprotonated dimer **13** reflects the strong preference of the alkyl-substituted ligand to retain an amino proton within its highly basic binding pocket. This is consistent with the relatively low frequency chemical shifts of the (N,N)μ_2-H protons of $[(^{Me_2tBu}LH)AeN''(THF)_n]$ (Ae = Ca, Sr and Ba, **Section 2.4.1.6**).

However, the coordination of a relatively hard Ca^{2+} cation seemingly stabilises the $[^{Me_2{}^tBu}L]^{2-}$ ligand sufficiently to enable some conversion to **13** (8% isolated yield), in contrast with the outcomes of reactions involving strontium and barium (**Section 4.4**).

4.3.3 IR spectroscopic analysis

The IR spectrum of **13** contains no N-H absorbances, consistent with the full deprotonation of both $[^{Me_2{}^tBu}L]^{2-}$ ligands. Conversely, the IR spectrum of **14** contains a signal at 3058 cm^{-1}, which is attributed to its N-H bond. The frequency of this vibration is red-shifted relative to the expected range for N-H absorbances, a phenomenon that has previously been reported for compounds containing intramolecular hydrogen bonds.[24-35]

Conversely, the IR spectrum of the corresponding proligand $^{Me_2{}^tBu}LH_2$ contains three signals at 3045, 3248 and 3338 cm^{-1}. The former (3045 cm^{-1}) is attributed to the intramolecular hydrogen bond, the value of which is red-shifted somewhat ($\Delta\nu$ = –13 cm^{-1}) relative to the absorbance attributed to the $[^{Me_2{}^tBu}LH]^-$ ligand in the IR spectrum of **14**. This reflects the strengthened intramolecular H-bond of $[^{Me_2{}^tBu}LH]^-$ that results from its anionic charge. The other signals (3248 and 3338 cm^{-1}) are assigned to the vibrational modes of the terminal N-H bond observed in the crystal structure of $^{Me_2{}^tBu}LH_2$ (**Figure 4.3b**). No analogous signals are present in the IR spectra of **13** or **14**.

4.3.4 *In situ* NMR spectroscopic analysis

The insolubility of isolated samples of **13** and **14** in hydrocarbons precluded a direct assessment of their solution-state structures. However, monitoring the 2:1 reaction of $^{Me_2{}^tBu}LH_2$ with $[CaN''_2]_2$ in C_6D_6 *in situ* by ^1H NMR spectroscopy provided insight into the mechanism by which **13** and **14** form.

An initial ^{1}H spectrum recorded after *ca*. 10 minutes at 25 °C (**Figure 4.4a**) showed the full consumption of the two starting materials, the release of two equivalents of HN" and the exclusive formation of an intermediate that is proposed to be the dimeric species [($^{Me_2}{}^{t}$BuLH)CaN"]$_2$ (**Scheme 4.4a**). This intermediate is characterised by the presence of a diagnostic (N,N)μ$_2$-H singlet at δ = 9.68 ppm with an integral value of two. The aromatic region consists of three naphthyl signals (δ = 7.15, 7.06 and 6.69 ppm), each

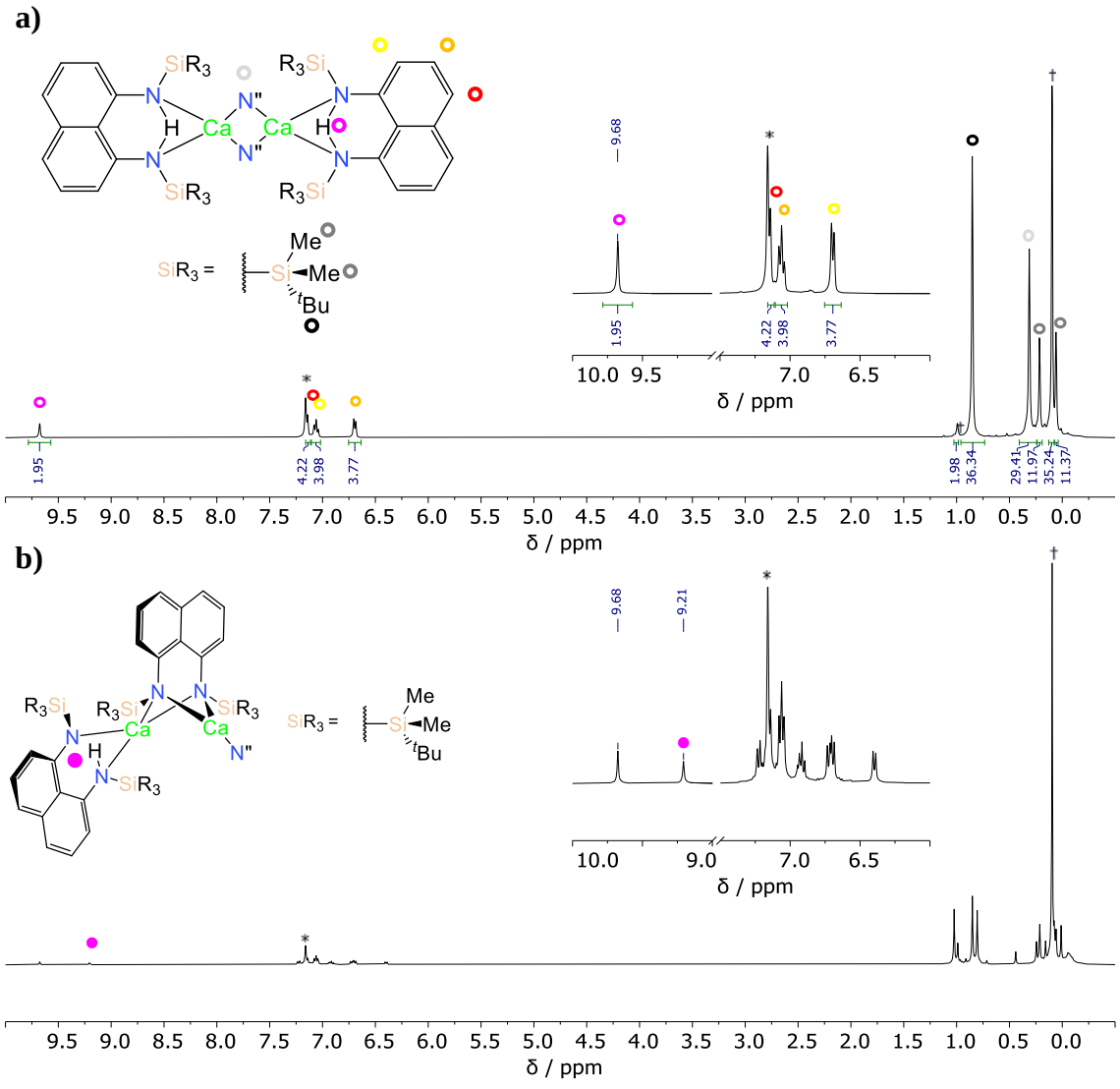


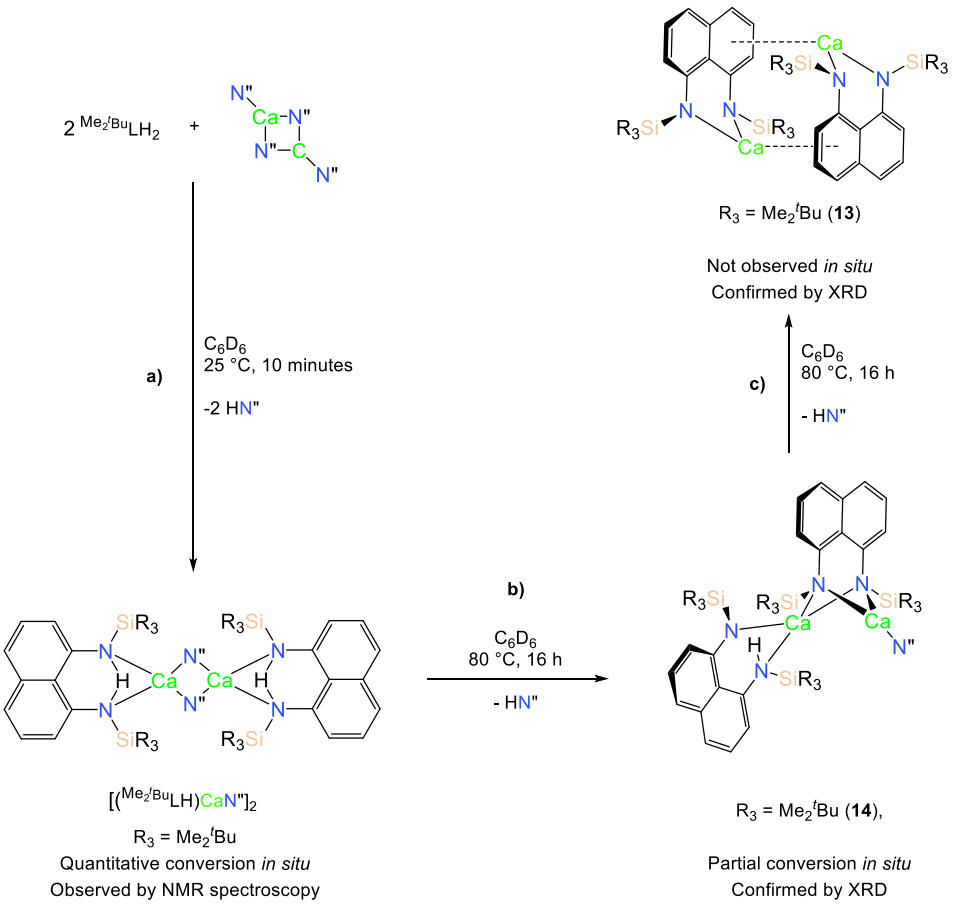
Figure 4.4 *in situ* ^{1}H NMR spectra (C_6D_6, 298 K, 400 MHz) of **a)** [($^{Me_2}{}^{t}$BuLH)CaN"]$_2$ and **b)** a mixture of [($^{Me_2}{}^{t}$BuLH)CaN"]$_2$ and [($^{Me_2}{}^{t}$BuLH)Ca(μ-$^{Me_2}{}^{t}$BuL)CaN"] (**14**), which form after 10 minutes at 25 °C and 16 hours at 80 °C respectively when $^{Me_2}{}^{t}$BuLH$_2$ is reacted with [CaN"$_2$]$_2$ in a 2:1 ratio in C_6D_6. Expansions show (N,N)μ$_2$-H and aromatic regions

integrating to four. Furthermore, the methyl region consists of a *tert*-butyl singlet at δ = 0.85 ppm which integrates to 36, as well as two singlets each integrating to 12 (δ = 0.21 and 0.06 ppm) that are assigned as the methyl protons of the $SiMe_2$ substituents. Together, these resonances suggest the formation of two equivalent $[^{Me_2{}^tBu}LH]^-$ ligands that are each coordinated to a Ca^{2+} cation in a κ^2-N,N′-bidentate manner. The presence of two distinct $SiMe_2$ singlets suggests the structure has some form of asymmetry, though the absence of crystallographic data precludes a confident assignment of the exact structure. It is proposed that the two Ca^{2+} cations are bridged by two $[\mu_2\text{-N''}]^-$ ligands that have been retained from the $[CaN''_2]_2$ starting material,[19] with their methyl protons resonating as a singlet at δ = 0.31 ppm.

The exclusive formation of $[(^{Me_2{}^tBu}LH)CaN'']_2$ demonstrates the improved selectivity of the protonolysis reaction when conducted in C_6D_6, which contrasts with the formation of multiple species when the same reaction is carried out in THF-d_8 (**Table 2.3** and **2.4**). $[(^{Me_2{}^tBu}LH)CaN'']_2$ can be viewed as a dimeric, THF-free analogue of the intermediate species $[(^{R_3}LH)AeN''(THF)_n]$ (**Section 2.4.1.1**). The incomplete deprotonation of $^{Me_2{}^tBu}LH_2$ at 25 °C in C_6D_6 contrasts with the generally fast full deprotonation of the phenyl-substituted proligands $^{Ph_2Me}LH_2$ and $^{Ph_3}LH_2$ under the same conditions (**Section 3.6**). This further demonstrates the enhanced basicity that results from the incorporation of bulky electron-donating silyl substituents.

Heating the reaction mixture at 80 °C for 16 hours resulted in the growth of new resonances in all regions of the spectrum as well as an increase in the integral value of the HN'' singlet at δ = 0.10 ppm, suggesting that further protonolysis had occurred (**Figure 4.4b**). However, incomplete consumption of the $[(^{Me_2{}^tBu}LH)CaN'']_2$ signals

demonstrated the stability and persistence of this intermediate in solution. This is consistent with the moderate and low isolated yields of **14** (53%) and **13** (8%) respectively. While the new signals could not be confidently assigned, it seems likely that they result from the formation of **14** following the release of an additional equivalent of HN" from $[(^{Me_2tBu}LH)CaN"]_2$ (**Scheme 4.4b**). This is supported by the growth of a new (N,N)μ_2-H signal at δ = 9.21 ppm, assigned as the amino proton of the single $[^{Me_2tBu}LH]^-$ ligand in **14**. Further heating results in little change to the spectrum, with no signals attributed to the minor product **13** observed. However, some conversion to **13** is confirmed by its isolation and characterisation by X-ray diffraction (**Scheme 4.4c**).



Scheme 4.4 Mechanism for the formation of $[(^{Me_2tBu}L)Ca]_2$ (**13**) *via* the two intermediate species $[(^{Me_2tBu}LH)CaN"]_2$ and $[(^{Me_2tBu}LH)Ca(\mu\text{-}^{Me_2tBu}L)CaN"]$ (**14**) that form at 25 °C and 80 °C respectively following the 2:1 reaction of $^{Me_2tBu}LH_2$ with $[CaN"_2]_2$ in C_6D_6.

This suggests that **13** crystallises immediately upon cooling the reaction mixture, and is therefore not observed in solution in subsequent NMR spectra recorded at 25 °C.

4.3.5 NMR spectroscopic analysis in THF-d_8

Isolated samples of **13** and **14** dissolve readily in THF-d_8, enabling the recording of NMR spectra that provide insight into the speciation of **13** and **14** into monomeric THF adducts.

4.3.5.1 NMR spectroscopic analysis of [(^{Me_2tBu}L)Ca]$_2$ (13)

The ^{1}H NMR spectrum of **13** recorded in THF-d_8 (**Figure 4.5**) is highly reminiscent of the corresponding spectra of the monomeric magnesium complex [(^{Me_2tBu}L)Mg(THF)$_2$] (**5**) and the dimeric complexes **6**–**11**. The simple spectrum consists of three naphthyl resonances (δ = 6.65, 6.48 and 6.35 ppm) as well as *tert*-butyl and methyl singlets at δ = 0.88 and 0.14 ppm respectively. In addition, the ^{13}C{^{1}H} NMR spectrum consists of only six naphthyl signals and three alkyl resonances, while the ^{29}Si NMR spectrum contains a single signal. Together, these spectra are fully consistent with the conversion

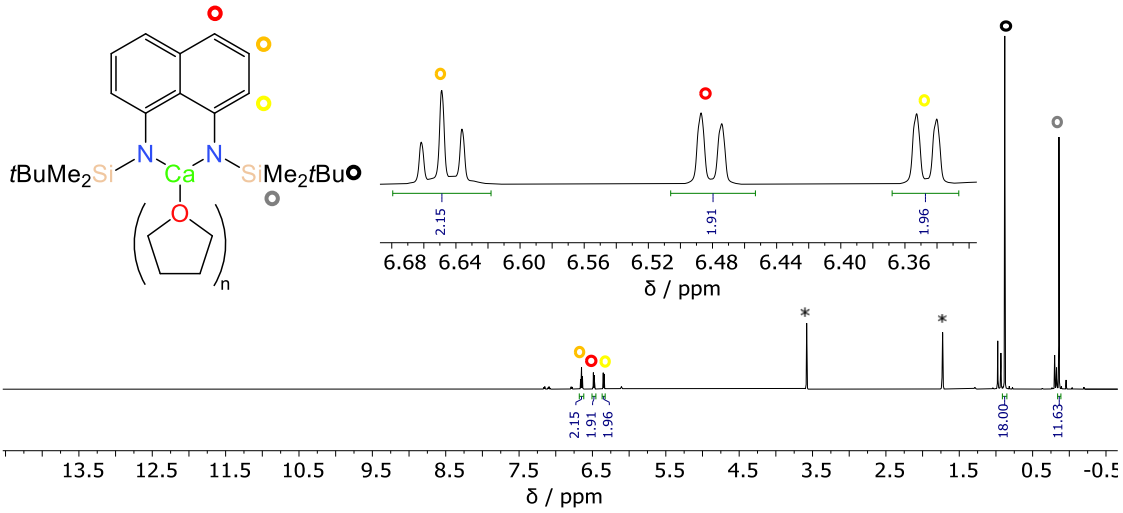


Figure 4.5 ^{1}H NMR spectrum (C_4D_8O, 298 K, 600.4 MHz) of [(^{Me_2tBu}L)Ca(THF)$_n$], formed when [(^{Me_2tBu}L)Ca]$_2$ (**13**) is dissolved in THF. * denotes residual protio fraction of C_4D_8O. Expansion shows naphthyl region.

of the dimeric complex **13** into the monomeric THF adduct [($^{Me_2{}^tBu}$L)Ca(THF)$_n$], in which the [$^{Me_2{}^tBu}$L]$^{2-}$ ligand chelates Ca^{2+} in a C_{2v}-symmetric κ^2-N,N′-bidentate manner.

4.3.5.2 NMR spectroscopic analysis of [($^{Me_2{}^tBu}$LH)Ca(μ-$^{Me_2{}^tBu}$L)CaN"] (14)

NMR spectra of **14** in THF-d_8 are more complex as a consequence of the speciation of the heteroleptic bimetallic complex in solution. Comparison with the NMR spectra of **13** reveals that the signals attributed to [($^{Me_2{}^tBu}$L)Ca(THF)$_n$] are also present in the corresponding spectra of **14**. This confirms that [($^{Me_2{}^tBu}$L)Ca(THF)$_n$] is also formed when **14** is dissolved in THF. However, additional signals are also observed. The aromatic region of the ^{1}H NMR spectrum (**Figure 4.6**) contains three additional naphthyl resonances (δ = 6.56, 6.15 and 5.99 ppm), while additional *tert*-butyl and methyl singlets

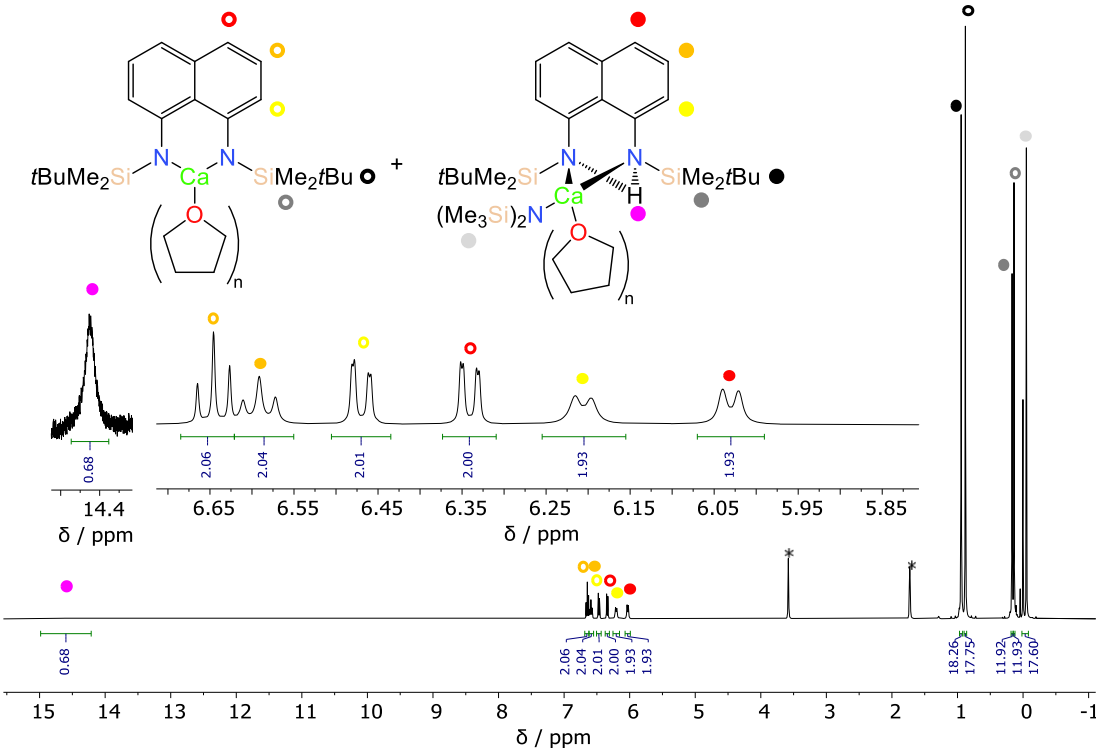
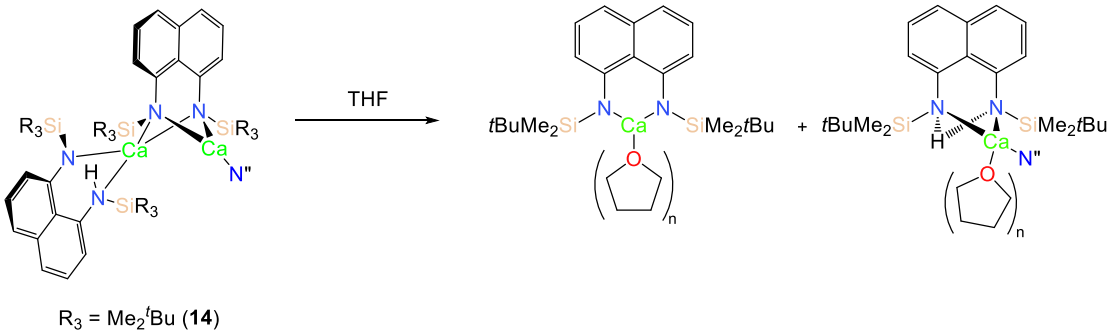


Figure 4.6 ^{1}H NMR spectrum (C_4D_8O, 298 K, 400 MHz) of [($^{Me_2{}^tBu}$L)Ca(THF)$_n$] and [($^{Me_2{}^tBu}$LH)CaN"(THF)$_n$], formed in a 1:1 ratio when [($^{Me_2{}^tBu}$LH)Ca(μ-$^{Me_2{}^tBu}$L)CaN"] (**14**) is dissolved in THF. * denotes residual protio fraction of C_4D_8O. Expansions show (N,N)-μ$_2$H and naphthyl regions.

are also observed (δ = 0.95 and 0.16 ppm respectively). A diagnostic (N,N)μ$_2$-H singlet is also present at δ = 14.86 ppm, as well as a [N"]$^-$ singlet at δ = –0.06 ppm. This suggests that the monoanionic [^{Me_2tBu}LH]$^-$ and [N"]$^-$ ligands observed in the solid state are retained in solution, and that further protonolysis to form HN" (which is not observed) and a second equivalent of [(^{Me_2tBu}L)Ca(THF)$_n$] does not take place. Furthermore, the ^{13}C{^{1}H} NMR spectrum contains additional signals (six naphthyl and three alkyl) consistent with the presence of an additional C_s-symmetric [^{Me_2tBu}LH]$^-$ fragment in solution. In addition, the ^{29}Si NMR spectrum contains a broad signal at δ = –5.71 ppm, which is assigned as the silicon atoms of the [^{Me_2tBu}LH]$^-$ fragment. This is confirmed by the presence of $^2J_{Si\text{-}H}$ correlations between this ^{29}Si NMR signal and the respective ^{1}H NMR signals of the methyl and *tert*-butyl substituents of the [^{Me_2tBu}LH]$^-$ ligand in the two-dimensional ^{29}Si-^{1}H HMBC spectrum. Based on these spectra, it is tentatively proposed that [(^{Me_2tBu}LH)CaN"(THF)$_n$] is the other solution-phase complex that forms upon the dissolution of **14** in THF-d_8. The result is the formation of a 1:1 mixture of [(^{Me_2tBu}L)Ca(THF)$_n$] and [(^{Me_2tBu}LH)CaN"(THF)$_n$] (**Scheme 4.5**). This confirms the solid-state formulation of **14** as an aggregate of the THF-free analogues of these complexes.

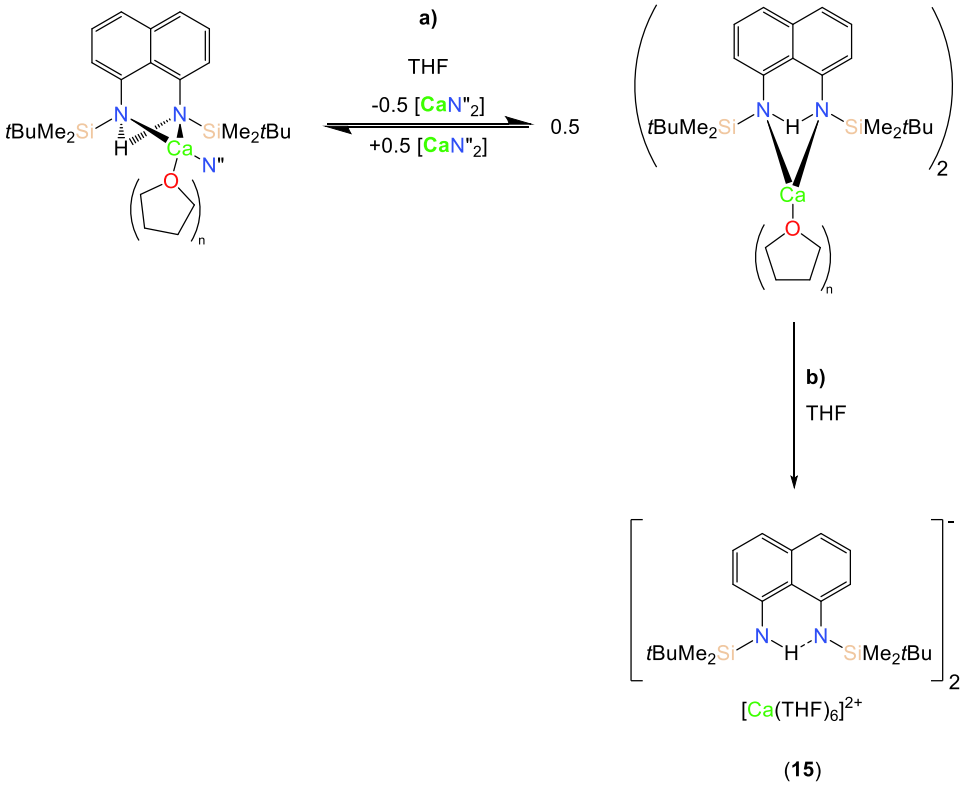


Scheme 4.5 Speciation of [(^{Me_2tBu}LH)Ca(μ-^{Me_2tBu}L)CaN"] (**14**) into a 1:1 mixture of [(^{Me_2tBu}L)Ca(THF)$_n$] and [(^{Me_2tBu}LH)CaN"(THF)$_n$] when dissolved in THF.

The formation of [(^{Me_2tBu}LH)CaN"(THF)$_n$] when **14** is dissolved in THF lends credence to the proposed structures of the intermediate species [(^{R_3}LH)AeN"(THF)$_n$] that generally form *in situ* when the protonolysis of ^{R_3}LH$_2$ with [AeN"$_2$] (Ae = Ca, Sr and Ba) is conducted in THF (**Section 2.4.1.1**). Indeed, the (N,N)μ_2-H signal at δ = 14.86 ppm in the ^{1}H spectrum of **14** in THF-d_8 agrees well with the presence of an analogous signal at δ = 14.77 in the corresponding spectrum of [(^{Me_2tBu}LH)CaN"(THF)$_n$] generated *in situ* (**Figure A.19**). No degradation of [(^{Me_2tBu}L)Ca(THF)$_n$] and [(^{Me_2tBu}LH)CaN"(THF)$_n$] *via* the elimination of their silyl substituents was observed over time at room temperature or upon heating, in contrast with the solution-phase degradation of the phenyl-substituted complexes **6**–**11** in THF. This provides further evidence that bulky alkyl substituents stabilise solution-phase complexes bearing [^{R_3}LH]$^-$ ligands.

However, the heteroleptic formulation of [(^{Me_2tBu}LH)CaN"(THF)$_n$] renders it susceptible to ligand redistribution. Consequently, the dissolution of **14** in THF also results in the instantaneous formation of the homoleptic species [(^{Me_2tBu}LH)$_2$Ca(THF)$_n$] and [(THF)$_n$CaN"$_2$] *via* a Schlenk equilibrium with [(^{Me_2tBu}LH)CaN"(THF)$_n$] (**Scheme 4.6a**). The dynamic solution-phase structure of [(^{Me_2tBu}LH)CaN"(THF)$_n$] is evidenced by the broadness of the resonances attributed to the [^{Me_2tBu}LH]$^-$ and [N"]$^-$ ligands, suggesting that these signals are time-averaged across both homo- and heteroleptic species. Further, an additional singlet at δ = 0.00 ppm suggests the presence of [(THF)$_n$CaN"$_2$] in solution: the summation of the integral of this signal with that of the signal at δ = –0.06 ppm is required to reach the total of 18 expected for protons in [N"]$^-$ environments. The presence of both [(THF)$_n$CaN"$_2$] and [(^{Me_2tBu}LH)CaN"(THF)$_n$] in solution is further supported by the presence of two [N"]$^-$ signals in both the ^{13}C{^{1}H} (δ = 5.9 and 5.6 ppm) and ^{29}Si

(–15.15 and –15.38 ppm) NMR spectra. That [(^{Me_2tBu}LH)CaN"(THF)$_n$] is subject to ligand redistribution was confirmed by the crystallisation of the SSIP [^{Me_2tBu}LH]$_2$[Ca(THF)$_6$] (**15**) from THF solutions of **14** (**Scheme 4.6b**).



Scheme 4.6 a) Schlenk equilibrium between the heteroleptic species [(^{Me_2tBu}LH)CaN"(THF)$_n$] and the homoleptic species [(^{Me_2tBu}LH)$_2$Ca(THF)$_n$] and [(THF)$_n$CaN"$_2$], **b)** Conversion of [(^{Me_2tBu}LH)$_2$Ca(THF)$_n$] into the SSIP [^{Me_2tBu}LH]$_2$[Ca(THF)$_6$] (**15**).

4.3.6 X-ray crystallographic analysis of [^{Me_2tBu}LH]$_2$[Ca(THF)$_6$] (15)

Yellow single crystals of the unexpected species [^{Me_2tBu}LH]$_2$[Ca(THF)$_6$] (**15**) suitable for an X-ray diffraction study grew when a THF solution of **14** was left to stand at 25 °C for 16 hours. Compound **15** crystallises in the $P2_1/n$ space group as a SSIP that consists of a 2:1 ratio of [^{Me_2tBu}LH]$^-$ and [Ca(THF)$_6$]$^{2+}$ molecular ions (**Figures 4.7**–**4.10**, **Table 4.3**).

The asymmetric unit consists of a single monoanionic $[^{Me_2tBu}LH]^-$ fragment and half a dicationic $[Ca(THF)_6]^{2+}$ complex, as well as one co-crystallised THF molecule. A full empirical $[^{Me_2tBu}LH]_2[Ca(THF)_6]$ unit consisting of a second crystallographically identical $[^{Me_2tBu}LH]^-$ fragment and the other half of the $[Ca(THF)_6]^{2+}$ complex is generated by a (–X+1, –Y+1, –Z+1) symmetry operation (**Figure 4.7**, **Table 4.3**).

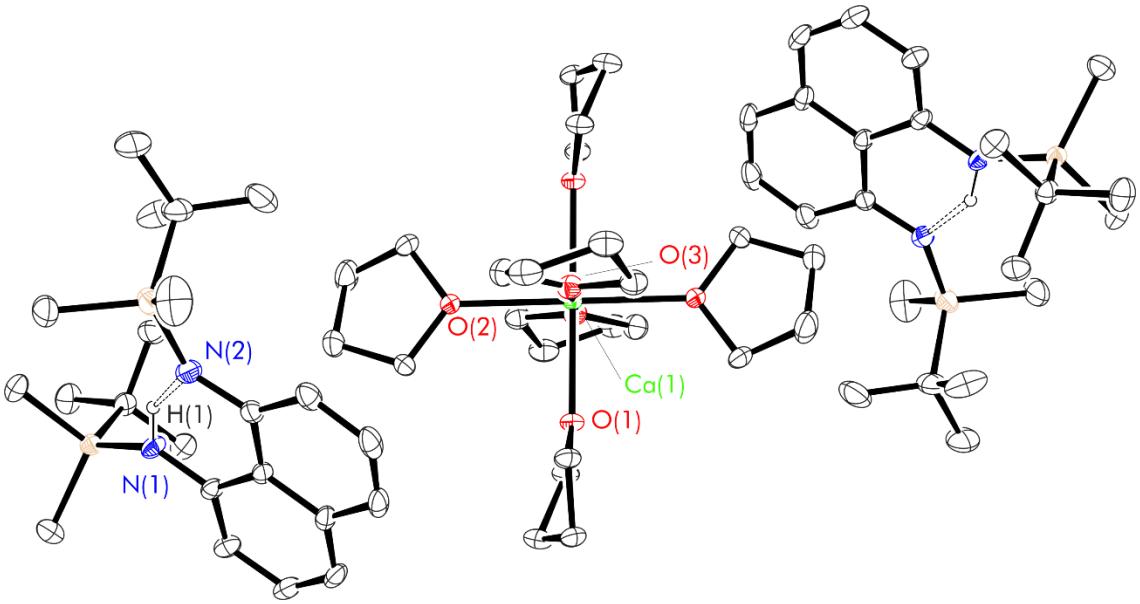


Figure 4.7 Thermal displacement ellipsoid drawing (30% probability) of $[^{Me_2tBu}LH]_2[Ca(THF)_6]$ (**15**). The $[^{Me_2tBu}LH]_2[Ca(THF)_6]$ unit is generated by a (–X+1, –Y+1, –Z+1) symmetry operation. All non-amino hydrogen atoms gave been omitted for clarity.

The charge-separated structure of **15** results in its crystallisation as an extended ionic lattice (**Figure 4.8**). The unit cell consists of a body-centred $[Ca(THF)_6]^{2+}$ complex which is surrounded by four symmetry-related $[^{Me_2tBu}LH]^-$ WCAs. Charge balance is provided by eight symmetry-related $[Ca(THF)_6]^{2+}$ molecules located at the vertices of the unit cell.

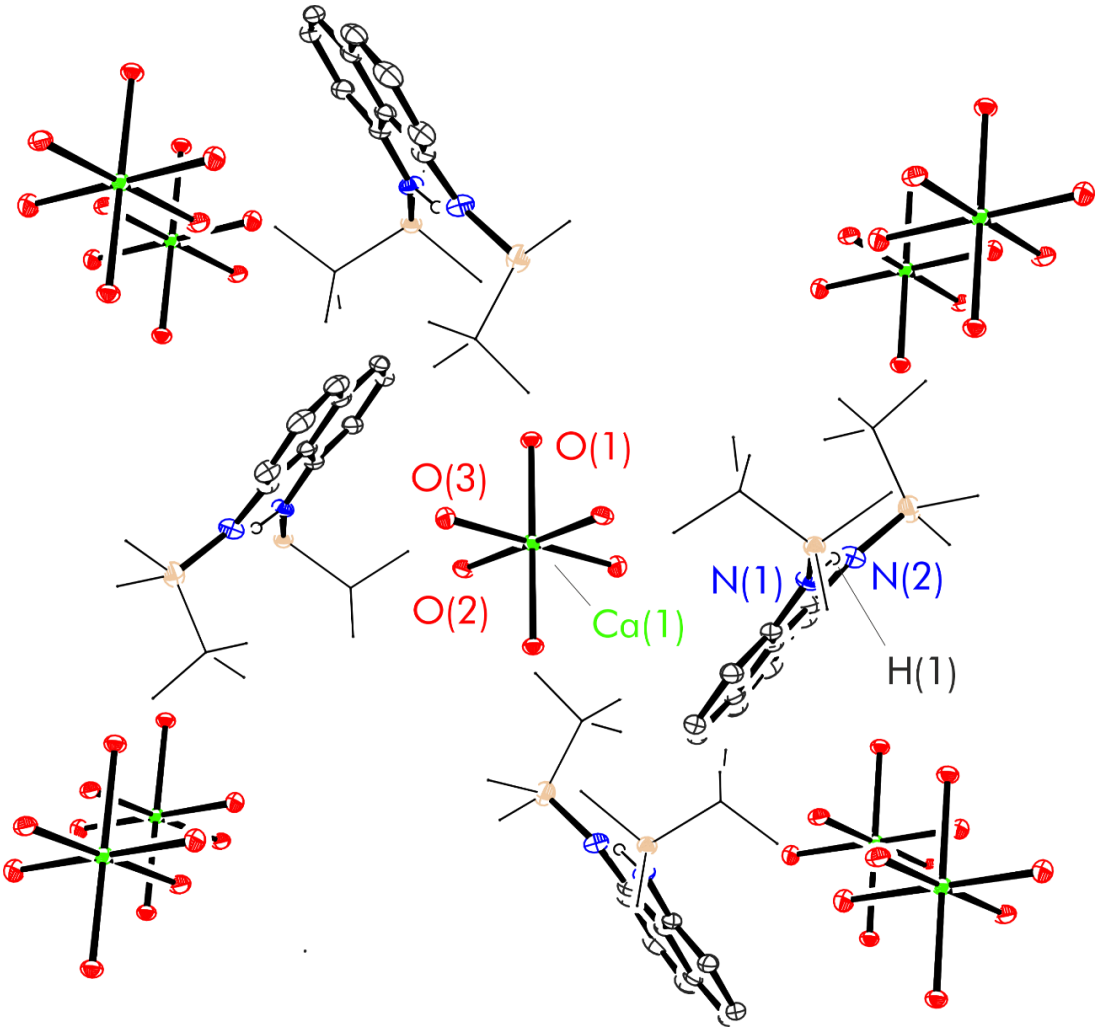


Figure 4.8 Thermal displacement ellipsoid drawing (30% probability) of the unit cell of $[^{Me_2{}^tBu}LH]_2[Ca(THF)_6]$ (**15**). All non-amino hydrogen atoms, coordinated THF carbon atoms and co-crystallised THF molecules have been omitted and alkyl groups are wireframed for clarity.

The empirical $[^{Me_2{}^tBu}LH]_2[Ca(THF)_6]$ unit of **15** can be viewed as a "sandwich" complex consisting of a large $[Ca(THF)_6]^{2+}$ dication between two $[^{Me_2{}^tBu}LH]^-$ WCAs. This sandwich motif has been reported previously for other SSIPs of the form $[Ca(THF)_6][WCA]_2$.[36] No Ca-N bonding interactions are present, with the shortest Ca-N distance (Ca(1)-N(1) = 6.820(2) Å) well outside the sum of the respective covalent radii (Σr_{cov}(Ca,N) = 2.42 Å[20]). In addition, there are no π-facial or agostic interactions between

Table 4.3 Experimental metrical parameters (bond lengths in Å and angles in °) in $[^{Me_2tBu}LH]_2[Ca(THF)_6]$ (**15**). Selected parameters from $^{Me_2tBu}LH_2$, **14**, **16** and **17** are presented for the sake of comparison. ***a***: only metrics from one $[^{Me_2tBu}LH]^-$ ligand are presented and atom labels are altered for clarity.

	15	**$^{Me_2tBu}LH_2$**	**14**	**16**	**17[a]**
N(1)-H(1)	1.06(2)	0.83(2)	0.82(2)	0.81(2)	0.869(1)
N(2)-H(1)	1.62(3)	2.11(2)	2.08(3)	2.01(3)	1.981(1)
N(1)-N(2)	2.583(2)	2.812(2)	2.758(2)	2.713(2)	2.702(2)
N(1)-C(1)	1.374(3)	1.387(2)	1.427(2)	1.420(3)	1.415(2)
N(2)-C(8)	1.371(3)	1.443(1)	1.386(2)	1.380(3)	1.376(2)
N(1)-Si(1)	1.705(2)	1.742(1)	1.772(2)	1.769(2)	1.755(1)
N(2)-Si(2)	1.709(2)	1.773(1)	1.728(1)	1.720(2)	1.715(2)
Ca(1)-O(1)	2.329(1)	-	-	-	-
Ca(1)-O(2)	2.348(2)	-	-	-	-
Ca(1)-O(3)	2.338(1)	-	-	-	-
N(1)-H(1)-N(2)	150(2)	142(1)	140(2)	145(3)	139.6(1)
O(1)-Ca(1)-O(2)	91.60(5)	-	-	-	-
O(1)-Ca(1)-O(3)	89.15(5)	-	-	-	-
O(2)-Ca(1)-O(3)	89.97(5)	-	-	-	-

Ca^{2+} and the $[^{Me_2tBu}LH]^-$ fragments. However, short contacts are present between the $[^{Me_2tBu}LH]^-$ and $[Ca(THF)_6]^{2+}$ counterions due to the formation of C-H--π interactions between both faces of the naphthalene π-system of the former and the six THF ligands of the latter (**Figures 4.9** and **4.10**), which range between 2.704(2) Å and 2.895(3) Å in

length. Similar interactions have been reported previously for SSIPs featuring the $[Ca(THF)_6]^{2+}$ cation and carbanions with conjugated π-systems.[36–38]

The coordination of six THF ligands results in the coordinative saturation of Ca^{2+}. The three distinct Ca-O bond lengths (Ca(1)-O(1) = 2.329(1) Å, Ca(1)-O(2) = 2.348(2) Å and Ca(1)-O(3) = 2.338(1) Å) are very similar with respect to one another, and are within the range (2.323–2.375 Å) of those in previously reported $[Ca(THF)_6]^{2+}$ cations.[36–47] Furthermore, the O-Ca-O bond angles between neighbouring THF ligands deviate from orthogonality by at most 1.6° (O(1)-Ca(1)-O(2) = 91.60(5)° , O(1)-Ca(1)-O(3) = 89.15° and O(2)-Ca(1)-O(3) = 89.97°), resulting in a near-idealised six-coordinate octahedral coordination geometry. Otherwise, the $[Ca(THF)_6]^{2+}$ cation is unremarkable and very similar to those in previously reported SSIPs.[36–47]

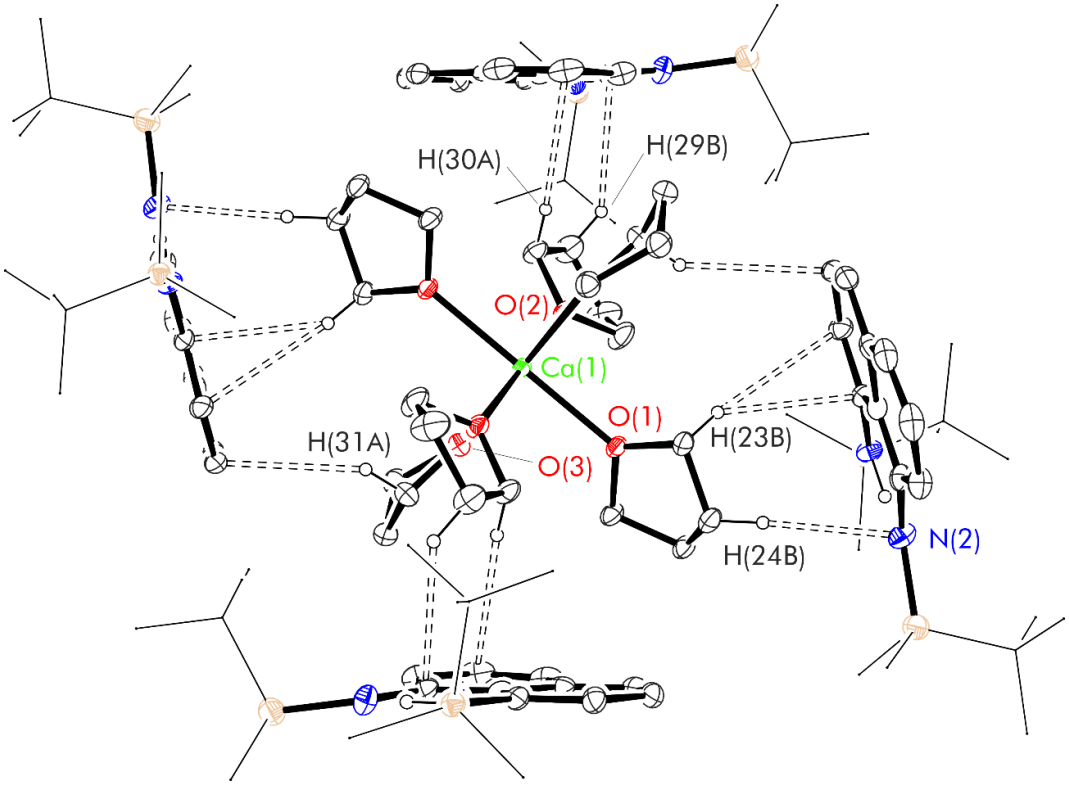


Figure 4.9 Thermal displacement ellipsoid drawing (30% probability) of the $[Ca(THF)_6]^{2+}$ cation and its C-H--π interactions four $[^{Me_2{}^tBu}LH]^-$ anions in the extended structure of $[^{Me_2{}^tBu}LH]_2[Ca(THF)_6]$ (**15**). Selected hydrogen atoms been omitted for clarity.

The amino proton of the $[^{Me_2{}^tBu}LH]^-$ anion was located in the difference map. Free refinement of this proton resulted in a long N(1)-H(1) bond length of 1.06(2) Å. This is significantly lengthened relative to the corresponding distances in the structures of the proligand $^{Me_2{}^tBu}LH_2$ (0.83(2) Å) and the coordinated $[^{Me_2{}^tBu}LH]^-$ ligands in **14** (0.82(2) Å) **16** (0.81(2) Å) and **17** (0.869(1) Å). The formation of an intramolecular hydrogen bond with the adjacent amide donor results in a N(2)-H(1) distance of 1.62(3) Å, which is significantly shorter than those in the proligand (2.11(2) Å), **14** (2.08(3) Å) **16** (2.01(3) Å) and **17** (1.981(1) Å). These N-H distances must be treated with caution due to the inherent inaccuracy with which X-ray crystallography locates hydrogen atoms.[48] However, the more reliable N(1)-N(2) distance in **15** (2.583(2) Å), is significantly shorter than the corresponding distances in the proligand (2.812(2) Å), **14** (2.758(2) Å) **16** (2.713(3) Å) and **17** (2.702(2) Å).

Notably, the N-N distance decreases in the order $^{Me_2{}^tBu}LH_2$ > **14** (Ae = Ca) > **16** (Ae = Sr) > **17** (Ae = Ba) > **15** (WCA). This trend reflects the increase in charge density and consequently stronger hydrogen bond of the $[^{Me_2{}^tBu}LH]^-$ fragment that results from deprotonation, coordination to progressively more electropositive Ae^{2+} centres and, finally, full dissociation as a WCA. Together, these metrics confirm the stabilisation of the formally anionic nitrogen donor of the $[^{Me_2{}^tBu}LH]^-$ WCA *via* the formation of a very strong intramolecular hydrogen bond. This "naked" amide donor is further stabilised through the formation of an intermolecular CH--N interaction (N(2)-H(24B) = 2.615(2) Å) with a β-hydrogen atom of one of the coordinated THF molecules of the $[Ca(THF)_6]^{2+}$ cation (**Figure 4.10**).

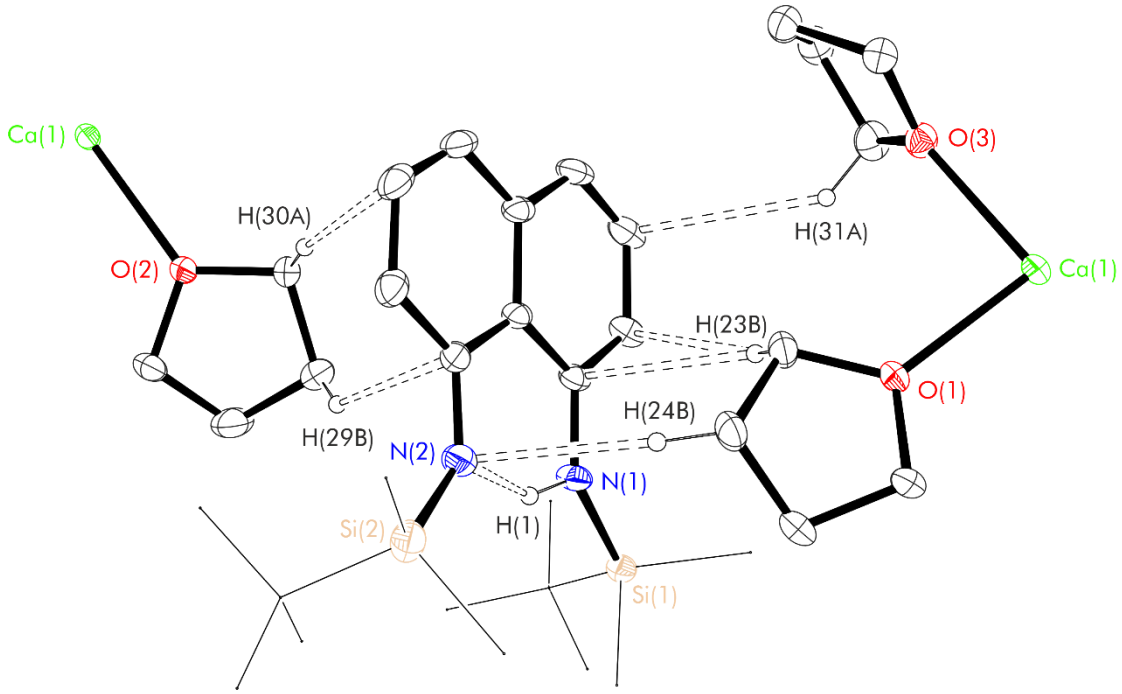


Figure 4.10 Thermal displacement ellipsoid drawing (30% probability) of the $[^{Me_2{}^tBu}LH]^-$ weakly-coordinating anion (WCA) and its C-H--π and C-H--N interactions with coordinated THF molecules of the $[Ca(THF)_6]^{2+}$ cation in the extended structure of $[^{Me_2{}^tBu}LH]_2[Ca(THF)_6]$ (**15**). Selected hydrogen atoms have been omitted and silyl substituents are wireframed for clarity.

Short N(1)-C(1) and N(2)-C(8) bond lengths (1.374(3) and 1.371(2) Å respectively) and the trigonal planar geometries of both nitrogen atoms (Σ{∠N(1)} = Σ{∠N(2)} = 360(1)°) demonstrate the delocalisation of negative charge across the conjugated π-system of the $[^{Me_2{}^tBu}LH]^-$ anion. Consequently, the $[^{Me_2{}^tBu}LH]^-$ anion is highly planar (C(1–10)-plane$_{C(1)\text{-}C(10)}$ = 0.007(2)–0.039(2) Å). Additionally, the two N-Si distances (N(1)-Si(1) = 1.705(2) Å, N(2)-Si(2) = 1.709(2) Å) are shorter than the corresponding bonds in the proligand, **14**, **16** and **17** (**Table 4.3**). This demonstrates the stabilisation conferred to the $[^{Me_2{}^tBu}LH]^-$ anion by the negative hyperconjugation of its nitrogen lone pairs with the Si-C σ* orbitals of its $SiMe_2{}^tBu$ groups. Notably, there is also no statistically significant difference between the two N-Si distances, reflecting the

delocalisation of negative charge across both nitrogen donors and consequently both N-Si bonds. The same is true for the statistically indistinguishable N(1)-C(1) and N(2)-C(8) bonds in **15** (*vide supra*). This contrasts with the coordinated $[^{Me_2{}^tBu}LH]^-$ anions in **14**, **16** and **17**, where the concentration of negative charge on the deprotonated nitrogen results in correspondingly shorter N-Si and N-C bonds than the N(H)-Si and N(H)-C bonds formed by the protonated nitrogen in each case.

Unfortunately, the decomposition of **15** *in vacuo* (presumably resulting from the loss of THF) prevented the isolation of pure material, precluding further spectroscopic analysis.

4.3.6.1 Comparison with previously reported WCAs and SSIPs

The $[^{Me_2{}^tBu}LH]^-$ WCA in **15** has no direct literature precedent. Previously reported SSIPs containing $[Ca(THF)_6]^{2+}$ cations feature more conventional WCAs including highly conjugated carbanions (e.g. triphenylmethyl,[38] fluorenyl,[36] difluoranthenyl[41] and cyclopentadienyl[37]), borates,[39,40,47] zincates,[42] alanates[43,45] and transition metal complexes[39,44,46] which do not possess electronegative donor atoms. In contrast, the $[^{Me_2{}^tBu}LH]^-$ anion possesses two hard nitrogen donors and generally acts as a chelating ligand, as shown by the crystal structures of **14**, **16** and **17**. However, the bulky $[N(Si^tBu_2)_2]^-$ anion that features in the crystal structure of the strontium SSIP $[Sr(THF)_6I][N(Si^tBu_2)_2]$ (**IV**, **Scheme 4.1**) demonstrates the ability of bulky *tert*-butylsilyl substituents to prevent anionic amide donors from coordinating to Ae^{2+} in the presence of THF,[16] a phenomenon that is replicated in the structure of **15**. Furthermore, the stabilisation of fluorenyl WCAs within alkaline earth SSIPs *via* the incorporation of less bulky trimethylsilyl substituents that enable negative hyperconjugation has also been reported previously by Harder and co-workers.[36]

The crystallisation of **15** following its formation *via* ligand redistribution is unusual, with most previously reported examples of SSIPs containing $[Ca(THF)_6]^{2+}$ cations having been synthesised rationally.[36-41,43,45-47] However, the crystallisation of the calcium zincate species $[Ca(THF)_6][\{Zn(\eta^1\text{-}CH_2C(CH_3)CH_2)_3\}_2]$ has previously been attributed to its formation *via* the Schlenk equilibrium by Okuda and co-workers.[42] Additionally, Sarazin, Carpentier and co-workers reported the spontaneous formation of $[Ca(THF)_6][B(C_6F_5)_4]_2$ upon the dissolution of a heteroleptic BDI-supported SSIP in THF.[44]

4.3.6.2 Factors influencing the formation of a SSIP

The crystallisation of **15** as a SSIP is surprising. With the exception of the associated species $[(^{Ph_3}L)Sr(THF)_3]$ (**12**), all other compounds discussed in **Chapters 2**–**4** bearing $[^{R_3}LH]^-$ or $[^{R_3}L]^-$ ligands are highly soluble in THF. This is consistent with the generally high solubility of strongly polarised coordination complexes in the strong donor solvent.[36] Furthermore, the crystal structure of **14** demonstrates that Ca^{2+} can accommodate the coordination of both $[^{Me_2{}^tBu}LH]^-$ and $[^{Me_2{}^tBu}L]^{2-}$ ligands in a κ^2-N,N′-bidentate manner. Therefore, the associated species $[(^{Me_2{}^tBu}LH)_2Ca(THF)_n]$ was expected to be stable in solution following its formation *via* ligand redistribution (**Scheme 4.6a**, *vide supra*), much like its heavier congeners (Ae = Sr and Ba, *vide infra*) which do not crystallise as SSIPs.

However, the coordination of THF by the oxophillic Ca^{2+} cation[49] necessitates either a higher coordination number or the dissociation of $[^{Me_2{}^tBu}LH]^-$ as a WCA. That the latter outcome is observed in the solid state suggests that the coordination of THF results in excessive steric clash between the two bulky $[^{Me_2{}^tBu}LH]^-$ ligands, which is relieved upon their dissociation. While Ca^{2+} is no longer coordinated by any formally anionic donors in

15, this is compensated for by the formation of six strong Ca-O bonds within a stable $[Ca(THF)_6]^{2+}$ cation. The formation of **15** is also driven by the stability of the $[^{Me_2{}^tBu}LH]^-$ anion. This is conferred by the aforementioned intermolecular C-H--π and CH--N interactions with the $[Ca(THF)_6]^{2+}$ cation, the strong intramolecular NH--N hydrogen bond and, finally, the delocalisation of negative charge across both the aromatic π-system as well as the bulky silyl substituents *via* negative hyperconjugation. Therefore, the stabilisation of both the cationic and anionic components facilitates their co-crystallisation as a SSIP, with further stabilisation then conferred by the resulting lattice enthalpy.

4.3.6.3 Outlook

While the characterisation of the $[^{Me_2{}^tBu}LH]^-$ WCA within the SSIP **15** is of note, this serendipitous result is likely due to a confluence of factors that are specific to this particular system (*vide supra*). Consequently, the further application of $[^{R_3}LH]^-$ fragments as WCAs is unlikely, as these species generally act as chelating ligands (as demonstrated by **14**, **16** and **17**).

4.4 Characterisation of strontium and barium complexes

4.4.1 X-ray crystallographic analysis

Slow cooling of the reaction mixtures resulting from both the 2:1 and 3:1 reactions of $^{Me_2{}^tBu}LH_2$ with $[AeN''_2]_2$ (Ae = Sr and Ba) at 80 °C in benzene resulted in the growth of crystals of $[\{(^{Me_2{}^tBu}LH)Ae\}_2(\mu\text{-}^{Me_2{}^tBu}L)]$ (Ae = Sr (**16**) and Ba (**17**)) suitable for X-ray diffraction studies. The two compounds, which crystalise in the *C*2/*c* (**16**) and $P\bar{1}$ (**17**) space groups respectively, are largely isostructural. Consequently, the structure of **16** is first discussed (**Figure 4.11**), with relevant comparisons then drawn with the structure of **17** and the related complex **14** (**Table 4.4**).

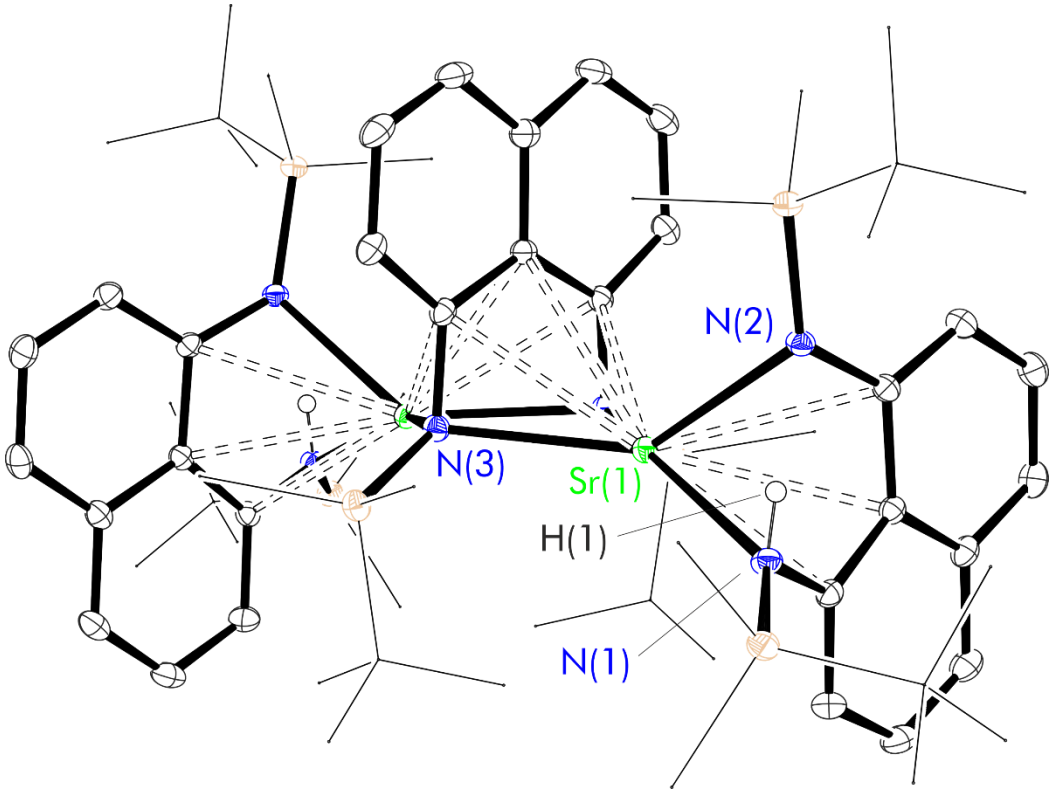


Figure 4.11 Thermal displacement ellipsoid drawing (30% probability) of $[\{(^{Me_2{}^tBu}LH)Sr\}_2(\mu\text{-}^{Me_2{}^tBu}L)]$ (**16**). The full bimetallic structure is generated by a (–X+1, Y, –Z+1/2) symmetry operation. Silyl substituents are wireframed and all non-amino hydrogen atoms have been omitted for clarity.

4.4.1.1 Crystal structure of [{(^{Me_2tBu}LH)Sr}$_2$(μ-^{Me_2tBu}L)] (16)

Complex **16** has a "triple-decker" bimetallic structure consisting of two Sr^{2+} cations, which are bridged by a dianionic [μ-^{Me_2tBu}L]$^{2-}$ ligand and each capped by monoanionic [^{Me_2tBu}LH]$^-$ ligands. The structure of **16** is therefore similar to that of **14**, with the exception that in **16** an additional [^{Me_2tBu}LH]$^-$ ligand is substituted in place of the monodentate [N'']$^-$ ligand that is present in **14**. The equivalence of the two capping monoanionic ligands in **16** confers C_2 symmetry to its structure: the asymmetric unit consists of a [(^{Me_2tBu}LH)Sr]$^+$ unit and one half of the bridging [μ-^{Me_2tBu}L]$^{2-}$ fragment, with the full bimetallic structure then generated by a two-fold rotation about a C_2 axis through the C(28)-C(29) bond of the central bridging ligand. This results in two crystallographically identical [(^{Me_2tBu}LH)Sr]$^+$ units bridged by a C_2-symmetric [μ-^{Me_2tBu}L]$^{2-}$ ligand. Each Sr^{2+} cation is coordinated by both a [^{Me_2tBu}LH]$^-$ fragment and a [μ-^{Me_2tBu}L]$^{2-}$ ligand. Both ligands coordinate in a κ^2-N,N′-bidentate manner, resulting in two four-coordinate Sr^{2+} centres with highly distorted tetrahedral coordination geometries (Σ{∠(Sr(1)} = 671.4(1)°, τ_4 = 0.48[18]).

The [μ-^{Me_2tBu}L]$^{2-}$ ligand coordinates to both Sr^{2+} cations *via* its two tetrahedral μ$_2$-N donors (Σ{∠(N(3)} = 650.6(2)°). The two faces of the naphthalene backbone also form η^3-π-facial interactions with the two Sr^{2+} cations (Sr(1)-centroid$_{C(24),C(29),C(24)}$* = 2.772(1) Å, * refers to symmetry related atoms). This results in a central [(μ-^{Me_2tBu}L)Ae$_2$]$^{2+}$ motif (analogous to that in **14**) consisting of a non-planar, four-membered Sr_2N_2 metallacycle (N(3)-Sr(1)-Sr(1)*-N(3)* = 166.18(12)°, Sr(1)-N(3)-N(3)*-Sr(1)* = 170.42(8)°).

Table 4.4 Experimental metrical parameters (bond lengths in Å and angles in °) in [{($^{Me_2{}^tBu}$LH)Ae}$_2$(μ-$^{Me_2{}^tBu}$L)] (Ae = Sr (**16**) and Ba (**17**)). *a*: selected metrics presented and atom labels altered for clarity.

	16	**17**[a]
Space group	*C*2/*c*	$P\bar{1}$
Ae(1)-N(1)	2.885(2)	3.004(1)
Ae(1)-N(2)	2.535(1)	2.675(2)
Ae(1)-N(3)	2.566(1)	2.760(1)
Ae(1)-N(3)*	2.574(1)	2.691(1)
N(1)-H(1)	0.81(2)	0.869(1)
N(2)-H(1)	2.01(3)	1.981(1)
Ae(1)-Ae(2)	4.2178(6)	4.5638(1)
N(1)-N(2)	2.713(2)	2.702(2)
N(3)-N(3)*	2.916(2)	2.956(2)
Ae(1)-Plane$_{C(1)-C(10)}$	2.3180(1)	2.492(1)
Ae(1)-Plane$_{C(23)-C(32)}$	2.1084(1)	2.302(1)
N(1)-Ae(1)-N(2)	59.65(5)	56.47(4)
N(3)-Ae(1)-N(3)*	69.12(5)	65.67(4)
Plane$_{C(1)-C(10)}$-Plane$_{C(23)-C(32)}$ fold	3.2423(1)	6.22(4)
Plane$_{C(1)-C(10)}$-Plane$_{C(1)-C(10)*}$ fold	1.18731(4)	1.87(4)
N(3)-Ae(1)-Ae(1)*-N(3)*	166.18(12)	165.88(8)
Ae(1)-N(3)-N(3)*-Ae(1)*	170.42(8)	170.83(5)

The Sr^{2+} cations therefore sit significantly out of the plane of the naphthalene backbone (Sr(1)-plane$_{C(24)-C(29)}$ = 2.1084(1) Å), which is highly planar (C(24–29)-plane$_{C(24)-C(29)}$ = 0.000(2)–0.032(2) Å) having not distorted to accommodate either Sr^{2+} cation in plane. This results in a narrow N(3)-Sr(1)-N(3)* bite angle (69.12(5)°) and a relatively short N(3)-N(3)* distance (2.916(2) Å). The Sr(1)-Sr(1)* distance in **16** (4.2178(6) Å) is longer than that of the nitrogen-bridged dimer **7** (3.7726(4) Å), but much shorter than that of the naphthalene-bridged dimer **10** (4.8750(5) Å).

The monoanionic charges of the two $[^{Me_2{}^tBu}LH]^-$ ligands results from their retention of an amino proton, H(1), in their metal binding pocket. H(1) was located in the difference map and freely refined, with its presence further confirmed by NMR and IR spectroscopy (*vide infra*). The structure of the $[^{Me_2{}^tBu}LH]^-$ ligand in **16** is very similar to that in **14**. H(1) is localised on a single formally neutral amino donor, resulting in a short N(1)-H(1) bond (0.81(2) Å). An intramolecular hydrogen bond (N(2)-H(1) = 2.01(3) Å, N(1)-H(1)-N(2) = 145(3)°) with the adjacent formally anionic amide donor is also present. The lengths of the two N-H bonds in **16** are statistically indistinguishable from the equivalent metrics in **14**. The intramolecular hydrogen bond results in a very short N(1)-N(2) distance (2.713(2) Å), while the naphthalene ring is distorted somewhat in order to accommodate both the retention of H(1) and the coordination of Sr(1) by the two nitrogen donors. The electron-rich naphthalene ring also interacts with the Sr^{2+} cation *via* the formation of η^3-π-facial Sr^{2+}-naphthyl interactions (Sr(1)-centroid$_{C(1),C(10),C(9)}$ = 2.7779(10) Å). Furthermore, the lower charge density of the protonated nitrogen donor is reflected by a N(1)-Sr(1) bond length (2.885(2) Å) that is over 0.3 Å longer than the other N-Sr bonds formed by the deprotonated N-donors in **16** (N(2)-Sr(1) = 2.535(1) Å, N(3)-Sr(1) = 2.566(1) Å and N(3)-Sr(1)* = 2.573(1) Å). The occupation of the metal binding pockets

of the two [^{Me_2tBu}LH]$^-$ ligands by their amino protons results in Sr(1) lying out of the plane of the naphthalene backbone (Sr(1)-plane$_{C(1)\text{-}C(10)}$ = 2.3180(1) Å). Consequently, Sr(1) resides between the planes defined by the [^{Me_2tBu}LH]$^-$ and [μ-^{Me_2tBu}L]$^{2-}$ ligands. These are tilted slightly with respect to one another, resulting in a small acute interplanar fold angle of 3.2423(1)°. Similarly, while the two symmetry-related [^{Me_2tBu}LH]$^-$ ligands are necessarily related by a twofold rotation, they are also non-parallel with respect to one another, ($\angle_{fold}$(plane$_{C(1)\text{-}C(10)}$-plane$_{C(1)^*\text{-}C(10)^*}$) = 1.18731(4)°). Sr(1) lies around 0.2 Å closer to the dianionic bridging ligand than the monoanionic capping ligand due to its stronger ionic attraction to the former. The rotation of the three ligands relative to one other is apparent when the structure of **16** is viewed down its Sr-Sr axis (**Figure 4.12**), with this arrangement seemingly minimising steric clash between bulky silyl substituents.

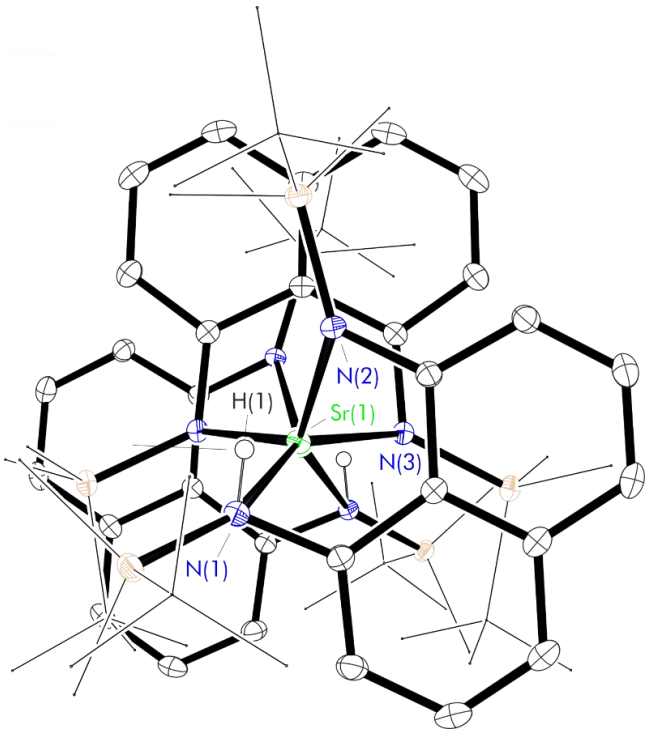


Figure 4.12 Thermal displacement ellipsoid drawing (30% probability) of [{(^{Me_2tBu}LH)Sr}$_2$(μ-^{Me_2tBu}L)] (**16**). Silyl substituents are wireframed and all non-amino hydrogen atoms have been omitted for clarity.

4.4.1.2 Crystal structure of [{(^{Me_2tBu}LH)Ba}$_2$(μ-^{Me_2tBu}L)] (17)

The structure of the barium congener **17** (**Figure 4.13**) is very similar to that of **16**. The primary difference between the structures of the two congeners is that the asymmetric unit of **17** consists of the entire "triple-decker" structure, with two crystallographically distinct [(^{Me_2tBu}LH)Ba]$^+$ units bridged by a [^{Me_2tBu}L]$^{2-}$ ligand that does not have a C_2 rotation axis through its central C-C bond. However, despite this crystallographic asymmetry the structure of **17** still displays *pseudo*-C_2 symmetry, with notable parameters that are symmetry related in **16** generally having very similar values to each other in **17**. As such, selected metrics are presented in **Table 4.4** for comparison with those of **16**. As expected, the Ae-N bond lengths in **17** are longer than those in **16** due to the larger ionic radius of Ba^{2+}. This results in narrower N-Ba-N bite angles as the Ba^{2+} cations sit further from the mean planes of both the [^{Me_2tBu}LH]$^-$ and [μ-^{Me_2tBu}L]$^{2-}$ ligands (**Table 4.4**).

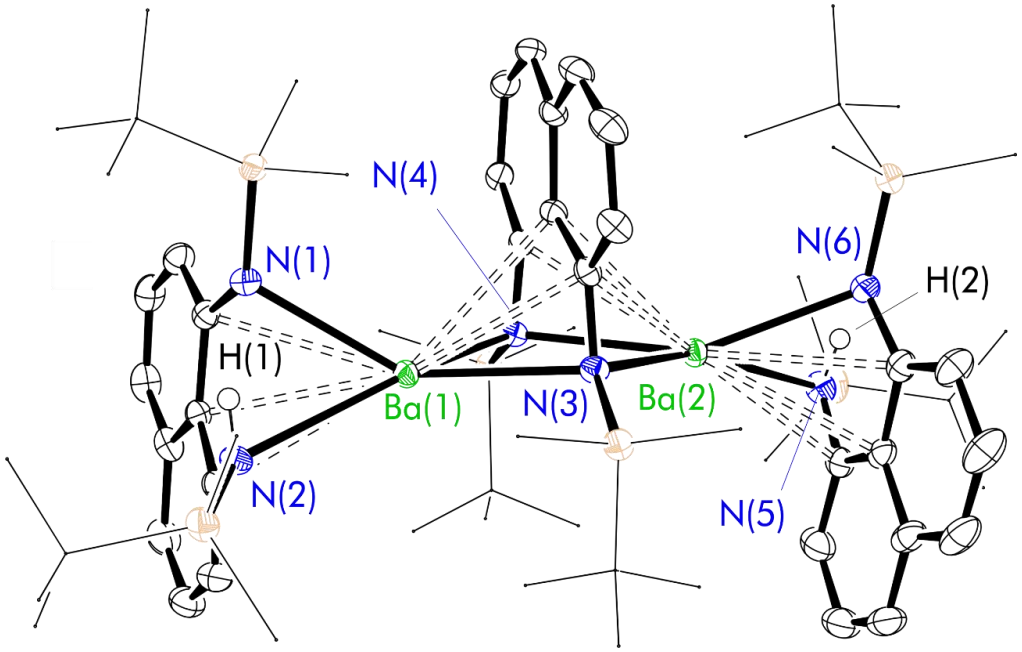
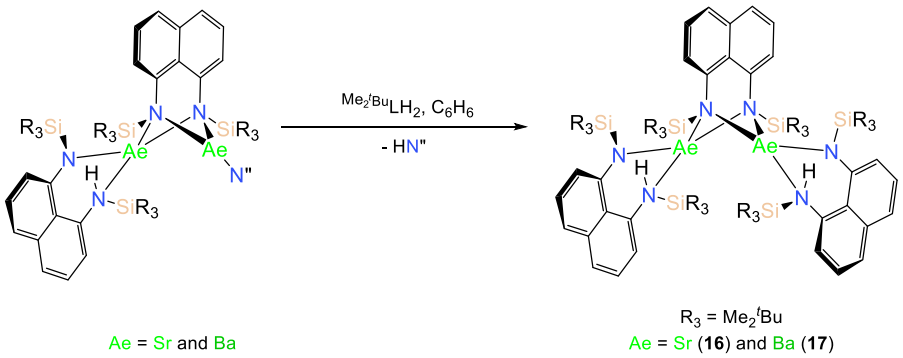


Figure 4.13 Thermal displacement ellipsoid drawing (30% probability) of [{(^{Me_2tBu}LH)Ba}$_2$(μ-^{Me_2tBu}L)] (**17**). Silyl substituents are wireframed and all non-amino hydrogen atoms have been omitted for clarity.

4.4.2 Discussion of "triple-decker" formation

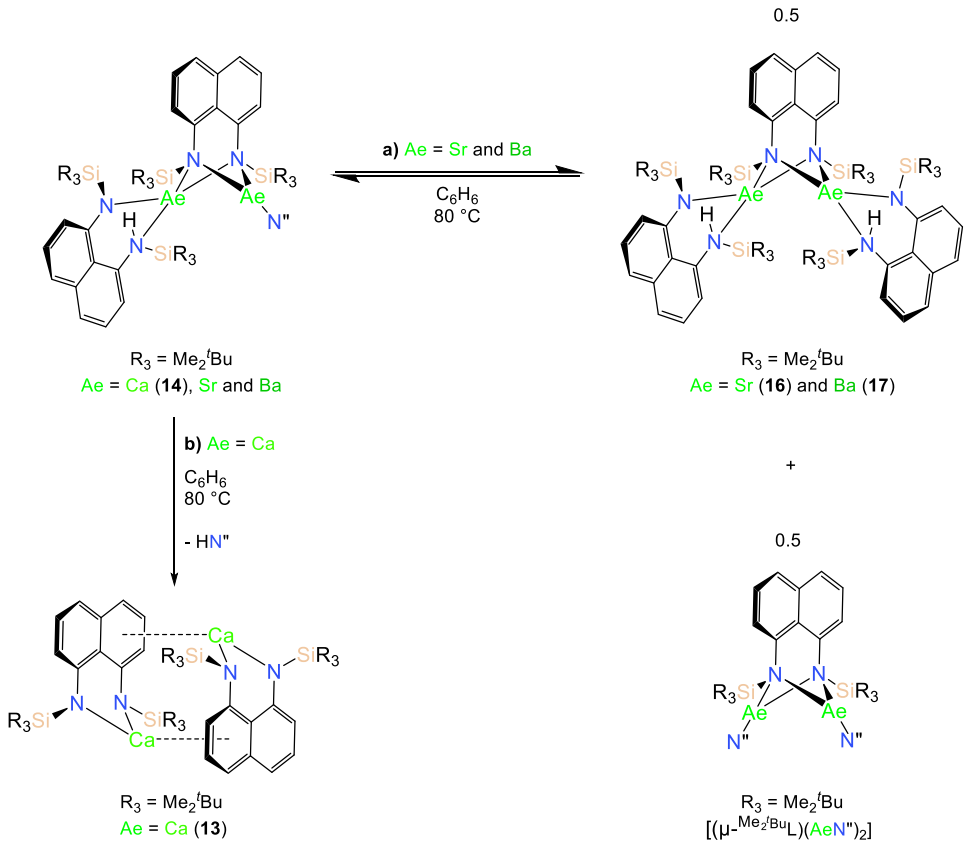
No 1,8-*bis*(silylamido)naphthalene complexes exhibiting this bimetallic "triple-decker" structural motif have been reported previously. The formation of **16** and **17** when a 3:1 ratio of $^{Me_2tBu}LH_2$ to $[AeN''_2]_2$ is employed can be attributed to the reaction of the third equivalent of proligand with an intermediate of the form $[(^{Me_2tBu}LH)Ae(\mu\text{-}^{Me_2tBu}L)AeN'']$ (Ae = Sr and Ba) that is analogous to the calcium congener **14** (**Scheme 4.7**).



Scheme 4.7 Reaction of the intermediate species $[(^{Me_2tBu}LH)Ae(\mu\text{-}^{Me_2tBu}L)AeN'']$ with $^{Me_2tBu}LH_2$ in benzene to form the "triple-decker" complexes $[\{(^{Me_2tBu}LH)Ae\}_2(\mu\text{-}^{Me_2tBu}L)]$ (Ae = Sr (**16**) and Ba (**17**)).

However, it is less clear how **16** and **17** form when a 2:1 $^{Me_2tBu}LH_2$ to $[AeN''_2]_2$ ratio is employed, as the 3:2 ligand to metal ratio of these complexes does not equal that of the starting materials in this case. It is proposed that in the absence of a third equivalent of proligand to react with, the intermediate $[(^{Me_2tBu}LH)Ae(\mu\text{-}^{Me_2tBu}L)AeN'']$ undergoes ligand redistribution in solution upon heating. This results in the formation of **16** and **17** as well as the proposed side product $[(\mu\text{-}^{Me_2tBu}L)(AeN'')_2]$ (**Scheme 4.8a**). **16** and **17** subsequently crystallise from the reaction mixture upon cooling, though in much smaller quantities than when a 3:1 ratio is employed. It is notable that ligand redistribution is the outcome of heating in these cases, rather than further protonolysis. This contrasts with the partial conversion of the calcium intermediate **14** into the fully deprotonated dimer

13 (**Scheme 4.8b**), and can be attributed to the higher kinetic lability of the heavier congeners strontium and barium enabling the facile exchange of the monoanionic $[^{Me_2{}^tBu}LH]^-$ and $[N'']^-$ ligands. This favours the formation of the "triple-decker" motif in which both Ae^{2+} cations have a four-coordinate geometry, in contrast to **14** where one Ae^{2+} cation is three-coordinate and **13** where each is only coordinated by two nitrogen donors. That $[(^{Me_2{}^tBu}L)Ae]_2$ (Ae = Sr and Ba) have not been isolated also reflects the more ionic Ae-N bonds formed by the more electropositive heavy Ae^{2+} cations. This results in the retention of more negative charge density by the $[^{Me_2{}^tBu}LH]^-$ ligand, further enhancing its basicity and preventing the abstraction of its amino proton by the remaining equivalent



Scheme 4.8 a) Formation of $[\{(^{Me_2{}^tBu}LH)Ae\}_2(\mu\text{-}^{Me_2{}^tBu}L)]$ (Ae = Sr (**16**) and Ba (**17**)) and proposed side-product $[(\mu\text{-}^{Me_2{}^tBu}L)(AeN'')_2]$ *via* ligand redistribution of the intermediate species $[(^{Me_2{}^tBu}LH)Ae(\mu\text{-}^{Me_2{}^tBu}L)AeN'']$ (Ae = Sr and Ba); **b)** Intramolecular protonolysis of **14** to from **13**.

of $[N'']^-$ even upon heating. This is in agreement with the relative low frequency (N,N)μ_2-H chemical shifts of $[(^{R3}LH)AeN''(THF)_n]$ complexes consisting of both bulky alkyl substituents and large Ae^{2+} cations (**Section 2.4.16**), which could also not be further deprotonated upon heating.

4.4.3 IR spectroscopic analysis

The IR spectra of **16** and **17** each contain an N-H absorption at 3055 cm^{-1}, and 3056 cm^{-1} respectively. These signals have very similar wavenumbers to the N-H signal in the IR spectrum of **14** (3058 cm^{-1}), and are redshifted relative to the expected range for N-H bonds,[24-35] thus confirming the presence of the hydrogen-bonded amino protons observed in the solid-state structures of **16** and **17**.

4.4.4 *In situ* NMR spectroscopic analysis

Isolated samples of **16** and **17** were found to be poorly soluble in alkanes and arenes, preventing a direct assessment of their solution-state structures in non-donor solvents. However, the mechanism of their formation *in situ* could be probed by monitoring the 2:1 and 3:1 reactions of $^{Me_2tBu}LH_2$ with $[AeN''_2]_2$ (Ae = Sr and Ba) in C_6D_6 by ^1H NMR spectroscopy.

The 2:1 reactions resulted in the formation of the intermediate species $[(^{Me_2tBu}LH)AeN'']_2$ (Ae = Sr and Ba) at 25 °C (see **Scheme 4.4a**). Subsequent heating resulted in the growth of additional signals that likely result from the formation of $[(^{Me_2tBu}LH)Ae(\mu\text{-}^{Me_2tBu}L)AeN'']$ (Ae = Sr and Ba, see **Scheme 4.4b**), followed by their conversion into **16** and **17** *via* ligand redistribution (see **Scheme 4.8a**). Both outcomes are consistent with the outcome of the analogous reaction with $[CaN''_2]_2$ (**Section 4.3.4**).

However, the corresponding 3:1 reactions resulted in different outcomes. An initial spectrum recorded at 25 °C for the 3:1 reaction of $^{Me_2tBu}LH_2$ with $[SrN''_2]_2$ resulted in a ^1H NMR spectrum (**Figure 4.14**) that both differs from the outcome of the corresponding 2:1 reaction and is inconsistent with the immediate formation of **16** at room temperature. The spectrum consists of two sets of sharp ligand signals. Inspection of the integral values of these suggests the presence of two non-equivalent *C*$_s$-symmetric $[^{Me_2tBu}LH]^-$ ligand environments that are present in a 2:1 ratio. Notably, there are two high frequency amino singlets at δ = 11.21 and 10.23 ppm that integrate to 1 and 2 respectively. In addition, the integral value of 54 for the HN'' singlet at δ = 0.10 ppm confirms the release of three equivalents of the amine by-product, while a singlet integrating to *ca.* 18 at δ = 0.20 ppm implies the retention of one $[N'']^-$ equivalent.

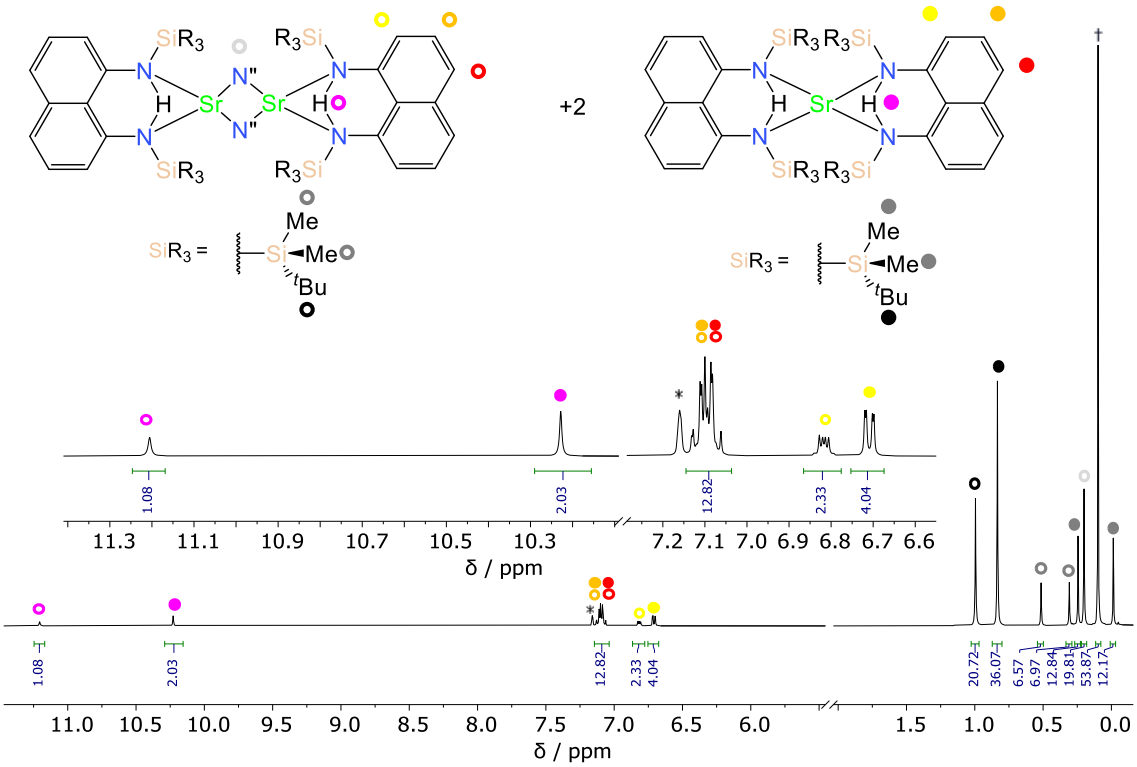


Figure 4.14 ^1H NMR spectrum (C_6D_6, 298 K, 400 MHz) of a proposed 1:2 mixture of $[(^{Me_2tBu}LH)SrN'']_2$ and $[(^{Me_2tBu}LH)_2Sr]$ that forms upon the 3:1 reaction of $^{Me_2tBu}LH_2$ and $[SrN''_2]_2$ at 25 °C in C_6D_6. † denotes HN'', * denotes residual protio fraction of C_6D_6. Expansion shows (N,N)-μ_2H and naphthyl regions.

It is tentatively suggested that the reaction mixture consists of a 1:2 ratio of the intermediate species $[(^{Me_2{}^tBu}LH)SrN"]_2$ and the side product $[(^{Me_2{}^tBu}LH)_2Sr]$. It is proposed that the formation of one equivalent of $[(^{Me_2{}^tBu}LH)SrN"]_2$ results from the 2:1 reaction of $[SrN"_2]_2$ with the proligand (*vide infra*), while the formation of two equivalents of $[(^{Me_2{}^tBu}LH)_2Sr]$ results from the corresponding 4:1 reaction. This outcome is consistent with the overall 3:1 $^{Me_2{}^tBu}LH_2$:$[SrN"_2]_2$ stoichiometry of the reaction.

However, subsequent spectra recorded after heating at 80 °C contained new ligand resonances and HN" signals with higher relative integral values. This suggests that conversion of $[(^{Me_2{}^tBu}LH)SrN"]_2$ and $[(^{Me_2{}^tBu}LH)_2Sr]$ into **16** occurs at 80 °C due to both ligand redistribution and further protonolysis. While **16** does not crystallise prior to heating, it deposits in moderate yield (50%) upon cooling the reaction mixture after 16 hours at 80 °C, further demonstrating that heating is required for its formation.

Conversely, an initial spectrum recorded at 25 °C in C_6D_6 for the 3:1 reaction of $^{Me_2{}^tBu}LH_2$ with $[BaN"_2]_2$ resulted in a ^{1}H NMR spectrum that is consistent with the formation of **17**, with no intermediates or side products observed (**Figure 4.15**). This spectrum consists of three naphthyl signals (δ = 7.08, 6.94 and 6.63 ppm) which each integrate to six relative to a high frequency amino singlet (δ = 11.15 ppm) that integrates to two. The methyl region consists of only three signals: a broad *tert*-butyl singlet (δ = 0.94 ppm) and a very broad methyl singlet (δ = 0.30 ppm) are assigned to the $SiMe_2{}^tBu$ groups of the ligands, while the integral value of 72 for the HN" singlet at δ = 0.10 ppm confirms the release of four equivalents of HN". This suggests that the high kinetic lability of Ba^{2+} enables the formation of **17** at room temperature. Furthermore, **17** seemingly has a fluxional solution-phase structure in which the two remaining amino protons rapidly exchange

between ligand fragments, which themselves are exchanging between terminal and bridging positions. This results in ligand signals that are time-averaged across both $[^{Me_2{}^tBu}LH]^-$ and $[^{Me_2{}^tBu}L]^{2-}$ environments. That **17** forms rapidly at room temperature, whereas the strontium congener **16** requires heating, further demonstrates the exceptional kinetic lability of Ba^{2+}.[50] Unfortunately, spectra recorded in toluene-d_8 were more complex, precluding the recording of informative low temperature NMR spectra.

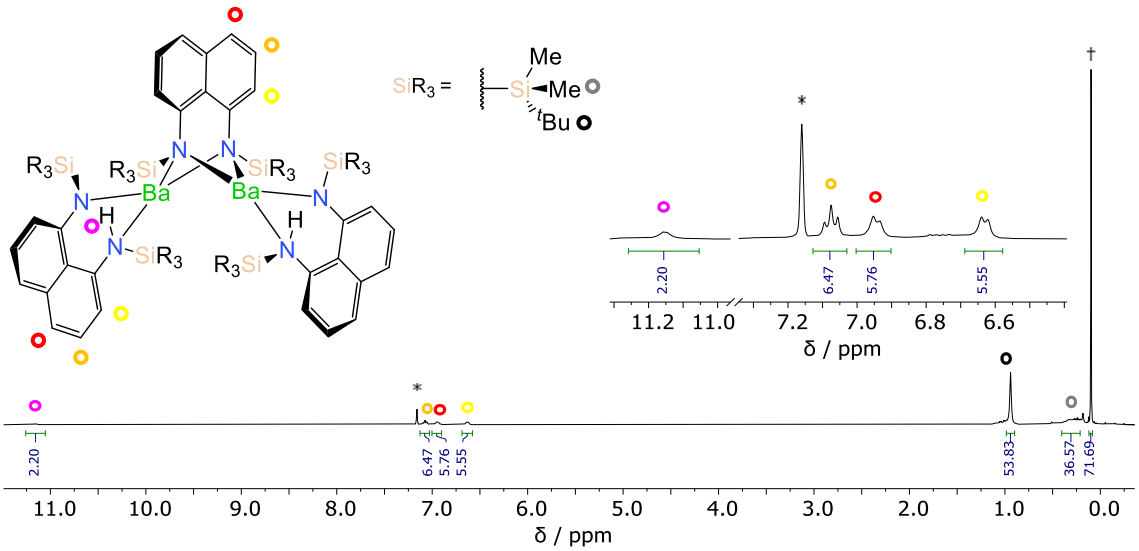


Figure 4.15 ^{1}H NMR spectrum (C_6D_6, 298 K, 400 MHz) of $[\{(^{Me_2{}^tBu}LH)Ba\}_2(\mu\text{-}^{Me_2{}^tBu}L)]$ (**17**) that forms upon the 3:1 reaction of $^{Me_2{}^tBu}LH_2$ and $[BaN''_2]_2$ at 25 °C in C_6D_6. † denotes HN'', * denotes residual protio fraction of C_6D_6. Expansion shows (N,N)-μ_2H and naphthyl regions.

4.4.5 NMR spectroscopic analysis in THF-d_8

Complexes **16** and **17** each dissolve readily in THF-d_8, enabling the recording of NMR spectra that provide insight into their speciation into monomeric THF adducts. As the NMR spectra of **16** and **17** are very similar with respect to one another, those of **16** are discussed as a representative example.

The ^{1}H NMR spectrum of **16** (**Figure 4.16**) is consistent with the speciation of the former into a 1:1 mixture of the monomeric THF adducts [(^{Me_2tBu}L)Sr(THF)$_n$] and [(^{Me_2tBu}LH)$_2$Sr(THF)$_n$], (**Scheme 4.9**). The aromatic region consists of six signals: three of these (δ = 6.75, 6.46 and 6.22 ppm) each integrate to four, whereas the other three resonances (δ = 6.61, 6.46, and 6.31ppm) integrate to only two. Further, the alkyl region consists of two *tert*-butyl singlets at δ = 0.92 and 0.86 ppm which integrate to 36 and 18 respectively, as well as two methyl singlets at δ = 0.21 and 0.11 ppm which integrate to 24 and 12 respectively. Finally, a high frequency amino singlet with an integral value of 2 resonates at δ = 13.16 ppm. These signals confirm that both [^{Me_2tBu}LH]$^{-}$ and [^{Me_2tBu}L]$^{2-}$ ligands are present in a 2:1 ratio, with the integral values of signals assigned to the

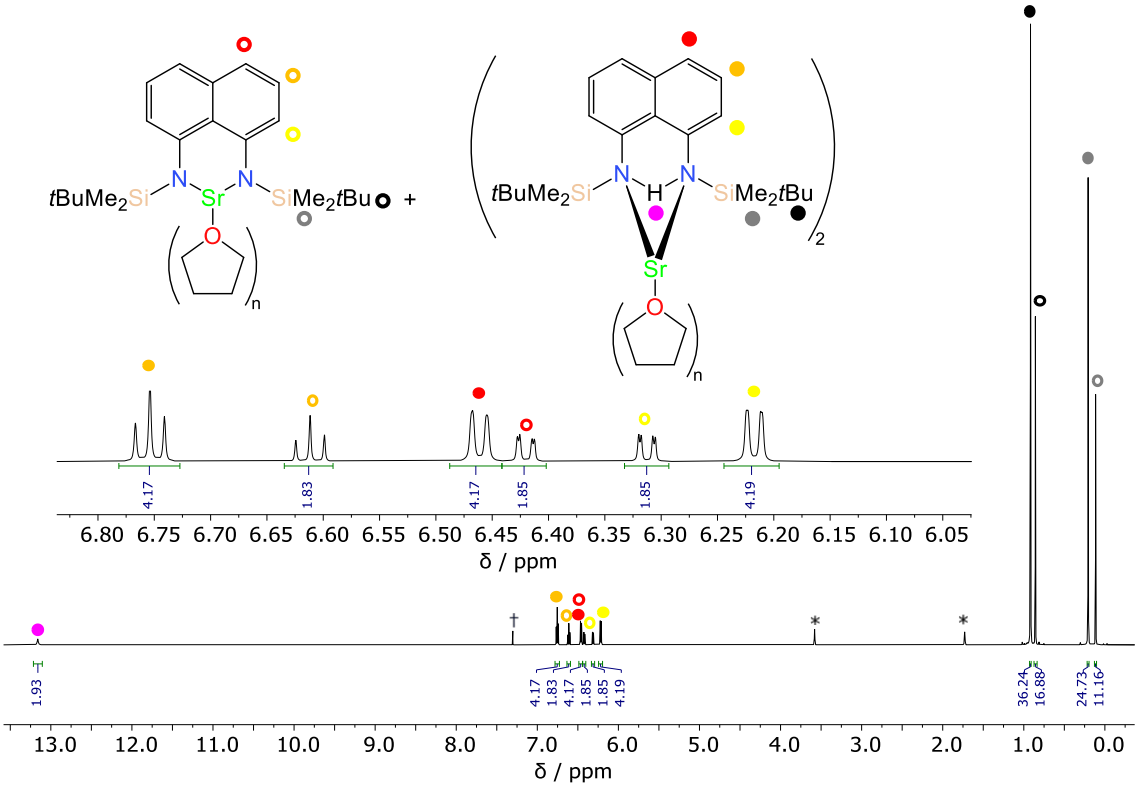


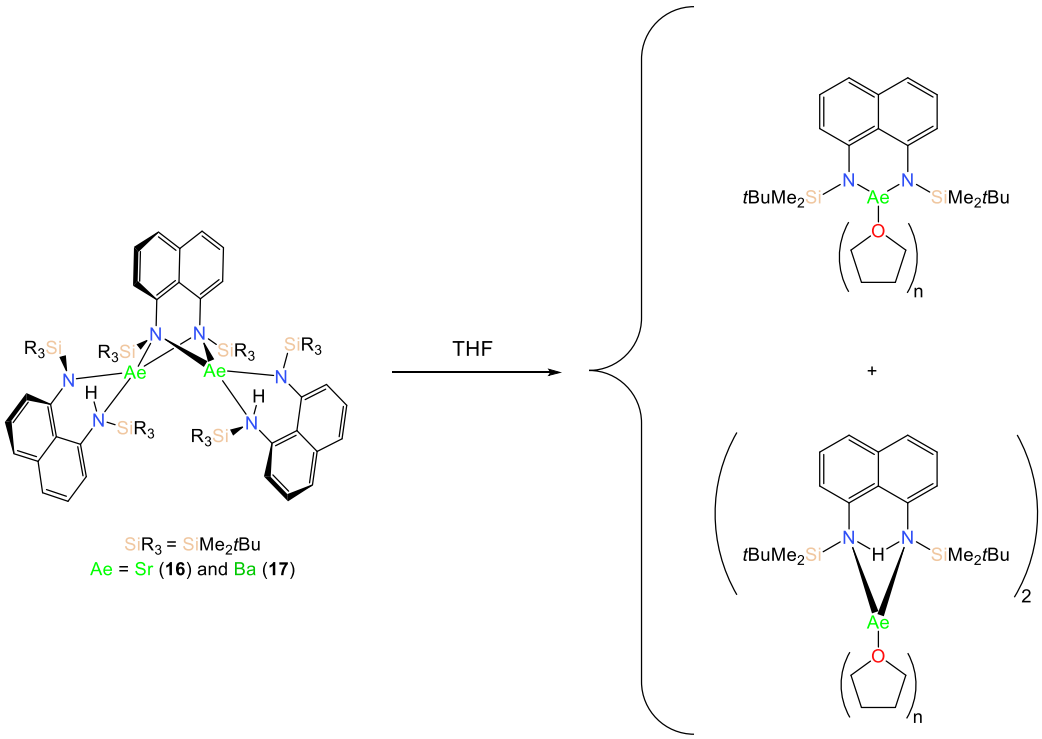
Figure 4.16 ^{1}H NMR spectrum (C_4D_8O, 298 K, 600.4 MHz) of [(^{Me_2tBu}L)Sr(THF)$_n$] and [(^{Me_2tBu}LH)$_2$Sr(THF)$_n$], formed in a 1:1 ratio when [{(^{Me_2tBu}LH)Sr}$_2$(μ-^{Me_2tBu}L)] (**16**) is dissolved in THF.

† denotes co-crystallised benzene, * denotes residual protio fraction of C_4D_8O.

Expansion shows naphthyl region.

monoanionic ligand all double those of the corresponding signals attributed to the dianionic ligand. This provides good evidence for the solid-state composition of **16**, in which the same 2:1 ratio is observed.

The ^{1}H NMR signals of these complexes suggest that they each have a plane of symmetry through their C(9)-C(10) axes. The ^{13}C{^{1}H} NMR spectrum of **16** in THF-d_8 has an aromatic region consisting of 12 signals (six for each complex), consistent with these observations. Notably, a $^{2}J_{C\text{-}H}$ correlation between the (N,N)μ$_2$-H ^{1}H NMR signal and the 1,8-C_{10}H$_6$ naphthyl ^{13}C{^{1}H} NMR signal of the [^{Me_2tBu}LH]$^-$ ligands is present in the two dimensional ^{13}C{^{1}H}-^{1}H HMBC spectrum. Furthermore, the ^{29}Si NMR spectrum of **16** consists of two sharp singlets at δ = –3.54 and –14.94 ppm, which are assigned as the silicon atoms of [(^{Me_2tBu}LH)$_2$Sr(THF)$_n$] and [(^{Me_2tBu}L)Sr(THF)$_n$] respectively.



Scheme 4.9 Speciation of [{(^{Me_2tBu}LH)Ae}$_2$(μ-^{Me_2tBu}L)] (Ae = Sr (**16**) and Ba (**17**)) into the monomeric adducts [(^{Me_2tBu}L)Ae(THF)$_n$] and [(^{Me_2tBu}LH)$_2$Ae(THF)$_n$] in THF.

4.4.6 Comparative ^{1}H NMR spectroscopic analysis

4.4.6.1 [(^{Me_2tBu}LH)CaN"(THF)$_n$] and [(^{Me_2tBu}LH)$_2$Ae(THF)$_n$] (Ae = Sr and Ba)

The signals assigned to the homoleptic complexes [(^{Me_2tBu}LH)$_2$Ae(THF)$_n$] (Ae = Sr and Ba) that form upon the dissolution of **16** and **17** in THF are sharp. This contrasts with the broad signals attributed to the heteroleptic complex [(^{Me_2tBu}LH)CaN"(THF)$_n$] that is proposed to form when **14** is dissolved in THF (**Figure 4.6**). This is consistent with the homoleptic structure of [(^{Me_2tBu}LH)$_2$Ae(THF)$_n$] precluding the formation of additional species *via* ligand redistribution, whereas the heteroleptic species [(^{Me_2tBu}LH)CaN"(THF)$_n$] has a more dynamic structure as it is subject to a Schlenk equilibrium (**Scheme 4.6a**). Notably, SSIPs of the form [^{Me_2tBu}LH]$_2$[Ae(THF)$_n$] (Ae = Sr and Ba) analogous to **15** (Ae = Ca) did not crystallise from THF solutions of **16** and **17**. This suggests that [(^{Me_2tBu}LH)$_2$Ae(THF)$_n$] (Ae = Sr and Ba) have more conventional associated solution-phase structures, with the larger Sr^{2+} and Ba^{2+} cations more readily accommodating the coordination of both two bulky [^{Me_2tBu}LH]$^-$ ligands and THF.

However, despite this structural variance between [(^{Me_2tBu}LH)CaN"(THF)$_n$] and [(^{Me_2tBu}LH)$_2$Ae(THF)$_n$] (Ae = Sr and Ba), the ^{1}H NMR chemical shifts of their bridging amino protons, δ(μ_2-H) (**Table 4.5**), display the same trend ($\delta_{Ca} > \delta_{Sr} > \delta_{Ba}$) as that discussed in **Chapter 2**. This can again be attributed to increasing Ae^{2+} size and electropositivity resulting in more ionic Ae-N bonds and more basic amide donors, with (N,N)μ_2-H more shielded as a consequence.

Table 4.5 Chemical shifts of the bridging amino protons, δ(μ$_2$-H), of the complexes [($^{Me_2{}^tBu}$LH)CaN"(THF)$_n$] and [($^{Me_2{}^tBu}$LH)$_2$Ae(THF)$_n$] (Ae = Sr and Ba) formed respectively when **14**, **16** and **17** are dissolved in THF-d_8 (600 MHz, 298 K). *a*: [($^{Me_2{}^tBu}$LH)CaN"(THF)$_n$] exists in equilibrium with the homoleptic species [($^{Me_2{}^tBu}$LH)$_2$Ca(THF)$_n$] and [(THF)$_n$CaN"$_2$].

Compound	δ(μ$_2$-H)
[($^{Me_2{}^tBu}$LH)CaN"(THF)$_n$]^a	14.86
[($^{Me_2{}^tBu}$LH)$_2$Sr(THF)$_n$]	13.09
[($^{Me_2{}^tBu}$LH)$_2$Ba(THF)$_n$]	12.65

4.4.6.2 [($^{Me_2{}^tBu}$L)Ae(THF)$_n$]

The formation of [($^{Me_2{}^tBu}$L)Ae(THF)$_n$] (Ae = Sr and Ba) upon the dissolution of **16** and **17** in THF provides the first evidence that the formation of strontium and barium complexes bearing only dianionic [$^{Me_2{}^tBu}$L]$^{2-}$ ligands is possible. This is despite the attempted synthesis of these complexes *via* protonolysis in THF resulting in only the formation of [$^{Me_2{}^tBu}$LH]$^-$ ligands (**Section 2.4.1.7**), while the analogous reactions in benzene resulting in the aggregated species **16** and **17** that feature both [$^{Me_2{}^tBu}$LH]$^-$ and [$^{Me_2{}^tBu}$L]$^{2-}$ ligands. These outcomes have precluded the isolation of either the monomeric THF adducts [($^{Me_2{}^tBu}$L)Ae(THF)$_n$] or THF-free dimers of the form [($^{Me_2{}^tBu}$L)Ae]$_2$ (Ae = Sr and Ba) analogous to the calcium species **13**.

However, the formation of [($^{Me_2{}^tBu}$L)Ae(THF)$_n$] upon the dissolution of **16** and **17** in THF suggests that this is a synthetic issue resulting from the insufficient basicity of [AeN"$_2$]$_2$

precluding full deprotonation to exclusively form $[^{Me_2{}^tBu}L]^{2-}$ ligands, rather than the $[(^{Me_2{}^tBu}L)Ae]$ unit being inherently unstable. Heating the 1:1 mixtures of $[(^{Me_2{}^tBu}L)Ae(THF)_n]$ and $[(^{Me_2{}^tBu}LH)_2Ae(THF)_n]$ (Ae = Sr and Ba) that result from the dissolution of **16** and **17** in THF at 80 °C resulted in no changes to their ^{1}H NMR spectra. This demonstrates the thermal stability of these species, in contrast with the phenyl-substituted complexes **6**–**11** that spontaneously degrade upon their conversion into monomeric THF adducts. This is consistent with the observation that bulky alkyl substituents prevent the thermal degradation of the intermediate species $[(^{R_3}LH)AeN"(THF)_n]$ *in situ* (**Chapter 2.4.1.5**).

4.4.7 Comparative ^{29}Si NMR spectroscopic analysis

As discussed in **Section 3.7.1**, the chemical shifts of the ^{29}Si NMR signals corresponding to the silyl substituents of **13**–**17**, $\delta(SiR_3)$, act as a useful probe for investigating the charge density of the ligands in these alkyl-substituted complexes (**Table 4.6, Figure 4.17**). Full comparative analysis of the complexes $[(^{Me_2{}^tBu}L)Ae(THF)_n]$ (Ae = Mg, Ca, Sr and Ba) was enabled by both the isolation of the magnesium congener $[(^{Me_2{}^tBu}L)Mg(THF)_2]$ (**5**) (**Section 2.3**) and the formation of its heavier congeners upon the dissolution of **13**, **14, 16** and **17** in THF. As expected, the ^{29}Si NMR singlet shifts to progressively lower frequencies as the size of Ae^{2+} and ionic character of the two Ae-N bonds both increase, resulting in more charge dense $[^{Me_2{}^tBu}L]^{2-}$ ligands with more shielded silicon centres.

Notably, for a given metal the ^{29}Si NMR signal of $[(^{Me_2{}^tBu}L)Ae(THF)_n]$ is shifted to a significantly higher frequency than the analogous signals in the ^{29}Si NMR spectra of the corresponding phenyl-substituted complexes $[(^{Ph_3}L)Ae(THF)_n]$ and $[(^{Ph_2Me}L)Ae(THF)_n]$

(Ae = Ca, Sr and Ba, **Section 3.7.1**). This demonstrates the reduced degree to which the negative charge of the $[^{Me_2{}^tBu}L]^{2-}$ ligand is withdrawn by its alkyl-substituted SiR_3 groups relative to the phenyl substituted variants.

Table 4.6 Chemical shifts of the SiR_3 groups, $\delta(SiR_3)$, of $[(^{Me_2{}^tBu}L)Ae(THF)_n]$ (Ae = Mg, Ca, Sr and Ba), $[(^{Me_2{}^tBu}LH)CaN''(THF)_n]$ and $[(^{Me_2{}^tBu}LH)_2Ae(THF)_n]$ (Ae = Sr and Ba) in THF-d_8 (600 MHz, 298 K). *a*: $[(^{Me_2{}^tBu}LH)CaN''(THF)_n]$ exists in equilibrium with the homoleptic species $[(^{Me_2{}^tBu}LH)_2Ca(THF)_n]$ and $[(THF)_nCaN''_2]$.

Compound	**$\delta(SiR_3)$**
$[(^{Me_2{}^tBu}L)Mg(THF)_2]$	–5.54
$[(^{Me_2{}^tBu}L)Ca(THF)_n]$	–13.16
$[(^{Me_2{}^tBu}L)Sr(THF)_n]$	–14.95
$[(^{Me_2{}^tBu}L)Ba(THF)_n]$	–15.77
$[(^{Me_2{}^tBu}LH)CaN''(THF)_n]^a$	–5.71
$[(^{Me_2{}^tBu}LH)_2Sr(THF)_n]$	–3.46
$[(^{Me_2{}^tBu}LH)_2Ba(THF)_n]$	–2.39

Additionally, the formation of $[(^{Me_2{}^tBu}LH)CaN''(THF)_n]$ and $[(^{Me_2{}^tBu}LH)_2Ae(THF)_n]$ (Ae = Sr and Ba) upon the dissolution of **14**, **16** and **17** in THF enables comparison with the ^{29}Si NMR signals of these complexes. The $[^{Me_2{}^tBu}LH]^-$ ligands of these species are monoanionic, in contrast with the dianionic ligands of $[(^{Me_2{}^tBu}L)Ae(THF)]$. This results in the ^{29}Si NMR signal of the $[^{Me_2{}^tBu}LH]^-$ ligand resonating at a consistently higher frequency than the $[^{Me_2{}^tBu}L]^{2-}$ ligand upon coordination to a given element

($\Delta\delta$ = 7.45 (Ca), 11.49 (Sr) and 13.38 (Ba) ppm) due to the lower negative charge density of the former.

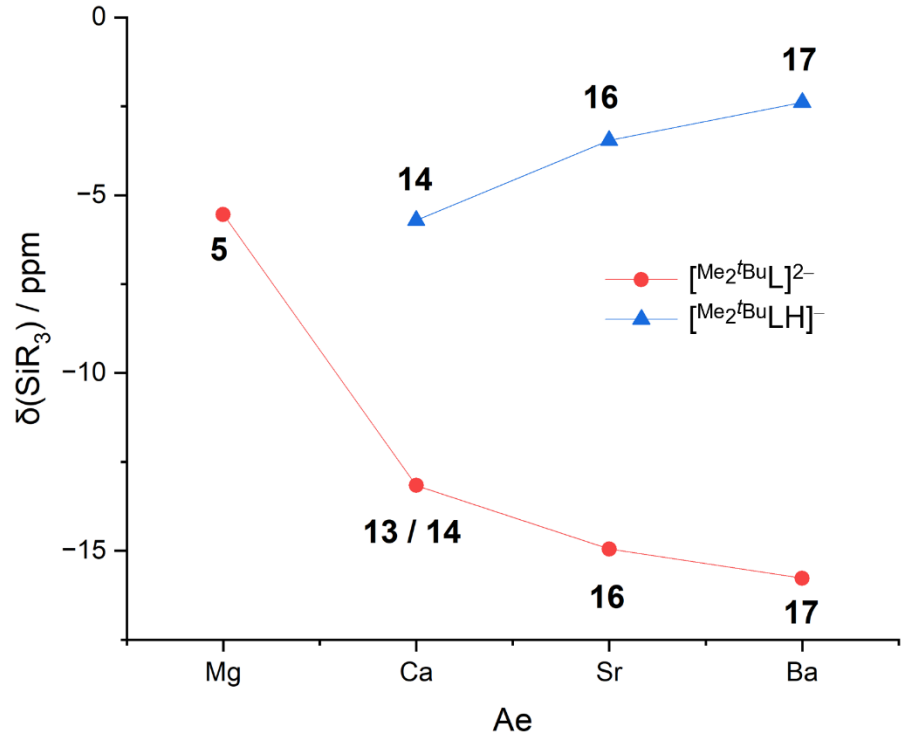
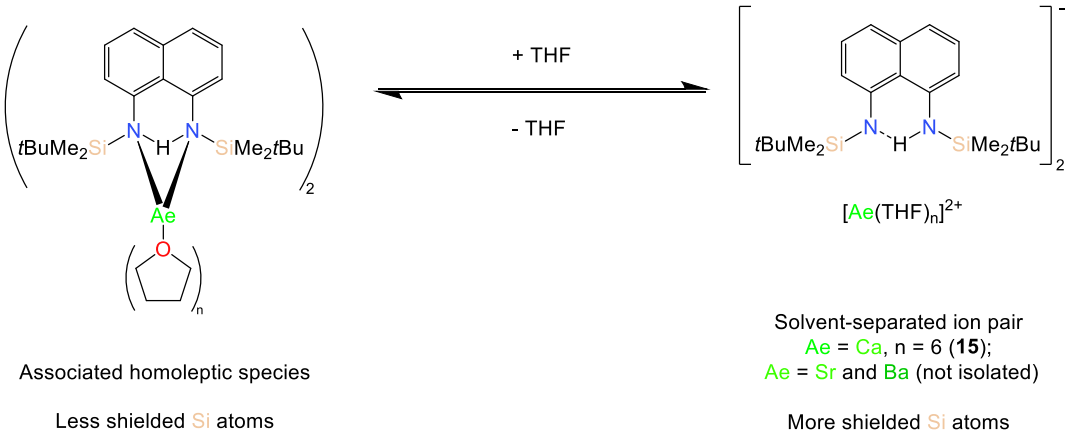


Figure 4.17 Chemical shifts of the SiR_3 ^{29}Si NMR signals, $\delta(SiR_3)$, of the $[^{Me_2t Bu}L]^{2-}$ ligands of $[(^{Me_2t Bu}L)Ae(THF)_n]$ (Ae = Mg, Ca, Sr and Ba) and the $[^{Me_2t Bu}LH]^-$ ligands of $[(^{Me_2t Bu}LH)CaN''(THF)_n]$ and $[(^{Me_2t Bu}LH)_2Ae(THF)_n]$ (Ae = Sr and Ba) that form when **5**, **13**, **14**, **16** and **17** are dissolved in THF-d_8 (600 MHz, 298 K).

Notably however, the ^{29}Si NMR signal of the monoanionic $[^{Me_2t Bu}LH]^-$ ligand increases in frequency with greater Ae^{2+} size. This contrasts with the trend observed for $[(^{Me_2t Bu}L)Ae(THF)_n]$, and seems counterintuitive based on the electronic rationale applied in that case. Instead, it is proposed that this trend results from a solution-phase equilibrium between the associated coordination complexes $[(^{Me_2t Bu}LH)_2Ae(THF)_n]$ and

the charge-separated species $[^{Me_2{}^tBu}LH]_2[Ae(THF)_n]$ (**Scheme 4.10**), the formation of which was verified by the crystallisation of **15** (**Section 4.3.6**).



Scheme 4.10 Proposed equilibrium between the associated homoleptic species $[(^{Me_2{}^tBu}LH)_2Ae(THF)_n]$ and the SSIP $[^{Me_2{}^tBu}LH]_2[Ae(THF)_n]$ in THF.

The full cleavage of the Ae-N bonds in the SSIP form likely results in more shielded silicon atoms, as minimal negative charge density is donated to Ae^{2+} by $[^{Me_2{}^tBu}LH]^-$. Therefore, the formation of the charge-separated species results in a time-averaged ^{29}Si NMR signal that is shifted to a lower frequency. The crystallisation of **15**, but not the strontium and barium congeners, demonstrates that the SSIP form is favoured by the greater oxophilicity of Ca^{2+}. Therefore, increasing Ae^{2+} size reduces the contribution of the more shielded SSIP form to the ^{29}Si NMR signal relative to that of the less shielded associated form, and results in the observed increase in chemical shift.

4.5 Conclusions

Full deprotonation of the alkyl-substituted proligand $^{Me_2tBu}LH_2$ afforded $[(^{Me_2tBu}L)Ca]_2$ (**13**), the naphthalene-bridged structure of which was rationalised on steric grounds. In other cases, the full deprotonation of $^{Me_2tBu}LH_2$ was precluded by the high basicity of its bulky *tert*-butyl substituted nitrogen donors. This resulted in the isolation of the heteroleptic bimetallic intermediate species $[(^{Me_2tBu}LH)Ca(\mu\text{-}^{Me_2tBu}L)CaN"]$ (**14**) and the bimetallic side-products $[\{(^{Me_2tBu}LH)Ae\}_2(\mu\text{-}^{Me_2tBu}L)]$ (Ae = **16** and **17**). The solid-state structures of **13**, **14**, **16** and **17** were characterised by X-ray diffraction, IR spectroscopy and elemental analysis. The dissolution of **13**, **14**, **16** and **17** in THF resulted in their speciation into stable monomeric adducts, which were characterised by multinuclear NMR spectroscopy.

Notably, the solvent-separated ionic pair (SSIP) $[^{Me_2tBu}LH]_2[Ca(THF)_6]$ (**15**) crystallised from a THF solution of **14**. Unexpectedly, the $[^{Me_2tBu}LH]^-$ fragment acts as a weakly coordinating anion (WCA) in the crystal structure of **15**, rather than as a chelating ligand. The formation of a SSIP was attributed to the oxophilicity of Ca^{2+} and the stability conferred to the $[^{Me_2tBu}LH]^-$ WCA by its strong intramolecular hydrogen bond, delocalised π-system and $SiMe_2{}^tBu$ groups.

While full characterisation of **13**–**17** provided useful insight into the properties of alkaline earth complexes supported by alkyl-substituted 1,8-*bis*(silylamido)naphthalene ligands, the onward reactivity of these complexes was not pursued. Instead, an alternative di(amido)siloxane ligand scaffold was investigated as a platform for the more straightforward synthesis of novel alkaline earth complexes.

4.6 References

1 I. Krossing and I. Raabe, *Angew. Chemie Int. Ed.*, 2004, **43**, 2066–2090.

2 I. M. Riddlestone, A. Kraft, J. Schaefer and I. Krossing, *Angew. Chemie Int. Ed.*, 2018, **57**, 13982–14024.

3 I. Krossing, *Chem. Eur. J.*, 2001, **7**, 490–502.

4 A. G. Massey and A. J. Park, *J. Organomet. Chem.*, 1964, **2**, 245–250.

5 S. J. Lancaster, A. Rodriguez, A. Lara-Sanchez, M. D. Hannant, D. A. Walker, D. H. Hughes and M. Bochmann, *Organometallics*, 2002, **21**, 451–453.

6 D. Seebach, H. Siegel, K. Mullen, K. Hiltbrunner, A. J. Kos, G. W. Spitznagel, C. Rohde, D. Arad, K. N. Houk and B. Konrad Seppelt, *Angew. Chemie Int. Ed.*, 1993, **32**, 1025–1027.

7 Y. Sarazin and J. F. Carpentier, *Chem. Rev.*, 2015, 115, 3564–3614.

8 Y. Sarazin, B. Liu, T. Roisnel, L. Maron and J. F. Carpentier, *J. Am. Chem. Soc.*, 2011, **133**, 9069–9087.

9 Y. Sarazin, V. Poirier, T. Roisnel and J. F. Carpentier, *Eur. J. Inorg. Chem.*, 2010, **2010**, 3423–3428.

10 B. Liu, V. Dorcet, L. Maron, J. F. Carpentier and Y. Sarazin, *Eur. J. Inorg. Chem.*, 2012, **2012**, 3023–3031.

11 K. Thum, J. Pahl, J. Eyselein, H. Elsen, J. Langer and S. Harder, *Chem. Commun.*, 2021, **57**, 5278–5281.

12 K. Thum, J. Martin, H. Elsen, J. Eyselein, L. Stiegler, J. Langer and S. Harder, *Eur. J. Inorg. Chem.*, 2021, **2021**, 2643–2653.

13 J. Pahl, S. Brand, H. Elsen and S. Harder, *Chem. Commun.*, 2018, **54**, 8685–8688.

14 J. Pahl, A. Friedrich, H. Elsen and S. Harder, *Organometallics*, 2018, **37**, 2901–2909.

15 K. Thum, A. Friedrich, J. Pahl, H. Elsen, J. Langer and S. Harder, *Chem. Eur. J.*, 2021, **27**, 2513–2522.

16 C. Knüpfer, L. Klerner, J. Mai, J. Langer and S. Harder, *Chem. Sci*, 2024, **15**, 4386–4395.

17 S. Harder, *Chem. Rev.*, 2010, **110**, 3852–3876.

18 L. Yang, D. R. Powell and R. P. Houser, *Dalton Trans.*, 2007, 955–964.

19 M. Westerhausen and W. Schwarz, *ZAAC*, 1991, **604**, 127–140.

20 P. Pyykkö, *J. Phys. Chem. A*, 2015, **119**, 2326–2337.

21 R. Guthardt, C. Bruhn, C. Färber and U. Siemeling, *Organometallics*, 2020, **39**, 4174–4177.

22 L. Pauling, *The Chemical Bond*, Cornell University Press, Ithaca, New York, 1967.

23 P. P. Power, *Nature*, 2010, **463**, 171–177.

24 E. Arunan, G. R. Desiraju, R. A. Klein, J. Sadlej, S. Scheiner, I. Alkorta, D. C. Clary, R. H. Crabtree, J. J. Dannenber, P. Hobza, H. G. Kjaergaard, A. C. Legon, B. Mennucci and D. J. Nesbitt, *Pure Appl. Chem.*, 2011, **83**, 1637–1641.

25 P. E. Hansen, M. Vakili, F. S. Kamounah and J. Spanget-Larsen, *Mol. 2021, Vol. 26, Page 7651*, 2021, **26**, 7651.

26 B. Brzezinski, Z. Rozwadowski, T. Dziembowska and G. Zundel, *J. Mol. Struct.*, 1998, **440**, 73–

79.

27 R. L. Jones, L. J. Morris, C. G. Collins Rice, Z. R. Turner and D. O'Hare, *Phys. Chem. Chem. Phys.*, 2023, **25**, 15463–15468.

28 S. Majumder, M. Fleck, C. R. Lucas and S. Mohanta, *J. Mol. Struct.*, 2012, **1020**, 127–133.

29 S. Hazra, S. Majumder, M. Fleck, R. Koner and S. Mohanta, *Polyhedron*, 2009, **28**, 2871–2878.

30 V. Vasylyeva, L. Catalano, C. Nervi, R. Gobetto, P. Metrangolo and G. Resnati, *CrystEngComm*, 2016, **18**, 2247–2250.

31 X. Wang, K. Q. Zhao, M. R. J. Elsegood and C. Redshaw, *Supramol. Chem.*, 2018, **30**, 404–410.

32 A. K. Asatkar, V. K. Verma, T. A. Jain, R. Singh, S. K. Gupta and R. J. Butcher, *Acta Crystallogr. Sect. E Struct. Reports Online*, 2011, **67**, o2724–o2725.

33 D. Esteban-Gómez, C. Platas-Iglesias, F. Avecilla, A. De Blas and T. Rodríguez-Blas, *Eur. J. Inorg. Chem.*, 2007, **2007**, 1635–1643.

34 S. Ghosh, R. R. Gowda, R. Jagan and D. Chakraborty, *Dalton Trans.*, 2015, **44**, 10410–10422.

35 Z. Rozwadowski, T. Dziembowska, G. Schroeder and B. Brzezinski, *J. Mol. Struct.*, 1998, **444**, 221–225.

36 S. Harder, F. Feil and T. Repo, *Chem. Eur. J.*, 2002, **8**, 1991–1999.

37 G. B. Deacon, C. M. Forsyth, F. Jaroschik, P. C. Junk, D. L. Kay, T. Maschmeyer, A. F. Masters, J. Wang and L. D. Field, *Organometallics*, 2008, **27**, 4772–4778.

38 S. Harder, S. Müller and E. Hübner, *Organometallics*, 2004, **23**, 178–183.

39 J. Langer, S. Krieck, H. Görls, G. Kreisel, W. Seidel and M. Westerhausen, *New J. Chem.*, 2010, **34**, 1667–1677.

40 B. Liu, V. Dorcet, L. Maron, J. F. Carpentier and Y. Sarazin, *Eur. J. Inorg. Chem.*, 2012, **2012**, 3023–3031.

41 I. L. Fedushkin, A. N. Lukoyanov, S. Dechert and H. Schumann, *Eur. J. Inorg. Chem.*, 2004, **2004**, 2421–2424.

42 C. Lichtenberg, P. Jochmann, T. P. Spaniol and J. Okuda, *Angew. Chemie Int. Ed.*, 2011, **50**, 5753–5756.

43 S. Krieck, H. Görls and M. Westerhausen, *Inorg. Chem. Commun.*, 2008, **11**, 911–913.

44 S. Perruchas, F. Simon, S. Uriel, N. Avarvari, K. Boubekeur and P. Batail, *J. Organomet. Chem.*, 2002, **643**–**644**, 301–306.

45 S. Krieck, H. Görls and M. Westerhausen, *Organometallics*, 2008, **27**, 5052–5057.

46 S. Krieck, H. Görls and M. Westerhausen, *Chem. – An Asian J.*, 2010, **5**, 272–277.

47 N. Romero, L. Vendier, C. Dinoi and M. Etienne, *Dalton Trans.*, 2014, **43**, 10114–10119.

48 J. S. McMullen, R. Huo, P. Vasko, A. J. Edwards and J. Hicks, *Angew. Chemie Int. Ed.*, 2022, **62**, e2022152.

49 M. J. Harvey and T. P. Hanusa, *Organometallics*, 2000, **19**, 1556–1566.

50 P. M. Chapple and Y. Sarazin, *Eur. J. Inorg. Chem.*, 2020, **2020**, 3321–3346.

Chapter 5

Synthesis, characterisation and reactivity of di(amido)siloxane alkaline earth complexes

5.1 Introduction

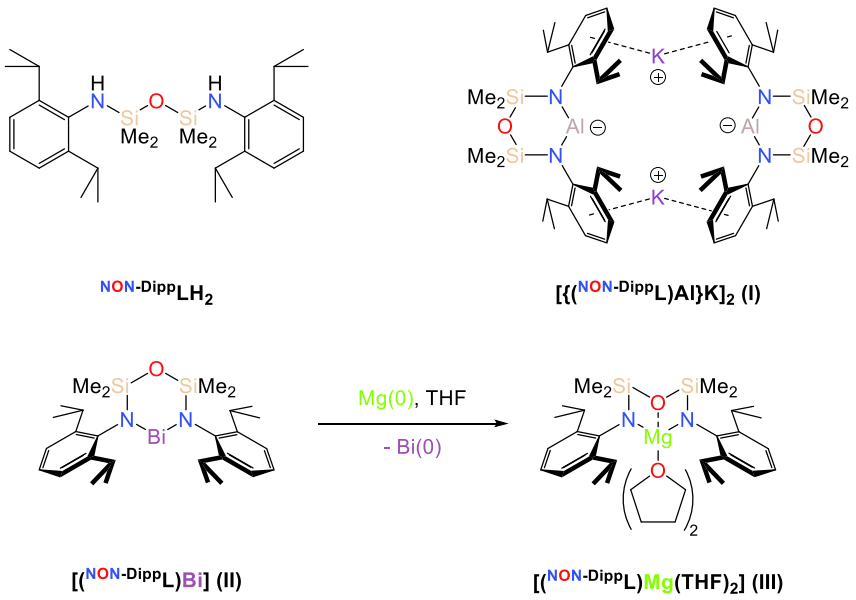
5.1.1 Overview

Chapter 5 discusses the synthesis and characterisation of four novel dimeric alkaline earth complexes supported by a flexible di(amido)siloxane ligand. Collaboration with Ms. Andrea O'Reilly (supervised by Profs. Martyn P. Coles and J. Robin Fulton, Victoria University of Wellington) enabled the comparison of these dimeric THF-free species with five THF adducts supported by the same ligand. The attempted synthesis of low-valent alkaline earth complexes resulted in the characterisation of two heterobimetallic molecular magnesium hydroxide complexes featuring a rearranged ligand backbone.

5.1.2 Di(amido)siloxane ligands

The di(amino)siloxane proligand, $^{NON\text{-}Dipp}LH_2$ ($O(SiMe_2NHDipp)_2$, Dipp = 2,6-di*iso*propylphenyl), and the corresponding dianionic di(amido)siloxane ligand, $[^{NON\text{-}Dipp}L]^{2-}$ ($[O(SiMe_2NDipp)_2]^{2-}$), were first reported in 2002 by Leznoff and co-workers (**Chart 5.1**).[1] This built on previous work in which analogous ligands featuring alternative N-alkyl or -aryl substituents were reported.[2–8]

The $[^{NON\text{-}Dipp}L]^{2-}$ ligand consists of a flexible siloxane tether bridging between two anionic nitrogen donors. The siloxane group is a poor dative donor due to the negative hyper-conjugation of its lone pairs with the Si-C σ* orbitals of its $SiMe_2$ groups.[9] Consequently, there are numerous reported examples of complexes in which the $[^{NON\text{-}Dipp}L]^{2-}$ ligand is coordinated to p-block elements (Al, Ge, Sn, In, Bi, Pb, Sb) in a κ^2-N,N′-bidentate manner.[2,10–17] This has been exemplified by a number of low-valent species reported by Coles and co-workers, with notable examples including the potassium aluminyl complex $[\{(^{NON\text{-}Dipp}L)Al\}K]_2$ (**I**, **Chart 5.1**)[18] and the bismuth(II) radical $[(^{NON\text{-}Dipp}L)Bi]$ (**II**, **Chart 5.1**).[17] These complexes demonstrate the kinetic stability conferred to reactive main-group species by the bulky Dipp substituents of the $[^{NON\text{-}Dipp}L]^{2-}$ ligand, which are also able to form stabilising π-facial interactions with metal cations. Notably, the over-reduction of **II** with metallic magnesium resulted in the isolation of the monomeric magnesium complex $[(^{NON\text{-}Dipp}L)Mg(THF)_2]$ (**III, Chart 5.1**), in which the $[^{NON\text{-}Dipp}L]^{2-}$ ligand is coordinated to the oxophillic Mg^{2+} centre in a κ^3-N,O,N′-tridentate manner.[17] Complex **III** was the only previously reported example



$^{NON\text{-}Dipp}LH_2$ $[\{(^{NON\text{-}Dipp}L)Al\}K]_2$ (I)

$[(^{NON\text{-}Dipp}L)Bi]$ (II) $[(^{NON\text{-}Dipp}L)Mg(THF)_2]$ (III)

Chart 5.1 The $^{NON\text{-}Dipp}LH_2$ proligand and selected metal complexes supported by the dianionic $[^{NON\text{-}Dipp}L]^{2-}$ ligand in both κ^2-N,N′-bidentate and κ^3-N,O,N′-tridentate coordination modes.

of an alkaline earth complex supported by the $[^{NON\text{-}Dipp}L]^{2-}$ ligand prior to the inception of this Thesis research. The κ^3-N,O,N′-tridentate coordination mode has also been reported for di(amido)siloxane complexes featuring oxophillic actinides (Th, U),[1,19–23] yttrium,[24,25] scandium[26] and other transition metals (Cr, Mn, Fe, Co, Zr).[1,5,7,27]

The $[^{NON\text{-}Dipp}L]^{2-}$ ligand is generally robust when chelated to a metal cation. However, its conversion into a mixed amide/alkoxide "NNO" $[^{NNO\text{-}Dipp}L]^{2-}$ ($[(Dipp)NSiMe_2N(Dipp)SiMe_2O]^{2-}$) ligand *via* an intramolecular 1,3-silyl retro-Brook rearrangement has been reported when the dilithium salt $[(^{NON\text{-}Dipp}L)Li_2]$ is dissolved in THF (**Chart 5.2a**).[28] Very recently, Coles and co-workers reported the rearrangement of the "NON" complex $K[(^{NON\text{-}Dipp}L)Al\{CH_2CH_2C(N^iPr)_2\}]$, into the "NNO" complex $K[(^{NNO\text{-}Dipp}L)Al\{CH_2CH_2C(N^iPr)_2\}]$ upon heating at 80 °C (**IV** and **V** respectively, **Chart 5.2b**).[29]

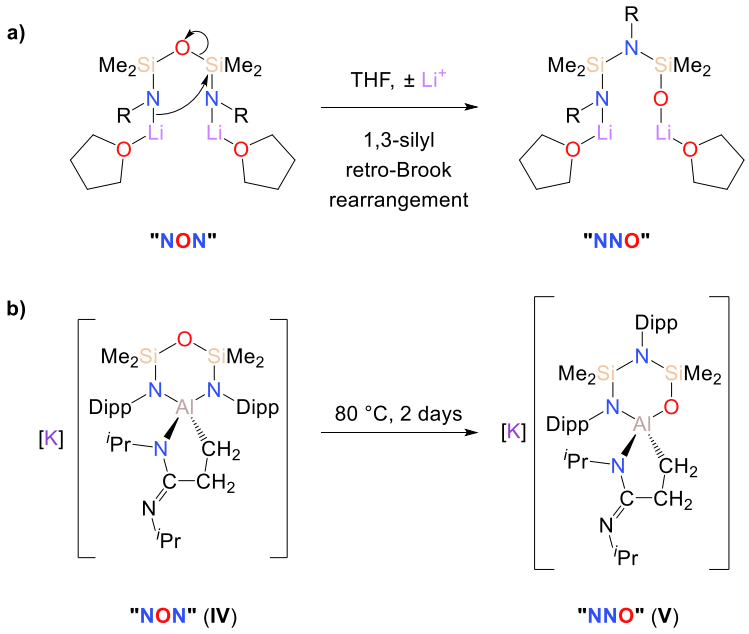
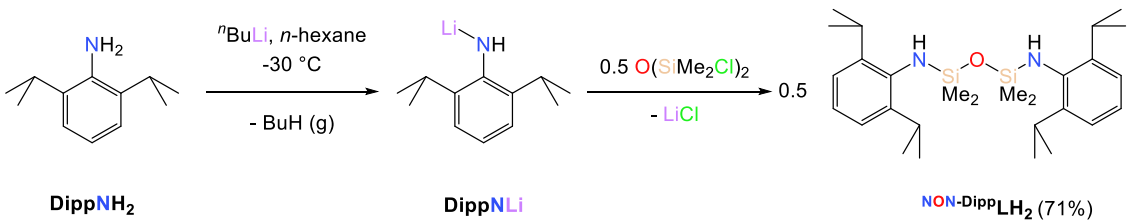


Chart 5.2 a) Rearrangement of a generic "NON" dilithium di(amido)siloxane into a "NNO" mixed amide/alkoxide form *via* a 1,3-silyl retro-Brook rearrangement in THF;
b) Rearrangement of the "NON" complex $K[(^{NON\text{-}Dipp}L)Al\{CH_2CH_2C(N^iPr)_2\}]$ (**IV**) into the "NNO" complex $K[(^{NON\text{-}Dipp}L)Al\{CH_2CH_2C(N^iPr)_2\}]$ (**V**).

5.2 Proligand synthesis

The synthesis of alkaline earth complexes bearing the $[^{NON\text{-}Dipp}L]^{2-}$ ligand scaffold was expected to pose less synthetic challenges than the 1,8-*bis*(silylamido)naphthalene ($^{R_3}LH_2$) ligands investigated in **Chapters 2**–**4**. It was proposed that the flexible ligand backbone would more readily facilitate both the deprotonation of the $^{NON\text{-}Dipp}LH_2$ proligand and the chelation of the larger Ae^{2+} cations (Ae = Ca, Sr and Ba).

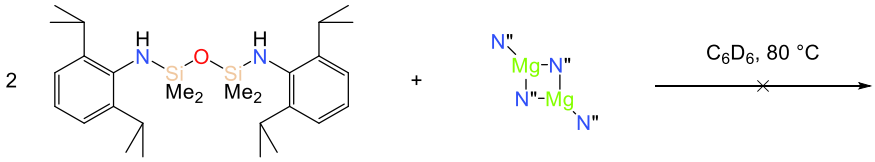
The proligand $^{NON\text{-}Dipp}LH_2$ was synthesised according to a reported two-step, one pot procedure (**Scheme 5.1**).[1] The 1:1 reaction of 2,6-di*iso*propylaniline ($DippNH_2$) with *n*-butyllithium in *n*-hexane generated the corresponding lithium amide (DippNHLi) intermediate *in situ*. The subsequent addition of 0.5 eq. 1,3-dichloro-1,1,3,3-tetramethyldisiloxane resulted in the elimination of lithium chloride and afforded the proligand $^{NON\text{-}Dipp}LH_2$ as an orange oil in 71% overall yield. The ^{1}H NMR spectrum of $^{NON\text{-}Dipp}LH_2$ in THF-d_8 contains a diagnostic singlet at δ = 3.35 ppm corresponding to its two equivalent amino protons. This singlet notably resonates at a significantly lower frequency than those in the analogous ^{1}H NMR spectra of $^{R_3}LH_2$ (δ = 5.39–6.67 ppm, **Table 2.1**). This results from the flexibility of $^{NON\text{-}Dipp}LH_2$ precluding the formation of a strongly deshielding intramolecular hydrogen-bond, in contrast with the rigid structure of $^{R_3}LH_2$, and suggests that deprotonation of $^{NON\text{-}Dipp}LH_2$ should be facile.



Scheme 5.1 Synthesis of $^{NON\text{-}Dipp}LH_2$.

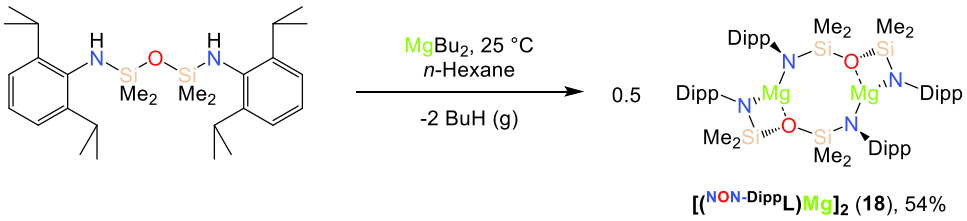
5.3 Synthesis of di(amido)siloxane magnesium complexes

The 2:1 reaction of $^{NON\text{-}Dipp}LH_2$ with $[MgN"_2]_2$ in benzene proved unproductive (**Scheme 5.2**), with the ^1H NMR spectrum of the reaction mixture showing no consumption of the two starting materials after 1 week at 80 °C. The same reaction in THF (in which $[MgN"_2]$ exists as a monomeric THF adduct) also proved unsuccessful. This was unexpected given the previously reported structure of $[(^{NON\text{-}Dipp}L)Mg(THF)_2]$ (**III**, **Chart 5.1**),[17] which demonstrates that Mg^{2+} can accommodate the coordination of the $[^{NON\text{-}Dipp}L]^{2-}$ ligand in κ^3-N,O,N′-tridentate manner. This suggests that $[MgN"_2]_2$ is insufficiently reactive to deprotonate $^{NON\text{-}Dipp}LH_2$ due to both the strength of its Mg-N bonds and its sterically congested dimeric structure,[30] in contrast with the more reactive heavier $[AeN"_2]_2$ (Ae = Ca, Sr and Ba) congeners (*vide infra*).



Scheme 5.2 Unsuccessful 2:1 reaction of $^{NON\text{-}Dipp}LH_2$ with $[MgN"_2]_2$ in benzene.

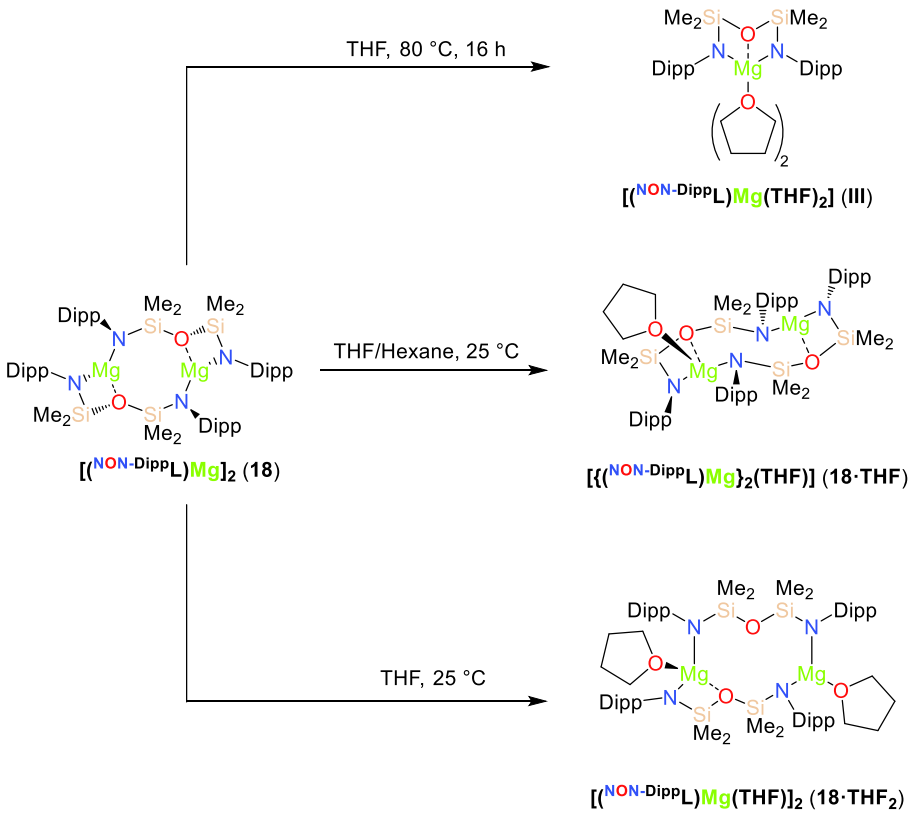
Conversely, the 1:1 reaction of $^{NON\text{-}Dipp}LH_2$ with the stronger base di-*n*-butylmagnesium in either benzene or *n*-hexane afforded the dimeric complex $[(^{NON\text{-}Dipp}L)Mg]_2$ (**18**) in moderate yield (54%) *via* alkane elimination (**Scheme 5.3**).



Scheme 5.3 Synthesis of $[(^{NON\text{-}Dipp}L)Mg]_2$ (**18**) *via* alkane elimination.

Complex **18** crystallises directly from the reaction mixture, enabling its facile isolation and characterisation by X-ray crystallography, multinuclear NMR and IR spectroscopy and elemental analysis.

Quantitative conversion of **18** into the monomeric THF adduct **III** was possible by heating a THF solution of the former at 80 °C for 16 hours. However, results obtained in collaboration with Ms. Andrea O'Reilly showed that the recrystallisation of **18** from THF/*n*-hexane (1:1) and THF results in its conversion into the intermediate dimeric THF adducts [{($^{NON\text{-}Dipp}$L)Mg}$_2$(THF)] (**18·THF**) and [($^{NON\text{-}Dipp}$L)Mg(THF)]$_2$ (**18·THF$_2$**) respectively (**Scheme 5.4**). Complexes **18·THF and 18·THF$_2$** were also characterised by X-ray crystallography.



Scheme 5.4 Conversion of [($^{NON\text{-}Dipp}$L)Mg]$_2$ (**18**) into the THF adducts [($^{NON\text{-}Dipp}$L)Mg(THF)$_2$] (**III**), [{($^{NON\text{-}Dipp}$L)Mg}$_2$(THF)] (**18·THF**) and [($^{NON\text{-}Dipp}$L)Mg(THF)]$_2$ (**18·THF$_2$**).

5.3.1 X-ray crystallographic analysis

5.3.1.1 X-ray crystal structure of [($^{NON\text{-}Dipp}$L)Mg]$_2$ (18)

Dissolution of **18** in benzene at 80 °C followed by slow cooling to room temperature afforded colourless single crystals suitable for an X-ray diffraction study. Complex **18** crystallises in the *C*2/*c* space group (**Figure 5.1**, **Table 5.1**). The asymmetric unit of **18** (**Figure 5.1a**) consists of a [$^{NON\text{-}Dipp}$L]$^{2-}$ ligand coordinated to Mg^{2+} in a κ^2-N,O-bidentate manner (Mg(1)-N(1) = 1.987(1) Å, Mg(1)-O(1) = 2.066(1) Å), resulting in the formation of a four-membered MgNSiO metallacycle. Full deprotonation of the ligand was confirmed by the absence of any N-H absorbances in the IR spectrum of **18**. The coordination of the siloxane group by the highly oxophillic Mg^{2+} cation[31] is consistent with the previously reported structure of **III**.[17]

The full dimeric structure of **18** (**Figure 5.1b**) is generated by a twofold rotation axis, and consists of a central eight-membered $Mg_2N_2Si_2O_2$ metallacycle. This has a "boat-like" conformation in which the two four-membered MgNSiO rings are *syn* with respect to one another beneath the central eight-membered ring, with two NDipp substituents projected above the opposite face. The pendant amide donor, N(2), does not coordinate to Mg(1) (Mg(1)-N(2) = 3.551(1) Å >> Σr_{cov}(Mg,N) = 2.10[32]), but does coordinate to the symmetry equivalent Mg(1) centre in a κ^1-N-monodentate manner (Mg(1)-N(2)* = 1.999(1) Å, * refers to symmetry related atoms). Consequently, each ligand adopts a κ^2-N,O-κ^1-N′ coordination mode, which has only very recently been reported elsewhere for a dimeric ytterbium hydride complex.[25] This results in a distorted trigonal pyramidal coordination geometry at each Mg^{2+} centre ($\Sigma\{\angle Mg(1)\}$ = 345.63(8)°). The small ionic radius of Mg^{2+} seemingly precludes the four-coordinate geometry that would result from the dimerisation of two [($^{NON\text{-}Dipp}$L)Mg] units in which the ligand is coordinated in a

κ^3-N,O,N′-μ-κ^1-N manner, in contrast with the heavier [($^{NON\text{-}Dipp}$L)Ae]$_2$ congeners (**Section 5.4**).

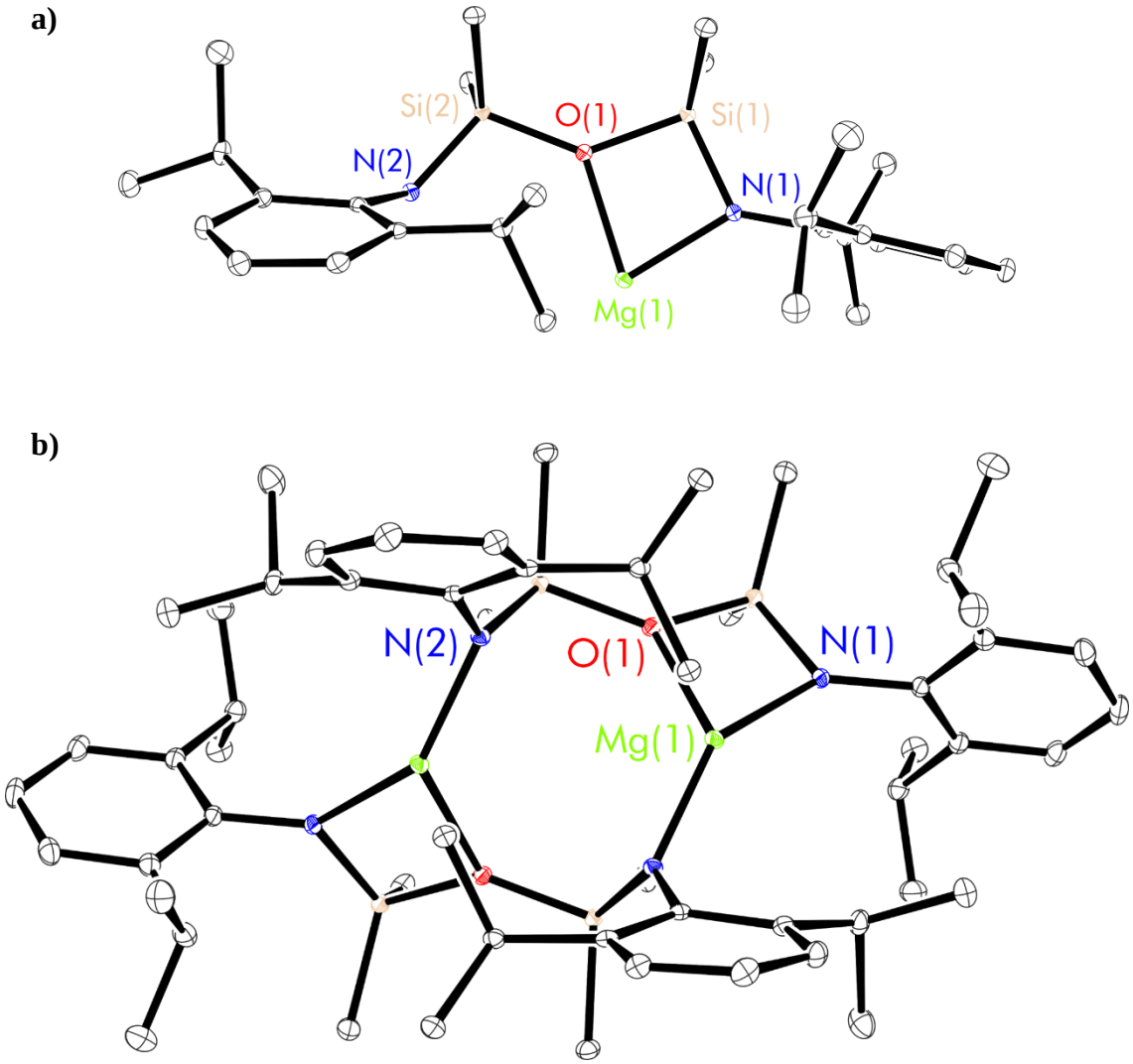


Figure 5.1 Thermal displacement ellipsoid drawing (30% probability) of **a)** asymmetric unit and **b)** full dimeric structure of [($^{NON\text{-}Dipp}$L)Mg]$_2$ (**18**) generated by a (–X+1, Y, –Z+1/2) symmetry operation. All hydrogen atoms have been omitted for clarity.

The central Mg_2N_2 diamond core that is present in the structure of [MgN"$_2$]$_2$ is absent in **18**,[30] rationalising the lack of conversion of the dimeric precursor into **18**. This results in a long Mg-Mg distance of 4.1130(9) Å. It is notable that this separation is significantly longer than the reported range for Mg-Mg bonds in both “neutral” magnesium(I) dimers

(2.971–3.196 Å)[33,34] and the Mg-Mg distance of 3.2124(11) Å in the "anionic" [{($CH_2SiMe_2NDipp)_2Mg$}$Na]_2$ dimer reported by Hill and co-workers (**XLVII**, **Scheme 1.17**).[35] This suggests that significant structural rearrangement may be necessary to accommodate the reduction of **18** (**Section 5.5**).

Table 5.1 Selected metrical parameters (bond lengths in Å, angles in °) of [($^{NON\text{-}Dipp}$L)Mg]$_2$ (**18**).

* refers to symmetry related atoms.

	18
Space group	*C*2/*c*
Mg(1)-N(1)	1.987(1)
Mg(1)-N(2)*	1.999(1)
Mg(1)-O(1)	2.066(1)
Mg(1)-N(2)	3.551(1)
Mg(1)-Mg(1)*	4.1130(9)
N(1)-Mg(1)-N(2)*	143.05(5)
N(1)-Mg(1)-O(1)	76.22(4)
N(2)*-Mg(1)-O(1)	126.25(5)

5.3.1.2 X-ray crystal structures of [{($^{NON\text{-}Dipp}$L)Mg}$_2$(THF)] (18·THF) and [($^{NON\text{-}Dipp}$L)Mg(THF)]$_2$ (18·THF$_2$)

Results obtained in collaboration with Ms. Andrea O'Reilly showed that complexes **18·THF** and **18·THF$_2$** (**Figures 5.2** and **5.3** respectively, **Table 5.2**) both crystallise in the $P2_1/n$ space group. The structure of **18·THF** (**Figure 5.2**) is similar to that of **18**, with the κ^2-N,O-κ^1-N′ coordination mode of the two [$^{NON\text{-}Dipp}$L]$^{2-}$ ligands retained. The coordination geometry at Mg(1) is now tetrahedral (Σ{∠Mg(1)} = 649.68(18)°,

τ_4 = 0.72[36]) due to the coordination of a single equivalent of THF (Mg(1)-O(3) = 2.051(2) Å), while the trigonal planar geometry observed in **1** is retained at Mg(2) ($\Sigma\{\angle$Mg(2)$\}$ = 356.88(13)°). The increased steric congestion that results from the coordination of THF to Mg(1) has resulted in the widening of the central eight-membered $Mg_2N_2Si_2O_2$ metallacycle. This is reflected by an increase of 0.487(1) Å in the Mg-Mg distance in **18·THF** (Mg(1)-Mg(2) = 4.6000(9) Å) relative to **18**. The $Mg_2N_2Si_2O_2$ metallacycle in **18·THF** has a "chair-like" conformation with the two four-membered MgNSiO rings *anti* with respect to one another, in contrast with the "boat-like" structure of **18**. The Mg-N and Mg-O bonds are shorter for Mg(2) than for Mg(1) (**Table 5.2**), reflecting the increased steric congestion that results from the coordination of THF to the latter.

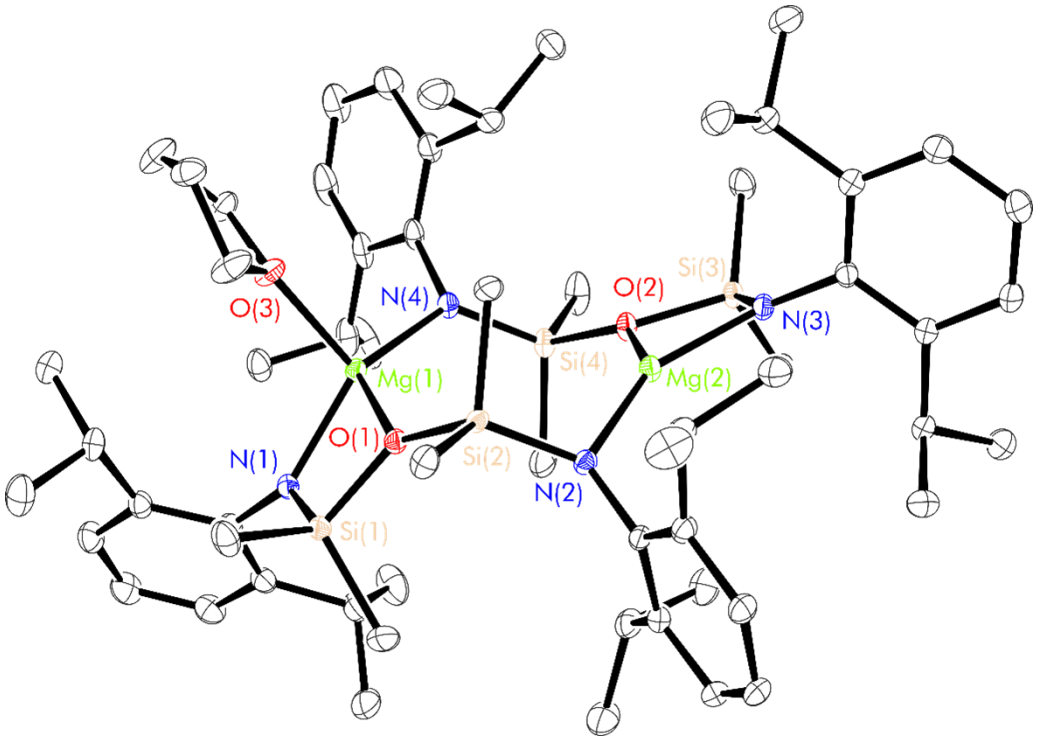


Figure 5.2 Thermal displacement ellipsoid drawing (30% probability) of [{($^{NON\text{-}Dipp}$L)Mg}$_2$(THF)] (**18·THF**). All hydrogen atoms have been omitted for clarity. Produced using data obtained in collaboration with Ms. Andrea O'Reilly.

The structure of **18·THF₂** (**Figure 5.3**) varies significantly relative to those of **18** and **18·THF**. One molecule of THF is coordinated to each Mg^{2+} centre (Mg(1)-O(3) = 2.046(1) Å, Mg(2)-O(4) = 2.018(1) Å). However, while Mg(1) has the same tetrahedral coordination geometry as in **18·THF** ($\Sigma\{\angle Mg(1)\}$ = 650.70(10)°, τ_4 = 0.76[36]), the coordination of THF to Mg(2) has displaced the silylether group (Mg(2)-O(2) = 3.549(1) Å >> Σr_{cov}(Mg,O) = 2.02 Å[32]), resulting in the retention of a trigonal planar coordination geometry ($\Sigma\{\angle Mg(2)\}$ = 357.26(8)°). Consequently, **18·THF₂** consists of a central 10-membered $Mg_2N_3O_2Si_3$ metallacycle. One $[^{NON\text{-}Dipp}L]^{2-}$ ligand retains the κ^2-N,O-κ^1-N′ coordination mode observed exclusively in **18** and **18·THF**, while the other instead bridges between the two Mg centres in an alternative κ^1-N-κ^1-N' manner. This is reminiscent of a report from Hill and co-workers, in which the solvation of

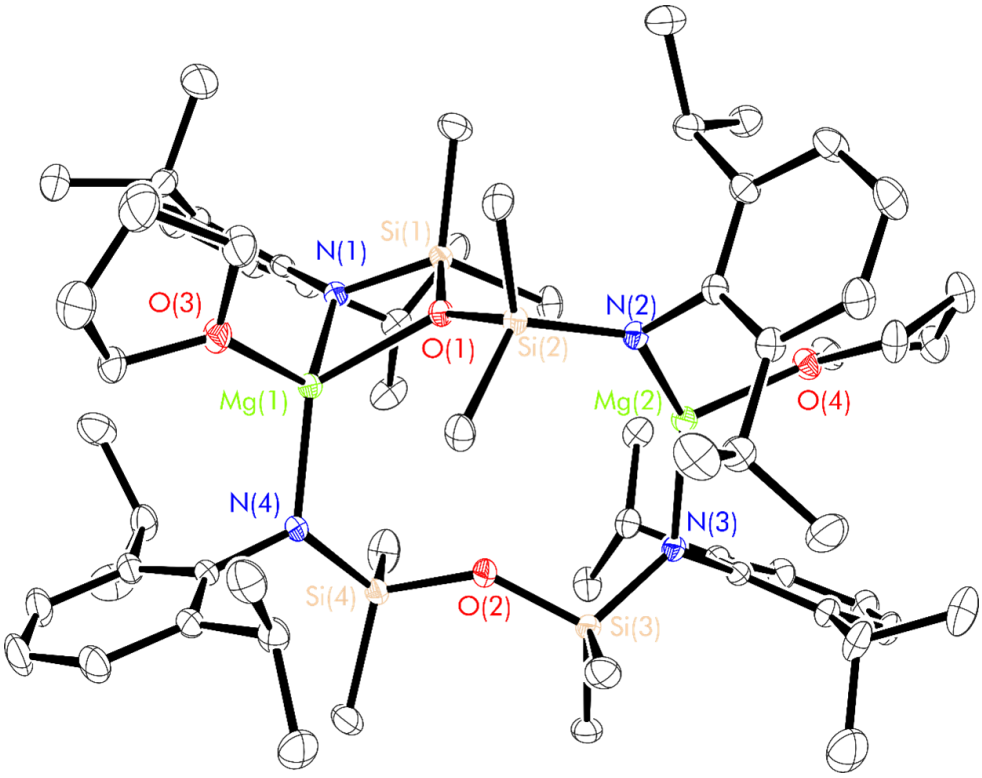


Figure 5.3 Thermal displacement ellipsoid drawing (30% probability) of $[(^{NON\text{-}Dipp}L)Mg(THF)]_2$ (**18·THF₂**). All hydrogen atoms have been omitted for clarity. Produced using data obtained in collaboration with Ms. Andrea O'Reilly.

$[\{(CH_2SiMe_2NDipp)_2Mg\}Na]_2$ resulted in the extrusion of sodium metal and the formation of a 14-membered metallacycle in which two $[(CH_2SiMe_2NDipp)_2]^{2-}$ ligands bridge between two three-coordinate Mg^{2+} centres (**L**, **Scheme 1.18c**).[37] Similar motifs have also been reported for transition metal complexes (Fe, Cr) bearing di(amido)siloxane ligands.[8,38] This rearrangement likely results from the increased steric congestion that occurs upon coordination of a second equivalent of THF to **18·THF**, which is relieved upon the formation of **18·THF$_2$** *via* ring expansion. This is reflected by a Mg(1)-Mg(2) distance in **18·THF$_2$** (5.2386(7) Å) that is 0.639(1) Å longer than that of **18·THF**.

Table 5.2 Selected bond lengths (in Å) in $[\{(^{NON\text{-}Dipp}L)Mg\}_2(THF)]$ (**18·THF**) and $[(^{NON\text{-}Dipp}L)Mg(THF)]_2$ (**18·THF$_2$**). Data obtained in collaboration with Ms. Andrea O'Reilly.

	18·THF	**18·THF$_2$**
Space group	$P2_1/n$	$P2_1/n$
Mg(1)-N(1)	2.035(2)	2.0626(9)
Mg(1)-N(4)	2.019(2)	2.000(1)
Mg(1)-O(1)	2.128(2)	2.133(1)
Mg(1)-O(3)	2.051(2)	2.046(1)
Mg(2)-N(3)	1.950(2)	1.992(1)
Mg(2)-N(2)	1.969(2)	2.003(1)
Mg(2)-O(2)	2.040(2)	3.549(1)
Mg(2)-O(4)	-	2.018(1)
Mg(1)-Mg(2)	4.6000(9)	5.2386(7)

5.3.2 NMR spectroscopic analysis

Complex **18** dissolves fully in THF, enabling the recording of NMR spectra at 25 °C. An initial ^{1}H NMR spectrum recorded prior to heating (**Figure 5.4a**) has an aromatic region consisting of a doublet (δ = 6.94 ppm) and triplet (δ = 6.74 ppm). These two signals are mutually coupled ($^{3}J_{H\text{-}H}$ = 7.5 Hz) and are respectively assigned as the *meta* and *para* protons of the phenyl rings of the Dipp groups. While a single broad methine resonance (δ = 4.08 ppm) is also clear, the extremely broad and overlapping signals observed in the lower frequency methyl region are more challenging to confidently assign. This suggests that **18** has a highly fluxional dimeric solution-phase structure when dissolved in THF, in which it is assumedly solvated to form **18·THF$_2$**. It is also possible that an equilibrium between **18·THF$_2$** and **18·THF** further contributes to the observed signal broadening.

However, heating a THF solution of **18** at 80 °C for 16 hours results in the consumption of the broad resonances observed prior to heating. A ^{1}H NMR spectrum recorded subsequently consists of a mutually coupled ($^{3}J_{H\text{-}H}$ = 7.5 Hz) doublet and triplet (δ = 6.88 and 6.62 ppm respectively), a sharp methine heptet (δ = 4.09 ppm) and a single sharp $SiMe_2$ singlet (δ = 0.12 ppm). In addition, two distinct *iso*propyl methyl doublets (δ = 1.19 and 1.09 ppm) each integrating to twelve are also present. Furthermore, two *iso*propyl methyl signals (δ = 26.5 and 26.1 ppm) are present in the corresponding ^{13}C{^{1}H} NMR spectrum, while the corresponding ^{29}Si NMR spectrum contains a single sharp singlet (δ = –14.75 ppm). Together, these spectra imply the conversion of the dimeric species **18**/**18·THF**/**18·THF$_2$** into the monomeric THF adduct [($^{NON\text{-}Dipp}$L)Mg(THF)$_2$] (**III**, **Chart 5.1**), for which very similar NMR spectra recorded in C_6D_6 have been reported.[17] The previously reported X-ray crystal structure of **III** (**Figure 5.7a**) exhibits a square pyramidal coordination geometry at Mg^{2+} with a THF ligand in

the apical position. This is consistent with the observed asymmetry of the *iso*propyl methyl groups in solution, which assumedly results from restricted rotation of the Dipp groups.

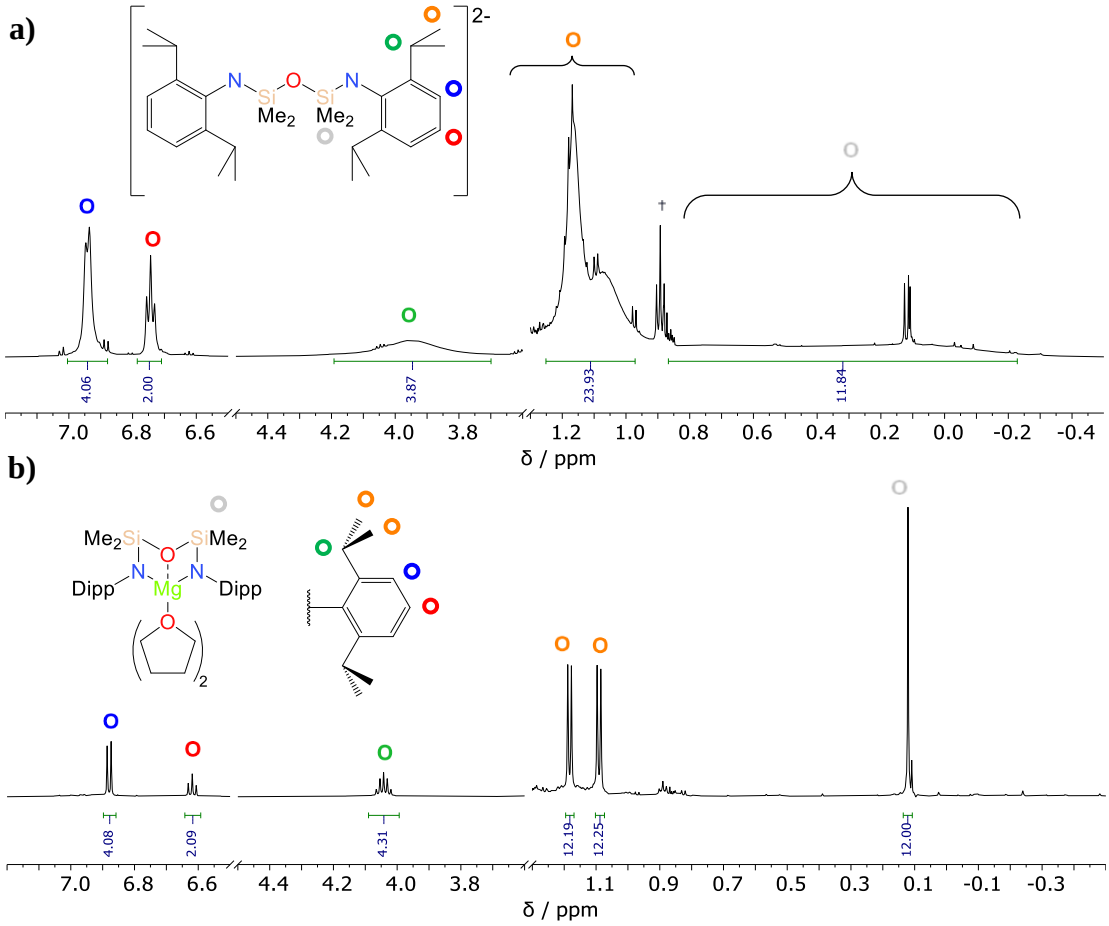


Figure 5.4 ^{1}H NMR spectra (C_4D_8O, 298 K, 600 MHz) of [($^{NON\text{-}Dipp}$L)Mg]$_2$ (**18**) after

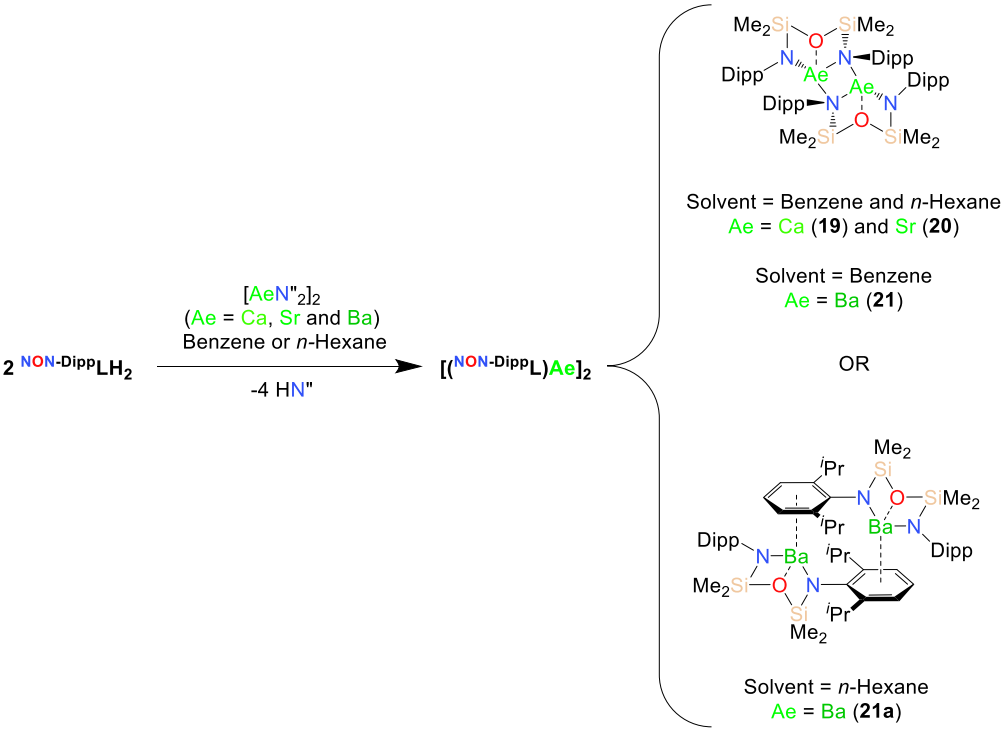
a) 10 minutes at room temperature and **b)** heating for 16 hours at 80 °C in THF-d_8. † denotes *n*-hexane.

Complex **18** is poorly soluble in hydrocarbons, preventing the recording of informative NMR spectra of the THF-free dimeric species at room temperature. However, NMR spectra could be recorded in toluene-d_8 at 80 °C. The ^{1}H NMR spectrum (**Figure A.48**) is similar to that recorded at 25 °C in THF-d_8, and consists of two aromatic resonances (δ = 6.96 and 6.85 ppm), an *iso*propyl heptet (δ = 3.57 ppm) and a $SiMe_2$ singlet (δ = 0.39 ppm) which are relatively sharp. However, a very broad signal at δ = 0.39 ppm is also present, and is attributed to the methyl protons of the *iso*propyl

groups. The corresponding $^{13}C\{^{1}H\}$ NMR spectrum (**Figure A.49**) also contains a broadened methyl signal at δ = 24.8 ppm, and is fully consistent with the ^{1}H NMR spectrum. Together, these spectra suggest that **18** has a fluxional solution-phase structure when dissolved in toluene at 80 °C, in contrast with the highly unsymmetrical structure observed in the solid state. While the dimeric structure of **18** is likely retained under these conditions, the rapid reversible exchange of the two nitrogen donors between the two distinct positions observed in the solid state seemingly results in a time-averaged C_{2v}-symmetric spectrum

5.4 Synthesis of calcium, strontium and barium complexes

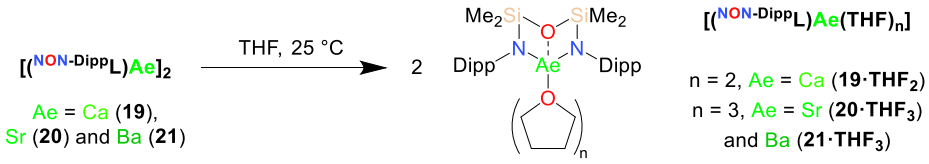
The 2:1 reaction of $^{NON\text{-}Dipp}LH_2$ with $[AeN''_2]_2$ (Ae = Ca, Sr and Ba) in either benzene or *n*-hexane resulted in the formation of the dimeric complexes $[(^{NON\text{-}Dipp}L)Ae]_2$ (Ae = Ca (**19**), 65%, Sr (**20**), 57%, Ba (**21/21a**), 48%; **Scheme 5.5**).



Scheme 5.5 Synthesis of $[(^{NON\text{-}Dipp}L)Ae]_2$ (Ae = Ca (**19**), Sr (**20**) and Ba (**21** and **21a**)) in benzene and *n*-hexane.

All three complexes exhibit dimeric nitrogen-bridged structures when crystallised from benzene (**19**, **20** and **21**). Conversely, while the nitrogen bridged structure is retained when the calcium and strontium congeners are crystallised from *n*-hexane, the barium congener (**21a**) instead crystallises as a weakly associated aryl-bridged dimer.

The dissolution of **19**–**21** in THF results in their instantaneous conversion into the monomeric THF adducts [($^{NON\text{-}Dipp}$L)Ae(THF)$_n$] (n = 2, Ae = Ca (**19·THF$_2$**); n = 3, Ae = Sr (**20·THF$_3$**) and Ba (**21·THF$_3$**)) at 25 °C (**Scheme 5.6**). No intermediate dimeric THF adducts were observed either in the solid state or in solution, in contrast with the magnesium complexes **18·THF** and **18·THF$_2$**.



Scheme 5.6 Conversion of [($^{NON\text{-}Dipp}$L)Ae]$_2$ into the monomeric THF adducts [($^{NON\text{-}Dipp}$L)Ae(THF)$_n$] (n = 2, Ae = Ca (**19·THF$_2$**); n = 3, Ae = Sr (**20·THF$_3$**) and Ba (**21·THF$_3$**)).

5.4.1 X-ray crystallographic analysis

5.4.1.1 X-ray crystal structures of nitrogen-bridged [($^{NON\text{-}Dipp}$L)Ae]$_2$ (Ae = Ca (19), Sr (20) and Ba (21))

Layering a benzene solution of $^{NON\text{-}Dipp}$LH$_2$ (2 eq.) over a benzene solution of [AeN"$_2$]$_2$ (1 eq., Ae = Ca, Sr and Ba) resulted in the growth of colourless single crystals of **19**–**21** suitable for X-ray diffraction. Complexes **19**–**21** crystallise as largely isostructural nitrogen-bridged dimers in the *C*2/*c* space group (**Figure 5.5**, **Table 5.3**).

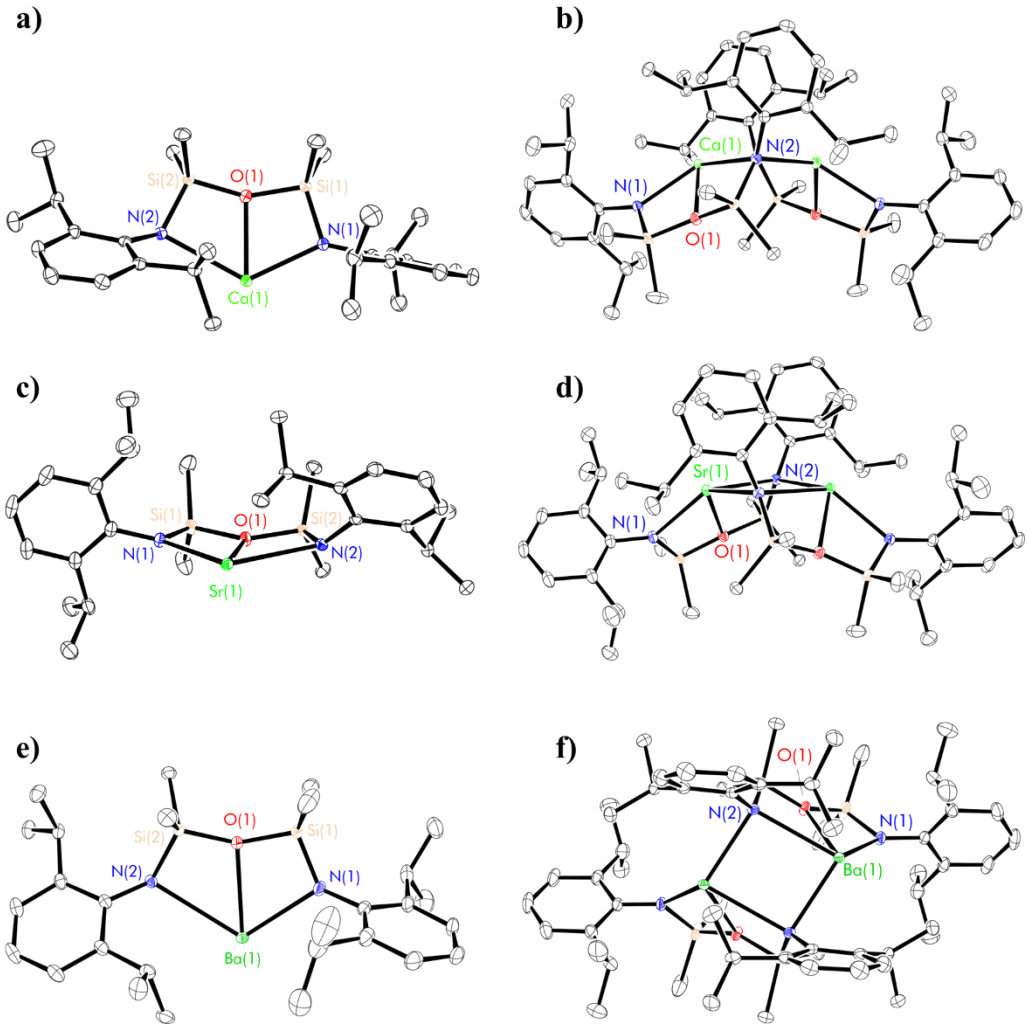


Figure 5.5 Thermal displacement ellipsoid drawings (30% probability) of **a)** asymmetric unit and **b)** full dimeric structure of [($^{NON\text{-}Dipp}$L)Ca]$_2$ (**19**); **c)** asymmetric unit and **d)** full dimeric structure of [($^{NON\text{-}Dipp}$L)Sr]$_2$ (**20**); **e)** asymmetric unit and **f)** full dimeric structure of [($^{NON\text{-}Dipp}$L)Ba]$_2$ (**21**). The full dimeric structures are generated by a (–X+1, Y, –Z+1/2) symmetry operation in each case, All hydrogen atoms have been omitted for clarity.

In all cases the asymmetric unit (**Figure 5.5a**, **c** and **e**) consists of the [$^{NON\text{-}Dipp}$L]$^{2-}$ ligand coordinated to Ae^{2+} in a κ^3-N,O,N′-tridentate manner. This contrasts with the structure of the magnesium congener **18** (**Figure 5.1a**), suggesting that the larger ionic radii of Ca^{2+}, Sr^{2+} and Ba^{2+} facilitate the coordination of an additional bulky amide donor. The Ae-N and Ae-O bonds lengthen with increasing Ae^{2+} size as expected (**Table 5.3**). Coordination

of the silylether donor to Ae^{2+} is consistent with the structure of the magnesium congener **18**, and can be rationalised by considering both the oxophilicity of the heavier congeners and their preference for high coordination numbers. [31,39,40] The resulting six-membered AeN_2Si_2O metallacycle consists of two four-membered AeNSiO rings. These are folded with respect to one another about the Ae-O axis, resulting in an "open-book" conformation. Both the acute fold angle between the two four-membered AeNSiO rings (14.58(4)° (**19**) > 13.04(4)° (**20**) > 8.56(5)° (**21**)) and the N(1)-Ae(1)-N(2) bite angle (126.01(3)° (**19**) > 119.22(3)° (**20**) > 112.61(4)° (**21**)) decrease with increasing Ae^{2+} size as a more planar "open-book" conformation is better accommodated. The wide bite angle of the $[^{NON\text{-}Dipp}L]^{2-}$ ligand in the asymmetric units of **19**–**21** results in highly exposed Ae^{2+} cations, which are further stabilised by dimerisation.

The full pentacyclic dimeric structures (**Figure 5.5b**, **d** and **f**) each consist of two $[(^{NON\text{-}Dipp}L)Ae]$ units bridged by a central Ae_2N_2 ring that has been retained from the $[AeN''_2]_2$ precursors.[41–43] A twofold rotation axis through the Ae_2N_2 centroid confers C_2 symmetry. The two AeN_2Si_2O rings of each asymmetric unit are *syn* with respect to one another beneath the central Ae_2N_2 ring, which the Dipp substituents of the two μ_2-N(2) atoms are projected above. The Ae_2N_2 ring is somewhat puckered, but approaches planarity with increasing Ae^{2+} size (N(2)-Ae(1)-Ae(1)*-N(2)* = 168.54(5)° (**19**) < 172.13(6) (**20**) < 174.02(5)° (**21**)). Two tetrahedral μ_2-N donors, N(2) ($\Sigma\{\angle N(2)\}$ = 653.9(1)° (**19**), 654.2(1)° (**20**), 653.3(2)° (**21**)), bridge between the two four-coordinate Ae^{2+} centres, while the terminal N(1) and O(1) donors are trigonal planar. The coordination geometry at Ae^{2+} is constrained by the chelating ligand, and is best described as a distorted AeN_3 trigonal pyramid that becomes less planar with increasing Ae^{2+} size ($\Sigma\{N\text{-}Ae(1)\text{-}N\}$ = 345.73(6)° (**19**), 337.45(6)° (**20**), 320.70(7)° (**21**)), with the additional

siloxane donor subtending the N(1)-Ae(1)-N(2) bite angle. The bond between Ae^{2+} and the terminal nitrogen donor, N(1), is the shortest in all cases, with the non-bridging Ae(1)-N(2) bond the longest and the bridging Ae(1)-N(2)* bond intermediate between the two (**Table 5.3**). Additional coordinative saturation is provided by the formation of agostic interactions between Ae^{2+} and the isopropyl substituents of the two Dipp groups that are projected above the Ae_2N_2 ring (Ca-H$_{i\text{Pr}}$ = 2.3988(4)–2.7382(3) Å, Sr-H$_{i\text{Pr}}$ = 2.4834(4)–2.8890(3) Å, Ba-H$_{i\text{Pr}}$ = 2.6428(4)–3.1030(3) Å). In addition, the larger Sr^{2+} (**20**) and Ba^{2+} (**21**) cations are further stabilised by respective η^1- and η^2-π-facial interactions with the Dipp substituent of the N(2) donor to which they are coordinated *via* a bridging interaction (Sr(1)-C(17)* = 3.029(1) Å), Ba(1)-centroid$_{C(17),C(18)}$* = 3.077(1) Å). The stabilisation of low-coordinate complexes of the heavier Ae^{2+} cations by agostic and π-facial interactions is consistent with both literature precedent[44,45] and the structures of the 1,8-*bis*(silylamido)naphthalene alkaline earth complexes presented in **Chapters 3** and **4**.

The dimeric structures of **19**–**21** are therefore comparable to that of **18**, with the exception that the accommodation of a four-coordinate geometry by the heavier congeners results in a much shorter Ae(1)-N(2)* distances (2.686(1) Å (**19**) < 2.798(1) Å (**20**) < 2.970(1) Å (**21**) < 3.551(1) Å (**18**)). Consequently, the two Ae^{2+} centres are brought into close proximity by the κ^3-N,O,N′-μ-κ^1-N′ coordination mode of the ligand in the heavier congeners. This results in Ca-Ca (3.7151(8) Å (**19**) and Sr-Sr (3.9504(8) Å (**20**)) distances that are shorter than the Mg-Mg distance (4.1130(9) Å) in **18**, while the Ba-Ba distance (4.1561(8) Å (**21**)) is only slightly longer due to the extremely large ionic radius of Ba^{2+}. While this dimerisation mode has not been previously reported for any complexes of the bulky [$^{\text{NON-Dipp}}$L]$^{2-}$ ligand, related chromium and cobalt dimers bearing

a less bulky *N*-mesityl substituted ligand are known.[1,28] There are also a number of related examples of N-bridged dimers in which the two AeN_2Si_2O rings are *anti* with respect to one another, again supported by di(amido)siloxane ligands with less bulky N-aryl or N-alkyl substituents.[1,5,14,38] Nitrogen-bridged dimeric motifs are also present in various previously reported alkaline earth complexes supported by chelating di(amido) ligands and in complexes **6**–**9** (**Chapter 2**).[46–49]

Table 5.3 Selected metrical parameters (bond lengths in Å, angles in °) in $[(^{NON\text{-}Dipp}L)Ae]_2$ crystallised from benzene (Ae = Mg (**18**), Ca (**19**), Sr (**20**) and Ba (**21**).

* refers to symmetry related atoms.

	18	**19**	**20**	**21**
Space group	*C*2/*c*	*C*2/*c*	*C*2/*c*	*C*2/*c*
Ae(1)-N(1)	1.987(1)	2.340(1)	2.473(1)	2.582(1)
Ae(1)-N(2)	3.551(1)	2.686(1)	2.798(1)	2.970(1)
Ae(1)-N(2)*	1.999(1)	2.3787(9)	2.541(1)	2.714(1)
Ae(1)-O(1)	2.066(1)	2.3494(8)	2.5086(9)	2.672(1)
Ae(1)-Ae(1)*	4.1130(9)	3.7151(8)	3.9504(8)	4.1561(8)
N(1)-Ae(1)-N(2)	125.62(4)	126.01(3)	119.22(3)	112.61(4)
N(1)-Ae(1)-N(2)*	143.05(5)	134.41(4)	133.79(4)	122.09(4)
N(2)-Ae(1)-N(2)*	86.69(4)	85.31(3)	84.44(3)	86.00(4)

5.4.1.2 X-ray crystal structure of aryl-bridged $[(^{NON\text{-}Dipp}L)Ba]_2$ (21a)

Complexes **19–21** were targeted with a view to assessing their suitability as precursors for the synthesis of novel low-valent alkaline earth complexes. However, **19**–**21** each

co-crystallise with a single molecule of benzene, which could not be removed *in vacuo*. Previous literature reports have demonstrated that the high reactivity of low-valent alkaline earth complexes can result in the reduction of benzene to form "low-valent synthons" containing the $[C_6H_6]^{2-}$ dianion, precluding the isolation of true low-valent species (see **Sections 1.3** and **1.5**).[50–52] Consequently, the isolation of benzene-free analogues of **19**–**21** was targeted. Layering a *n*-hexane solution of $^{NON\text{-}Dipp}LH_2$ (2 eq.) over an *n*-hexane solution of $[AeN"_2]_2$ (Ae = Ca, Sr and Ba) resulted in the growth of colourless crystals of **19**, **20** and **21a** suitable for X-ray diffraction.

The calcium and strontium congeners **19** and **20** crystallise from *n*-hexane with structures that are isostructural with those obtained from benzene, so will not be discussed further. However, the barium congener **21a** was found to crystallise as large blocks, rather than the thin plates that **19**–**21** crystallise as. X-ray crystallographic analysis confirmed this macroscopic variance resulted from a change in molecular structure. While **21a** also crystallises as a C_2-symmetric dimer in the *C*2/*c* space group, dimerisation now occurs *via* two Ba^{2+}-aryl η^5-π-facial interactions (**Figure 5.6**, **Table 5.4**).

The Ae_2N_2 ring present in **19**–**21** has been broken, resulting in marked increases in both the Ba(1)-N(2)* (2.714(1) Å (**21**) vs 3.702(2) Å (**21**)) and Ba-Ba (4.1561(8) Å (**21**) vs 4.7644(6) Å (**21a**)) distances, as well as a shortening of the Ba(1)-centroid$_{C(17)\text{-}C(22)}$* distance (3.920(1) Å (**21**) vs 2.862(1) Å (**21a**)) and planarisation of the otherwise tetrahedral nitrogen donor ($\Sigma\{\angle N(2)\}$ = 653.3(2)° (**21**) vs 358.8(2)° (**21a**)). While no other $[^{NON\text{-}Dipp}L]^{2-}$ complexes have been reported to dimerise in this manner, related ligands with less bulky 2,6-dimethylphenyl substituents have been shown to support similar aryl-bridged Pb(II) and Sn(II) dimers.[14] That Ba^{2+} interacts with an aryl ring instead of an additional "hard" amide donor in this case reflects its greater size,

electropositivity and consequent preference for "soft" multihaptic π-facial interactions that provide greater coordinative saturation,[39] and is consistent with the structures of the 1,8-*bis*(silylamido)naphthalene barium complexes **9** and **11** (**Chapter 3**).

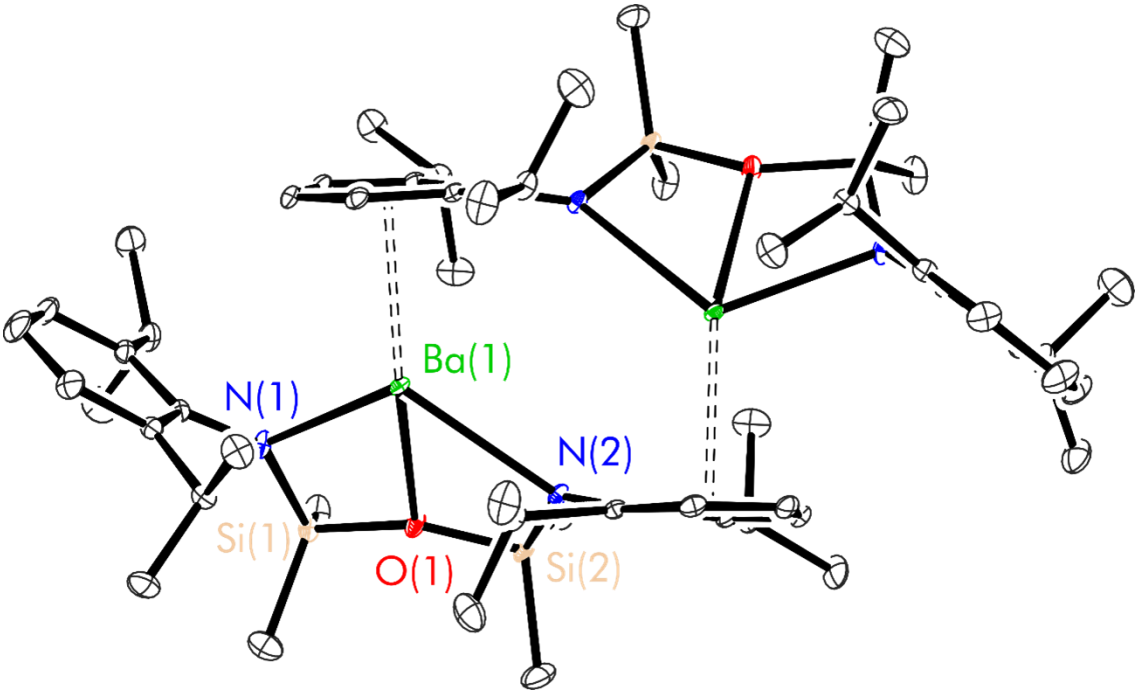


Figure 5.6 Thermal displacement ellipsoid drawing (30% probability) of the aryl-bridged complex [($^{NON\text{-}Dipp}$L)Ba]$_2$ (**21a**) generated by a (–X+1, Y, –Z +3/2) symmetry operation. All hydrogen atoms have been omitted for clarity.

Besides the change in the hybridisation state of N(2) (*vide supra*), the asymmetric unit of **21** shows little variation from that of **21a**, with the κ^3-N,O,N′-tridnetate coordination mode of [$^{NON\text{-}Dipp}$L]$^{2-}$ to Ba^{2+} retained. However, there are small but significant decreases in the Ba(1)-N(1) (2.5821(1) Å (**21**), 2.569(2) Å (**21a**)), Ba(1)-N(2) (2.970(1) Å (**21**), 2.799(1) Å (**21a**)) and Ba(1)-O(1) (2.672(1) Å (**21**), 2.651(1) Å (**21a**)) bond lengths, reflecting the reduced steric congestion at Ba^{2+} that results from the exchange of the bulky amide donor for the aryl π-system. Notably, the structure of **21a** does not contain any co-crystallised *n*-hexane, with its absence from isolated samples confirmed by NMR spectroscopy and elemental analysis. Furthermore, the presence of a η^2-π-facial

interaction in the structure of **21** suggests that there is little difference in energy with the "slipped" η^5- structure of **21a**. Together, this suggests that the variation in dimerisation mode between **21** and **21a** likely results from changes in crystal packing forces.

Table 5.4 Selected metrical parameters (bond lengths in Å, angles in °) in $[(^{NON\text{-}Dipp}L)Ba]_2$ crystallised from *n*-hexane (**21a**). * refers to symmetry related atoms.

	21a
Ae(1)-N(1)	2.569(2)
Ae(1)-N(2)	2.799(1)
Ae(1)-N(2)*	3.702(2)
Ae(1)-O(1)	2.651(1)
$Ae(1)\text{-}Centroid_{C(17)\text{-}C(22)}$*	2.862(1)
Ae(1)-Ae(1)*	4.7644(6)
N(1)-Ae(1)-N(2)	114.57(5)
$N(1)\text{-}Ae(1)\text{-}Centroid_{C(17)\text{-}C(22)}$*	112.49(4)
$N(2)\text{-}Ae(1)\text{-}Centroid_{C(17)\text{-}C(22)}$*	128.01(3)

5.4.1.3 X-ray crystal structures of $[(^{NON\text{-}Dipp}L)Ae(THF)_n]$

Results obtained in collaboration with Ms. Andrea O'Reilly showed that the slow evaporation of THF solutions of **19**–**21** at 25 °C affords colourless crystals of the monomeric THF adducts $[(^{NON\text{-}Dipp}L)Ae(THF)_n]$ (n = 2, Ae = Ca (**19·THF$_2$**); n = 3, Ae = Sr (**20·THF$_3$**) and Ba (**21·THF$_3$**)) suitable for X-ray diffraction studies. Complexes **19·THF$_2$**, **20·THF$_3$** and **21·THF$_3$** crystallise in the $P2_1/c$, $P2_1$ and $Pca2_1$ space groups respectively (**Figure 5.7**, **Table 5.5**).

The structure of **19·THF$_2$** (**Figure 5.7b**) is very similar to that of the previously reported magnesium congener [($^{NON\text{-}Dipp}$L)Mg(THF)$_2$] (**Figure 5.7a**).[17] In both cases, two THF molecules are coordinated to a five-coordinate Ae^{2+} cation with a distorted trigonal-bipyramidal coordination geometry (τ_5 = 0.70 (**III**), 0.82 (**19·THF$_2$**)).[53] The axial positions are occupied by one THF molecule and the siloxane tether, while the equatorial plane comprises the second THF molecule and the two amide donors of a [$^{NON\text{-}Dipp}$L]$^{2-}$ ligand that is coordinated in a κ^3-N,O,N′-tridentate manner.

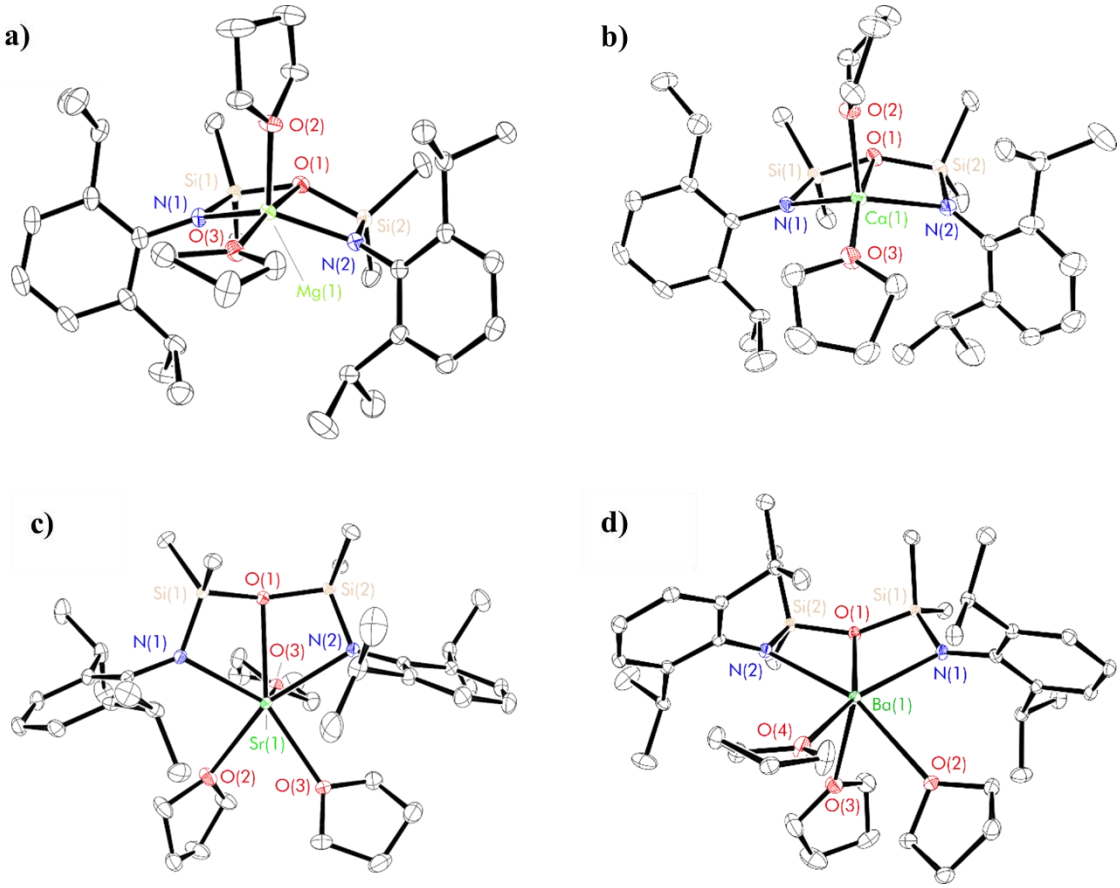


Figure 5.7 Thermal displacement ellipsoid drawings (30% probability) of **a)** [($^{NON\text{-}Dipp}$L)Mg(THF)$_2$], **b)** [($^{NON\text{-}Dipp}$L)Ca(THF)$_2$] (**19·THF$_2$**), **c)** [($^{NON\text{-}Dipp}$L)Sr(THF)$_3$] (**20·THF$_3$**) and **d)** [($^{NON\text{-}Dipp}$L)Ba(THF)$_3$] (**21·THF$_3$**). All hydrogen atoms have been omitted for clarity. a) produced using data published in reference 17, b), c) and d) produced using data obtained in collaboration with Ms. Andrea O'Reilly.

Conversely, the structures of **20·THF$_3$** and **21·THF$_3$** each exhibit an additional coordinated THF molecule, resulting in six-coordinate Sr^{2+} and Ba^{2+} centres with pentagonal pyramidal coordination geometries. In both cases the apical position is occupied by a THF molecule, with the equatorial plane occupied by two additional THF molecules and a $[^{NON\text{-}Dipp}L]^{2-}$ ligand coordinated in a κ^3-N,O,N′-tridentate manner.

The coordination of an additional equivalent of THF by the heavier Ae^{2+} congeners is accommodated by their large ionic radii, and is consistent with previously reported monomeric alkaline earth THF adducts supported by chelating diamido ligands.[54–57] The Ae-N and Ae-O bonds lengthen while the N(1)-Ae(1)-N(2) bite angle contracts with increasing Ae^{2+} ionic radius (**Table 5.5**).

Table 5.5 Selected metrical parameters (bond lengths in Å, angles in °) in [($^{NON\text{-}Dipp}$L)Ae(THF)$_n$] (n = 2, Ae = Mg (**III**)[16] and Ca (**19·THF$_2$**); n = 3, Ae = Sr (**20·THF$_3$**) and Ba (**21·THF$_3$**). Metrics for **III** reproduced from reference 17, metrics for **19·THF$_2$**, **20·THF$_3$** and **21·THF$_3$** obtained in collaboration with Ms. Andrea O'Reilly.

	III[17]	**19·THF$_2$**	**20·THF$_3$**	**21·THF$_3$**
Space group	$P2_12_12_1$	$P2_1/c$	$P2_1$	$Pca2_1$
Ae(1)-N(1)	2.040(2)	2.313(1)	2.564(2)	2.619(2)
Ae(1)-N(2)	2.041(2)	2.285(1)	2.507(3)	2.676(3)
Ae(1)-O(1)	2.308(2)	2.490(1)	2.627(2)	2.889(3)
Ae(1)-O(2)	2.065(2)	2.337(1)	2.557(4)	2.838(3)
Ae(1)-O(3)	2.047(2)	2.323(1)	2.510(3)	2.689(2)
Ae(1)-O(4)	-	-	2.591(2)	2.772(3)
N(1)-Ae(1)-N(2)	129.1(1)	119.59(5)	114.48(8)	109.33(8)

Notably, no intermediate dimeric THF adducts analogous to **18·THF** and **18·THF$_2$** crystallised from THF solutions of **19**–**21**. This is likely due to the similarities between the [($^{NON\text{-}Dipp}$L)Ae] units of the dimeric species **19**–**21** and their monomeric analogues [($^{NON\text{-}Dipp}$L)Ae(THF)$_n$], which both feature the coordination of the [$^{NON\text{-}Dipp}$L]$^{2-}$ ligand in a κ^3-N,O,N′-tridentate manner. Consequently, little structural rearrangement is required upon the coordination of THF, which readily outcompetes the Ae-N and π-facial interactions that facilitate the dimerisation of **19**–**21** in the absence of the strong donor solvent. Conversely, conversion of **18** into its monomeric analogue **III** requires a more significant structural rearrangement due to the alternative κ^2-N,O-κ^1-N′ coordination mode of the ligand in the former. In addition, the smaller ionic radius of Mg^{2+} results in significantly reduced kinetic lability relative to the heavier Ae^{2+} congeners.[58] Consequently, a higher temperature of 80 °C is required to disrupt the dimeric structure of **18**, which instead forms the stable dimeric intermediates **18·THF** and **18·THF$_2$** at 25 °C, in contrast with the heavier congeners **19–21** which are readily converted to monomers at lower temperatures.

5.4.2 NMR spectroscopic analysis

The dimeric complexes **19**–**21** are poorly soluble in non-donor solvents, precluding a direct assessment of their solution-phase structures. However, their high solubility in THF enabled the recording of informative NMR spectra corresponding to the analogous monomeric THF adducts [($^{NON\text{-}Dipp}$L)Ae(THF)$_n$] that form in solution (*vide supra*). The ^{1}H NMR spectrum of the barium congener **21b** in THF-d_8 (in which it is converted to **21·THF$_3$**) is presented as a representative example (**Figure 5.8**). The spectrum consists of five signals, corresponding to the *meta* (δ = 6.80 ppm, d, 4H) and *para* (δ = 6.39 ppm, t, 2H) protons of the aryl ring, the methine (δ = 3.97 ppm, sept, 4H) and methyl

(δ = 1.12 ppm, d, 24H) protons of the isopropyl substituents and the silylmethyl protons (δ = 0.10 ppm, s, 12H) of the tetramethylsiloxane backbone. No amino singlet is observed, confirming the full deprotonation of the $[^{NON\text{-}Dipp}L]^{2-}$ ligand. This is consistent with the absence of N-H absorbances in IR spectra of solid samples of **19**–**21**. Furthermore, the corresponding $^{13}C\{^{1}H\}$ NMR spectrum consists of four aromatic (δ = 152.4, 141.6, 123.1 and 115.6 ppm) and three alkyl (δ = 27.5, 26.0 and 5.5 ppm) signals, while the ^{29}Si NMR spectrum contains a single signal at δ = –26.22 ppm. The corresponding NMR spectra of **19** and **20** in THF-d_8 vary little with respect to those of **21**, and only differ due to minor variations of the chemical shifts of signals that are consistently present in each. Notably, the chemical shift of the ^{29}Si NMR singlet shifts to progressively lower frequencies as Ae^{2+} size increases (δ_{Mg} = –14.75 ppm > δ_{Ca} = –19.77 ppm > δ_{Sr} = –23.74 ppm > δ_{Ba} = –26.22 ppm). This can be attributed to the more ionic bonding of the heavier congeners, which results in more electron density being retained by the $[^{NON\text{-}Dipp}L]^{2-}$ ligand. Consequently, the silicon atoms are better shielded due to enhanced negative hyperconjugation with the lone pairs of the ligand's

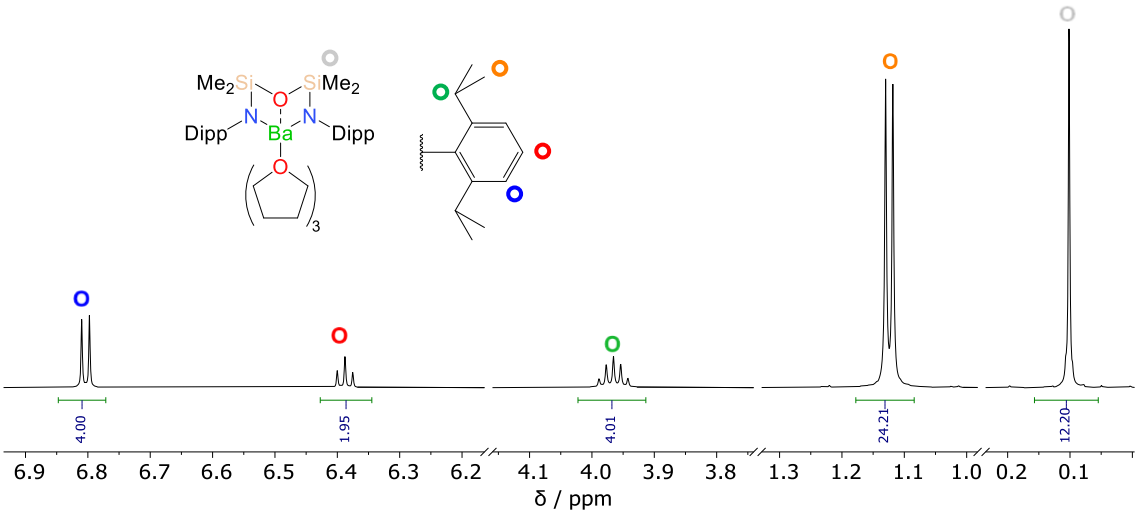


Figure 5.8 ^{1}H NMR spectrum (C_4D_8O, 298 K, 600.4 MHz) of $[(^{NON\text{-}Dipp}L)Ba]_2$ (**21a**) in THF-d_8, in which it exists as the monomeric THF adduct $[(^{NON\text{-}Dipp}L)Ba(THF)_3]$ (**21·THF**$_3$).

donor atoms. This trend is consistent with those observed for the monomeric THF adducts [(^{R3}L)Ae(THF)$_n$] discussed in **Chapters 3** and **4**.

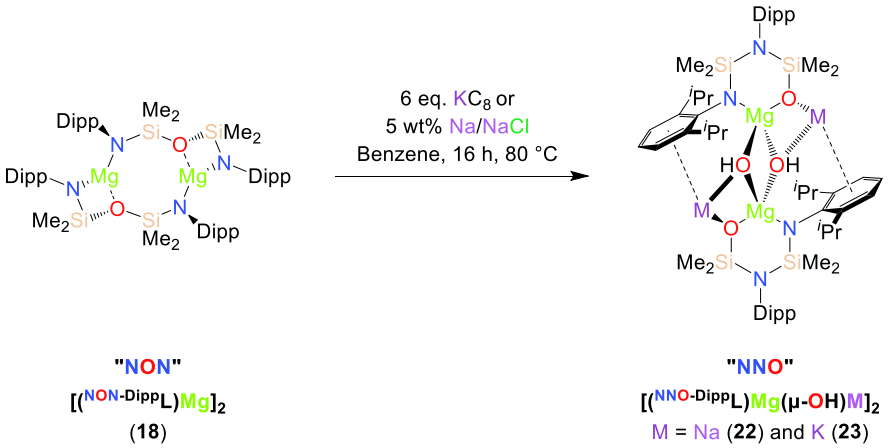
Together, these spectra confirm the conversion of the dimeric species **19**–**21** into monomeric THF adducts with *C*2$_v$-symmetric solution-phase structures when dissolved in THF at 25 °C, and are very similar to the corresponding spectra of [($^{NON\text{-}Dipp}$L)Mg(THF)$_2$] in THF-d_8 (**Figure 5.4b**). However, only a single *iso*propyl methyl doublet integrating to 24 is present in the ^{1}H NMR spectra of **19**–**21**, in contrast with the two doublets each integrating to 12 in the spectrum of the magnesium congener. No splitting of this doublet was observed for the heavier congeners even in spectra recorded at –80 °C. This reflects the greater kinetic lability of the larger Ae^{2+} cations, which results in greater fluxionality in solution and the loss of any asymmetry that is observed on the NMR timescale for [($^{NON\text{-}Dipp}$L)Mg(THF)$_2$].

5.5 Attempted synthesis of low-valent alkaline earth complexes

5.5.1 Synthesis of [($^{NNO\text{-}Dipp}$L)Mg(μ-OH)M]$_2$ (M = Na (22) and K (23))

The conversion of [($^{NON\text{-}Dipp}$L)Mg]$_2$ into low-valent species was targeted. One equivalent of **18** was reacted with six equivalents of either 5 wt% Na/NaCl or KC_8 in benzene, with the poor arene solubility of the **18** necessitating a temperature of 80 °C (**Scheme 5.7**). After stirring for 16 hours, the reaction mixtures were filtered and left to stand for three days at 25 °C. This reproducibly resulted in the growth of small colourless crystals of [($^{NNO\text{-}Dipp}$L)Mg(μ-OH)M]$_2$ (M = Na (**22**) and K (**23**)). Notably, the "NON" ligand present in **18** has rearranged into a "NNO" form in **22** and **23**. This is highly reminiscent of previous reports from Leznoff and co-workers describing the rearrangement of di(amido)siloxane dilithium salts (**Chart 5.2a**),[28] as well as a very recent report from

Coles and co-workers detailing the conversion of K[($^{NON\text{-}Dipp}$L)Al{$CH_2CH_2C(N^iPr)_2$}] into K[($^{NNO\text{-}Dipp}$L)Al{$CH_2CH_2C(N^iPr)_2$}] (**IV** and **V** respectively, **Chart 5.2b**).[59] While the attempted reduction of **18** has successfully introduced two alkali metal cations into the dimeric structures of **22** and **23**, the Mg^{2+} cations have not been reduced. Instead, charge balance is provided by two bridging hydroxide anions. Complexes **22** and **23** were characterised by X-ray diffraction and NMR spectroscopy.



Scheme 5.7 Conversion of [($^{NON\text{-}Dipp}$L)Mg]$_2$ (**18**) to [($^{NNO\text{-}Dipp}$L)Mg(μ-OH)M]$_2$ (M = Na (**22**) and K (**23**)).

5.5.2 Attempted reduction of [($^{NON\text{-}Dipp}$L)Ae]$_2$ (Ae = Ca (19), Sr (20) and Ba (21)).

The attempted reduction of [($^{NON\text{-}Dipp}$L)Ae]$_2$ (Ae = Ca (**19**), Sr (**20**) and Ba (**21**)) was inconclusive. While the poor solubility of **19**–**21** in hydrocarbons hindered their solution-phase reactivity, their reactions with both KC_8 and 5 wt% K/KI in benzene were attempted (**Scheme 5.8**). This resulted in the reaction mixture changing colour from colourless to brown. ^{1}H NMR spectra of the reaction mixtures recorded in C_6D_6 consisted of the five proton environments expected for the [$^{NON\text{-}Dipp}$L]$^{2-}$ ligand, thus demonstrating the selective formation of new species which have improved arene solubility relative to **19**–**21**. Notably, no evidence was found for the formation of "NNO" fragments, in contrast with the analogous reactions of the magnesium congener (*vide infra*). Furthermore, the addition of benzophenone to the reaction mixtures (following the

exclusion of excess reducing agent *via* filtration) resulted in the formation of blue solutions, suggesting that the reaction mixture may consist of stable species capable of reductive reactivity.[60] Unfortunately, no products could be isolated or crystallographically characterised.



Scheme 5.8 Inconclusive results obtained following the attempted reductions of [($^{NON\text{-}Dipp}$L)Ae]$_2$ (Ae = Ca (**19**), Sr (**20**) and Ba (**21**)) with potassium reducing agents in C_6D_6.

5.5.3 X-ray crystallographic analysis

Complexes **22** and **23** crystallise in the $P2_1/n$ and $P2_1/c$ space groups respectively (**Figure 5.9**, **Table 5.6**). As they have very similar structures, metrical parameters from **22** are discussed as a representative example. The asymmetric unit consists of a single [($^{NNO\text{-}Dipp}$L)Mg(μ-OH)Na] fragment, with the full pentacyclic dimeric structure generated by inversion. This motif results from the coordination of each magnesium cation by two [μ_3-OH]$^-$ anions. The two distinct Mg-O(H) bond lengths (1.980(1) Å and 1.991(1) Å) are similar to those reported for related dimeric molecular magnesium hydroxides supported by chelating anionic ligands (1.891(1)–1.982(1) Å).[61–66] The magnesium centres are also chelated by a mixed amide/alkoxide [$^{NNO\text{-}Dipp}$L]$^{2-}$ ligand in a κ^2-N,O-bidentate manner (Mg(1)-N(1) = 1.998(1) Å, Mg(1)-O(1) = 1.920(1) Å, N(1)-Mg(1)-O(1) = 112.88(5)°). No dative interaction is formed between Mg^{2+} and the nitrogen donor of the bulky DippN(SiMe$_2$)$_2$ group (Mg(1)-N(2) = 3.281(1) Å > Σr_{cov}(Mg,N) = 2.10 Å[32]). This is consistent with previously reported structures containing "NNO" ligands of this type,[28,29] and contrasts with the coordination of the less hindered siloxane tether exhibited by **18**–**21**. This results in magnesium adopting a four-coordinate

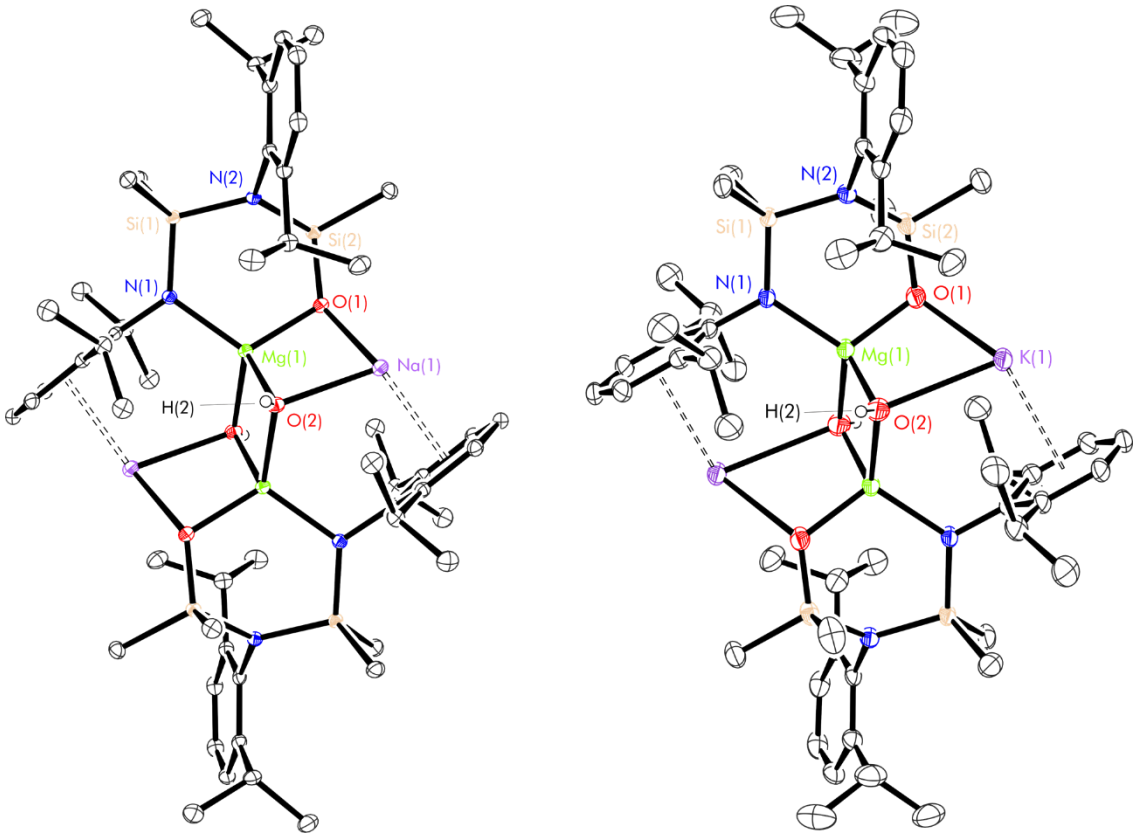


Figure 5.9 Thermal displacement ellipsoid drawings (30% probability) of **a)** [($^{NNO\text{-}Dipp}$L)Mg(μ-OH)Na]$_2$ (**22**) and **b)** [($^{NNO\text{-}Dipp}$L)Mg(μ-OH)K]$_2$ (**23**). The full dimeric structures are generated by a (–X+1, –Y+1, –Z+1) symmetry operation in each case. All non-hydroxyl protons have been omitted for clarity.

tetrahedral coordination geometry ($\Sigma\{\angle Mg(1)\}$ = 654.0(1)°, τ_4 = 0.81[36]). The μ_2-O alkoxide donor of the [$^{NNO\text{-}Dipp}$L]$^{2-}$ ligand also coordinates to Na^+ in a κ^1-O-monodentate manner (Na(1)-O(1) = 2.221(1) Å), with the Na^+ cation also coordinated by a proximal hydroxide anion (Na(1)-O(2)* = 2.399(1) Å). The [μ_3-OH]$^-$ anions consequently bridge between one sodium and two magnesium cations, resulting in a tricyclic $Mg_2Na_2O_4$ "ladder". This consists of a central planar Mg_2O_2 diamond core as well as two four-membered MgO_2Na rings, which are necessarily antiparallel with respect to one another and are tilted relative to the former (O(1)-Mg(1)-O(2) = 119.47°(4), Na(1)-O(2)-Mg(1) = 107.95(5)°). This results in the full eight-membered metallacycle adopting a "chair" conformation.

Table 5.6 Selected metrical parameters (bond lengths in Å, angles in °) in [($^{NNO\text{-}Dipp}$L)Mg(μ-OH)M]$_2$ (M = Na (**22**) and K (**23**)). * refers to symmetry related atoms.

a: some atom labels have been changed clarity.

	22	**23**^{a}
Mg(1)-N(1)	1.998(1)	2.023(2)
Mg(1)-O(1)	1.920(1)	1.908(2)
Mg(1)-O(2)	1.980(1)	1.991(2)
Mg(1)-O(2)*	1.991(1)	1.986(2)
M(1)-O(1)	2.221(1)	2.563(2)
M(1)-O(2)*	2.399(1)	2.883(2)
M(1)-Centroid$_{C(1)\text{-}C(6)}$	2.467(1)	2.847(1)
Mg(1)-Mg(1)*	2.9705(7)	2.967(1)
O(2)-O(2)*	2.636(1)	2.649(3)
N(1)-Mg(1)-O(1)	112.88(5)	110.28(9)
O(2)-Mg(1)-O(2)*	83.18(4)	83.53(8)
Mg(1)-O(2)-Mg(1)*	96.82(5)	96.47(9)
Mg(1)-O(1)-M(1)	93.20(4)	100.25(8)
Mg(1)-O(2)-M(1)*	86.24(4)	88.49(7)
O(1)-M(1)-O(2)*	79.83(4)	67.39(6)
O(1)-M(1)-Centroid$_{C(1)\text{-}C(6)}^{*}$	142.46(4)	133.21(5)
O(2)-M(1)-Centroid$_{C(1)\text{-}C(6)}^{*}$	106.23(3)	99.46(5)

In addition, the Na^+ cations also form η^6-π-facial Na^+-aryl interactions with the phenyl ring of the proximal NDipp group (Mg(1)-centroid$_{C(1)\text{-}C(6)}$ = 2.447(1) Å). Further coordinative saturation is provided by agostic interactions with the C-H bonds of

*iso*propylmethyl groups both within each [($^{NNO\text{-}Dipp}$L)Mg(μ-OH)Na]$_2$ molecule and between dimers in the extended structure. While the Mg-Mg distance in **22** (2.9705(7) Å) is significantly shorted relative to that of **18** (4.1130(9) Å), this results from the strong ionic Mg-O interactions formed with the small hydroxide anions, rather than the formation of a Mg(I)-Mg(I) bond. Furthermore, the O-O separation between the two hydroxide anions (2.6363(19) Å) is significantly longer than the longest reported O-O bond in a crystallographically characterised neutral hydrogen peroxide (1.510 Å),[67] thus confirming the Mg^{2+} oxidation state required for charge balance. The protons of the two hydroxide anions were located in the difference map and freely refined, with the alternative presence of either one peroxide (O_2^{2-}) or two oxide (O^{2-}) anions respectively excluded by the long O-O separation and the need for charge balance.

5.5.4 NMR spectroscopic analysis

While the crystallisation of **22** and **23** was reproducible, they could not be isolated in sufficient quantities for further analysis. However, conducting the 6:1 reactions of **18** with 5 wt% Na/NaCl and KC_8 in C_6D_6 enabled the recording of informative NMR spectra of the products **22** and **23** *in situ*. The *in situ* ^{1}H NMR spectrum of **23** is presented as a representative example (**Figure 5.10**). In addition to some unknown signals, this spectrum consists of two distinct sets of Dipp resonances that are fully consistent with the intramolecular rearrangement of the [$^{NON\text{-}Dipp}$L]$^{2-}$ ligand into a [$^{NNO\text{-}Dipp}$L]$^{2-}$ fragment. The corresponding ^{13}C{^{1}H} NMR spectrum also displays signals consistent with the presence of Dipp groups in two distinct chemical environments. Furthermore, the asymmetry of the [$^{NNO\text{-}Dipp}$L]$^{2-}$ ligand is demonstrated by the presence two $SiMe_2$ signals in the ^{1}H (δ = 0.19 and 0.13 ppm), ^{13}C{^{1}H} (4.5 and 4.1 ppm) and ^{29}Si (–13.44 and –14.15 ppm) NMR spectra.

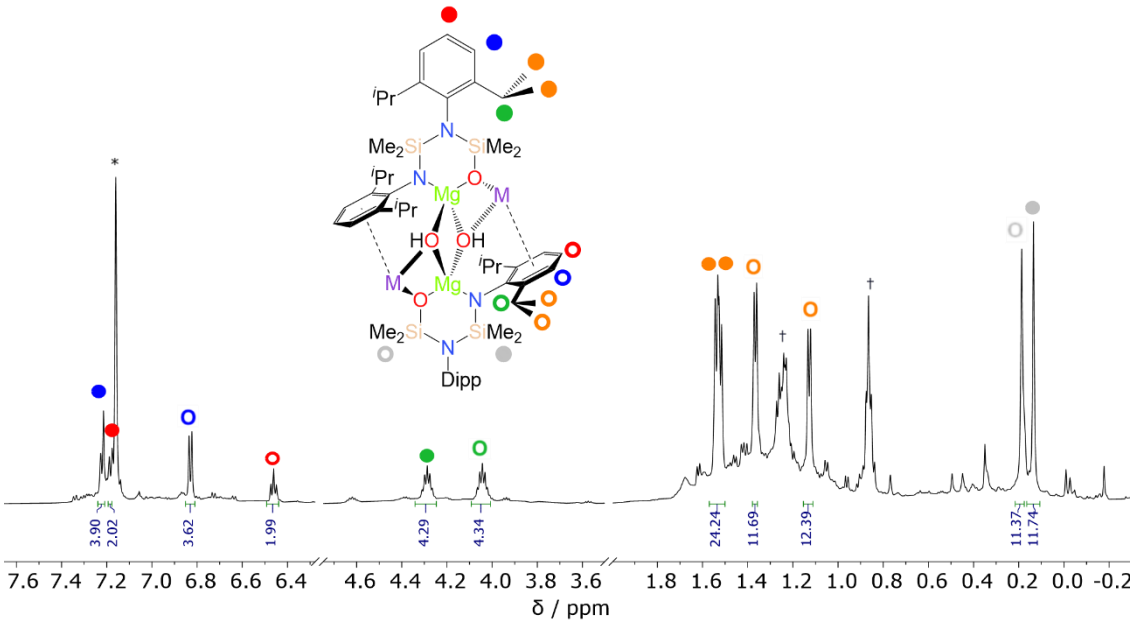


Figure 5.10 ^{1}H NMR spectrum (C_6D_6, 298 K, 600 MHz) of [($^{NNO\text{-}Dipp}$L)Mg(μ-OH)K]$_2$ (**23**) generated *in-situ* by heating 1 eq. of [($^{NON\text{-}Dipp}$L)Mg]$_2$ with 6 eq. KC_8 at 80 °C for 16 hours. † denotes an unknown by-product present in solution, * denotes C_6D_6.

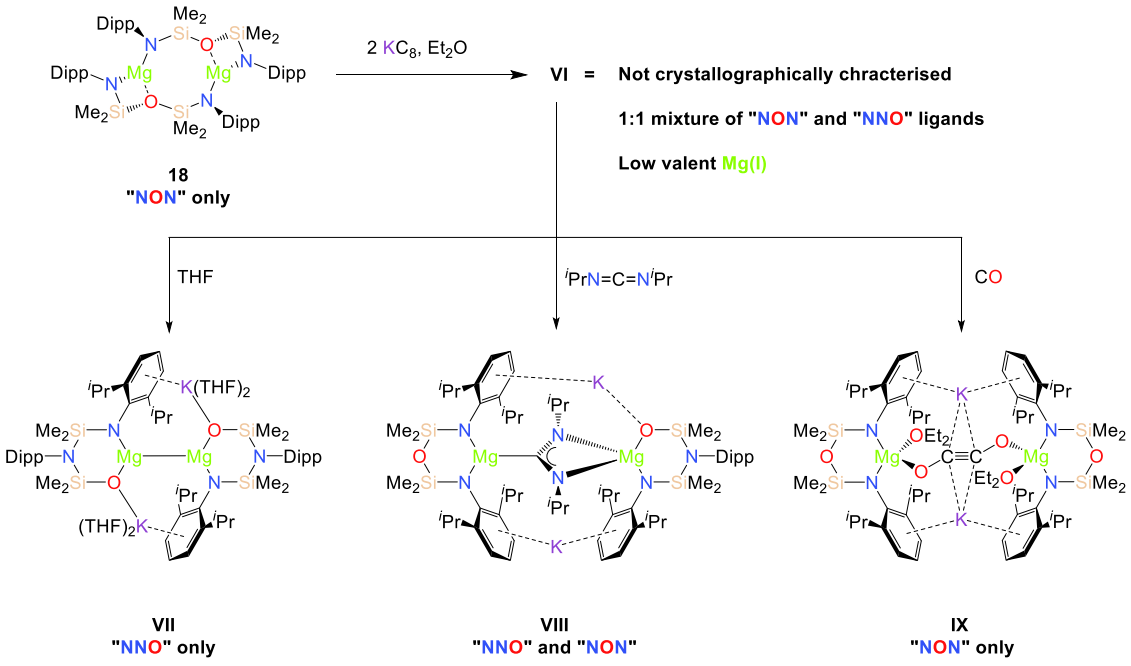
A 2D NOESY spectrum contains cross-peaks between the higher frequency *iso*propyl methyl signals (δ = 1.54 and 1.52 ppm) and both $SiMe_2$ singlets in the ^{1}H NMR spectrum. Conversely, the lower frequency *iso*propyl doublets (δ = 1.37 and 1.13 ppm) each form only one cross-peak with the $SiMe_2$ singlet at 0.13 ppm. The latter was therefore assigned as the N-$SiMe_2$-N group, with the higher frequency $SiMe_2$ singlet at 0.19 ppm consequently assigned as the N-$SiMe_2$-O group. This enabled the confident assignment of the lower and higher frequency *iso*propyl doublets as the methyl protons of the [(Dipp)N$SiMe_2$]$^-$ and [(Dipp)N($SiMe_2$)$_2$] groups respectively, with analysis of additional 2D correlation spectra then enabling the full assignment of the other ^{1}H, ^{13}C{^{1}H} and ^{29}Si NMR signals.

That each of the two Dipp groups produce two distinct *iso*propylmethyl doublets suggests that their rotation is restricted in solution on the NMR timescale. However, the other chemical environments of the [$^{NNO\text{-}Dipp}$L]$^{2-}$ ligand each result in only one ^{1}H NMR signal.

This suggests that the dimeric, centrosymmetric solid-state dimeric structure of **23** is retained in solution. The protons of the hydroxide ligands could not be confidently assigned to any signals in the ^{1}H NMR spectrum. However, the absence of OH resonances in ^{1}H NMR spectra of molecular magnesium hydroxides has been reported previously.[63]

5.5.5 Discussion of 22 and 23 and comparison with low-valent complexes

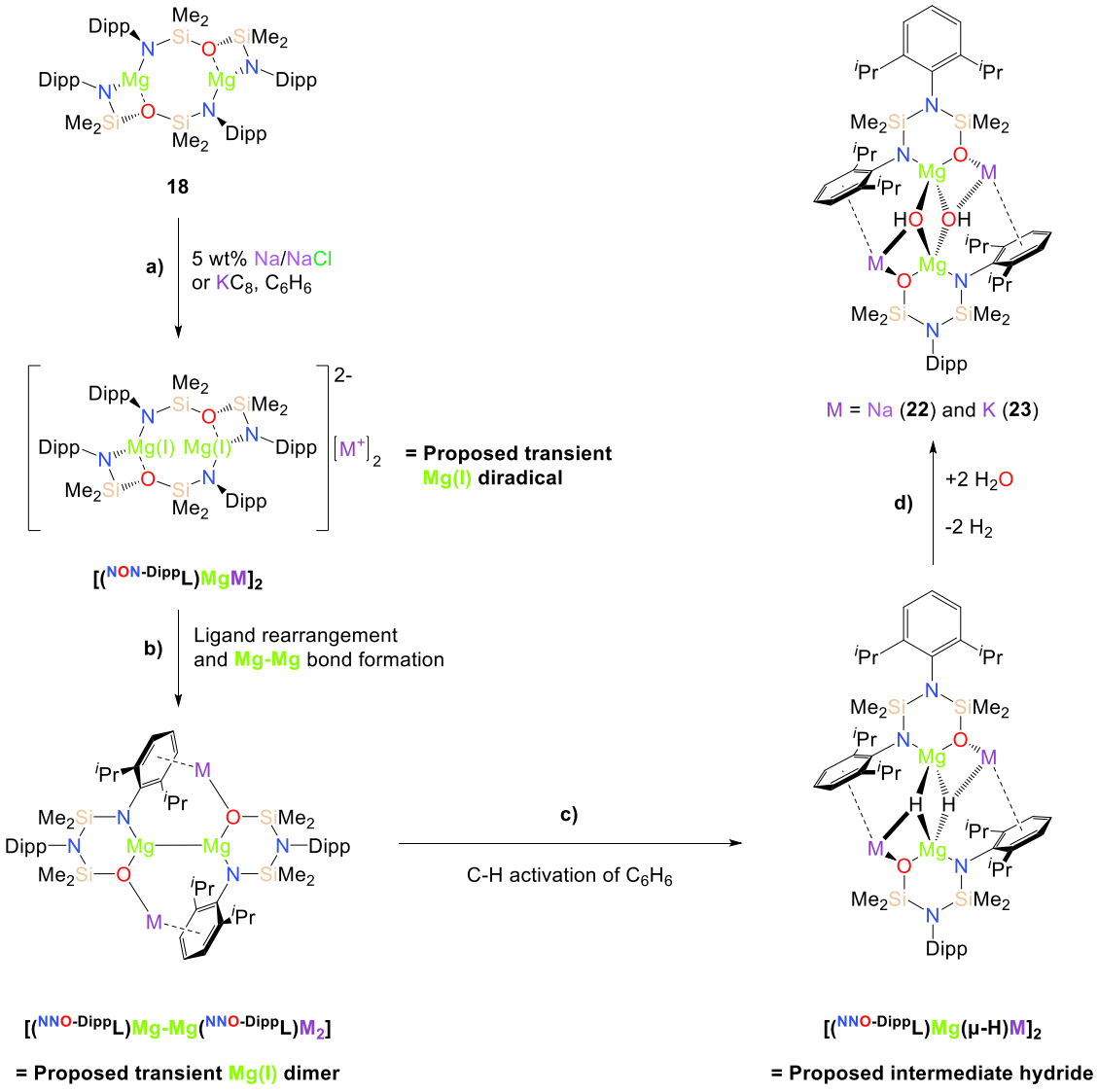
The formation of **22** and **23** contrasts with results published very recently in collaboration with Coles and co-workers, which showed that the reduction of **18** with potassium graphite in diethyl ether (rather than benzene) resulted in a different outcome (**Scheme 5.9**).[68] While isolable, the initial product(s) of this reaction (**VI**) could not be crystallographically characterised. However, the formation of reduced Mg(I) centres chelated by both "NON" and "NNO" ligands (present in a 1:1 ratio) was confirmed. Subsequent recrystallisation from THF afforded [($^{\text{NNO-Dipp}}$L)Mg-Mg($^{\text{NNO-Dipp}}$L)][K(THF)$_2$]$_2$ (**VII**), a Mg(I) dimer consisting of a Mg(I)-Mg(I) bond between two anionic [($^{\text{NNO-Dipp}}$L)Mg(I)]$^-$ units. However, the reactions of the initial product **VI** with di*iso*propylcarbodiimide and carbon monoxide afforded the complexes [($^{\text{NNO-Dipp}}$L)Mg{C(N^{i}Pr)$_2$}Mg($^{\text{NON-Dipp}}$L)]K$_2$ (**VIII**) and [{($^{\text{NON-Dipp}}$L)Mg(Et$_2$O)}$_2$(C$_2$O$_2$)]K$_2$ (**IX**) respectively. The former (**VIII**) consists of both "NNO" and "NON" ligands, while the latter (**IX**) consists of only "NON" ligands, in contrast with the exclusive incorporation of "NNO" ligands in both the Mg(I) dimer **VII** and in complexes **22** and **23**. These results provide verification for the rearrangement of the [$^{\text{NON-Dipp}}$L]$^{2-}$ ligand into the [$^{\text{NNO-Dipp}}$L]$^{2-}$ form upon the reduction of **18** with alkali metal reducing agents, while demonstrating that the outcome of these reactions is complex and highly solvent-dependent.



Scheme 5.9 Summary of results published in collaboration with Coles and co-workers relating to the conversion of [($^{NON\text{-}Dipp}$L)Mg]$_2$ (**18**) into the intermediate **VI**, and the subsequent isolation of [($^{NNO\text{-}Dipp}$L)Mg-Mg($^{NNO\text{-}Dipp}$L)][K(THF)$_2$]$_2$ (**VII**), [($^{NNO\text{-}Dipp}$L)Mg{C(N^{i}Pr)$_2$}Mg($^{NON\text{-}Dipp}$L)]K$_2$ (**VIII**) and [{($^{NON\text{-}Dipp}$L)Mg(Et$_2$O)}$_2$(C$_2$O$_2$)]K$_2$. Adapted from reference 68.

Based on these results, it is proposed that the reduction of **18** in benzene initially results in the formation of the transient Mg(I) diradical species [($^{NON\text{-}Dipp}$L)MgM]$_2$ (M = Na and K, **Scheme 5.10a**). This necessitates the rearrangement of the "NON" ligand into an "NNO" form to accommodate the formation of the Mg(I) dimer [($^{NNO\text{-}Dipp}$L)Mg-Mg($^{NNO\text{-}Dipp}$)M$_2$] (**Scheme 5.10b**), which is analogous to the solvated complex **VII**. It is proposed that this heterobimetallic low-valent species is insufficiently stabilised in the absence of a donor solvent, resulting in the subsequent formation of the proposed heterobimetallic hydride intermediate [($^{NNO\text{-}Dipp}$L)Mg(μ-H)M]$_2$ (**Scheme 5.10c**) *via* the C-H activation of the solvent. Finally, hydrolysis of [($^{NNO\text{-}Dipp}$L)Mg(μ-H)M]$_2$ with

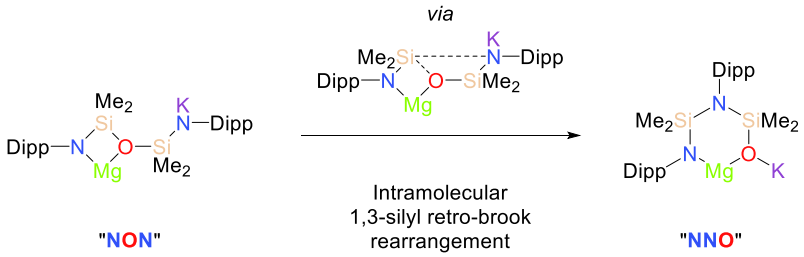
adventitious water result in conversion to the corresponding hydroxides **22** and **23** (**Scheme 5.10d**).



Scheme 5.10 Proposed mechanism for the conversion of [(NON-DippL)Mg]$_2$ (**18**) into [(NNO-DippL)Mg(μ-OH)M] (M = Na (**22**) and K (**23**).

While the stage at which ligand rearrangement occurs cannot be conclusively determined, the results obtained by Coles and co-workers suggest that it occurs immediately upon the reduction of **18** to low-valent species. Notably, the Mg-Mg distance in **18** (4.1130(9) Å) is too long to accommodate the formation of an Mg(I)-Mg(I) bond, suggesting that significant structural rearrangement is required to enable the quenching of transient Mg(I)

radicals formed upon reduction (**Scheme 5.10b**). This process can be attributed to a 1,3-silyl retro-Brook rearrangement of the "NON" form of the ligand in an analogous manner to previous literature reports (**Chart 5.2**).[28,29] It is proposed that coordination of an anionic amide donor to an alkali metal cation introduced by reduction enables the dissociation of the former from the Mg^{2+} centre to which it is coordinated in **18**. This pendant amide group is consequently able to attack the siloxane backbone, resulting in conversion into the mixed amide/alkoxide "NNO" ligand (**Scheme 5.11**).



Scheme 5.11 Simplified mechanism illustrating the conversion of the "NON" ligand present in $[(^{NON\text{-}Dipp}L)Mg]_2$ (**18**) into the "NNO" ligand present in $[(^{NNO\text{-}Dipp}L)Mg(\mu\text{-}OH)M]_2$ (M = Na (**22**) and K (**23**)) *via* a 1,3-silyl retro-Brook rearrangement.

This process is presumably also favoured by the reduced bulk of the alkoxide donor of the "NNO" ligand, the formation of which therefore reduces steric congestion at the small Mg^{2+} centre. A computational investigation of the conversion of **IV** into **V** supported the assertion that ligand rearrangement is facilitated by the alkali metal cation, and is thermodynamically favoured on steric grounds.[29] Notably, the reported temperature of 80 °C required for the thermal rearrangement of **IV** into **V** is the same as that employed in the synthesis of **22** and **23** due to the poor solubility of **18** in benzene.

The subsequent formation of the intermediate hydride species $[(^{NNO\text{-}Dipp}L)Mg(\mu\text{-}H)M]_2$ (**Scheme 5.10c**) is supported by a previous report from Hicks and co-workers. The attempted reduction of neutral magnesium and calcium complexes supported by a related

chelating diamido "NON" ligand in benzene resulted in the formation of isolable dimeric heterobimetallic hydride species (**LIII**, **Scheme 1.21a**).[69] Furthermore, while Hill and co-workers have reported the successful isolation of a heterobimetallic low-valent magnesium complex $[\{(CH_2SiMe_2NDipp)_2Mg\}Na]_2$ (**XLVII**, **Scheme 1.17**),[35] the attempted synthesis of an analogous beryllium complex instead resulted in the isolation of an anionic phenylberyllate (**LI**, **Scheme 1.19**).[70] The C-H activation of benzene by transient low-valent species was proposed in both cases, and has also been reported for other strongly reducing alkaline earth complexes.[33,51]

Complexes **22** and **23** can each be classified as heterobimetallic molecular magnesium hydroxides, which have no direct literature precedent. However, a number of related molecular magnesium hydroxides supported by monoanionic β-diketiminato,[63–65] *tris*(pyrazolyl)hydroborato,[66] *bis*(phosphoranyl)methanediide[62] and 1,3,5-triazapentadiene[61] ligands have been reported. In all cases, the isolation of these complexes resulted from either the deliberate or inadvertent hydrolysis of magnesium complexes with labile nucleophilic ligands, supporting the proposed formation of **22** and **23** *via* the surreptitious hydrolysis of an intermediate hydride (**Scheme 5.10d**).

5.6 Conclusions

The four dimeric alkaline earth complexes $[(^{NON\text{-}Dipp}L)Ae]_2$ (Ae = Mg (**18**), Ca (**19**), Sr (**20**) and Ba (**21**)) bearing a flexible di(amido)siloxane ligand were successfully isolated and characterised by X-ray diffraction, NMR and IR spectroscopy and elemental analysis. While the $[^{NON\text{-}Dipp}L]^{2-}$ ligand adopts a κ^2-N,O-κ^1-N′ coordination mode in **18** to relieve steric congestion resulting from the small ionic radius of Mg^{2+}, a κ^3-N,O,N′-κ^1-N′-tridentate coordination mode is readily accommodated by the heavier

congeners **19–21**. While **19** and **20** crystallise as nitrogen-bridged dimers from both arenes and alkanes, crystallisation of the barium congener was found to be solvent dependent. While crystallisation from benzene resulted in the same nitrogen-bridged structure observed in the lighter congeners (**21**), crystallisation from *n*-hexane resulted in an alternative aryl-bridged motif (**21a**).

Results obtained in collaboration with Coles and co-workers showed that the coordination of THF to **18** at 25 °C results in the formation of the dimeric THF adducts [{($^{NON\text{-}Dipp}$L)Mg}$_2$(THF)] (**18·THF**) and [($^{NON\text{-}Dipp}$L)Mg(THF)]$_2$ (**18·THF$_2$**), which were characterised by X-ray diffraction. Conversion to the previously reported monomeric adduct [($^{NON\text{-}Dipp}$L)Mg(THF)$_2$] was afforded by heating a THF solution of **18** at 80 °C. Conversely, dissolution of **19**–**21** in THF resulted in their rapid full conversion into the corresponding monomeric THF adducts [($^{NON\text{-}Dipp}$L)Ae(THF)$_n$] (n = 2, Ae = Ca (**19·THF$_2$**); n = 3, Ae = Sr (**20·THF$_3$**) and Ba (**21·THF$_3$**)) at 25 °C, which were characterised by X-ray diffraction and NMR spectroscopy.

While the attempted reductions of the heavier congeners **19**–**21** were inconclusive, the reactions of the magnesium dimer **18** with alkali metal reducing agents in benzene afforded the dimeric heterobimetallic molecular magnesium hydroxide complexes [($^{NNO\text{-}Dipp}$L)Mg(μ-OH)M]$_2$ (M = Na (**22**) and K (**23**)), which were characterised by X-ray diffraction and NMR spectroscopy. Complexes **22** and **23** exhibit a rearranged "NNO" ligand, which forms *via* an intramolecular 1,3-silyl retro-Brook rearrangement of the "NON" ligand. The formation of **22** and **23** contrasts with results published in collaboration with Coles and co-workers, which showed that conducting the reduction of **18** in diethyl ether results in the formation of stable low-valent species. The hydroxide groups in **22** and **23** were proposed to originate from the hydrolysis of an intermediate

hydride species that forms following the C-H activation of benzene by transient low-valent species.

5.7 References

1 D. B. Leznoff, G. Mund, K. C. Jantunen, P. H. Bhatia, A. J. Gabert and R. J. Batchelor, *J. Nucl. Sci. Technol.*, 2002, **39**, 406–409.

2 U. Wannagat and F. Rabet, *Inorg. Nucl. Chem. Lett.*, 1970, **6**, 155–162.

3 K. Wiegel and H. Bürger, *ZAAC - J. Inorg. Gen. Chem.*, 1976, **426**, 301–308.

4 H. Bürger and K. Wiegel, *ZAAC - J. Inorg. Gen. Chem.*, 1976, **419**, 157–162.

5 A. J. Elias, H. W. Roesky, W. T. Robinson and G. M. Sheldrick, *J. Chem. Soc. Dalton Trans.*, 1993, 495–500.

6 N. A. H. Male, M. Thornton-Pett and M. Bochmann, *J. Chem. Soc. Dalton Trans.*, 1997, **2**, 2487–2494.

7 N. A. H. Male, M. Thornton-Pett and M. Bochmann, *J. Chem. Soc. Dalton Trans.*, 1997, **9**, 2487–2494.

8 G. Mund, A. J. Gabert, R. J. Batchelor, J. F. Britten and D. B. Leznoff, *Chem. Commun.*, 2002, **24**, 2990–2991.

9 F. Dankert and C. von Hänisch, *Eur. J. Inorg. Chem.*, 2021, **2021**, 2907–2927.

10 R. J. Schwamm and M. P. Coles, *Chem. Eur. J.*, 2019, **25**, 14183–14191.

11 R. J. Schwamm and M. P. Coles, *Eur. J. Inorg. Chem.*, 2022, **2022**, e202200064.

12 R. J. Schwamm, A. J. Edwards, C. M. Fitchett and M. P. Coles, *Dalton Trans.*, 2019, **48**, 2953–2958.

13 R. J. Schwamm, M. D. Anker, M. Lein, M. P. Coles and C. M. Fitchett, *Angew. Chemie Int. Ed.*, 2018, **57**, 5885–5887.

14 R. J. Schwamm, C. A. von Randow, A. Mouchfiq, M. J. Evans, M. P. Coles and J. Robin Fulton, *Eur. J. Inorg. Chem.*, 2021, **2021**, 3466–3473.

15 M. D. Anker, Y. Altaf, M. Lein and M. P. Coles, *Dalton Trans.*, 2019, **48**, 16588–16594.

16 M. P. Coles and M. J. Evans, *Chem. Commun.*, 2023, **59**, 503–519.

17 R. J. Schwamm, J. R. Harmer, M. Lein, C. M. Fitchett, S. Granville and M. P. Coles, *Angew. Chemie Int. Ed.*, 2015, **54**, 10630–10633.

18 R. J. Schwamm, M. D. Anker, M. Lein and M. P. Coles, *Angew. Chemie Int. Ed.*, 2019, **58**, 1489–1493.

19 K. C. Jantunen, F. Haftbaradaran, M. J. Katz, R. J. Batchelor, G. Schatte and D. B. Leznoff, *Dalton Trans.*, 2005, 3083–3091.

20 C. E. Hayes and D. B. Leznoff, *Organometallics*, 2010, **29**, 767–774.

21 K. C. Jantunen, R. J. Batchelor and D. B. Leznoff, *Organometallics*, 2004, **23**, 2186–2193.

22 C. E. Hayes, Y. Sarazin, M. J. Katz, J. F. Carpentier and D. B. Leznoff, *Organometallics*, 2013, **32**, 1183–1192.

23 C. E. Hayes, R. H. Platel, L. L. Schafer and D. B. Leznoff, *Organometallics*, 2012, **31**, 6732–6740.

24 M. J. Evans, M. D. Anker and M. P. Coles, *Inorg. Chem.*, 2021, **60**, 4772–4778.

25 M. D. Anker, M. J. Evans, S. A. Cameron and G. Laufersky, *Polyhedron*, 2024, **247**, 116741.

26 G. Navickaite, *Synthesis of polymeric materials derived from abundant natural feedstocks using non-toxic heavy metals*, D.Phil Thesis, University of Oxford, 2024.

27 E. W. Y. Wong, A. K. Das, M. J. Katz, Y. Nishimura, R. J. Batchelor, M. Onishi and D. B. Leznoff, *Inorg. Chim. Acta*, 2006, **359**, 2826–2834.

28 F. Haftbaradaran, G. Mund, R. J. Batchelor, J. F. Britten and D. B. Leznoff, *Dalton Trans.*, 2005, 2343–2345.

29 A. O'Reilly, M. G. Gardiner, C. L. McMullin, J. R. Fulton and M. P. Coles, *Chem. Commun.*, 2024, **64**, 881–884.

30 M. Westerhausen and W. Schwarz, *ZAAC*, 1992, **609**, 39–44.

31 K. P. Kepp, *Inorg. Chem.*, 2016, **55**, 9461–9470.

32 P. Pyykkö, *J. Phys. Chem. A*, 2015, **119**, 2326–2337.

33 J. C. Mullins, K. Yuvaraj, Y. Jiang, G. P. Van Trieste, A. Maity, D. C. Powers and C. Jones, *Chem. Eur. J.*, 2022, **28**, e202202103.

34 S. P. Green, C. Jones and A. Stasch, *Angew. Chemie Int. Ed.*, 2008, **47**, 9079–9083.

35 H.-Y. Liu, R. J. Schwamm, S. E. Neale, M. S. Hill, C. L. McMullin and M. F. Mahon, *J. Am. Chem. Soc.*, 2021, **143**, 17851–17856.

36 L. Yang, D. R. Powell and R. P. Houser, *Dalton Trans.*, 2007, 955–964.

37 H.-Y. Liu, S. E. Neale, M. S. Hill, M. F. Mahon, C. L. Mcmullin, E. Richards, M. S. Hill and C. L. M C Mullin, *Angew. Chemie Int. Ed.*, 2022, **62**, e202213670.

38 A. K. Das, Z. Moatazedi, G. Mund, A. J. Bennet, R. J. Batchelor and D. B. Leznoff, *Inorg. Chem.*, 2007, **46**, 366–368.

39 P. M. Chapple and Y. Sarazin, *Eur. J. Inorg. Chem.*, 2020, **2020**, 3321–3346.

40 M. S. Hill, D. J. Liptrot and C. Weetman, *Chem. Soc. Rev.*, 2016, 45, 972–988.

41 M. Westerhausen and W. Schwarz, *ZAAC*, 1991, **606**, 177–190.

42 C. D. Schaeffer and J. J. Zuckerman, *J. Am. Chem. Soc.*, 1974, **96**, 7160–7162.

43 M. Westerhausen and W. Schwarz, *ZAAC*, 1991, **604**, 127–140.

44 Y. Sarazin and J. F. Carpentier, *CHAPTER 4: Secondary (Agostic Si-H/Electrostatic C-F) interactions in alkaline earth-based catalysts*, Royal Society of Chemistry, 2019.

45 J. Pahl, S. Brand, H. Elsen and S. Harder, *Chem. Commun.*, 2018, **54**, 8685–8688.

46 P. Stegner, C. Färber, J. Oetzel, U. Siemeling, M. Wiesinger, J. Langer, S. Pan, N. Holzmann, G. Frenking, U. Albold, B. Sarkar and S. Harder, *Angew. Chemie Int. Ed.*, 2020, **59**, 14615–14620.

47 C. Jones, D. T. Nguyen, C. Helling and M. J. Evans, *Inorg. Chem.*, 2024, **63**, 5718–5726.

48 M. J. C. Dawkins, A. N. Simonov and C. Jones, *Dalton Trans.*, 2020, **49**, 6627–6634.

49 L. Lameyer, O. A. Salah, S. Deuerlein, T. Stey and D. Stalke, *ZAAC*, 2004, **630**, 1801–1806.

50 J. Mai, B. Rösch, J. Langer, S. Grams, M. Morasch, S. Harder, J. Mai, B. Rösch, J. Langer, S. Grams, M. Morasch and S. Harder, *Eur. J. Inorg. Chem.*, 2023, **26**, e202300421.

51 J. Mai, M. Morasch, D. Jędrzkiewicz, J. Langer, B. Rösch and S. Harder, *Angew. Chemie Int. Ed.*, 2022, **62**, e202212463.

52 M. J. Evans, J. Mullins, R. Mondal and C. Jones, *Chem. Eur. J.*, 2024, **30**, e202401005.

53 A. W. Addison, T. N. Rao, J. Reedijk, J. Van Rijn and G. C. Verschoor, *J. Chem. Soc. Dalton Trans.*, 1984, 1349–1356.

54 L. Orzechowski, G. Jansen and S. Harder, *J. Am. Chem. Soc.*, 2006, **128**, 14676–14684.

55 L. Orzechowski and S. Harder, *Organometallics*, 2007, **26**, 5501–5506.

56 B. Freitag, C. A. Fischer, J. Penafiel, G. Ballmann, H. Elsen, C. Färber, D. F. Piesik and S. Harder, *Dalton Trans.*, 2017, **46**, 11192–11200.

57 R. K. Kottalanka, H. Adimulam, J. Bhattacharjee, H. Vignesh Babu and T. K. Panda, *Dalton Trans.*, 2014, **43**, 8757–8766.

58 S. Harder and J. Langer, *Nat. Rev. Chem.*, 2023, **7**, 843–853.

59 A. O'Reilly, M. G. Gardiner, C. L. McMullin, J. R. Fulton and M. P. Coles, *Chem. Commun.*, 2024, **60**, 881–884.

60 S. Sinhababu, M. R. Radzhabov, J. Telser and N. P. Mankad, *J. Am. Chem. Soc.*, 2022, **13**, jacs.1c13108.

61 I. Pernik, B. J. Maitland, A. Stasch and C. Jones, *Can. J. Chem.*, 2018, **96**, 513–521.

62 J. Guo, J. S. Lee, M. C. Foo, K. C. Lau, H. W. Xi, K. H. Lim and C. W. So, *Organometallics*, 2010, **29**, 939–944.

63 L. F. Sánchez-Barba, D. L. Hughes, S. M. Humphrey and M. Bochmann, *Organometallics*, 2006, **25**, 1012–1020.

64 M. Arrowsmith, B. Maitland, G. Kociok-Köhn, A. Stasch, C. Jones and M. S. Hill, *Inorg. Chem.*, 2014, **53**, 10543–10552.

65 S. Nembenna, S. Singh, S. S. Sen, H. W. Roesky, H. Ott and D. Stalke, *ZAAC*, 2011, **637**, 201–205.

66 P. Ghosh and G. Parkin, *Inorg. Chem.*, 1996, **35**, 1429–1430.

67 R. A. Wiscons, M. K. Bellas, J. C. Bennion and A. J. Matzger, *Cryst. Growth Des.*, 2018, **18**, 7701–7707.

68 A. O'Reilly, M. D. Haynes, Z. R. Turner, C. L. McMullin, S. Harder, D. O'Hare, J. R. Fulton and M. P. Coles, *Chem. Commun.*, 2024, **60**, 7204–7207.

69 J. S. McMullen, R. Huo, P. Vasko, A. J. Edwards and J. Hicks, *Angew. Chemie Int. Ed.*, 2022, **62**, e2022152.

70 K. G. Pearce, M. S. Hill and M. F. Mahon, *Chem. Commun.*, 2023, **59**, 1453–1456.

Chapter 6

Experimental details and characterisation data

6.1 General details

6.1.1 Air- and moisture-sensitive compounds

All air- and moisture-sensitive manipulations were carried out under an inert atmosphere of dinitrogen, employing standard Schlenk line techniques and a MBraun Unilab glove box. Glassware was oven-dried at temperatures greater than 150 °C prior to use.

6.1.2 Commercially supplied reagents

1,8-diaminonaphthalene (Sigma Aldrich), *n*-butyllithium (1.6 M or 2.5 M solution in hexanes; Sigma Aldrich), trimethylsilylchloride (Sigma Aldrich), dimethyl*tert*butylsilylchloride (Sigma Aldrich), tri*iso*propylsilylchloride (Sigma Aldrich), diphenylmethylsilylchloride (Sigma Aldrich), triphenylsilylchloride (Sigma Aldrich), magnesium *bis*(hexamethyldisilazide) (Sigma Aldrich), anhydrous calcium iodide (Sigma Aldrich), anhydrous strontium iodide (Sigma Aldrich), anhydrous barium iodide (Sigma Aldrich), 1,3-dichloro-1,1,3,3-tetramethyldisiloxane (Sigma Aldrich and Thermo Fisher Scientific) and di-*n*-butyl magnesium (1.0 M in heptane, Sigma Aldrich) were used as received. Hexamethyldisilazane (Sigma Aldrich), methanol-d_1 (Sigma Aldrich) and 2,6-di*iso*propylaniline (Apollo Scientific) were dried over calcium hydride, freeze-pump-thaw degassed three times and stored over pre-activated 3 Å molecular

sieves prior to use. Sodium metal (Sigma Aldrich) and potassium metal (Sigma Aldrich) were purchased as chunks suspended in mineral oil, and were washed with *n*-pentane, dried *in vacuo* and stored under nitrogen prior to use. Sodium chloride (Sigma Aldrich) and potassium iodide (Sigma Aldrich) were ground to fine powders and dried according to a reported procedure prior to use.[1] Graphite (Sigma Aldrich) was dried by heating at 150 °C overnight *in vacuo* prior to use. Potassium hydride (Sigma Aldrich) was purchased as a 30 wt% dispersion in mineral oil. Excess oil was decanted away before the solid was washed thoroughly with diethyl ether until a free-flowing powder was obtained, which was dried *in vacuo* prior to use. Celite (Sigma Aldrich) was dried at 150 °C under reduced pressure (10^{-3} mbar) for at least 48 hours before use. Molecular sieves (Sigma Aldrich) were dried *in vacuo* at 140 °C for 48 hours prior to use.

6.1.3 Synthesis of literature compounds

1,8-{(R_3Si)NH}$_2C_{10}H_6$ ($^{R_3}LH_2$, R_3 = Me_3, $Me_2{}^tBu$ and Ph_2Me),[2] $KN(SiMe_3)_2$,[3] $[(THF)_2Ae\{N(SiMe_3)_2\}_2]$ (Ae = Ca, Sr and Ba),[4,5] $[Ae\{N(SiMe_3)_2\}_2]_2$ (Ae = Ca, Sr and Ba),[6,7] $O\{SiMe_2NH(2,6\text{-}{}^iPr_2C_6H_3)\}_2$ ($^{NON\text{-}Dipp}LH_2$),[8] 5 wt% Na/NaCl,[1] 5 wt% K/KI[1] and potassium graphite (KC_8)[9] were prepared according to literature procedures. 1,8-{($^iPr_3Si$)NH}$_2C_{10}H_6$ ($^{iPr_3}LH_2$) was synthesised by Dr. Zoë Turner according to a literature procedure.[2]

6.1.4 Solvent preparation

Protio solvents (*n*-pentane, *n*-hexane, toluene, benzene) were dried using an MBraun SPS-800 solvent purification system, stored over a potassium mirror, and degassed under partial pressure prior to use. Tetrahydrofuran was distilled from sodium/benzophenone, stored over pre-activated 3 Å molecular sieves, and degassed under partial pressure prior

to use. Diethyl ether was distilled from sodium/benzophenone, stored over a potassium mirror, and degassed under partial pressure prior to use.

Deuterated solvents were refluxed under partial pressure over potassium (benzene-d_6, toluene-d_8) or dried over calcium hydride (tetrahydrofuran-d_8), distilled, freeze-pump-thaw degassed three times, and stored over pre-activated 3 or 4 Å molecular sieves.

6.1.5 Solution NMR spectroscopy

^{1}H NMR spectra were recorded at 298 K, unless otherwise stated, on Bruker AVIII 400 nanobay or Bruker AVIII 500 or Bruker NEO 600 spectrometers. ^{13}C{^{1}H} NMR spectra were recorded on the same spectrometers at operating frequencies of 100, 125 and 151 MHz respectively, as were ^{29}Si NMR spectra at operating frequencies of 80, 99 and 119 MHz respectively. ^{2}H NMR spectra were recorded on a Bruker AVIII 500 spectrometer at an operating frequency of 77 MHz. Two dimensional ^{1}H-^{1}H, ^{13}C-^{1}H and ^{29}Si-^{1}H correlation experiments were used, when necessary, to confirm ^{1}H, ^{13}C and ^{29}Si assignments. NMR spectra were referenced internally to residual protio solvent (^{1}H) or solvent (^{13}C) resonances and are reported relative to tetramethylsilane (δ = 0 ppm). Chemical shifts are quoted in δ (ppm) and coupling constants in Hertz. Air-sensitive samples were prepared in a glovebox under an inert atmosphere, using dry deuterated solvents in 5 mm J-Young's tap NMR tubes.

6.1.6 Fourier transform infrared (FTIR) spectroscopy

Samples were prepared in a glove box under a dinitrogen atmosphere as pellets pressed with anhydrous potassium bromide, which was dried above 150 °C at 10^{-6} mbar for 24 hours prior to use. FTIR spectra were measured using a Nicolet iS5 ThermoScientific spectrometer, with a background spectrum run prior to the sample and subtracted from the sample spectrum.

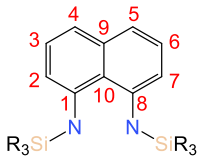
6.1.7 Elemental analysis

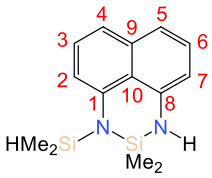
Samples were prepared in a glove box under a nitrogen atmosphere and sealed in glass vials. CHN analyses were carried out in duplicate either at the University of Erlangen-Nuremberg or by Ms Orla McCullough at London Metropolitan University.

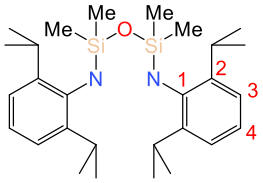
6.1.8 Single crystal X-ray diffraction (XRD)

Single crystal X-ray diffraction data collection and structure determination for compounds **1**, **3**, **4**, **5**, **6**, **7**, **8**, **9**, **10**, **11**, **13**, **16**, **17**, **19**, **20** and **21**, were performed by Dr. Zoë Turner, Dr. Louis Morris, Dr. Clement Collins-Rice and Dr. Aisling Roper (University of Oxford), for compounds **18**, **22** and **23** by Dr. Jens Langer (University of Erlangen-Nuremberg), for compounds **18·THF**, **18·THF$_2$**, **19·THF$_2$**, **20·THF$_3$** and **21·THF$_3$** by Prof. Martyn Coles and co-workers (Victoria University of Wellington), and for ^{Me3}LH$_2$, ^{Me2tBu}LH$_2$, **12**, **14**, **15**, **19**, **20** and **21a** by the author, Mr. Matthew Haynes. Crystals were mounted on MiTeGen MicroMounts using perfluoropolyether oil and rapidly transferred to a goniometer head on a diffractometer fitted with an Oxford Cryostream open-flow nitrogen cooling device.[10] Data collections were carried out at 150 K using an Oxford Diffraction Supernova diffractometer using mirror-monochromated Cu Kα radiation (λ = 1.54178 Å) or Mo Kα radiation (λ = 0.71073 Å) and the data processed using CrysAlisPro.[11] The structures were solved using direct methods (SIR-92),[12] a flipping algorithm (SUPERFLIP),[13] or intrinsic phasing (SHELXT)[14] and refined by full-matrix least squares procedures using the WinGX software suite,[15] CRYSTALS,[16] or the SHELXL[17] refinement package implemented in Olex2.[18] Where required, interplanar distances and angles were calculated using Olex2[18] and molecular structures were generated using Ortep (with ellipsoids shown at 30% probability).[19]

6.1.9 Ligand numbering schemes

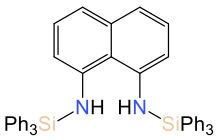






6.2 Experimental details for Chapter 2

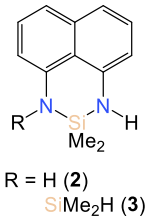
6.2.1 Synthesis of $^{Ph3}LH_2$ (1); adapted from reference 2.



1,8-diaminonaphthalene (4.00 g, 25.3 mmol) was dissolved in tetrahydrofuran (50 mL). The resulting deep purple solution was cooled to −30 °C, then *n*-butyllithium (1.6 M in hexanes, 31.6 mL, 50.6 mmol, 2 eq.) was added dropwise over 20 minutes. The reaction mixture was allowed to warm to room temperature and stirred for 2 hours. The resulting green suspension was cooled to −30 °C. A solution of triphenylsilylchloride (14.9 g, 50.6 mmol, 2 eq.) in tetrahydrofuran (50 mL) was added dropwise over 20 minutes to form a dark brown suspension. The reaction mixture was allowed to warm to room temperature and stirred for 16 hours. All solvents were removed and the resulting yellow residue dried *in vacuo* for 2 hours. The residue was extracted with toluene (4 x 20 mL) and filtered through Celite. The resulting colourless solution was concentrated *in vacuo* to ~10 mL. The addition of *n*-pentane (40 mL) and storage at −30 °C resulted in the precipitation of a white solid, which was isolated by filtration, washed with *n*-pentane (3 x 10 mL) and dried *in vacuo* for 1 hour. $^{Ph3}LH_2$ (4.57 g, 6.77 mmol, 27% (**1**)) was isolated as a white powder. The toluene/*n*-pentane filtrate was left to stand at room temperature, resulting in the growth of large colourless crystals suitable for an X-ray diffraction study. ^{1}H NMR (C_4D_8O, 298 K, 600 MHz): δ (ppm) = 7.53 (m, 12H, 2,6-$C_6\boldsymbol{H_5}$), 7.31 (dt, $^3J_{H\text{-}H}$ = 7.4, $^4J_{H\text{-}H}$ = 1.4 Hz, 6H, 4-$C_6\boldsymbol{H_5}$), 7.20 (m, 12H, 3,5-$C_6\boldsymbol{H_5}$), 7.11 (dd, $^3J_{H\text{-}H}$ = 8.2,

$^{4}J_{H\text{-}H}$ = 1.1 Hz, 2H, 4,5-$C_{10}\boldsymbol{H_6}$), 6.86 (t, *J* = $^{3}J_{H\text{-}H}$ = 7.8 Hz, 2H, 3,6-$C_{10}\boldsymbol{H_6}$), 6.74 (dd, $^{3}J_{H\text{-}H}$ = 7.5, $^{4}J_{H\text{-}H}$ = 1.1 Hz, 2H, 2,7-$C_{10}\boldsymbol{H_6}$), 6.67 (s, br, 2H, N***H***). $^{13}C\{^{1}H\}$ NMR (C_4D_8O, 298 K, 151 MHz): δ (ppm) = 144.6 (1,8-$\boldsymbol{C_{10}}H_6$), 138.2 (10-$\boldsymbol{C_{10}}H_6$), 136.7 (2,6-$\boldsymbol{C_6}H_5$), 135.5 (1-$\boldsymbol{C_6}H_5$), 130.6 (4-$\boldsymbol{C_6}H_5$), 128.8 (3,5-$\boldsymbol{C_6}H_5$), 126.1 (3,6-$\boldsymbol{C_{10}}H_6$), 122.2 (9-$\boldsymbol{C_{10}}H_6$), 121.1 (4,5-$\boldsymbol{C_{10}}H_6$), 117.1 (2,7-$\boldsymbol{C_{10}}H_6$).^{29}Si NMR (C_4D_8O, 298 K, 119 MHz): δ (ppm) = –19.89 (***Si***Ph_3). IR (KBr): 3312, 2204, 3269, 3065, 3056, 3021, 1576, 1427, 1412, 1290, 1111, 1027, 739, 714, 697, 516 cm^{-1}. Anal. calcd for $C_{46}H_{36}N_2Si_2$: C, 81.85; H, 5.67; N, 4.15. Found: C, 81.68; H, 5.83; N, 3.97.

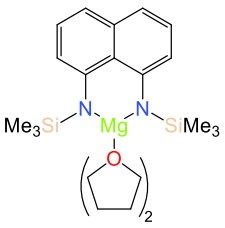
6.2.2 Synthesis of $^{\mu\text{-}Me_2}LH_2$ (2) and $^{Me_2H\text{-}\mu\text{-}Me_2}LH$ (3)



1,8-diaminonaphthalene (4.00 g, 25.3 mmol) was dissolved in tetrahydrofuran (40 mL). The resulting deep purple solution was cooled to −30 °C. *n*-Butyllithium (1.6 M in hexanes, 31.6 mL, 50.6 mmol, 2 eq.) was added dropwise over 20 minutes, with the reaction mixture then allowed to warm to room temperature and stirred for 2 hours. The resulting green suspension was cooled to −30 °C. A solution of dimethylsilylchloride (5.62 mL, 50.6 mmol, 2 eq.) was added dropwise over 20 minutes to form an orange suspension. The reaction mixture was allowed to warm to room temperature and stirred for 16 hours. All solvents were removed and the resulting brown residue dried *in vacuo* for 2 hours. The residue was extracted with *n*-pentane (4 x 20 mL) and filtered to yield an orange solution. All volatiles were removed *in vacuo* to yield an orange powder. Recrystallisation from *n*-pentane yielded the major product $^{\mu\text{-}Me_2}LH_2$ (**2**) as pink needle-like crystals, which were isolated by filtration and dried *in vacuo* for one hour (2.07 g, 9.66 mmol, 37%). NMR spectra of **2** were consistent with a previous report.[20] Concentration of the orange filtrate to *ca*. 5 mL and storage at −30 °C resulted in the formation of pink needle-like crystals of the minor

product $^{Me_2H\text{-}\mu\text{-}Me_2}$LH (**3**) suitable for an X-ray diffraction study. The solvent was decanted and the crystals dried *in vacuo* for one hour to yield **3** (0.364 g, 1.34 mmol, 5%) as a pink microcrystalline solid. ^{1}H NMR (C_6D_6, 298 K, 400 MHz): δ (ppm) = 7.30 (dd, $^3J_{H\text{-}H}$ = 8.2, $^3J_{H\text{-}H}$ = 1.1 Hz, 1H, 4-C_{10}***H*****$_6$**), 7.24–7.18 (overlapping m, 2H, 5,6-C_{10}***H*****$_6$**), 7.15 (t, $^3J_{H\text{-}H}$ = 7.7 Hz, 1H, 3-C_{10}***H*****$_6$**), 6.78 (dd, $^3J_{H\text{-}H}$ = 7.6, $^4J_{H\text{-}H}$ = 1.1 Hz, 1H, 2-C_{10}***H*****$_6$**), 6.25 (m, $^3J_{H\text{-}H}$ = 5.8, $^4J_{H\text{-}H}$ = 2.8 Hz, 1H, 7-C_{10}***H*****$_6$**), 4.73 (hept, $^3J_{H\text{-}H}$ = 3.6 Hz, 1H, $SiMe_2$***H***), 3.36 (s, br, 1H, N***H***), 0.31 (d, $^3J_{H\text{-}H}$ = 3.6 Hz, 6H, Si(*C*H_3)$_2$H), 0.19 (s, 6H, μ$_2$-Si(C***H*****$_3$**)$_2$). ^{13}C{^{1}H} NMR (C_6D_6, 298 K, 101 MHz): δ (ppm) = 143.5 (8-***C*****$_{10}$**H_6), 143.2 (1-***C*****$_{10}$**H_6), 137.6 (10-***C*****$_{10}$**H_6), 127.0 (4-***C*****$_{10}$**H_6), 126.2 (6-***C*****$_{10}$**H_6), 120.6 (5-***C*****$_{10}$**H_6), 118.5 (9-***C*****$_{10}$**H_6), 118.3 (3-***C*****$_{10}$**H_6), 113.6 (2-***C*****$_{10}$**H_6), 109.6 (7-***C*****$_{10}$**H_6), 2.5 (Si(***C***H_3)$_2$H), –1.4 (μ$_2$-Si(***C***H_3)$_2$) ^{29}Si NMR (C_6D_6, 298 K, 119 MHz): δ (ppm) = - 6.75 (s, μ$_2$-***Si***Me_2), –13.00 (s, ***Si***Me_2H). Anal. Calcd. for $C_{14}H_{20}N_2Si_2$: C, 61.71; H, 7.40; N, 10.28. Found: C, 61.86; H, 7.46; N, 10.21.

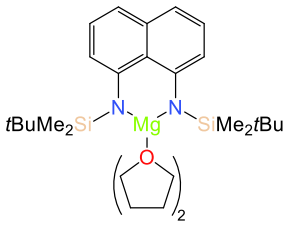
6.2.3 Synthesis of [(^{Me_3}L)Mg(THF)$_2$] (4)



A solution of $^{Me_3}LH_2$ (250 mg, 0.826 mmol) in THF (5 mL) was added dropwise to a stirred solution of [MgN"$_2$]$_2$ (286 mg, 0.413 mmol, 0.5 eq.) in THF (5 mL) at room temperature. The resulting brown solution was refluxed at 80 °C for 24 hours. All volatiles were removed *in vacuo* to yield a brown solid, which was washed with cold (−78 °C) *n*-pentane (3 x 5 mL), isolated by filtration and dried *in vacuo* for one hour. [(^{Me_3}L)Mg(THF)$_2$] (210 mg, 0.448 mmol, 54% (**4**)) was isolated as a beige powder. Yellow crystals suitable for an X-ray diffraction study were grown by storing a saturated THF/*n*-hexane (1:1) solution at −30 °C. ^{1}H NMR (C_4D_8O, 298 K, 500 MHz): δ (ppm) = 6.71 (t, $^3J_{H\text{-}H}$ = 7.7 Hz, 2H, 3,6-C_{10}***H*****$_6$**), 6.57 (dd, $^3J_{H\text{-}H}$ = 7.8, $^4J_{H\text{-}H}$ = 1.4 Hz, 2H,

4,5-$C_{10}\boldsymbol{H_6}$), 6.41 (dd, $^{3}J_{H\text{-}H}$ = 7.5, $^{4}J_{H\text{-}H}$ = 1.3 Hz, 2H, 2,7-$C_{10}\boldsymbol{H_6}$), 3.62 (m, 4H, THF), 1.78 (m, 4H, THF), 0.11 (s, 18H, Si(C$\boldsymbol{H_3}$)$_3$). ^{13}C{^{1}H} NMR (C_4D_8O, 298 K, 126 MHz): δ (ppm) = 158.8 (1,8-$\boldsymbol{C_{10}}H_6$), 140.4 (9-$\boldsymbol{C_{10}}H_6$), 129.0 (10-$\boldsymbol{C_{10}}H_6$), 124.9 (3,6-$\boldsymbol{C_{10}}H_6$), 115.7 (2,7-$\boldsymbol{C_{10}}H_6$), 115.6 (4,5-$\boldsymbol{C_{10}}H_6$), 68.4 (THF), 26.5 (THF), 3.2 (Si($\boldsymbol{C}H_3$)$_3$). ^{29}Si NMR (C_4D_8O, 298 K, 99 MHz): δ (ppm) = –11.07 ($\boldsymbol{Si}Me_3$). IR (KBr): 3042, 2956, 2992, 1544, 1418, 1365, 1243, 1063, 901, 827, 742 cm^{-1}. Anal. calcd. for $C_{24}H_{40}MgN_2O_2Si_2$: C, 61.45; H, 8.60; N, 5.97. Found: C, 60.71; H, 8.49; N, 5.93.

6.2.4 Synthesis of [(^{Me_2tBu}L)Mg(THF)$_2$] (5)

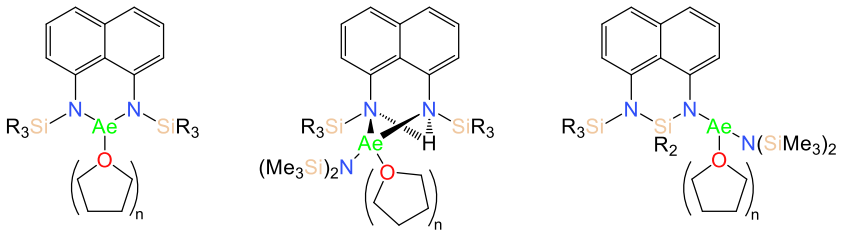


A solution of $^{Me_2tBu}LH_2$ (387 mg, 1.00 mmol) in THF (5 mL) was added dropwise to a stirred solution of [MgN"$_2$]$_2$ (345 mg, 0.500 mmol, 0.5 eq.) in THF (5 mL) at room temperature to form a brown solution, which was refluxed at 80 °C for 72 hours. All volatiles were removed *in vacuo* to yield a brown solid, which was washed with cold (−78 °C) *n*-pentane (3 x 5 mL), isolated by filtration and dried *in vacuo* for one hour. [(^{Me_2tBu}L)Mg(THF)$_2$] (308 mg, 0.557 mmol, 56% (**5**)) was isolated as an orange powder. Colourless crystals suitable for an X-ray diffraction study were grown by storing a saturated THF/*n*-hexane (1:1) solution at −30 °C. ^{1}H NMR (C_4D_8O, 298 K, 600 MHz): δ (ppm) = 6.72 (t, $^{3}J_{H\text{-}H}$ = 7.6 Hz, 2H, 3,6-$C_{10}\boldsymbol{H_6}$), 6.65 (dd, $^{3}J_{H\text{-}H}$ = 7.9, $^{4}J_{H\text{-}H}$ = 1.4 Hz, 2H, 4,5-$C_{10}\boldsymbol{H_6}$), 6.56 (dd, $^{3}J_{H\text{-}H}$ = 7.4, $^{4}J_{H\text{-}H}$ = 1.4 Hz, 2H, 2,7-$\boldsymbol{C_{10}H_6}$), 3.64–3.60 (m, THF), 1.79–1.76 (m, THF), 0.79 (s, 18H, SiC(C$\boldsymbol{H_3}$)$_3$), 0.14 (s, 12H, Si(C$\boldsymbol{H_3}$)$_2$^{t}Bu). ^{13}C{^{1}H} NMR (C_4D_8O, 298 K, 151 MHz): δ (ppm) = 158.7 (1,8-$\boldsymbol{C_{10}}H_6$), 140.2 (9-$\boldsymbol{C_{10}}H_6$), 129.9 (10-$\boldsymbol{C_{10}}H_6$), 125.2 (3,6-$\boldsymbol{C_{10}}H_6$), 119.1 (2,7-$\boldsymbol{C_{10}}H_6$), 116.7 (4,5-$\boldsymbol{C_{10}}H_6$), 68.4 (THF), 29.2 (SiC($\boldsymbol{C}H_3$)$_3$), 26.5 (THF), 21.54 (Si$\boldsymbol{C}Me_3$), 0.2 (Si($\boldsymbol{C}H_3$)$_2$^{t}Bu). ^{29}Si NMR (C_4D_8O, 298 K, 119 MHz): δ (ppm) = −5.54 ($\boldsymbol{Si}Me_2$^{t}Bu). IR (KBr): 2947, 2926, 2850, 1583, 1541,

1418, 1360, 1273, 1057, 904, 832 cm^{-1}. Anal. calcd. for $C_{30}H_{52}MgN_2O_2Si_2$: C, 65.13; H, 9.47; N, 5.06. Found: C, 65.08; H, 9.37; N, 4.83.

6.2.5 General procedure for the reaction of $^{R3}LH_2$ with $[(THF)_2AeN"_2]$ in THF-d_8

A solution of $^{R3}LH_2$ (0.050 mmol, 1 eq.; R_3 = Me_3, $Me_2{}^tBu$, $^iPr_3$, Ph_2Me and Ph_3) in THF-d_8 (0.25 mL) was added dropwise to a solution of $[(THF)_2Ae\{N(SiMe_3)_2\}_2]$ (0.050 mmol, 1 eq.; Ae = Ca, Sr and Ba) in THF-d_8 (0.25 mL). This resulted in the formation of bright yellow reaction mixtures, which were transferred to J-Youngs' tap NMR tubes. ^{1}H NMR spectra were recorded as soon as possible following the initial room temperature reaction (*ca*. 10 minutes), with further spectra recorded at various time intervals after the reaction mixtures were left to stand at room temperature, then heated at various temperatures. The complexes $[(^{R3}LH)Ae\{N(SiMe_3)_2\}(THF)_n]$ (Ae = Ca, Sr and Ba; R_3 = Me_3, $Me_2{}^tBu$, $^iPr_3$, Ph_2Me and Ph_3), $[(^{R3}L)Ae(THF)_n]$ (Ae = Ca, R_3 = $Me_2{}^tBu$, $^iPr_3$, Ph_2Me and Ph_3; Ae = Ca, Sr and Ba, R_3 = Ph_3) and $[(^{R3\text{-}\mu\text{-}R2}L)Ae\{N(SiMe_3)_2\}(THF)_n]$ (Ae = Ca, Sr and Ba, R_3 = Me_3, Ph_2Me and Ph_3) formed in solution (see **Tables 6.1**–**3**), but were not isolated.



$[(^{R3}L)Ae(THF)_n]$ $[(^{R3}LH)AeN"(THF)_n]$ $[(^{R3\text{-}\mu\text{-}R2}L)AeN"(THF)_n]$

Table 6.1 Maximum percentage conversion of $^{R_3}LH_2$ (R_3 = Me_3, $Me_2{}^tBu$, $^iPr_3$, Ph_2Me and Ph_3) into [(^{R_3}LH)AeN"$(THF)_n$] (Ae = Ca, Sr and Ba) in THF-d_8 with relevant reaction temperatures and times.

R_3	Ca	Sr	Ba
Me_3	>99% after 10 mins at 25 °C. Intermediate.	>99% after 10 mins at 25 °C. Intermediate.	>99% after 10 mins at 25 °C. Intermediate.
$Me_2{}^tBu$	44% after 16 at 80 °C. Equilibrium mixture.	>99% after 10 mins at 25 °C. Final product.	>99% after 10 mins at 25 °C. Final product.
$^iPr_3$	55% after 72 h at 80 °C. Equilibrium mixture.	50% after 24 h at 80 °C Equilibrium mixture.	90% after 10 mins at 25 °C. Equilibrium mixture.
Ph_2Me	>99% after 10 mins at 25 °C. Intermediate.	>99% after 10 mins at 25 °C. Intermediate.	>99% after 10 mins at 25 °C. Intermediate.
Ph_3	>99% after 16 h at 25 °C. Intermediate.	>99% after 10 mins at 25 °C. Intermediate.	>99% after 10 mins at 25 °C. Intermediate.

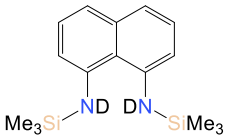
Table 6.2 Maximum percentage conversion of $^{R_3}LH_2$ (R_3 = Me_3, $Me_2{}^tBu$, $^iPr_3$, Ph_2Me and Ph_3) into [(^{R_3}L)Ae$(THF)_n$] (Ae = Ca, Sr and Ba) in THF-d_8 with relevant reaction temperatures and times.

R_3	Ca	Sr	Ba
Me_3	Not observed.	Not observed.	Not observed.
$Me_2{}^tBu$	39% after 16 h at 80 °C. Equilibrium mixture.	Not observed.	Not observed.
$^iPr_3$	4% after 72 h at 80 °C. Equilibrium mixture.	Not observed.	Not observed.
Ph_2Me	>99% after 16 h at 25 °C. Reversible.	Not observed.	Not observed.
Ph_3	>99% after 3 h at 80 °C. Reversible.	63% after 2 h at 60 °C. Reversible.	31% after 24 h at 25 °C. Reversible.

Table 6.3 Maximum percentage conversion of $^{R_3}LH_2$ (R_3 = Me_3, $Me_2{}^tBu$, $^iPr_3$, Ph_2Me and Ph_3) into [($^{R_3\text{-}\mu\text{-}R_2}L$)AeN"(THF)$_n$] (Ae = Ca, Sr and Ba) in THF-d_8 with relevant reaction temperatures and

R_3	Ca	Sr	Ba
Me_3	>99% after 16 h at 80 °C. Final product.	>99% after 16 h at 80 °C. Final product.	>99% after 16 h at 80 °C. Final product.
$Me_2{}^tBu$	Not observed.	Not observed.	Not observed.
$^iPr_3$	Not observed.	Not observed.	Not observed.
Ph_2Me	>99% after 16 h at 80 °C. Final product.	>99% after 16 h at 80 °C. Final product.	>99% after 16 h at 80 °C. Final product.
Ph_3	>99% after 1 month at 110 °C. Final product	>99% after 16 h at 80 °C. Final product.	>99% after 3 h at 50 °C. Final product.

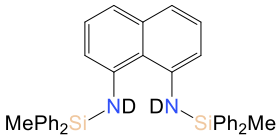
6.2.6 Synthesis of $^{Me_3}LD_2$



$^{Me_3}LH_2$ (500 mg, 1.65 mmol, 1 eq.) was dissolved in *n*-hexane (10 mL). The solution was cooled to −30 °C, then *n*-butyllithium (2.5 M in hexanes, 2.00 mL, 4.99 mmol, 3 eq.) was added dropwise over 10 minutes. The reaction mixture was allowed to warm to room temperature and stirred for two hours. The reaction mixture was cooled again to −30 °C, with methanol-d_1 (203 μL, 4.99 mmol, 3 eq.) then added. The reaction mixture was allowed to warm to room temperature, which resulted in the precipitation of a white solid. The solution was filtered, then all solvents were removed and the resulting solid dried *in vacuo* for 1 hour. $^{Me_3}LD_2$ (354 mg, 1.16 mmol, 70%) was isolated as an off-white powder. ^1H, $^{13}C\{^1H\}$ and ^{29}Si NMR spectroscopic data in THF-d_8 were in full agreement with those of $^{Me_3}LH_2$,[2] with the

exception that the NH signal at δ = 6.38 ppm was fully supressed. ^{2}H NMR (C_4H_8O, 77 MHz, 298 K): δ (ppm) = 6.29 ppm (s, br, N***D***).

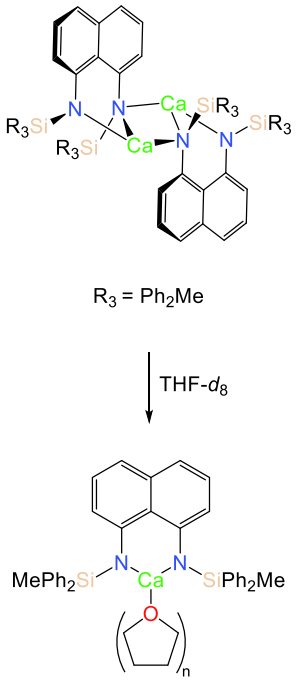
6.2.7 Synthesis of $^{Ph_2Me}LD_2$



$^{Ph_2Me}LH_2$ (920 mg, 1.67 mmol, 1 eq.) was dissolved in toluene (10 mL). The solution was cooled to −30 °C, then *n*-butyllithium (1.6 M in hexanes, 2.00 mL, 5.01 mmol, 3 eq.) was added dropwise over 10 minutes. The reaction mixture was allowed to warm to room temperature and stirred for two hours. The reaction mixture was cooled again to −30 °C, with methanol-d_1 (204 μL, 5.01 mmol, 3 eq.) then added. The reaction mixture was allowed to warm to room temperature, which resulted in the precipitation of a white solid. The solution was filtered, then all solvents were removed and the resulting solid dried *in vacuo* for 1 hour. $^{Ph_2Me}LD_2$ (847 mg, 1.53 mmol, 92%) was isolated as an off-white powder. ^{1}H, ^{13}C{^{1}H} and ^{29}Si NMR spectroscopic data in THF-d_8 were in full agreement with those of $^{Ph_2Me}LH_2$,[2] with the exception that the NH signal at δ = 6.65 ppm was fully supressed. ^{2}H NMR (C_4H_8O, 77 MHz, 298 K): δ (ppm) = 6.61 ppm (s, br, N***D***).

6.3 Experimental details for Chapter 3

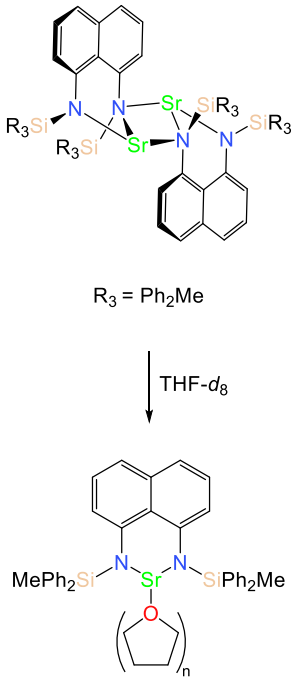
6.3.1 Synthesis of [(^{Ph_2Me}L)Ca]$_2$ (6)



A solution of $^{Ph_2Me}LH_2$ (276 mg, 0.500 mmol, 2 eq.) in benzene (2 mL) was carefully layered over a solution of [CaN"$_2$]$_2$ (180 mg, 0.250 mmol, 1 eq.) in benzene (2 mL). The amber-coloured reaction mixture was left to stand for 16 hours, resulting in the growth of pale-yellow crystals suitable for an X-ray diffraction study. The solution was decanted and the crystals washed with benzene (3 x 0.5 mL) and *n*-pentane (3 x 1 mL), then dried *in vacuo* for 1 hour. [(^{Ph_2Me}L)Ca]$_2$ (166 mg, 0.141 mmol, 56% (**6**)) was isolated as a pale yellow crystalline solid. IR (KBr): 3065, 3047, 2952, 1578, 1542, 1427, 1268, 1110, 1055, 701 cm^{-1}. Anal. Calcd. for $C_{72}H_{64}Ca_2N_4Si_4$: C, 73.42; H, 5.48; N, 4.76. Found: C, 73.21; H, 5.44; N, 4.34.

Dissolution of [(^{Ph_2Me}L)Ca]$_2$ in THF-d_8 resulted in conversion to [(^{Ph_2Me}L)Ca(THF)$_n$], which could be characterised by multinuclear NMR spectroscopy. ^{1}H NMR (C_4D_8O, 298 K, 600 MHz): δ (ppm) = 7.70 (dd, $^3J_{H\text{-}H}$ = 7.4, $^4J_{H\text{-}H}$ = 2.0 Hz, 8H, 2,6-$C_6\boldsymbol{H_5}$), 7.18–7.11 (m, 12H, 3,5-$C_6\boldsymbol{H_5}$ and 4-$C_6\boldsymbol{H_5}$ overlapping), 6.59 (t, $^3J_{H\text{-}H}$ = 7.5, 2H, 3,6-$C_{10}\boldsymbol{H_6}$), 6.56 (dd, $^3J_{H\text{-}H}$ = 7.8, $^4J_{H\text{-}H}$ = 1.9 Hz, 2H, 4,5-$C_{10}\boldsymbol{H_6}$), 6.45 (dd, $^3J_{H\text{-}H}$ = 7.1, $^4J_{H\text{-}H}$ 1.9 Hz, 2H, 2,7-$C_{10}\boldsymbol{H_6}$), 0.61 (s, 6H, Si(C$\boldsymbol{H_3}$)Ph$_2$). ^{13}C{^{1}H} NMR (C_4D_8O, 298 K, 151 MHz): δ (ppm) = 159.3 (1,8-$\boldsymbol{C_{10}}H_6$), 145.2 (1-$\boldsymbol{C_6}H_5$), 142.0 (9-$\boldsymbol{C_{10}}H_6$), 136.2 (2,6-$\boldsymbol{C_6}H_5$), 129.4 (10-$\boldsymbol{C_{10}}H_6$), 128.5 (4-$\boldsymbol{C_6}H_5$), 128.2 (3,5-$\boldsymbol{C_6}H_5$), 125.7 (3,6-$\boldsymbol{C_6}H_{10}$), 119.0 (2,7-$\boldsymbol{C_6}H_{10}$), 115.2 (4,5-$\boldsymbol{C_6}H_{10}$), 1.6 (Si($\boldsymbol{C}H_3$)Ph$_2$). ^{29}Si NMR (C_4D_8O, 298 K, 119 MHz): δ (ppm) = –27.98 (N$\boldsymbol{Si}$Ph$_2$Me).

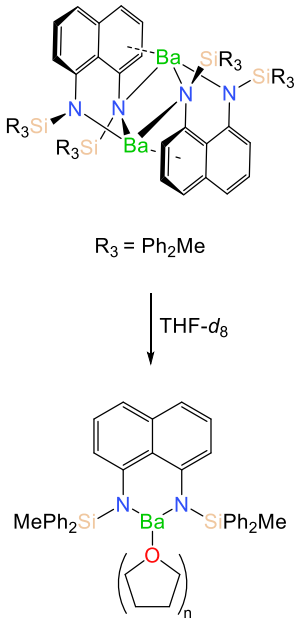
6.3.2 Synthesis of [(^{Ph_2Me}L)Sr]$_2$ (7)



A solution of $^{Ph_2Me}LH_2$ (551 mg, 1.00 mmol, 2 eq.) in benzene (2 mL) was carefully layered over a solution of [SrN"$_2$]$_2$ (409 mg, 0.500 mmol, 1 eq.) in benzene (3 mL). The amber-coloured reaction mixture was left to stand for 16 hours, resulting in the growth of bright yellow crystals suitable for an X-ray diffraction study. The solution was decanted and the crystals washed with benzene (3 x 1 mL) and *n*-pentane (3 x 2 mL), then dried *in vacuo* for 1 hour. [(^{Ph_2Me}L)Sr]$_2$ (465 mg, 0.365 mmol, 73% (**7**)) was isolated as a bright yellow crystalline solid. IR (KBr) = 3044, 2953, 1541, 1424, 1366, 1105, 1054, 886, 701 cm^{-1}. Anal. Calcd. for $C_{72}H_{64}N_4Si_4Sr_2$: C, 67.94; H, 5.07; N, 4.40. Found: C, 68.03; H, 5.16; N, 4.11.

Dissolution of [(^{Ph_2Me}L)Sr]$_2$ in THF-d_8 resulted in conversion to [(^{Ph_2Me}L)Sr(THF)$_n$], which could be characterised by multinuclear NMR spectroscopy. ^{1}H NMR (C_4D_8O, 298 K, 600 MHz): δ (ppm) = 7.75 (m, 8H, 2,6-$C_5\boldsymbol{H_6}$), 7.16–7.06 (m, 12H, 3,5-$C_5\boldsymbol{H_6}$ and 4-$C_5\boldsymbol{H_6}$ overlapping), 6.57 (t, $^3J_{H\text{-}H}$ = 7.6 Hz, 2H, 3,6-$C_{10}\boldsymbol{H_6}$), 6.52 (dd, $^3J_{H\text{-}H}$ = 7.9, $^4J_{H\text{-}H}$ = 1.5 Hz, 2H, 4,5-$C_{10}\boldsymbol{H_6}$), 6.44 (dd, $^3J_{H\text{-}H}$ = 7.4, $^4J_{H\text{-}H}$ = 1.5 Hz, 2H, 2,7-$C_{10}\boldsymbol{H_6}$), 0.58 (s, 6H, Si(C$\boldsymbol{H_3}$)Ph$_2$). ^{13}C{^{1}H} NMR (C_4D_8O, 298 K, 151 MHz): δ (ppm) = 160.0 (1,8-$\boldsymbol{C_{10}}H_6$), 145.5 (1-$\boldsymbol{C_6}H_5$), 142.0 (9-$\boldsymbol{C_{10}}H_6$), 136.3 (2,6-$\boldsymbol{C_6}H_5$), 130.3 (10-$\boldsymbol{C_{10}}H_6$), 128.3 (4-$\boldsymbol{C_6}H_5$), 128.1 (3,5-$\boldsymbol{C_6}H_5$), 125.5 (3,6-$\boldsymbol{C_{10}}H_6$), 119.1 (2,7-$\boldsymbol{C_{10}}H_6$), 114.5 (4,5-$\boldsymbol{C_{10}}H_6$), 2.0 (Si($\boldsymbol{C}H_3$)Ph$_2$). ^{29}Si NMR (C_4D_8O, 298 K, 119 MHz): δ (ppm) = –29.39 (N$\boldsymbol{Si}$Ph$_2$Me).

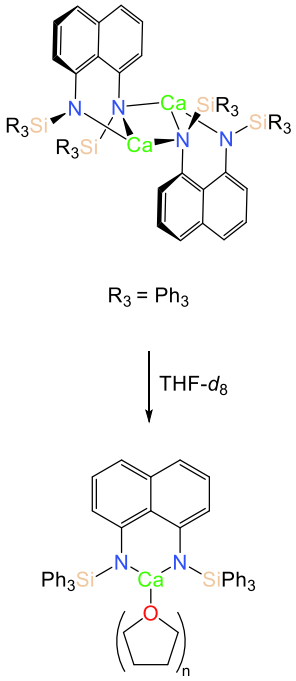
6.3.3 Synthesis of [(^{Ph_2Me}L)Ba]$_2$ (8)



A solution of $^{Ph_2Me}LH_2$ (551 mg, 1.00 mmol, 2 eq.) in benzene (2 mL) was carefully layered over a solution of [BaN"$_2$]$_2$ (459 mg, 0.500 mmol, 1 eq.) in benzene (3 mL). The amber-coloured reaction mixture was left to stand for 16 hours, resulting in the growth of bright yellow crystals suitable for an X-ray diffraction study. The solution was decanted and the crystals washed with benzene (3 x 1 mL) and *n*-pentane (3 x 2 mL), then dried *in vacuo* for 1 hour. [(^{Ph_2Me}L)Ba]$_2$·(C$_6$H$_6$) (560 mg, 0.386 mmol, 77% (**8**)) was isolated as a bright yellow crystalline solid. IR (KBr): 3038, 3012, 2952, 1532, 1424, 1365, 1319, 1106, 1068, 894, 736 cm^{-1}. Anal. Calcd. for C$_{72}$H$_{64}$Ba$_2$N$_4$Si$_4$·(C$_6$H$_6$): C, 64.59; H, 4.86; N, 3.86. Found: C, 63.87; H, 4.55; N, 3.46.

Dissolution of [(^{Ph_2Me}L)Ba]$_2$ in THF-d_8 resulted in conversion to [(^{Ph_2Me}L)Ba(THF)$_n$], which could be characterised by multinuclear NMR spectroscopy. ^{1}H NMR (C$_4$D$_8$O, 298 K, 600 MHz): δ (ppm) = 7.72 (dd, $^3J_{H\text{-}H}$ = 7.6, $^4J_{H\text{-}H}$ = 1.7 Hz, 8H, 2,6-C$_6$***H*****$_5$**), 7.20–7.08 (m, 12H, 3,5-C$_6$***H*****$_5$** and 4-C$_6$***H*****$_5$** overlapping), 6.59 (t, $^3J_{H\text{-}H}$ = 7.7 Hz, 2H, 3,6-C$_{10}$***H*****$_6$**), 6.52 (dd, $^3J_{H\text{-}H}$ = 7.8, $^4J_{H\text{-}H}$ = 1.4 Hz, 2H, 4,5-C$_{10}$***H*****$_6$**), 6.39 (dd, $^3J_{H\text{-}H}$ = 6.8, $^4J_{H\text{-}H}$ = 1.4 Hz, 2H, 2,7-C$_{10}$***H*****$_6$**), 0.62 (s, 6H, Si(C***H*****$_3$)Ph$_2$). ^{13}C{^{1}H} NMR (C$_4$D$_8$O, 298 K, 151 MHz): δ (ppm) = 158.9 (1,8-***C*****$_{10}$**H$_6$), 145.3 (1-***C*****$_6$**H$_5$), 142.3 (9-***C*****$_{10}$**H$_6$), 136.3 (2,6-***C*****$_6$**H$_5$), 129.4 (10-***C*****$_{10}$**H$_6$), 128.4 (4-***C*****$_6$**H$_5$), 128.2 (3,5-***C*****$_6$**H$_5$), 125.7 (3,6-***C*****$_{10}$**H$_6$), 118.5 (2,7-***C*****$_{10}$**H$_6$), 114.1 (4,5-***C*****$_{10}$**H$_6$), 1.6 (Si(***C***H$_3$)Ph$_2$). ^{29}Si NMR (C$_4$D$_8$O, 298 K, 119 MHz): δ (ppm) = −30.64 (N***Si***Ph$_2$Me).

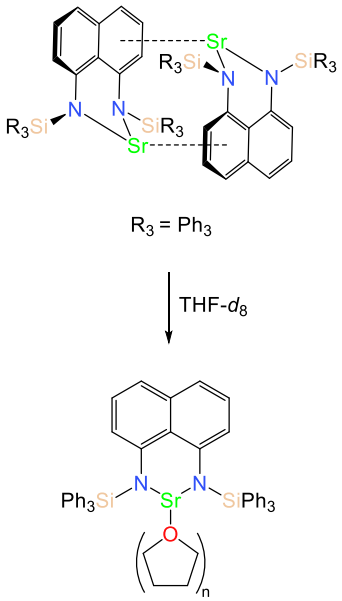
6.3.4 Synthesis of [(^{Ph3}L)Ca]$_2$ (9)



A solution of $^{Ph3}LH_2$ (254 mg, 0.376 mmol, 2 eq.) in benzene (2 mL) was added to a solution of [CaN"$_2$]$_2$ (136 mg, 0.188 mmol, 1 eq.) in benzene (2 mL). The yellow reaction mixture was left to stand for 16 hours, then lyophilised to yield a bright yellow powder. Benzene (10 mL) was added and refluxed at 100 °C to redissolve the yellow solid. Slow cooling of the solution to 25 °C resulting in the growth of bright yellow crystals suitable for an X-ray diffraction study. The solution was decanted and the crystals washed with benzene (0.5 mL) and *n*-pentane (3 x 0.5 mL) then dried *in vacuo* for 1 hour. [(^{Ph3}L)Ca]$_2$ (98 mg, 0.069 mmol, 37% (**9**)) was isolated as a yellow crystalline solid. IR (KBr): 3066, 3049, 2992, 1544, 1427, 1279, 1103, 881, 832, 703 cm^{-1}. Anal. Calcd. for $C_{92}H_{72}Ca_2N_4Si_4$: C, 77.48; H, 5.09; N, 3.93. Found: C, 77.70; H, 5.20; N, 3.15.

Dissolution of [(^{Ph3}L)Ca]$_2$ in THF-d_8 resulted in conversion to [(^{Ph3}L)Ca(THF)$_n$], which could be characterised by multinuclear NMR spectroscopy. ^{1}H NMR (C_4D_8O, 298 K, 600 MHz): δ (ppm) = 7.70 (d, $^3J_{H-H}$ = 7.3 Hz, 12H, 2,6-C_6***H*****$_5$**), 7.16 (t, $^3J_{H-H}$ = 7.5 Hz, 6H, 4-C_6***H*****$_5$**), 7.06 (t, $^3J_{H-H}$ = 7.4 Hz, 12H, 3,5-C_6***H*****$_5$**), 6.66–6.62 (m, 4H, 4,5-C_{10}***H*****$_6$** and 2,7-C_{10}***H*****$_6$** overlapping), 6.55 (t, $^3J_{H-H}$ = 7.6 Hz, 2H, 3,6-C_{10}***H*****$_6$**).^{13}C{^{1}H} NMR (C_4D_8O, 298 K, 151 MHz): δ (ppm) = 158.6 (1,8-***C*****$_{10}$**H_6), 143.1 (1-***C*****$_6$**H_5), 141.7 (9-***C*****$_{10}$**H_6), 137.2 (2,6-***C*****$_6$**H_5), 129.5 (10-***C*****$_{10}$**H_6), 128.7 (4-***C*****$_6$**H_5), 128.3 (3,5-***C*****$_6$**H_5), 125.6 (3,6-***C*****$_{10}$**H_6), 120.5 (2,7-***C*****$_{10}$**H_6), 116.1 (4,5-***C*****$_{10}$**-H_6). ^{29}Si NMR (C_4D_8O, 298 K, 119 MHz): δ (ppm) = −31.57 (N***Si***Ph_3).

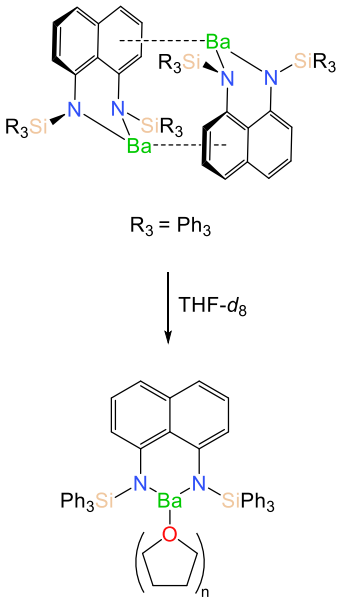
6.3.5 Synthesis of [(^{Ph3}L)Sr]$_2$ (10)



A solution of $^{Ph3}LH_2$ (254 mg, 0.375 mmol, 2 eq.) in benzene (2 mL) was carefully layered over a solution of [SrN"$_2$]$_2$ (172 mg, 0.188 mmol, 1 eq.) in benzene (2 mL). The amber-coloured reaction mixture was left to stand for 16 hours, resulting in the growth of bright yellow crystals suitable for an X-ray diffraction study. The solution was decanted and the crystals washed with benzene (3 x 0.5 mL) and *n*-pentane (3 x 1 mL), then dried *in vacuo* for 1 hour. [(^{Ph3}L)Sr]$_2$ (225 mg, 0.148 mmol, 79% (**10**)) was isolated as a bright yellow crystalline solid. IR (KBr): 3065, 3043, 1533, 1424, 1364, 1327, 1105, 830, 704, 516 cm^{-1}. Anal. Calcd. for $C_{92}H_{72}N_4Si_4Sr_2$: C, 72.64; H, 4.77; N, 3.68. Found: C, 71.72; H, 4.24; N, 3.30.

Dissolution of [(^{Ph3}L)Sr]$_2$ in THF-d_8 resulted in conversion to [(^{Ph3}L)Sr(THF)$_3$] (**12**), which could be characterised by multinuclear NMR spectroscopy. ^{1}H NMR (C_4D_8O, 298 K, 600 MHz): δ (ppm) = 7.70 (dd, $^3J_{H\text{-}H}$ = 7.9, $^4J_{H\text{-}H}$ = 1.5 Hz, 12H. 2,6-C_6***H*****$_5$**), 7.16 (ddt, $^3J_{H\text{-}H}$ = 8.8, 6.9, $^4J_{H\text{-}H}$ = 1.4 Hz, 6H, 4-C_6***H*****$_5$**), 7.05 (t, $^3J_{H\text{-}H}$ = 7.4 Hz, 12H, 3,5-C_6***H*****$_5$**), 6.59 (dd, $^3J_{H\text{-}H}$ = 7.6, $^4J_{H\text{-}H}$ = 1.6 Hz, 2H, 4,5-C_{10}***H*****$_6$**), 6.56 (dd, $^3J_{H\text{-}H}$ = 7.6, $^4J_{H\text{-}H}$ = 1.6 Hz, 2H, 2,7-C_{10}***H*****$_6$**), 6.52 (t, $^3J_{H\text{-}H}$ = 7.5 Hz, 2H, 3,6-C_{10}***H*****$_6$**). ^{13}C{^{1}H} NMR (C_4D_8O, 298 K, 151 MHz): δ (ppm) = 158.6 (1,8-***C*****$_{10}$**H_6), 143.5 (1-*C*$_6$H$_5$), 142.2 (9-***C*****$_{10}$**H_6), 137.2 (2,6-***C*****$_6$**H_5), 129.3 (10-***C*****$_{10}$**H_6), 128.7 (4-***C*****$_6$**H_5), 128.3 (3,5-***C*****$_6$**H_5), 125.6 (3,6-***C*****$_{10}$**H_6), 120.4 (2,7-***C*****$_{10}$**H_6), 115.5 (4,5-***C*****$_{10}$**H_6). ^{29}Si NMR (C_4D_8O, 298 K, 119 MHz): δ (ppm) = −32.92 (N***Si***Ph$_3$).

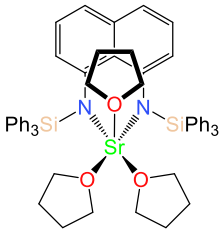
6.3.6 Synthesis of [(^{Ph3}L)Ba]$_2$ (11)



A solution of ^{Ph3}LH$_2$ (254 mg, 0.375 mmol, 2 eq.) in benzene (2 mL) was carefully layered over a solution of [BaN"$_2$]$_2$ (172 mg, 0.188 mmol, 1 eq.) in benzene (3 mL). The amber-coloured reaction mixture was left to stand for 16 hours, resulting the growth of bright yellow crystals suitable for an X-ray diffraction study. The solution was decanted and the crystals washed with benzene (3 x 0.5 mL) and *n*-pentane (3 x 1 mL), then dried *in vacuo* for 1 hour. [(^{Ph3}L)Ba]$_2$ (244 mg, 0.151 mmol, 80% (**11**)) was isolated as a bright yellow crystalline solid. IR (KBr): 3065, 3042, 1531, 1426, 1325, 1105, 900, 703, 514 cm^{-1}. Anal. Calcd. for $C_{92}H_{72}Ba_2N_4Si_4$: C, 68.18; H, 4.48; N, 3.46. Found: C, 67.75; H, 4.32; N, 3.22.

Dissolution of [(^{Ph3}L)Ba]$_2$ in THF-d_8 resulted in conversion to [(^{Ph3}L)Ba(THF)$_n$], which could be characterised by multinuclear NMR spectroscopy. ^{1}H NMR (C_4D_8O, 298 K, 600 MHz): δ (ppm) = 7.69 (d, $^3J_{H-H}$ = 7.2 Hz, 12H, 2,6-C_6***H*****$_5$**), 7.16 (t, $^3J_{H-H}$ = 7.4 Hz, 6H, 4-C_6***H*****$_5$**), 7.06 (t, $^3J_{H-H}$ = 7.4 Hz, 12H, 3,5-C_6***H*****$_5$**), 6.58 (dd, $^3J_{H-H}$ = 7.1, $^4J_{H-H}$ = 2.2 Hz, 2H, 4,5-C_{10}***H*****$_6$**), 6.54 (m, 4H, 3,6-C_{10}***H*****$_6$** and 2,7-C_{10}***H*****$_6$** overlapping). ^{13}C{^{1}H} NMR (C_4D_8O, 298 K, 151 MHz): δ (ppm) = 157.8 (1,8-***C*****$_{10}$**H_6), 143.3 (1-***C*****$_6$**H_5), 142.3 (9-***C*****$_{10}$**-H_6), 137.2 (2,6-***C*****$_6$**H_5), 129.2 (10-***C*****$_{10}$**H_6), 128.7 (4-***C*****$_6$**H_5), 128.3 (3,5-***C*****$_6$**H_5), 125.7 (3,6-***C*****$_{10}$**H_6), 120.0 (2,7-***C*****$_{10}$**H_6), 114.9 (4,5-***C*****$_{10}$**H_6). ^{29}Si NMR (C_4D_8O, 298 K, 119 MHz): δ (ppm) = −34.23 (N***Si***Ph_3).

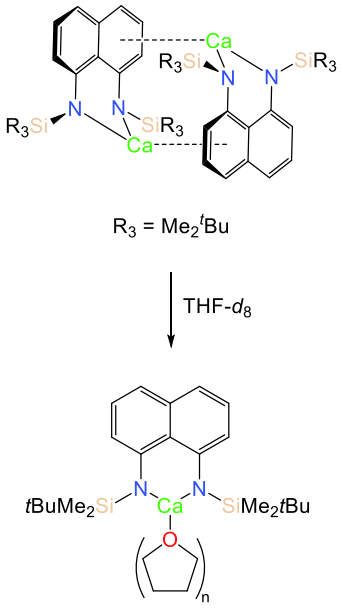
6.3.7 Synthesis of [(^{Ph_3}L)Sr(THF)$_3$] (12)



Dissolution of [(^{Ph_3}L)Sr]$_2$ (30 mg, 20 μmol (**10**)) in THF (0.5 mL) resulted in the growth of large block-like yellow crystals of [(^{Ph_3}L)Sr(THF)$_3$] (**12**) suitable for an X-ray diffraction study when left to stand at 25 °C for 24 hours. Complex **12** was not isolated on a preparative scale.

6.4 Experimental details for Chapter 4

6.4.1 Synthesis of [(^{Me_2tBu}L)Ca]$_2$ (13)

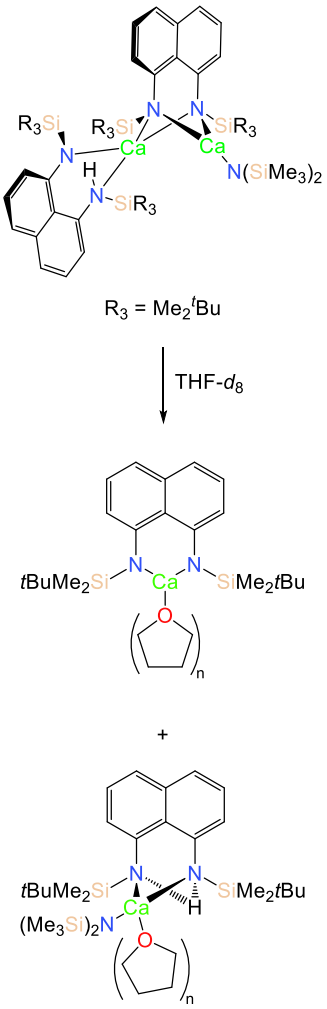


A solution of ^{Me_2tBu}LH$_2$ (250 mg, 0.646 mmol, 2 eq.) in benzene (2 mL) was added to a stirred solution of [CaN"$_2$]$_2$ (233 mg, 0.323 mmol, 1 eq.) in benzene (2 mL). The amber-coloured reaction mixture was heated at 80 °C and stirred for 16 hours. The solution was slowly cooled to 25 °C and left to stand for 16 hours, resulting in the growth of a small crop of bright yellow crystals suitable for an X-ray diffraction study. The solution was filtered and lyophillised, yielding a pale-yellow powder. This was redissolved in benzene (3 mL) at 100 °C, with the resulting solution then allowed to cool to room temperature and left to stand for 16 hours. This yielded a larger crop of yellow crystals, which were isolated by filtration, washed with cold *n*-pentane (−78 °C, 3 x 0.5 mL) and dried *in vacuo* for 1 hour. [(^{Me_2tBu}L)Ca]$_2$ (22 mg, 0.026 mmol, 8% (**13**)) was isolated as a bright yellow crystalline solid. IR (KBr): 2954, 2925, 2853, 1570, 1533, 1431, 1372, 1308, 1258, 1078, 819 cm^{-1}. Anal. calc. for $C_{46}H_{78}Ca_2N_4Si_4$: C, 62.21; H, 8.54; N, 6.59.

Despite repeated elemental analysis of crystalline samples of **13**, satisfactory agreement with the calculated values were not obtained. Best result: C, 61.09; H, 7.55; N, 5.58.

Dissolution of $[(^{Me_2{}^tBu}L)Ca]_2$ in THF-d_8 resulted in conversion to $[(^{Me_2{}^tBu}L)Ca(THF)_n]$, which could be characterised by multinuclear NMR spectroscopy. ^{1}H NMR (C_4D_8O, 298 K, 600 MHz): δ (ppm) = 6.65 (t, $^3J_{H\text{-}H}$ = 7.6 Hz, 2H, 3,6-C_{10}***H*****$_6$**), 6.48 (dd, $^3J_{H\text{-}H}$ = 7.9, $^4J_{H\text{-}H}$ = 1.2 Hz, 2H, 4,5-C_{10}***H*****$_6$**), 6.35 (dd, $^3J_{H\text{-}H}$ = 7.6, $^4J_{H\text{-}H}$ = 1.2 Hz, 2H, 2,7-C_{10}***H*****$_6$**), 0.88 (s, 18H, C(C***H*****$_3$**$)_3$), 0.14 (s, 12H, Si(C***H*****$_3$**$)_2$). ^{13}C{^{1}H} NMR (C_4D_8O, 298 K, 151 MHz): δ (ppm) = 159.9 (1,8-***C*****$_{10}$**H_6), 142.6 (9-***C*****$_{10}$**H_6), 128.9 (10-***C*****$_{10}$**H_6), 125.6 (4,5-***C*****$_{10}$**H_6), 118.5 (2,7-***C*****$_{10}$**H_6), 114.2 (3,6-***C*****$_{10}$**H_6), 29.7 (SiC(***C***$H_3)_3$), 22.0 (Si***C***Me_3), −0.1 (Si(***C***$H_3)_2{}^t$Bu). ^{29}Si NMR (C_4D_8O, 298 K, 119 MHz): δ (ppm) = –13.16 (***Si***$Me_2{}^t$Bu).

6.4.2 Synthesis of [(^{Me_2tBu}LH)Ca(μ-^{Me_2tBu}L)Ca{N(SiMe$_3$)$_2$}] (14)

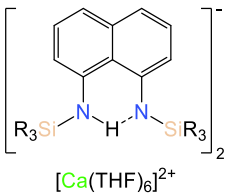


A solution of ^{Me_2tBu}LH$_2$ (250 mg, 0.646 mmol, 2 eq.) in *n*-hexane (2 mL) was added to a stirred solution of [CaN"$_2$]$_2$ (233 mg, 0.323 mmol, 1 eq.) in *n*-hexane (2 mL). The amber-coloured reaction mixture was heated at 80 °C and stirred for hours. The solution was slowly cooled to 25 °C and left to stand for 16 hours, resulting in the growth of a small crop of bright yellow crystals of [(^{Me_2tBu}L)Ca]$_2$ (**13**). The reaction mixture was filtered and concentrated *in vacuo*, resulting in the growth beige crystals suitable for an X-ray diffraction study. These were isolated by filtration, washed with cold *n*-pentane (−78 °C, 3 x 0.5 mL) and dried *in vacuo* for 1 hour. [(^{Me_2tBu}LH)Ca(μ-^{Me_2tBu}L)Ca{N(SiMe$_3$)$_2$}] (174 mg, 0.172 mmol, 53% (**14**)) was isolated as a pale brown crystalline solid. IR (KBr): 3058, 2957, 2930, 2855, 1556, 1266, 1058, 1022, 828 cm^{-1}. Anal. calcd. for $C_{53}H_{91}Ca_2N_5Si_6$: C, 59.40; H, 9.07; N, 6.93. Found: C, 59.23; H, 9.13; N, 6.56.

Dissolution of [(^{Me_2tBu}LH)Ca(μ-^{Me_2tBu}L)Ca{N(SiMe$_3$)$_2$}] in THF-*d*$_8$ resulted in conversion to a 1:1 mixture of [(^{Me_2tBu}LH)Ca{N(SiMe$_3$)$_2$}(THF)$_n$] and [(^{Me_2tBu}L)Ca(THF)$_n$], which could each be characterised by multinuclear NMR spectroscopy (*Note: all reported signals are for [(^{Me_2tBu}LH)Ca{N(SiMe$_3$)$_2$}(THF)$_n$]; Additional ^{1}H, ^{13}C{^{1}H} and ^{29}Si signals present are the same as those assigned as [(^{Me_2tBu}L)Ca(THF)$_n$] in THF-d$_8$ NMR spectra of* ***13*****).** ^{1}H NMR (THF-d$_8$, 298 K,

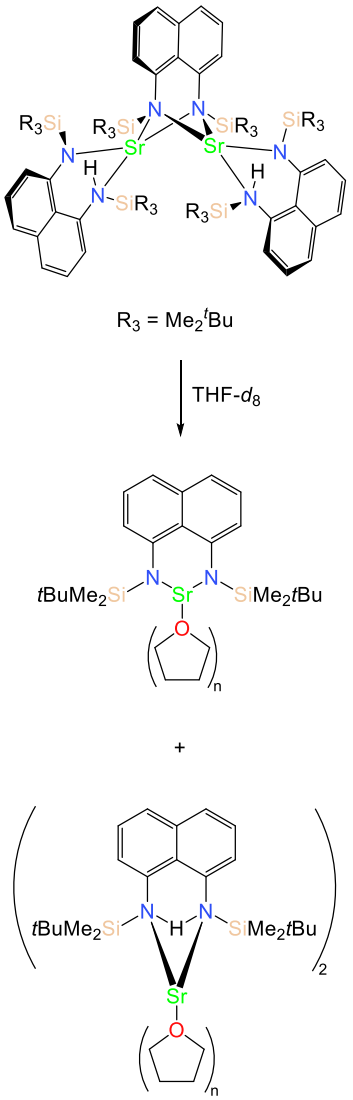
400 MHz): δ (ppm) = 14.86 (s, 1H, (N,N)μ$_2$-***H***), 6.56 (t, $^3J_{H\text{-}H}$ = 7.7 Hz, 2H, 3,6-C$_{10}$***H$_6$***), 6.15 (d, $^3J_{H\text{-}H}$ = 7.8 Hz, 2H, 4,5-C$_{10}$***H$_6$***), 5.99 (d, $^3J_{H\text{-}H}$ = 7.7 Hz, 2H, 2,7-C$_{10}$***H$_6$***), 0.95 (s, 18H, C(C***H$_3$***)$_3$), 0.16 (s, 12H, Si(C***H$_3$***)$_2$), 0.00 (s, 6H, N(Si(C***H$_3$***)$_3$)$_2$), −0.06 (s, 12H, N(Si(C***H$_3$***)$_3$)$_2$). ^{13}C{^{1}H} NMR (THF-d$_8$, 298 K, 151 MHz): δ (ppm) = 159.5 (1,8-***C$_{10}$***H$_6$), 140.4 (9-***C$_{10}$***H$_6$), 126.3 (3,6-***C$_{10}$***H$_6$), 122.9 (10-***C$_{10}$***H$_6$), 110.4 (4,5-***C$_{10}$***H$_6$), 110.0 (2,7-***C$_{10}$***H$_6$), 28.7 (C(***C***H$_3$)$_3$), 21.3 (Si***C***Me$_3$), 5.9 (N(Si(***C***H$_3$)$_2$)$_2$), 5.6 (N(Si(***C***H$_3$)$_3$)$_2$), –1.4 (Si(***C***H$_3$)$_2$). ^{29}Si NMR (THF-d$_8$, 298 K, 119 MHz): δ (ppm) = −5.71 (***Si***Me$_2$^{t}Bu), –15.15 (N(***Si***Me$_3$)$_2$).

6.4.3 Synthesis of [^{Me_2tBu}LH]$_2$[Ca(THF)$_6$] (15)



Dissolution of [(^{Me_2tBu}LH)Ca(μ-^{Me_2tBu}L)Ca{N(SiMe$_3$)$_2$}] (30 mg, 30 μmol) in THF (0.5 mL) resulted in the growth of yellow crystals of [^{Me_2tBu}LH]$_2$[Ca(THF)$_6$] (**15**) suitable for an X-ray diffraction study when left to stand for 72 hours at 25 °C. The isolation and further characterisation of **15** was not possible due to its decomposition *in vacuo*.

6.4.4 Synthesis of [{(^{Me_2tBu}LH)Sr}$_2$(μ-^{Me_2tBu}L)] (16)

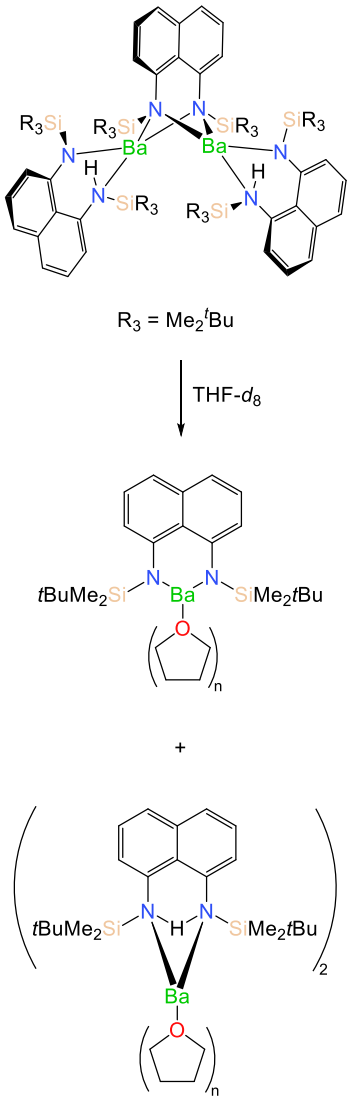


A solution of $^{Me_2tBu}LH_2$ (194 mg, 0.500 mmol, 3 eq.) in benzene (1 mL) was added dropwise to a stirred solution of [SrN"$_2$]$_2$ (137 mg, 0.167 mmol, 1 eq.) in benzene (2 mL). The amber-coloured reaction mixture was heated at 80 °C for 16 hours. Slow cooling of the solution to 25 °C resulting in the growth of yellow crystals suitable for an X-ray diffraction study. The solution was decanted and the crystals washed with benzene (3 x 0.5 mL), and *n*-pentane (3 x 1 mL) then dried *in vacuo* for 1 hour. [{(^{Me_2tBu}LH)Sr}$_2$(μ-^{Me_2tBu}L)] (112 mg, 0.084 mmol, 50% (**16**)) was isolated as a pale yellow crystalline solid. IR (KBr): 3324, 3250, 3055, 2956, 2930, 2854, 1563, 1403, 1252, 1062, 876, 830, 666 cm^{-1}. Anal. Calcd. for $C_{66}H_{110}N_6Si_6Sr_2$: C, 59.54; H, 8.33; N, 6.31. Found: C, 60.12; H, 8.63; N, 6.17.

Dissolution of [{(^{Me_2tBu}LH)Sr}$_2$(μ-^{Me_2tBu}L)] in THF-d_8 resulted in conversion to a 1:1 mixture of [(^{Me_2tBu}LH)$_2$Sr(THF)$_n$] and [(^{Me_2tBu}L)Sr(THF)$_n$], which could each be characterised by multinuclear NMR spectroscopy. **[(^{Me_2tBu}LH)$_2$Sr(THF)$_n$]:** ^{1}H NMR (C_4D_8O, 298 K, 600 MHz): δ (ppm) = 13.16 (s, 2H, (N,N)μ$_2$-***H***,), 6.75 (t, $^3J_{H\text{-}H}$ = 7.8 Hz, 4H, 3,6-C_{10}***H*****$_6$**), 6.46 (dd, $^3J_{H\text{-}H}$ = 7.9, $^4J_{H\text{-}H}$ 1.2 Hz, 4H, 4,5-C_{10}***H*****$_6$**), 6.22 (dd, $^3J_{H\text{-}H}$ = 7.6, $^4J_{H\text{-}H}$ = 1.2 Hz, 4H, 2,7-C_{10}***H*****$_6$**), 0.92 (s, 36H, C(C***H*****$_3$)$_3$), 0.21 (s, 24H, Si(C***H*****$_3$)$_2$). ^{13}C{^{1}H} NMR (C_4D_8O, 298 K, 151 MHz): δ (ppm) = 157.6 (1,8-***C*****$_{10}$**H_6), 140.4 (9-***C*****$_{10}$**H_6), 127.0

(3,6-***C*****$_{10}$**H$_6$), 122.6 (10-***C*****$_{10}$**H$_6$), 113.3 (4,5-***C*****$_{10}$**H$_6$), 112.2 (2,7-***C*****$_{10}$**H$_6$), 28.7 (SiC(***C***H$_3$)$_3$), 21.4 (Si***C***Me$_3$), –1.1 (Si(***C***H$_3$)$_2$^{t}Bu). ^{29}Si NMR (C$_4$D$_8$O, 298 K, 119 MHz): δ (ppm) = −3.54 (***Si***Me$_2$^{t}Bu). **[(Me$_2$^{t}BuL)Sr(THF)$_n$]:** ^{1}H NMR (C$_4$D$_8$O, 298 K, 600 MHz): δ (ppm) = 6.61 (t, $^3J_{H\text{-}H}$ = 7.6 Hz, 2H, 3,6-C$_{10}$***H*****$_6$**), 6.46 (dd, $^3J_{H\text{-}H}$ = 7.9, $^4J_{H\text{-}H}$ = 1.4 Hz, 2H, 4,5-C$_{10}$***H*****$_6$**), 6.31 (dd, $^3J_{H\text{-}H}$ = 7.5, $^4J_{H\text{-}H}$ = 1.4 Hz, 2H, 2,7-C$_{10}$***H*****$_6$**), 0.86 (s, 18H, C(C***H*****$_3$**)$_3$), 0.11 (s, 12H, Si(C***H*****$_3$**)$_2$). ^{13}C{^{1}H} NMR (C$_4$D$_8$O, 298 K, 151 MHz): δ (ppm) = 160.7 (1,8-***C*****$_{10}$**H$_6$), 142.3 (9-***C*****$_{10}$**H$_6$), 130.4 (10-***C*****$_{10}$**H$_6$), 125.3 (3,6-***C*****$_{10}$**H$_6$), 118.7 (2,7-***C*****$_{10}$**H$_6$), 113.3 (4,5-***C*****$_{10}$**H$_6$), 29.6 (SiC(***C***H$_3$)$_3$), 22.1 (Si***C***Me$_3$), −0.0 (Si(***C***H$_3$)$_2$^{t}Bu). ^{29}Si NMR (C$_4$D$_8$O, 298 K, 119 MHz): δ (ppm) = –14.94 (***Si***Me$_2$^{t}Bu).

6.4.5 Synthesis of [{(^{Me_2tBu}LH)Ba}$_2$(μ-^{Me_2tBu}L)] (17)



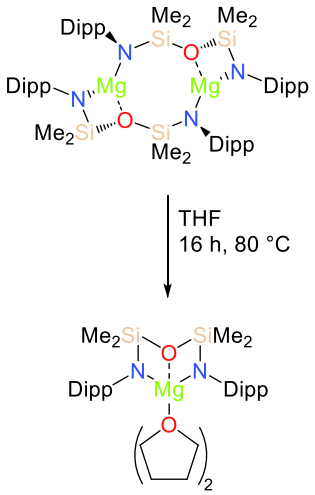
A solution of $^{Me_2tBu}LH_2$ (194 mg, 0.500 mmol, 3 eq.) in benzene (2 mL) was added to a stirred solution of [BaN"$_2$]$_2$ (167 mg, 0.250 mmol, 1 eq.) in benzene (3 mL). The amber-coloured reaction mixture was heated at 80 °C for 16 hours. Slow cooling of the solution to 25 °C resulting in the growth of yellow crystals suitable for an X-ray diffraction study. The solution was decanted and the crystals washed with benzene (3 x 0.5 mL) and *n*-pentane (3 x 1 mL), then dried *in vacuo* for 1 hour. [{(^{Me_2tBu}LH)Ba}$_2$(μ-^{Me_2tBu}L)] (188 mg, 0.131 mmol, 79% (**17**)) was isolated as a pale yellow crystalline solid. IR (KBr): 3324, 3249, 3056, 2951, 2928, 2881, 2852, 1562, 1463, 1402, 1252, 1061, 873, 832, 762, 665, 572, 478 cm^{-1}. Anal. Calcd. for $C_{66}H_{110}Ba_2N_6Si_6$: C, 55.40; H, 7.75; N, 5.87. Found: C, 55.84; H, 7.81; N, 5.61.

Dissolution of [{(^{Me_2tBu}LH)Ba}$_2$(μ-^{Me_2tBu}L)] in THF-d_8 resulted in conversion to a 1:1 mixture of [(^{Me_2tBu}LH)$_2$Ba(THF)$_n$] and [(^{Me_2tBu}L)Ba(THF)$_n$], which could each be characterised by multinuclear NMR spectroscopy. **[(^{Me_2tBu}LH)$_2$Ba(THF)$_n$]**:^{1}H NMR (C_4D_8O, 298 K, 600 MHz): δ (ppm) = 12.65 (s, 2H, (N,N)μ$_2$-***H***), 6.84 (t, $^3J_{H\text{-}H}$ = 7.8 Hz, 4H, 3,6-C_{10}***H$_6$***), 6.55 (dd, $^3J_{H\text{-}H}$ = 7.9, $^4J_{H\text{-}H}$ 1.2 Hz, 4H, 4,5-C_{10}***H$_6$***), 6.28 (dd, $^3J_{H\text{-}H}$ = 7.6, $^4J_{H\text{-}H}$ 1.3 Hz, 4H, 2,7-C_{10}***H$_6$***), 0.92 (s, 36H, C(C***H$_3$***)$_3$), 0.24 (s, 24H, Si(C***H$_3$***)$_2$). ^{13}C{^{1}H} NMR (C_4D_8O, 298 K, 151 MHz): δ (ppm) = 157.6 (1,8-***C$_{10}$***H$_6$), 140.7 (9-***C$_{10}$***H$_6$),

128.5 (3,6-$\boldsymbol{C_{10}}H_6$), 121.7 (10-$\boldsymbol{C_{10}}H_6$), 113.6 (4,5-$\boldsymbol{C_{10}}H_6$), 113.2 (2,7-$\boldsymbol{C_{10}}H_6$), 28.6 (SiC($\boldsymbol{C}H_3)_3$), 21.3 (Si$\boldsymbol{C}Me_3$), –1.1 (Si($\boldsymbol{C}H_3)_2{}^t$Bu). ^{29}Si NMR (C_4D_8O, 298 K, 119 MHz): δ (ppm) = –2.41 (***Si***$Me_2{}^t$Bu). **[($^{Me_2{}^tBu}$L)Ba(THF)$_n$]**: ^{1}H NMR (C_4D_8O, 298 K, 600 MHz): δ (ppm) = 6.63 (t, $^3J_{H\text{-}H}$ = 7.6 Hz, 2H, 3,6-$C_{10}\boldsymbol{H_6}$), 6.43 (dd, $^3J_{H\text{-}H}$ = 7.8, $^4J_{H\text{-}H}$ = 1.4 Hz, 2H, 4,5-$C_{10}\boldsymbol{H_6}$), 6.28 (dd, $^3J_{H\text{-}H}$ = 7.4, $^4J_{H\text{-}H}$ = 1.4 Hz, 2H, 2,7-$C_{10}\boldsymbol{H_6}$), 0.86 (s, 18H, C($C\boldsymbol{H_3}$)$_3$), 0.13 (s, 6H, C($C\boldsymbol{H_3}$)$_3$). ^{13}C{^{1}H} NMR (C_4D_8O, 298 K, 151 MHz): δ (ppm) = 159.7 (1,8-$\boldsymbol{C_{10}}H_6$), 142.6 (9-$\boldsymbol{C_{10}}H_6$), 129.6 (10-$\boldsymbol{C_{10}}H_6$), 125.5 (3,6-$\boldsymbol{C_{10}}H_6$), 118.6 (2,7-$\boldsymbol{C_{10}}H_6$), 113.1 (4,5-$\boldsymbol{C_{10}}H_6$), 29.5 (SiC($\boldsymbol{C}H_3)_3$), 22.1 (Si$\boldsymbol{C}Me_3$), −0.4 (Si($\boldsymbol{C}H_3)_2{}^t$Bu). ^{29}Si NMR (C_4D_8O, 298 K, 119 MHz): δ (ppm) = –15.79 (***Si***$Me_2{}^t$Bu).

6.5 Experimental details for Chapter 5

6.5.1 Synthesis of [($^{NON\text{-}Dipp}$L)Mg]$_2$ (18)



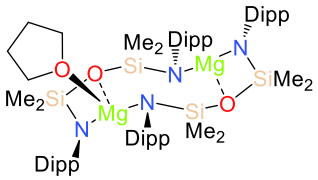
A solution of di-*n*-butylmagnesium in hexanes (0.75 M, 2.75 mL, 2.06 mmol, 1 eq.) was added dropwise to a stirred solution of $^{NON\text{-}Dipp}LH_2$ (1.00 g, 2.06 mmol, 1 eq.) in hexanes (3 mL) at 25 °C. The reaction mixture was stirred for 30 minutes then left to stand for 16 hours, resulting in the formation of a white crystalline solid. The solution was decanted and the solid washed with cold *n*-pentane (3 x 0.5 mL), then dried *in vacuo* for 3 hours. [($^{NON\text{-}Dipp}$L)Mg]$_2$ (562 mg, 1.11 mmol, 54% (**18**)) was isolated as a white crystalline solid. Colourless single crystals suitable for an X-ray diffraction study were grown by dissolving a sample in benzene at 80 °C, followed by slow cooling to room temperature. IR (KBr): 2960, 2867, 1458, 1313, 1257, 1040,

848, 818, 745, 542 (cm^{-1}). Anal. calcd. for $C_{56}H_{92}Mg_2N_4O_2Si_4$: C, 66.31; H, 9.14; N, 5.52. Found: C, 65.92; H, 9.58; N, 5.09.

^{1}H NMR (500 MHz, C_7D_8, 373 K): δ (ppm) = 6.96 (d, $^3J_{H-H}$ = 7.6, 4H, 3,5-$C_6\boldsymbol{H_3}$), 6.88 (t, $^3J_{H-H}$ = 7.6, 2H, 4-$C_6\boldsymbol{H_3}$), 3.57 (hept, $^3J_{H-H}$ = 6.9, 4H, C***H***Me_2), 1.07 (s, br, 24H, CH(C***H*****$_3$**)$_2$), 0.39 (s, 12H, Si(C***H*****$_3$**)$_2$). ^{13}C{$_1$H} NMR (126 MHz, C_7D_8, 373 K): δ (ppm) 145.4 (1-***C*****$_6$**H_3), 143.7 (2,6-***C*****$_6$**H_3), 124.0 (3,5-***C*****$_6$**H_3), 122.0 (4-***C*****$_6$**H_3), 28.7 (***C***HMe_2), 24.8 (CH(***C***H_3)$_2$), 3.8 (Si(***C***H_3)$_2$).

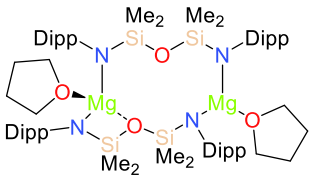
Heating a THF-d_8 solution of [($^{NON\text{-}Dipp}$L)Mg]$_2$ at 80 °C for 16 hours resulted in conversion to the previously reported complex [($^{NON\text{-}Dipp}$L)Mg(THF)$_2$],[21] which could be characterised by multinuclear NMR spectroscopy. ^{1}H NMR (C_4D_8O, 298 K, 600 MHz): δ (ppm) = 6.88 (d, $^3J_{H-H}$ = 7.5 Hz, 8H, 3,5-$C_6\boldsymbol{H_3}$), 6.62 (t, $^3J_{H-H}$ = 7.5 Hz, 4H, 4-$C_6\boldsymbol{H_3}$), 4.04 (hept, $^3J_{H-H}$ = 6.9 Hz, 8H, C***H***Me_2), 1.18 (d, $^3J_{H-H}$ = 6.8 Hz, 24H, CH(C***H*****$_3$**)$_2$), 1.09 (d, $^3J_{H-H}$ = 6.9 Hz, 24H, CH(C***H*****$_3$**)$_2$), 0.12 (s, 24H, Si(C***H*****$_3$**)$_2$). ^{13}C{^{1}H} NMR (C_4D_8O, 298 K, 151 MHz): δ (ppm) = 150.1 (1-***C*****$_6$**H_3), 144.7 (2,6-***C*****$_6$**H_3), 123.6 (3,5-***C*****$_6$**H_3), 119.3 (4-***C*****$_6$**H_3), 27.4 (***C***HMe_2), 26.5 (CH(***C***H_3)$_2$), 26.1 (CH(***C***H_3)$_2$), 4.6 (Si(***C***H_3)$_2$). ^{29}Si NMR (C_4D_8O, 298 K, 119 MHz): δ (ppm) = –14.75 (O***Si***Me_2N).

6.5.2 Synthesis of [{($^{NON\text{-}Dipp}$L)Mg}$_2$(THF)] (18·THF)



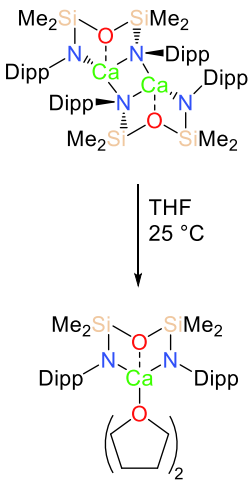
Slow evaporation of a THF/*n*-hexane (1:1) solution of [($^{NON\text{-}Dipp}$L)Mg]$_2$ (**18**) resulted in the growth of colourless single crystals of [{($^{NON\text{-}Dipp}$L)Mg}$_2$(THF)] (**18·THF**) suitable for an X-ray diffraction study. Complex **18·THF** was not isolated. *Note: this procedure was developed by Ms. Andrea O'Reilly (Victoria University of Wellington).*

6.5.3 Synthesis of [($^{NON\text{-}Dipp}$L)Mg(THF)]$_2$ (**18·THF$_2$**)



Slow evaporation of a THF solution of [($^{NON\text{-}Dipp}$L)Mg]$_2$ (**18**) resulted in the growth of colourless single crystals of [($^{NON\text{-}Dipp}$L)Mg(THF)]$_2$ (**18·THF$_2$**) suitable for an X-ray diffraction study. Complex **18·THF$_2$** was not isolated. *Note: this procedure was developed by Ms. Andrea O'Reilly (Victoria University of Wellington).*

6.5.4 Synthesis of [($^{NON\text{-}Dipp}$L)Ca]$_2$ (**19**)

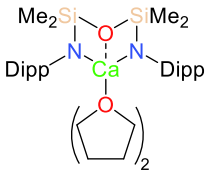


A solution of $^{NON\text{-}Dipp}$LH$_2$ (500 mg, 1.03 mmol, 2 eq.) in *n*-hexane (2.5 mL) was layered over a solution of [CaN"$_2$]$_2$ (372 mg, 0.52 mmol, 1 eq.) in *n*-hexane (2.5 mL). The reaction mixture was left to stand for 16 hours, resulting in the formation of colourless crystals. The solution was decanted and the crystalline solid washed with *n*-pentane (3 x 0.5 mL), then dried *in vacuo* for 1 hour. [($^{NON\text{-}Dipp}$L)Ca]$_2$·(C$_6$H$_{14}$) (383 mg, 0.34 mmol, 65% (**19**)) was isolated as a colourless crystalline solid. IR (KBr): 2963, 2928, 2866, 1424, 1254, 1038, 959, 788 cm^{-1}. Anal. calcd. for C$_{56}$H$_{92}$Ca$_2$N$_4$O$_2$Si$_4$·(C$_6$H$_{14}$): C, 65.78; H, 9.44; N, 4.95. Found: C, 65.52; H, 9.29; N, 4.92. Colourless single crystals of **19** suitable for X-ray diffraction studies were grown by conducting the reaction on a smaller scale (25 mg $^{NON\text{-}Dipp}$LH$_2$) in benzene (0.5 mL) or *n*-hexane (0.5 mL).

Dissolving **19** in THF-d_8 resulted in conversion to [($^{NON\text{-}Dipp}$L)Ca(THF)$_2$] (**19·THF$_2$**), which could be characterised by multinuclear NMR spectroscopy.^{1}H NMR (C$_4$D$_8$O, 298 K, 600 MHz): δ (ppm) = 6.83 (d, $^3J_{H\text{-}H}$ = 7.5 Hz, 8H, 3,5-C$_6$***H*$_3$**), 6.49 (t, $^3J_{H\text{-}H}$ = 7.5 Hz, 4H, 4-C$_6$***H*$_3$**), 3.95 (hept, $^3J_{H\text{-}H}$ = 7.0 Hz, 8H, C***H***Me$_2$), 1.12 (d, $^3J_{H\text{-}H}$ = 7.0 Hz,

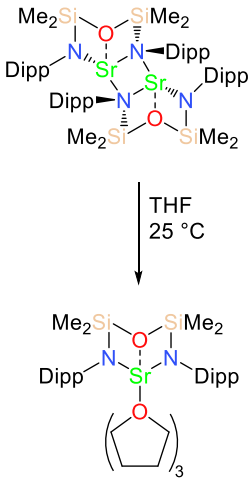
48H, CH(C***H*****3**)2), 0.13 (s, 24H, Si(C***H*****3**)2). $^{13}C\{^{1}H\}$ NMR (C_4D_8O, 298 K, 151 MHz): δ (ppm) = 151.2 (1-***C*****6**H_3), 142.4 (2,6-***C*****6**H_3), 123.0 (3,5-***C*****6**H_3), 117.3 (4-***C*****6**H_3), 27.7 (***C***HMe_2), 25.8 (CH(***C***H_3)2), 4.9 (Si(***C***H_3)2). ^{29}Si NMR (C_4D_8O, 298 K, 119 MHz): δ (ppm) = –19.77 (O***Si***Me_2N).

6.5.5 Synthesis of [(NON-DippL)Ca(THF)2] (19·THF2)



Slow evaporation of a THF solution of [(NON-DippL)Ca]2 (**19**) resulted in the growth of colourless single crystals of [(NON-DippL)Ca(THF)2] (**19·THF**2) suitable for an X-ray diffraction study. Complex **19·THF**2 was not isolated. *Note: this procedure was developed by Ms. Andrea O'Reilly (Victoria University of Wellington).*

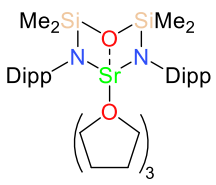
6.5.6 Synthesis of [(NON-DippL)Sr]2 (20)



A solution of NON-DippLH2 (500 mg, 1.03 mmol, 2 eq.) in *n*-hexane (2.5 mL) was carefully layered over a solution of [SrN"2]2 (422 mg, 0.52 mmol, 1 eq.) in *n*-hexane (5 mL). The reaction mixture was left to stand for 16 hours, resulting in the formation of colourless crystals. The solution was decanted and the crystalline solid washed with *n*-pentane (3 x 0.5 mL), then dried *in vacuo* for 1 hour. [NON-DippLSr]2·(C_6H_{14}) (362 mg, 0.29 mmol, 57% (**20**)) was isolated as a colourless crystalline solid. IR (KBr): 3055, 2960, 2866, 1587, 1421, 1259, 990, 781, 686 cm^{-1}. Anal. calcd. for $C_{56}H_{92}Sr_2N_4O_2Si_4$·($C_6H_{14}$): C, 60.97; H, 8.77; N, 4.51. Found: C, 60.50; H, 8.47; N, 4.59. Colourless single crystals of **20** suitable for X-ray diffraction studies were grown by conducting the reaction on a smaller scale (25 mg NON-DippLH2) in benzene (0.5 mL) or *n*-hexane (0.5 mL).

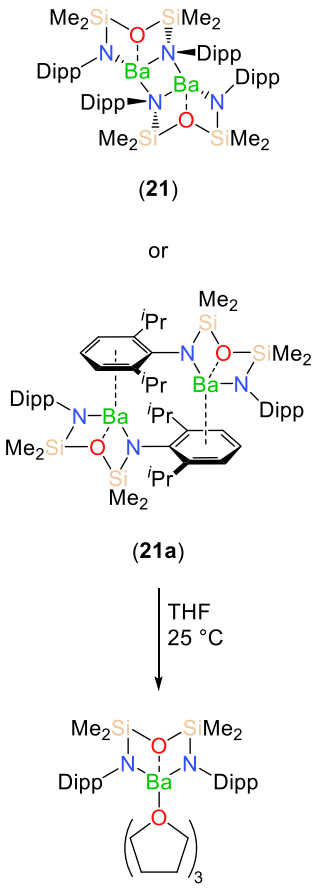
Dissolving **20** in THF-d_8 resulted in conversion to [($^{NON\text{-}Dipp}$L)Sr(THF)$_3$] (**20·THF**$_3$), which could be characterised by multinuclear NMR spectroscopy. ^{1}H NMR (C_4D_8O, 298 K, 600 MHz): δ (ppm) = 6.80 (d, $^3J_{H\text{-}H}$ = 7.5 Hz, 8H, 3,5-C_6***H*****$_3$**), 6.42 (t, $^3J_{H\text{-}H}$ = 7.5 Hz, 4H, 4-C_6***H*****$_3$**), 3.98 (hept, $^3J_{H\text{-}H}$ = 6.9 Hz, 8H, C***H***Me_2), 1.13 (d, $^3J_{H\text{-}H}$ = 6.9 Hz, 48H, CH(C***H*****$_3$)$_2$), 0.10 (s, 24H, Si(C***H*****$_3$)$_2$). ^{13}C{^{1}H} NMR (C_4D_8O, 298 K, 151 MHz): δ (ppm) = 153.6 (1-***C*****$_6$H$_3$), 142.1 (2,6-***C*****$_6$H$_3$), 123.1 (3,5-***C*****$_6$H$_3$), 116.1 (4-***C*****$_6$H$_3$), 27.6 (***C***HMe_2), 25.9 (CH(***C***H_3)$_2$), 5.2 (Si(***C***H_3)$_2$). ^{29}Si NMR (C_4D_8O, 298 K, 119 MHz): δ (ppm) = –23.74 (O***Si***Me_2N).

6.5.7 Synthesis of [($^{NON\text{-}Dipp}$L)Sr(THF)$_3$] (20·THF$_3$)



Slow evaporation of a THF solution of [($^{NON\text{-}Dipp}$L)Sr]$_2$ (**20**) resulted in the growth of colourless single crystals of [($^{NON\text{-}Dipp}$L)Sr(THF)$_3$] (**20·THF**$_3$) suitable for an X-ray diffraction study. Complex **20·THF**$_3$ was not isolated. *Note: this procedure was developed collaboration with Ms. Andrea O'Reilly (Victoria University of Wellington).*

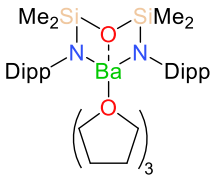
6.5.8 Synthesis of [($^{NON\text{-}Dipp}$L)Ba]$_2$ (21)



A solution of $^{NON\text{-}Dipp}$LH$_2$ (500 mg, 1.03 mmol, 2 eq.) in *n*-hexane (2.5 mL) was carefully layered over a solution of [BaN"$_2$]$_2$ (473 mg, 0.52 mmol, 1 eq.) in *n*-hexane (5 mL). The reaction mixture was left to stand for 48 hours, resulting in the formation of large colourless crystals. The solution was decanted and the crystals washed with cold *n*-pentane (0.5 mL), then dried *in vacuo* for 1 hour. [($^{NON\text{-}Dipp}$L)Ba]$_2$ (302 mg, 0.25 mmol, 48% (**21a**)) was isolated as a colourless crystalline solid. IR (KBr): 3043, 2957, 2863, 1411, 1341, 1249, 995, 771 cm^{-1}. Anal. calcd. for $C_{56}H_{92}Ba_2N_4O_2Si_4$: C, 54.23; H, 7.48; N, 4.52. Found: C, 54.20; H, 7.52; N, 4.46. Colourless single crystals of [($^{NON\text{-}Dipp}$L)Ba]$_2$ suitable for X-ray diffraction studies were grown by conducting the reaction on a smaller scale (25 mg $^{NON\text{-}Dipp}$LH$_2$) in benzene (0.5 mL) or *n*-hexane (0.5 mL) (**21** and **21a** respectively).

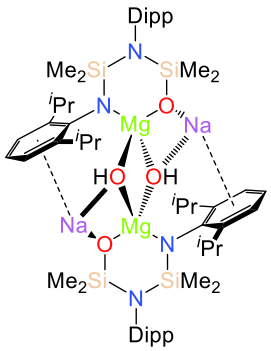
Dissolving **21** in THF-d_8 resulted in conversion to [($^{NON\text{-}Dipp}$L)Ba(THF)$_3$] (**21·THF$_3$**), which could be characterised by multinuclear NMR spectroscopy. ^{1}H NMR (C_4D_8O, 298 K, 600 MHz): δ (ppm) = 6.80 (d, $^3J_{H\text{-}H}$ = 7.5 Hz, 8H, 3,5-C$_6$***H*$_3$**), 6.39 (t, $^3J_{H\text{-}H}$ = 7.5 Hz, 4H, 4-C$_6$***H*$_3$**), 3.97 (hept, $^3J_{H\text{-}H}$ = 7.0 Hz, 8H, C***H***Me$_2$), 1.12 (d, $^3J_{H\text{-}H}$ = 7.0 Hz, 48H, CH(C***H*$_3$**)$_2$), 0.10 (s, 24H, Si(C***H*$_3$**)$_2$). ^{13}C{^{1}H} NMR (C_4D_8O, 298 K, 151 MHz): δ (ppm) = 152.4 (1-***C*$_6$**H$_3$), 141.6 (2,6-***C*$_6$**H$_3$), 123.1 (3,5-***C*$_6$**H$_3$), 115.6 (4-***C*$_6$**H$_3$), 27.5 (***C***HMe$_2$), 26.0 (CH(***C***H$_3$)$_2$), 5.5 (Si(***C***H$_3$)$_2$). ^{29}Si NMR (C_4D_8O, 298 K, 119 MHz): δ (ppm) = –26.22 (O***Si***Me$_2$N).

6.5.9 Synthesis of [($^{NON\text{-}Dipp}$L)Ba(THF)$_3$] (21·THF$_3$)



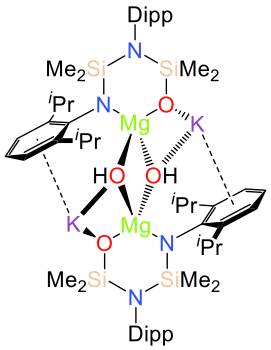
Slow evaporation of a THF solution of [($^{NON\text{-}Dipp}$L)Ba]$_2$ (**21**) resulted in the growth of colourless single crystals of [($^{NON\text{-}Dipp}$L)Ba(THF)$_3$] (**21·THF$_3$**) suitable for an X-ray diffraction study. Complex **21·THF$_3$** was not isolated. *Note: this procedure was developed by Ms. Andrea O'Reilly (Victoria University of Wellington).*

6.5.10 Synthesis of [($^{NNO\text{-}Dipp}$L)Mg(μ-OH)Na]$_2$ (22)



[($^{NON\text{-}Dipp}$L)Mg]$_2$ (20 mg, 20 μmol, 1 eq.) and 5 wt% Na/NaCl (54 mg, 118 μmol, 6 eq.) were suspended in benzene (0.5 mL). The reaction mixture was heated at 80 °C and stirred for 16 hours, then filtered. The resulting pale brown solution was left to stand for 3 days, resulting in the growth of small colourless crystals of [($^{NNO\text{-}Dipp}$L)Mg(μ-OH)Na]$_2$ (**22**). Complex **22** was not isolated on a preparative scale.

6.5.11 Synthesis of [($^{NNO\text{-}Dipp}$L)Mg(μ-OH)K]$_2$ (23)



[($^{NON\text{-}Dipp}$L)Mg]$_2$ (20 mg, 20 μmol, 1 eq.) and potassium graphite (16 mg, 188 μmol, 6 eq.) were suspended in benzene (0.5 mL). The reaction mixture was heated at 80 °C and stirred for 16 hours, then filtered. The resulting pale brown solution was left to stand for 3 days, resulting in the growth of small colourless crystals of [($^{NNO\text{-}Dipp}$L)Mg(μ-OH)K]$_2$ (**23**). Complex **23** was not isolated on a preparative scale. Multinuclear NMR spectra were obtained by monitoring the reaction *in situ* in C_6D_6. ^{1}H NMR (C_6D_6, 298 K, 600 MHz): δ (ppm) = 7.22 (m, 4H, (3,5-C_6***H*$_3$**)N(SiMe$_2$)$_2$), 7.19 (m, 2H, (4-C_6***H*$_3$**)N(SiMe$_2$)$_2$), 6.83 (d, $^3J_{H\text{-}H}$ = 7.5 Hz, 4H, (3,5-C_6***H*$_3$**)NMg), 6.46 (t,

$^{3}J_{H\text{-}H}$ = 7.5 Hz, 2H, (4-C_6***H*****$_3$**)NMg), 4.28 (hept, $^{3}J_{H\text{-}H}$ = 7.5 Hz, 4H, {2,6-Ph(C***H***Me_2)$_2$}NMg), 4.04 (hept, $^{3}J_{H\text{-}H}$ = 6.7 Hz, 4H, {2,6-Ph(C***H***Me_2)$_2$)}N($SiMe_2$)$_2$), 1.54 (d, $^{3}J_{H\text{-}H}$ = 6.9 Hz, 12H, {2,6-Ph(CH(C***H*****$_3$**)$_2$)}N($SiMe_2$)$_2$), 1.52 (d, $^{3}J_{H\text{-}H}$ = 6.9 Hz, 12H, {2,6-Ph(CH(C***H*****$_3$**)$_2$}N($SiMe_2$)$_2$), 1.37 (d, $^{3}J_{H\text{-}H}$ = 6.9 Hz, 12H, {2,6-Ph(CH(C***H*****$_3$**)$_2$)}NMg), 1.13 (d, $^{3}J_{H\text{-}H}$ = 6.8 Hz, 12H, {2,6-Ph(CH(C***H*****$_3$**)$_2$)}NMg), 0.19 (s, 12H, N{Si(C***H*****$_3$**)$_2$}O), 0.13 (s, 12H, N{Si(C***H*****$_3$**)$_2$}N). $^{13}C\{^{1}H\}$ NMR (C_6D_6, 298 K, 151 MHz): δ (ppm) = 153.9 ((1-***C*****$_6$**H_3)NMg), 147.4 ((2,6-***C*****$_6$**H_3)NMg), 147.1 ((2,6-***C*****$_6$**H_3)N($SiMe_2$)$_2$), 145.2 ((1-***C*****$_6$**H_3)N($SiMe_2$)$_2$), 124.4 ((4-***C*****$_6$**H_3)N($SiMe_2$)$_2$), 124.0 ((3,5-***C*****$_6$**H_3)N($SiMe_2$)$_2$), 123.2 ((3,5-***C*****$_6$**H_3)NMg), 118.6 ((4-***C*****$_6$**H_3)NMg), 28.53 ({2,6-Ph(***C***HMe_2)$_2$}N($SiMe_2$)$_2$), 26.9 ({2,6-Ph(CH(***C***H_3)$_2$)$_2$}NMg), 26.6 ({2,6-Ph(CH(***C***H_3)$_2$)$_2$}N($SiMe_2$)$_2$), 25.9 ({2,6-Ph(***C***HMe_2)$_2$}NMg), 25.3 ({2,6-Ph(CH(***C***H_3)$_2$)$_2$}NMg), 24.3 ({2,6-Ph(CH(***C***H_3)$_2$)$_2$}N($SiMe_2$)$_2$), 4.5 (N{Si(***C***H_3)$_2$}N), 4.1 (N{Si(***C***H_3)$_2$}O). ^{29}Si NMR (C_6D_6, 298 K, 119 MHz): δ (ppm) = –13.44 (N(***Si***Me_2)O), –14.15 (N(***Si***Me_2)N).

6.6 References

1 J. Hicks, M. Juckel, A. Paparo, D. Dange and C. Jones, *Organometallics*, 2018, **37**, 4810–4813.

2 L. H. Gade, C. H. Galka, K. W. Hellmann, R. M. Williams, L. De Cola, I. J. Scowen and M. McPartlin, *Chem. Eur. J.*, 2002, **8**, 3732–3746.

3 J. A. Spivey and D. B. Collum, *J. Am. Chem. Soc.*, 2024, **146**, 17827–17837.

4 T. M. Cameron, X. Chongying, A. G. Dipasquale and A. L. Rheingold, *Organometallics*, 2008, **27**, 1596–1604.

5 Y. Sarazin, R. H. Howard, D. L. Hughes, S. M. Humphrey and M. Bochmann, *Dalton Trans.*, 2006, **60**, 340–350.

6 P. P. Power, *Inorg. Synth.*, 2018, **37**, 24–26.

7 B. A. Vaartstra, J. C. Huffman, W. E. Streib and K. G. Caulton, *Inorg. Chem.*, 1991, **30**, 121–125.

8 K. C. Jantunen, F. Haftbaradaran, M. J. Katz, R. J. Batchelor, G. Schatte and D. B. Leznoff, *Dalton Trans.*, 2005, 3083–3091.

9 D. M. Ottmers and H. F. Rase, *Carbon N. Y.*, 1966, **4**, 125–127.

10 B. J. Cosier and A. M. Glazer, *J. Appl. Crystallogr.*, 1986, **19**, 105–107.

11 *CrysAlisPRO, Journal, Oxford Diffraction / Agilent Technologies UK Ltd.*

12 A. Altomare, G. Cascarano, C. Giacovazzo and A. Guagliardi, *J. Appl. Crystallogr.*, 1993, **26**, 343–350.

13 L. Palatinus and G. Chapuis, *J. Appl. Crystallogr.*, 2007, **40**, 786–790.

14 G. M. Sheldrick, *Acta Crystallogr. A*, 2015, **71**, 3–8.

15 L. J. Farrugia, *J. Appl. Crystallogr.*, 2012, **45**, 849–854.

16 P. W. Betteridge, J. R. Carruthers, R. I. Cooper, K. Prout and D. J. Watkin, *J. Appl. Crystallogr.*, 2003, **36**, 1487–1487.

17 G. M. Sheldrick, *Acta Crystallogr. Sect. C Struct. Chem.*, 2015, **71**, 3–8.

18 O. V. Dolomanov, L. J. Bourhis, R. J. Gildea, J. A. K. Howard and H. Puschmann, *J. Appl. Crystallogr.*, 2009, **42**, 339–341.

19 L. J. Farrugia, *J. Appl. Crystallogr.*, 1997, **30**, 565–565.

20 S. Danièle, C. Drost, B. Gehrhus, S. M. Hawkins, P. B. Hitchcock, M. F. Lappert, P. G. Merle and S. G. Bott, *Dalton Trans.*, 2001, 3179–3188.

21 R. J. Schwamm, J. R. Harmer, M. Lein, C. M. Fitchett, S. Granville and M. P. Coles, *Angew. Chemie Int. Ed.*, 2015, **54**, 10630–10633.

Chapter 7

Conclusions

This Thesis research has centred around the development of novel alkaline earth coordination complexes supported by chelating diamido ligands. Systems based on both rigid and tuneable 1,8-*bis*(silylamido)naphthalene ligands as well as more flexible di(amido)siloxane ligands have been investigated. The reactions of di(amido)siloxane alkaline earth complexes with alkali metal reducing agents were also assessed. In total, the solid-state structures of 26 novel alkaline earth complexes have been characterised by X-ray diffraction and, in most cases, IR spectroscopy and elemental analysis. The solution-phase structures of numerous species were also probed using NMR spectroscopy. The key conclusions are presented below.

i) Novel alkaline earth complexes supported by 1,8-*bis*(silylamido)naphthalene ligands

Synthesis:

The reactions of a series of 1,8-*bis*(silylamino)naphthalene proligands ($^{R_3}LH_2$ = 1,8-{$(R_3Si)NH\}_2C_{10}H_6$; R_3 = Me_3, $Me_2{}^tBu$, $^iPr_3$, Ph_2Me and Ph_3), with alkaline earth *bis*(hexamethyldisilazide) bases ([AeN''_2], Ae = Mg, Ca, Sr and Ba, N'' = $[N(SiMe_3)_2]^-$) in THF were assessed. Though the monomeric magnesium complexes [(^{R_3}L)$Mg(THF)_2$] (R_3 = Me_3 (**4**) and $Me_2{}^tBu$ (**5**)) could be isolated, no isolable complexes

of the heavier congeners calcium, strontium and barium were obtained. While the formation of the target species [(^{R_3}L)Ae(THF)$_n$] was possible in some cases, the formation of the stable intermediate species [(^{R_3}LH)AeN"(THF)$_n$] was generally favoured. This synthetic route was also significantly hindered by thermal degradation, which in some cases resulted in the formation of the unsymmetrical heteroleptic species [($^{R_3\text{-}\mu\text{-}R_2}$L)AeN"(THF)$_n$] *via* a proposed intramolecular σ-bond metathesis reaction. Detailed *in situ* NMR spectroscopic analysis demonstrated the sensitivity of these reactions to the exact metal and ligand substituents employed in each case, and were rationalised based on various competing stereoelectronic demands.

Gratifyingly, a THF-free synthetic route proved more successful. The 2:1 reactions of the phenyl-substituted proligands ^{Ph_2Me}LH$_2$ and ^{Ph_3}LH$_2$ with the dimeric precursors [AeN"$_2$]$_2$ (Ca, Sr and Ba) in benzene afforded smooth conversion to the dimeric species [(^{R_3}L)Ae]$_2$ (R_3 = Ph_2Me, Ae = Ca (**6**), Sr (**7**) and Ba (**8**); R_3 = Ph_3, Ae = Ca (**9**), Sr (**10**) and Ba (**11**)) at 25 °C. The facile synthesis of **6**–**11** was attributed to the enhanced acidity conferred by their electron-withdrawing phenyl substituents and, in most cases, their rapid crystallisation from the reaction mixture.

Conversely, the corresponding THF-free reactions employing the alkyl-substituted proligand ^{Me_2tBu}LH$_2$ required a temperature of 80 °C to facilitate conversion to isolable products. The target complex [(^{Me_2tBu}L)Ca]$_2$ (**13**) as well as the unexpected bimetallic intermediate [(^{Me_2tBu}LH)Ca(μ-^{Me_2tBu}L)CaN"] (**14**) and bimetallic side products [{(^{Me_2tBu}LH)Ae}$_2$(μ-^{Me_2tBu}L)] (Ae = Sr (**16**) and Ba (**17**)) were isolated. These more varied outcomes were attributed to the enhanced basicity and stability that are conferred to the [^{Me_2tBu}LH]$^-$ ligand by its bulky, electron-donating *tert*-butyl substituents.

Solid-state structural properties:

The dimeric phenyl-substituted complexes **6**–**11** displayed two distinct dimerisation modes. Complexes **6**–**9** were found to have nitrogen-bridged structures, whereas **10** and **11** were found to have naphthalene-bridged structures. This variance was attributed to both the weaker amide donors that result from additional electron-withdrawing phenyl substituents and the preferential formation of π-facial interactions with softer, multihaptic ligands by the heavier congeners strontium and barium. Complex **13** was also found to have a naphthalene-bridged dimeric structure analogous to those of **10** and **11** due to steric factors. Conversely, **14**, **16** and **17** exhibited nitrogen-bridged structures that result from the hard amide donors and strong intramolecular hydrogen bonds of their alkyl-substituted ligands.

Solution-phase behaviour:

Complexes **6**–**11**, **13**, **14**, **16** and **17** were all found to be poorly soluble in non-donor solvents. However, their dissolution in THF resulted in the speciation of these aggregated bimetallic species into monomeric adducts. Comparative analysis of the ^{29}Si NMR spectra of these adducts confirmed the respective electron-withdrawing and electron-donating influences exerted by phenyl and *tert*-butyl substituents. Additional structural verification was provided by the crystallisation of both [(^{Ph_3}L)Sr(THF)$_3$] (**12**) and, notably, the solvent-separated ion pair [$^{Me_2{}^tBu}$LH]$_2$[Ca(THF)$_6$] (**15**) from THF. The latter outcome was attributed to the high oxophilicity of Ca^{2+} and the stability conferred to the [$^{Me_2{}^tBu}$LH]$^-$ weakly-coordinating anion by its strong intramolecular hydrogen bond, delocalised π-system and silyl substituents.

ii) Novel alkaline earth complexes supported by di(amido)siloxane ligands

Synthesis:

The four dimeric di(amido)siloxane alkaline earth complexes $[(^{NON\text{-}Dipp}L)Ae]_2$ ($[^{NON\text{-}Dipp}L]^{2-} = [O(SiMe_2NDipp)_2]^{2-}$, Ae = Mg (**18**), Ca (**19**), Sr (**20**) and Ba (**21**)) were isolated *via* THF-free protonolysis procedures. The straightforward synthesis of **18**–**21** was aided by the flexibility and reduced basicity of the di(amido)siloxane ligand.

Solid-state structural properties:

The structure of **18** was found to consist of two three-coordinate, trigonal planar Mg^{2+} centres, with dimerisation resulting from the κ^2-N,O-κ^1-N′ coordination mode of the $[^{NON\text{-}Dipp}L]^{2-}$ ligand. Conversely, the larger ionic radii of the heavier Ae^{2+} congeners were found to enable the accommodation of a κ^3-N,O,N′-κ^1-N′ coordination mode in **19**–**21**. However, the crystallisation of the barium congener from *n*-hexane instead resulted in an aryl-bridged structure (**21a**), an outcome that was attributed to a combination of crystal packing forces and the preferential formation of π-facial interactions by Ba^{2+}.

Solution-phase behaviour:

While **18**–**21** display poor hydrocarbon solubility, **18** was found to have a fluxional solution-phase structure when dissolved in arenes at 80 °C. NMR spectroscopic analysis combined with X-ray crystallographic data obtained in collaboration with Ms. Andrea O'Reilly also enabled the characterisation of the dimeric THF adducts $[\{(^{NON\text{-}Dipp}L)Mg\}_2(THF)]$ and $[(^{NON\text{-}Dipp}L)Mg(THF)]_2$ (**18·THF** and **18·THF₂** respectively) and monomeric adducts $[(^{NON\text{-}Dipp}L)Ae(THF)_n]$ (n = 2, Ae = Ca (**19·THF₂**); n = 3, Ae = Sr (**20·THF₃**) and Ba (**21·THF₃**)).

ii) Attempted reduction of di(amido)siloxane alkaline earth complexes

The attempted reduction of the heavier congeners **19**–**21** did not yield conclusive outcomes, and may be worthy of further study. Conversely, the reactions of the magnesium dimer **18** with alkali metal reducing agents afforded the dimeric heterobimetallic molecular magnesium hydroxide complexes $[(^{NNO\text{-}Dipp}L)Mg(\mu\text{-}OH)M]_2$ ($[^{NNO\text{-}Dipp}L]^{2-}$ = $[OSiMe_2NDippSiMe_2NDipp]^{2-}$, M = Na (**22**) and K (**23**)), which were characterised by X-ray crystallography and NMR spectroscopy. The presence of rearranged "NNO" ligands in **22** and **23** was attributed to an intramolecular 1,3-silyl retro-Brook rearrangement. The hydroxide groups in **22** and **23** were proposed to originate from the hydrolysis of an intermediate hydride species that results from the C-H activation of benzene by transient low-valent species. The isolation of **22** and **23** contrasted with the isolation of stable low-valent species by Coles and co-workers when the reduction of **18** was conducted in diethyl ether, demonstrating the solvent-dependency of this system.

iv) Final remarks

The exclusion of THF and the use of carefully chosen dianionic ancillary ligands facilitated the crystallisation of numerous aggregated alkaline earth complexes that could be isolated and structurally characterised. In agreement with literature precedent, these structures were found to be dominated by the formation of ionic Ae-N interactions, though in some cases the heavier Ae^{2+} congeners preferentially formed softer π-facial interactions. The exact solid-state structure adopted in each case was found to be highly sensitive to the steric and electronic properties of the ancillary ligand.

The dissolution of these aggregated alkaline earth complexes in THF consistently resulted in their speciation into monomeric adducts, which in many cases displayed dynamic solution-phase behaviour. However, the poor solubility of these species in non-donor solvents, combined with the propensity of both 1,8-*bis*(silylamido)naphthalene and di(amido)siloxane ligands for rearrangement, largely precluded an investigation of the onward reactivity of these complexes. Further investigations could employ mechanochemical methods to attempt the solid-state conversion of the compounds discussed in this study into more reactive species. Alternatively, the direct synthesis of heterobimetallic s-block species supported by dianionic ligands could be pursued *via* the reactions of suitable proligands with heterobimetallic precursors.

Appendix

Supplementary data for Chapters 2–5

A.1 Appendix for Chapter 2

A.1.1 NMR spectra of isolated compounds

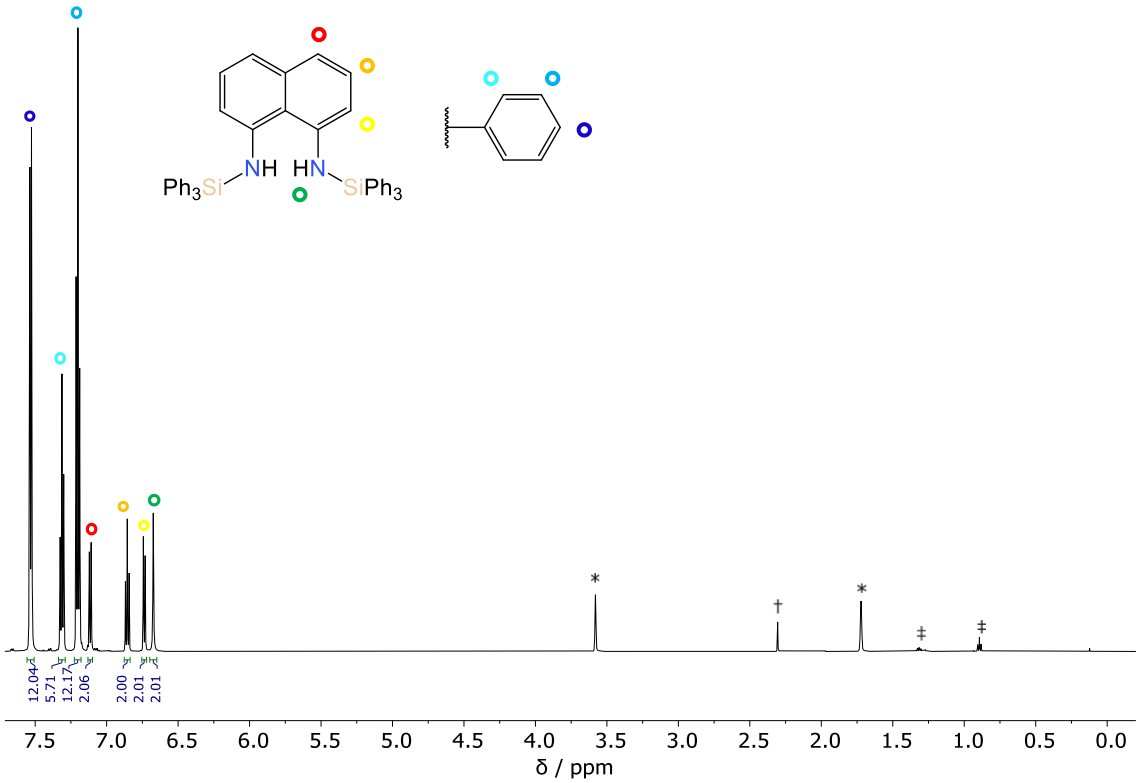


Figure A.1 ^{1}H NMR spectrum (C_4D_8O, 298 K, 600.4 MHz) of $^{Ph_3}LH_2$ (**1**). ‡ denotes n-pentane, †, denotes toluene, * denotes residual protio fraction of C_4D_8O.

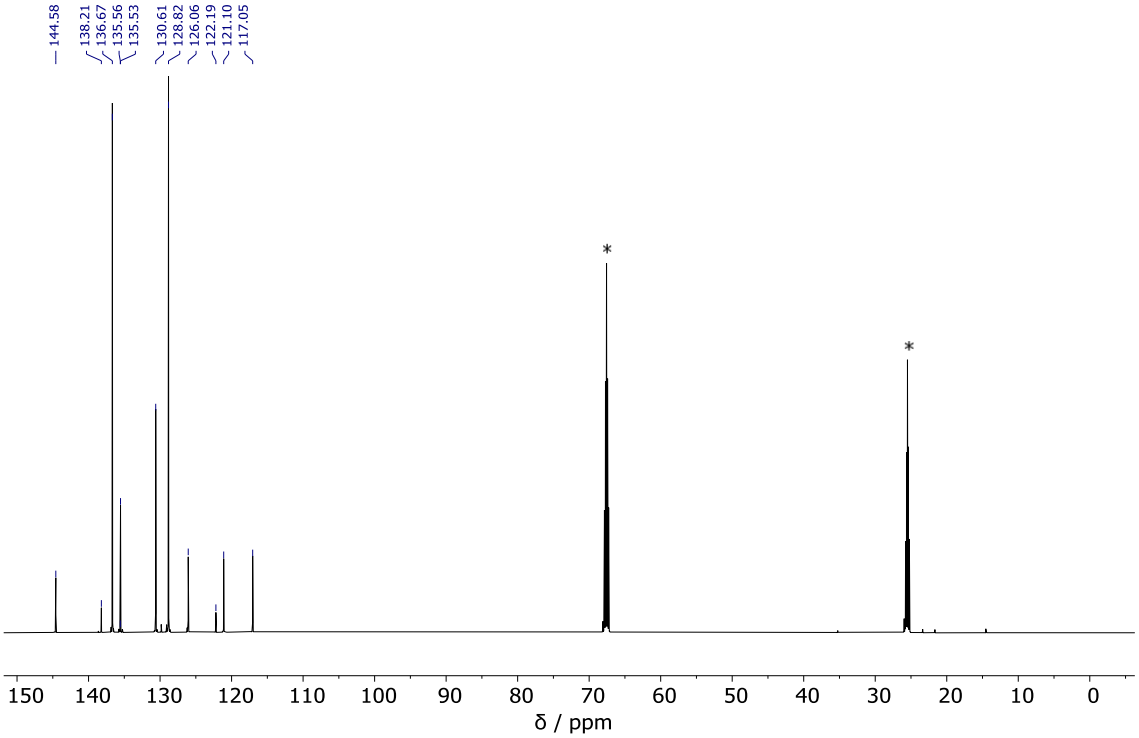


Figure A.2 $^{13}C\{^{1}H\}$ NMR spectrum (C_4D_8O, 298 K, 151.0 MHz) of $^{Ph_3}LH_2$ (**1**). * denotes C_4D_8O.

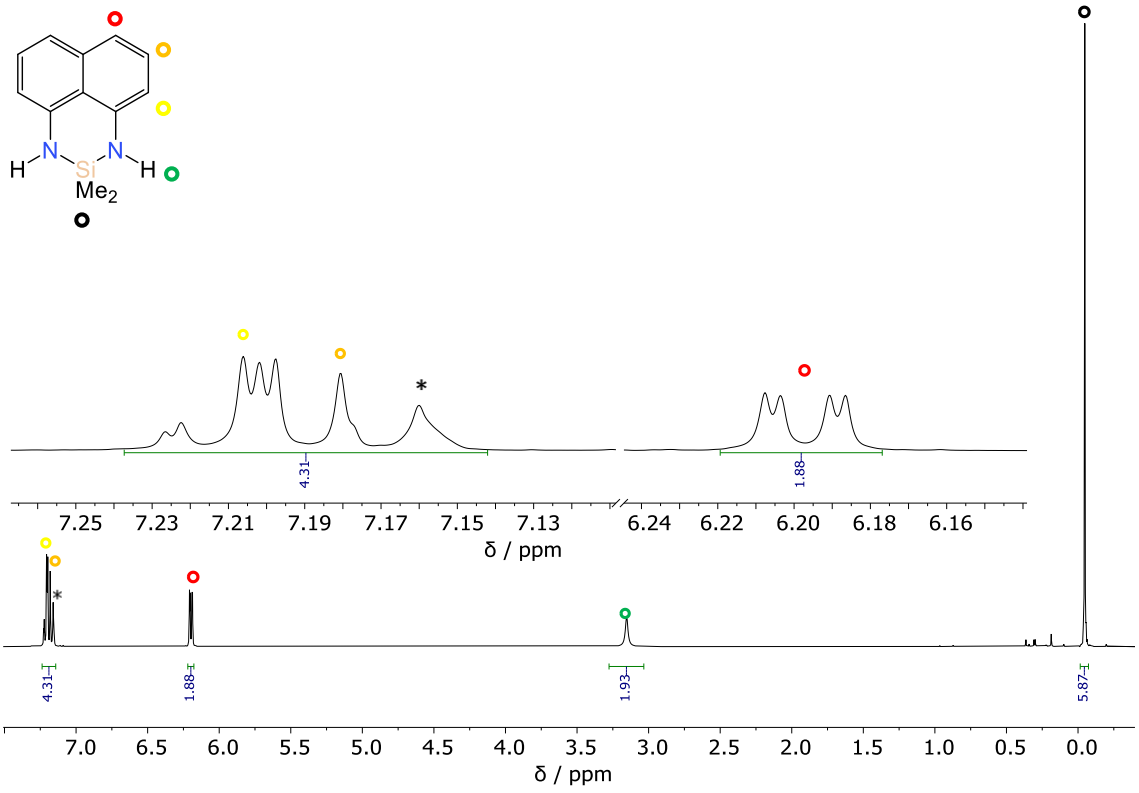


Figure A.3 ^{1}H NMR spectrum (C_6D_6, 298 K, 400 MHz) of $^{\mu\text{-}Me_2}LH_2$ (**2**).

* denotes residual protio fraction of C_6D_6.

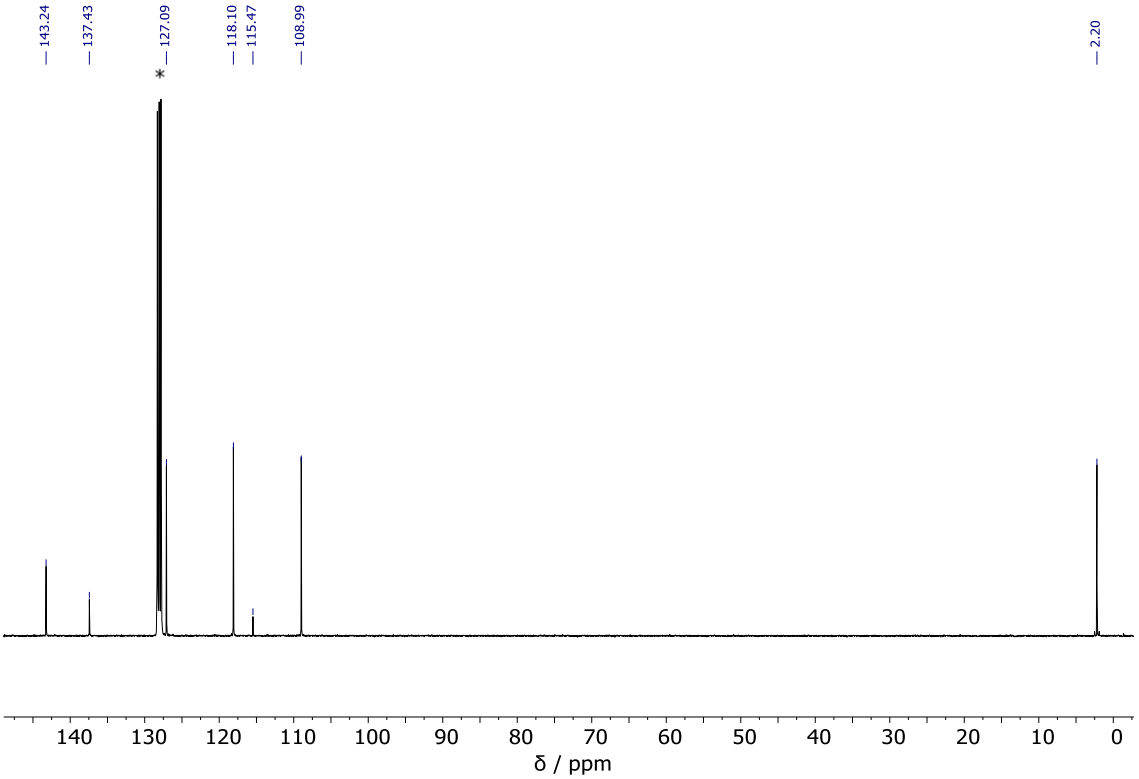


Figure A.4 $^{13}C\{^{1}H\}$ NMR spectrum (C_6D_6, 298 K, 100.6 MHz) of $^{\mu\text{-}Me_2}LH_2$ (**2**). * denotes C_6D_6.

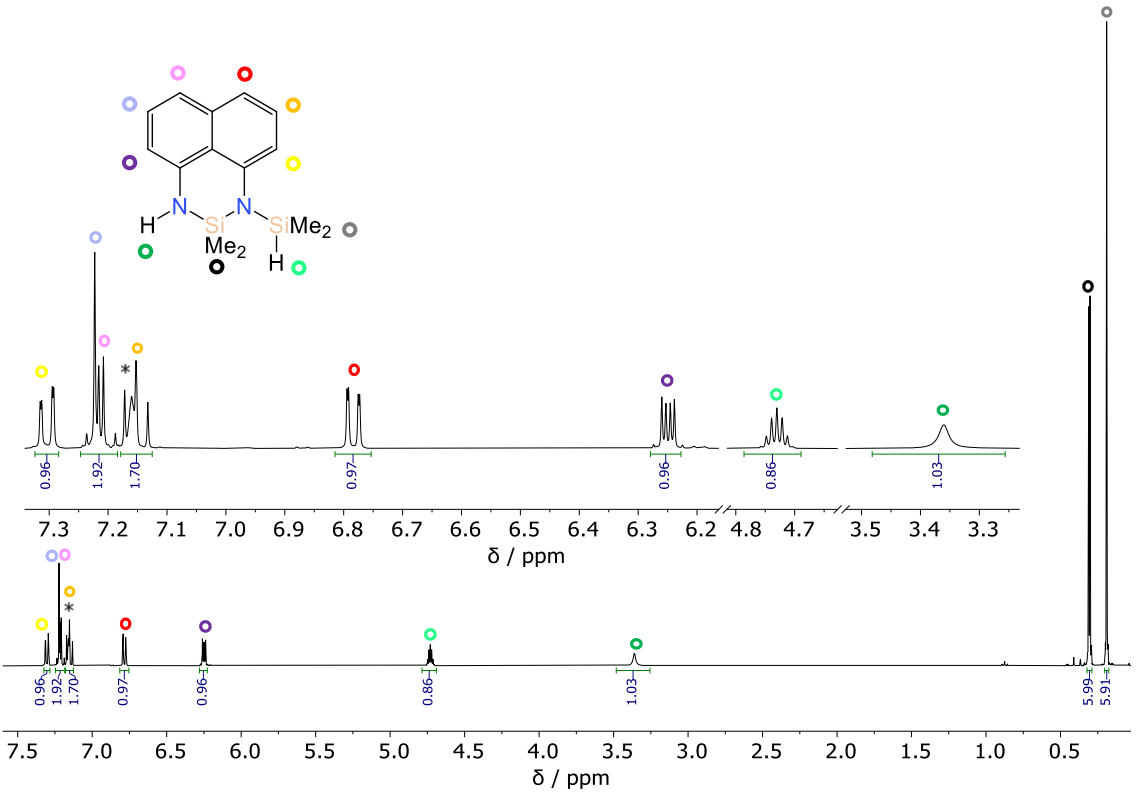


Figure A.5 ^{1}H NMR spectrum (C_6D_6, 298 K, 400 MHz) of $^{Me_2H\text{-}\mu\text{-}Me_2}LH$ (**3**).

* denotes residual protio fraction of C_6D_6.

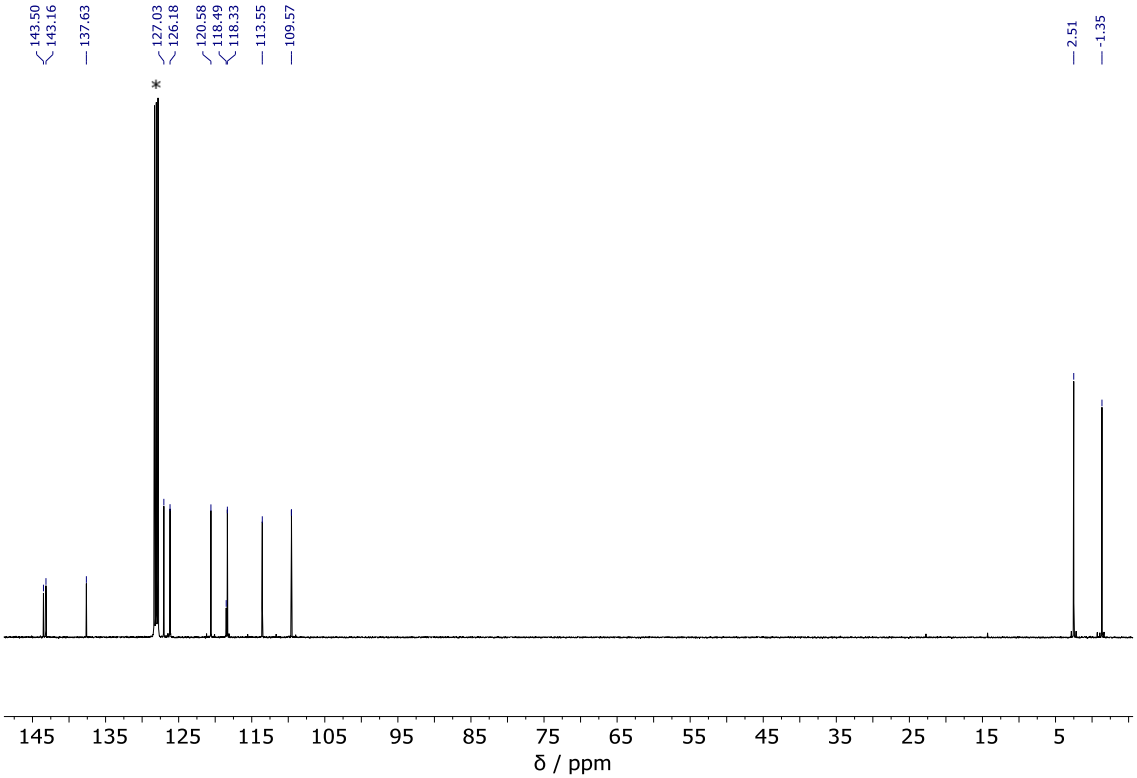


Figure A.6 $^{13}C\{^{1}H\}$ NMR spectrum (C_6D_6, 298 K, 100.6 MHz) of $^{Me_2H\text{-}\mu\text{-}Me_2}LH$ (**3**). * denotes C_6D_6.

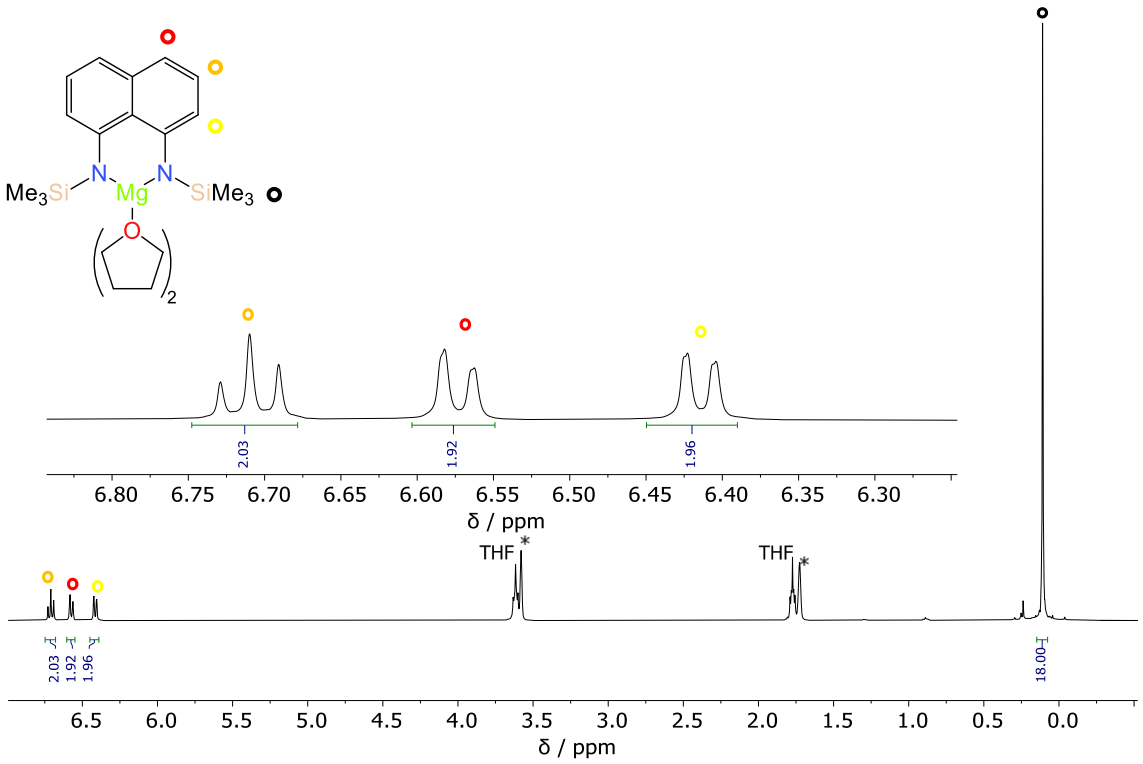


Figure A.7 ^{1}H NMR spectrum (C_4D_8O, 298 K, 400 MHz) of $[(^{Me_3}L)Mg(THF)_2]$ (**4**).* denotes residual protio fraction of C_4D_8O. Expansion shows naphthyl region.

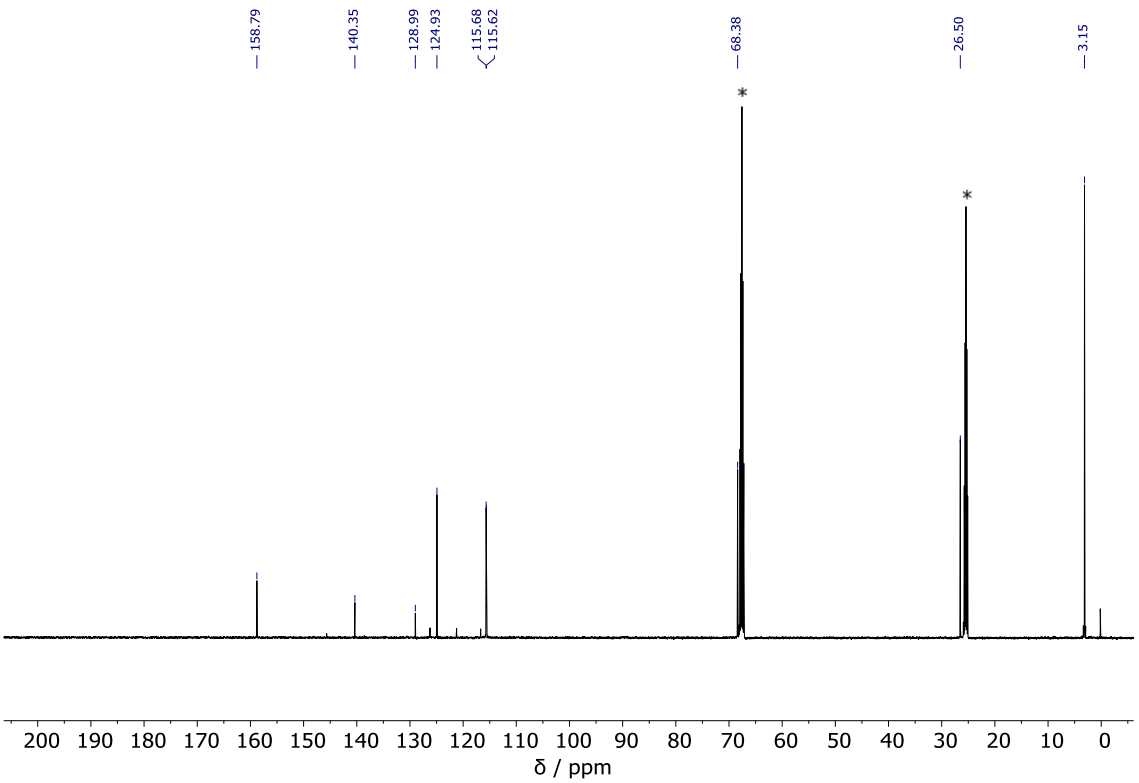


Figure A.8 $^{13}C\{^{1}H\}$ NMR spectrum (C_4D_8O, 298 K, 125 MHz) of [(^{Me_3}L)Mg(THF)$_2$] (**4**).* denotes C_4D_8O.

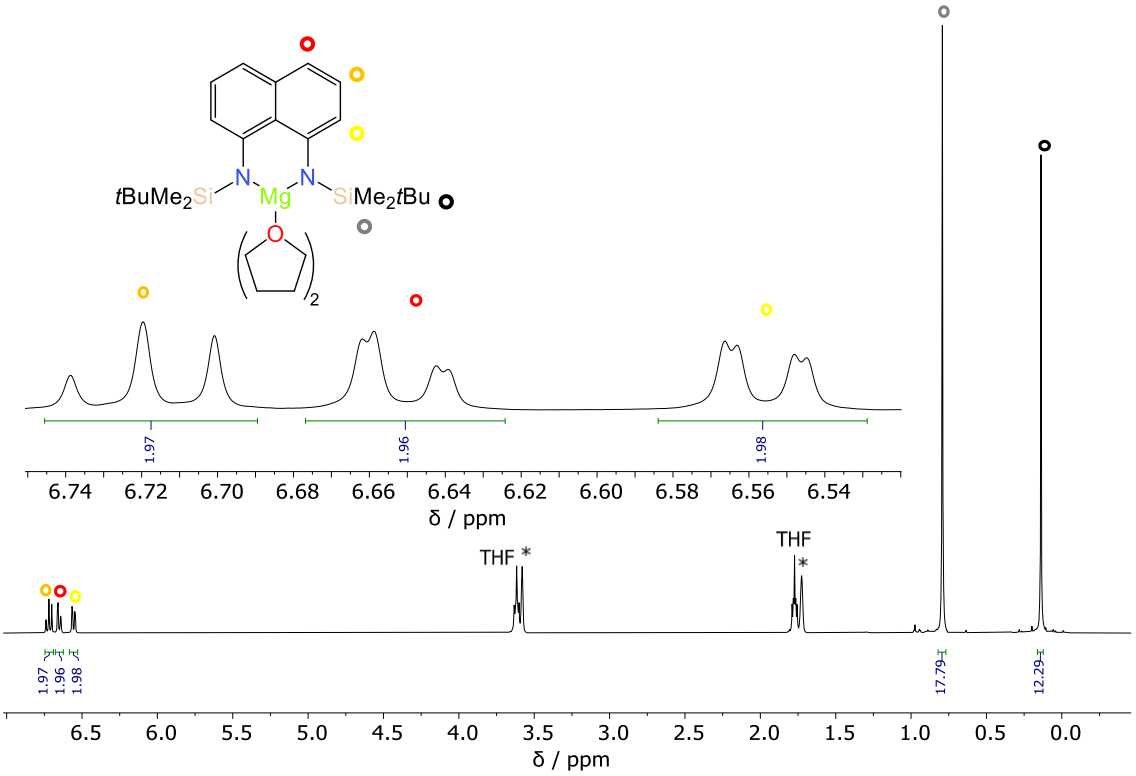


Figure A.9 ^{1}H NMR spectrum (C_4D_8O, 298 K, 400 MHz) of [($^{Me_2{}^{t}Bu}$L)Mg(THF)$_2$] (**5**).* denotes residual protio fraction of C_4D_8O. Expansion shows naphthyl region.

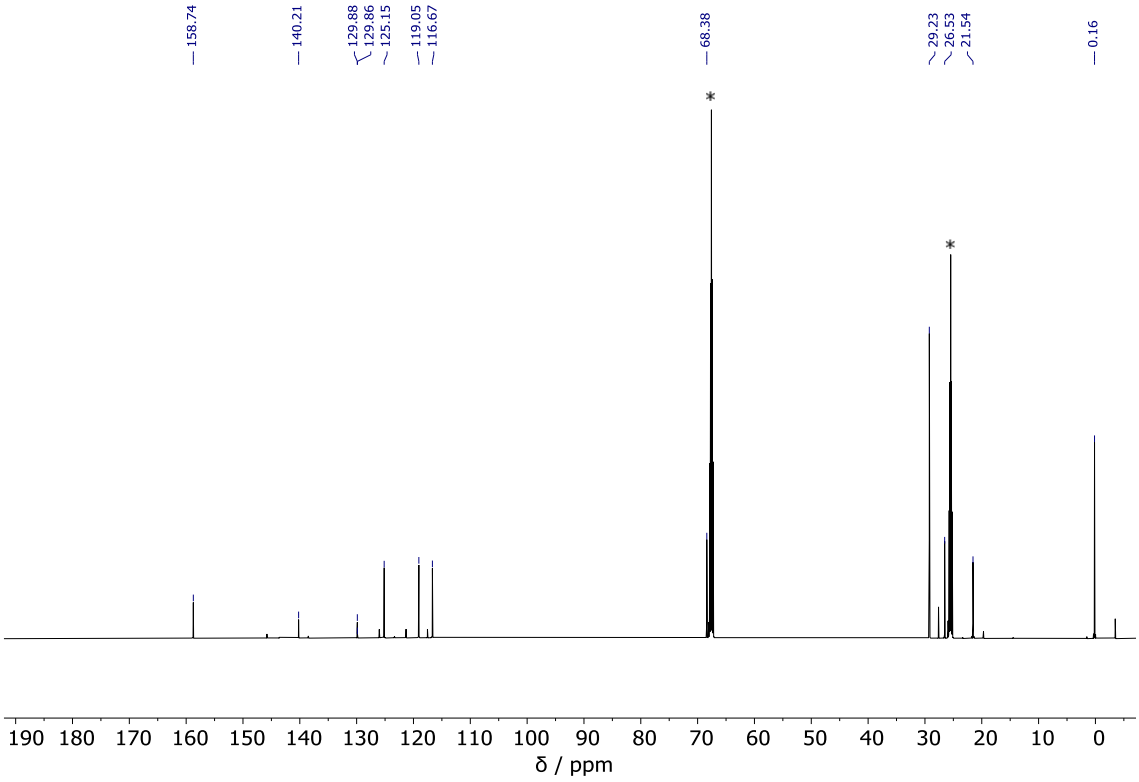


Figure A.10 $^{13}C\{^{1}H\}$ NMR spectrum (C_4D_8O, 298 K, 151 MHz) of [($^{Me_2{}^tBu}$L)Mg(THF)$_2$] (**5**).

* denotes C_4D_8O.

A.1.2 *In situ* NMR spectra

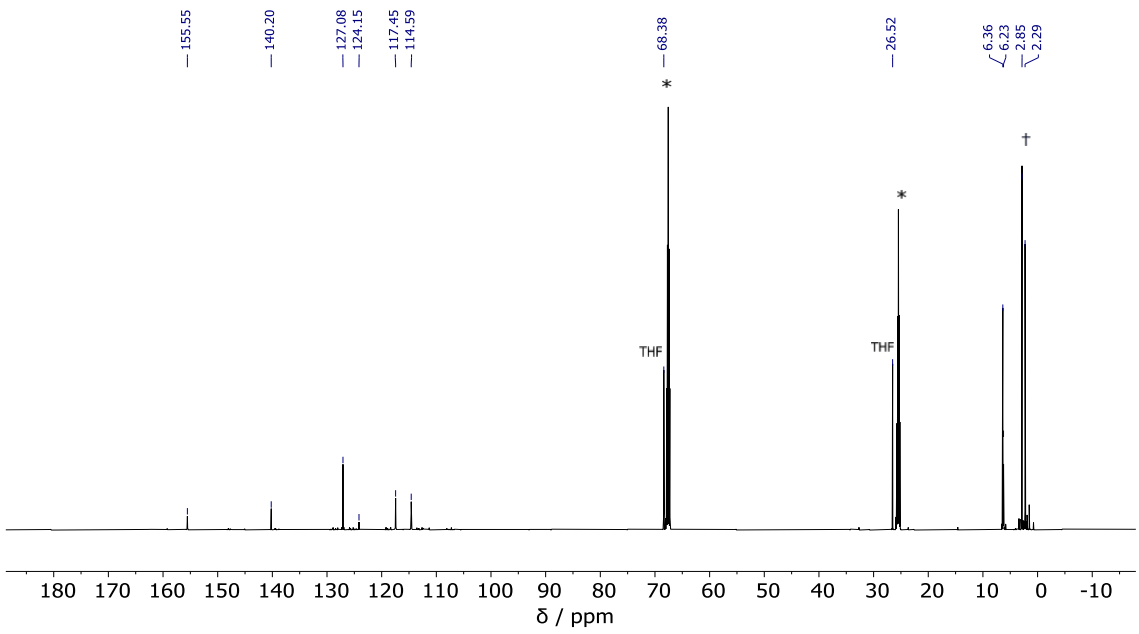


Figure A.11 $^{13}C\{^{1}H\}$ NMR spectra (C_4D_8O, 298 K, 151.0 MHz) of [(^{Me_3}LH)SrN"(THF)$_n$] prepared *in situ* from $^{Me_3}LH_2$ and [SrN"$_2$(THF)$_2$]. † denotes HN", * denotes C_4D_8O.

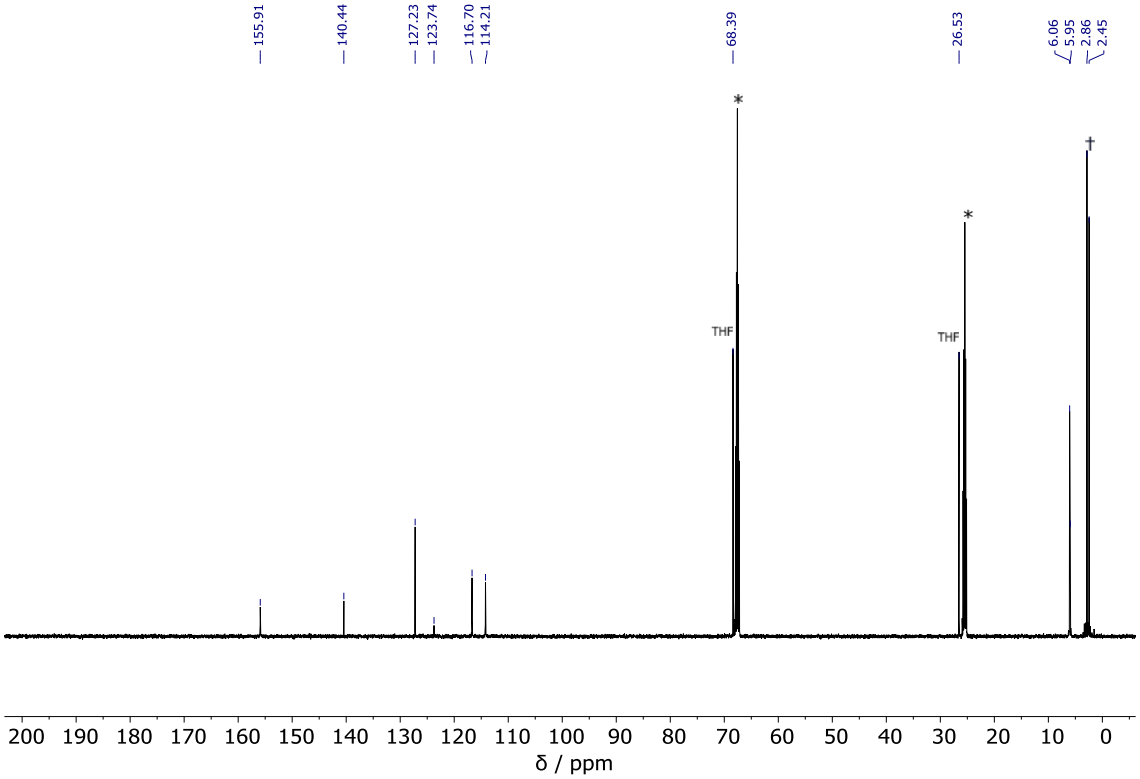


Figure A.12 $^{13}C\{^{1}H\}$ NMR spectrum (C_4D_8O, 298 K, 126 MHz) of [(^{Me3}LH)BaN"(THF)$_n$] prepared *in situ* from $^{Me3}LH_2$ and [BaN"$_2$(THF)$_2$]. † denotes HN", * denotes C_4D_8O.

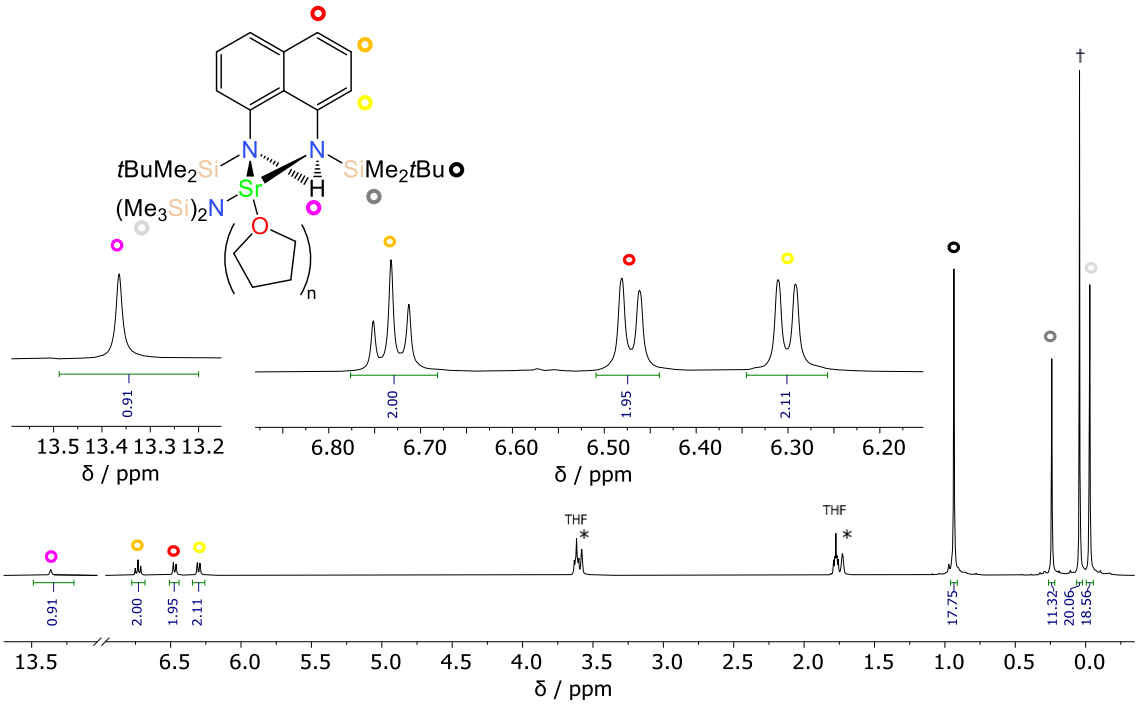


Figure A.13 ^{1}H NMR spectrum (C_4D_8O, 298 K, 400 MHz) of [(^{Me2tBu}LH)SrN"(THF)$_n$] prepared in situ from $^{Me2tBu}LH_2$ and [SrN"$_2$(THF)$_2$]. † denotes HN", * denotes residual protio fraction of C_4D_8O.

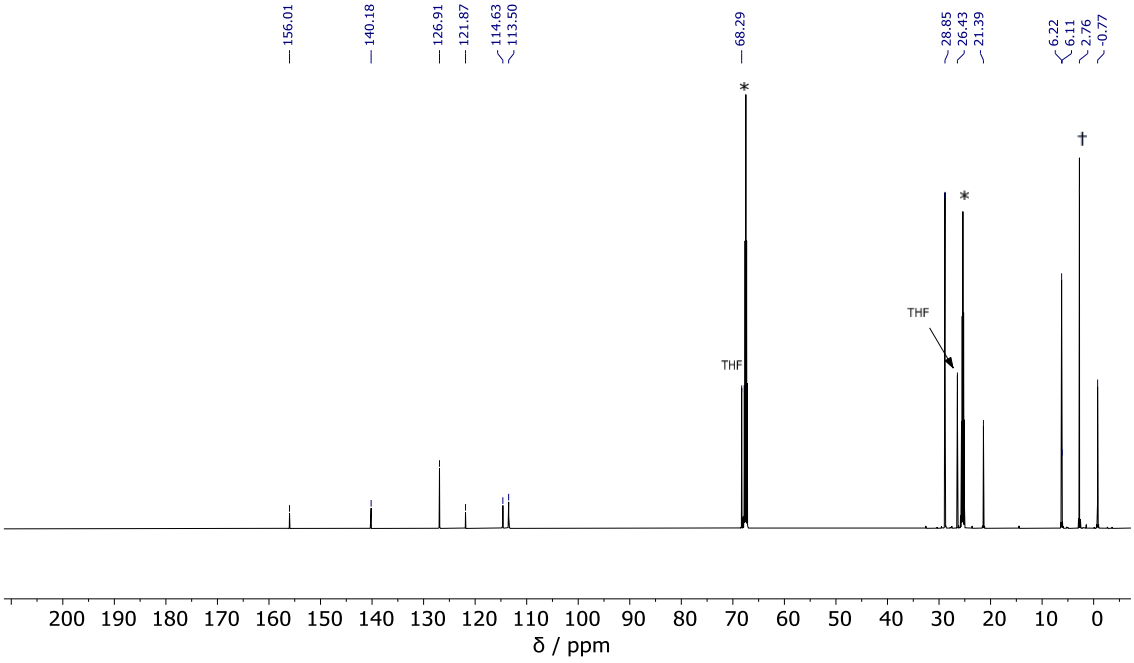


Figure A.14 $^{13}C\{^{1}H\}$ NMR spectrum (C_4D_8O, 298 K, 151.0 MHz) of [($^{Me_2{}^tBu}$LH)SrN"(THF)$_n$] prepared in situ from $^{Me_2{}^tBu}LH_2$ and [SrN"$_2$(THF)$_2$]. † denotes HN", * denotes C_4D_8O.

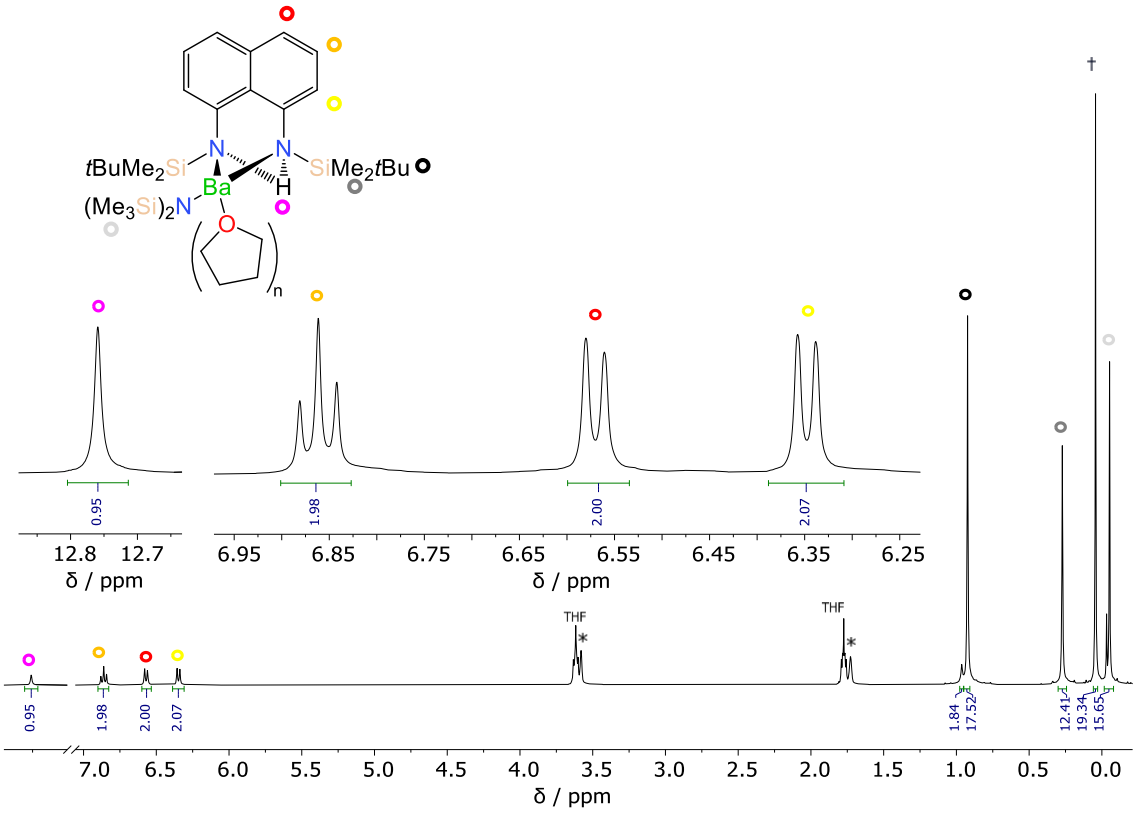


Figure A.15 ^{1}H NMR spectrum (C_4D_8O, 298 K, 400 MHz) of [($^{Me_2{}^tBu}$LH)BaN"(THF)$_n$] prepared in situ from $^{Me_2{}^tBu}LH_2$ and [BaN"$_2$(THF)$_2$]. † denotes HN", * denotes residual protio fraction of C_4D_8O.

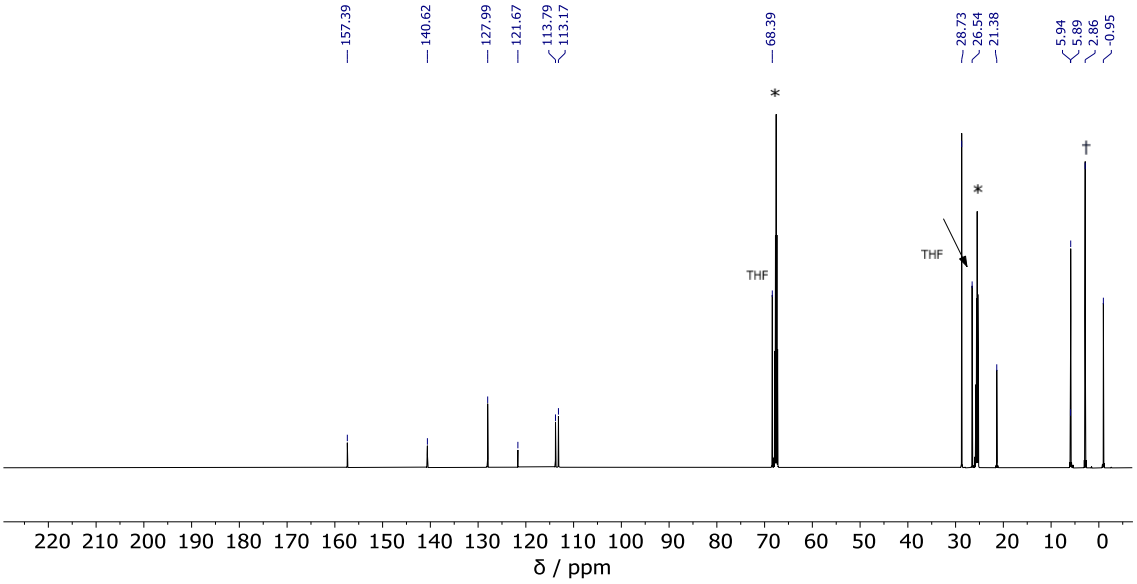


Figure A.16 $^{13}C\{^{1}H\}$ NMR spectrum (C_4D_8O, 298 K, 151.0 MHz) of [($^{Me_2{}^tBu}$LH)BaN"(THF)$_n$] prepared in situ from $^{Me_2{}^tBu}LH_2$ and [BaN"$_2$(THF)$_2$]. † denotes HN", * denotes C_4D_8O.

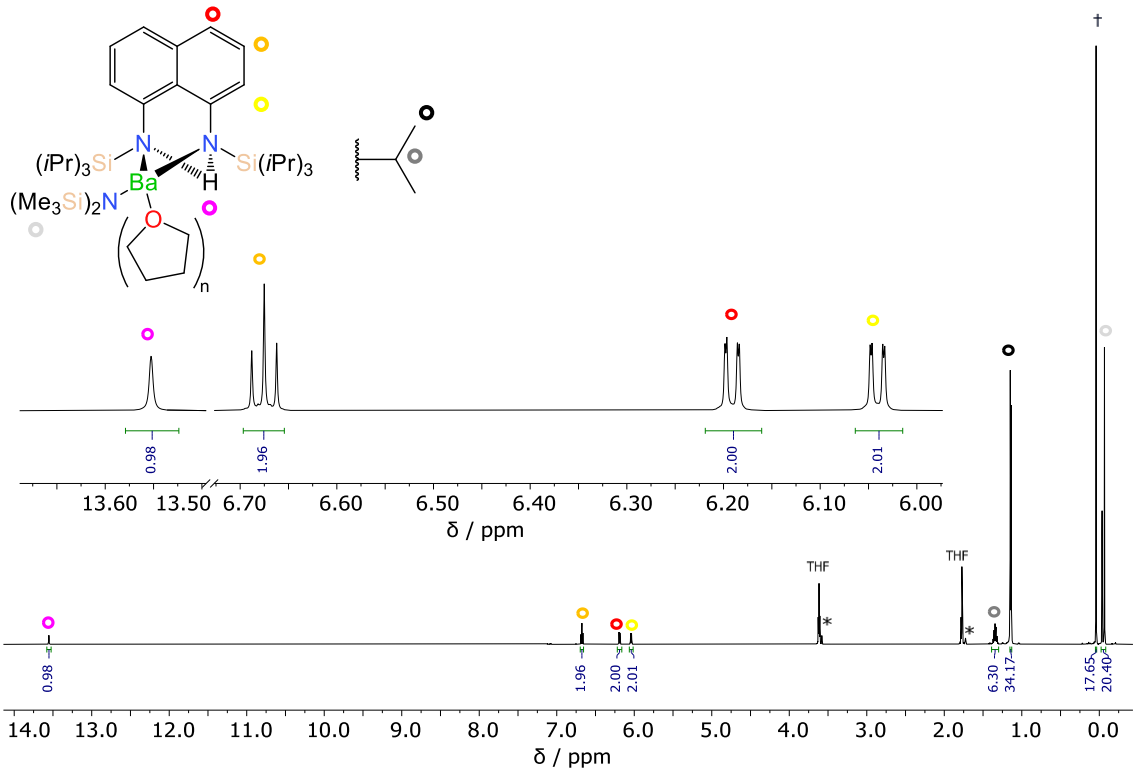


Figure A.17 ^{1}H NMR spectrum (C_4D_8O, 298 K, 600 MHz) of [(^{iPr_3}LH)BaN"(THF)$_n$] prepared *in situ* from $^{iPr_3}LH_2$ and [BaN"$_2$(THF)$_2$]. † denotes HN", * denotes residual protio fraction of C_4D_8O.

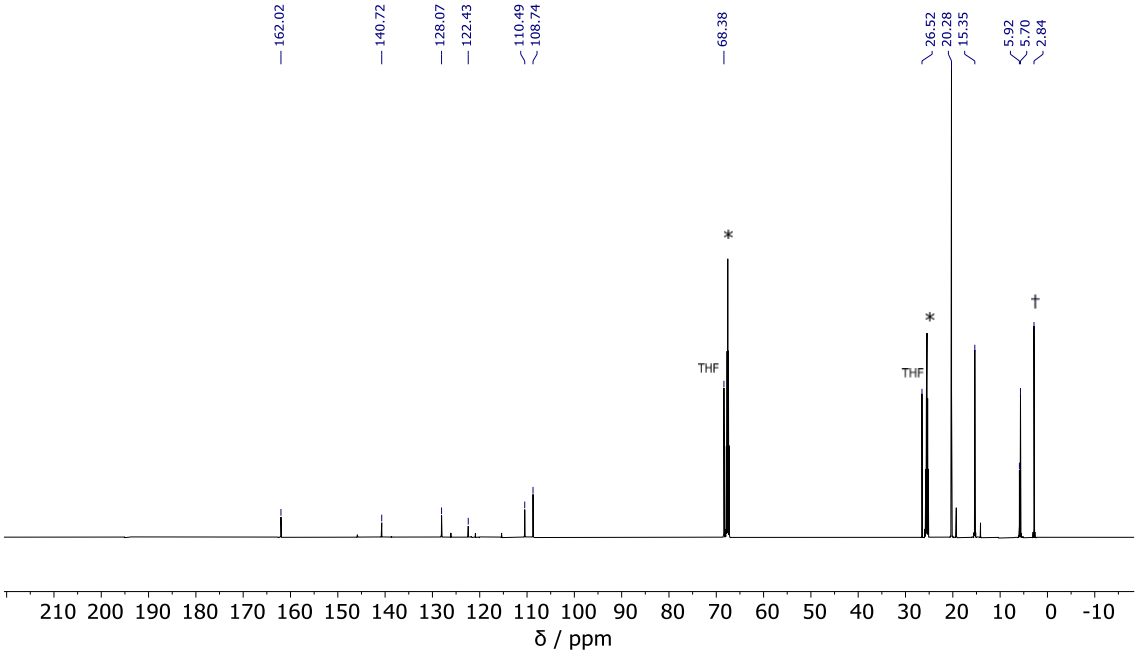


Figure A.18 $^{13}C\{^{1}H\}$ NMR spectrum (C_4D_8O, 298 K, 151.0 MHz) of [($^{i}Pr_3$LH)BaN"(THF)$_n$] prepared in situ from $^{i}Pr_3LH_2$ and [BaN"$_2$(THF)$_2$]. † denotes HN", * denotes C_4D_8O.

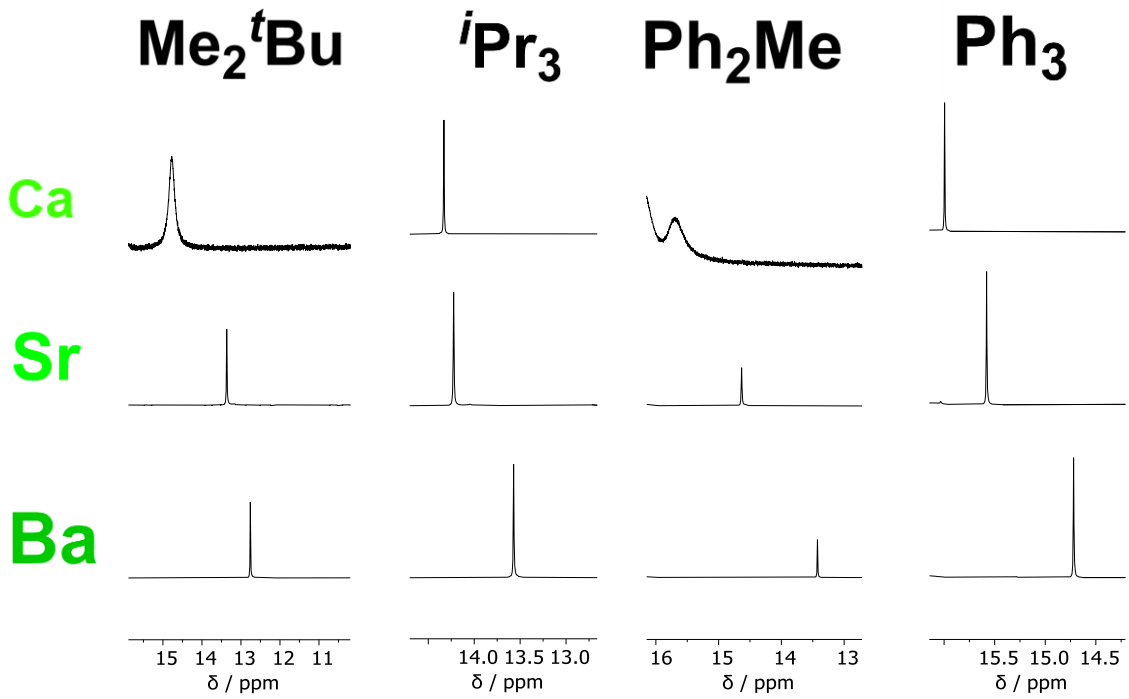


Figure A.19 (N,N)μ_2-H regions of the ^{1}H NMR spectra (C_4D_8O, 298 K, 400 MHz) of [(^{R3}LH)AeN"(THF)$_n$] prepared in situ from $^{R3}LH_2$ and AeN"$_2$(THF)$_2$ (R_3 = Me$_2$^{t}Bu, $^{i}Pr_3$, Ph$_2$Me and Ph$_3$; Ae = Ca, Sr and Ba).

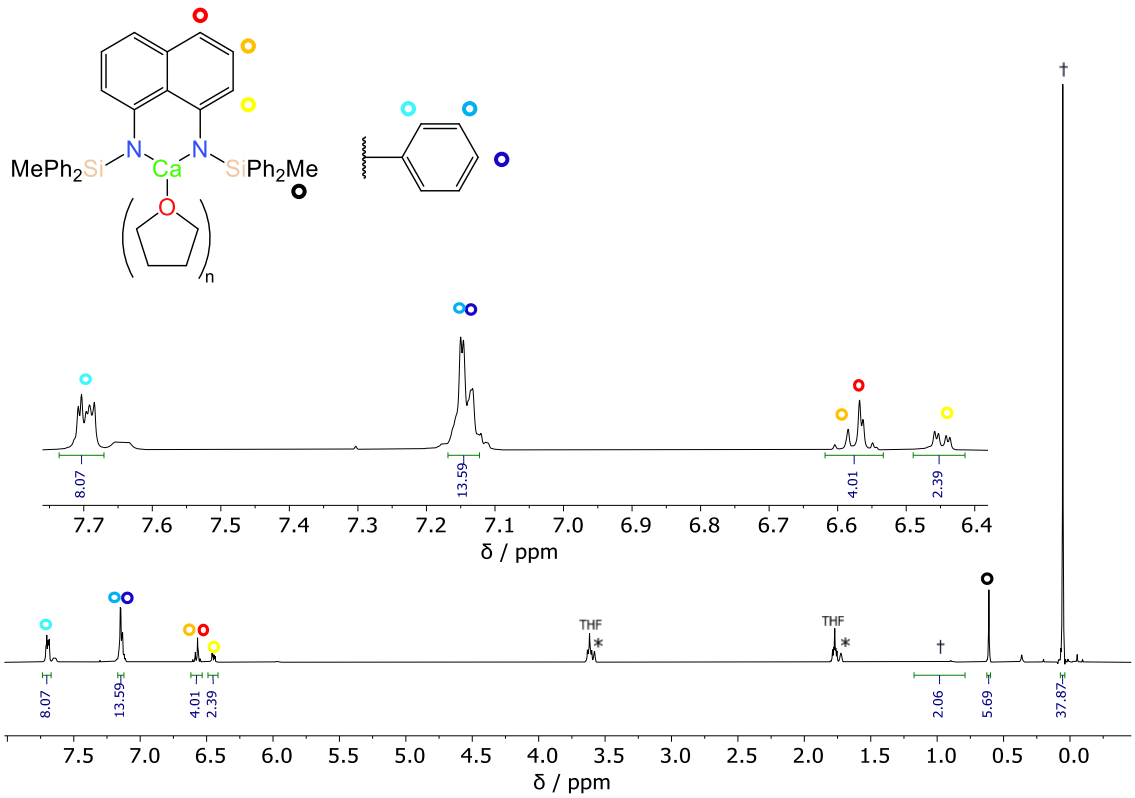


Figure A.20 ^{1}H NMR spectrum (C_4D_8O, 298 K, 400 MHz) of [(^{Ph_2Me}L)Ca(THF)$_n$] prepared *in situ* after leaving a reaction mixture of $^{Ph_2Me}LH_2$ and [CaN"$_2$(THF)$_2$] to stand for 16 h at 25 °C. † denotes HN", * denotes residual protio fraction of C_4D_8O.

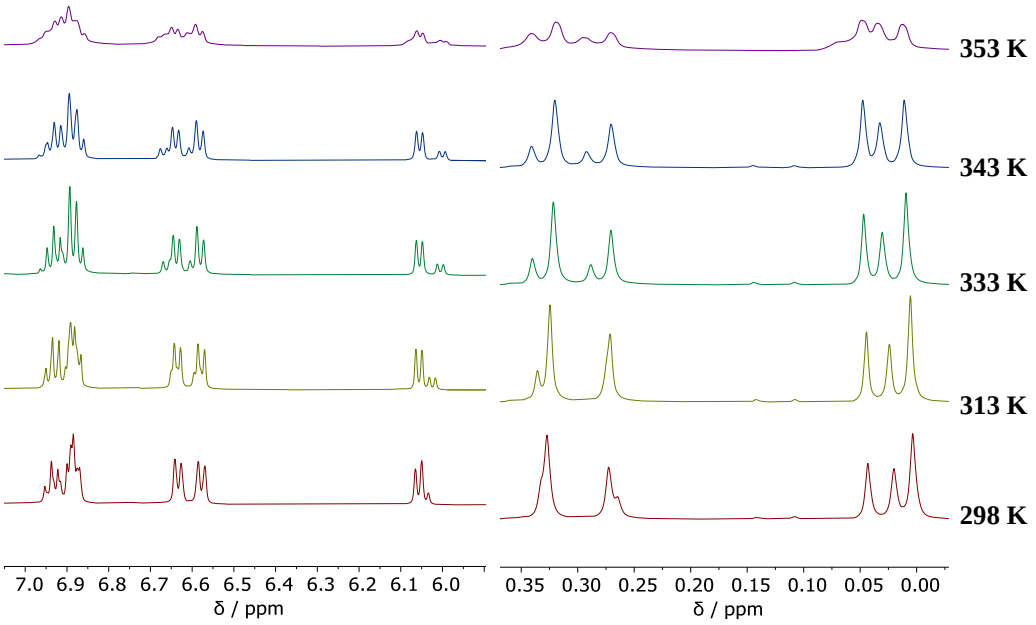


Figure A.21 Variable temperature ^{1}H NMR spectra (C_4D_8O, 499.9 MHz) of [($^{Me_3\text{-}\mu\text{-}Me_2}$L)CaN"(THF)$_n$], prepared *in situ* from $^{Me_3}LH_2$ and [CaN"$_2$(THF)$_2$] at 80 °C for 16 h.

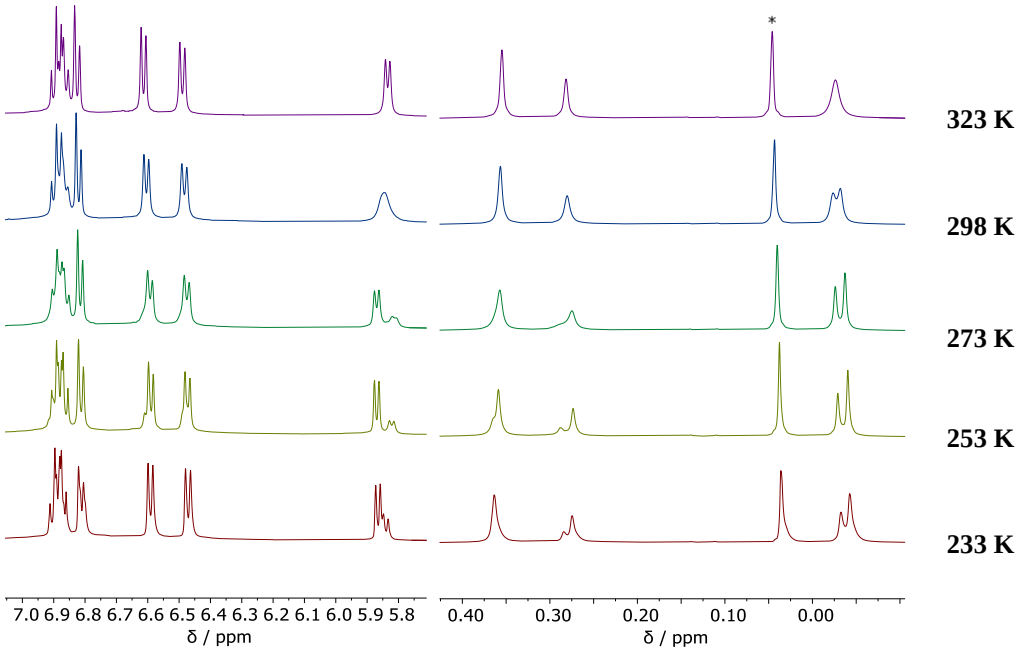


Figure A.22 Variable temperature ^{1}H NMR spectra (C_4D_8O, 499.9 MHz) of [(^{Me3}-μ-^{Me2}L)BaN"(THF)$_n$] prepared *in situ* by heating $^{Me3}LH_2$ and [BaN"$_2$(THF)$_2$] at 80 °C for 16 h. * denotes HN".

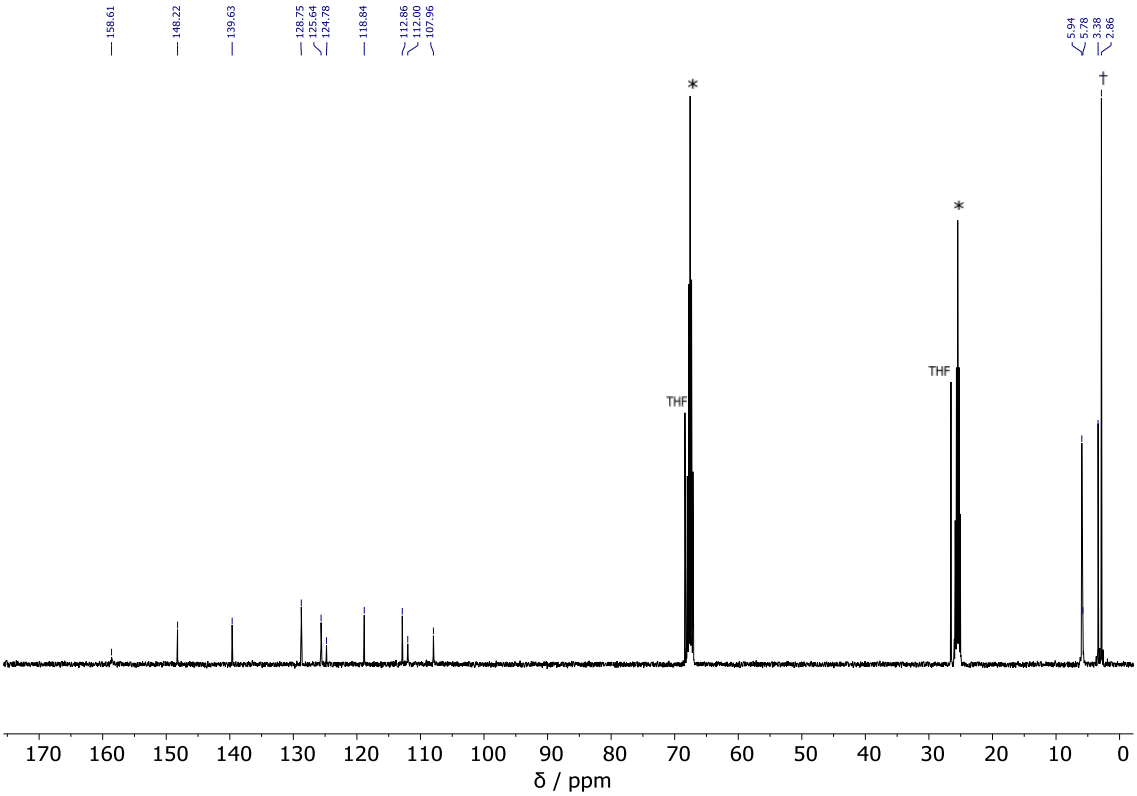


Figure A.23 ^{13}C{^{1}H} NMR spectrum (C_4D_8O, 298 K, 100.6 MHz) of [(^{Me3}-μ-^{Me2}L)BaN"(THF)$_n$], prepared *in situ* by heating $^{Me3}LH_2$ and [BaN"$_2$(THF)$_2$] at 80 °C for 16 h. † denotes HN", * denotes C_4D_8O.

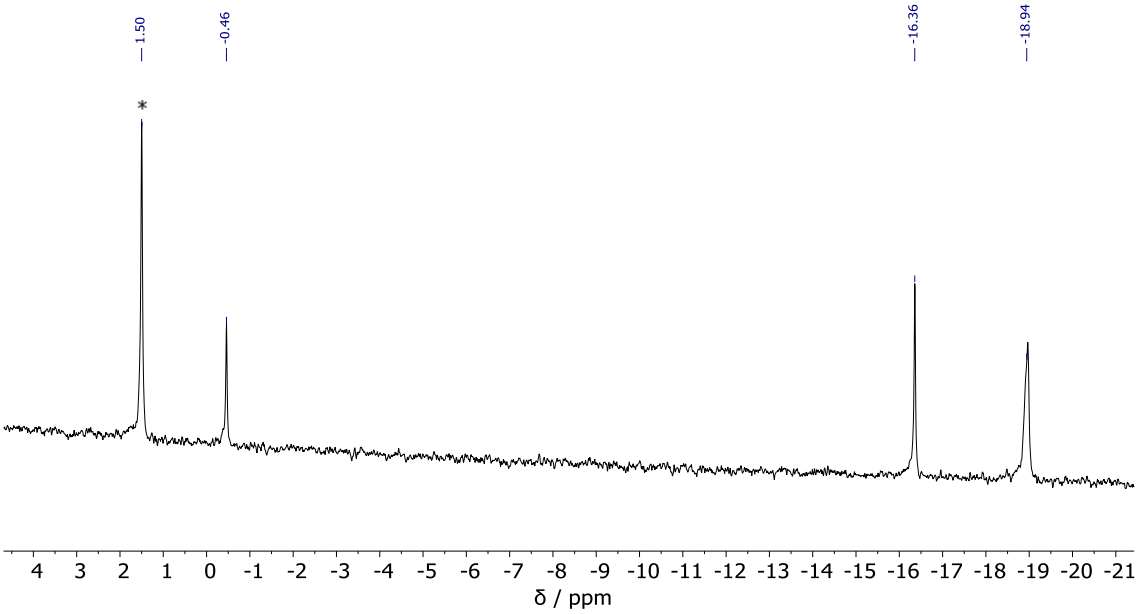


Figure A.24 ^{29}Si NMR spectrum (C_4D_8O, 298 K, 119 MHz) of [(^{Me_3}-μ-^{Me_2}L)BaN"(THF)$_n$], prepared *in situ* by heating $^{Me_3}LH_2$ and [BaN"$_2$(THF)$_2$] at 80 °C for 16 h. * denotes HN".

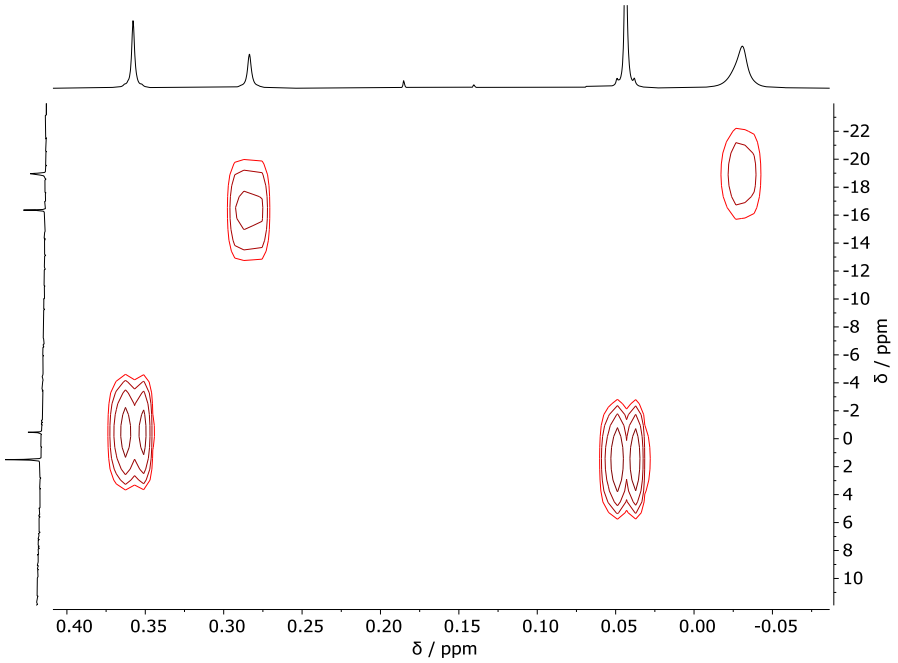


Figure A.25 dimensional ^{29}Si-^{1}H HMBC NMR spectrum (C_4D_8O, 298 K) of [(^{Me_3}-μ-^{Me_2}L)BaN"(THF)$_n$], prepared *in situ* by heating $^{Me_3}LH_2$ and [BaN"$_2$(THF)$_2$] at 80 °C for 16 h.

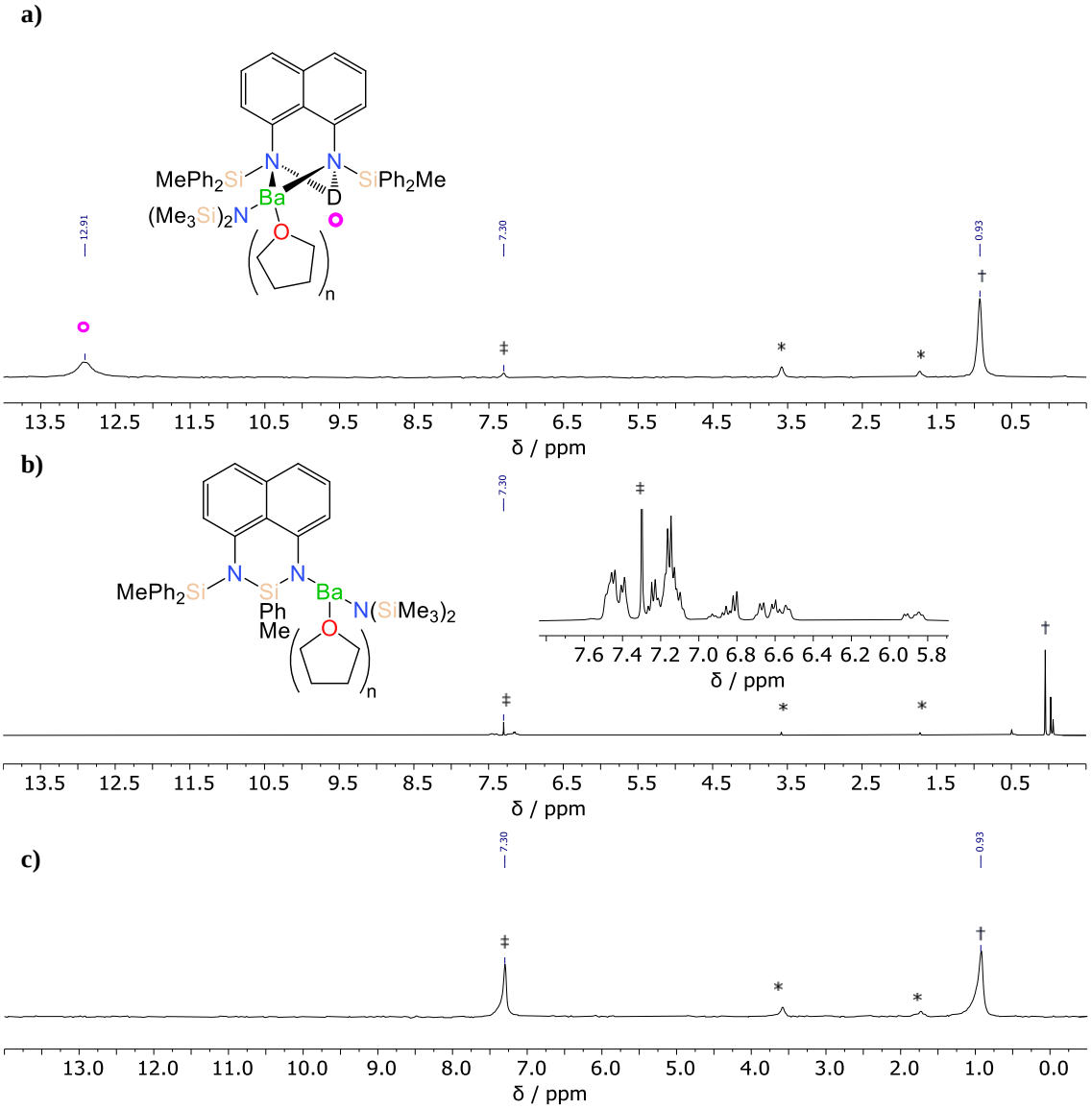


Figure A.26 a) ^{2}H NMR spectrum (C_4H_8O, 298 K, 77 MHz) of [(^{Ph_2Me}LD)BaN"(THF)$_n$], **b)** ^{1}H NMR spectrum (C_4D_8O, 298 K, 400 MHz) of [($^{Ph_2Me\text{-}\mu\text{-}PhMe}$L)BaN"(THF)$_n$] and **c)** ^{2}H NMR spectrum (C_4H_8O, 298 K, 92 MHz) of [($^{Ph_2Me\text{-}\mu\text{-}PhMe}$L)BaN"(THF)$_n$]. Expansion in **b)** shows aromatic region (broad and overlapping signals are not assigned). ‡ denotes C_6H_5D, † denotes DN", * denotes residual protio/deuterio fraction of THF-d_8/THF.

A.1.3 X-ray crystallographic data

Table A.1 Experimental crystallographic data for $^{Me_3}LH_2$, $^{Me_2{}^tBu}LH_2$ and $^{Ph_3}LH_2$ (**1**).

Complex	**$^{Me_3}LH_2$**	**$^{Me_2{}^tBu}LH_2$**	**1**
		Crystal data	
File name	004mdh24	003mdh24	012ccr22
Chemical formula	$C_{16}H_{26}N_2Si_2$	$C_{22}H_{38}N_2Si_2$	$C_{46}H_{38}N_2Si_2$
M_r	302.57	386.72	674.99
Crystal system, space group	Orthorhombic, *Pbca*	Monoclinic, $P2_1/n$	Triclinic, $P\bar{1}$
Temperature (K)	150	150	150
a, *b*, *c* (Å)	6.9308 (1), 19.8358 (2), 26.5103 (2)	15.8085 (1), 7.9751 (1), 18.9730 (2)	11.3470 (3), 13.2059 (3), 24.8531 (5)
α, *β*, *γ* (°)	90, 90, 90	90, 103.913 (1), 90	81.2550 (17), 77.0739 (19), 82.0233 (18)
V (Å^3)	3644.58 (7)	2321.83 (4)	3566.32 (15)
Z	8	4	4
Radiation type	Cu *K*α	Cu *K*α	Cu *K*a
μ (mm^{-1})	1.70	1.43	1.17
Crystal size (mm)	0.18 × 0.11 × 0.05	0.12 × 0.04 × 0.04	0.16 × 0.15 × 0.03
		Data Collection	
Diffractometer	SuperNova, Dual, Cu at home/near, Atlas	SuperNova, Dual, Cu at home/near, Atlas	Oxford Diffraction SuperNova
Absorption correction	Multi-scan *CrysAlis PRO* 1.171.43.95a (Rigaku Oxford Diffraction, 2023) Empirical absorption correction using spherical harmonics, implemented in SCALE3 ABSPACK scaling algorithm.	Multi-scan *CrysAlis PRO* 1.171.43.95a (Rigaku Oxford Diffraction, 2023) Empirical absorption correction using spherical harmonics, implemented in SCALE3 ABSPACK scaling algorithm.	Multi-scan *CrysAlis PRO* (Rigaku Oxford Diffraction, 2017)
T_{min}, T_{max}	0.954, 1.000	0.976, 1.000	0.86, 0.97
No. of measured, independent and observed [$I > 2\sigma(I)$] reflections	53010, 3815, 3304	38129, 4807, 4144	57465, 14727, 11823

R_{int}	0.041	0.039	0.048
Refinement			
$R[F^2 > 2\sigma(F^2)]$, $wR(F^2)$, S	0.030, 0.085, 1.03	0.030, 0.084, 1.04	0.049, 0.136, 1.03
No. of reflections	3815	4807	14724
No. of parameters	195	253	917
No. of restraints	-	-	16
$(\Delta/\sigma)_{max}$	-	-	-
$\Delta\rho_{max}$, $\Delta\rho_{min}$ (e Å^{-3})	0.28, −0.20	0.29, −0.19	0.70, −0.50
Absolute structure	-	-	-

Table A.2 Experimental crystallographic data for $^{Me_2H\text{-}\mu\text{-}Me_2}$LH (**3**), [(^{Me_3}L)Mg(THF)$_2$] (**4**) and [($^{Me_2{}^tBu}$L)Mg(THF)$_2$] (**5**)

Complex	**3**	**4**	**5**
		Crystal data	
File name	007zrt21	008zrt22	005zrt22
Chemical formula	$C_{14}H_{20}N_2Si_2$	$C_{24}H_{40}MgN_2O_2Si_2$	$C_{30}H_{52}MgN_2O_2Si_2$
M_r	272.50	469.07	553.22
Crystal system, space group	Monoclinic, $P2_1/c$	Monoclinic, $C2/c$	Triclinic, $P\bar{1}$
Temperature (K)	150	150	150
a, b, c (Å)	9.4539 (1), 22.7711 (3), 21.2705 (3)	22.2086 (2), 12.1186 (1), 19.9744 (2)	10.6149 (3), 11.1516 (3), 15.2078 (4)
α, β, γ (°)	90, 96.112 (1), 90	90, 94.936 (1), 90	70.623 (2), 78.813 (2), 72.252 (2)
V (Å^3)	4552.99 (10)	5355.92 (8)	1608.74 (8)
Z	12	8	2
Radiation type	Cu $K\alpha$	Cu Ka	Cu Ka
μ (mm^{-1})	1.99	1.60	1.40
Crystal size (mm)	0.31 × 0.12 × 0.09	0.30 × 0.18 × 0.14	0.35 × 0.13 × 0.11
		Data Collection	
Diffractometer	SuperNova, Dual, Cu at home/near, Atlas	SuperNova, Dual, Cu at home/near, Atlas	SuperNova, Dual, Cu at home/near, Atlas
Absorption correction	Gaussian *CrysAlis PRO* 1.171.41.93a (Rigaku Oxford Diffraction, 2020) Numerical absorption correction based on gaussian integration over a multifaceted crystal model Empirical absorption correction using spherical harmonics, implemented in SCALE3 ABSPACK scaling algorithm.	Gaussian *CrysAlis PRO* 1.171.41.93a (Rigaku Oxford Diffraction, 2020) Numerical absorption correction based on gaussian integration over a multifaceted crystal model Empirical absorption correction using spherical harmonics, implemented in SCALE3 ABSPACK scaling algorithm.	Gaussian *CrysAlis PRO* 1.171.41.93a (Rigaku Oxford Diffraction, 2020) Numerical absorption correction based on gaussian integration over a multifaceted crystal model Empirical absorption correction using spherical harmonics, implemented in SCALE3 ABSPACK scaling algorithm.
T_{min}, T_{max}	0.574, 1.000	0.521, 1.000	0.679, 1.000
No. of measured, independent and	25974, 9247, 7564	31845, 5483, 5138	20116, 6554, 6086

observed [$I > 2\sigma(I)$] reflections			
R_{int}	0.033	0.025	0.019
Refinement			
$R[F^2 > 2\sigma(F^2)]$, $wR(F^2)$, S	0.036, 0.101, 1.02	0.029, 0.080, 1.05	0.033, 0.092, 1.04
No. of reflections	9247	5483	6554
No. of parameters	691	286	344
No. of restraints	43	-	-
$(\Delta/\sigma)_{max}$	-	-	-
$\Delta\rho_{max}$, $\Delta\rho_{min}$ (e Å^{-3})	0.30, −0.31	0.25, −0.24	0.74, −0.46
Absolute structure	-	-	-
Absolute structure parameter	-	-	-

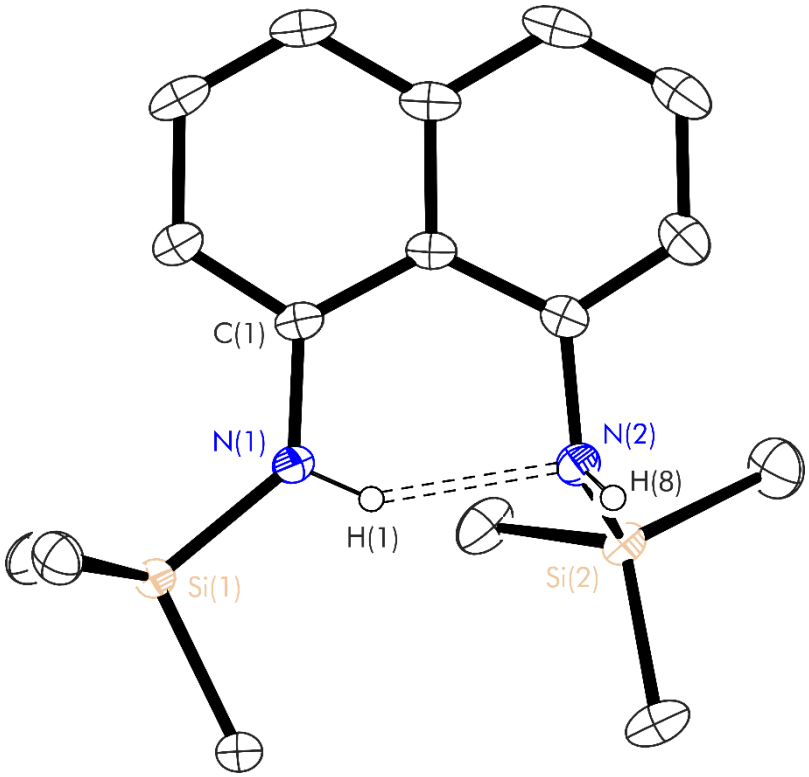


Figure A.27 Thermal displacement ellipsoid drawing (30% probability) of $^{Me_3}LH_2$. All non-amino hydrogen atoms have been omitted for clarity.

Table A.3 Experimental metrical parameters (bond lengths in Å and angles in °) in $^{Me_3}LH_2$, $^{Me_2{}^tBu}LH_2$ and $^{Ph_3}LH_2$ (**1**).

	$^{Me_3}LH_2$	$^{Me_2{}^tBu}LH_2$	**1**
N(1)-H(1)	0.82(2)	0.83(2)	0.87(2)
N(2)-H(8)	0.79(2)	0.87(2)	0.86(2)
N(2)-H(1)	2.03(2)	2.11(2)	2.11(2)
N(1)-C(1)	1.384(2)	1.387(2)	1.449(3)
N(2)-C(8)	1.438(2)	1.443(1)	1.390(3)
N(1)-Si(1)	1.729(1)	1.742(1)	1.741(2)
N(2)-Si(2)	1.747(1)	1.773(1)	1.733(2)
N(1)-N(2)	2.754(2)	2.812(2)	2.827(2)
H(1)-N(1)-C(1)	112(1)	112(1)	111(1)
H(1)-N(1)-Si(1)	116(1)	118(1)	113(1)
C(1)-N(1)-Si(1)	131.83(9)	128.50(9)	123.4(1)
H(8)-N(2)-C(8)	112(1)	110(1)	115(1)
H(8)-N(2)-Si(2)	114(1)	110(1)	117(1)
C(8)-N(2)-Si(2)	123.18(9)	117.75(8)	127.7(2)
N(1)-H(1)-N(2)	146(2)	142(1)	140(2)

Table A.4 Experimental metrical parameters (bond lengths in Å and angles in °) in $^{Me_2H\text{-}\mu\text{-}Me_2}$LH (**3**).

	3
N(2)-H(2E)	0.78(3)
Si(1)-H(2D)	1.39(2)
N(1)-C(1)	1.413(2)
N(2)-C(8)	138.1(2)
N(1)-Si(1)	1.744(1)
N(1)-Si(2)	1,764(1)
N(2)-Si(1)	1.723(1)
N(1)-N(2)	2.692(2)
C(1)-N(1)-Si(1)	123.6(1)
C(1)-N(1)-Si(2)	122.7(1)
Si(1)-N(1)-Si(2)	113.73(8)
H(2E)-N(2)-C(8)	116(2)
H(2E)-N(2)-Si(1)	117(2)
C(8)-N(2)-Si(1)	127.3(1)
N(1)-Si(1)-N(2)	101.88(7)
Si(1)-N(1)-Si(2)	113.73(8)

A.2 Appendix for Chapter 3

A.2.1 NMR spectra of isolated compounds

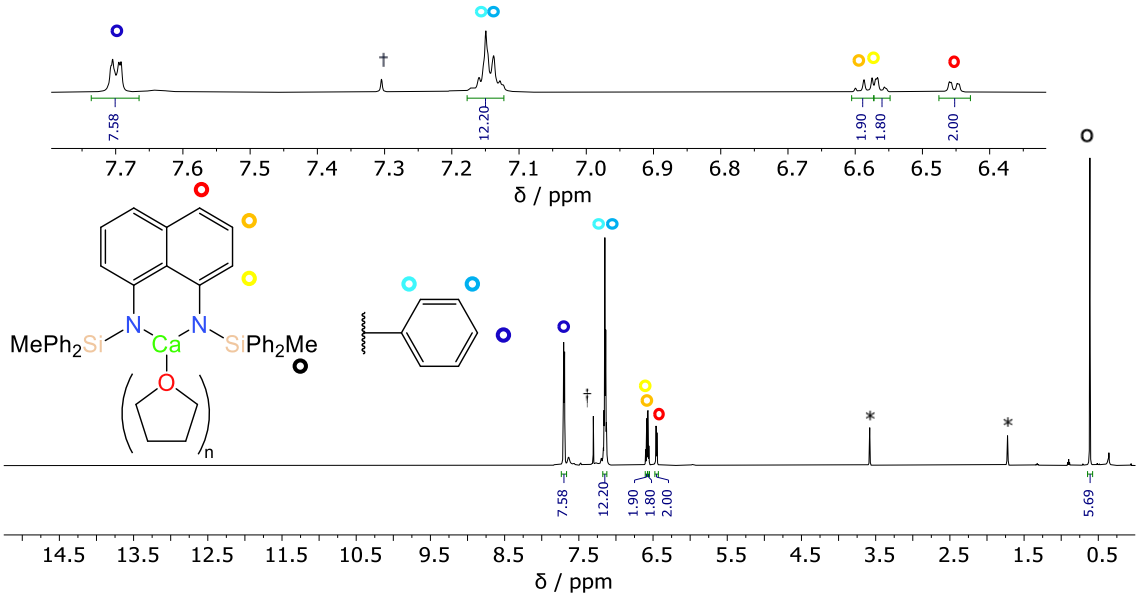


Figure A.28 ^{1}H NMR spectrum (C_4D_8O, 298 K, 600.4 MHz) of [(^{Ph_2Me}L)Ca(THF)$_n$], formed when [(^{Ph_2Me}L)Ca]$_2$ (**6**) is dissolved in THF. † denotes co-crystalllised benzene, * residual protio fraction of denotes C_4D_8O.

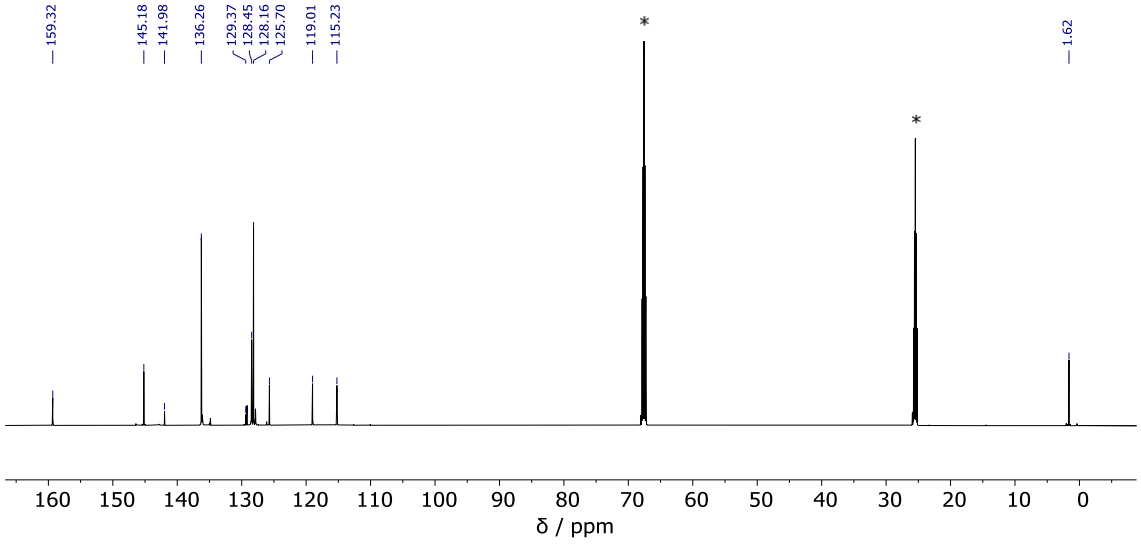


Figure A.29 ^{13}C{^{1}H} NMR spectrum (C_4D_8O, 298 K, 151.0 MHz) of [(^{Ph_2Me}L)Ca(THF)$_n$], formed when [(^{Ph_2Me}L)Ca]$_2$ (**6**) is dissolved in THF. * denotes C_4D_8O.

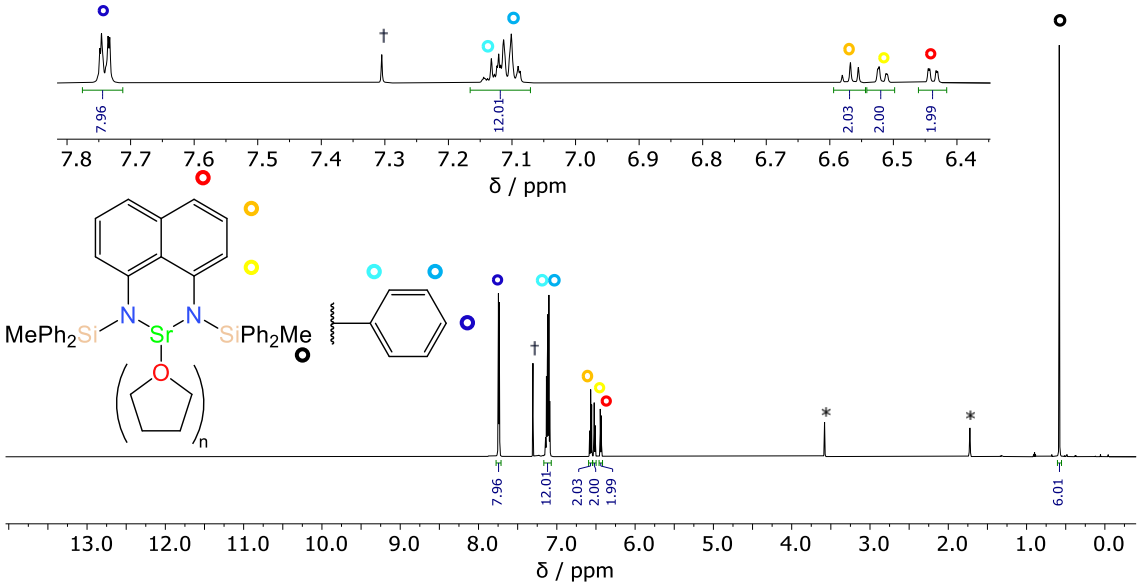


Figure A.30 ^{1}H NMR spectrum (C_4D_8O, 298 K, 600.4 MHz) of [(^{Ph_2Me}L)Sr(THF)$_n$], formed when [(^{Ph_2Me}L)Sr]$_2$ (**7**) is dissolved in THF. † denotes co-crystallised benzene, * denotes residual protio fraction of C_4D_8O. Expansion shows aromatic region.

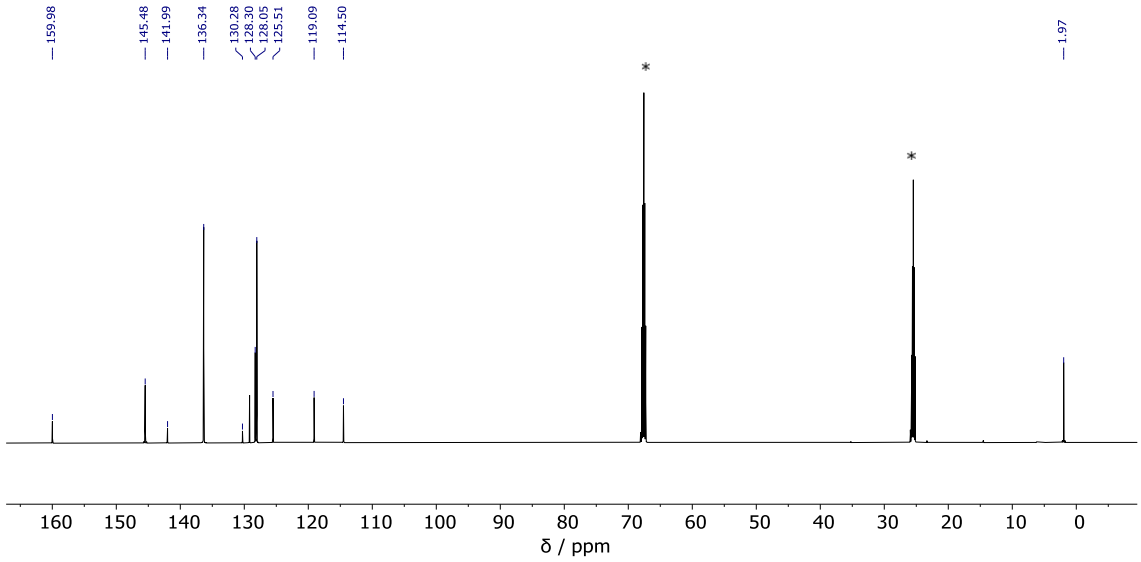


Figure A.31 ^{1}H NMR spectrum (C_4D_8O, 298 K, 600.4 MHz) of [(^{Ph_2Me}L)Sr(THF)$_n$], formed when [(^{Ph_2Me}L)Sr]$_2$ (**7**) is dissolved in THF. † denotes co-crystallised benzene, * denotes residual protio fraction of C_4D_8O. Expansion shows aromatic region.

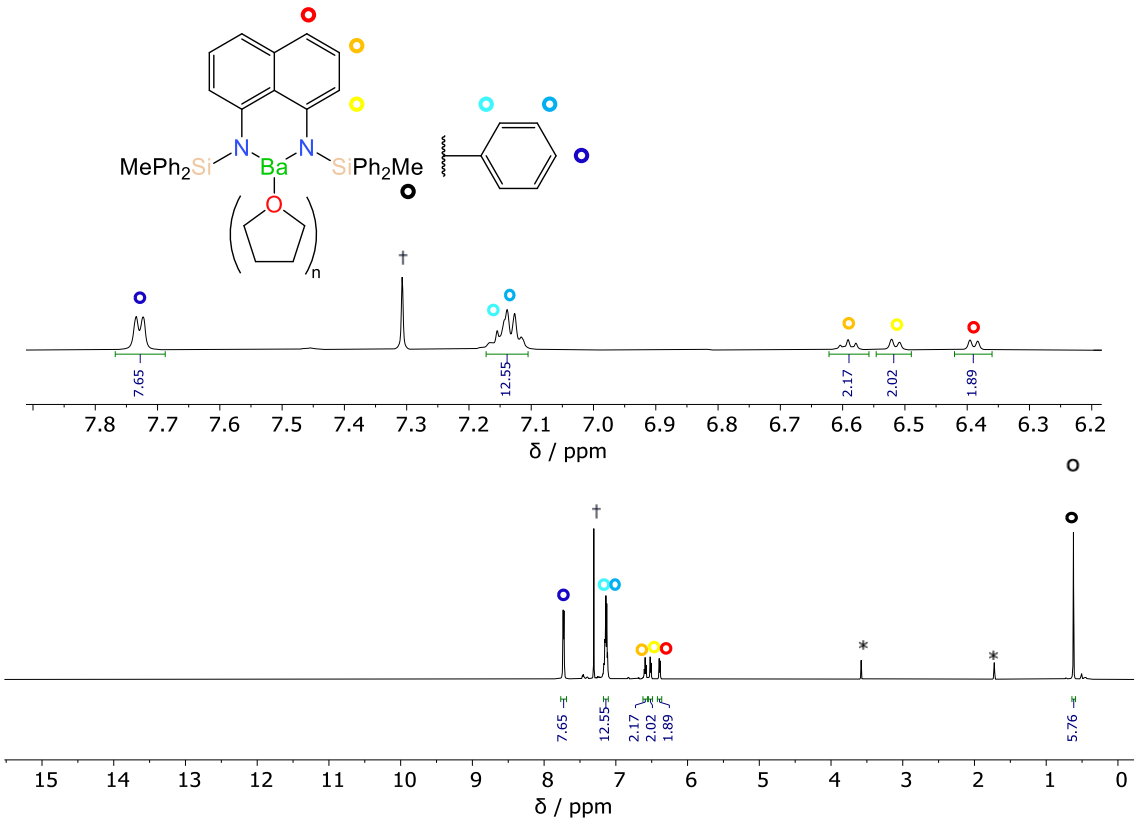


Figure A.32 ^{1}H NMR spectrum (C_4D_8O, 298 K, 600.4 MHz) of [(^{Ph_2Me}L)Ba(THF)$_n$], formed when [(^{Ph_2Me}L)Ba]$_2$ (**8**) is dissolved in THF. † denotes co-crystallised benzene, * denotes residual protio fraction of C_4D_8O. Expansion shows aromatic region.

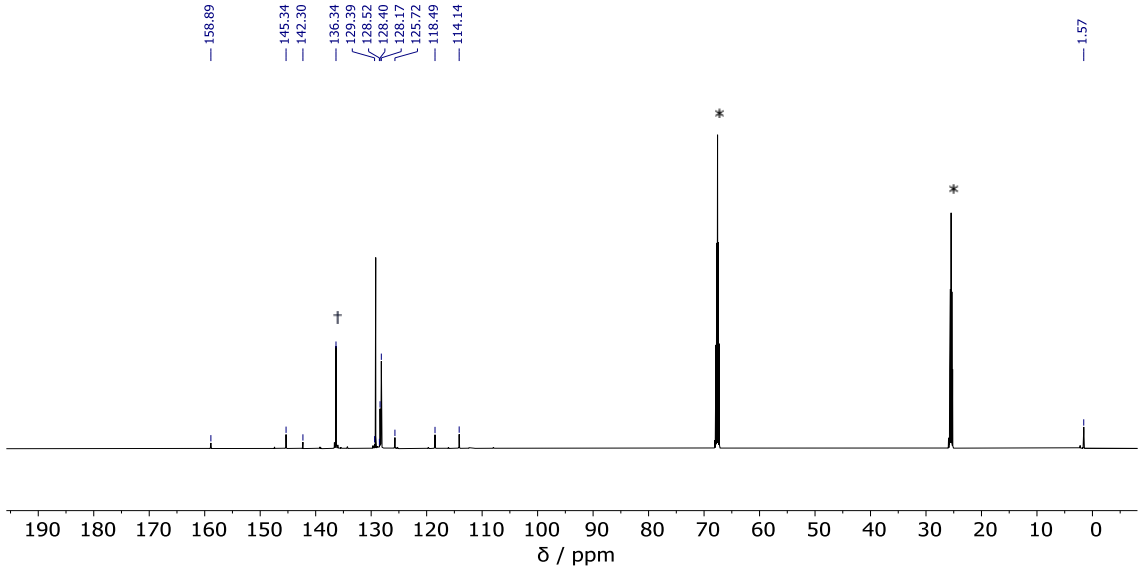


Figure A.33 ^{13}C{^{1}H} NMR spectrum (C_4D_8O, 298 K, 151.0 MHz) of [(^{Ph_2Me}L)Ba(THF)$_n$], formed when [(^{Ph_2Me}L)Ba]$_2$ (**8**) is dissolved in THF. † denotes co-crystallised benzene, * denotes C_4D_8O.

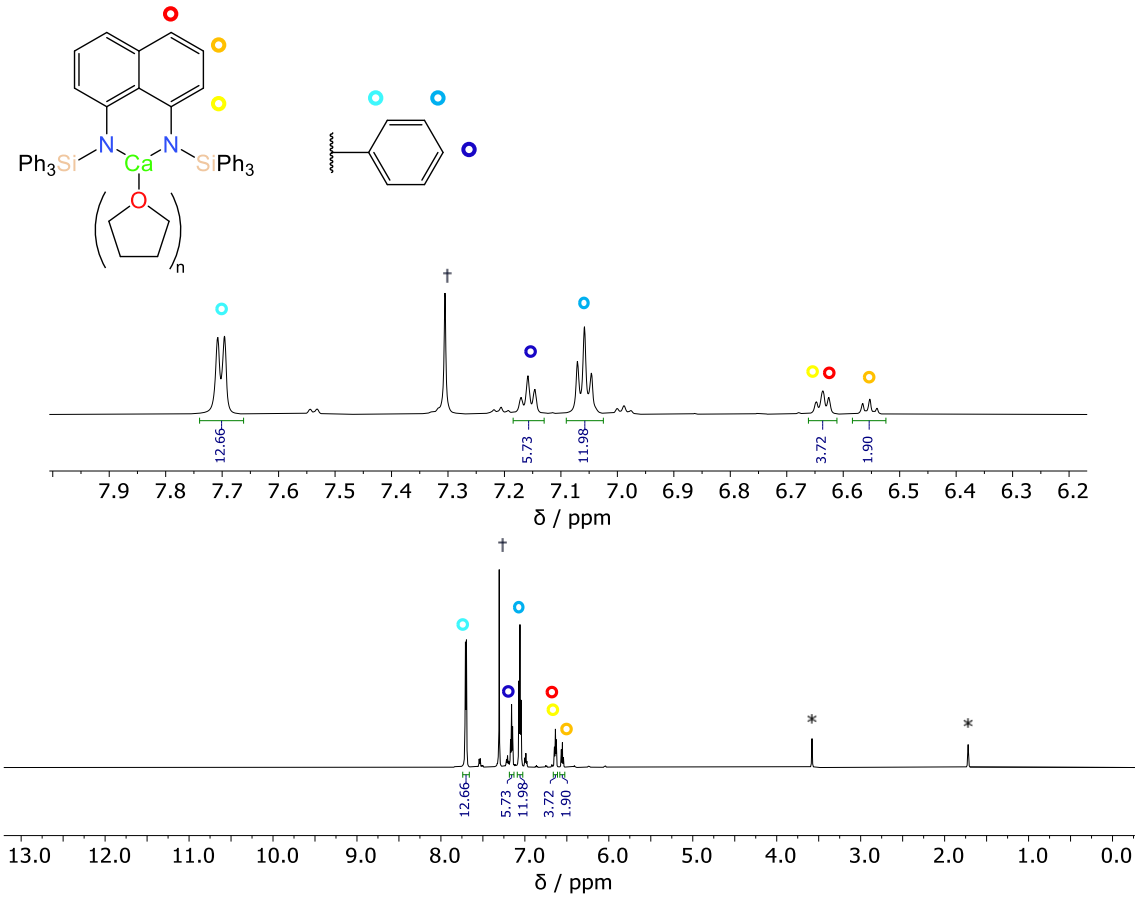


Figure A.34 ^{1}H NMR spectrum (C_4D_8O, 298 K, 600.4 MHz) of [(^{Ph3}L)Ca(THF)$_n$], formed when [(^{Ph3}L)Ca]$_2$ (**9**) is dissolved in THF. † denotes co-crystallised benzene, * denotes residual protio fraction of C_4D_8O. Expansion shows aromatic region.

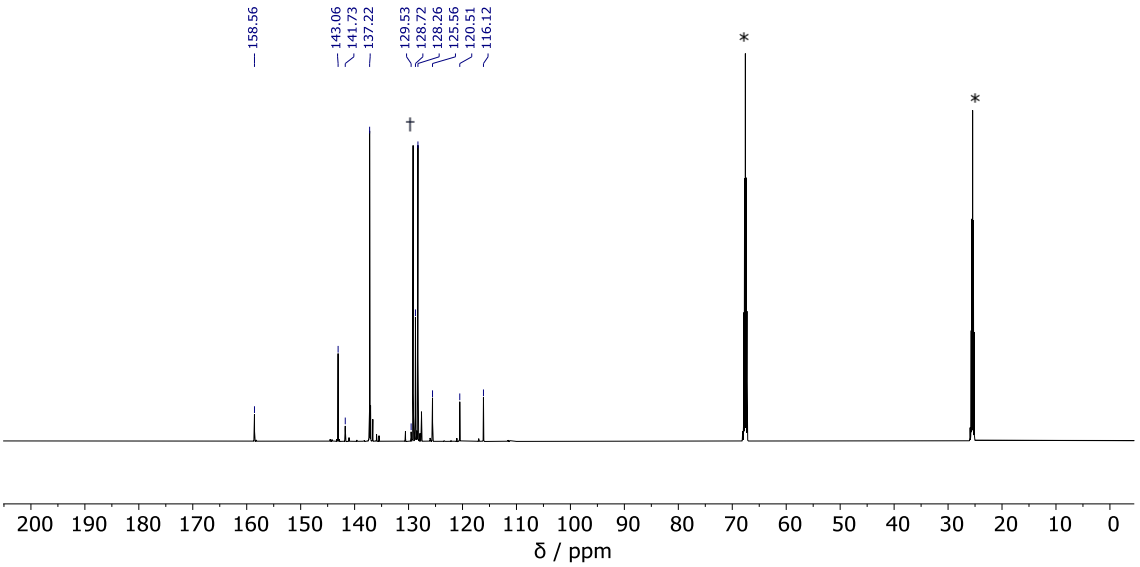


Figure A.35 ^{13}C{^{1}H} NMR spectrum (C_4D_8O, 298 K, 151.0 MHz) of [(^{Ph3}L)Ca(THF)$_n$], formed when [(^{Ph3}L)Ca]$_2$ (**9**) is dissolved in THF. † denotes co-crystallised benzene, * denotes C_4D_8O.

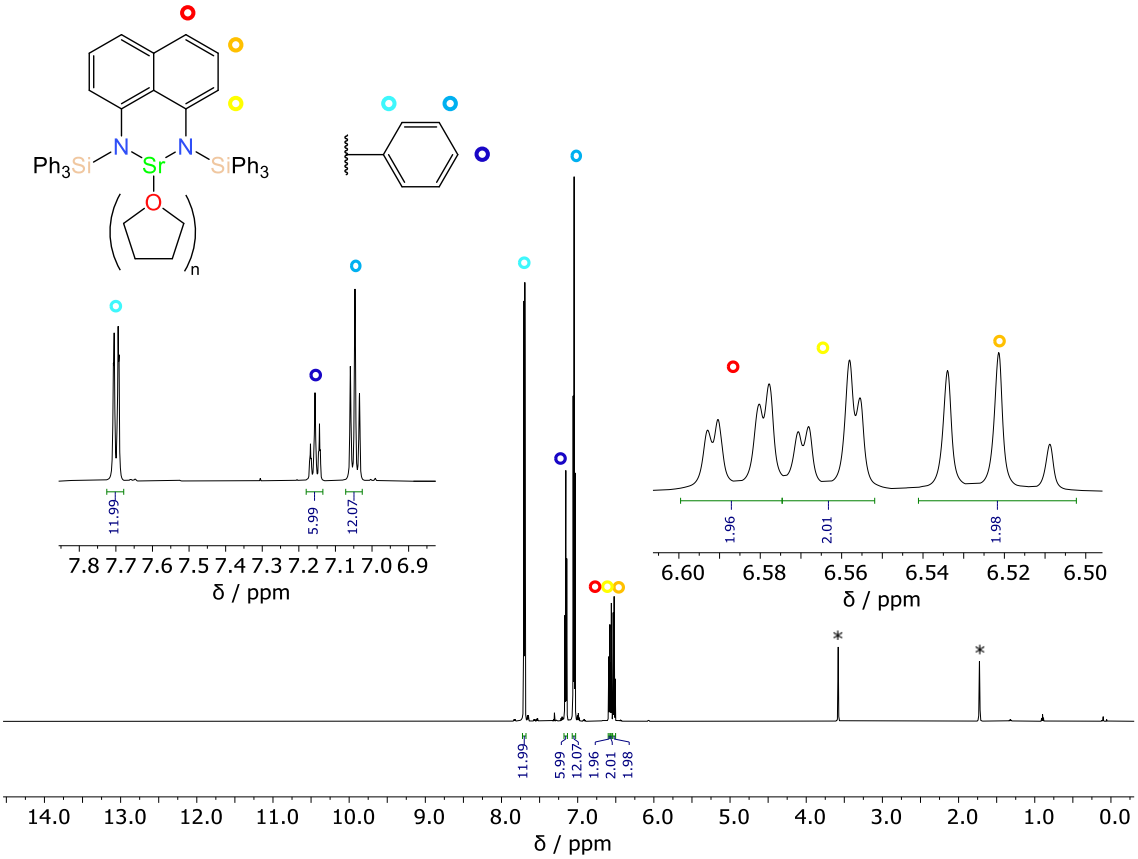


Figure A.36 ^{1}H NMR spectrum (C_4D_8O, 298 K, 600.4 MHz) of [(^{Ph3}L)Sr(THF)$_3$] (**12**), formed when [(^{Ph3}L)Sr]$_2$ (**10**) is dissolved in THF. * denotes residual protio fraction of C_4D_8O. Expansions show phenyl and naphthyl regions.

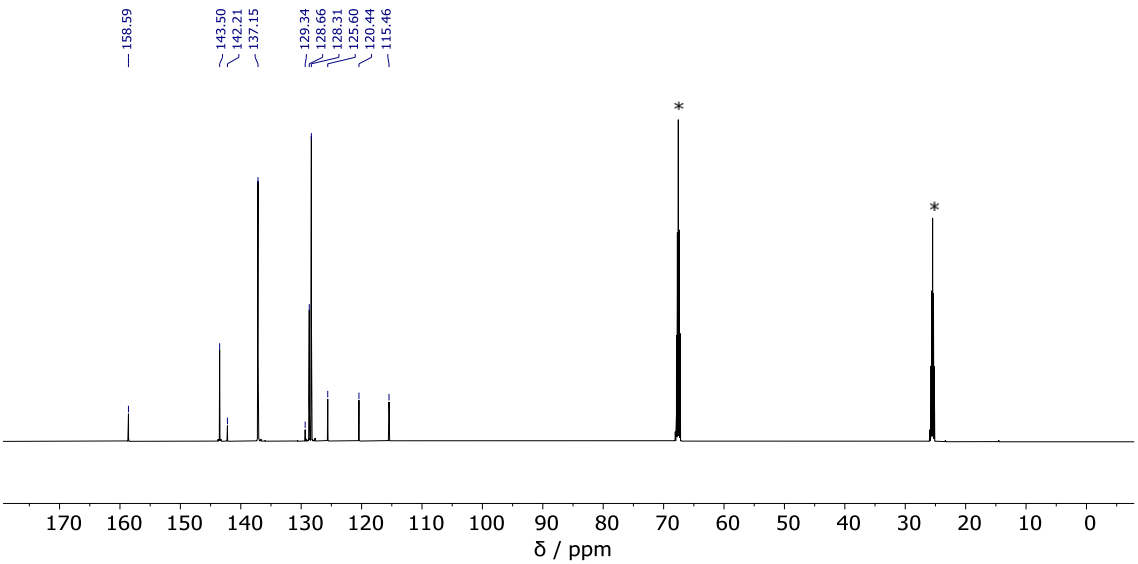


Figure A.37 ^{13}C{^{1}H} NMR spectrum (C_4D_8O, 298 K, 151.0 MHz) of [(^{Ph3}L)Sr(THF)$_3$] (**12**), formed when [(^{Ph3}L)Sr]$_2$ (**10**) is dissolved in THF. * denotes C_4D_8O.

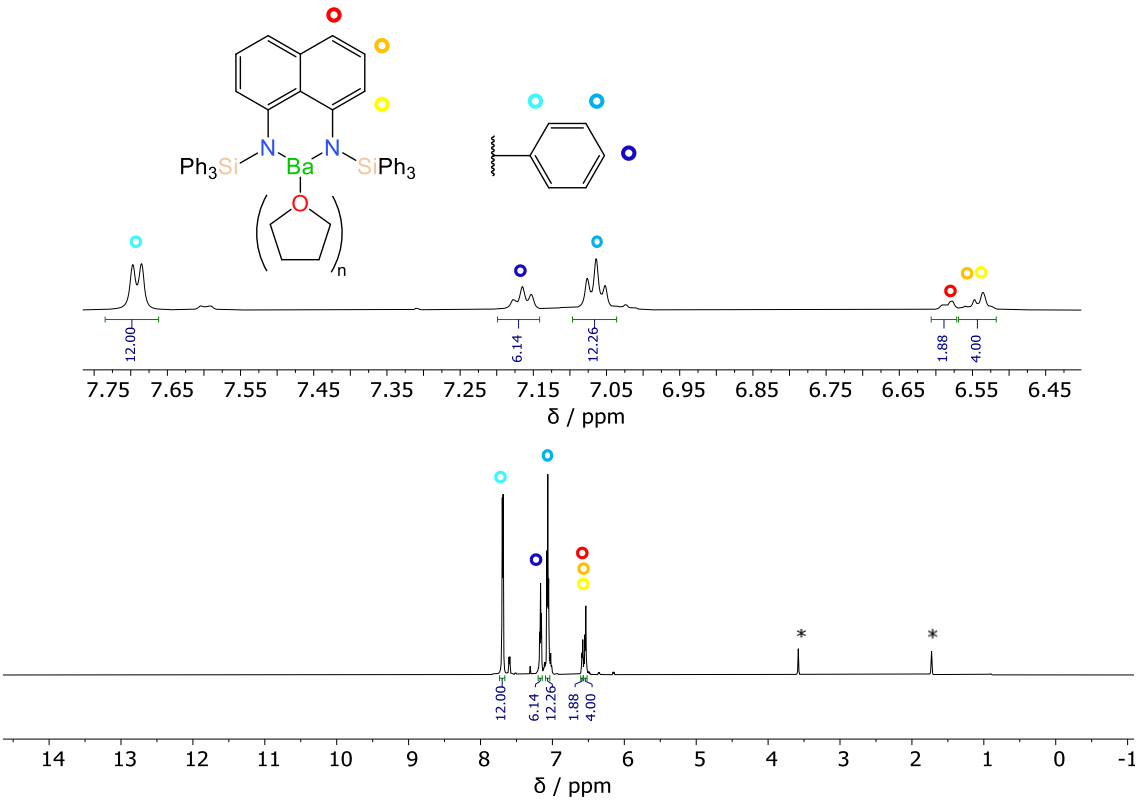


Figure A.38 ^{1}H NMR spectrum (C_4D_8O, 298 K, 600.4 MHz) of [(^{Ph3}L)Ba(THF)$_n$], formed when [(^{Ph3}L)Ba]$_2$ (**11**) is dissolved in THF. * denotes residual protio fraction of C_4D_8O. Expansion shows aromatic region.

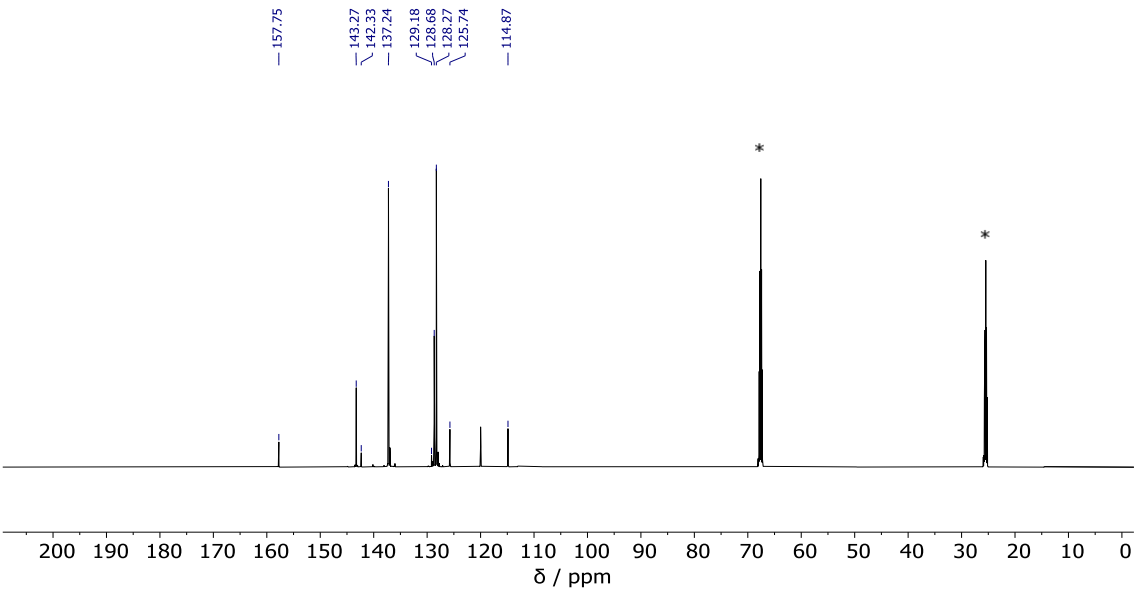


Figure A.39 ^{13}C{^{1}H} NMR spectrum (C_4D_8O, 298 K, 151.0 MHz) of [(^{Ph3}L)Ba(THF)$_n$], formed when [(^{Ph3}L)Ba]$_2$ (**11**) is dissolved in THF. * denotes C_4D_8O.

A.2.2 X-ray crystallographic data

Table A.5 Experimental crystallographic data for [(^{Ph_2Me}L)Ca]$_2$ (**6**), [(^{Ph_2Me}L)Sr]$_2$ (**7**) and [(^{Ph_2Me}L)Ba]$_2$ (**8**).

Complex	**6**	**7**	**8**
		Crystal data	
File name	028ljm23	015ccr23	023ljm23
Chemical formula	$C_{36}H_{32}CaN_2Si_2 \cdot 1(C_6H_6)$	$C_{72}H_{64}N_4Si_4Sr_2 \cdot 2(C_6H_6)$	$C_{36}H_{32}BaN_2Si_2 \cdot 2.5(C_6H_6)$
M_r	667.00	1429.09	881.45
Crystal system, space group	Monoclinic, $P2_1/c$	Monoclinic, $P2_1/c$	Monoclinic, $P2_1/c$
Temperature (K)	100	100	150
a, b, c (Å)	10.6141 (4), 30.2492 (9), 11.3302 (3)	10.7971 (4), 30.4296 (9), 11.2367 (3)	17.48618 (16), 14.15228 (13), 17.31503 (17)
α, β, γ (°)	90, 109.192 (4), 90	90, 110.094 (3), 90	90, 98.5389 (9), 90
V (Å^3)	3435.6 (2)	3467.10 (19)	4237.44 (7)
Z	4	2	4
Radiation type	Mo Ka	Mo Ka	Cu Ka
μ (mm^{-1})	0.29	1.66	8.11
Crystal size (mm)	0.09 × 0.08 × 0.05	0.15 × 0.10 × 0.01	0.17 × 0.11 × 0.03
		Data Collection	
Diffractometer	XtaLAB Synergy R, DW system, HyPix-Arc 150	XtaLAB Synergy DW	SuperNova, Dual, Cu at home/near, Atlas
Absorption correction	Multi-scan *CrysAlis PRO* 1.171.42.83a (Rigaku Oxford Diffraction, 2023) Empirical absorption correction using spherical harmonics, implemented in SCALE3 ABSPACK scaling algorithm.	Multi-scan *CrysAlis PRO* (Rigaku Oxford Diffraction, 2017)	Gaussian *CrysAlis PRO* 1.171.42.72a (Rigaku Oxford Diffraction, 2022) Numerical absorption correction based on gaussian integration over a multifaceted crystal model Empirical absorption correction using spherical harmonics, implemented in SCALE3 ABSPACK scaling algorithm.

T_{min}, T_{max}	0.970, 1.000	0.78, 0.98	0.425, 0.893
No. of measured, independent and observed [$I > 2\sigma(I)$] reflections	41333, 7876, 6624	34630, 7936, 6051	29177, 8741, 7564
R_{int}	0.041	0.073	0.046
Refinement			
$R[F^2 > 2\sigma(F^2)]$, $wR(F^2)$, S	0.058, 0.139, 1.16	0.049, 0.143, 1.01	0.033, 0.090, 1.05
No. of reflections	7876	7936	8741
No. of parameters	481	461	507
No. of restraints	264	662	-
$(\Delta/\sigma)_{max}$	-	-	-
$\Delta\rho_{max}$, $\Delta\rho_{min}$ (e Å^{-3})	0.52, −0.29	0.86, −0.72	1.27, −0.96
Absolute structure	-	-	-
Absolute structure parameter	-	-	-

Table A.6 Experimental crystallographic data for [(^{Ph3}L)Ca]$_2$ (**9**), [(^{Ph3}L)Sr]$_2$ (**10**) and [(^{Ph3}L)Ba]$_2$ (**11**).

Complex	**9**	**10**	**11**
		Crystal data	
File name	010ccr23	014ljm23	011ccr23
Chemical formula	$2(C_{92}H_{72}Ca_2N_4Si_4)\cdot 7(C_6H_6)$	$C_{46}H_{36}N_2Si_2Sr\cdot 3(C_6H_6)$	$C_{92}H_{72}Ba_2N_4Si_4\cdot 6(C_6H_6)$
M_r	3399.04	994.89	2089.20
Crystal system, space group	Triclinic, $P\bar{1}$	Monoclinic, $P2_1/c$	Monoclinic, $P2_1/c$
Temperature (K)	100	150	100
a, b, c (Å)	13.2212 (1), 26.0129 (2), 27.9342 (3)	16.9507 (2), 17.3350 (2), 17.6684 (2)	16.8045 (2), 17.5673 (2), 17.4740 (2)
α, β, γ (°)	72.1918 (8), 86.2964 (8), 76.4975 (8)	90, 99.032 (1), 90	90, 97.8264 (12), 90
V (Å^3)	8893.79 (14)	5127.32 (10)	5110.44 (10)
Z	2	4	2
Radiation type	Mo $K\alpha$	Cu $K\alpha$	Mo $K\alpha$
μ (mm^{-1})	0.24	2.23	0.87
Crystal size (mm)	0.22 × 0.13 × 0.11	0.15 × 0.09 × 0.03	0.13 × 0.11 × 0.05
		Data Collection	
Diffractometer	XtaLAB Synergy R, DW system, HyPix-Arc 150	SuperNova, Dual, Cu at home/near, Atlas	XtaLAB Synergy R, DW system, HyPix-Arc 150
Absorption correction	Multi-scan *CrysAlis PRO* (Rigaku Oxford Diffraction, 2017)	Multi-scan *CrysAlis PRO* 1.171.42.72a (Rigaku Oxford Diffraction, 2022) Empirical absorption correction using spherical harmonics, implemented in SCALE3 ABSPACK scaling algorithm.	Multi-scan *CrysAlis PRO* (Rigaku Oxford Diffraction, 2017)
T_{min}, T_{max}	0.86, 0.97	0.815, 1.000	0.83, 0.96
No. of measured, independent and observed [$I > 2\sigma(I)$] reflections	186203, 44053, 34917	65375, 10679, 8452	98019, 12671, 10702

R_{int}	0.036	0.073	0.043
Refinement			
$R[F^2 > 2\sigma(F^2)]$, $wR(F^2)$, S	0.045, 0.131, 1.00	0.036, 0.087, 1.02	0.043, 0.127, 1.04
No. of reflections	44053	10679	12669
No. of parameters	2215	622	622
No. of restraints	-	-	-
$(\Delta/\sigma)_{max}$	-	-	-
$\Delta\rho_{max}$, $\Delta\rho_{min}$ (e Å^{-3})	0.71, −0.43	0.52, −0.34	3.36, −0.93
Absolute structure	-	-	-
Absolute structure parameter	-	-	-

A.3 Appendix for Chapter 4

A.3.1 NMR spectra of isolated compounds

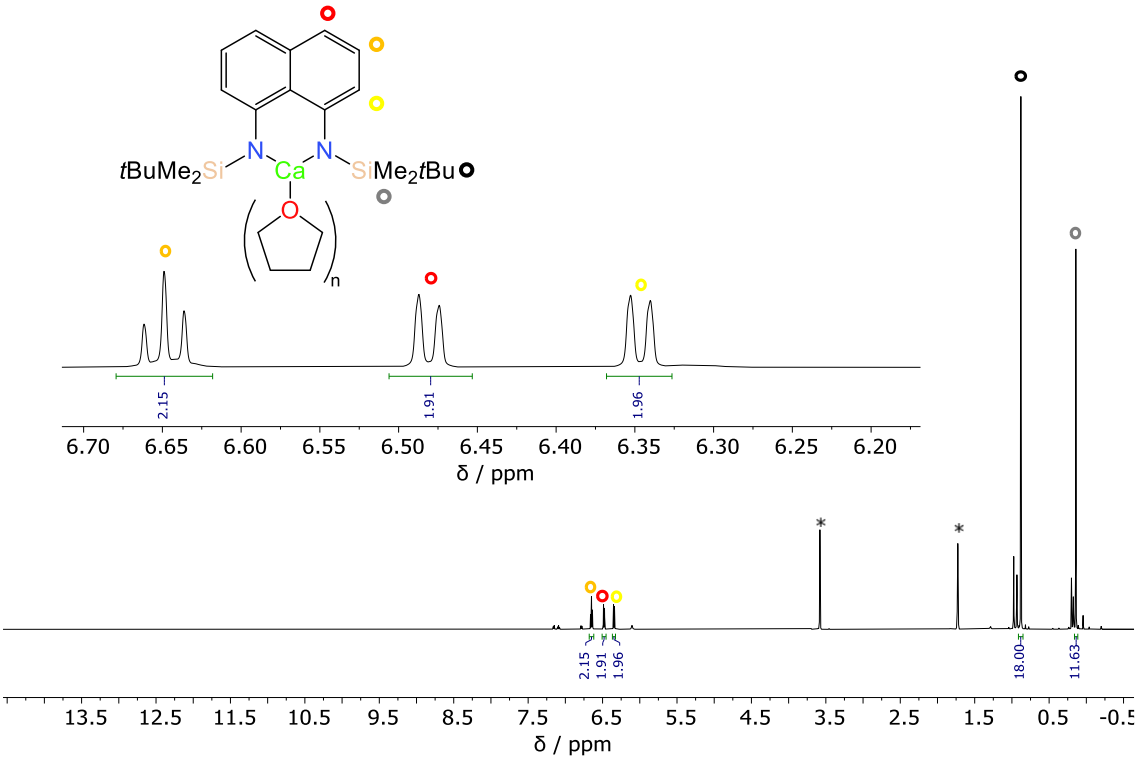


Figure A.40 ^{1}H NMR spectrum (C_4D_8O, 298 K, 600.4 MHz) of [(^{Me_2tBu}L)Ca(THF)$_n$], formed when [{(^{Me_2tBu}L)Ca}$_2$ (**13**) is dissolved in THF. * denotes residual protio fraction of C_4D_8O. Expansion shows naphthyl regions.

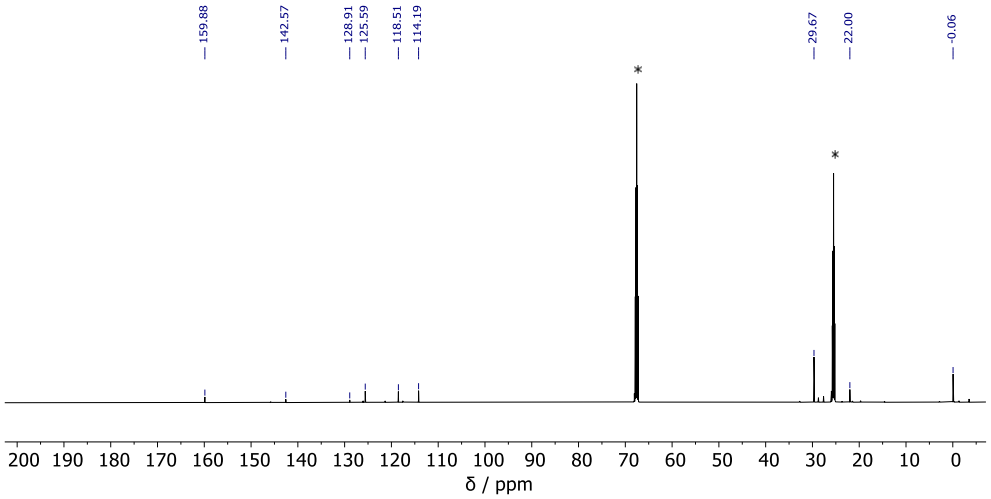


Figure A.41 ^{13}C{^{1}H} NMR spectrum (C_4D_8O, 298 K, 151.0 MHz) [(^{Me_2tBu}L)Ca(THF)$_n$], formed when [{(^{Me_2tBu}L)Ca}$_2$ (**13**) is dissolved in THF. * denotes C_4D_8O.

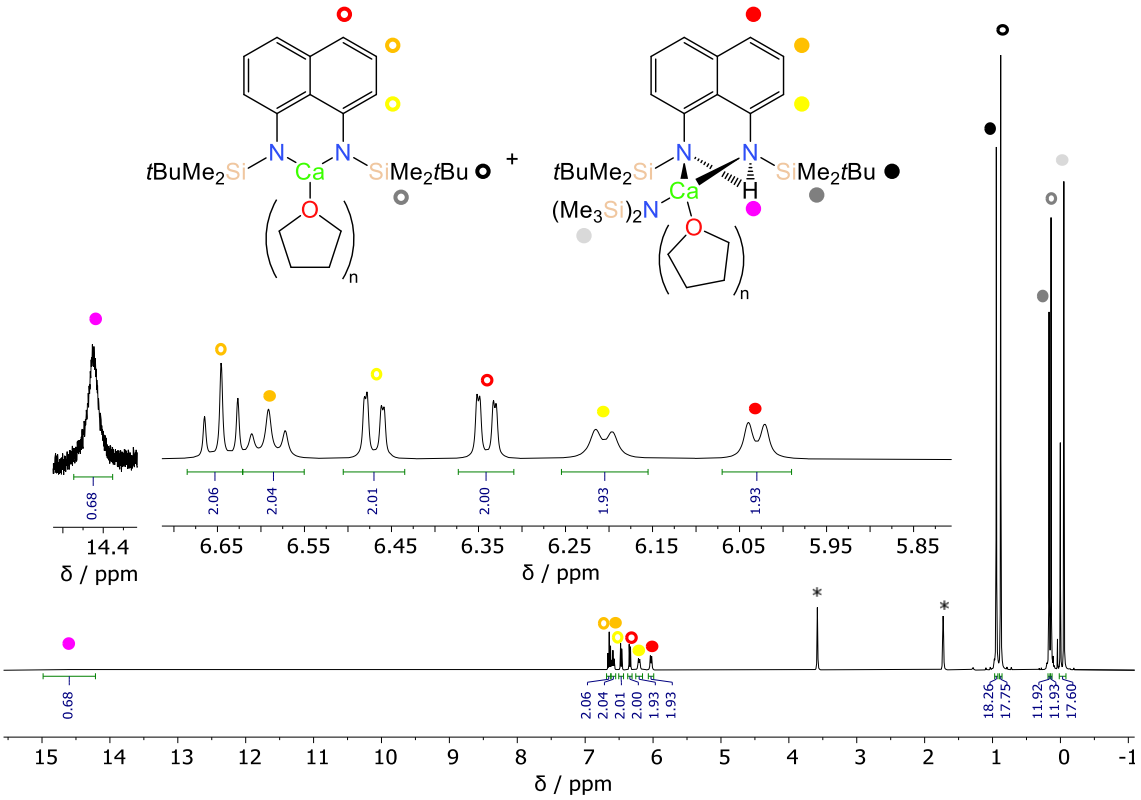


Figure A.42 ^{1}H NMR spectrum (C_4D_8O, 298 K, 400 MHz) of [($^{Me_2{}^tBu}$L)Ca(THF)$_n$] and [($^{Me_2{}^tBu}$LH)$_2$Ca(N(SiMe$_3$)$_2$)(THF)$_n$], formed in a 1:1 ratio when [($^{Me_2{}^tBu}$LH)Ca(μ-$^{Me_2{}^tBu}$L)Ca(N(SiMe$_3$)$_2$)] (**14**) is dissolved in THF. * denotes residual protio fraction of C_4D_8O. Expansions show (N,N)μ$_2$-H and naphthyl regions.

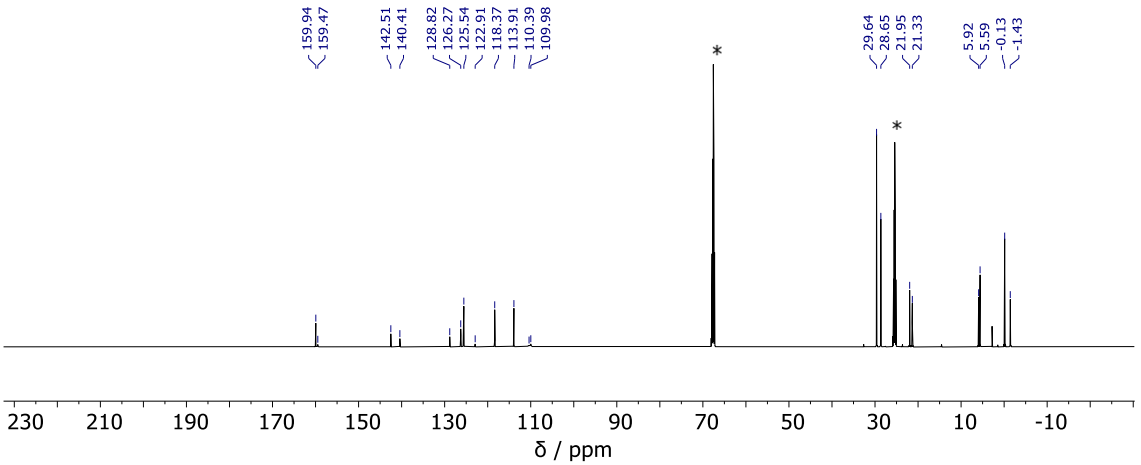


Figure A.43 ^{13}C{^{1}H} NMR spectrum (C_4D_8O, 298 K, 151.0 MHz) of [($^{Me_2{}^tBu}$L)Ca(THF)$_n$] and [($^{Me_2{}^tBu}$LH)$_2$Ca{N(SiMe$_3$)$_2$}(THF)$_n$], formed in a 1:1 ratio when [($^{Me_2{}^tBu}$LH)Ca(μ-$^{Me_2{}^tBu}$L)Ca{N(SiMe$_3$)$_2$}] (**14**) is dissolved in THF. * denotes C_4D_8O.

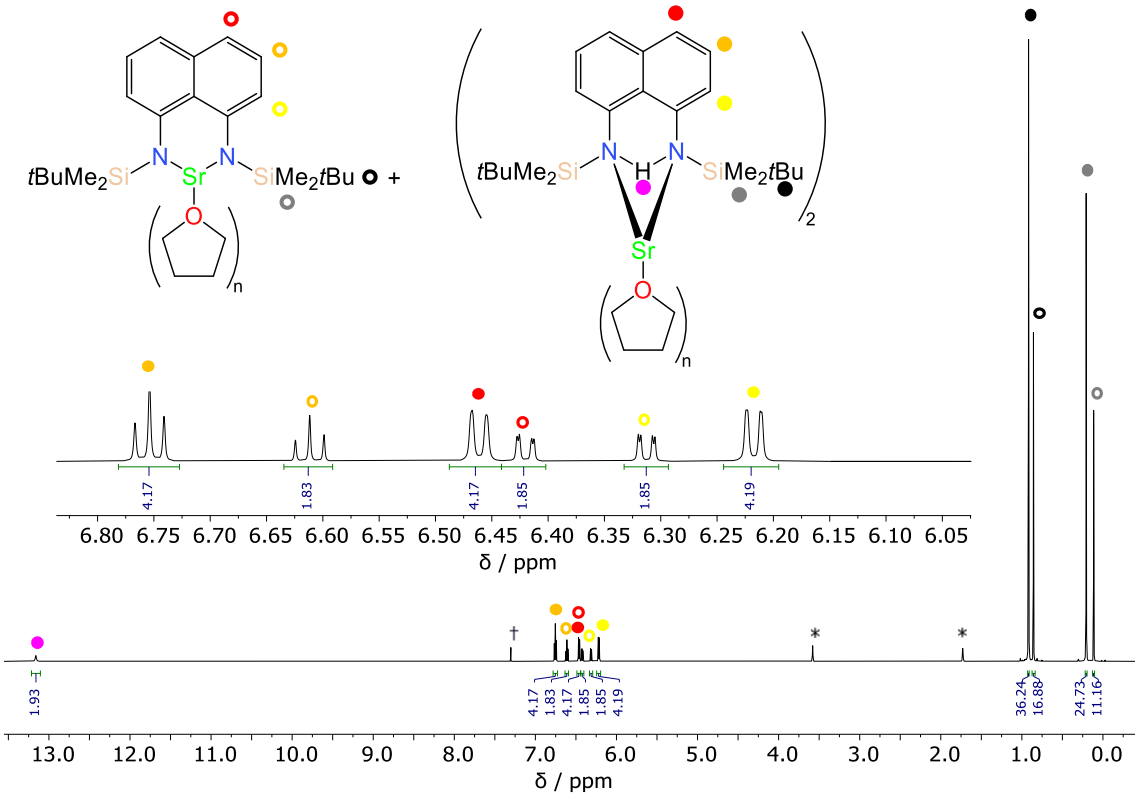


Figure A.44 ^{1}H NMR spectrum (C_4D_8O, 298 K, 600.4 MHz) of [(^{Me_2tBu}L)Sr(THF)$_n$] and [(^{Me_2tBu}LH)$_2$Sr(THF)$_n$], formed in a 1:1 ratio when [{(^{Me_2tBu}LH)Sr}$_2$(μ-^{Me_2tBu}L)] (**16**) is dissolved in THF. † denotes co-crystallised benzene, * denotes residual protio fraction of C_4D_8O. Expansion shows naphthyl regions.

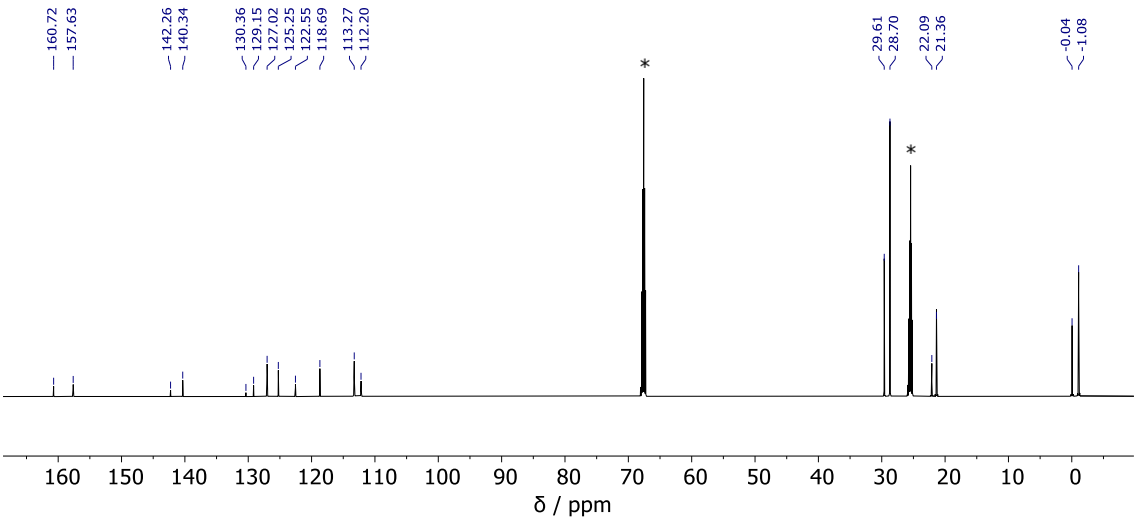


Figure A.45 ^{13}C{^{1}H} NMR spectrum (C_4D_8O, 298 K, 151.0 MHz) [(^{Me_2tBu}L)Sr(THF)$_n$] and [(^{Me_2tBu}LH)$_2$Sr(THF)$_n$], formed in a 1:1 ratio when [{(^{Me_2tBu}LH)Sr}$_2$(^{Me_2tBu}L)] (**16**) is dissolved in THF. * denotes C_4D_8O.

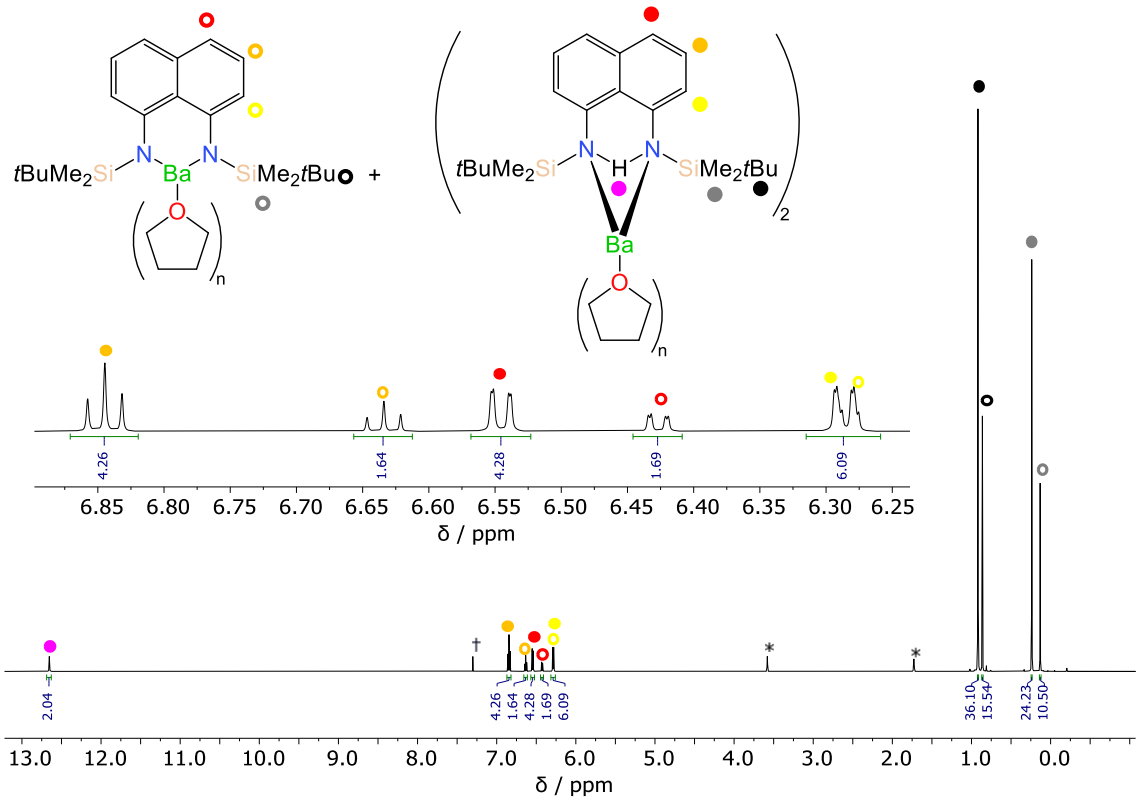


Figure A.46 ^{1}H NMR spectrum (C_4D_8O, 298 K, 600.4 MHz) of [(^{Me_2tBu}L)Ba(THF)$_n$] and [(^{Me_2tBu}LH)$_2$Ba(THF)$_n$], formed in a 1:1 ratio when [{(^{Me_2tBu}LH)Ba}$_2$(^{Me_2tBu}L)] (**17**) is dissolved in THF. † denotes co-crystallised benzene, * denotes residual protio fraction of C_4D_8O. Expansion shows naphthyl region.

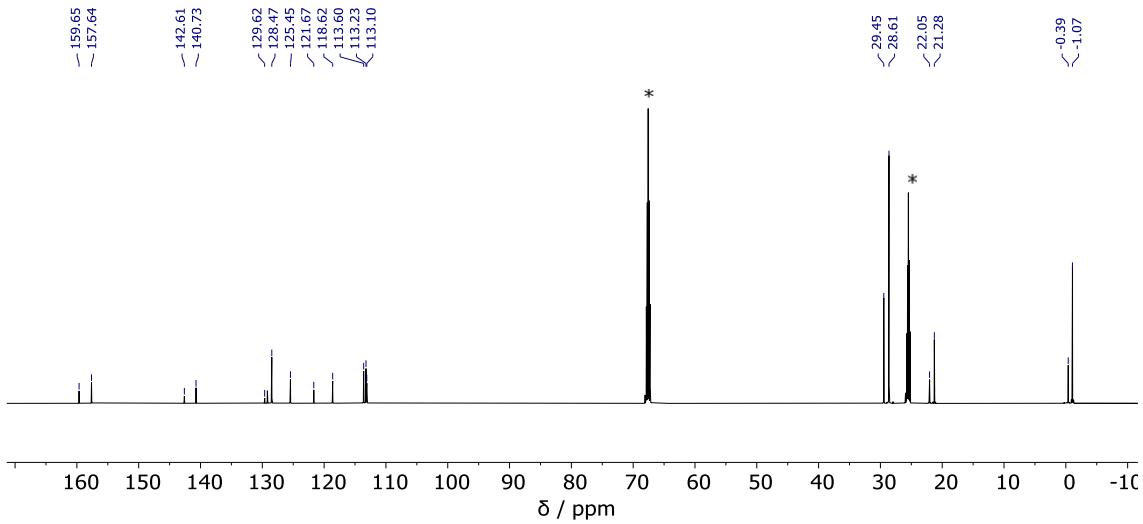


Figure A.47 ^{13}C{^{1}H} NMR spectrum (C_4D_8O, 298 K, 151.0 MHz) [(^{Me_2tBu}L)Ba(THF)$_n$] and [(^{Me_2tBu}LH)$_2$Ba(THF)$_n$], formed in a 1:1 ratio when [{(^{Me_2tBu}LH)Ba}$_2$(^{Me_2tBu}L)] is dissolved in THF. * denotes C_4D_8O.

A.3.2 X-ray crystallographic data

Table A.7 Experimental crystallographic data for [{($^{Me_2{}^tBu}$L)Ca]$_2$ (**13**), [($^{Me_2{}^tBu}$LH)Ca(μ-$^{Me_2{}^tBu}$L)Ca{N(SiMe$_3$)$_2$}]$_2$ (**14**) and [$^{Me_2{}^tBu}$LH]$_2$[Ca(THF)$_6$] (**15**).

Complex	**13**	**14**	**15**
		Crystal data	
File name	012ccr23	017mdh24	018mdh24
Chemical formula	$C_{28}H_{42}CaN_2Si_2$	$C_{50}H_{91}Ca_2N_5Si_6$	$C_{76}H_{138}CaN_4O_8Si_4$
M_r	502.91	1010.97	1388.34
Crystal system, space group	Monoclinic, $P2_1$	Triclinic, $P1$	Monoclinic, $P2_1/n$
Temperature (K)	100	150	150
a, b, c (Å)	10.7547 (2), 26.1127 (3), 11.3128 (2)	11.1116 (2), 12.2743 (2), 24.2443 (4)	13.4860 (1), 16.6595 (1), 18.9695 (1)
α, β, γ (°)	90, 117.692 (3), 90	81.992 (1), 77.513 (1), 69.022 (1)	102.543 (1)
V (Å^3)	2813.12 (11)	3007.45 (9)	4160.16 (5)
Z	4	2	2
Radiation type	Mo Ka	Cu Kα	Cu Kα
μ (mm^{-1})	0.33	3.05	1.60
Crystal size (mm)	0.13 × 0.08 × 0.04	0.17 × 0.06 × 0.04	0.14 × 0.10 × 0.04
		Data Collection	
Diffractometer	Oxford Diffraction SuperNova	SuperNova, Dual, Cu at home/near, Atlas	SuperNova, Dual, Cu at home/near, Atlas
Absorption correction	Multi-scan *CrysAlis PRO* (Rigaku Oxford Diffraction, 2017)	Multi-scan *CrysAlis PRO* 1.171.43.95a (Rigaku Oxford Diffraction, 2023) Empirical absorption correction using spherical harmonics, implemented in SCALE3 ABSPACK scaling algorithm.	Multi-scan *CrysAlis PRO* 1.171.43.95a (Rigaku Oxford Diffraction, 2023) Empirical absorption correction using spherical harmonics, implemented in SCALE3 ABSPACK scaling algorithm.
T_{min}, T_{max}	0.93, 0.99	0.794, 1.000	0.622, 1.000
No. of measured, independent and observed [$I > 2\sigma(I)$]	52783, 25034, 20240	66502, 12449, 11119	97324, 8670, 8014

reflections			
R_{int}	0.030	0.030	0.042
Refinement			
$R[F^2 > 2\sigma(F^2)]$, $wR(F^2)$, S	0.044, 0.112, 0.95	0.029, 0.083, 1.04	0.055, 0.162, 1.06
No. of reflections	25034	12449	8670
No. of parameters	595	598	462
No. of restraints	1	-	7
$(\Delta/\sigma)_{max}$	-	-	-
$\Delta\rho_{max}$, $\Delta\rho_{min}$ (e Å^{-3})	1.62, −0.63	0.54, −0.32	1.69, −0.58
Absolute structure	-	-	-
Absolute structure parameter	-	-	-

Table A.8 Experimental crystallographic data for

[{($^{Me_2{}^tBu}$LH)Ae}$_2$(μ-$^{Me_2{}^tBu}$L)] (Ae = Sr (**16**) and Ba (**17**)).

Complex	**16**	**17**
	Crystal data	
File name	015ljm23	016ccr23
Chemical formula	$C_{33}H_{55}N_3Si_3Sr \cdot C_3H_3$	$C_{66}H_{110}Ba_2N_6Si_6$
M_r	704.74	1430.83
Crystal system, space group	Monoclinic, *C*2/*c*	Triclinic, $P\bar{1}$
Temperature (K)	150	100
a, *b*, *c* (Å)	25.8829 (5), 11.4649 (2), 26.4924 (5)	11.66777 (9), 16.96452 (13), 19.78397 (11)
α, *β*, *γ* (°)	90, 106.609 (2), 90	101.9301 (6), 94.3177 (5), 108.9949 (7)
V (Å^3)	7533.5 (3)	3579.51 (5)
Z	8	2
Radiation type	Cu *K*α	Mo *K*α
μ (mm^{-1})	3.10	1.24
Crystal size (mm)	0.16 × 0.14 × 0.1	0.16 × 0.12 × 0.08
	Data Collection	
Diffractometer	SuperNova, Dual, Cu at home/near, Atlas	Rigau XtaLAB Synergy DW
Absorption correction	Gaussian *CrysAlis PRO* 1.171.42.72a (Rigaku Oxford Diffraction, 2022) Numerical absorption correction based on gaussian integration over a multifaceted crystal model Empirical absorption correction using spherical harmonics, implemented in SCALE3 ABSPACK scaling algorithm.	Multi-scan *CrysAlis PRO* (Rigaku Oxford Diffraction, 2017)
T_{min}, T_{max}	0.945, 1.000	0.86, 0.91
No. of measured, independent and observed [$I > 2\sigma(I)$]	38807, 7841, 6606	130442, 21766, 19551

reflections		
R_{int}	0.030	0.030
Refinement		
$R[F^2 > 2\sigma(F^2)]$, $wR(F^2)$, S	0.028, 0.069, 1.05	0.024, 0.066, 0.96
No. of reflections	7841	21766
No. of parameters	408	721
No. of restraints	-	-
$(\Delta/\sigma)_{max}$	-	-
$\Delta\rho_{max}$, $\Delta\rho_{min}$ (e Å^{-3})	0.44, −0.31	2.61, −0.59
Absolute structure	-	-
Absolute structure parameter	-	-

A.4 Appendix for Chapter 5

A.4.1 NMR spectra of isolated compounds

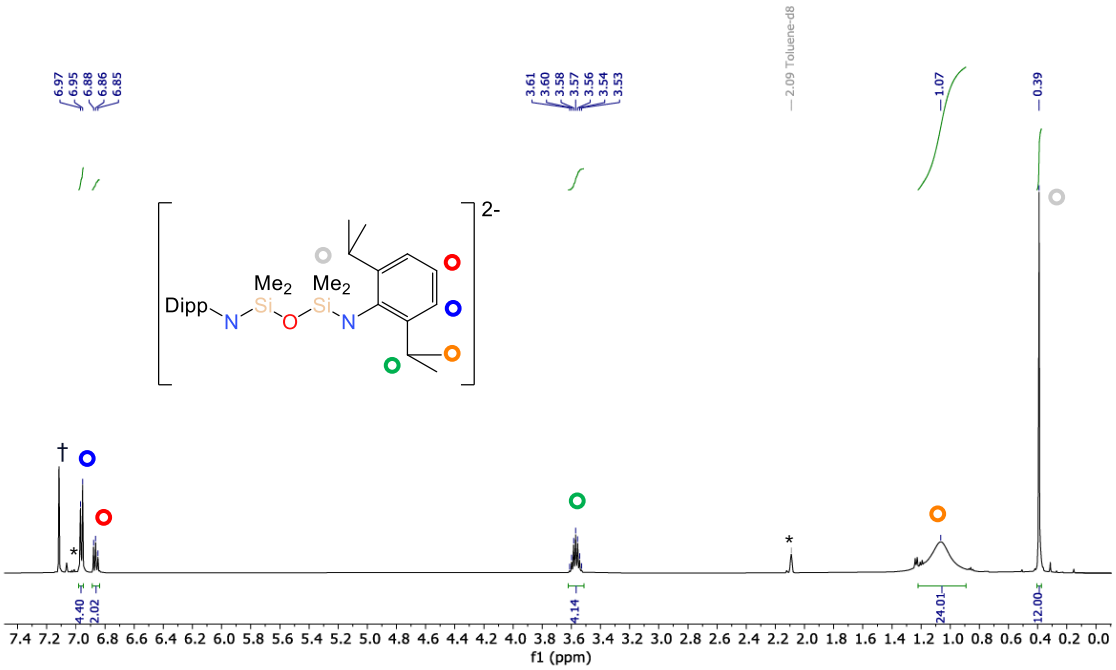


Figure A.48 ^{1}H NMR spectrum (C_7D_8, 373 K, 500 MHz) of [($^{NON\text{-}Dipp}$L)Mg]$_2$ (**18**). † denotes co-crystallised benzene, * denotes residual protio fraction of C_7D_8. Reproduced with permission from Prof. Martyn Coles and Ms. Andrea O'Reilly.

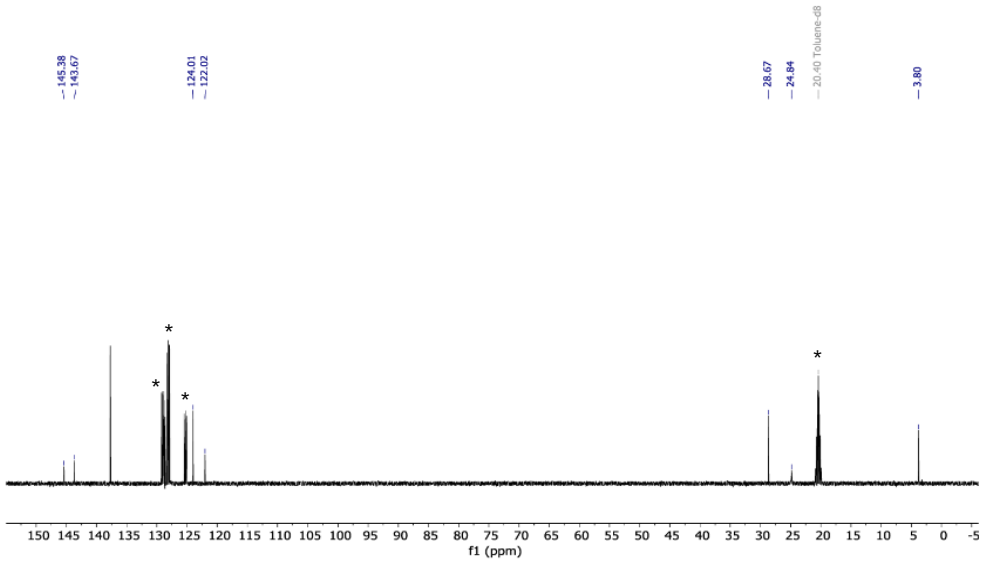


Figure A.49 ^{13}C{^{1}H} NMR spectrum (C_7D_8, 373 K, 126 MHz) of [($^{NON\text{-}Dipp}$L)Mg]$_2$ (**18**). * denotes residual protio fraction of C_7D_8. Reproduced with permission from Prof. Martyn Coles and Ms. Andrea O'Reilly.

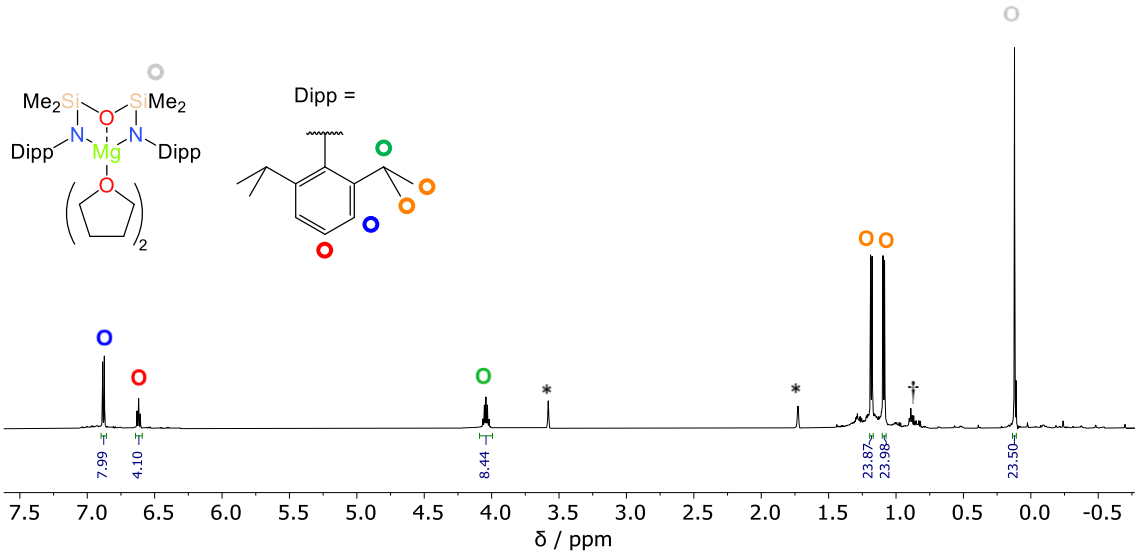


Figure A.50 ^{1}H NMR spectrum (C_4D_8O, 298 K, 600 MHz) of [($^{NON\text{-}Dipp}$L)Mg(THF)$_2$], formed when a THF solution of [($^{NON\text{-}Dipp}$L)Mg]$_2$ (**18**) is heated at 80 °C for 16 h. †, denotes *n*-hexane, * denotes residual protio fraction of C_4D_8O.

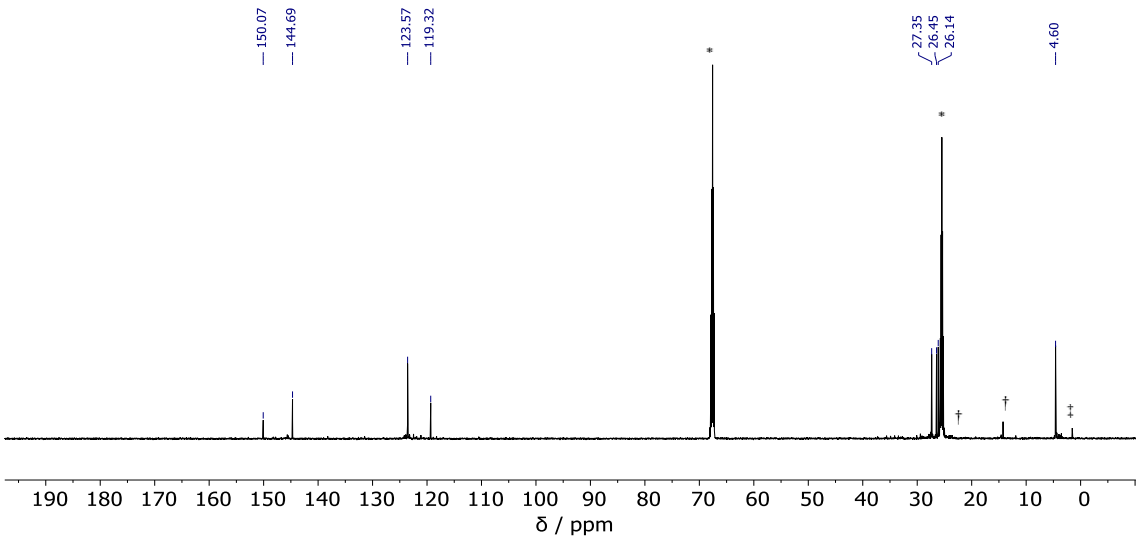


Figure A.51 ^{13}C{^{1}H} NMR (C_4D_8O, 298 K, 151 MHz) of [($^{NON\text{-}Dipp}$L)Mg(THF)$_2$], formed when a THF solution of [($^{NON\text{-}Dipp}$L)Mg]$_2$ (**18**) is heated at 80 °C for 16 h. †, denotes *n*-hexane, * denotes C_4D_8O.

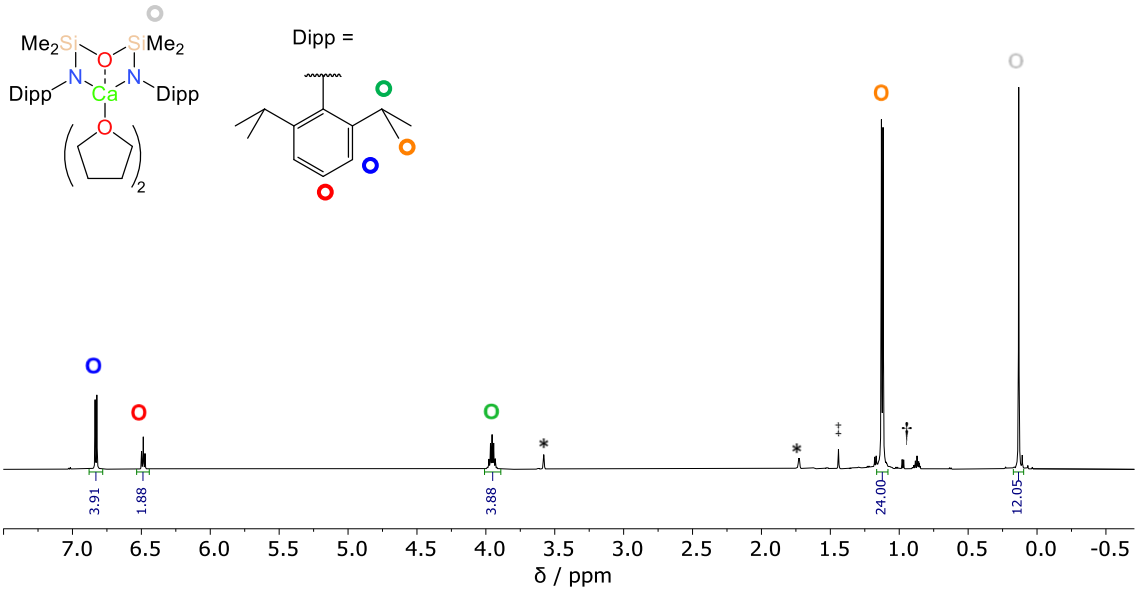


Figure A.52 ^{1}H NMR spectrum (C_4D_8O, 298 K, 600 MHz) of [($^{NON\text{-}Dipp}$L)Ca(THF)$_2$] (**19·THF$_2$**), formed when [($^{NON\text{-}Dipp}$L)Ca]$_2$ (**19**) is dissolved in THF. ‡ denotes cyclohexane, † denotes *n*-hexane, * denotes residual protio fraction of C_4D_8O.

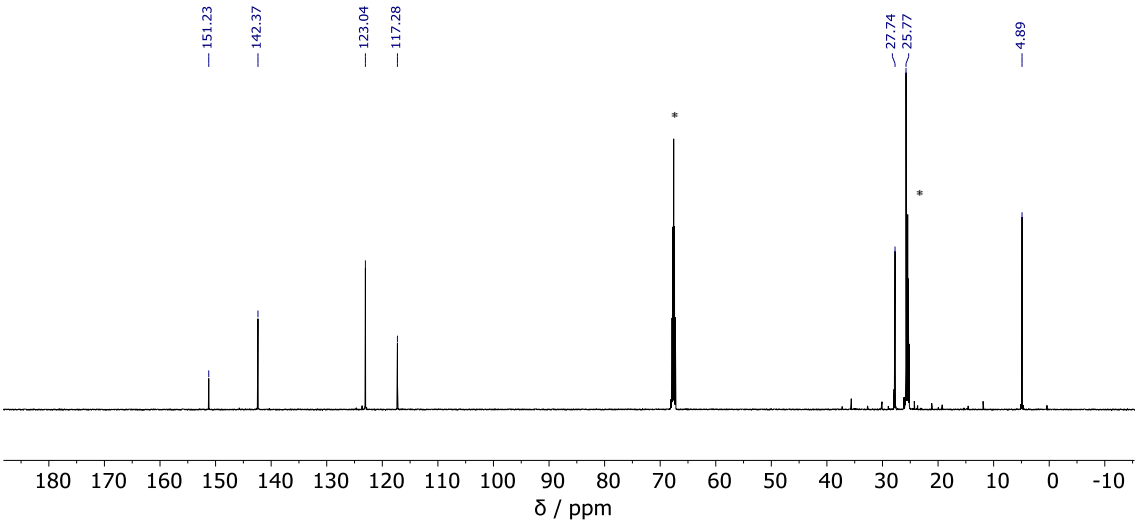


Figure A.53 ^{13}C{^{1}H} NMR spectrum (C_4D_8O, 298 K, 151 MHz) of [($^{NON\text{-}Dipp}$L)Ca(THF)$_2$] (**19·THF$_2$**), formed when [($^{NON\text{-}Dipp}$L)Ca]$_2$ (**19**) is dissolved in THF. * denotes residual protio fraction of C_4D_8O.

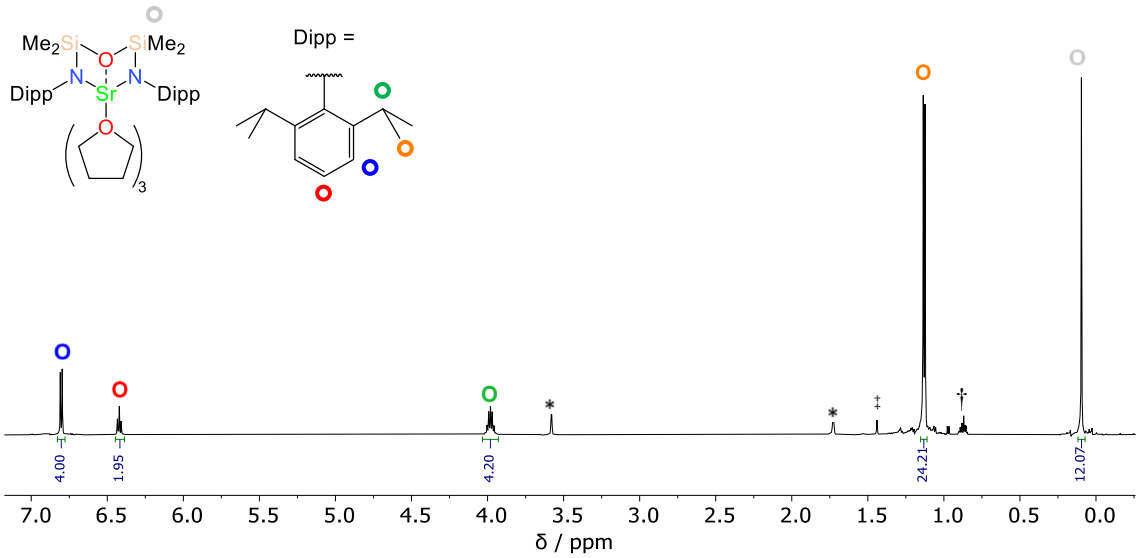


Figure A.54 ^{1}H NMR spectrum (C_4D_8O, 298 K, 600 MHz) of [($^{NON\text{-}Dipp}$L)Sr(THF)$_3$] (**20·THF$_3$**), formed when [($^{NON\text{-}Dipp}$L)Sr]$_2$ (**20**) is dissolved in THF. ‡ denotes cyclohexane, † denotes *n*-hexane, * denotes residual protio fraction of C_4D_8O.

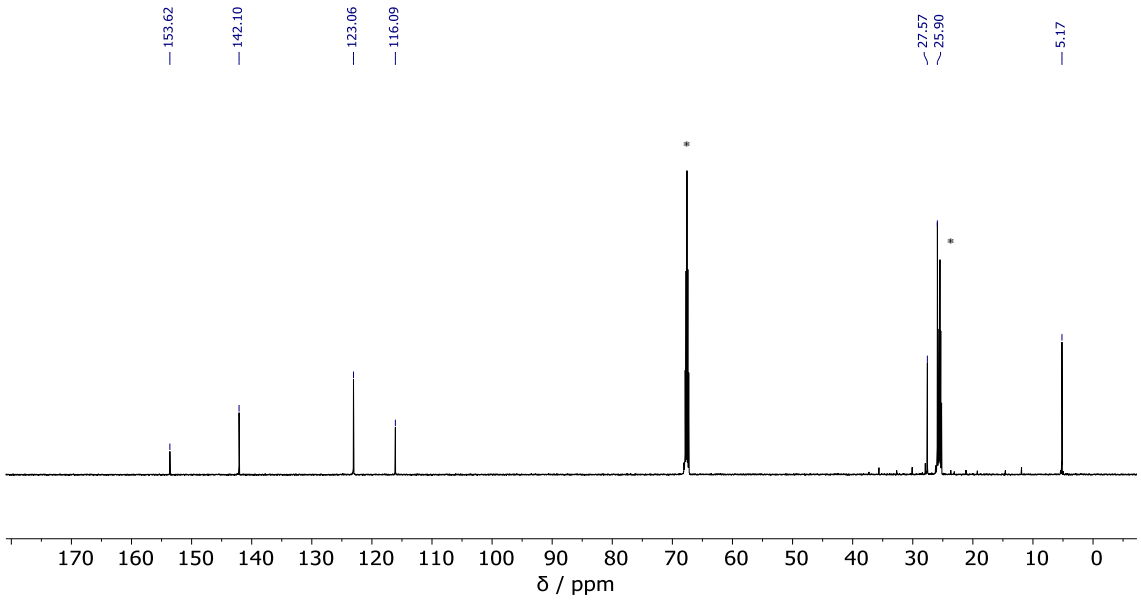


Figure A.55 ^{13}C{^{1}H} NMR spectrum (C_4D_8O, 298 K, 151 MHz) of [($^{NON\text{-}Dipp}$L)Sr(THF)$_3$] (**20·THF$_3$**), formed when [($^{NON\text{-}Dipp}$L)Sr]$_2$ (**20**) is dissolved in THF. * denotes residual protio fraction of C_4D_8O.

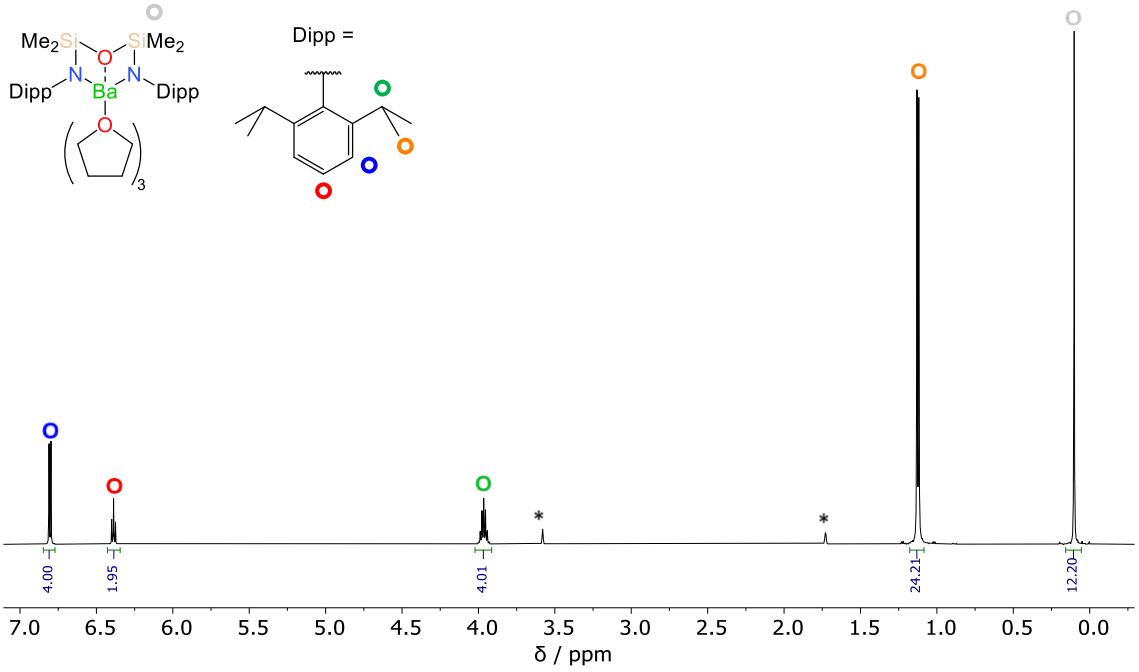


Figure A.56 ^{1}H NMR spectrum (C_4D_8O, 298 K, 600 MHz) of [($^{NON\text{-}Dipp}$L)Ba(THF)$_3$] (**21·THF$_3$**), formed when [($^{NON\text{-}Dipp}$L)Ba]$_2$ (**21**) is dissolved in THF. * denotes residual protio fraction of C_4D_8O.

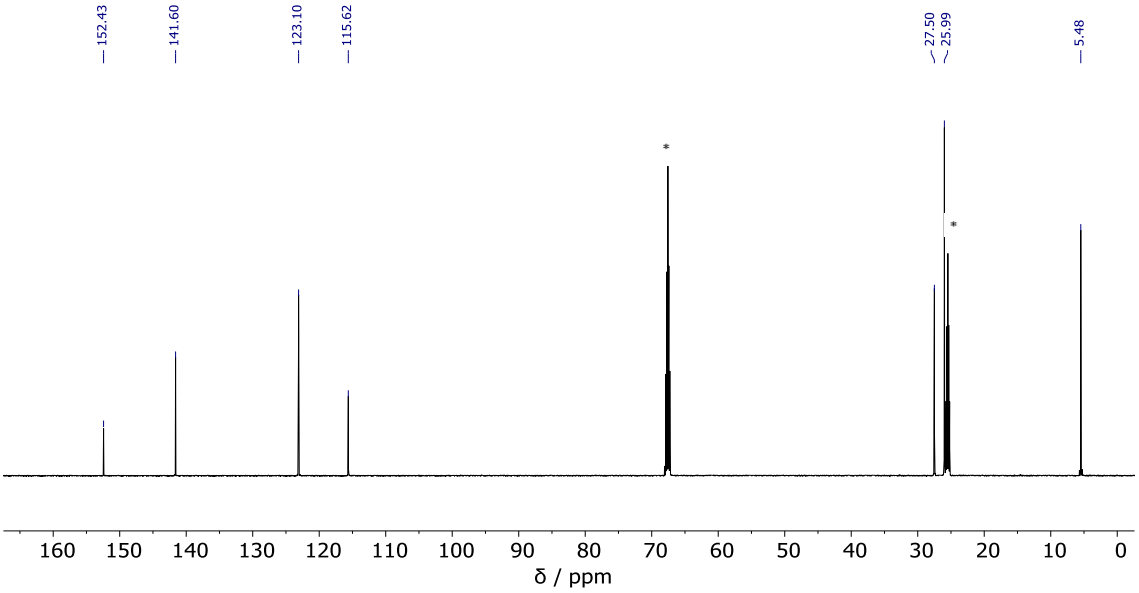


Figure A.57 ^{13}C{^{1}H} NMR spectrum (C_4D_8O, 298 K, 151 MHz) of [($^{NON\text{-}Dipp}$L)Ba(THF)$_3$] (**21·THF$_3$**), formed when [($^{NON\text{-}Dipp}$L)Ba]$_2$ (**21**) is dissolved in THF. * denotes residual protio fraction of C_4D_8O.

A.4.2 *In situ* NMR spectra

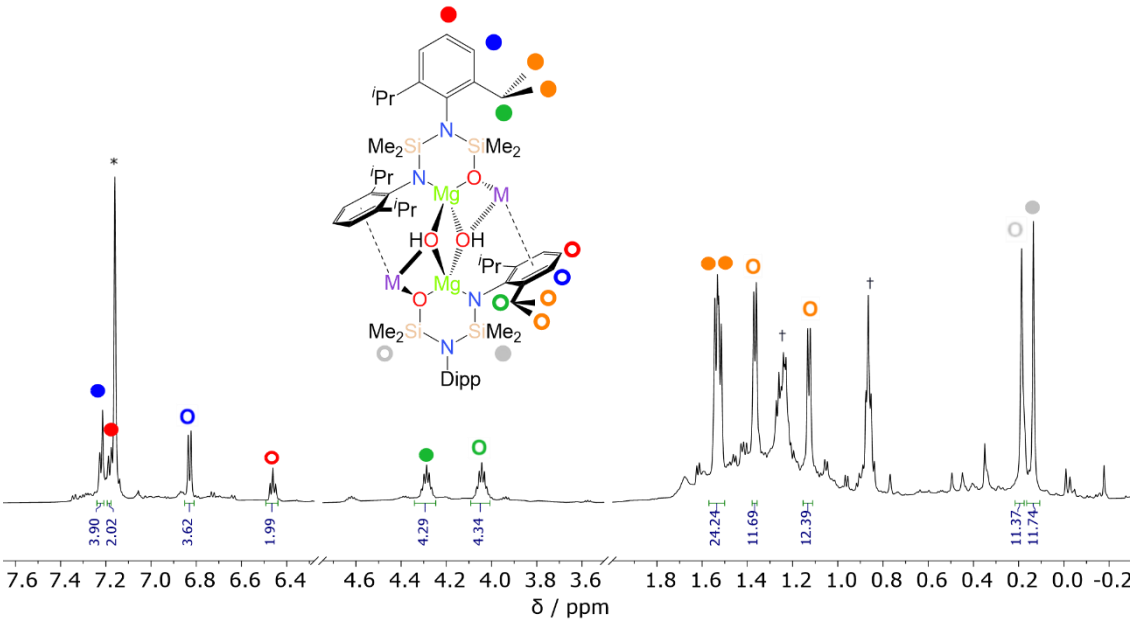


Figure A.58 ^{1}H NMR spectrum (C_6D_6, 298 K, 600 MHz) of [($^{NNO\text{-}Dipp}$L)Mg(μ-OH)K]$_2$ (**23**) generated *in-situ* by heating 1 eq. of [($^{NON\text{-}Dipp}$L)Mg]$_2$ with 6 eq. KC_8 at 80 °C for 16 h.

† denotes an unknown by-product present in solution, * denotes C_6D_6.

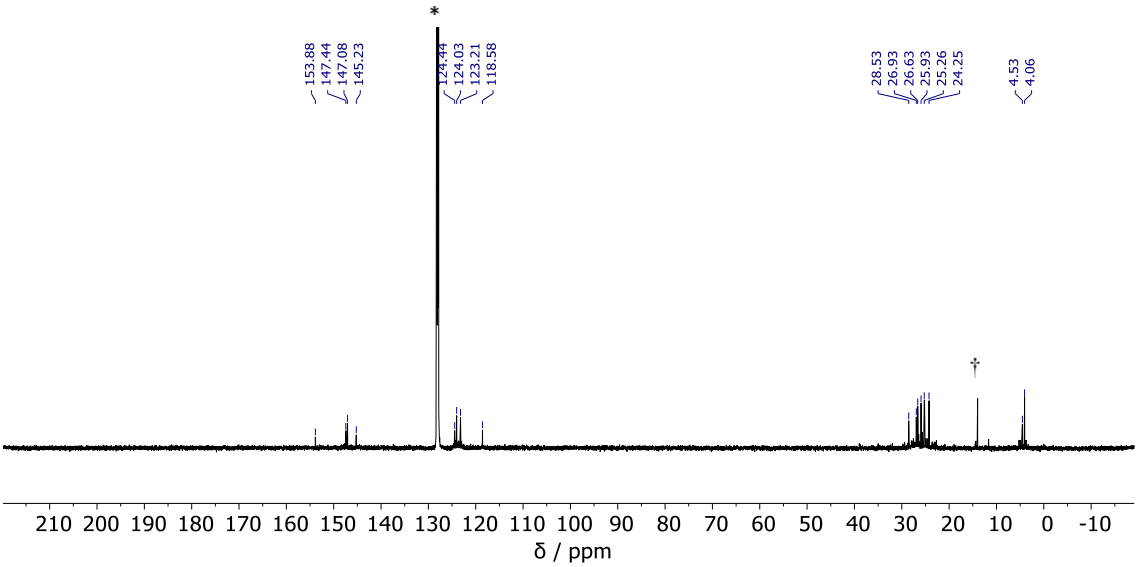


Figure A.59 ^{13}C{^{1}H} NMR spectrum (C_6D_6, 298 K, 600 MHz) of [($^{NNO\text{-}Dipp}$L)Mg(μ-OH)K]$_2$ (**23**) generated *in-situ* by heating 1 eq. of [($^{NON\text{-}Dipp}$L)Mg]$_2$ with 6 eq. KC_8 at 80 °C for 16 h.

† denotes an unknown by-product present in solution, * denotes C_6D_6.

A.4.3 X-ray crystallographic data

Table A.9 Experimental crystallographic data for [($^{NON\text{-}Dipp}$L)Mg]$_2$ (**18**), [($^{NON\text{-}Dipp}$L)Mg}$_2$(THF)] (**18·THF**) and [($^{NON\text{-}Dipp}$L)Mg(THF)]$_2$ (**18·THF$_2$**). Data for **18·THF** and **18·THF$_2$** reproduced with permission from Prof. Martyn Coles and Ms. Andrea O'Reilly.

Complex	**18**	**18·THF**	**18·THF$_2$**
		Crystal data	
File name	hasj231005a	X24-SAB008_SQUEEZED	X24-AOR9-100-THF_SQUEEZED_150K
Chemical formula	$C_{56}H_{92}Mg_2N_4O_2Si_4 \cdot C_6H_6$	$C_{66}H_{114}Mg_2N_4O_3Si_4 \cdot 0.5(C_6H_6)$	$C_{64}H_{108}Mg_2N_4O_4Si_4 \cdot 3(C_4H_8O)$
M_r	1092.42	1211.64	1374.83
Crystal system, space group	Monoclinic, *C*2/*c*	Monoclinic, $P2_1/n$	Monoclinic, $P2_1/n$
Temperature (K)	100	119.99(10)	149.99(10)
a, *b*, *c* (Å)	31.7643 (4), 10.2434 (1), 19.3380 (2)	13.29922(14), 35.7370(3), 15.62092(17)	21.3834(3), 13.93371(15), 27.2300(3)
α, *β*, *γ* (°)	90, 98.303 (1), 90	90, 103.0217(10), 90	90, 102.0079(12), 90
V (Å^3)	6226.14 (12)	7233.30(12)	7935.64(16)
Z	4	4	3
Radiation type	Cu *K*a	Cu *K*α	Cu *K*α
μ (mm^{-1})	1.42	1.27	1.252
Crystal size (mm)	0.40 × 0.24 × 0.03	0.373 × 0.212 × 0.157	0.23 × 0.119 × 0.085
		Data Collection	
Diffractometer	SuperNova, Dual, Cu at home/near, AtlasS2	SuperNova, Dual, Cu at home/near, EosS2	SuperNova, Dual, Cu at home/near, EosS2
Absorption correction	Gaussian *CrysAlis PRO* 1.171.42.72a (Rigaku Oxford Diffraction, 2022) Numerical absorption correction based on gaussian integration over a multifaceted crystal model Empirical absorption correction using spherical harmonics, implemented in SCALE3 ABSPACK	Gaussian CrysAlisPro 1.171.40.53 (Rigaku Oxford Diffraction, 2019) Numerical absorption correction based on gaussian integration over a multifaceted crystal model. Empirical absorption correction using spherical harmonics, implemented in SCALE3 ABSPACK scaling algorithm.	Gaussian CrysAlisPro 1.171.40.53 (Rigaku Oxford Diffraction, 2019). Numerical absorption correction based on gaussian integration over a multifaceted crystal model. Empirical absorption correction using spherical harmonics, implemented in SCALE3 ABSPACK scaling algorithm.

	scaling algorithm.		
T_{min}, T_{max}	0.444, 1.000	0.577, 1.000	0.666, 1.000
No. of measured, independent and observed [$I > 2\sigma(I)$] reflections	10597, 5979, 5270	52183, 14216, 13055	55164, 15587, 13191
R_{int}	0.029	0.0236	0.0307
Refinement			
$R[F^2 > 2\sigma(F^2)]$, $wR(F^2)$, S	0.033, 0.084, 1.03	0.0528, 0.1514, 1.032	0.055, 0.162, 1.06
No. of reflections	5979	14216	15587
No. of parameters	388	716	746
No. of restraints	51	-	-
$(\Delta/\sigma)_{max}$	-	-	-
$\Delta\rho_{max}$, $\Delta\rho_{min}$ (e Å^{-3})	0.29, −0.28	1.118, −0.77	0.971, −0.326
Absolute structure	-	-	-
Absolute structure parameter	-	-	-

Table A.10 Experimental crystallographic data for [($^{NON\text{-}Dipp}$L)Ca]$_2$ (**19**), [($^{NON\text{-}Dipp}$L)Sr]$_2$ (**20**) and [($^{NON\text{-}Dipp}$L)Ba]$_2$ (**21**) crystallised from benzene.

Complex	**19**	**20**	**21**
		Crystal data	
File name	071mhar23	069mhar23	051mhar23
Chemical formula	$C_{56}H_{92}Ca_2N_4O_2Si_4 \cdot C_6H_6$	$C_{56}H_{92}N_4O_2Si_4Sr_2 \cdot C_6H_6$	$C_{56}H_{92}Ba_2N_4O_2Si_4 \cdot C_6H_6$
M_r	1123.96	1219.04	1318.48
Crystal system, space group	Monoclinic, *C*2/*c*	Monoclinic, *C*2/*c*	Monoclinic, *C*2/*c*
Temperature (K)	150	150	150
a, *b*, *c* (Å)	30.8158 (2), 10.5849 (1), 19.6876 (2)	30.63227 (12), 10.88063 (5), 19.72812 (8)	29.62654 (9), 11.41698 (4), 20.02024 (7)
α, *β*, *γ* (°)	90, 94.094 (1), 90	90, 92.7130 (4), 90	90, 93.5715 (3), 90
V (Å^3)	6405.36 (10)	6567.98 (5)	6758.61 (4)
Z	4	4	4
Radiation type	Cu *K*a	Cu *K*a	Cu *K*a
μ (mm^{-1})	2.59	3.16	9.99
Crystal size (mm)	0.24 × 0.22 × 0.09	0.2 × 0.18 × 0.03	0.27 × 0.18 × 0.15
		Data Collection	
Diffractometer	SuperNova, Dual, Cu at home/near, Atlas	SuperNova, Dual, Cu at home/near, Atlas	SuperNova, Dual, Cu at home/near, Atlas
Absorption correction	Multi-scan *CrysAlis PRO* 1.171.42.72a (Rigaku Oxford Diffraction, 2022) Empirical absorption correction using spherical harmonics, implemented in SCALE3 ABSPACK scaling algorithm.	Multi-scan *CrysAlis PRO* 1.171.42.72a (Rigaku Oxford Diffraction, 2022) Empirical absorption correction using spherical harmonics, implemented in SCALE3 ABSPACK scaling algorithm.	Gaussian *CrysAlis PRO* 1.171.41.93a (Rigaku Oxford Diffraction, 2020) Numerical absorption correction based on gaussian integration over a multifaceted crystal model Empirical absorption correction using spherical harmonics, implemented in SCALE3 ABSPACK scaling algorithm.
T_{min}, T_{max}	0.641, 1.000	0.642, 1.000	0.497, 1.000
No. of measured, independent and observed [$I > 2\sigma(I)$]	86957, 6721, 6368	84520, 6865, 6399	89686, 7053, 6907

reflections			
R_{int}	0.035	0.032	0.036
Refinement			
$R[F^2 > 2\sigma(F^2)]$, $wR(F^2)$, S	0.027, 0.077, 1.05	0.021, 0.057, 1.05	0.018, 0.046, 1.03
No. of reflections	6721	6865	7053
No. of parameters	346	353	350
No. of restraints	-	-	30
$(\Delta/\sigma)_{max}$	-	-	-
$\Delta\rho_{max}$, $\Delta\rho_{min}$ (e Å^{-3})	0.26, −0.27	0.46, −0.44	0.57, −0.70
Absolute structure	-	-	-
Absolute structure parameter	-	-	-

Table A.11 Experimental crystallographic data for [($^{NON\text{-}Dipp}$L)Ca]$_2$ (**19**), [($^{NON\text{-}Dipp}$L)Sr]$_2$ (**20**) and [($^{NON\text{-}Dipp}$L)Ba]$_2$ (**21a**) crystallised from *n*-hexane.

Complex	**19**	**20**	**21a**
		Crystal data	
File name	002mdh24	005mdh24	009mdh24
Chemical formula	$C_{56}H_{92}Ca_2N_4O_2Si_4 \cdot C_6H_{14}$	$C_{56}H_{92}N_4O_2Si_4Sr_2 \cdot C_6H_{14}$	$C_{56}H_{92}Ba_2N_4O_2Si_4$
M_r	1132.02	1227.10	1240.37
Crystal system, space group	Monoclinic, *C*2/*c*	Monoclinic, *C*2/*c*	Monoclinic, *C*2/*c*
Temperature (K)	150	150	150
a, *b*, *c* (Å)	31.405 (3), 10.7081 (9), 19.7961 (13)	31.1544 (2), 10.9816 (1), 19.7810 (1)	18.5088 (2), 17.9946 (2), 19.4082 (3)
α, *β*, *γ* (°)	90, 92.787 (8), 90	90, 93.440 (1), 90	90, 109.429 (1), 90
V (Å^3)	6649.3 (10)	6755.38 (8)	6095.96 (14)
Z	4	4	4
Radiation type	Cu *K*α	Cu *K*α	Cu *K*α
μ (mm^{-1})	2.49	3.07	11.04
Crystal size (mm)	0.15 × 0.06 × 0.04	0.15 × 0.13 × 0.05	0.18 × 0.16 × 0.12
		Data Collection	
Diffractometer	SuperNova, Dual, Cu at home/near, Atlas	SuperNova, Dual, Cu at home/near, Atlas	SuperNova, Dual, Cu at home/near, Atlas
Absorption correction	Multi-scan *CrysAlis PRO* 1.171.43.95a (Rigaku Oxford Diffraction, 2023) Empirical absorption correction using spherical harmonics, implemented in SCALE3 ABSPACK scaling algorithm.	Multi-scan *CrysAlis PRO* 1.171.43.95a (Rigaku Oxford Diffraction, 2023) Empirical absorption correction using spherical harmonics, implemented in SCALE3 ABSPACK scaling algorithm.	Multi-scan *CrysAlis PRO* 1.171.43.95a (Rigaku Oxford Diffraction, 2023) Empirical absorption correction using spherical harmonics, implemented in SCALE3 ABSPACK scaling algorithm.
T_{min}, T_{max}	0.696, 1.000	0.807, 1.000	0.573, 1.000
No. of measured, independent and observed [$I > 2\sigma(I)$] reflections	40355, 6929, 4365	76112, 7046, 6211	71967, 6380, 6225
R_{int}	0.105	0.035	0.045
		Refinement	

$R[F^2 > 2\sigma(F^2)]$, $wR(F^2)$, S	0.058, 0.184, 1.02	0.029, 0.079, 1.06	0.019, 0.051, 1.06
No. of reflections	6929	7046	6380
No. of parameters	347	319	319
No. of restraints	-	-	-
$(\Delta/\sigma)_{max}$	-	-	-
$\Delta\rho_{max}$, $\Delta\rho_{min}$ (e Å^{-3})	0.35, −0.40	0.75, −0.65	0.90, −0.81
Absolute structure	-	-	-
Absolute structure parameter	-	-	-

Table A.12 Experimental crystallographic data for [($^{NON\text{-}Dipp}$L)Ca(THF)$_2$] (**19·THF$_2$**), [($^{NON\text{-}Dipp}$L)Sr(THF)$_3$] (**20·THF$_3$**) and [($^{NON\text{-}Dipp}$L)Ba(THF)$_3$] (**21·THF$_3$**). Reproduced with permission from Prof. Martyn Coles and Ms. Andrea O'Reilly.

Complex	**19·THF$_2$**	**20·THF3**	**21·THF$_3$**
		Crystal data	
File name	X23-AOR6-084a	X24-AOR6-053-THF	X24-AOR6-083-THF
Chemical formula	$C_{36}H_{62}CaN_2O_3Si_2$	$C_{40}H_{70}N_2O_4Si_2Sr$	$C_{40}H_{70}BaN_2O_4Si_2$
M_r	667.13	786.78	836.5
Crystal system, space group	Monoclinic, $P2_1/c$	Monoclinic, $P2_1$	Orthorhombic, $Pca2_1$
Temperature (K)	120.01(11)	120.00(10)	119.99(10)
a, b, c (Å)	10.30216(17), 20.9676(4), 18.5303(3)	10.86671(12), 18.7432(2),11.11722(12)	17.2911(2), 14.4444(2), 17.4395(3)
α, β, γ (°)	90, 93.4268(16), 90	90, 107.5561(12), 90	90, 90, 90
V (Å^3)	3995.62(12)	2158.86(4)	4355.70(11)
Z	4	2	4
Radiation type	Cu $K\alpha$	Cu $K\alpha$	Cu $K\alpha$
μ (mm^{-1})	2.181	2.561	7.913
Crystal size (mm)	0.297 × 0.112 × 0074	0.158 × 0.098 × 0.079	0.213 × 0.141 × 0.0.107
		Data Collection	
Diffractometer	SuperNova, Dual, Cu at home/near, EosS2	SuperNova, Dual, Cu at home/near, EosS2	SuperNova, Dual, Cu at home/near, EosS2
Absorption correction	Gaussian CrysAlisPro 1.171.40.53 (Rigaku Oxford Diffraction, 2019). Numerical absorption correction based on gaussian integration over a multifaceted crystal model. Empirical absorption correction using spherical harmonics, implemented in SCALE3 ABSPACK scaling algorithm.	Gaussian CrysAlisPro 1.171.40.53 (Rigaku Oxford Diffraction, 2019). Numerical absorption correction based on gaussian integration over a multifaceted crystal model. Empirical absorption correction using spherical harmonics, implemented in SCALE3 ABSPACK scaling algorithm.	Gaussian CrysAlisPro 1.171.40.53 (Rigaku Oxford Diffraction, 2019). Numerical absorption correction based on gaussian integration over a multifaceted crystal model. Empirical absorption correction using spherical harmonics, implemented in SCALE3 ABSPACK scaling algorithm
T_{min}, T_{max}	0.626, 1.000	0.764, 1.000	0.36, 0.74
No. of measured, independent and	27707, 7859, 6876	12925, 6637 , 6507	17670, 7245, 7043

observed [$I > 2\sigma(I)$] reflections			
R_{int}	0.0317	0.0374	0.0632
Refinement			
$R[F^2 > 2\sigma(F^2)]$, $wR(F^2)$, S	0.0369, 0.0985, 1.03	0.027, 0.067, 1.022	0.0206, 0.0505, 1.024
No. of reflections	7859	6637	7245
No. of parameters	487	455	454
No. of restraints	27	10	1
$(\Delta/\sigma)_{max}$	-	-	-
$\Delta\rho_{max}$, $\Delta\rho_{min}$ (e Å^{-3})	0.506, −0.381	0.477, −0.307	0.386, −0.417
Absolute structure	-	-	-
Absolute structure parameter	-	-	-

Table A.13 Experimental crystallographic data for [($^{NNO\text{-}Dipp}$L)Mg(μ-OH)M]$_2$ (M = Na (**22**) and K (**23**)).

Complex	**22**	**23**
	Crystal data	
File name	hasj231116a	hasj231025a
Chemical formula	$C_{56}H_{94}Mg_2N_4Na_2O_4Si_4 \cdot 2(C_6H_6)$	$C_{56}H_{94}K_2Mg_2N_4O_4Si_4$
M_r	1250.52	1126.53
Crystal system, space group	Monoclinic, $P2_1/n$	Monoclinic, $P2_1/c$
Temperature (K)	100	100
a, b, c (Å)	12.3531 (2), 16.2015 (2), 17.9195 (2)	10.7972 (5), 17.1932 (5), 17.5399 (6)
α, β, γ (°)	90, 92.869 (1), 90	90, 103.061 (4), 90
V (Å^3)	3581.89 (8)	3171.8 (2)
Z	2	2
Radiation type	Cu $K\alpha$	Cu $K\alpha$
μ (mm^{-1})	1.42	2.58
Crystal size (mm)	0.25 × 0.17 × 0.12	0.22 × 0.20 × 0.06
	Data Collection	
Diffractometer	SuperNova, Dual, Cu at home/near, AtlasS2	SuperNova, Dual, Cu at home/near, AtlasS2
Absorption correction	Multi-scan *CrysAlis PRO* 1.171.42.72a (Rigaku Oxford Diffraction, 2022) Empirical absorption correction using spherical harmonics, implemented in SCALE3 ABSPACK scaling algorithm.	Gaussian *CrysAlis PRO* 1.171.42.72a (Rigaku Oxford Diffraction, 2022) Numerical absorption correction based on gaussian integration over a multifaceted crystal model Empirical absorption correction using spherical harmonics, implemented in SCALE3 ABSPACK scaling algorithm.
T_{min}, T_{max}	0.775, 1.000	0.595, 1.000
No. of measured, independent and observed [$I > 2\sigma(I)$] reflections	13521, 6877, 6225	11926, 6090, 5111
R_{int}	0.028	0.028
	Refinement	
$R[F^2 > 2\sigma(F^2)]$, $wR(F^2)$, S	0.033, 0.090, 1.04	0.054, 0.152, 1.05

No. of reflections	6877	6090
No. of parameters	395	341
No. of restraints	0	-
$(\Delta/\sigma)_{max}$	-	-
$\Delta\rho_{max}$, $\Delta\rho_{min}$ (e Å^{-3})	0.33, −0.27	0.45, −0.45
Absolute structure	-	-
Absolute structure parameter	-	-